Investigating mTORC2/AKT-mediated regulation of FOXO1: a novel therapeutic strategy for chronic lymphocytic leukaemia?

Michael William Moles

BSc (Hons) (*Exon.*)

Submitted in fulfilment of the requirements for the Degree of Doctor of Philosophy

College of Medical, Veterinary & Life Sciences

University of Glasgow

September 2020

Abstract

The pathogenesis of chronic lymphocytic leukaemia (CLL) is inextricably linked to the tumour microenvironment, a 'sanctuary site' wherein CLL cells engage B cell receptor (BCR) signalling and form interactions with non-malignant accessory cells. 'Crosstalk' within the microenvironment elicits survival and proliferative signals that facilitate therapy resistance and outgrowth of malignant clones. Therefore, eliminating the signals that orchestrate these events is crucial to prevent disease progression. The advent of small molecule inhibitors targeting BCR signalling components have proven clinically effective. However, these treatments are not always available (or indeed suitable) for every patient and drug resistance has been reported. Thus, there is a need to identify novel treatment strategies that have the ability to improve CLL patient outcomes.

Several oncogenic pathways emanating from microenvironment communication converge upon the PI3K-AKT-mTOR axis in CLL cells. Surprisingly, little is known about the functional importance of mTOR signalling in CLL pathogenesis. mTOR exists in two protein complexes, mTORC1 and mTORC2, which coordinate growth, survival and proliferation signals downstream of PI3K-AKT signalling. Despite encouraging preclinical data with the mTORC1-selective inhibitor rapamycin, the rapalogue everolimus only had modest anti-tumour activity in a CLL clinical trial. Clinical activity of mTORC1-selective inhibitors is limited due to abrogation of a S6K-mediated negative feedback loop modulating mTORC2 activity, which results in activation of AKT-mediated pro-survival signalling. The development of 'second generation' ATP-competitive mTOR inhibitors avoid these issues by inhibiting both mTORC1 and mTORC2. As such, this investigation sought to address whether inhibition of mTORC1/2 with the dual mTOR kinase inhibitor AZD8055 would represent an effective therapeutic approach for CLL.

The data presented in this thesis demonstrates that mTOR is an effector of BCR crosslinking *in vitro*, playing a role in the coordination cellular behaviours emanating from BCR engagement (BCR-PI3K-AKT) in CLL cells. mTORC1 (4E-BP1$^{T37/46}$ and S6$^{S235/236}$) and mTORC2 (AKT^{S473}) activities were effectively targeted by the 'second generation' mTOR kinase inhibitor AZD8055 (and its clinical analogue AZD2014), which disabled pro-survival feedback loops associated with

rapamycin treatment. At the molecular level, AZD8055 inhibited mTOR signalling downstream of $F(ab')_2$-mediated BCR ligation and stromal cell (NT-L/CD40L) co-cultures, highlighting the ability of this compound to disrupt various microenvironmental stimuli. On a functional level, AZD8055 elicited potent inhibitory effects on CLL growth and proliferation, but only moderately affected cell viability *in vitro*. For these reasons, AZD8055 anti-tumour activity appeared to be limited as a monotherapy. A synergistic combination of AZD8055 and the BTK inhibitor ibrutinib promoted cell death, augmented cell size contraction and arrested proliferation, indicating that simultaneous inhibition of mTOR kinase and BTK in CLL cells evokes anti-tumour activity via targeted inhibition of multiple oncogenic pathways *and* at different levels within the same pathway.

In search of a mechanism of action, we proposed that the combination treatment conferred a more robust inhibition of AKT kinase activity. Among other methods, AKT promotes cell survival and proliferation via negative regulation of FOXO transcription factors. FOXOs are widely regarded as tumour suppressors, which regulate several cellular behaviours including cell cycle arrest and apoptosis. Our data demonstrated that BCR crosslinking negatively regulated FOXO1 (the most abundant FOXO in CLL cells) by AKT-dependent $FOXO1^{T24}$ phosphorylation, subsequent nuclear export and reduced DNA-binding activity. Like normal B cells, these data suggested that FOXO1 inactivation was an important consequence of BCR engagement in CLL cells. For this reason, we hypothesised that inhibiting BCR signalling would unleash FOXO1 tumour suppressor activity. We showed that elimination of BCR signal transduction, via AZD8055 or ibrutinib mono- and combination therapy, re-engaged FOXO1 DNA-binding activity by preventing FOXO1 nuclear export, which suggested that FOXO1 was an effector of BCR signalling inhibition that mediated treatment response. Through pharmacological FOXO1 inhibition, we demonstrated that FOXO1 activity contributed to the cytotoxic, cell-contracting and cytostatic effects of the combination treatment, indicating that FOXO1 functions as a tumour suppressor in this context.

In conclusion, these studies highlight the potential for AZD8055/2014 as a drug partner for novel combination strategies in the treatment of CLL. Indeed, these data suggest that AZD8055/2014 could be combined with agents targeting

proximal BCR signalling components (BTK, PI3K or SYK) or perhaps pro-survival signals (BCL2). Furthermore, reactivation of FOXO1 activity or other inactivated ‘genetically intact’ tumour suppressors (via targeted inhibition of negative regulators) represents an interesting treatment strategy for CLL. Collectively, these data provide valuable information that has the potential to inform subsequent pre-clinical investigations and future CLL clinical trials.

Table of Contents

List of Tables

List of Figures

Acknowledgement

First and foremost, I would like to express my heartfelt gratitude to my primary supervisor Dr. Alison Michie. You have always supported me, encouraged me and been there when it's all gone horribly wrong. Our regular chats (usually over a pint or two) have meant a great deal. I could not have asked for a better mentor to guide me through this PhD. Thank you.

I would also like to thank my second supervisor Dr. Heather Jørgensen. Your support, guidance and teaching have equipped me with skills needed to complete this PhD and beyond.

Here's to the Michie's: Jodie (Jobbie/Judy), Jen, Hassan, Natasha, Ailsa, Emilio, Alison M^{C}Caig and the countless undergrads/masters' students. You've got me through this PhD. Thank you for everything. I'm lucky to call you my pals. I will be back soon, for sure. Gie it laldy!

A special thank you to Hugh "Shuggie" Forgie, for whom this PhD studentship was named. Hugh, together with his wife Mags, raised a tremendous amount of money for POG-LRC, by cycling from Glasgow to Malaga, which provided the funding for this PhD studentship specialising in CLL research. Sadly, Hugh did not quite make it through to see the finished product, dying peacefully of CLL at the Beatson on Saturday 5th September 2020. He will be missed by all who knew him. Thank you to Hugh, and all the patients who willingly donated samples that contributed to the completion of this PhD.

To everyone at the POG-LRC, past and present: your guidance, help, kindness and friendship made this PhD all the more worthwhile. I wish you all the best for the future. Thank you. Keep at it.

Thank you to all my friends and family. A lot has been sacrificed in pursuit of this PhD: cancelled nights out, missed weekends away and unattended family occasions. You're understanding, unconditional love and endless support have not gone unnoticed. I will make it up to all of you.

Finally, I would like to thank my wonderful wife Nora. Thank you for leaving your life in Hamburg to join me in Glasgow. Thank you for putting up with the early mornings, late evenings and lost weekends. Thank you for supporting me through it all. Without you, this would not have been possible.

Author's Declaration

I declare that this thesis is the result of my own work (except where explicit reference is made to the contribution of others) and has not been submitted to any other institution.

Michael William Moles

September 2020

Definitions/Abbreviations

1L	First-line
3AC	3-a-Aminocholestane
4E-BP1	Eukaryotic translation initiation factor 4E-binding protein 1
7-AAD	7-Aminoactinomycin D
ABC-DLBCL	Activated B-cell-like subtype Diffuse large B-cell lymphoma
AID	Activation-induced cytidine deaminase
AKT	Protein kinase B
AML	Acute myeloid leukaemia
AMPK	AMP-activated protein kinase
APRIL	A proliferation-inducing ligand
ATCC	American Type Culture Collection
ATL	Adult T-cell leukaemia
ATM	Ataxia-telangiectasia mutated
B2M	$ß_2$-microglobulin
BAFF	B cell activating factor
BAK	BCL2-antagonist/killer
BAX	Bcl-2-associated X protein
BBC3 (PUMA)	Bcl-2-binding component 3
BCA	Bicinchoninic acid
BCL2	B-cell lymphoma 2
BCL2-L1 (BCL-xL)	B-cell lymphoma-extra large
BCL2-L11 (BIM)	Bcl-2-like protein 11
BCP-ALL	B-cell precursor acute lymphoblastic leukaemia
BCR	B cell receptor
BH3	BCL2 homology 3
BIM el	Bcl-2-like protein 11 isotype extra large
BIM l	Bcl-2-like protein 11 isotype large
BIM s	Bcl-2-like protein 11 isotype small
BL	Burkitt’s lymphoma
BM	Bone marrow
BSA	Bovine serum albumin
BTK	Bruton's tyrosine kinase
CCL19	C-C Motif Chemokine Ligand 19
CCND2	Cyclin D2
CCNG2	Cyclin G2
CD40L	CD40 ligand
CDK2	Cyclin-dependent kinase 2
CDKI	Cyclin-dependent kinase inhibitor
CDKN1A (p21 CIP1)	CDK-interacting protein 1
CDKN1B (p27 KIP1)	Cyclin-dependent kinase inhibitor 1B

cDNA	complementary DNA
ChIP-seq	Chromatin immunoprecipitation-sequencing
cHL	Classical Hodgkin lymphoma
CI	Combination index
CK	Complex karyotype
CK1	Casein kinase 1
CK2	Casein kinase 2
CLL	Chronic lymphocytic leukaemia
CLL-IPI	CLL International Prognostic Index
CML	Chronic myeloid leukaemia
CO2	Carbon dioxide
COMBO	Combination
CR	Complete response
CRM1	Chromosomal region maintenance 1
CSR	Class switch recombination
CTLA-4	Cytotoxic T-lymphocyte-associated protein 4
CTV	CellTrace Violet
CXCL12	C-X-C motif chemokine 12
DAB	3,3'-Diaminobenzidine
DAG	Diacylglycerol
DAPI	4',6-diamidino-2-phenylindole
DBD	DNA-binding domain
DISC	Death-inducing signalling complex
DLBCL	Diffuse large B-cell lymphoma
DMEM	Dulbecco's Modified Eagle Medium
DMSO	Dimethyl sulfoxide
DNA	Deoxyribonucleic acid
DNA-PK	DNA-dependent protein kinase
DSMZ	Deutsche Sammlung von Mikroorganismen und Zellkulturen
DZ	Dark zone
EBV	Epstein-Barr virus
EC_{50}	Half maximal effective concentration
EDTA	Ethylenediaminetetraacetic acid
ERIC	European Research Initiative on CLL
ERK	Extracellular signal-regulated kinase
ESCCA	European Society for Clinical Cell Analysis
Eμ-TCL1	Eμ-T-cell leukemia/lymphoma protein 1
F(ab')	Fragment antibody binding
FBS	Fetal bovine serum
Fc	Fragment crystallisable
FCR	Fludarabine-cyclophosphamide-rituximab
FDA	US Food and Drug Administration
FHRE	Forkhead response element
FL	Follicular lymphoma
FOX	Forkhead Box

FOXO	Forkhead Box Class O
FOXO1	Forkhead Box Class O1
FOXO1-A3	Constitutively active FOXO1-AAA mutant
FOXO1-DN	Dominant-negative FOXO1
FOXO3	Forkhead Box Class O3
FOXO4	Forkhead Box Class O4
FOXO6	Forkhead Box Class O6
FR	Framework region
G0	Resting phase/quiescence
G1	Gap 1 phase
G2	Gap 2 phase
GADD45A	Growth Arrest And DNA Damage Inducible Alpha
GAP	GTPase activating protein
GC	Germinal centre
GCB-DLBCL	Germinal centre B-cell subtype Diffuse large B-cell lymphoma
GCLLSG	German CLL study group
GEP	Gene expression profiling
GF	Growth factor
GSEA	Gene set enrichment analysis
GSK3α/β	Glycogen synthase kinase 3 alpha/beta
H	Heavy
HCDR3	Heavy complementarity determining region 3
HEK293T	Human embryonic kidney 293 cells (SV40 T-antigen)
hESCs	Human embryonic stem cells
HRS	Hodgkin and Reed/Sternberg
IF	Immunofluorescence
Ig	Immunoglobulin
IgD	Immunoglobulin D
IGF1R	Insulin-like growth factor 1 receptor
IgM	Immunoglobulin M
IGVH	Immunoglobulin heavy-chain variable region
IGVL	Immunoglobulin light-chain variable region
IHC	Immunohistochemistry
IL-21	Interleukin-21
IL-4	Interleukin-4
IP3	Inositol-1,2,5-triphosphate
ITAMs	Immunoreceptor tyrosine-based activation motifs
ITIMs	Immunoreceptor tyrosine-based inhibition motifs
iwCLL	International Workshop on CLL
JNK	c-Jun N-terminal kinase
L	Light
LB	Luria Broth
LMP	Latent Membrane Protein
LN	Lymph node
LYN	Tyrosine-protein kinase Lyn

LZ	Light zone
M	Mitosis/mitotic phase
M	Molar
M-CLL	IGVH-mutated CLL
mAbs	Monoclonal antibodies
MAPK	Mitogen-activated protein kinase
MCL-1	Induced myeloid leukemia cell differentiation protein
MDM2	Mouse double minute 2 homolog
MEK	Mitogen-activated protein kinase kinase
miRNA	MicroRNA
mM	Millimolar
MOMP	Mitochondrial outer membrane permeabilization
mRNA	Messenger RNA
MSC	Mesenchymal stem cell
mTOR	Mechanistic target of rapamycin
mTORC1	Mechanistic target of rapamycin complex 1
mTORC2	Mechanistic target of rapamycin complex 2
NES	Nuclear export sequences
NF-AT	Nuclear factor of activated T cells
NF-κB	Nuclear factor kappa-light-chain-enhancer of activated B cells
NHL	Non-Hodgkin lymphoma
NLCs	Nurse-like cells
NLS	Nuclear localisation sequences
nM	Nanomolar
NOTCH1	Neurogenic locus notch homolog protein 1
NT-L	Mouse fibroblast L cells
OR	Overall response
OS	Overall survival
PB	Peripheral blood
PBMCs	Peripheral blood mononuclear cells
PBS	Phosphate-buffered saline
PD-1	Programmed cell death protein 1
PDCD4	Programmed cell death protein 4
PDK1	Phosphoinositide-dependent kinase-1
PFA	Paraformaldehyde
PFS	Progression-free survival
PH	Pleckstrin homology
PI	Propidium iodide
PI3K	Phosphoinositide 3-kinase
PI3Kδ	PI3K isoform p110δ
PIKK	PI3K-related protein kinases
PIP2	Phosphatidylinositol(4,5)P_2
PIP_3	Phosphatidylinositol(3,4,5)P_3
PKA	Protein Kinase A
PKC	Protein Kinase C

PLCγ2	Phospholipase C gamma 2
pre-B	Precursor B cells
pro-B	Progenitor B cells
PS	Phosphatidylserine
PTEN	Phosphatase and tensin homolog
PTLD	Posttransplant lymphoproliferative disorder
PVDF	Polyvinylidene Fluoride
R-CHOP	Rituximab, cyclophosphamide, doxorubicin, vincristine and prednisone
R/R	Relapsed/Refractory
R&D	Research and development
RAPTOR	Regulatory protein associated with mTOR
RICTOR	Rapamycin insensitive companion of mTOR
RNA	Ribonucleic acid
RNA-seq	RNA sequencing
RPMI	Roswell Park Memorial Institute
RT	Room temperature
RT-qPCR	Real time quantitative reverse transcription PCR
RTK	Receptor tyrosine kinase
S	Synethesis phase
S6	Ribosomal protein S6
S6K1	p70-S6 Kinase 1
Scr	Scrambled
SDF-1α	Stromal cell-derived factor 1-alpha
SESN3	Sestrin 3
SH2	Src-homology 2
SHIP1	SH2-domain-containing inositol 5'-phosphatase 1
SHM	Somatic hypermutation
SHP-1	SH2 domain-containing tyrosine phosphatase-1
shRNA	Short hairpin RNA
sIgM	Surface IgM
SIN1	MAPK Associated Protein 1
SINE	Selective inhibitors of nuclear export
SKP2	S-phase kinase-associated protein 2
SLOs	Secondary lymphoid organs
SNBTS	Scottish National Blood Transfusion Service
SYK	Spleen associated tyrosine kinase
TB	Terrific Broth
TME	Tumour microenvironment
TNF	Tumour necrosis factor
TP53 (p53)	Cellular tumour antigen p53
TSC1/2	Tuberous sclerosis 1/2
U-CLL	IGVH-unmutated CLL
UK	United Kingdom
USP7	Ubiquitin-specific-processing protease 7
V(D)J	Variable(Diversity)Joining

WES	Whole-exome sequencing
WGS	whole-genome sequencing
WT	Wild type
XPO1	Exportin 1
ZAP-70	ζ chain associated protein kinase 70
µM	Micromolar

1 Introduction

1.1 Chronic lymphocytic leukaemia (CLL)

A compartmentalised malignancy of mature B lymphocytes, CLL is characterised by the relentless expansion and progressive infiltration of $CD19^+$ $CD23^+$ $CD5^+$ B cells in the blood, bone marrow (BM) and secondary lymphoid organs (SLOs) (1, 2). CLL is a heterogenous disease with contrasting (and somewhat polarising) prognoses (2, 3). Clinical behaviour (and disease progression) largely mirrors the underlying complexity in disease biology (3), which informs prognosis and therapeutic strategies. For example, immunoglobulin heavy-chain variable region (*IGVH*) gene mutational status (4, 5), genetic aberrations (6) and the ectopic/aberrant expression of signalling molecules (7, 8) are implicated in CLL pathogenesis and represent essential markers for prognostic stratification. Disease progression is inextricably linked to the tumour microenvironment (TME), a 'sanctuary site' wherein CLL cells engage B cell receptor (BCR) signalling and form interactions with non-malignant accessory cells, which promotes cell survival and proliferation (9). The emergence of BCR signalling inhibitors (10) and BH3 mimetics (11) have demonstrated excellent clinical activity and transformed the treatment landscape for CLL patients. However, these treatments are not always available (or indeed suitable) for every patient (12) and drug resistance has been reported (13, 14). These observations have focussed the spotlight on the identification of novel treatment strategies that have the ability to improve progression-free (PFS) and overall survival (OS) rates for CLL patients with unmet clinical needs.

1.1.1 CLL epidemiology

With an 'age-standardised' incidence of 5.7/100,000 persons each year in the United Kingdom (UK) (15), CLL is frequently described as the most common adult leukaemia in the 'Western' world (2). In reference to the UK's epidemiological data, there are ~3,800 newly diagnosed cases annually, which accounts for ~1 % of all new cancer diagnoses. CLL is predominantly a disease of the elderly, with the highest incidence in people aged between 85-89 (41 % of newly diagnosed cases are in people over the age of 75) (15). However, younger patients (≤55 years; median 50 years) diagnosed with CLL were reported to have a shorter

time to treatment compared to their 'elderly' (>55 years; median 67 years) counterparts, perhaps underscored by a disproportionate expression of poor prognostic disease biomarkers (16). Incidence rates are higher in males (7.9/100,000) than females (3.9/100,000), with 63 % of all newly diagnosed UK cases recorded in male patients (data correct as of 2017) (15). Interestingly, analysis of clinical data revealed that female CLL patients had reduced incidence of poor prognostic features, improved treatment responses and better survival rates (17). However, the reason(s) for this is not understood. The age-adjusted mortality rate stands at 1/100,000 persons each year in the UK, accounting for less than 1 % (947 deaths recorded) of all cancer deaths in 2017 (15). CLL patients with at least one family member (blood relative) with CLL, so-called 'familial CLL', is observed in ~5-10 % of all CLL patients (18), indicating the presence of heritable and/or common genetic risk factors (2). Indeed, blood relatives of patients with CLL are 8.5-times more susceptible of developing the disease (and elevated risk of developing other lymphoma subtypes) (2, 19). CLL is less common (5 to 10-times) in people of Asian descent compared to those with mainly European backgrounds (20), further demonstrating the presence of a genetic predisposition and/or aetiology for this malignancy. Of note, incidence rates in Asian people are unaffected by emigration to 'higher-risk' countries, indicating geographical factors are less important in this context (20). Finally, environmental factors have been associated with elevated risk of CLL including exposure to 'agent orange' (21), insecticides (22) and certain hair dyes (23).

1.1.2 CLL diagnosis, staging and prognostic stratification

This section refers to the International Workshop on CLL (iwCLL) guidelines (12, 24), which outlines 'agreed' recommendations for clinical diagnosis, staging and prognostic stratification.

1.1.2.1 Diagnosis

CLL is diagnosed via blood tests (including morphology) and immunophenotyping. An assessment of molecular genetics (cytogenetics and/or *TP53* mutation) or *IGVH* mutational status may assist prognosis, but is less commonly adopted for diagnostic purposes (24). A diagnosis requires the detection of ≥5 $x10^9$/L B cells in the peripheral blood (PB) for a continuous period of ≥3 months (12, 24).

Morphologically (as assessed by blood smears), CLL cells are typically small in size with a large 'dense' nucleus and only a thin rim of cytoplasm (2). The presence of 'smudge cells' on blood smears is another feature associated with CLL (12, 24). A joint project by the European Research Initiative on CLL (ERIC) and European Society for Clinical Cell Analysis (ESCCA) recently established a consensus list of "required" and "recommended" disease markers for the diagnosis of CLL (adopted by the iwCLL guidelines). The immunophenotype $CD19^+$, $CD5^+$, $CD20^+$, $CD23^+$, κ and λ immunoglobulin (Ig) light (L) chains was "required" for CLL diagnosis, while a number of other markers ($CD79b^+$, $CD81^+$ and $ROR1^+$, for example) were "recommended" for borderline cases (12, 25).

1.1.2.2 Staging

The Rai (26) and Binet (27) staging systems are widely adopted methods for stratifying CLL patients according to disease 'risk' following physical examination (2). The Rai staging system is largely based on lymphocytosis, which originally classified CLL patients into 5 stages (0 to IV) representing increased disease risk (26). This was later reduced to 3 'risk categories' that combined the 5 stages (28). In contrast, the Binet staging system is predominantly based on the number of affected lymphoid tissue groups (and the presence of anaemia or thrombocytopenia), which separates CLL patients into 3 stages (A, B and C) (27). CLL patients with Binet stage A disease are typically less likely to require therapy, whereas those with stage B or C (poorest prognosis) are associated with negative outcomes with reduced PFS and OS (Table 1.1) (Holroyd and M^{C}Caig; personal communication). The Rai system is mainly applied in the United States, while the Binet system is more widely used in Europe (2, 29).

Stage	Clinical features	Median life expectancy*
A	No anaemia/thrombocytopenia <3 lymphoid regions enlarged	13 years
B	No anaemia/thrombocytopenia ≥3 lymphoid regions enlarged	8 years
C	Anaemia (<10 g/dL) Thrombocytopenia (<100 x10^9/L)	2 years

Table 1.1 – The Binet clinical staging system (27) *(2)

1.1.2.3 Prognostic stratification

As a product of their time, the Rai and Binet staging systems do not account for the multitude of subsequently identified disease biomarkers that offer invaluable prognostic information (irrespective of clinical stage) (12). As such, various 'prognostic scores' have been devised (30-32). The CLL International Prognostic Index (CLL-IPI) combines clinical staging with essential prognostic variables (genetic and biological) to identify CLL patients in need of therapy (33). It uses a weighted system that 'grades' prognostic factors, including del(17p)/*TP53* mutation, *IGHV* mutational status, serum $ß_2$-microglobulin (B2M), clinical stage and patient age (12), to generate a 'risk score' (Table 1.2). Risk scores ultimately translate into 4 'risk categories/prognostic subgroups' that inform treatment decisions (33).

Variable	Adverse factor	Grading
del(17p)/*TP53*	Deleted/mutated	4
IGHV mutational status	Unmutated	2
B2M (mg/L)	>3.5	2
Clinical stage	Binet B/C or Rai I-IV	1
Age	>65 years	1
	Risk score	**0-10**

Table 1.2 - The CLL-IPI (33, 233)

The CLL-IPI has been validated in recent studies (34-36). Recently, Delgado *et al*. devised (and validated) an alternative prognostic model comprising only 2 prognostic biomarkers (*IGVH* mutational status and cytogenetics), simplifying the CLL-IPI (37).

1.1.3 CLL prognostic factors

Over the last 30 years, our understanding of CLL pathophysiology has fundamentally changed with the identification of several prognostic biomarkers associated with disease progression. These factors have transformed risk stratification and underpinned management strategies for CLL patients (expertly reviewed in (38)).

1.1.3.1 *IGVH* mutational status and 'stereotyped' B cell receptors (BCRs)

In normal B cell maturation, somatic hypermutation (SHM) of *IGVH* and Ig light-chain variable region (*IGVL*) genes is essential for the generation of affinity-enhanced antibodies in support of the adaptive immune response (39). In an early study, Fais *et al.* reported that approximately 51.6 % of CLL patients (cohort of 64 IgM$^+$ patients) had undergone SHM of their *IGVH* genes (mutated; M-CLL), whereas the others encoded *IGVH* genes corresponding to the most similar germline sequence (unmutated; U-CLL) (40). Two groups subsequently showed that these entities were implicated in disease progression and clinical outcome, with U-CLL patients (≥98 % sequence homology with germline) experiencing a more aggressive disease and poorer prognosis (irrespective of Binet stage) than their M-CLL counterparts (<98 % sequence homology with germline) (4, 5). These data were independently confirmed in a separate patient cohort (41) and recently validated (42). The presence or absence SHM in *IGVH* genes largely reflects the stage of maturation of the parent B cell (2), with U-CLL deriving from a pre-germinal centre (GC) CD5$^+$ B cell (absent SHM) and M-CLL originating from a CD5$^+$ B cell that has progressed through the GC reaction (Figure 1.1) (38, 43).

Analysis of *IGVH* gene sequences from 7,424 CLL patients revealed that nearly one-third of patients (30.4 %) displayed 'quasi-identical' or 'stereotyped' BCRs (44), i.e. the biased and, in some instances, identical usage of heavy complementarity determining region 3 (HCDR3) sequences (45). This study was preceded by several reports identifying BCR similarities among CLL patients (46-50), which collectively supported the theory of a common antigenic determinant in CLL development (51). The identification of 19 "major" stereotyped subsets highlighted the clinical significance of BCR stereotypy in CLL disease course (44). Subsets #1 and #8, for example, typically confer poor prognosis and are associated with the expression of U-CLL. In contrast, subset #4 patients express M-CLL and experience a relatively indolent disease. Intriguingly, subset #2 have an aggressive disease course irrespective of *IGVH* mutational status, expressing both U-CLL (40 %) and M-CLL (60 %) (44, 50, 52). The significance of BCR stereotypy in CLL pathogenesis and clinical behaviour has been comprehensively reviewed (45, 51).

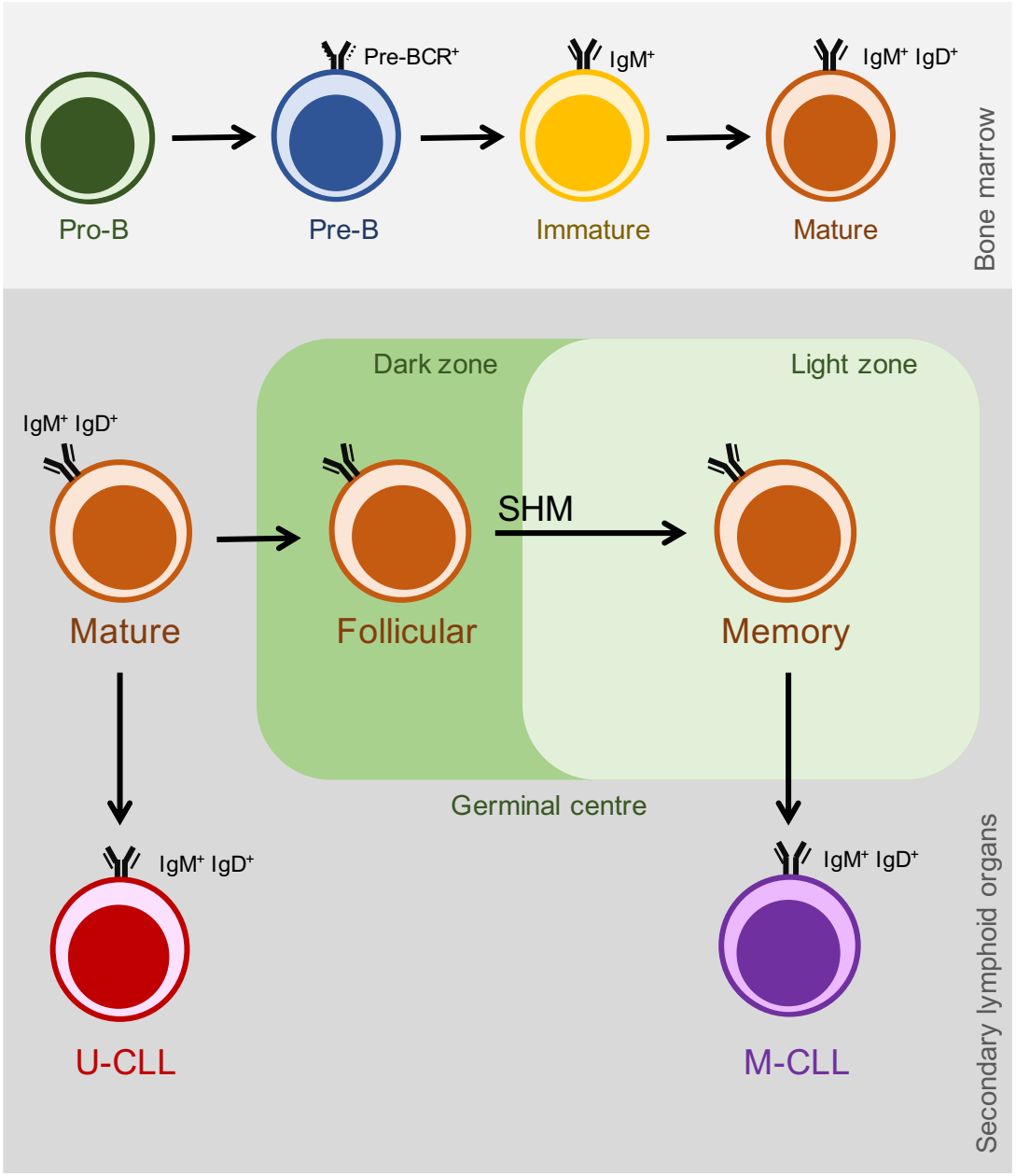

Figure 1.1 - BCR maturation and cellular origins of CLL cells (modified from (45))

1.1.3.2 Cytogenetic alterations and 'complex karyotype'

In their seminal study, Döhner *et al.* identified a spectrum of cytogenetic aberrations and assessed their clinical implications in a cohort of 325 CLL patients. These data showed that 82 % of CLL patients harboured cytogenetic alterations (52 % possessed at least one alteration) at the time of enrolment (median 15 months from diagnosis), with the majority possessing at least one of the following aberrations: 13q14 (del(13q)), 11q22-q23 (del(11q)) and 17p13 (del(17p)) or +12q13 (trisomy 12) (2, 6, 38). Del(13q) was the most frequent

cytogenetic aberration (55 % of patients), which conferred an indolent disease course (median survival time of 133 months) (2, 6). The deleted region in del(13q) encompasses the loci encoding the microRNAs (miRNAs) *mir15A* and *mir16A* (53), which negatively regulate the anti-apoptotic protein B cell lymphoma 2 (BCL2) (54). BCL2 overexpression as a consequence of *mir15A*/*mir16A* deletion favours survival in CLL cells (54-56), as evidenced by clinical activity of BH3 mimetic venetoclax in CLL clinical studies (38, 57, 58). Del(11q) is the next commonest cytogenetic aberration (~18 % of patients), which is associated with a more aggressive disease course (median survival time of 79 months) (6). Within this deleted region contains the locus encoding the cell cycle checkpoint kinase (DNA damage response) ataxia telangiectasia mutated (ATM) (59). Del(17p) occurs in ~7 % of patients and confers the poorest prognosis with rapid disease progression (median survival time of 32 months) (6). The deleted region encodes the tumour suppressor p53 (*TP53*) (60), which exhibits poor response to chemo- and chemoimmunotherapy (61, 62). Finally, trisomy 12 appears in ~16 % of patients and confers a more favourable prognosis (median survival time of 114 months), akin to 'normal karyotype' (median survival time of 111 months) (6). In recent years, the hierarchical classification system formulated by Döhner *et al.* (6) was reassessed in a cohort of 1,585 CLL patients (63). These results are summarised in Table 1.3.

	(6)		(63)	
Aberration	**Number of patients (%)**	**Median survival (months)**	**Number of patients (%)**	**Median survival (years)**
Del(13q)	178 (55)	133	624 (39)	not reached
Del(11q)	58 (18)	79	187 (12)	7
Trisomy 12	53 (16)	114	205 (13)	11
Del(17p)	23 (7)	32	193 (12)	5

Table 1.3 - Incidence of cytogenetic aberrations (including median survival): a comparison of the (6) and (63) studies

Over the last 10 years, studies have implicated 'complex karyotype' (CK), defined as the presence of ≥3 chromosome alterations (64), as an independent prognostic marker associated with poor prognosis and inferior survival (65). Studies by Rigolin *et al.* and Baliakas *et al.* independently demonstrated that CK

was present in ~15% of patients and significantly associated with U-CLL, del(17p)/*TP53* mutations and advanced clinical stage (66, 67). In line with these findings, CK was associated with worse response and/or disease progression (refractoriness) in patients treated with chemoimmunotherapy (68, 69) or targeted therapies (70, 71). More recently, the 5-year follow-up of single-agent ibrutinib-treated relapsed/refractory (R/R) CLL patients (phase 1b/2 study; #NCT01105247) showed that patients with CK had shorter PFS and OS compared with those without (72). Finally, Baliakas *et al*. recently postulated that CK is a heterogenous group with contrasting clinical behaviour. For example CK with ≥5 chromosomal aberrations had poor prognosis irrespective of other prognostic factors, whereas patients with CK and trisomy 12 conferred a relatively indolent disease course (73).

1.1.3.3 Recurrent somatic mutations and 'clonal evolution'

Whole-exome sequencing (WES) and whole-genome sequencing (WGS) studies have transformed our understanding of the genomic landscape of CLL (74, 75). Building upon previous studies (76, 77), Landau *et al*. evaluated the genomic complexity and/or heterogeneity in 538 CLL patients from different "non-overlapping" cohorts (76, 78). WES of this cohort identified >40 mutated CLL 'driver' genes, which were implicated in a small group of signalling pathways: Notch signalling (*NOTCH1*, *FBXW7*), inflammatory pathways (*MYD88*, *SAMHD1*, *RIPK1*), BCR signalling (*ITPKB*), MAPK/ERK pathway (*KRAS*, *NRAS*, *BRAF*, *MAP2K1*), MYC-related (*FBXW7*), DNA damage/cell cycle regulation (*ATM*, *TP53*, *POT1*, *CHEK2*), chromatin modelling (*ZMYM3*, *CHD2*) and RNA processing (*XPO1*, *SF3B1*). From a clinical point of view, *TP53* and *SF3B1* inactivating mutations were found to confer reduced PFS and OS in 278 pre-treatment CLL patients derived from the CLL8 cohort (74). Furthermore, patients with *TP53* mutations had reduced PFS and OS in response to chemotherapy (79, 80) and chemoimmunotherapy (81), based on the results of the CLL4 and CLL8 studies, respectively. Fortunately, BCR signalling inhibitors (ibrutinib, idelalisib) or BH3-mimetics (venetoclax) have improved PFS and OS for CLL patients with *TP53* aberrations (82-84), highlighting the efficacy of these treatment strategies.

'Clonal evolution', i.e. the adaptive ability of cancers to 'selection pressures' (e.g. treatment) via intra-tumoral genetic heterogeneity, is underscored by the

presence and/or complexity of sub-clonal ‘driver’ mutations (85). Studies have shown that intra-tumoral driver mutations (e.g. *TP53*, del(17p), *IKZF3*) are associated with progressive disease, treatment refractoriness and resistance (74, 86), driven by the ‘intrinsic’ or ‘extrinsic’ expansion of sub-clones (85). Indeed, the evolution of subpopulations has posed numerous challenges for CLL therapeutic strategies (74, 76), particularly targeted therapies (87-89). Landau *et al*. assessed clonal evolution in 59 R/R patients from the CLL8 cohort. In almost all cases (~96 %), WES analysis uncovered treatment-induced ‘clonal shifts’ among patients before (pre-treatment) and after relapse. Interestingly, the relapsed clone was detectable in ~30 % of the pre-treatment samples, some of which already possessed a driver mutation (e.g. *TP53*) (74). More recently, reports have highlighted the ability of ibrutinib to confer a selective pressure that facilitates sub-clonal evolution (87-89). Burger *et al*. demonstrated that ibrutinib-resistant clones were present prior to ibrutinib initiation (87), while Landau *et al*. identified early clonal shifts (within first 12 months ibrutinib therapy; prior to relapse) that were associated with aggressive disease (88). In line with these findings, Ahn *et al*. identified ibrutinib-resistance mutations (*BTK* (C481S) or *PLCG2* (R665W)) in single-agent ibrutinib-treated CLL patients up-to 15 months before disease progression (89). These studies highlighted the highly dynamic nature of CLL, which manifests as a collection of genetically divergent diseases (subclones) within an individual patient that undergo ‘clonal competition’ influenced by selection pressures (90).

1.1.3.4 Other prognostic parameters

Damle *et al*. demonstrated that CD38 expression levels were elevated among U-CLL patients and was associated with unfavourable treatment and/or disease outcome (4). A succession of studies subsequently confirmed CD38 as an important CLL prognostic marker with adverse disease progression, reduced treatment responsiveness and shorter OS (91-94). On a functional level, CD38 is a transmembrane glycoprotein that promotes CLL cell proliferation and survival via ligation to the adhesion molecule CD31. CD31 is expressed by non-malignant accessory cells of the CLL-TME (95).

High expression of ζ chain associated protein kinase 70 (ZAP-70) is considered a surrogate marker for U-CLL, which is associated with faster disease progression

and dismal survival (7, 8). Functionally, ectopic expression of ZAP-70 potentiates BCR signalling in CLL cells (96), analogous to its role in downstream of the T cell receptor (TCR) in T cells (97).

1.1.4 Treatment of CLL

The management of CLL has undergone significant changes in recent years with the advent of novel targeted therapies against signalling kinases and anti-apoptotic proteins (98). This section outlines CLL management strategies and recent results from clinical trials. The treatment of CLL was recently reviewed in (12) and (98).

1.1.4.1 CLL treatment algorithm

With reference to 'first line' (1L) treatment options, several parameters are considered: clinical stage, patient symptoms, patient 'fitness' and genetic risk (*TP53* mutational status). CLL patients with advanced (Binet stage C) or active disease will require some form of therapy (12). The 1L CLL treatment algorithm is presented in Table 1.4.

Stage	del(17p) or *TP53* mut	Fitness	*IGVH* mut (M/U)	Therapy
Binet A-B, Rai 0-II, inactive disease	Irrelevant	Irrelevant	Irrelevant	None
Active disease or Binet C or Rai III-IV	Yes	Irrelevant	Irrelevant	Ibrutinib/Acalabrutinib or Venetoclax + Obinutuzumab or Idelalisib + Rituximab
	No	Go go	M	FCR (BR >65 years) or ibrutinib or Venetoclax + Obinutuzumab
			U	Ibrutinib or FCR (BR >65 years) or Venetoclax + Obinutuzumab
		Slow go	M	Venetoclax + Obinutuzumab or Chlorambucil + Obinutuzumab or Ibrutinib/Acalabrutinib
			U	Venetoclax + Obinutuzumab or Ibrutinib/Acalabrutinib or Chlorambucil + Obinutuzumab

Table 1.4 - CLL 1L treatment (updated April 2020) (12)

Fitness: patients in good physical condition (Go go) or those with impaired physical condition (Slow go). Updated treatment options are highlighted in red and refer to recent EMA approval of Venetoclax + Obinutuzumab and recent presentations at ASH 2019 (Hallek, via Twitter 26.04.2020).

1.1.4.2 Chemotherapy

For many years, the alkylating agent chlorambucil remained the 'go-to' 1L treatment option for CLL patients (99). This was ultimately reassessed following the arrival of the purine analogue fludarabine (12, 100). Fludarabine demonstrated significantly higher complete response (CR) rates in previously untreated CLL patients compared to those who received chlorambucil (20 % and 4 %, respectively) (101). Ensuing preclinical studies showed that combining fludarabine with the alkylating agent cyclophosphamide potentiated cytotoxicity in CLL patient samples (102), which subsequently enhanced overall response (OR) rates compared to single-agent fludarabine in phase II clinical trials (fludarabine-cyclophosphamide; FC) (103, 104). Later, randomised trials (including the UK LRF- and German CLL Study Group (GCLLSG) CLL4 trials) confirmed the superiority of FC over fludarabine monotherapy as 1L treatment, evoking higher OR/CR rates and improved PFS (61, 105, 106). Off the back of these studies, the foundations for new management strategies that incorporated anti-CD20 monoclonal antibodies (mAbs), such as rituximab (62) and obinutuzumab (107), were established.

1.1.4.3 Chemoimmunotherapy

The CD20 antigen has proved to be an effective target in the treatment of B cell malignancies, particularly in combination with chemotherapeutic agents (108). Single-agent rituximab was shown to have clinical activity in CLL patients, but was less efficacious compared to other B cell leukaemia (109, 110). Building upon promising preclinical (111) and phase II clinical data (112), the influential phase III GCLLSG CLL8 trial demonstrated that combining rituximab with FC had superior clinical activity as 1L treatment than FC alone (fludarabine-cyclophosphamide-rituximab; FCR), with CR rates of 44.5 % and 22.9 %, respectively (62). Updated results from the CLL8 trial (median follow-up of 5.9 years) revealed that patients receiving FCR had improved median PFS (56.8 months vs. 32.9 months) and median OS (not reached vs. 86 months) compared to FC. Importantly, analysis of *IGVH* mutational status revealed that FCR

enhanced PFS and OS in M-CLL patients, whereas U-CLL patients responded poorly. Inferior PFS and OS were associated with M-CLL patients harbouring del(17p), while those with favourable cytogenetic aberrations (del(13q) and trisomy 12) had better outcomes (113). Comparable results were obtained in a separate study of FCR vs FC in previously untreated CLL patients (median follow-up of 12.8 years) from the MD Anderson Cancer Center (114). As such, FCR remains 1L therapy for physically 'fit' symptomatic CLL patients without *TP53* aberrations (12).

Combining the alkylating agent bendamustine with rituximab (bendamustine-rituximab; BR) similarly showed favourable response rates in R/R CLL patients (115) and as 1L therapy (116). In the proceeding phase III GCLLSG CLL10 trial, BR was compared to FCR in previously untreated physically 'fit' CLL patients with del(17p). Patients treated with FCR had a superior median PFS compared to those on the BR regimen (55.2 months vs. 41.7 months, respectively; median follow-up of 37.1 moths). However, FCR elicited more adverse and/or toxic effects, particularly in the over 65 age group (117). As a result, FCR remained standard 1L therapy for CLL patients, but BR was 'green-lit' as an alternative for physically 'fit' elderly patients (12).

In preclinical studies, the anti-CD20 mAb obinutuzumab (GA101) demonstrated enhanced anti-cancer activity compared to rituximab in *ex vivo* CLL cells. Importantly, obinutuzumab augmented the cytotoxic effect of chlorambucil in combination (118). A subsequent phase I trial of single-agent obinutuzumab showed encouraging OR rates of 43 % in pre-treated R/R CLL patients (119). After phase II trials assessing the combination of rituximab with chlorambucil (120, 121), the phase III GCLLSG CLL11 trial compared obinutuzumab-chlorambucil and rituximab-chlorambucil combination regimens with single-agent chlorambucil in previously untreated CLL patients with underlying conditions. Here, obinutuzumab-chlorambucil extended PFS compared to rituximab-chlorambucil or chlorambucil alone (median PFS of 26.7 vs. 16.3 vs. 11.1 months, respectively). Furthermore, obinutuzumab-chlorambucil resulted in superior CR rates than rituximab-chlorambucil (20.7 % vs. 7 %, respectively) (107). Obinutuzumab-chlorambucil is approved for 1L therapy in physically 'unfit' (slow go) CLL patients (12, 108).

1.1.4.4 BCR signalling inhibitors

BCR signalling is a central pathway in CLL pathogenesis (reviewed in (45, 122)). The advent of small-molecule BCR signalling inhibitors, such as ibrutinib and idelalisib, revolutionised the treatment landscape for CLL patients (and among patients with other B cell malignancies), particularly those with high-risk disease (45). BCR inhibitors typically antagonise TME communication, induce CLL cell death and arrest proliferation (123). From a clinical point of view, BCR inhibitors promote transient lymphocytosis alongside a concomitant reduction in lymphadenopathy (abnormal lymph node (LN) size) (45, 124). BCR signalling is described in more detail in section 1.2.

Ibrutinib (PCI-32765) is an irreversible, orally administrable Bruton's tyrosine kinase (BTK) inhibitor that covalently binds to a cysteine residue (C481) in the BTK active site (108, 125). In preclinical studies, Herman *et al*. showed that ibrutinib inhibited CpG oligonucleotide-induced CLL cell proliferation, antagonised 'microenvironmental' stimuli (CD40L, BAFF, TNF-α, IL-6, IL-4 and fibronectin) and overcame stromal cell survival signals *in vitro* (126). The same group later confirmed these findings *in vivo*, demonstrating that ibrutinib inhibited BCR and NF-κB pathways and diminished proliferation of LN- and BM-resident CLL cells (127). In a parallel study, ibrutinib downregulated BCR-induced chemokines CCL3 and CCL4 (*in vitro* and *in vivo*) and inhibited chemotaxis towards CXCL12 and CXCL13 (128). Later, de Rooij *et al*. further reported that ibrutinib thwarted BCR- and chemokine-induced adhesion and chemotaxis (129). In the Eμ-TCL1 CLL-like mouse model, ibrutinib delayed disease progression and induced lymphocytosis (128), similar to the observations in early phase I clinical trials (130). An ensuing multicentre phase Ib/II trial of ibrutinib monotherapy in poor prognostic R/R CLL patients demonstrated durable response rates, with PFS of 75 % and OS of 83 % (26 months follow-up), irrespective of high-risk genomic features (131). These findings led to clinical approval of ibrutinib for R/R CLL patients (108). At 5 years follow-up, the OR rate for single agent ibrutinib in previously untreated and R/R CLL patients was 89 %, with CR rates of 29 % for treatment naïve and 10 % for R/R patients. The PFS rate was 92 % in treatment naïve (median PFS not reached) and 44 % in R/R patients (median PFS of 51 months). Importantly, this trial demonstrated long term efficacy of ibrutinib in some high-risk R/R patients, particularly U-CLL

patients and those harbouring del(11q) (72). The efficacy of ibrutinib monotherapy over immunotherapy (RESONATE (132)), chemotherapy (RESONATE-2 (133)) or chemoimmunotherapy (Alliance (134)) has recently been established among high-risk R/R patients and as 1L therapy. Additionally, combining ibrutinib with BR showed robust response rates in R/R patients (HELIOS (135)). More recently, the highly selective irreversible BTK inhibitor acalabrutinib (ACP-196; calquence) has evoked encouraging response rates in R/R CLL patients, including those with del(17p) (136). Acalabrutinib has shown less off-target activity compared to ibrutinib (137). At a median follow up of 41 months, median PFS had not been reached (138).

Idelalisib (CAL-101) is a selective inhibitor of phosphoinositide 3'-kinase (PI3K) isoform p110δ (PI3Kδ) (12). In preclinical studies, idelalisib inhibited cellular migration towards CXCL12 and CXCL13, overcame survival signals downstream of BCR engagement and downregulated BCR ligation-induced AKT and ERK activation in primary CLL cells (139). Idelalisib was assessed as a monotherapy in a small cohort of severely high-risk R/R CLL patients, which demonstrated OR rates of 72 % and a median PFS of 15.8 months (83). In a phase III study, combining idelalisib with rituximab significantly extended OS (92 % vs. 80 % at 12 months) and median PFS (not reached vs. 5.5 months) compared to rituximab (plus placebo) in R/R CLL patients (140). Consequently, idelalisib and rituximab combination was approved for patients with refractory CLL (108). Final results from this trial reaffirmed the superior efficacy of idelalisib and rituximab over rituximab alone in R/R patients. Importantly, long-term idelalisib treatment was shown to be effective and devoid of unexpected adverse effects (141). Nevertheless, idelalisib is generally reserved for patients lacking alternative therapeutic options since it harbours a riskier safety profile than other targeted agents (108).

Other studies have investigated targeted inhibition of additional BCR signalling components including spleen tyrosine kinase (SYK) using R406 (142) or PRT318/P505-15 (143) and the SCR-family protein-tyrosine kinases using dasatinib (144, 145), which antagonised CLL survival/chemotaxis under conditions mimicking the CLL-TME.

Despite excellent clinical activity (45), emerging evidence demonstrates that CLL cells engage in elaborate feedback mechanisms to overcome targeted inhibition of BTK (87, 88, 146) and PI3K (147). Furthermore, acquired resistance mutations (due to continuous therapy) have been reported (148). Ibrutinib resistance is often associated with cysteine-to-serine mutations (C481S) affecting the ibrutinib-binding site within BTK (149) or gain-of-function mutations in phospholipase Cɣ2 (*PLCG2*) (150). As such, targeted therapies (monotherapies) are rarely curative (12), highlighting the need to identify alternative targets and/or design rational drug combinations. ARQ-531 is a potent, reversible BTK inhibitor that has been shown to abrogate BCR signalling in ibrutinib-resistant (BTK (C481S) and *PLCG2* mutants) CLL cells (151). In a phase I clinical trial, ARQ-531 showed anti-cancer activity as a monotherapy against ibrutinib-resistant R/R patients (152). Furthermore, the non-covalent BTK inhibitor vecabrutinib (SNS-062), which targets wild-type and mutated (C481S) BTK, has also demonstrated clinical activity in an ongoing phase Ib/II clinical trial in high-risk CLL patients relapsing on ibrutinib treatment (153).

1.1.4.5 BCL2 inhibitors: BH3 mimetics

The BCL2 protein family are critical regulators of the intrinsic apoptosis pathway, which contain shared BCL2 homology (BH) domains (154). BCL2 proteins are functionally grouped into 3 subfamilies: anti-apoptotic (BCL2, BCL-xL and MCL-1), pro-apoptotic multidomain (BAX and BAK) and pro-apoptotic BH3-only (BIM, NOXA and PUMA). The balance of pro- and anti-apoptotic proteins, and subsequent binding therein, govern cellular life or death decisions (108). BH3 mimetics functionally mimic (and displace) pro-apoptotic BH3-only proteins via binding to the hydrophobic groove on anti-apoptotic BCL2 proteins, which tips the balance to induce apoptosis (154). BCL2 overexpression is key aspect of aberrant CLL cell survival (155).

Following the inception of BH3 mimetics ABT-737 and navitoclax (ABT-263) (156), targeted inhibition of BCL2 by venetoclax (ABT-199) showed remarkable clinical activity in CLL, particularly in high-risk patients with del(17p)/*TP53* mutations, fludarabine refractoriness and/or U-CLL (57, 58, 84, 157). Furthermore, venetoclax performed favourably in CLL patients whose disease had progressed following treatment with BCR signalling inhibitors (158, 159).

Nevertheless, acquired resistance to venetoclax has been reported via mechanisms including treatment-induced clonal evolution (160) or Gly101Val mutations (14, 161), which is often a consequence of continuous targeted treatment (108). As such, the phase III MURANO trial was designed to assess fixed-duration venetoclax-rituximab treatment, which resulted in excellent PFS rates that were sustained 2-years after venetoclax discontinuation (162). The GCLLSG CLL14 trial of fixed-duration venetoclax-obinutuzumab combination compared to chlorabucil-obinutuzumab in patients with previously untreated CLL (and coexisting conditions) showed the superiority of venetoclax-obinutuzumab over chlorabucil-obinutuzumab, with an estimated PFS of 88.2 % and 64.1 %, respectively (median follow-up 28.1 months). Importantly, this benefit was similarly evident in high-risk patients with del(17p)/*TP53* mutations and U-CLL (163). As a result of this study, venetoclax-obinutuzumab was approved for 1L therapy (108). Following promising preclinical data (164), clinical studies are now assessing venetoclax combined with ibrutinib, such as the CLARITY (165), CAPTIVATE (166) and NCT02756897 (167) trials, in treatment naïve or R/R patients. These studies are ongoing and producing encouraging results.

1.1.5 The CLL microenvironment (CLL-TME)

CLL pathogenesis (and disease progression) is inextricably linked to the 'supportive' CLL-TME, a 'sanctuary site' wherein CLL cells engage B cell receptor (BCR) signalling and form interactions with non-malignant accessory cells (also referred to as the BM and LN microenvironment) (expertly reviewed in (9)). CLL cells continually traffic between the PB compartment and lymphoid 'sanctuary sites' (168), lured to- and retained within the permissive niche by tissue-derived secreted chemokine gradients (CXCL12, CXCL13) (169, 170) recognised by chemokine receptors (CXCR4, CXCR5) on CLL cells (9, 95, 171). Upon entering the lymphoid tissue, CLL cells interact with TME bystander cells and engage BCR signalling, which largely facilitate resistance to cytotoxic agents, promote 'active' disease and facilitate expansion of malignant clones (2, 122). On provision of adequate help, activated CLL cells proliferate in aptly named microanatomical sites known as 'proliferation centres' (also referred to as 'psuedofollicles', given their distinct nature over normal B cell follicles) (9), where they turnover up to 2 % of their leukaemic clone per day (172). Importantly, evidence indicates that the response of CLL cells to TME crosstalk

depends on inter-patient heterogeneity (for example IGVH mutational status, CD38 levels, *NOTCH1* mutations), which extends to intra-patient genetic variability between cellular subclones (173). Indeed, the CLL-TME (LN microenvironment) has emerged as a driver of 'clonal evolution', wherein proliferating LN-resident CLL cells acquire additional genetic aberrations (distinct from their PB counterparts) and facilitate expansion of 'dominant' subclones (90, 174). More recently, interactions between non-malignant cellular components (173), TME-induced immune dysfunction (175) and hypoxia-driven cellular metabolic reprogramming (176, 177) have emerged as 'hot topics' in CLL-TME investigations. Given the importance of the LN microenvironment in CLL pathogenesis, the identification and targeted inhibition of pathways mediating TME crosstalk has become a key therapeutic strategy (9). Until recently, however, our understanding of the intricate cellular communication networks was surprisingly limited. Recent studies have made inroads into the complexity of the CLL-TME (for example (178) and (179)), which promise to unlock insights into CLL disease biology and identify novel therapeutic targets. In this section, key cellular components and pathways implicated in TME crosstalk are discussed.

1.1.5.1 Cellular components of the CLL-TME

Two-way communication between CLL cells and T cells represent a critical interaction at the level of the CLL-TME (9). Activated (and autologous) $CD4^+$ T cells have been shown to sustain CLL cell survival and promote proliferation *in vitro* and *in vivo* (180, 181). Along these lines, Os *et al*. demonstrated that CLL cells operate as effective antigen presenting cells (APCs), akin to normal B cells (181). Importantly, immunohistochemical analysis demonstrated that proliferating ($Ki\text{-}67^+$) CLL cells colocalised with $CD4^+$ T cells in CLL patient LN biopsies (182, 183). Within the CLL-TME, Ghia *et al*. showed that a proportion of T cells expressed the costimulatory molecule CD40 ligand (CD40L/CD154) (182). CD40L engagement with CD40-expressing CLL cells *in vitro* promotes survival/proliferation (184, 185) via upregulation of anti-apoptotic proteins (186) and activation of PI3K-AKT, MAPK/ERK and NF-κB pathways (187, 188). Additionally, CD40L-triggered CD40 engagement has been shown to 'sensitise' CLL cells to further BCR signalling (189), retain CLL cells within the TME (190), promote T cell chemotaxis toward the LN (182) and potentiate CLL-T cell

interactions via CLL cell-mediated extracellular vesicle shedding (178). Other T cell factors similarly promote CLL survival/proliferation including interleukin-4 (IL-4) (192) and interleukin-21 (IL-21) (180). In CLL patients, the circulating T cell population is increased (193) and phenotypically skewed towards increased proportions of $CD8^+$ T cells (194), which correlate with advanced disease stage (195) and worse outcome (194). This being said, T cells derived from CLL patients appear to be functionally flawed (196, 197), which is perhaps indicative of increased expression of the exhaustion marker programmed cell death protein 1 (PD-1) (198) and immune-inhibitory molecule cytotoxic T-lymphocyte-associated protein 4 (CTLA-4) (199).

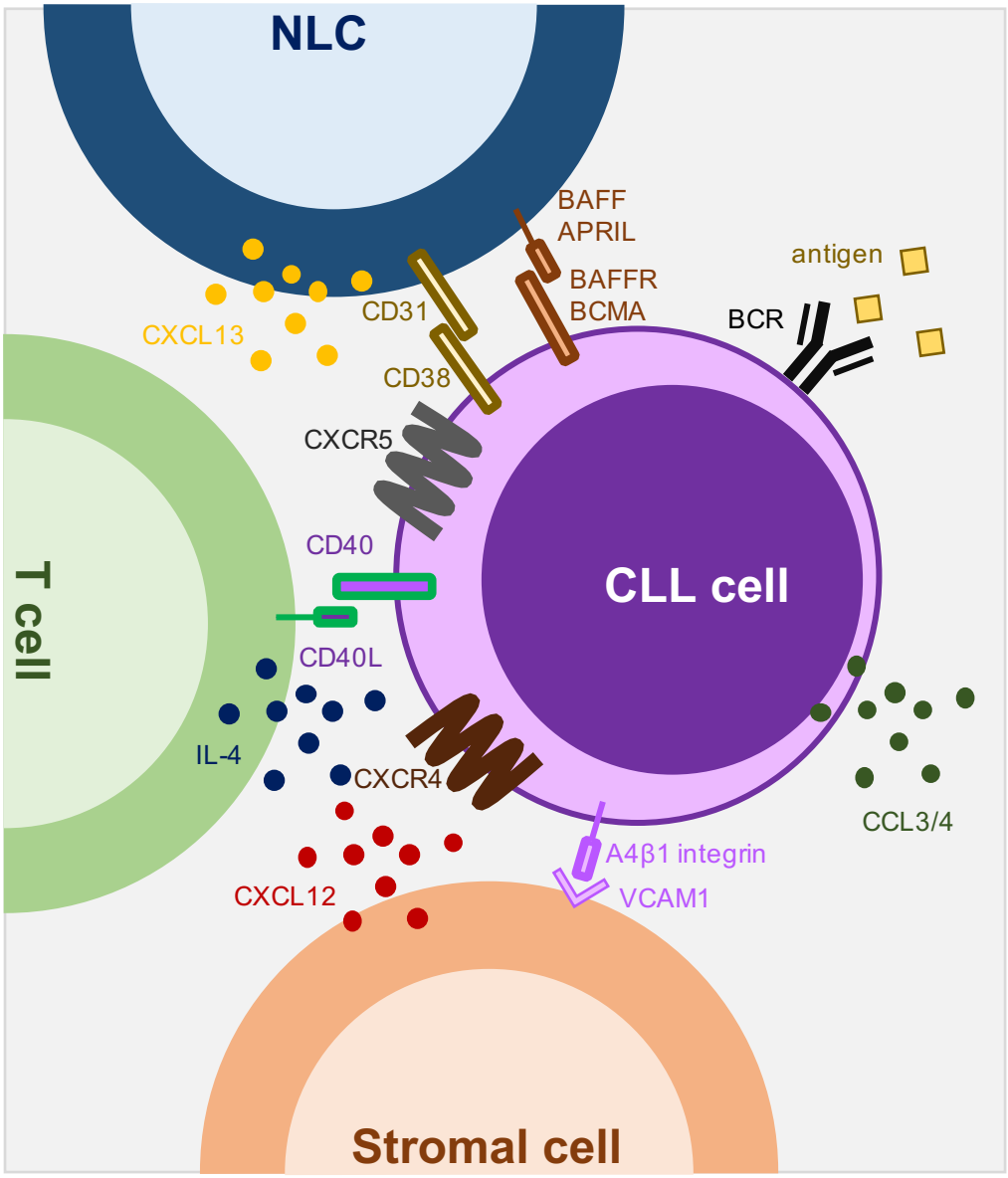

Figure 1.2 - The CLL-TME (modified from (2))

Of note, other cellular constituents of the CLL-TME similarly form elaborate communication networks that facilitate CLL disease progression (reviewed in (9)). In their study, Nishio *et al.* demonstrated that monocyte-derived nurse-like cells (NLCs) sustain CLL cell survival via expression of tumour necrosis factor (TNF) molecules B cell activating factor (BAFF) and a proliferation-inducing ligand (APRIL), which induce NF-κB signalling and upregulated MCL-1 expression in CLL cells (200). Perhaps most prominently, NLCs attract and preserve CLL cells within the LN niche via the production of CXCL12 and CXCL13 (170, 201) and expression of CD31 (202). Furthermore, NLC antigens trigger BCR activation in CLL cells, which supports CLL survival (203, 204). Integrated within the architecture of secondary lymphoid organs, stromal cells constitutively secrete chemokines, such as CXCL12, which lure CLL cells to the tissues via engagement with its cognate receptor CXCR4 on CLL cells (205). Moreover, stromal cells provide survival signals that protect CLL cells from cytotoxic agents (9), perhaps via activation of NOTCH signalling (206).

1.1.5.2 BCR activation in the CLL-TME

In their seminal study, Herishanu *et al.* identified the LN microenvironment as a key compartment in CLL pathogenesis (207), wherein CLL cells engage (auto-) antigens that activate BCR signalling resulting in enhanced survival, increased proliferation and ultimately disease progression (9). Gene expression profiling (GEP) was performed on CLL cells derived simultaneously from the PB, LN and BM compartments, which revealed marked differential expression between the distinctive niches. Gene set enrichment analysis (GSEA) subsequently demonstrated an overrepresentation of BCR-related genes (including BCR-dependent NF-κB and nuclear factor of activated T cells (NF-AT) gene sets) in LN-derived CLL cells, suggestive of BCR activation in the LN microenvironment. This was confirmed following the generation of a 'CLL-BCR gene signature' from BCR-stimulated CLL cells *in vitro*, which were enriched for genes upregulated in LN-resident CLL cells. Importantly, the 'BCR gene signature' was more highly expressed in LN-resident cells derived from U-CLL patients than those from M-CLL patients. The LN microenvironment was identified as the primary site of cell proliferation, wherein U-CLL cells expressed higher levels of proliferation-promoting genes E2F1 and C-MYC compared to M-CLL cells, which was associated with adverse clinical outcome (207). Taken together, this study demonstrated

activation of BCR signalling in the LN microenvironment *in vivo* and reflected the contrasting functional behaviours among U-CLL and M-CLL in the context of the CLL-TME.

The importance and/or relevance of BCR signal transduction (and participation of BCR signalling components in diverse pathways) in CLL-TME crosstalk was subsequently confirmed by preclinical *in vitro* and *in vivo* studies assessing BCR kinase inhibitors ibrutinib (126, 128, 129) and idelalisib (139, 208). Alongside the 'BCR-dependent' impact of BCR inhibitors on survival and proliferation, these reports highlighted many 'on-target, BCR-independent' effects on chemotaxis/adhesion (122), owing to the promiscuity of BCR kinases (BTK and PI3Kδ) embedded within chemokine- and integrin-signalling networks (209). As discussed, these studies paved the way for clinical trials, which have transformed management strategies for CLL patients (45).

1.1.5.3 Mimicking the CLL-TME *in vitro*

Mimicking the CLL-TME *in vitro* has enabled investigators to glean mechanistic insights into the interactions (and signalling networks therein) promoting CLL cell survival, proliferation and drug resistance within the CLL-TME. In a similar vein, modelling TME crosstalk has illuminated the mechanism(s) of action of therapeutic agents in preclinical studies, offering insights into potential clinical efficacy (reviewed in (210)).

For the first time, Bernal *et al.* demonstrated that BCR crosslinking using soluble $F(ab')_2$ fragments enhanced CLL cell survival via activation of NF-κB signalling and upregulation of anti-apoptotic protein MCL-1 (211). Furthermore, Nédellec *et al.* showed that CLL patients responded differently to $F(ab')_2$ fragments, with the functional consequence of BCR signalling being associated with prognostic subgroups (for example, ZAP-70 status, *IGVH* mutational status and CD38 expression) (212). Thus, *in vitro* BCR stimulation continues to reveal novel insights into CLL-TME crosstalk. However, in the absence of a standardised protocol, Rombout *et al.* showed that immobilised anti-IgM conferred a more robust and reliable BCR stimulus than soluble $F(ab')_2$ fragments, indicating the mode of *in vitro* BCR stimulation is equally important (213).

In early studies, co-culturing CLL cells with stromal cells (214) or CD40L (CD154)-expressing fibroblasts (187) prevented 'spontaneous' CLL apoptosis and initiated pro-survival pathways (210). These findings indicated that CLL-TME interactions (particularly with the stroma and T cells), could be recapitulated and/or mimicked *in vitro*. In their study, Willimott *et al*. demonstrated that co-culturing CLL cells on mouse fibroblast L cells (NT-L) improved CLL cell survival via a mechanism dependent upon physical cellular contact. Furthermore, NT-L cells stably transfected with CD40L supplemented with interleukin-4 (IL-4) induced CLL cell proliferation, whereas those cultured on NT-L remained largely quiescent (215). In a parallel study, the same group showed that culturing CLL cells on CD40L (+IL-4) induced expression of anti-apoptotic proteins MCL-1, BCL-xL and survivin, which reduced fludarabine-induced CLL cell apoptosis (186). An additional study showed that CD40L (+IL-4)-stimulated CLL cells were less sensitive to the BH3 mimetic ABT-737 due to upregulation of anti-apoptotic BCL-xL and BCL2-A1 (216). Therefore, mimicking CLL-TME interactions using the NT-L and CD40L (+IL-4) co-culture systems are applicable to 1) investigate underlying growth and survival pathways, and 2) address the cytotoxic and cytostatic ability of therapeutic agents to overcome signals emanating from the LN microenvironment. Later, Hamilton *et al*. compared the functional and phenotypic responses of different co-culture systems mimicking interactions in the CLL-TME: NT-L cells transfected with CD40L (T cell) or CD31 (NLC) and the endothelial cell line HMEC-1 (vascular system). Given the effect on cell survival and proliferation, the authors concluded that the CD40L/IL-4 system was perhaps best-placed to mimic the LN microenvironment (217).

It is important to note that this is not an exhaustive list. The CLL-TME has modelled by several distinct systems including co-cultures with activated T cells (180, 218), novel 3D co-culture systems of the BM niche (219), chemotaxis assays (128), CpG oligonucleotide stimulations (220) and *in vitro* models of hypoxia (177). Although highly relevant in CLL disease biology, they go beyond the scope of this thesis.

1.2 BCR signalling

BCR signalling plays a pivotal role in the growth, survival and proliferation of 'normal' and malignant B cells (122). In their review, ten Hacken *et al*. elegantly

summarised the evidence that implicates BCR signal transduction in CLL pathogenesis (45). For example, the clinical importance of *IGVH* mutation status (4, 5), existence of BCR stereotypy (44) and activation of the BCR in the CLL-TME (207) all point towards the notion that CLL disease progression depends upon BCR signal transduction (45). In this section, we overview BCR signalling in 'normal' B cells (BCR structure, development and signal propagation) and discuss the mechanisms, heterogeneity and functional importance of BCR activation in CLL cells.

1.2.1 BCR signalling in 'normal' B cells

BCR signalling is a key pathway in 'normal' B cell survival and development (221). In an early study, Lam *et al*. showed that deletion of the BCR (via inducible ablation of *IGVH* gene) resulted in apoptosis of mature B cells (222), demonstrating that a functioning BCR is required for B cell survival. Alongside a subsequent report (223), these data inferred that the maintenance of mature (and resting) B cells required 'tonic' signals, i.e. sustained 'low-level' signals emanating from the BCR in the absence of antigen-binding (224). Although the molecular events following 'antigenic' BCR activation are well characterised (225), the signalling pathways transmitting 'tonic' signals (and the cooperation with antigen-induced BCR stimulation) remain ill-defined (226, 227). Nevertheless, the prevailing dogma indicates that B cells are reliant upon both 'tonic' and antigen-mediated BCR activation (122).

1.2.1.1 V(D)J recombination

The assembly of a functioning BCR occurs in a 'stepwise' manner along a continuum of strictly regulated developmental stages throughout B cell maturation (228). Occurring within the BM, Ig heavy- (H) chain 'variable' (V), 'diversity' (D) and 'joining' (J) gene segments undergo functional rearrangements (facilitated by recombinase-activating gene (RAG) proteins) in an process known as V(D)J recombination (reviewed in (229)). Licensing the transition from progenitor B cells (pro-B) to precursor B cells (pre-B), this process generates an incredibly diverse Ig repertoire (specifically within HCDR3 regions), which underpins the specificity and/or restricted affinity of BCR molecules. Upon completion of subsequent Ig L chain (V and J) rearrangements,

the ‘pre-BCR’ (i.e. the BCR expressed on pre-B cells) becomes a ‘complete’ BCR (expressing the IgM isotype) expressed on newly-promoted immature B cells. Following the rejection of self-reactive BCRs, immature B cells develop into mature B cells expressing both IgM and IgD isotypes. Further maturation occurs within the SLOs following antigen engagement in a process known as SHM, where multiple mutations (facilitated by activation-induced cytidine deaminase (AID)) are introduced into the *IGVH* and *IGVL* genes to create higher-affinity BCRs for the selected antigen (45).

1.2.1.2 Structure of the BCR

The BCR is transmembrane heteromultimeric complex comprising a membrane-associated (and antigen-restricted) Ig (composed of two identical H- and two matching L-chains) non-covalently linked to the Igα (CD79A)/Igβ (CD79B) heterodimer (9). In mature B cells, the H-chain of surface Ig (sIg) is ordered into an assemblage of one V domain connected to three (IgD isotype) or four (IgM isotype) constant (C) domains (230), coupled with a short intracellular segment (231). The Ig can be subdivided into two functionally distinct portions: the ‘fragment antigen-binding’ (F(ab)) and ‘fragment crystallisable’ (Fc) regions. The F(ab) region (containing V domains) is responsible for antigen-binding, whereas the Fc region defines the Ig isotype (230). The ‘reassembled’ V domain within the H-chain (i.e. *IGVH* genes) possesses marked sequence diversity (particularly within HCDR3 regions) dictating the BCRs antigen specificity (232). Because the Ig is devoid innate signalling capacity (231), signal propagation is achieved via immunoreceptor tyrosine-based activation motifs (ITAMs) on the cytoplasmic tails of CD79A/CD79B (9), which are essential for B cell survival (223). In a resting state, the BCR is presumed to exist as a monomer or small oligomer on the cell surface (although this is debated), awaiting antigenic stimulation (Figure 1.3) (231).

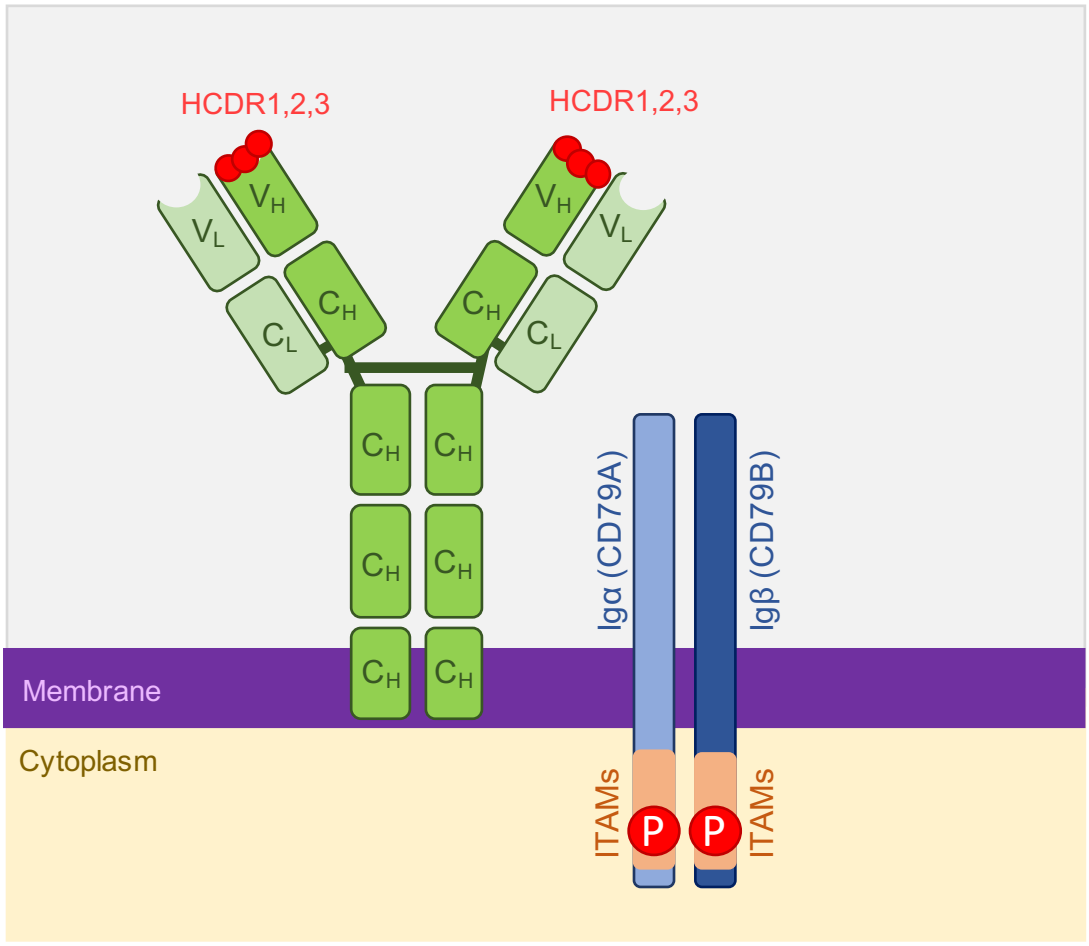

Figure 1.3 - The structure of the BCR (modified from (233))

1.2.1.3 BCR signal transduction

BCR signalling is initiated following antigen encounter, which triggers BCR 'clustering' and the formation of the 'signalosome' (225). In the early events of antigen engagement and/or 'signalosome' formation, the Src-family kinase LYN phosphorylates ITAMs on Ig-linked CD79A/CD79B, which recruits and activates the BCR-proximal kinase SYK (via Src-homology 2 (SH2) domains) (234). SYK facilitates signal propagation from the BCR complex to downstream signalling kinases via its association and phosphorylation of the adaptor molecule B-cell linker protein (BLNK) (235). BLNK operates as a scaffold that bridges the interface between SYK and downstream effectors including BTK and its substrate PLCγ2 (via SH2 domains) (236). Aberrations in BCR-associated kinases LYN (237), SYK (238, 239) and the TEC family kinase BTK (240) have deleterious effects on B cell development, signalling and function. Indeed, deficiencies in BTK function (BTK mutations) were shown to be involved in X-linked agammaglobulinemia

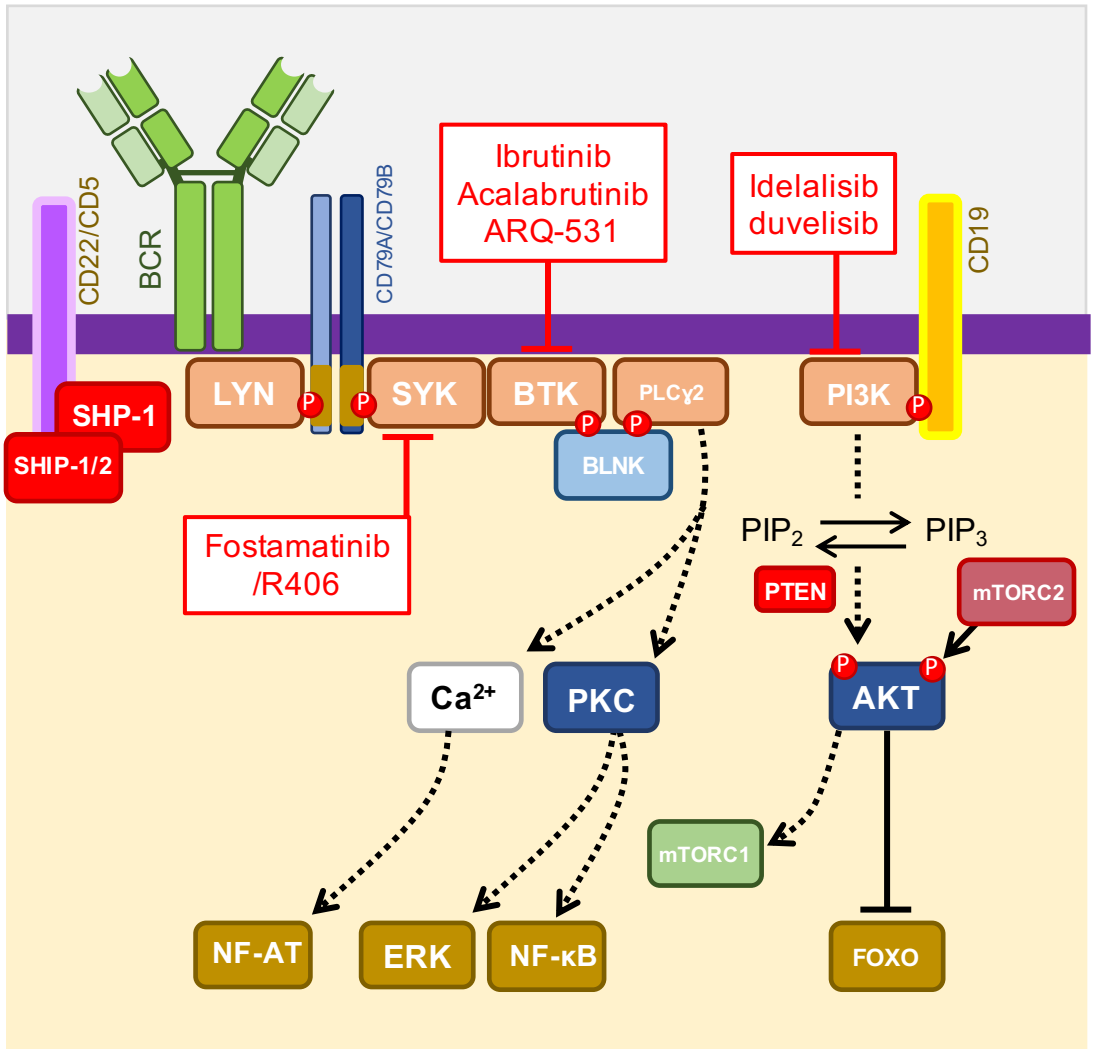

Figure 1.4 - BCR signalling (modified from (45))

(XLA) (241, 242). LYN- or SYK-dependent activation of BTK (at BTK^{Y551}, followed by autophosphorylation at BTK^{Y223}) transmits signals via PLCγ2 (via phosphorylation at multiple tyrosine residues e.g. $PLC\gamma2^{Y753}$) that ultimately leads to activation of downstream second messengers inositol-1,2,5-triphosphate (IP_3) and diacylglycerol (DAG) (235). IP_3 mobilises the release of intracellular Ca^{2+} and activates NF-AT-dependent transcription, while DAG (via activation of protein kinase Cβ (PKCβ)) leads to the activation of ERK1/2, Jun N-terminal kinase (JNK), p38 and NF-κB pathways (243). BCR engagement similarly promotes another 'branching point' facilitated by LYN-dependent phosphorylation of tyrosine residues (Y-X-X-M motifs) within the cytoplasmic tail of co-receptor molecule CD19, which creates docking sites for the p85 subunit (via the SH2 domain) of PI3K (234). PI3K is necessary for BTK activation (244, 245) and, perhaps most prominently, initiates downstream AKT-mTOR signalling (246). BCR signal integration *via* the PI3K-AKT-mTOR axis is expanded in section 1.3. In

addition to LYN's role as a facilitator of 'positive' BCR signalling, LYN possesses the ability to negatively modulate BCR signal transduction via phosphorylation of immunoreceptor tyrosine-based inhibition motifs (ITIMs) on inhibitory co-receptors FcγRIIB, CD5 and CD22 (235). Phosphorylation of ITIMs promote docking of inhibitory phosphatases SH2 domain-containing tyrosine phosphatase-1 (SHP-1) and SH2-domain-containing inositol 5'-phosphatase-1 and -2 (SHIP-1/-2), which tightly regulate the duration and strength of BCR signal transduction (Figure 1.4) (234).

1.2.2 BCR signalling in CLL cells

Beyond the prevailing view that CLL cells merely hijack the innate functional properties of BCR signal transduction in 'normal' B cells (122), increasing evidence indicates that BCR signalling is dysfunctional in CLL cells (247). Recent studies identified constitutive 'clustering' of the BCR on 'resting' CLL cells, similar to that observed on anti-IgM stimulated 'normal' B cells (247, 248). These findings aligned with studies demonstrating the appearance of an 'activated' phenotype (249) and support observations that upstream BCR signalling kinases LYN (250), SYK (251) and downstream PI3K (252) are constitutively activated (122). In their study, Ziegler *et al*. confirmed that CLL cells possess enhanced BCR responsiveness and demonstrated that BCR dysfunction (i.e. constitutive 'clustering') was strongly associated with disease severity (247). In the absence of mutations affecting the BCR (44) or downstream signalling modules (76) (as observed in activated B-cell-like (ABC) subtype-diffuse large B-cell lymphoma (DLBCL) (253)), these data supported the paradigm that CLL cells possess the ability for cell-autonomous BCR activation (247). Indeed, Dühren-von Minden *et al*. showed that CLL-derived BCRs undergo 'antigen-independent' activation via HCDR3-dependent binding of BCR-intrinsic epitopes located in the second framework region (FR2) (254). Binder *et al*. subsequently identified another 'self-recognition' epitope in the FR3 (255). Importantly, the capacity for cell-autonomous activation was restricted to BCRs from CLL cells (and not from other B cell malignancies) (122, 254). Although these studies highlighted the pathological importance of BCR stereotypy within HCDR3 regions, they did not explain the clinical heterogeneity associated with *IGVH* mutational status (122) and were unable to account for the contributions of 'extrinsic-antigens' towards CLL pathogenesis (122, 254).

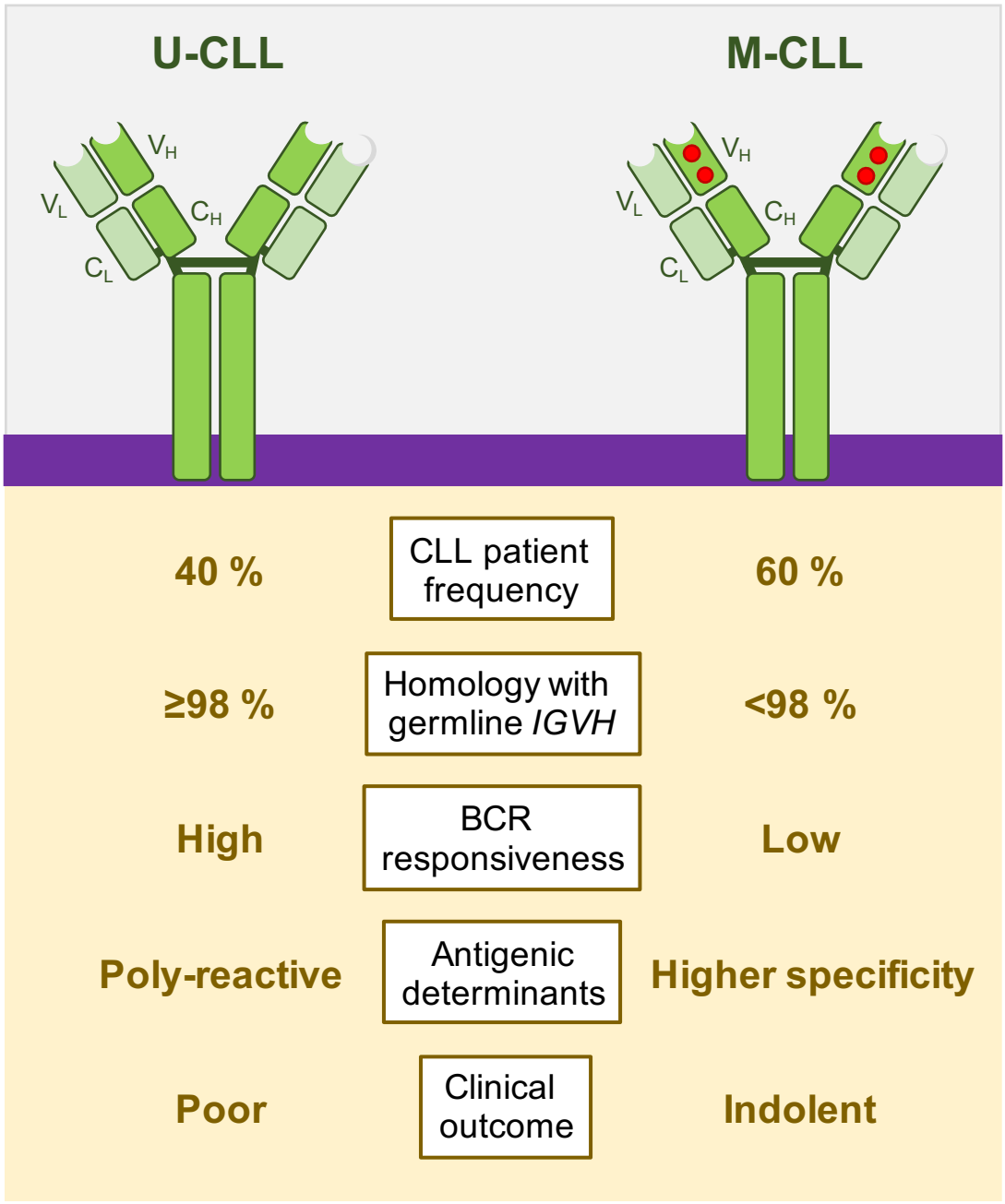

Figure 1.5 - Features of U-CLL and M-CLL patients (modified from (45))

While the underlying mechanisms remain obscure, surface IgM (sIgM) levels are often lower on CLL cells compared to 'normal' B cells, perhaps due to chronic activation (234). Nevertheless, the spatio-temporal dynamics of BCR activation represents a key determinant in CLL pathogenesis (9). Like mature B cells (222), Burger *et al*. postulated that CLL cell survival and expansion is reliant upon both 'tonic' and antigen-triggered BCR activation (122). On a functional level, the heterogenous outcome of BCR activation in CLL cells is governed by the innate properties of the cell (e.g. *IGVH* mutational status), the degree of stimulation and cooperation with bystander cells in the CLL-TME (256). With reference to

IGVH mutational status, antigen engagement of cells derived from U-CLL patients generally leads to 'positive' BCR signalling i.e. increased proliferation and/or survival (256). Along these lines, U-CLL cells typically have increased responsiveness (albeit homogenous) to BCR stimulation (234), express higher levels of sIgM (257) and tend to be associated with ectopic ZAP-70 expression (258). In contrast, cells from M-CLL patients are usually forced into a state of unresponsiveness or 'anergy' (256), characterised on a molecular level by increased activity of ERK1/2 and NF-AT (259). These functional differences align with disease severity and prognosis (256). U-CLL cells are generally more 'polyreactive', having been shown to recognise an array of autoantigens and microbial proteins (260-262), whereas M-CLL cells react to specific antigens with greater affinity (Figure 1.5) (9, 263). As mentioned earlier, the emergence of small-molecule BCR signalling inhibitors targeting BTK (ibrutinib) and PI3Kδ (idelalisib) have transformed outcomes for CLL patients, particularly those with high-risk disease (45). However, elaborate feedback mechanisms have been identified (13) and acquired resistance mutations have been reported (148). These observations have focussed the spotlight on the identification of novel treatment strategies directed towards 'targetable' BCR crosslinking-induced effectors that have the ability to improve CLL patient outcomes.

1.3 The PI3K-AKT-mTOR axis

Activated downstream of growth factor (GF) receptor stimulation (e.g. BCR, chemokine and adhesion molecules), the PI3K-AKT-mTOR signalling axis regulates (and coordinates) cellular behaviours including cell growth, proliferation, survival, metabolism and migration (264). With reference to the 'hallmarks of cancer' (265), it is unsurprising that cancerous neoplasms frequently harbour dysregulation and/or hyperactivation of the PI3K-AKT-mTOR axis (266). Indeed, B cell malignancies are no stranger to upregulated and/or constitutively active PI3K-AKT-mTOR signalling (267). As such, pharmacological inhibition of PI3K-AKT-mTOR has garnered much attention as a treatment option for this indication (268). For example, the PI3Kδ inhibitor idelalisib (in combination with rituximab) has been approved by the US Food and Drug Administration (FDA) for R/R CLL patients (108). This section gives an overview of PI3K-AKT-mTOR axis in CLL cells (with an emphasis on mTOR signalling) downstream of TME stimulation and highlights the preclinical and clinical

investigations using current mTOR inhibitors. Of note, the PI3K-AKT-mTOR signalling axis was recently reviewed (246, 269, 270).

1.3.1 PI3K-AKT signalling

There are 3 classes of PI3Ks in humans (I, II and III). Class I PI3Ks express 4 different isoforms (p110α (PI3Kα), p110ß (PI3Kß), p110δ (PI3Kδ) and p110ɣ (PI3Kɣ)), which form heterodimers with regulatory subunits (usually SH2-domain-containing p85) that control PI3K activity and localisation (269, 271). In B cells, PI3Kα and PI3Kδ operate redundantly at the pre-B cell stage (272), while PI3Kδ plays an essential role in mature B cell development and function (271, 273). Although signals emanating from multiple cell surface receptors converge on the PI3K-AKT axis (9), perhaps the best characterised is following BCR engagement (especially in the context of 'normal' and malignant B cells) (274). Importantly, PI3K-AKT integrates signals emanating from both 'tonic' (275) and antigen-induced BCR activation (235). BCR ligation-induced PI3K activation (via p85-induced binding to CD19) phosphorylates and catalyses the conversion of phosphatidylinositol(4,5)P_2 (PIP_2) to phosphatidylinositol(3,4,5)P_3 (PIP_3), a cytoplasmic membrane-associated second messenger that recruits (and activates) pleckstrin homology (PH)-domain containing effectors including BTK, phosphoinositide-dependent kinase-1 (PDK1) and the AGC serine/threonine kinase AKT (235, 269). PIP_3-mediated docking of PDK1 and AKT at the cytoplasmic plasma membrane promotes PDK1-dependent phosphorylation of AKT at T308 (AKT^{T308}) within the catalytic domain. 'Full' activation of AKT requires additional mechanistic target of rapamycin (mTOR) complex 2 (mTORC2)-dependent AKT phosphorylation at S473 (AKT^{S473}) within the hydrophobic motif (246). It has been proposed that PDK1-dependent AKT^{T308} phosphorylation enhances AKT kinase activity, which, in turn, phosphorylates mTORC2 component mSIN1 at T86 ($mSIN^{T86}$). Enhanced mTORC2 activity then phosphorylates AKT^{S473} in a positive feedback loop to 'fully' activate AKT (276). AKT promotes survival and proliferation via 'positive' and 'negative' regulation of downstream substrates, such as negative regulation of FOXO transcription factors (277), which control diverse cellular behaviours (246). PI3K-induced signal transduction is reduced by the activity of phosphatase and tensin homolog (PTEN), which dephosphorylates PIP_3 to PIP_2 thereby disabling recruitment of PH-domain containing effectors (269).

Evidence from Burkitt's lymphoma (BL) and germinal centre B-cell (GCB) subtype-DLBCL indicate that 'tonic' BCR signalling-induced PI3K-AKT signal transduction is central to pathogenesis (264).

1.3.1.1 PI3K-AKT signalling in CLL cells

Engagement of BCR (278), CD40 (279), CXCR4 (169) receptors or intimate contact with stromal cells (280) within the CLL-TME have been shown to activate PI3K-AKT signalling in CLL cells (122). PI3K-AKT activation in the context of CLL-TME communication has been reviewed (264, 271). Ringshausen *et al*. demonstrated that PI3K was constitutively active in CLL cells derived from the PB compartment (via detection of synthesised PI3P). Confoundingly, 'basal' activation of AKT (AKT^{S473}) was not observed. Instead, PKCδ activity (PDK1-dependent $PKC\delta^{T505}$ phosphorylation) was readily detected in freshly isolated CLL samples. Importantly, inhibition of PI3K (LY294002) resulted in CLL cell apoptosis (252). Interestingly, U-CLL patients possess increased levels of PI3K expression compared to their M-CLL counterparts (281), perhaps indicative of enhanced BCR responsiveness in poor prognostic patients (234). More recently, genetic and pharmacological (CZC24832) inhibition of PI3Kγ reduced CLL cell migration and adhesion, indicating that PI3Kγ has a unique role (distinct from PI3Kδ) in CLL cells. Furthermore, expression of PI3Kγ increased following CD40L (+IL-4) co-culture (282). In line with these data, the PI3Kδ/γ inhibitor duvelisib (IPI-145) antagonised CLL-TME stimuli *in vitro*, induced apoptosis and prevented chemotaxis towards CXCL12 (283). Detection of basal AKT activity in CLL cells appears to be contentious, which probably highlights experimental limitations and/or differences. However, we (284) and others (285, 286) have observed varying levels of AKT^{S473} phosphorylation among PB-derived CLL patient samples, which could indicate constitutive AKT activation or a 'functional snapshot' of prior stimulation. Notably, however, Zhuang *et al*. showed that pharmacological AKT inhibition (A-443654; median LC_{50} = 0.71 μM) induced cell death in CLL patient samples devoid of external stimulation, whereas 'normal PBMCs' were less sensitive (285). Furthermore, studies have shown that AKT plays a key role in cell cycle progression and proliferation of CLL cells in response to CD40L (+IL-4) (279) and CpG-oligodeoxynucleotides *in vitro* (287).

Like many other cancers, growing evidence indicates that PTEN is functionally comprised in CLL cells (reviewed in (288)). Shehata *et al.* reported that PTEN tumour suppressor activity was reduced by casein kinase 2 (CK2)-dependent phosphorylation, inasmuch as the CK2 inhibitor apigenin diminished $PTEN^{S380}$ phosphorylation and induced CLL cell apoptosis (290). Furthermore, others found that PTEN was downregulated by aberrant expression of PTEN-targeting miRNAs miR-26a, miR-214 (289) or miR-22 (291). More recently, Carra *et al.* demonstrated that inactivation of PTEN was instigated by upregulation of the de-ubiquitinase USP7, which resulted in aberrant cytoplasmic localisation of PTEN (288, 292). Collectively, these findings describe a pathophysiological state wherein aberrant PTEN inactivation could potentially lead to constitutive activation of PI3K-AKT-mTOR in CLL cells.

1.3.2 mTOR signalling

As an effector of PI3K activation (and a member of the PI3K-related protein kinases (PIKK) family), the serine/threonine protein kinase mTOR orchestrates diverse signals emanating from environmental inputs (e.g. GF receptor stimulation and nutrient sensing) to regulate many cellular behaviours including cell growth, metabolism, survival and proliferation (270). mTOR represents the catalytic subunit residing within 2 separate protein complexes: mTOR complex 1 (mTORC1) and mTORC2. mTORC1 comprises three main components: mTOR, regulatory protein associated with mTOR (RAPTOR) and mLST8, alongside two inhibitory subunits PRAS40 and DEPTOR. In contrast, mTORC2 contains mTOR, rapamycin insensitive companion of mTOR (RICTOR), mLST8, DEPTOR and regulatory subunits mSIN1 and PROTOR1/2 (293). Although the complexes are differentiated by their constituent components (and response to rapamycin), downstream substrates and functional output (270), the concerted activities of mTORC1 and mTORC2 represent key signalling nodes coordinating PI3K-AKT signalling-induced cell growth, survival and proliferation (Figure 1.6) (246).

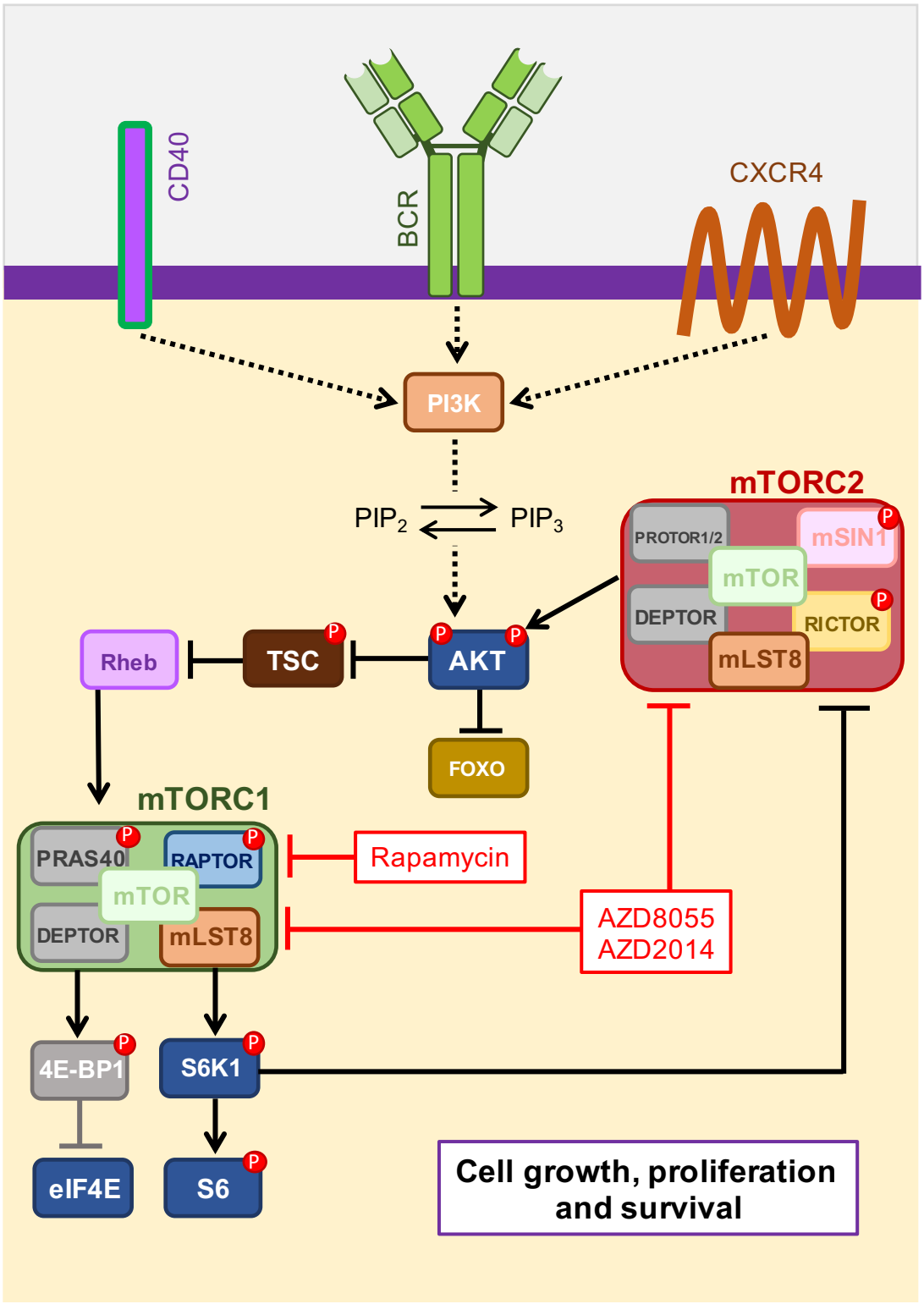

Figure 1.6 - mTOR signalling (modified from (233) and (294))

1.3.2.1 mTORC1

While mTORC1 plays a critical role integrating and modulating signalling pathways triggered by cellular stress (DNA damage, hypoxia and reduced ATP levels) and nutrient availability (amino acids) (293), this section will primarily

focus on mTORC1 signalling in response to GF receptor stimulation (via PI3K-AKT signalling).

AKT initiates mTORC1 activity via phosphorylation (and inactivation) of tuberous sclerosis complex 2 (TSC2), a tumour suppressor (and key negative regulator of mTORC1) functioning within the heterotrimeric TSC complex (TSC1, TSC2 and TBC1D7) (293). In the absence of stimulation, the TSC complex operates as a GTPase activating protein (GAP), which associates with (and functionally subdues) the GTPase Rheb. Upon AKT-dependent suppression of the TSC complex, the conversion of inactive Rheb-GDP to active Rheb-GTP permits binding and activation of mTORC1 (270). Furthermore, the activity of mTORC1 is controlled by AKT-dependent phosphorylation of mTORC1 inhibitory subunit PRAS40 at T246 ($PRAS40^{T246}$), which facilitates its disassociation from RAPTOR, enabling activation of downstream mTORC1 substrates (295). Of note, crosstalk with the MAPK/ERK pathway (and its effector $p90^{RSK}$) similarly activates mTORC1 via suppression of the TSC complex (266).

Within the mTORC1 complex, RAPTOR ensures correct mTORC1 localisation (293) and instigates the recruitment and association of mTORC1-specific substrates p70S6 Kinase 1 (S6K1) and eIF4E-Binding Protein 1 (4E-BP1) via their conserved TOR signalling (TOS) motifs (296). mTORC1-dependent phosphorylation of S6K1 and 4E-BP1 plays a key role in the regulation of cell growth (for example, via translation of proteins implicated in cell cycle progression) (266). Together with PDK1-dependent phosphorylation at T229 ($S6K1^{T229}$), mTORC1 directly phosphorylates (and activates) S6K1 at T389 ($S6K1^{T389}$). Activated S6K1 subsequently phosphorylates the 40S subunit component S6 ribosomal protein (S6) at S235/236 ($S6^{S235/236}$) (270). Most prominently, S6K1 directly contributes to cap-dependent mRNA translation (and protein synthesis) via triggering eIF4B activation (a positive regulator of the eIF4F complex) and marking PDCD4 (an inhibitor of eIF4A RNA helicase activity) for degradation (S6K1-dependent $PDCD4^{S67}$ phosphorylation) (293, 297). In the absence of stimulation, 4E-BP1 suppresses cap-dependent mRNA translation via its association with eIF4E, which disables the assembly of the eIF4F complex (270). mTORC1-dependent phosphorylation of 4E-BP1 at T37/46 ($4E\text{-}BP1^{T37/46}$) primes 4E-BP1 for further phosphorylation and subsequent dissociation from eIF4E, thereby enabling eIF4F

complex formation (298). Alongside its fundamental role in protein synthesis, mTORC1 functions to facilitate lipid/glucose metabolism (augmenting cell size/biomass) and repress autophagy/catabolism (protein turnover) (reviewed in (270)).

Importantly, S6K1 is embedded within negative feedback loops that modulate mTORC2 activity (293). S6K1 directly reduces mTORC2 activity via phosphorylation of mTORC2 component RICTOR at T1135 ($RICTOR^{T1135}$) (299), while S6K1 similarly inactivates insulin receptor substrate 1 (IRS1) (and subsequent PI3K-AKT activation) via downregulation of *IRS1* gene expression and phosphorylation-induced IRS1 depletion (300, 301). Finally, mTORC1 negates PI3K-AKT-mTORC2 signal transduction via phosphorylation (and stabilisation) of the mTORC1 negative regulator Grb10 (302, 303).

1.3.2.2 mTORC2

In the absence of PI3K-dependent generation of PIP_3, the regulatory mTORC2 subunit mSIN1 prevents mTORC2 activation via binding to its catalytic domain. Upon PI3K activation, the PH domain of mSIN1 interacts with PIP_3, thereby releasing the inhibitory effect on mTORC2 kinase activity (293, 304). As mentioned earlier, AKT-dependent $mSIN^{T86}$ phosphorylation (and enhanced mTORC2 activity) reciprocates phosphorylation of AKT^{S473} in a positive feedback loop that results in maximum kinase activity (276, 293).

Within the mTORC2 complex, RICTOR (the defining element of mTORC2) modulates the activity of downstream targets (305), akin to the function of mTORC1-specific (but unrelated) RAPTOR (293). Although AKT kinase activity does not require mTORC2-dependent AKT^{S473} phosphorylation to initiate effector functions, AKT^{S473} phosphorylation has been shown to stabilise PDK1-dependent AKT^{T308} phosphorylation (246, 306, 307). In this regard, mTORC2 modulates (in a substrate-specific manner (308)) AKT-dependent negative regulation of downstream substrates such as the FOXO transcription factors (277), glycogen synthase kinase 3 (GSK3) (309) and the TSC complex (310). Collectively, these ‘nodes’ control diverse cellular behaviours including cell growth, proliferation and survival (246). Like AKT, mTORC2 directly phosphorylates members of the

PKC family, which regulate actin cytoskeleton remodelling, chemotaxis and cell migration (293).

1.3.2.3 mTOR inhibitors

mTORC1 and mTORC2 are functionally distinguished and/or characterised, in part, by their sensitivity to rapamycin (otherwise known as sirolimus in clinical settings) (293). Rapamycin forms a complex with FKBP12 that binds allosterically to the FKBP12-rapamycin binding (FRB) domain within mTOR kinase (specifically mTORC1), which prevents binding of substrate molecules (269). While mTORC2-specific mTOR kinase equally possesses an FRB domain, mTORC2 is insensitive to rapamycin by virtue of RICTOR-mSIN1 complex, which creates a structural conformation that masks the ability of FKBP12-rapamycin to associate with the FRB domain (270). Although chronic exposure to rapamycin has been shown to reduce mTORC2 activity (via limiting the availability of mTOR kinase) (311), rapamycin is generally considered an allosteric mTORC1-selective inhibitor (293). Indeed, Choo *et al*. demonstrated that rapamycin differentially (and selectively) inhibits mTORC1 substrates, preferentially targeting S6K1 activity over 4E-BP1 (312). Although rapamycin is an effective cytostatic agent (313), its clinical derivatives (the 'rapalogues') CCI-779 (temsirolimus) and RAD001 (everolimus) have evoked limited anti-cancer activity in clinical trial (293). Clinical activity of mTORC1-selective inhibitors is insufficient due to incomplete blockade of 4E-BP1 phosphorylation (thus enabling eIF4E-mediated translation) (312) and abrogation of negative feedback loops modulating mTORC2 activity, which results in activation of AKT-mediated pro-survival signalling (293, 314-317).

To circumvent the problems associated with selective-mTORC1 inhibitors (rapalogues), 'second generation' ATP-competitive dual mTOR kinase inhibitors (targeting mTORC1 and mTORC2) were developed (293). The dual mTOR kinase inhibitor AZD8055 (and it's clinical analogue AZD2014 (vistusertib) (318)) has been shown to inhibit phosphorylation of mTORC1 (S6K1^{T389} and 4E-BP1$^{T37/46}$) and mTORC2 (AKT^{S473}) substrates and downstream proteins (S6$^{S235/236}$ and FOXO1^{T24}) (319). In pre-clinical studies, AZD8055 demonstrated *in vitro* activity against acute myeloid leukaemia (AML) (320), renal cell carcinoma (321) and breast cancer (322). The dual mTOR kinase inhibitor OSI-027 has similarly shown pre-

clinical activity in lymphomas (323). However, dual mTOR kinase inhibition has been shown to upregulate expression of receptor tyrosine kinases (RTK) via elimination of inhibitory feedback mechanisms, resulting in pro-survival signalling mediated by PI3K-dependent AKT^{T308} phosphorylation (324). In an attempt to sidestep these drawbacks, dual PI3K/mTOR inhibitors, such as PF-04691502 and SAR245409, have been developed, displaying positive results in pre-clinical investigations and phase I-II clinical trials (Table 1.5) (293).

Compound	Target	Phase	Disease	Reference
AZD2014 (Vistusertib)	mTORC1/2	I-II	AST, GBM, Prostate, Meningiomas, Lymphomas	(325)
MLN0128 (TAK228)	mTORC1/2	I-II	AST, Prostate, Thyroid, Breast, Liver, Sarcoma, MCC, MM	(326)
OSI-027	mTORC1/2	I	AST, Lymphomas	(327)
CC-223	mTORC1/2	I-II	NSCLC, NHL, MM	(328)
PF-04691502	PI3K/mTORC1/2	I-II	Breast, Endometrial, AST	(329)
VS-5584	PI3K/mTORC1/2	I	Metastatic cancer, Lymphomas	(330)
SAR245409 (Voxtalisib)	PI3K/mTORC1/2	I-II	AST, GBM, Ovarian, Breast, NHL	(331)
CC-115	mTORC1/2/DNA-PK	I-II	AST, GBM, CLL, Prostate	(332)

Table 1.5 - mTOR kinase inhibitors in clinical trials (333)
AST=Advanced Solid Tumours, GBM=Glioblastoma Multiforme, NSCLC=Non-Small Cell Lung Cancer, NHL=Non-Hodgkin Lymphoma, MCC=Merkel Cell Carcinoma, MM=Multiple Myeloma.

1.3.2.4 mTOR signalling in CLL

mTOR is aberrantly activated in various 'solid' and haematological cancers (294, 334), albeit seldom as a result of activating mutations in mTOR (335). Pathological overactivation of PI3K-AKT or MAPK/ERK signalling hijacks mTOR activity (270), inasmuch as mTOR becomes detached from 'normal' physiological cues and sustains cancer cell growth (334). Despite a plethora of studies delineating PI3K-AKT signalling in CLL pathogenesis (264), mTOR (as an important node within the PI3K-AKT axis) has garnered surprisingly little attention as a potential therapeutic target for CLL.

Early preclinical studies showed that pharmacological inhibition of mTORC1 (rapamycin) induced cell cycle arrest and apoptosis in CLL cells (313, 336, 337).

Indeed, Decker *et al*. demonstrated that rapamycin-induced G1 cell cycle arrest corresponded to decreased levels of cyclin D3, cyclin E and cyclin A, concluding that mTOR represents a putative therapeutic strategy to prevent accumulation of proliferative CLL cells within the LN microenvironment (313). Additionally, Åleskog *et al*. showed that CLL patient samples were vulnerable to rapamycin treatment, resulting in dose-dependent cell death irrespective of poor prognostic features (337). In line with these data, a recent drug-sensitivity screen demonstrated that a subset of M-CLL patients were particularly sensitive to everolimus treatment, with ~14 % of patients dependent upon mTOR signalling irrespective of BCR signalling capacity (338). In clinical trial, everolimus promoted redistribution of CLL cells from the tissues to the periphery in a subset of CLL patients, akin to the clinical manifestations observed with BCR signalling inhibitors. However, anti-cancer activity was modest, with only 18 % of patients achieving partial remission (339). Alongside the aforementioned limitations associated with prolonged mTORC1 inhibition (316, 317), an unpublished study showed that mTORC2 component RICTOR was overexpressed in CLL cells, which resulted in enhanced mTORC2 activity (340). Collectively, these data suggest that selective-mTORC1 inhibitors would have limited efficacy in CLL. As such, dual mTOR kinase inhibitors (284) and dual PI3K/mTOR inhibitors PF-04691502 (341) and SAR245409 (342) have been adopted in recent CLL pre-clinical investigations, which have resulted in enhanced CLL cell death and abrogation of CLL-TME stimuli. Moreover, the dual mTOR/DNA-dependent protein kinase (DNA-PK) inhibitor CC-115 has equally demonstrated pre-clinical and clinical potency in CLL (343). Thus, the role of mTOR signalling in CLL pathogenesis (and targeted inhibition thereof) warrants further investigation.

1.4 Forkhead Box (FOX) Class O (FOXO) transcription factors

Reciprocal positive-feedback between AKT and mTORC2 influences AKT substrate specificity by maximising kinase activity (293). Among other methods, AKT promotes cell survival and proliferation via negative regulation of FOXO transcription factors (246). Mammalian FOXOs (belonging to the evolutionary conserved FOX transcription factor superfamily) consist of 4 family members: FOXO1, FOXO3, FOXO4 and FOXO6 (344), which possess similarities in their structure, function and regulation (345). In terms of distribution patterns, FOXOs

are widely (albeit differentially) expressed in a tissue-specific manner (for example, *FOXO1* is abundantly expressed in adipose tissue), indicating individual FOXO family members have specific cellular functions (346). However, increasing evidence indicates that FOXOs can occupy similar expression patterns and fulfil overlapping (functionally redundant) roles (344). As context-dependent transcriptional activators *and* repressors, FOXOs operate as key regulators of diverse cellular processes including cell cycle arrest, apoptosis, metabolism, longevity and cell fate determination (347). FOXOs are unique among the FOX superfamily by virtue of an amino acid sequence (Gly-Asp-Ser-Asn-Ser) that flanks the DNA-binding domain, mediating interactions with the 'forkhead response element' (FHRE) or DNA consensus sequence 5′-(G/C)(T/A)AA(C/T)AA-3′ (346). FOXO subcellular localisation largely dictates transcriptional activity, which is influenced by multiple posttranslational modifications including FOXO nuclear export via AKT-dependent phosphorylation (345). Furthermore, nucleo-cytoplasmic shuttling is regulated by conserved nuclear localisation sequences (NLS) and nuclear export sequences (NES), enabling interactions between FOXOs and nuclear export/import machinery (346). FOXOs are widely considered to be '*bona fide*' tumour suppressors, evoking transcriptional programmes resulting in potent inhibitory effects on cell growth and survival (348). However, emerging evidence points towards an alternative paradigm whereby FOXOs operate as mediators of cellular homeostasis and/or resistance in both 'normal' and pathophysiological scenarios (344). In any case, dysregulation of FOXOs can result in a broad spectrum of diseases including cancer (347). This section gives an overview of FOXO regulation and its functional importance in 'normal' and malignant B cells. Of note, the role of FOXOs in the context of cancer has been recently reviewed (344, 347).

1.4.1 AKT-dependent FOXO regulation

FOXO subcellular localisation is regulated by multiple posttranslational (and posttranscriptional) modifications, which largely influence FOXO transcriptional activity (reviewed in (345)). Perhaps most prominently, AKT negatively regulates FOXO DNA-binding and transactivation via phosphorylation at conserved RxRxxS/T residues (344, 348). AKT phosphorylates FOXOs at 3 serine/threonine sites (located at the N-terminus, NLS (flanking the DBD) and proximal to the NES) that promote FOXO nuclear export: FOXO1 (T24, S256 and S319), FOXO3 (T32,

S253 and S315) and FOXO4 (T28, S193, S258) (347). FOXO6 transcriptional activity is abrogated by AKT-dependent phosphorylation (at T26 and S184), irrespective of inherent nucleo-cytoplasmic shuttling impairments (FOXO6 lacks the AKT phosphorylation site located at the C-terminus) (349). Importantly, Biggs *et al.* showed that FOXOs expressing mutant AKT phosphorylation sites were resistant to AKT-dependent phosphorylation and nuclear export (350). Furthermore, Brunet *et al.* demonstrated that removal of GF stimulation resulted in FOXO dephosphorylation, nuclear accumulation and enhanced transcriptional activity, indicating that FOXO cellular distribution represents a highly dynamic process (277). AKT-phosphorylated FOXOs are exported from the nucleus by interactions with 14-3-3 proteins, which operate as molecular scaffolds via binding to RSxpS/TxP and RxxxpSxP motifs (277, 348, 350-353). AKT-dependent FOXO1 (T24 and S256) and FOXO3 (T32 and S253) phosphorylation induces 14-3-3 binding (277, 345, 354, 355). 14-3-3 proteins exert various mechanism to control FOXO transcriptional activity. For example, the association with 14-3-3 proteins expose the FOXO NES (located at the C-terminus) and mask the availability of the NLS, thus preventing FOXO translocation back to the nucleus (345, 356, 357). Furthermore, 14-3-3 binding directly disrupts FOXO interactions with the FHRE via disturbing the FOXO DNA-binding interface (DNA-binding domain) (Figure 1.7) (354, 358-361). FOXO degradation is initiated following AKT-dependent phosphorylation and nuclear export, in a context-dependent manner (348, 362-364). The E3 ubiquitin ligase S-phase kinase-associated protein 2 (SKP2) (existing in the SCF^{SKP2} complex) interacts with and polyubiquitinates AKT-phosphorylated FOXOs for targeted degradation via the proteasome (364).

PI3K-AKT signalling is frequently hyperactivated in cancer, which nullifies FOXO activity as a result of the aforementioned mechanisms. Indeed, enhanced levels of AKT-dependent FOXO phosphorylation are often associated with aggressive disease and poor prognosis in various ‘solid’ and haematological malignancies (344, 347). As such, targeted inhibition of the PI3K-AKT-mTOR axis has been proposed as a strategy to unleash the tumour suppressive capabilities of FOXOs (365).

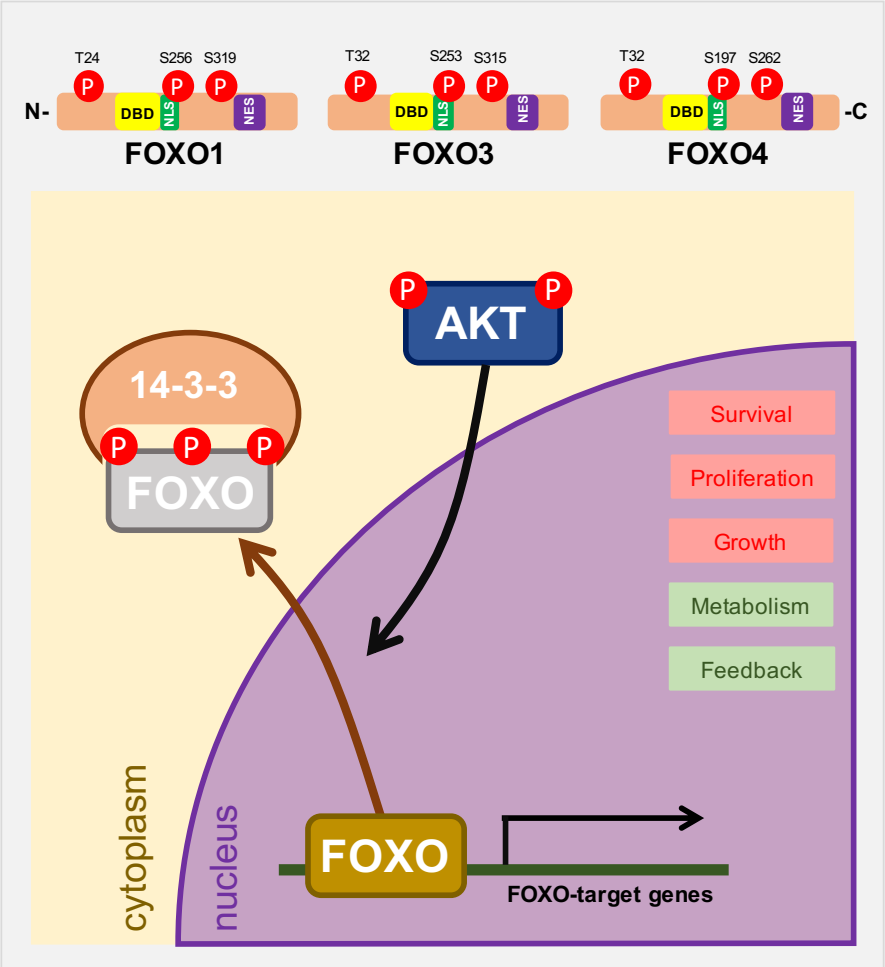

Figure 1.7 - AKT-dependent FOXO regulation (modified from (246))

1.4.2 Other mechanisms of FOXO regulation

AKT-dependent phosphorylation of FOXOs is the most well-studied (and perhaps the most influential) posttranslational modification governing FOXO activity (345). However, it is important to note that FOXO subcellular localisation, transcriptional activity and degradation are influenced by multiple co-occurring posttranslational and posttranscriptional modifications in a highly dynamic process. Indeed, FOXOs are key nodes at the nexus of several signalling pathways (348). Alongside AKT-dependent regulation, FOXO transcriptional activity (and subcellular localisation) is also negatively regulated via phosphorylation by MAPK/ERK (366, 367), cyclin-dependent kinase 2 (CDK2) (368) and casein kinase 1 (CK1) (369, 370) pathways. Conversely, oxidative stress-activated JNK phosphorylates FOXOs (and 14-3-3 proteins) to promote nuclear translocation and transcriptional activation (371). In response to intracellular energy depletion, AMP-activated protein kinase (AMPK) phosphorylation promotes FOXO

stability, nuclear accumulation and transcriptional activity (347, 372). Stress-induced FOXO-mediated transcription maintains cellular homeostasis (344). Although beyond the scope of this thesis, other posttranslational (acetylation, methylation and ubiquitination) and posttranscriptional (miRNAs) modifications impact FOXO functionality, often with dual 'positive' and 'negative' impacts in a context-specific manner, reviewed in (347, 373, 374).

1.4.3 FOXO-mediated induction of cell cycle arrest and apoptosis

Early studies demonstrated the ability of FOXOs to induce cell cycle arrest and apoptosis (either by FOXO overexpression or pharmacological PI3K-AKT inhibition) via upregulation of cytostatic and pro-apoptotic transcripts, which suggested that FOXOs operate as obligate tumour suppressors downstream of PI3K-AKT inactivation (277, 344, 375-379). Studies have subsequently identified a wide array of FOXO-regulated target genes, which have highlighted their role as mediators of growth arrest and cell death, in a context-specific manner (348, 380).

Cell cycle progression is a tightly regulated process involving the timely (and sequential) expression of cyclin dependent kinases (CDKs), cyclins and cyclin-dependent kinase inhibitors (CDKIs) along a succession of cell cycle phases (G0, G1, S, G2 and M) (365). FOXOs exert control over cell cycle progression at the G1/S transition via upregulation of CDKIs *CDKN1A* ($p21^{CIP1}$) and *CDKN1B* ($p27^{KIP1}$), which inhibit cyclin E-CDK2 and cyclin D-CDK4/6 complexes (376, 377, 381, 382). Furthermore, FOXOs have been shown to upregulate members of the INK4 family of CDKIs: *CDKN2B* ($p15^{INK4b}$), *CDKN2A* ($p16^{INK4a}$), *CDKN2C* ($P18^{INK4c}$) and *CDKN2D* ($p19^{INK4d}$), which elicit G1 cell cycle arrest via inhibition of the cyclin D-CDK4/6 complex (344). FOXOs can also upregulate the retinoblastoma (Rb) protein family member p130, which induces cellular 'quiescence' following cell cycle arrest via enhanced (and chronic) formation of the inhibitory p130/E2F complex (preventing transcription of genes necessary for S phase) (365, 376). Interestingly, Schmidt *et al.* demonstrated that FOXOs transcriptionally repress *CCND1* (cyclin D1) and *CCND2* (cyclin D2) expression (involved in cell cycle progression), inducing growth arrest independently of $p27^{KIP1}$ (378).

FOXOs are also implicated in the regulation of transcripts involved in the 'intrinsic' and 'extrinsic' apoptotic pathways, leading to the activation of caspase 3- and caspase 7-dependent programmed cell death (344). The 'intrinsic' pathway is initiated in response to apoptotic stimuli, which results in mitochondrial outer membrane permeabilization (MOMP). MOMP is initiated by the activity of BAK and BAX proteins (located on the outer mitochondrial membrane), which are activated by binding of pro-apoptotic BH3-only (BID, BIM, PUMA, and NOXA) proteins. Conversely, MOMP is inhibited by anti-apoptotic (BCL2, BCL-xL and MCL-1) proteins, which bind to (and nullify) pro-apoptotic proteins (383). FOXOs contribute to the 'intrinsic' pathway via upregulation of pro-apoptotic *BCL2-L11* (BIM) and *BBC3* (PUMA) proteins, while FOXO-mediated repression of *BCL2-L1* (BCL-xL) has been reported (344, 365). The 'extrinsic' pathway is triggered via engagement of 'death receptors' (FAS, TNFR1 and TRAILR1), which leads to the assembly of the 'death-inducing signalling complex' (DISC) (383). FOXOs contribute to the 'extrinsic' pathway via upregulation of 'death receptor' cognate ligands FASL and TRAIL (344, 365).

1.4.4 FOXO function in 'normal' B cells

FOXOs fulfil distinct roles throughout B cell maturation (reviewed in (384)). At the earliest stages of B cell development, Welinder *et al.* demonstrated that *Foxo1* expression was induced by E proteins E2A and HeLa E-box binding protein (HEB), which concertedly trigger differentiation of the common lymphoid progenitor (CLP) to the pro-B cell stage. Ablation of E2A or HEB resulted in a block at the CLP stage, which coincided with reduced *Foxo1* expression (385). The transition between the pro-B cell and pre-B cell stages is governed by successful V(D)J recombination facilitated by RAG proteins (228). Two groups showed that Foxo1 directly activated *Rag1* and *Rag2* transcription, which was reduced in Foxo1-depleted early B cells (386, 387). Importantly, Dengler *et al.* demonstrated that Foxo1-ablation (and not Foxo3) impaired V(D)J recombination in pro-B cells, while Foxo1 loss reduced L chain rearrangements in pre-B cells. Furthermore, Foxo1-deletion in pro-B cells blocked commitment to the pre-B cell stage via diminished IL-7Rα expression. Paradoxically, loss of Foxo1 at the pro-B cell stage induced apoptosis, which was associated with elevated *Bcl2-l11* expression and reduced *Bcl2-l1* (387). FOXO1 depletion induced apoptosis in pre-B cells (386), while FOXO1 activity evoked 'positive' (via increased cyclin D3

levels) (388) and 'negative' (via transcriptional activation of *BCL6*) (389) impacts on pre-B cell proliferation in a temporal-specific manner (384). In mature B cells, FOXO1 is the most abundantly expressed FOXO family member (390), which is downregulated (and inactivated) following BCR ligation via PI3K-AKT signalling (391). In their study, Yusuf *et al*. showed that PI3K-AKT-mediated FOXO1 inactivation was necessary for optimal B cell proliferation. Here, PI3K inhibition or expression of a constitutively active form of FOXO1 (FOXO1-A3), which is insensitive to AKT-dependent phosphorylation, promoted apoptosis and cell cycle arrest (390). Along these lines, Srinivasan *et al*. demonstrated that FOXO1 induced apoptosis of BCR-depleted B cells, which was rescued by ectopic expression of constitutively active PI3K. Furthermore, BCR-ablated B cells had elevated levels of FOXO-targets *BCL2-L11* and *CDKN1B* (275). Conversely, Dengler *et al*. revealed that conditional deletion of *Foxo1* (*CD21-Cre*$^{+}$) reduced LN-resident B cells, indicating Foxo1 is necessary for B cell maintenance. Interestingly, B cells lacking *Foxo1* also possessed impairments in BCR signalling and proliferation (387). In a subset of mature B cells, antigen encounter within the SLOs leads to the formation of the GC, a specialised microanatomical structure wherein mature B cells undergo rapid clonal expansion, Ig SHM and class switch recombination (CSR) to generate affinity-enhanced antibodies in support of the adaptive immune response (392). On a functional level, the GC is polarised into a highly proliferative 'dark zone' (DZ), which is the site of SHM, and a 'light zone' (LZ), where B cells undergo activation, CSR and selection (393). FOXO1 is abundantly expressed in B cells within the proliferative DZ compartment, where it instructs a gene expression programme favouring DZ formation (394, 395). Indeed, FOXO1 induces the expression of *CXCR4*, retaining B cells within the DZ (394). Furthermore, FOXO1 mediates transcription of *AICDA* (encoding AID), a key component involved in SHM and CSR (387). Along these lines, FOXO1 knockdown in GC-B cells impeded the formation of the DZ, CSR was defective, whereas normal SHM was maintained (384, 387, 394, 395).

1.4.5 The role of FOXOs in B cell malignancies

The diverse functionality of FOXO1 throughout B cell maturation is often hijacked in the development, maintenance and progression of B cell malignancies (comprehensively reviewed in (384)). In their study, Xie *et al*. demonstrated that FOXO1 was downregulated in classical Hodgkin lymphoma

(cHL) cell lines (and virtually absent in the majority of examined cHL patient samples) compared to 'normal' human tonsillar $CD19^+$ cells via overexpression of the FOXO1-targetting miR-183–miR-96–miR-182 cluster and constitutive activation of AKT and ERK kinases. Importantly, expression of FOXO1-A3 induced growth arrest and apoptosis, coinciding with enhanced levels of *CDKN1B* and *BCL2-L11*. The authors proposed that low FOXO1 expression contributed to cHL progression, suggesting that FOXO1 is a putative tumour suppressor (396). The roles of FOXOs in DLBCL, BL and B-cell precursor acute lymphoblastic leukaemia (BCP-ALL) are contradictory (384).

Szydlowski *et al*. demonstrated that FOXO1 was an effector of SYK inhibition (R406) in GCB-DLBCL, which is dependent upon 'tonic' BCR signalling. FOXO1 activation resulted in enhanced expression of BIM and $p27^{KIP1}$, while FOXO1 depletion shielded GCB-DLBCL cells from R406-induced apoptosis and cell cycle arrest (397). Conversely, *FOXO1* mutations have been reported in ~9 % of DLBCL patients, nearly half of which (~46 %) possess recurrent mutations in the N-terminal region. These mutations negated $FOXO1^{T24}$ phosphorylation, diminished binding to 14-3-3 proteins and promoted nuclear accumulation (398). Importantly, *FOXO1* mutations were associated with poor prognosis and worse response to therapy (384, 398, 399).

In BL, FOXOs have been purported as tumour suppressors by virtue of their antagonistic relationship with MYC (384), the defining oncogene in BL pathogenesis (400). In contrast, Kabrani *et al*. showed that recurrent FOXO1 mutations (preventing AKT-dependent $FOXO^{T24}$ phosphorylation) restricted FOXO1 to the nucleus, which promoted cell proliferation and survival. Nuclear FOXO1 depletion (via CRISPR/Cas9 editing) compromised tumour growth, indicating that nuclear FOXO1 is a key oncogenic event in BL (401).

In pre-BCR^+ BCP-ALL, Köhrer *et al*. showed that FOXO1 was a key effector of pre-BCR signalling inactivation. Pharmacological inhibition of SYK (PRT318) in pre-BCR^+ BCP-ALL cell lines blocked $FOXO1^{T24}$ phosphorylation, enhanced FOXO1 expression and promoted nuclear accumulation. Furthermore, ectopic FOXO1-A3 expression reduced cell viability, indicating that maintenance of pre-BCR^+ BCP-ALL required inactivation of FOXO1 (384, 402). In contrast, Wang *et al*. demonstrated that pharmacological or shRNA-mediated FOXO1 depletion induced

G1 cell cycle arrest and enhanced caspase-dependent cell death in pre-BCR$^-$ and pre-BCR$^+$ BCP-ALL cell lines (via CCND3 downregulation, reduced mTOR activity and increase p27^{KIP1}), indicating that BCP-ALL cell maintenance is reliant on FOXO1 expression (403).

Comparatively speaking, little evidence exists about the role of FOXOs in CLL disease biology. In their study, Palacios *et al*. demonstrated that proliferating CLL cells were dependent upon overexpression of miR-22, which downregulated PTEN activity and subsequently enhanced PI3K-AKT-FOXO1 signalling, specifically in 'proliferative' cells from U-CLL patients. Inactivated FOXO1 (cytoplasmic localisation) was associated with reduced levels of p27^{KIP1} (291). In line with these findings, Ticchioni *et al*. showed that 'homeostatic' chemokines (CXCL12, CCL21, CCL19 and CXCL13) induced CLL cell survival via PI3K-AKT-induced FOXO3A inactivation and correlated with reduced levels of BIM. Expression of 'triple mutant' FOXO3A (constitutively active) induced cell death, while FOXO3A siRNA enhanced 'basal' CLL survival (286). Collectively, these studies point towards a tumour suppressive role for FOXOs in CLL. However, scant evidence exists about endogenous FOXO expression levels (patient-derived cells and LN biopsies) or FOXO regulation downstream of BCR ligation in CLL.

1.4.6 FOXOs: tumour suppressors or promotors (or both)?

FOXOs have been generally regarded as 'classical' tumour suppressors due to their ability to induce cell cycle arrest and apoptosis (344). Indeed, a seminal report by Paik *et al*. demonstrated that conditional (and inducible) deletion of *Foxo1*, *Foxo3*, and *Foxo4* in adult mice (*Mx-Cre$^+$; Foxo1/3/4$^{L/L}$*) resulted in tumour phenotypes characterised by thymic lymphomas and widespread haemangiomas, indicating that FOXOs were '*bona fide*' tumour suppressors. Importantly, this study also highlighted the potential for functional redundancy and/or developmental compensation of FOXOs as 'dual' knockouts resulted in only mild cancer phenotypes (404). However, numerous reports (as described in B cell malignancies) also indicate that FOXOs can promote tumorigenesis by upholding cellular resilience and facilitating drug resistance (344). Indeed, FOXO 'activating' mutations have been linked with disease progression in BL (401) and DLBCL (398), while FOXO upregulation has been associated with poor prognosis in AML (405) and glioblastoma (344, 406). Interestingly, evidence now suggests

that FOXOs possess ‘dual faceted’ or ‘bimodal’ roles, i.e. FOXOs can be tumour suppressors *and* promotors within the same indication in a context-dependent manner (344). In their study, Hornsveld *et al*. demonstrated that either inducible activation or depletion of FOXOs repressed cell growth and metastasis in a model of metastatic breast cancer, indicating a role for FOXOs in tumour maintenance and metastasis formation. Indeed, the authors proposed that FOXO activity is finely tuned to support cancer cell homeostasis (408). As described, this supposed ‘two-faced’ behaviour has also been observed in pre-BCR^{+} BCP-ALL (402, 403). Akin to ‘normal’ B cells, these studies indicate that FOXO activity is maintained within an optimum that promotes cellular homeostasis, as deviations outside this range have deleterious effects on cell growth and survival (344, 403). Despite the depth of knowledge about FOXOs in ‘normal’ and ‘malignant’ scenarios, the functional importance of these transcription factors (whether ‘positive’, ‘negative’ or both) in CLL disease biology remains poorly understood.

1.5 Project aims

This thesis explores mTOR kinase as a potential therapeutic target in CLL. Along these lines, the efficacy of the dual mTOR kinase inhibitor AZD8055 is addressed, alongside its potential as a partner drug for the BTK inhibitor ibrutinib. We further investigate a mechanism of action for AZD8055 as a monotherapy (and in combination with ibrutinib), which centres on AKT-dependent regulation of FOXO transcription factors. As such, we aim to define whether targeting negative regulators of FOXOs represent a promising therapeutic strategy for CLL.

I. Ascertain the effect of AZD8055 treatment on CLL cells at a molecular and functional level - exploring a potential mechanism of action.

II. Address the regulation (phosphorylation, localisation and DNA-binding activity) of FOXO transcription factors as functional consequence of BCR ligation in CLL cells.

III. Investigate the functional importance (cell growth, proliferation and survival) of FOXOs as an effector of combined mTOR kinase and BTK inhibition in CLL cell lines.

2 Materials and Methods

2.1 Materials

2.1.1 Companies/Suppliers

Company/Supplier	Address
Applied Biosystems (Thermo Fisher Scientific)	Unit 3, Fountain Dr, Inchinnan, Renfrew PA4 9RF, UK
Abcam plc	Discovery Drive Cambridge Biomedical Campus, Cambridge CB2 0AX, UK
Active Motif	Office Park Nysdam, Avenue Reine Astrid 92, B-1310 La Hulpe, BE
Agilent Technologies LDA UK Ltd (DAKO)	Cheadle Royal Business Park, Stockport, Cheshire SK8 3GR, UK
AstraZeneca PLC	1 Francis Crick Avenue, Cambridge Biomedical Campus, Cambridge CB2 0AA, UK
BD Biosciences	Binningerstrasse 94, 4123 Allschwil, CH
Biolegend UK Ltd	4B, Highgate Business Centre, 33 Greenwood Pl, Kentish Town, London NW5 1LB, UK
Bioline	Edge Business Centre, Humber Rd, London NW2 6EW, UK
Carl Zeiss Ltd.	ZEISS House Building 1030, Cambourne Business Park, Cambourne, Cambridge CB23 6DW, UK
Cell Signalling Technology Europe BV (CST)	Dellaertweg 9b, 2316 WZ Leiden, NL
Clarivate Analytics	Friars House, Blackfriars Rd, London SE1 8EZ, UK
Fisher Scientific (Thermo Fisher Scientific)	Unit 3, Fountain Dr, Inchinnan, Renfrew PA4 9RF, UK
GE Healthcare	Amersham Pl, Little Chalfont HP7 9NA, UK
Griener Bio-One Ltd.	Unit 5 Brunel Way, Stonehouse GL10 3SX
Hendley-Essex Ltd	Oakwood Hill Industrial Estate Loughton IG10 3TZ, UK
Invitrogen (Thermo Fisher Scientific)	Unit 3, Fountain Dr, Inchinnan, Renfrew PA4 9RF, UK
LI-COR Biosciences GmbH	Siemensstraße 25, 61352 Bad Homburg vor der Höhe, DE
Merck Millipore	Merck KGaA, Frankfurter Strasse 250, Darmstadt, 64293, DE
Miltenyi Biotech	Friedrich-Ebert-Straße 68, 51429 Bergisch Gladbach, DE
New England Biolabs	75-77 Knowl Piece, Hitchin SG4 0TY, UK

Company/Supplier	Address
Olympus Life Sciences (KeyMed Ltd)	KeyMed House, Stock Road, Southend-on-Sea, Essex SS2 5QH, UK
PeproTech EC Ltd.	29 Margravine Rd, Hammersmith, London W6 8LL, UK
QIAGEN Ltd	Skelton House, Lloyd Street North, Manchester M15 6SH, UK
Sakura Europe	Flemingweg 10, 2408 AV Alphen aan den Rijn, NL
Santa Cruz Biotechnology	Bergheimer Str. 89-2, 69115 Heidelberg, DE
Sartorius GmbH	Otto-Brenner-Str. 20, 37079 Götingen, DE
Scientific Lab Supplies (SLS) Ltd.	204 Main St, Coatbridge, ML5 3RB, UK
Sigma-Aldrich Co Ltd.	Second Ave, Heatherhouse Industrial Estate, Irvine KA12 8NB, UK
STEMCELL Technologies	Cambridge Research Park, 8100 Beach Dr, Waterbeach, Cambridge CB25 9TL, UK
Stratech Scientific Ltd.	Cambridge House, St Thomas' Pl, Ely CB7 4EX, UK
Thermo Fisher Scientific	Unit 3, Fountain Dr, Inchinnan, Renfrew PA4 9RF, UK

Table 2.1 - Companies/Suppliers

2.1.2 Flow Cytometry

2.1.2.1 Antibodies/dyes

Antibodies/Dyes	Cat.	Supplier
7-AAD	559925	BD Biosciences
APC Annexin V	550475	BD Biosciences
APC-Cy7 Mouse Anti-Human CD19 (SJ25C1)	557791	BD Biosciences
APC-Cy7 Mouse Anti-Human CD45 (2D1)	557833	BD Biosciences
FITC Annexin V	556419	BD Biosciences
FITC Mouse Anti-Human CD5 (UCHT2)	555352	BD Biosciences
Human TruStain Fc Receptor Blocking Solution	422302	Biolegend
Pacific Blue anti-Human CD3 (UCHT1)	300431	Biolegend
PE-Cy7 Mouse Anti-Human CD19 (SJ25C1)	557835	BD Biosciences

Table 2.2 – Flow cytometry antibodies/dyes

2.1.3 Immunofluorescence

2.1.3.1 Antibodies/dyes

Antibody	Dilution	Cat.	Supplier
Fox01 (C29H4) Rabbit mAb	1:100	2880S	CST
Alexa Fluor 488 Goat anti-Rabbit, IgG (H+L)	1:500	A11008	ThermoFisher Scientific
Alexa Fluor 594 anti-mouse/human CD45R/B220 (RA3-6B2)	1:200	103254	Biolegend
P-Akt (S473) (D9E) XP Rabbit mAb	1:400	4060S	CST

Table 2.3 – Immunofluorescence antibodies/dyes

2.1.4 Immunohistochemistry

2.1.4.1 Antibodies

Antibody	Dilution	Cat.	Supplier
Fox01 (C29H4) Rabbit mAb	1:100	2880S	CST
P-Akt (S473) (D9E) XP Rabbit mAb	1:100	4060S	CST

Table 2.4 – IHC antibodies

2.1.5 Western blotting

2.1.5.1 Antibodies

Antibody	Dilution	Dilutent	Cat.	Supplier
14-3-3 (pan) Rabbit Ab	1:1000	5 % BSA/TBST	8312S	CST
4E-BP1 (53H11) Rabbit mAb	1:1000	5 % BSA/TBST	9644S	CST
Akt (pan) (C67E7) Rabbit mAb	1:1000	5 % BSA/TBST	4691S	CST
anti-Rat IgG-HRP	1:1000	2 % Milk/TBST	sc-2006	Santa Cruz
Anti-mouse IgG, HRP-linked Antibody	1:2000	2 % Milk/TBST	7076S	CST
Anti-rabbit IgG, HRP-linked Antibody	1:2000	2 % Milk/TBST	7074S	CST
Bcl-2 (124) Mouse mAb	1:1000	5 % BSA/TBST	15071S	CST

Antibody	Dilution	Dilutent	Cat.	Supplier
Bcl-xL Rabbit Ab	1:1000	5 % BSA/TBST	2762S	CST
beta-Tubulin Rabbit Ab	1:1000	5 % BSA/TBST	2146S	CST
BIM (C34C5) Rabbit mAb	1:1000	5 % BSA/TBST	2933S	CST
Btk (D3H5) Rabbit mAb	1:1000	5 % Milk/TBST	8547S	CST
CDK2 (78B2) Rabbit mAb	1:1000	5 % BSA/TBST	2546S	CST
Cdk4 (DCS-35) Mouse mAb	1:1000	5 % Milk/TBST	sc-23896	Santa Cruz
Cyclin D1 (92G2) Rabbit mAb	1:1000	5 % BSA/TBST	2978S	CST
cyclin D2 (34B1-3) Rat mAb	1:1000	5 % Milk/TBST	sc-452	Santa Cruz
Cyclin E1 (HE12) Mouse mAb	1:1000	5 % Milk/TBST	4129S	CST
Cyclin E2 Rabbit Ab	1:1000	5 % BSA/TBST	4132S	CST
Fox01 (C29H4) Rabbit mAb	1:1000	5 % BSA/TBST	2880S	CST
Fox03a (75D8) Rabbit mAb	1:1000	5 % BSA/TBST	2497S	CST
Fox04 Rabbit Ab	1:1000	5 % BSA/TBST	9472S	CST
GAPDH (D16H11) XP Rabbit mAb	1:2000	5 % Milk/TBST	5174S	CST
GSK-3beta (D5C5Z) XP Rabbit mAb	1:1000	5 % BSA/TBST	12456S	CST
IRDye 680RD Goat-anti Rabbit IgG	1:15000	TBST	926-68071	LI-COR
IRDye 800CW Goat-anti Mouse IgG	1:15000	TBST	827-08364	LI-COR
Lamin A/C Rabbit Ab	1:1000	5 % BSA/TBST	2032S	CST
Mcl-1 Rabbit Ab	1:1000	5 % BSA/TBST	4572S	CST
Monoclonal Anti-gamma-Tubulin antibody (Mouse)	1:1000	2 % Milk/TBST	T5326	Sigma
P-4E-BP1 (T37/46) Rabbit Ab	1:1000	5 % BSA/TBST	9459S	CST
P-Akt (S473) (D9E) XP Rabbit mAb	1:1000	5 % BSA/TBST	4060S	CST
P-Akt (T308) (D25E6) XP Rabbit mAb	1:1000	5 % BSA/TBST	13038S	CST
P-Btk (Y223) (D9T6H) Rabbit mAb	1:1000	5 % Milk/TBST	87141S	CST
P-Fox01 (S256) Rabbit Ab	1:1000	5 % BSA/TBST	9461S	CST

Antibody	Dilution	Dilutent	Cat.	Supplier
P-Fox01 (T24)/Fox03a (T32) Rabbit Ab	1:1000	5 % BSA/TBST	9464S	CST
P-GSK-3beta (S9) (D85E12) XP Rabbit mAb	1:1000	5 % BSA/TBST	5558S	CST
P-p44/42 MAPK (T202/Y204) (D13.14.4E) XP Rabbit mAb	1:1000	5 % BSA/TBST	4370S	CST
P-PRAS40 (T246) (C77D7) Rabbit mAb	1:1000	5 % BSA/TBST	2997S	CST
P-Rb (S780) Rabbit mAb	1:1000	5 % BSA/TBST	9307S	CST
P-Rb (S807/811) Rabbit mAb	1:1000	5 % BSA/TBST	9308S	CST
P-S6 Ribsomal Protein (S235/236) (D57.2.2E) XP Rabbit mAb	1:1000	5 % BSA/TBST	4858S	CST
p21 Waf1/Cip1 (12D1)	1:1000	5 % BSA/TBST	2947S	CST
p44/42 MAPK (Erk1/2) (137F5) Rabbit mAb	1:1000	5 % BSA/TBST	46953S	CST
PARP (46D11) Rabbit mAb	1:1000	5 % Milk/TBST	9532S	CST
PRAS40 (D23C7) XP Rabbit mAb	1:1000	5 % BSA/TBST	2691S	CST
Purified Mouse Anti-p27 [Kip1]	1:2000	5 % Milk/TBST	610241	BD
Rb (4H1) Mouse mAb	1:2000	5 % Milk/TBST	9309S	CST
S6 Ribsomal Protein (54D2) Mouse mAb	1:1000	5 % BSA/TBST	2317S	CST
Survivin (71G4B7) Rabbit mAb	1:1000	5 % BSA/TBST	2808S	CST

Table 2.5 – Western blot antibodies

2.1.6 RT-qPCR

2.1.6.1 TaqMan assays

Target	Assay ID	Supplier
BBC3	Hs00248075_m1	ThermoFisher Scientific
BCL2L1	Hs00236329_m1	ThermoFisher Scientific
BCL2L11	Hs00197982_m1	ThermoFisher Scientific
CCND1	Hs00765553_m1	ThermoFisher Scientific
CCND2	Hs00153380_m1	ThermoFisher Scientific
CCND3	Hs01017690_g1	ThermoFisher Scientific
CCNG2	Hs00171119_m1	ThermoFisher Scientific
CDKN1A	Hs00355782_m1	ThermoFisher Scientific

Target	Assay ID	Supplier
CDKN1B	Hs01597588_m1	ThermoFisher Scientific
FOXO1	Hs01054576_m1	ThermoFisher Scientific
FOXO3	Hs00818121_m1	ThermoFisher Scientific
FOXO4	Hs00936217_g1	ThermoFisher Scientific
GADD45A	Hs00169255_m1	ThermoFisher Scientific
GUSB	Hs00939627_m1	ThermoFisher Scientific
IGF1R	Hs00609566_m1	ThermoFisher Scientific
MCL1	Hs01050896_m1	ThermoFisher Scientific
SESN3	Hs00914870_m1	ThermoFisher Scientific
SOD2	Hs00167309_m1	ThermoFisher Scientific

Table 2.6 - TaqMan assays for RT-qPCR

2.2 Methods

This section will provide a broad description of the methods used to generate the data represented within this thesis. Please refer section 2.1 ‘Materials’, for specific information regarding suppliers, antibodies and TaqMan assays.

2.2.1 General Tissue Culture

2.2.1.1 Cell culture conditions

Cell culture methods were executed using sterile technique in a laminar flow hood. Cell cultures were maintained in a humidified incubator at 37 °C in 5 % carbon dioxide (CO_2). procedure

2.2.1.2 Cell culture media

Cell culture media containing supplements are herein referred to as ‘complete’ media. Unless otherwise stated, ‘complete RPMI’ consists of RPMI-1640 cell culture medium containing 10% FBS, 50 U/mL penicillin, 50 mg/mL streptomycin (1 % Pen Strep) and 2 mM L-glutamine (1 % L-glutamine) (ThermoFisher Scientific). ‘Complete DMEM’ consists of DMEM cell culture medium containing 10% FBS, 50 U/mL penicillin, 50 mg/mL streptomycin (1 % Pen Strep) and 2 mM L-glutamine (1 % L-glutamine) (ThermoFisher Scientific).

2.2.1.3 Primary CLL cells

Ethical approval was granted from the West of Scotland Research Ethics Committee, NHS Greater Glasgow and Clyde, UK. PB samples were drawn from (clinically-diagnosed) CLL patients after written informed consent. Patients were either treatment naïve or had not received therapy in the previous 3 months, unless otherwise stated. Peripheral blood mononuclear cells (PBMCs) from CLL patients were isolated by density gradient centrifugation using Histopaque-1077 Hybri-Max (Histopaque) (Sigma) according to the manufacturer's instructions. Briefly, PB samples (EDTA blood collection tubes (BD)) from CLL patients were diluted 1:1 with RT CLL wash buffer (PBS, 0.5 % FBS, 2 mM EDTA). Histopaque was aliquoted into reaction tubes (10 mL Histopaque into a 50 mL reaction tube for 30 mL PB sample or 4mL Histopaque into a 15 mL reaction tube for 10 mL PB sample). The sample was carefully layered on top of the Histopaque layer and centrifuged at 300*g* for 30 min at RT. Importantly, the temperature of the centrifuge was maintained at RT prior to centrifugation as differences in temperature would impact the enrichment of mononuclear cells. Moreover, it is imperative that the brake on the centrifuge is switched off to prevent disruption of the liquid interface as a result of sudden breaking. The white 'buffy' layer of mononuclear cells between the plasma:histopaque interface was harvested and transferred into a fresh 50 mL reaction tube (Greiner Bio-One). The cell suspension was washed with 4 volumes of CLL wash buffer and centrifuged at 300*g* for 10 min at RT. The cell pellet was resuspended with 10 mL CLL wash buffer and centrifuged at 300*g* for 10 min at RT. The pellet was then resuspended in a volume of CLL wash buffer (<40 mL) (418). The cells were counted before proceeding to flow cytometry to check the purity of CLL cells. PBMCs isolated from CLL patients were >90 % $CD19^+$ $CD5^+$ cells as determined by flow cytometry.

PB samples from CLL patients with low leukocyte counts, defined as <40 $x10^9$ leukocytes/L, were processed using the RosetteSep human B-cell enrichment cocktail (STEMCELL Technologies) according to the manufacturer's instructions. Briefly, the PB sample was transferred to a 50 mL reaction tube and 50 μL of the RosetteSep cocktail was added per mL of blood and incubated for 20 min at RT. The sample was then diluted 1:1 with RT CLL wash buffer. The protocol was then followed according to the Histopaque procedure described earlier. Following

enrichment, B cell purity was >90 % as determined by flow cytometry. Freshly isolated primary CLL cells were cultured at 1 x10^7 cells/mL in complete RPMI or cryopreserved (section 2.2.1.6).

Information about the primary samples used within this thesis, including patient pseudonym and prior treatment, can be found in Table 2.7. Of note, prognostic biomarkers such as Binet stage, ZAP-70 status, *IGVH* (*IGVH* mut) and *TP53* (*TP53* mut) mutational status and cytogenetic abnormalities (cytogenetics) are included. Hyphens (-) indicate prognostic information that was not assessed in the clinic. Moreover, whilst multiple cytogenetic alterations exist in CLL disease biology, not all are assessed in the clinic. For this reason, a patient with 'no del(11q)/del(17p)' indicates that del(11q) or del(17p) were not detected. Therefore, it is possible that undetected cytogenetic abnormalities may exist in the patient.

Patient ID	**Tx (Y/N)**	**Sex (M/F)**	**Binet**	**ZAP-70**	***IGVH* mut**	***TP53* mut (Y/N)**	**Cytogenetics**
CLL8	N	F	A	neg	U-CLL	-	del(11q)
CLL9	Y	F	B	neg	-	-	-
CLL18	Y	F	B	pos	U-CLL	Y	del(11q)
CLL28	N	F	A	pos	-	-	del(17p)
CLL32	N	F	C	pos	U-CLL	-	no del(11q)/del(17p)
CLL44	N	F	A	neg	M-CLL	-	no del(11q)/del(17p)
CLL46	N	F	A	pos	M-CLL	-	no del(11q)/del(17p)
CLL57	N	M	C	pos	-	-	no del(11q)/del(17p)
CLL69	Y	M	A	pos	U-CLL	-	no del(11q)/del(17p)
CLL72	N	F	A	pos	-	-	no del(11q)/del(17p)
CLL80	N	M	C	neg	-	-	del(17p)
CLL84	Y	M	B	neg	U-CLL	-	del(11q)
CLL85	Y	F	A	-	-	-	del(11q)
CLL90	Y	F	B	pos	-	-	no del(11q)/del(17p)
CLL93	Y	M	C	pos	-	-	del(17p)
CLL95	Y	M	B	-	-	N	no del(11q)/del(17p)
CLL109	N	M	-	-	-	-	del(17p)
CLL113	Y	F	C	pos	-	-	del(17p)

Patient ID	Tx (Y/N)	Sex (M/F)	Binet	ZAP-70	*IGVH* mut	*TP53* mut (Y/N)	Cytogenetics
CLL116	N	M	A	pos	-	-	no del(11q)/del(17p)
CLL118	N	M	A	pos	-	-	del(11q)
CLL119	N	F	B	-	-	-	del(17p)
CLL123	N	M	A	-	-	-	no del(11q)/del(17p)
CLL126	N	M	B	pos	-	-	no del(11q)/del(17p)
CLL132	N	F	B	pos	-	-	del(17p)
CLL138	Y	F	A	pos	-	-	no del(11q)/del(17p)
CLL139	N	F	-	pos	-	-	del(11q)
CLL142	Y	F	B	pos	-	-	no del(11q)/del(17p)
CLL143	Y	F	C	pos	-	-	del(11q)
CLL144	N	M	B	pos	-	-	del(17p)
CLL147	N	M	C	pos	-	-	no del(11q)/del(17p)
CLL148	Y	M	B	pos	-	-	del(11q)
CLL149	N	M	A	-	-	-	del(17p)
CLL150	N	M	A	pos	-	-	no del(11q)/del(17p)
CLL151	N	M	B	-	-	-	del(11q)
CLL155	Y	M	B	-	-	-	del(11q)
CLL157	N	M	-	-	-	-	del(11q)
CLL165	N	M	C	-	-	-	del(11q)
CLL168	N	M	B	-	-	-	Tri12 del(13q)
CLL169	N	F	C	-	-	-	del(11q)
CLL170	Y	F	-	-	-	-	-
CLL172	N	M	-	-	-	-	no del(11q)/del(17p)
CLL184	N	M	-	-	-	-	no del(11q)/del(17p)

Table 2.7 - CLL patients (including clinical staging and prognostic stratification)
Tx = prior therapy (yes or no); Binet Stage (A, B or C); ZAP-70 status (positive or negative); *IGVH* mutational status (U- or M-CLL); *TP53* somatic mutation (yes or no); cytogenetics (as explained); Hyphens (-) indicate prognostic information that was not assessed in the clinic

2.2.1.4 Buffy coat samples

'Buffy coats' provide an enriched source of leukocytes enabling isolation of large numbers of immune cells. Buffy coat samples from healthy individuals were obtained from the Scottish National Blood Transfusion Service (SNBTS) following volunteer blood donations. To select for B cells, we adopted the RosetteSep human B-cell enrichment cocktail or human CD19 Microbeads (Miltenyi), which

provide a method for negative or positive selection of $CD19^+$ B cells, respectively.

The protocol for the RosetteSep human B-cell enrichment cocktail was followed according to the manufacturer's instructions for buffy coat samples. Of note, it was important that the concentration of nucleated cells did not exceed 5 $x10^7$ cells/mL. Briefly, 50 μL of the RosetteSep cocktail was added per mL of buffy coat suspension and incubated for 20 min at RT. The sample was then diluted with two volumes of PBS and gently mixed. The sample was then layered on an appropriate volume of Histopaque and centrifuged for 20 min at 1200*g* at RT with the break off. The enriched cells were removed from the histopaque:plasma interface and washed twice with PBS, as per the protocol described earlier.

The protocol for human CD19 Microbeads using MACS separation technology was followed according to the manufacturer's instructions. Importantly, cells were kept cold throughout the procedure and solutions were pre-cooled. In brief, buffy coat samples underwent density gradient centrifugation with Histopaque according the manufacturer's instructions. The cell suspension was counted to adjust the concentration of cells to meet the requirements of the protocol. Before commencing magnetic labelling, the cell suspension was passed through a 30 μm cell strainer (Sartorius) to create a single-cell suspension. At this point, 5 $x10^5$ cells were removed from the suspension as a pre-enrichment control and transferred to a FACS tube (BD Biosciences). The remaining cells were centrifuged at 300*g* for 10 min and resuspended at a concentration of 1 $x10^7$ cells/80 μL PBS. 20 μL of CD19 Microbeads was added per 1 $x10^7$ cells and incubated for 15 min at 4 °C. Following incubation with the microbeads, the cells were washed with 2 mL PBS per 1 $x10^7$ cells. After a second centrifugation step, up to 1 $x10^9$ cells were resuspended in 3 mL PBS. The cell suspension subsequently underwent magnetic separation using 'LS' MACS columns (Miltenyi) placed in the magnetic field of a suitable MACS Separator (Miltenyi). The protocol for MACS separation was followed according to the manufacturer's instructions.

Following enrichment, B cell purity was >90 % as determined by flow cytometry. Cell pellets of enriched B cells were generated and used immediately or 'snap frozen' until further use. B cells derived from healthy donors are herein referred to as 'healthy donor B cells' or 'healthy $CD19^+$'.

2.2.1.5 Cell lines

As a general rule, the procedure for maintaining cell lines were performed in accordance with ATCC or DSMZ guidelines. Where 'working' stocks of cell lines existed, a new vial was thawed once the passage number had reached 20.

Cell line	Origin	Culture conditions	Details
MEC-1	EBV-transformed PB-derived CLL cells from a male (61 years; 1993) patient with evidence of prolymphocytoid transformation. MEC-1 cells are $CD5^-$ $CD19^+$ and possess del(17p) (409).	**DMEM (10% FBS; 1% P/S; 1% L-glutamine);** Maintain at about 0.5-2.0 x10^6 cells/ml; optimal split ratio 1:3 every 2-3 days; Culture upright in T75^2 culture flasks (409).	The MEC-1 CLL cell line was a gift from Dr Joseph Slupsky (University of Liverpool, UK)
HG-3	Transformed PB-derived CLL cells from a male (70 years; 1998) patient. The patient was Rai stage II at diagnosis. HG-3 cells are $CD5^+$ $CD19^+$ and possess del(13q) (410).	**RPMI (10% FBS; 1% P/S; 1% L-glutamine);** Maintained at 0.5-1 x 10^6 cells/ml; optimal split ratio 1:3 every 2-3 days; Culture upright in T75^2 culture flasks (410).	The HG-3 CLL cell line was a gift from Dr Joseph Slupsky (University of Liverpool, UK)
NT-L	Mouse fibroblast L cells were derived from subcutaneous connective tissue and represent a suitable transfection host (411).	**RPMI (10% FBS; 1% P/S; 1% L-glutamine);** Passage cells at 70 % confluency; optimal split ratio 1:4 to 1:10 every 2-3 days; Culture in T75^2 culture flasks (411).	The NT-L cell line was a gift from Prof J. Gordon (University of Birmingham, UK)

Cell line	Origin	Culture conditions	Details
CD40L	Mouse fibroblast L cells (as above) stably transfected with CD154 (CD40L).	**RPMI (10% FBS; 1% P/S; 1% L-glutamine);** Passage cells at 70 % confluency; optimal split ratio 1:4 to 1:10 every 2-3 days; Culture in T75^2 culture flasks.	The CD40L cell line was a gift from Prof J. Gordon (University of Birmingham, UK)
HEK293T (293T)	The HEK293T cell line is version of human embryonic kidney 293 cells, containing the SV40 T-antigen (412).	**DMEM (10% FBS; 1% P/S; 1% L-glutamine);** Seed out at ~1-3 x 10^6 cells; Passage cells at 70 % confluency; optimal split ratio 1:3 to 1:8 every 2-3 days; Culture in T75^2 culture flasks (412).	

Table 2.8 - Cell lines (origin, culture conditions and further details)

2.2.1.6 Cryopreservation of cells

Freshly isolated PB CLL cells that were not directly required for experimentation were cryopreserved for long-term storage in our CLL cell bank. In brief, primary CLL cell suspensions were counted and resuspended at a concentration of 5 x10^7–1 x10^8 cells/mL in cell freezing solution (FBS, 10 % DMSO). The cells were then aliquoted into cryovials (Greiner Bio-One) and quickly transferred to a Mr. Frosty™ freezing container (ThermoFisher Scientific), which was subsequently placed at -80 °C to slowly freeze the cells at a controlled rate of 1 °C/min. After overnight (O/N) storage at -80 °C, the cells were transferred to liquid nitrogen storage. Cryopreservation of cell lines was performed to create 'master' and 'working' stocks to ensure the continual supply of back-up cells. Importantly, cells should only be cryopreserved at the maximum growth rate or almost at confluency.

As suspension cells, MEC-1 and HG-3 cells were cryopreserved using similar methods to primary CLL cells. Following an initial period of expansion of one 'master' stock vial, the cells were inspected for contamination, counted and subsequently resuspended in cell freezing solution at a concentration of 4–8 x10^6

cells/mL to create multiple new 'working' stocks. The cells were then slowly frozen in accordance with the protocol for primary CLL cells.

As with the suspension cultures, adherent NT-L, CD40L and HEK293T cells were expanded to create multiple working stocks. Once the cells had reached 70–80 % confluency, the cells were washed twice with 10 mL PBS (adding gently to avoid disturbing the cell layer). The cells were then detached using 1 mL pre-warmed Trypsin-EDTA (0.5 %; Thermo Fisher Scientific) for <3 min, ensuring gentle dissociation to minimise damage to the cells. The cells were viewed under a microscope to observe detachment. Once >90 % of the cells were detached, 9 mL complete medium was added to the cell suspension to establish a viable cell count. The cells were subsequently resuspended in cell freezing solution at a concentration of 4–8 x10^6 cells/mL and slowly frozen as per the standard protocol.

2.2.1.7 Thawing cryopreserved cells

Frozen primary CLL cells were thawed quickly (<2 min) in a 37 °C water bath and transferred to a 15 mL reaction tube (one vial per reaction tube) (Greiner Bio-One). The cells were diluted slowly (dropwise) over 10 min using 10 mL pre-warmed 'DAMP' solution (PBS, 10 U/mL DNase I, 1 % HSA, 2.5 mM Magnesium Chloride ($MgCl_2$), 8.2 mM Tri-Sodium Citrate ($Na_3C_6H_5O_7$)). The cell suspension was centrifuged at 300*g* and then resuspended in 10 mL complete RPMI. After a final centrifugation step, the cells were resuspended in complete RPMI at a concentration of 1 x 10^7 cells/mL and cultured O/N to recover prior to beginning an experiment. Following recovery, a viable cell count was obtained. Of note, primary CLL cells were cultured upright in an appropriately sized culture flask (Greiner Bio-One).

Cell lines were thawed quickly in a 37 °C water bath and transferred to a 15 mL reaction tube. The cells were diluted slowly (dropwise) using 10 mL pre-warmed complete medium. Following centrifugation at 300*g*, the cells were resuspended in 10 mL complete medium and transferred to an appropriately sized culture flask. The cells were observed daily to monitor cell recovery before commencing the first passage. Experiments commenced only when the cells looked healthy

and had reached at least the second passage. Of note, when necessary, cell lines were expanded to create 'working' stocks from 'master' stocks of cell lines.

2.2.1.8 Drug treatments

AZD8055, AZD2014, ibrutinib, rapamycin and AS1842856 were solubilised in DMSO (Sigma) to make 10 mM stock solutions. AZD5363 was solubilised in DMSO to make a 100 mM stock solution. Stock solutions were stored in 10 μL aliquots for up to 2 years at -80 °C. Once thawed, aliquots were stored at 4 °C for up to a week. Unless otherwise stated, the standard working concentration of each drug used in experiments was as follows:

Drug	Stock concentration (mM)	Working concentration (μM)
AZD8055	10	0.1
AZD2014	10	0.5
Ibrutinib	10	1
Rapamycin	10	0.01
AS1842856	10	0.03
AZD5363	100	1

Table 2.9 - Drugs (stock solutions and working concentrations). All drugs purchased from Stratech Scientific.

Working concentrations were made by diluting stock solutions in appropriate cell culture media, depending on the cells being examined. DMSO was used as a vehicle control (vehicle) or 'no drug control' (NDC) in drug treatments. Unless otherwise stated, cells were incubated with the appropriate working concentration of drug or vehicle for the entirety of the treatment period.

Prior to F(ab')$_2$ stimulations (section 2.2.1.9), cells were 'pre-treated' with drug for 30 min. In NT-L and CD40L/IL-4 co-cultures (with the exception of the primary CLL cell proliferation assay), primary CLL cells were co-cultured O/N with the stromal cells before starting the drug treatment for the indicated time period (section 2.2.1.10).

2.2.1.9 F(ab')$_2$ stimulation

F(ab')$_2$ fragments (Stratech Scientific) are polyclonal IgM-specific secondary antibodies generated by pepsin digestion of IgG antibodies (413). In context, the

use of F(ab')$_2$ fragments represent an established method of stimulating and initiating antigen-dependent BCR signalling in CLL cells (213). F(ab')$_2$ fragments were solubilised in a sterile-filtered liquid at a concentration of 1.3 mg/mL and stored for up to a year at 4 °C. Depending on the application, 1 x10^7/mL primary CLL cells or 1 x10^6/mL MEC-1 cells were seeded into tissue culture plates and stimulated with 10 μg/mL F(ab')$_2$ fragments diluted directly into the culture medium for the indicated time period. Following the indicated stimulation period, the cells were harvested and processed for downstream applications.

2.2.1.10 Short-term NT-L and CD40L/IL-4 co-culture systems

NT-L and CD40L cells are immortalised stromal cells utilised in an established *in vitro* co-culture system designed to mimic the CLL-T cell interactions within the CLL-TME (186).

Depending on the downstream application, 3 x10^5/mL NT-L or CD40L cells were seeded into cell culture plates and left for 2 h to adhere. Freshly isolated or thawed cryopreserved CLL cells were counted and subsequently added to the stromal cells at a ratio of 25:1 (CLL cell:stromal cell) in complete RPMI. For CD40L co-cultures, complete growth medium was supplemented with 10 ng/mL interleukin-4 (IL-4) diluted directly into the culture medium. This co-culture system is commonly known as the CD40L/IL-4 system. Recombinant human IL-4 (PeproTech) was reconstituted in dH_2O to make a 10 μg/mL stock solution and stored in 10 μL aliquots for up to 3 months at -80 °C. The co-cultures were incubated O/N prior to treating the cells with drug or vehicle control. The length of incubation refers to the drug treatment period.

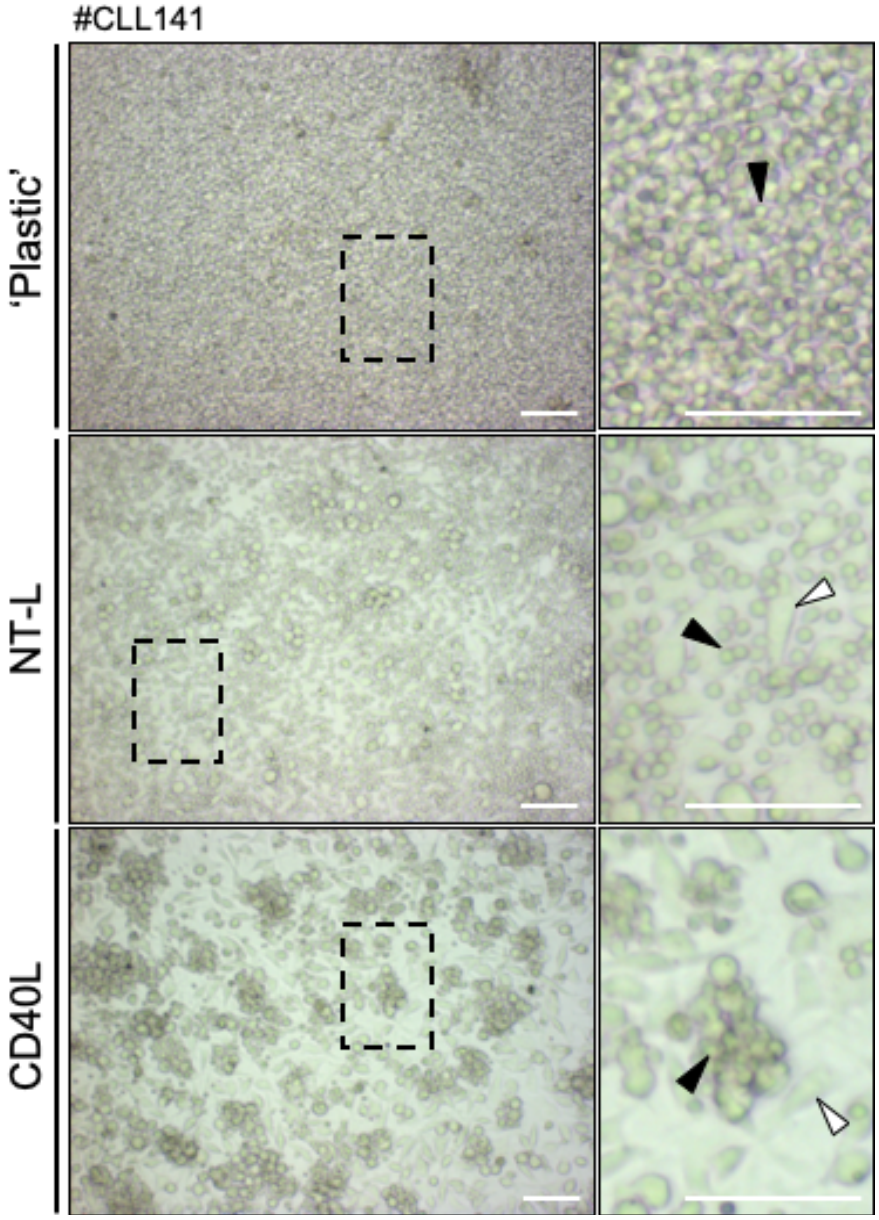

Figure 2.1 – CLL cells co-cultured with NT-L / CD40L
Representative micrograph images (20x) of 'plastic' (top panel), NT-L (middle panel) and CD40L (bottom panel) co-cultures after 48 h incubation. CLL patient pseudonym CLL141. Dashed boxes (left panel) represent a region of interest (ROI) within the field of view that have been scaled (right panel) to more easily identify primary CLL cells (black arrows) and NT-L / CD40L stromal cells (white arrows). Of note, primary CLL cells form close interactions with CD40L cells, demonstrated as large 'clumps' surrounding CD40L cells. Scale bar = 50 μm.

2.2.2 Flow cytometry

The working concentration of fluorochrome-linked antibodies and dyes used in flow cytometry panels were determined in accordance with the manufacturer's recommendations. Data generated by flow cytometry were acquired on a FACSCanto II analyser (BD Biosciences) connected to FACSDiva software (BD Biosciences). Data analysis was performed with FlowJo v10 software (Tree Star, Inc.).

2.2.2.1 CLL patient samples

On receipt of a PB CLL sample, 30 µL whole blood was transferred to a FACS tube under sterile conditions and stained in the presence of Human TruStain Fc receptor block (Biolegend) with the 'primary CLL cell' panel for 30 min at 4 °C, protected from light. Importantly, unstained and 'fluorescence minus one' (FMO) controls were run alongside the test samples.

Component	Volume (uL)/Test
Human TruStain Fc Receptor Blocking Solution	1
APC-Cy7 Mouse Anti-Human CD45	2.5
FITC Mouse Anti-Human CD5	2.5
PE-Cy7 Mouse Anti-Human CD19 (clone SJ25C1)	2.5
PBS to a final volume of 100 uL	

Table 2.10 - Primary CLL FACS panel

Immediately after incubation with the antibody panel, 500 µL EasyLyse™ erythrocyte-lysing reagent (DAKO) was added to the blood and mixed immediately. The sample was incubated with the lysing reagent for 10-15 min at RT prior to acquisition on the flow cytometer. Of note, if the samples were not analysed within 45 min, they were placed on ice and acquired within 2 h.

Following density gradient centrifugation of a PB CLL sample (section 2.2.1.3), the lymphocyte fraction was counted and 1 x10^6 viable cells were transferred to a FACS tube. Following centrifugation at 300*g* for 5 min at RT, the cell pellet was resuspended in 100 µL PBS and stained in the presence of Human TruStain Fc receptor block with the 'primary CLL cell panel' for 30 min at 4 °C, protected from light. Of note, unstained were run alongside the test samples. After the incubation period, the cells underwent a final washing (1 mL PBS) and centrifugation (300*g* for 5 min at RT) step. The cell pellet was then resuspended in 400 µL PBS and subsequently acquired on the flow cytometer.

For both methods, the percentage of $CD19^+$ $CD5^+$ cells in patient CLL samples were determined by flow cytometry. A $CD45^+$ population composed of >90 % $CD19^+$ $CD5^+$ cells was considered acceptable.

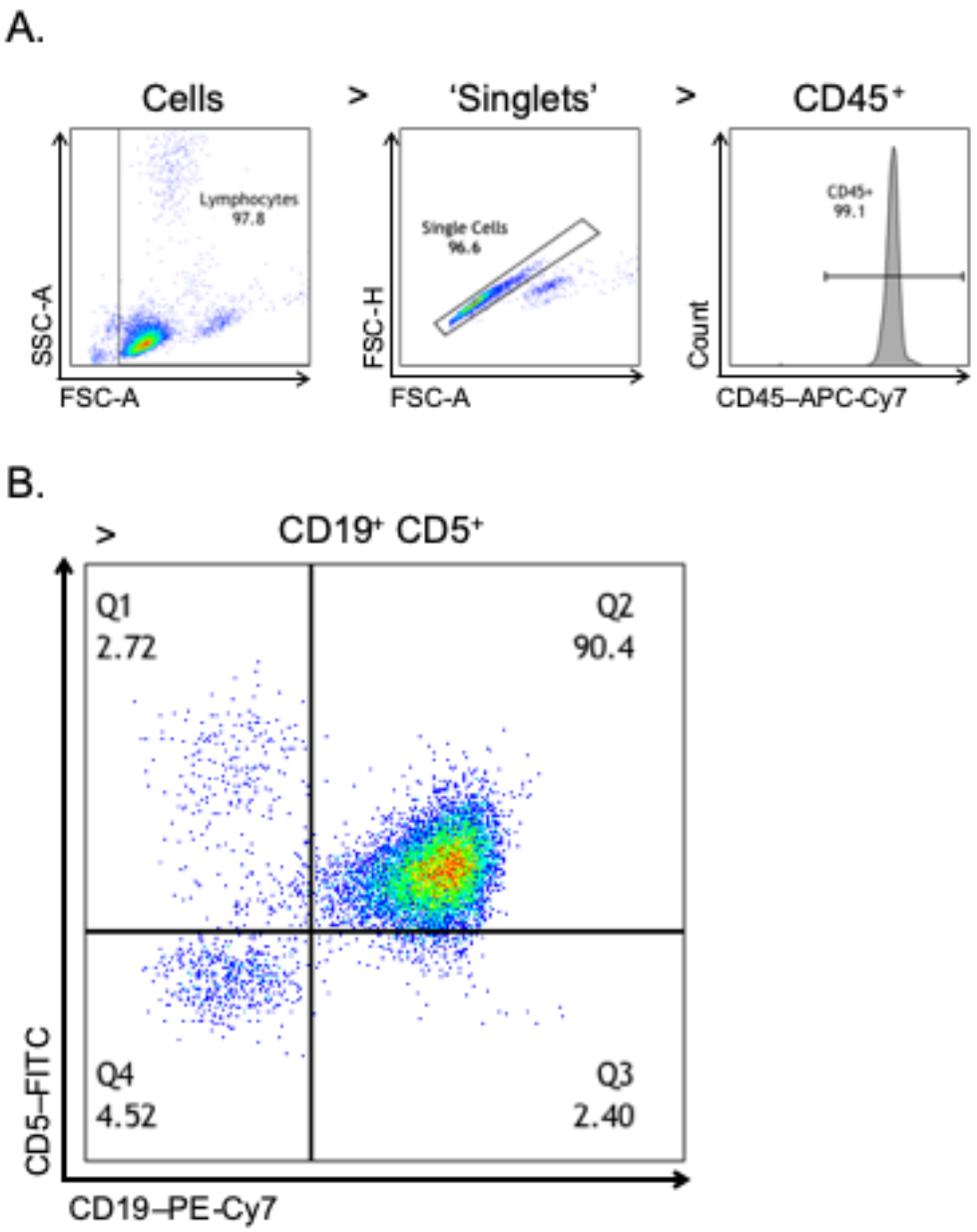

Figure 2.2 – Gating strategy for CLL patient-derived PBMCs
After density gradient centrifugation, PBMCs from CLL patients were stained with the 'primary CLL cell panel'. The following describes the gating strategy performed to identify $CD19^+$ $CD5^+$ CLL cells by flow cytometry. **(A)** Forward scatter (FSC) and side scatter (SSC) were used to gate all cells and exclude dead cells - including the lymphocyte population (left panel) - and subsequently selected for single cell events or 'singlets' (middle panel). Further analysis was performed to select for $CD45^+$ cells using a univariate histogram (right panel). **(B)** A bivariate histogram was then used to identify $CD19^+$ $CD5^+$ cells from the $CD45^+$ population. PBMCs derived from CLL patients were typically >90 % $CD19^+$ $CD5^+$ cells.

2.2.2.2 Buffy coat samples

Following B cell selection using the RosetteSep human B-cell enrichment cocktail or human CD19 Microbeads (section 2.2.1.4), the cell suspension was counted and 5 $x10^5$ cells were transferred to FACS tubes. The cells were then centrifuged at 300*g* for 5 min and the resultant cell pellet was washed with 1 mL PBS. After another centrifugation step, the cell pellet was resuspended in 100 μL PBS and

stained in the presence of Human TruStain Fc receptor block with an anti-CD19 antibody for 30 min at 4 °C, protected from light (Table 2.11). Following the incubation period, the cells were washed with 1 mL PBS and centrifuged at 300*g* for 5 min. The cells were then resuspended in 400 μL PBS and analysed on the flow cytometer. B cell purity was determined by the percentage of $CD19^+$ cells. A population >90 % $CD19^+$ cells was considered acceptable. The remaining cells were pelleted, snap-frozen and stored at -80 °C.

Component	Volume (uL)/Test
Human TruStain Fc Receptor Blocking Solution	1
APC-Cy7 Mouse Anti-Human CD19	2.5
PBS to a final volume of 100 uL	

Table 2.11 - 'Buffy coat' FACS panel

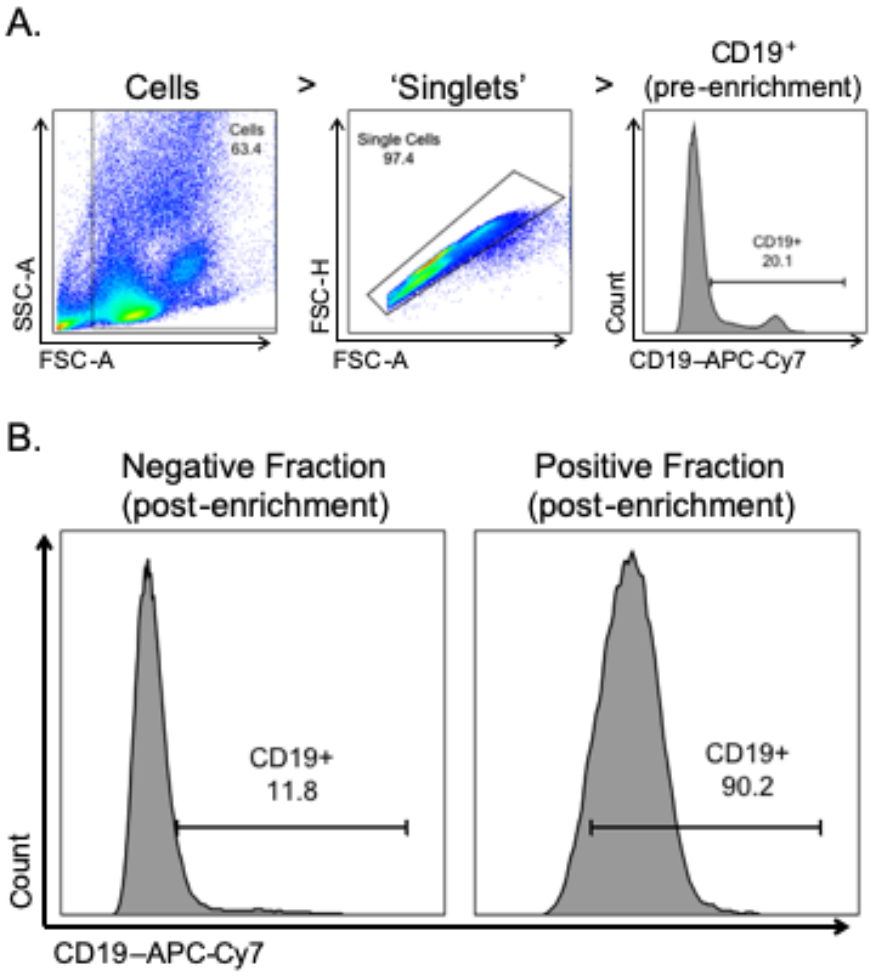

Figure 2.3 - Gating strategy for isolated 'buffy coat' samples
$CD19^+$ B cells were negatively or positively selected from buffy coat samples using the RosetteSep human B-cell enrichment cocktail or CD19 Microbeads, respectively. The following describes the

gating strategy performed to identify $CD19^+$ B cells using CD19 Microbeads (MACS separation technology) by flow cytometry. **(A)** FSC and SSC were used to gate all cells - including the lymphocyte population (left panel) - and subsequently selected for singlets (middle panel). Following density gradient centrifugation, ~5 $x10^5$ cells were removed from the cell suspension to assess the percentage of $CD19^+$ cells prior to CD19 enrichment (right panel). **(B)** After enrichment, the percentage of $CD19^+$ cells were examined using the 'negative' (flow-through) and 'positive' ($CD19^+$) fractions generated from MACS separation. Following CD19 enrichment, the positive fraction cell was typically >90 % $CD19^+$ cells.

2.2.2.3 Apoptosis assay

Dual Annexin V/7-AAD staining enables the discrimination of viable (Annexin V^{neg}, 7-AAD^{neg}), early apoptotic (Annexin V^{pos}, 7-AAD^{neg}) or late apoptotic (Annexin V^{pos}, 7-AAD^{pos}) cells following treatment and/or stimulation.

Unless otherwise stated, Annexin V/7-AAD staining was performed following drug treatments for a defined time period. After the treatment period had finished, cells were harvested and transferred to FACS tubes. The cells were then washed 1 mL HBSS (ThermoFisher Scientific) and centrifuged at 300*g* for 5 min. Of note, HBSS must contain calcium as it is required for the binding of Annexin V to phosphatidylserine (PS) molecules. After another centrifugation step, the cells were resuspended in 100 μL HBSS and stained at a concentration of 5 $x10^5$ cells/100 μL HBSS with Annexin V/7-AAD (Table 2.12). The cells were incubated for 15 min at RT, protected from light. Following incubation, 400 μL HBSS was added to each FACS tube prior to analysis. Of note, a further centrifugation step after staining was omitted as 7-AAD forms complexes in equilibrium with DNA.

Primary CLL cells / MEC-1 / HG-3	
Component	**Volume (uL)/Test**
FITC/APC Annexin V	2.5
7-AAD	2.5
HBSS to a final volume of 100 uL	

Table 2.12 - Apoptosis FACS panel (primary CLL, MEC-1 and HG-3 cells)

Annexin V/7-AAD staining was also performed to assess cell viability following CLL cell co-culture with NT-L/CD40L cells. To discriminate between primary CLL cells and stromal cells inadvertently harvested at the end of the treatment

period, cells were stained with a human anti-CD45 antibody prior to commencing Annexin V/7-AAD staining. In brief, cells were resuspended in 100 μL HBSS and stained in the presence of Human TruStain Fc receptor block with an anti-CD45 antibody (Table 2.13) for 30 min at 4 °C, protected from light. Following the incubation period, the cells were washed with 1 mL HBSS and centrifuged at 300*g* for 5 min. The cells were resuspended in 100 μL HBSS and subsequently underwent the Annexin V/7-AAD staining protocol described earlier.

NT-L / CD40L CLL co-cultures	
Component	**Volume (uL)/Test**
Human TruStain Fc Receptor Blocking Solution	1
APC-Cy7 Mouse Anti-Human CD45	2.5
HBSS to a final volume of 100 uL **==> 30 min incubation at 4 'C, followed by washing step**	
FITC Annexin V	2.5
7-AAD	2.5
HBSS to a final volume of 100 uL	

Table 2.13 - Apoptosis FACS panel (NT-L / CD40L CLL co-cultures)

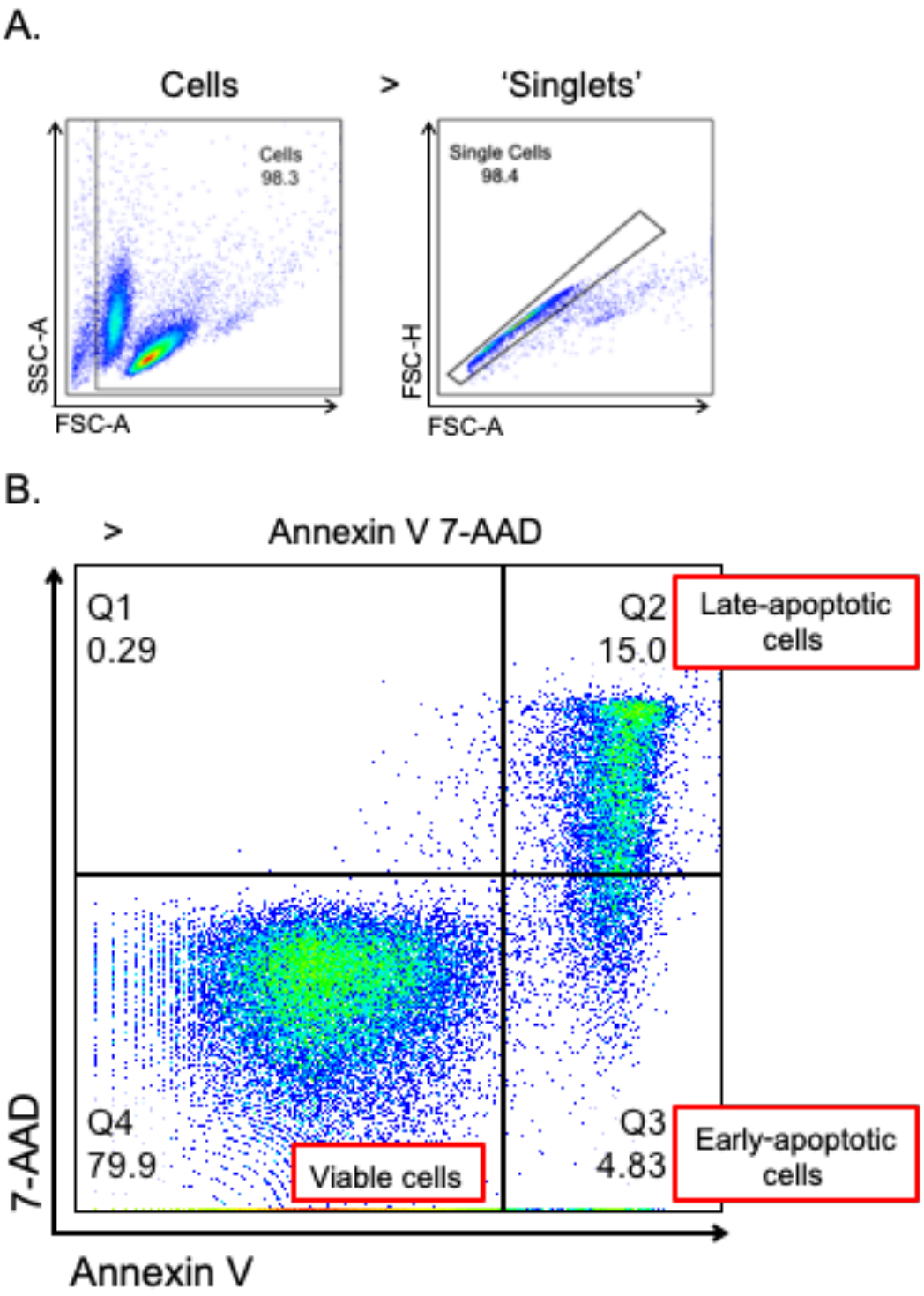

Figure 2.4 - Gating strategy for Annexin V/7-AAD staining
Following drug treatment and/or stimulation, primary CLL cells or cell lines were stained with Annexin V/7-AAD staining to assess cell viability. The following describes the gating strategy performed to discriminate between viable and non-viable cells by flow cytometry. **(A)** FSC and SSC were used to gate both viable/non-viable cells (left panel) and subsequently selected for singlets (right panel). **(B)** A bivariate histogram was then used to identify intact or viable cells (Annexin V negative, 7-AAD negative), early apoptotic (Annexin V positive, 7-AAD negative) and late apoptotic cells (Annexin V positive, 7-AAD positive). The percentages of the aforementioned populations were examined using a quadrant gate.

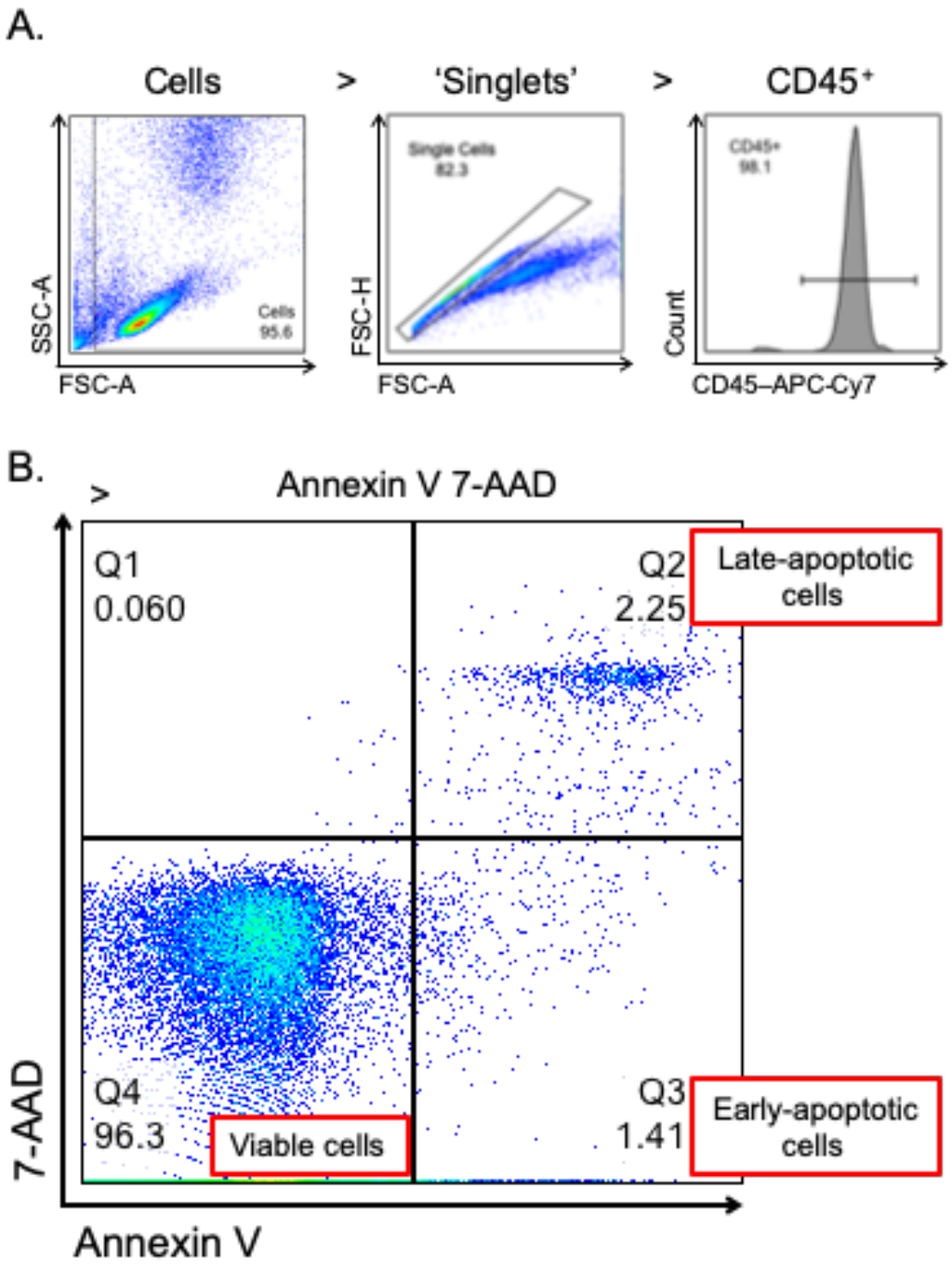

Figure 2.5 - Gating strategy for Annexin V/7-AAD staining (NT-L / CD40L co-cultures)
Annexin V/7-AAD staining was performed following drug treatments and/or stimulation. Assessing CLL cell viability after incubation with NT-L or CD40L cells requires discrimination between primary CLL cells (human) and stromal cells (mouse). The following describes the gating strategy for Annexin V 7-AAD staining after NT-L / CD40L co-cultures by flow cytometry. **(A)** FSC and SSC were used to gate all viable cells (including CLL and stromal cells) (left panel) and subsequently selected for singlets (middle panel). Further analysis was performed to distinguish between CLL cells and mouse stromal cells using a human-specific anti-CD45 antibody. $CD45^+$ cells were selected using a univariate histogram (right panel). **(B)** A bivariate histogram was then used to identify intact or viable cells (Annexin V negative, 7-AAD negative), early apoptotic (Annexin V positive, 7-AAD negative) and late apoptotic cells (Annexin V positive, 7-AAD positive). The percentages of the aforementioned populations were examined using a quadrant gate.

2.2.2.4 Cell cycle analysis by propidium Iodide (PI) staining

Cell cycle analysis by PI staining was performed to quantify the DNA content of cells in response to cell stimulation and/or drug treatment. Following cell stimulation and/or drug treatment, 1 x10^6 cells/mL were harvested, transferred to FACS tubes and washed twice in 1 mL ice-cold PBS. The cells were then fixed by adding 1 mL ice-cold 80 % ethanol (Sigma) dropwise (1 min) to the cell pellet while vortexing. Of note, vortexing ensured compete fixation of all cells and minimised clumping. The cells were fixed for at least 30 min or stored <5 days at -20 °C. At the end of fixation, cells were washed twice in 1 mL ice-cold PBS. Cells were centrifuged at 850*g* for 5 min to minimise cell loss from spinning out of ethanol. Importantly, as PI stains both DNA and RNA, the latter must be removed with ribonucleases. Following the final centrifugation step, the cells were resuspended with 400 μL PI/RNase staining buffer (BD Biosciences) and incubated for 15 min at RT, protected from light. Of note, acquisition of cells on the flow cytometer was performed slowly at 'low' to discriminate between cell cycle phases.

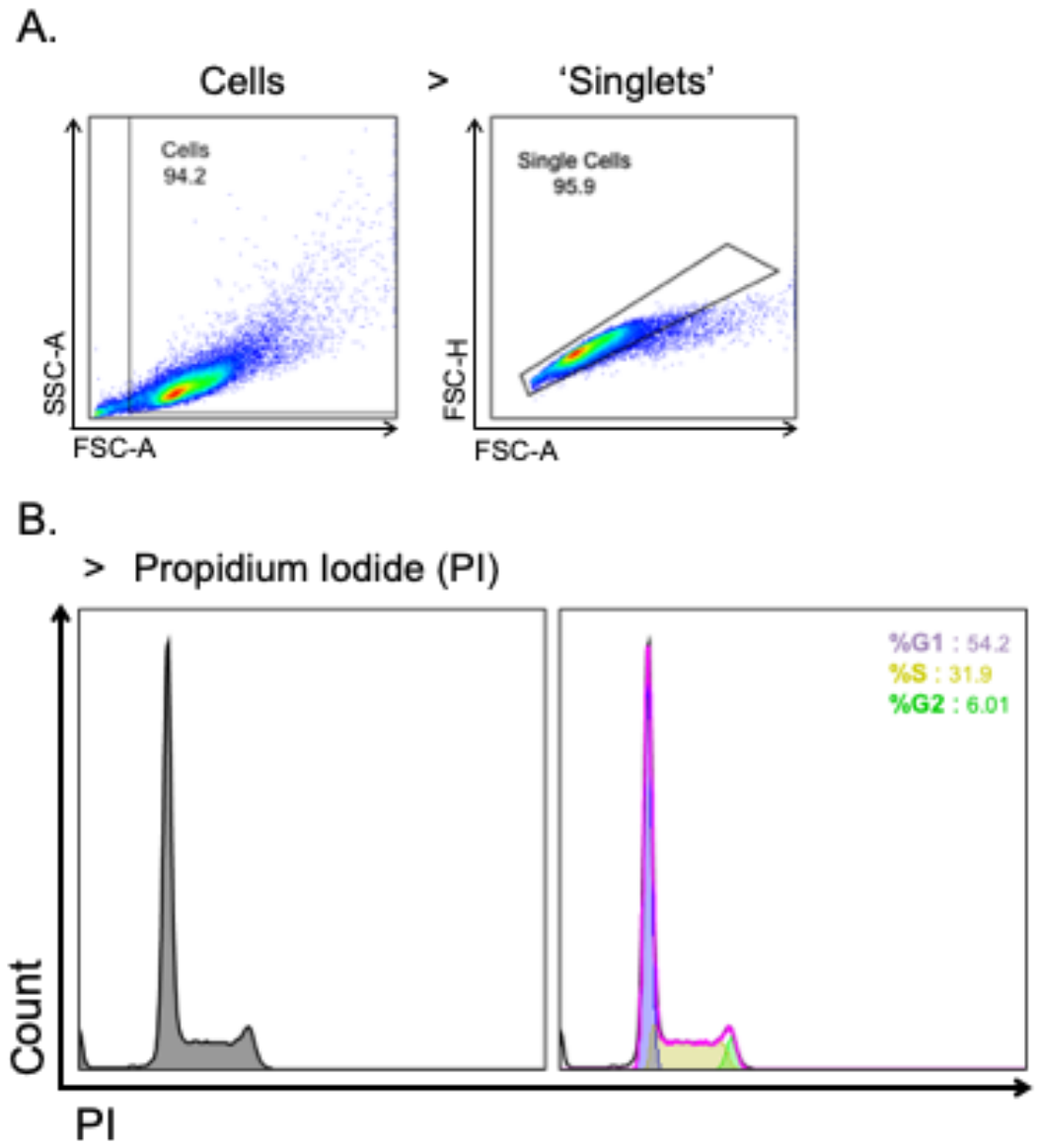

Figure 2.6 - Cell cycle analysis by propidium iodide (PI) staining
Cell cycle analysis by propidium iodide (PI) staining was performed to quantify the proportion of cells in each phase of the cell cycle (G1/0, S and G2) in response to cell stimulation and/or drug treatment. The following describes the gating strategy performed to assess DNA content of cells. **(A)** FSC and SSC were used to gate cells (left panel) and subsequently select for singlets (right panel). **(B)** DNA content was examined by PI staining using a univariate histogram (left panel) to identify each phase of the cell cycle. This data was further processed using univariate modelling based on the Watson Pragmatic algorithm (right panel) to quantify the percentage population in cell cycle phase G1 (purple), S (yellow) and G2 (green).

2.2.2.5 CellTrace Violet cell proliferation assay

CellTrace Violet (CTV) is a cell-permeable dye used to trace multiple cell divisions using dye dilution by flow cytometry (414). Cell proliferation was assessed in primary CLL cells, HG-3 and MEC-1 cells in response to stimulation and/or drug treatment. Despite differences in the experimental design, the labelling protocol for both primary cells and cells lines remains the same – albeit differences in cell number.

To induce primary CLL cell proliferation, an established method was used that adopts CD40L co-cultures (section 2.2.1.10). A key difference to the co-cultures described earlier is the omission of IL-4 and addition of interleukin-21 (IL-21). IL-21 was used to promote CLL cell proliferation *in vitro* as a component of long-term CD40L co-cultures. Recombinant human IL-21 (PeproTech) was solubilised in dH_2O to make a 50 μg/mL stock solution and stored in 10 μL aliquots for up to 3 months at -80 °C. Primary CLL cells were stimulated with 25 ng/mL IL-21 diluted directly into the culture medium. We and others have found IL-21 to be a stronger proliferative signal that confers robust proliferation of CLL cells co-cultured on CD40L (180). Importantly, CTV dye should be prepared immediately prior to use by adding 20 μL DMSO to one vial of CTV reagent, creating a 5 mM stock concentration.

CD40L cells were seeded (depending on the experimental design and the number of wells required) into a 12-well culture plate at a concentration of 5 $x10^4$ cells/mL and left for 2 h to adhere to the plate. Of note, 5 $x10^4$ NT-L cells were seeded for co-cultures acting as a non-proliferative control. Freshly isolated or thawed cryopreserved CLL cells were counted and transferred to a 15 mL reaction tube. The cells were centrifuged at 300*g* for 5 min and resuspended in 10 mL pre-warmed PBS. Following another centrifugation step, the cells were resuspended in pre-warmed PBS at a concentration of 1 $x10^7$ cells/mL. An aliquot of cells was removed and transferred to a FACS tube for an unstained day 0 control. To label the cells, 1 μL CTV dye was added per mL of cell suspension, creating a 5 μM working concentration. The cells were then incubated for 20 min in a 37 °C water bath, protected from light. After the incubation period, 5 times the original staining volume of complete growth medum was added to the cells. After a 5 min incubation period, the cells were centrifuged and subsequently resuspended in fresh pre-warmed complete RPMI at a concentration of 1.25 $x10^6$ cells/mL. An aliquot of CTV labelled cells was removed at this step to represent day 0 CTV-labelled cells. 1.25 $x10^6$ labelled CLL cells (1 mL) was subsequently added to the co-cultures (25:1 ratio) in complete RPMI supplemented with 25 ng/mL IL-21. The co-cultures were incubated for 1 h before drug treatment commenced.

Cell proliferation was assessed on day 0, 3, 6 and 9. For each timepoint, fresh NT-L and CD40L cells were seeded and left to adhere to the plates (as above). CTV labelled CLL cells were then harvested and resuspended in fresh complete RPMI (+IL-21). The cells were then added to the stromal cells and incubated for 1 h before treatment with fresh drugs commenced.

For each timepoint, cells were harvested and transferred to FACS tubes. Cells were centrifuged at 300*g* for 5 min and resuspended in HBSS. After another centrifugation, the cell pellet was resuspended in 100 μL HBSS. The cells were then stained in the presence of Human TruStain Fc receptor block with the cell proliferation panel (Table 2.14) for 30 min at 4 °C, protected from light. Following the incubation period, the cells were washed with HBSS and centrifuged at 300*g*. The cell pellet was then resuspended in 100 μL HBSS and stained with Annexin V/7-AAD for 15 min at RT, protected from light. Following this, 400 μL HBSS was added to the cells and subsequently acquired on the flow cytometer.

Component	Volume (uL)/Test
Human TruStain Fc Receptor Blocking Solution	1
APC-Cy7 Mouse Anti-Human CD45	2.5
HBSS to a final volume of 100 uL **==> 30 min incubation at 4 'C, followed by washing step**	
FITC Annexin V	2.5
7-AAD	2.5
HBSS to a final volume of 100 uL	

Table 2.14 - Cell proliferation FACS panel

As immortalised cell lines, HG-3 and MEC-1 cells do not require external stimuli to undergo proliferation. As such, CD40L co-cultures or IL-21 were not required. The protocol for labelling HG-3 and MEC-1 cells with CTV dye was similar to primary CLL cells. The amendments to this protocol are outlined below. HG-3 and MEC-1 cells were resuspended in PBS at a concentration of 2 x10^6 cells/mL prior to labelling with CTV dye. Moreover, HG-3 and MEC-1 cells were

resuspended in complete DMEM or complete RPMI, respectively. Proliferation was assessed on day 0, 1, 2, 3. The cells to be assessed were harvested and transferred to FACS tubes. Cells were centrifuged at 300*g* for 5 min and resuspended in HBSS. After another centrifugation step, the cell pellet was resuspended in 100 μL of HBSS. The cells were then stained with Annexin V/7-AAD for 15 min at RT, protected from light. At the end of the incubation period, 400 μL HBSS was added to the cells and subsequently acquired on the flow cytometer.

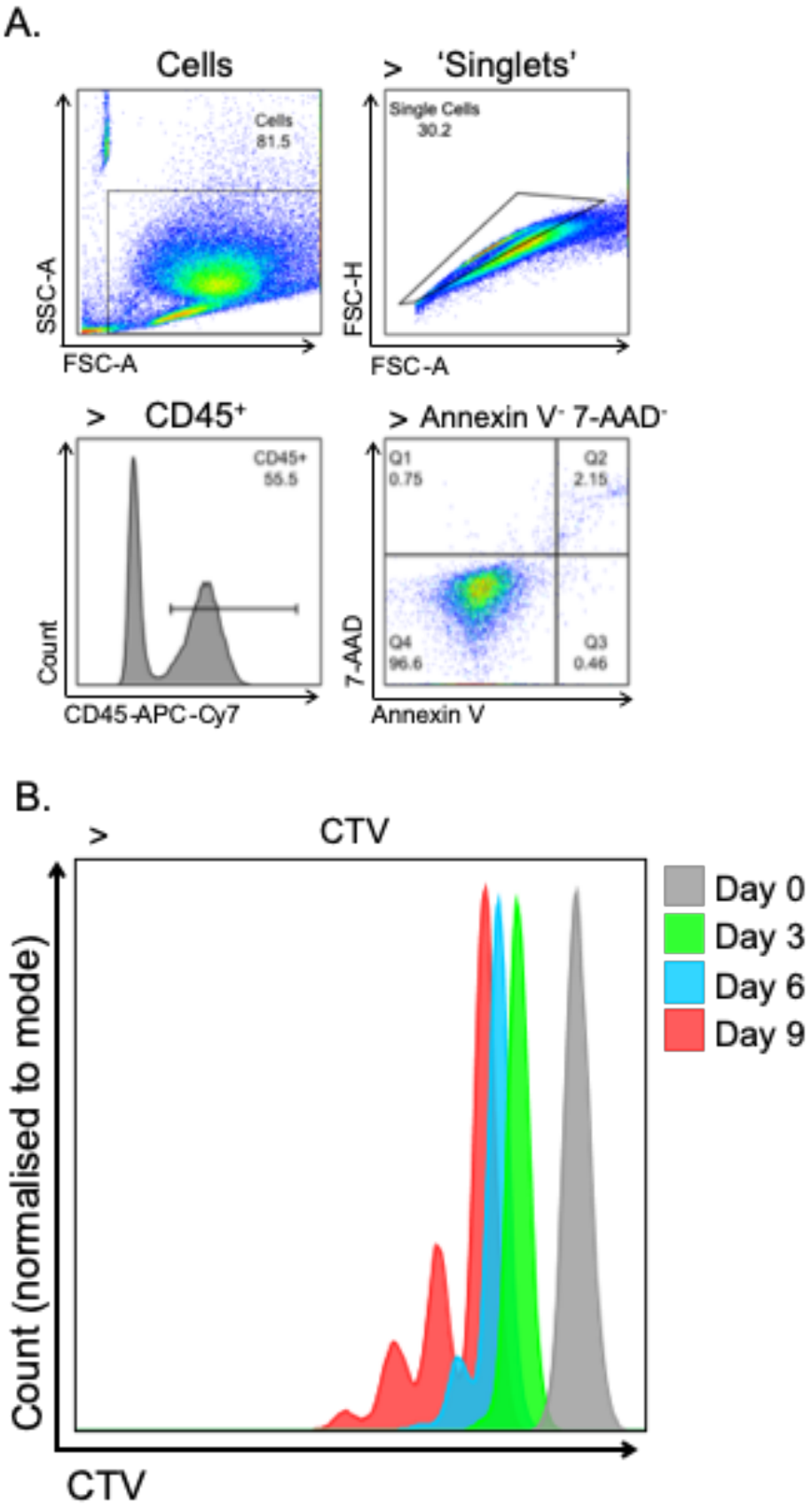

Figure 2.7 - Gating strategy for the CTV cell proliferation assay (primary CLL cells)
Proliferation of primary CLL cells was assessed following drug treatment and/or stimulation. CLL cell proliferation can be induced by CD40L (+IL-21) co-cultures. Monitoring proliferation can be achieved by labelling CLL cells with CTV. The dye is diluted with each cell division. Each 'peak' represents a population of cells that have undergone cell division. The greater the number of peaks, the more cell divisions a population of cells have completed. The following describes the

gating strategy performed to assess proliferation of primary CLL cells. **(A)** FSC and SSC were used to gate cells (top-left panel) and subsequently select for singlets (top-right panel). Next, a univariate histogram was used to select for $CD45^+$ cells (bottom-left panel). Of these $CD45^+$ cells, Annexin V/7-AAD staining was performed to select for viable cells (Annexin V^- 7-AAD^-) (bottom-right panel). **(B)** Of the viable cells gated, a univariate histogram was used to examine fluorescent intensity of CTV-labelled cells (bottom-right panel) across 4 timepoints: day 0 (grey), day 3 (green), day 6 (blue) and day 9 (red). 10,000 Q4 (Annexin V^- 7-AAD^-) events were recorded.

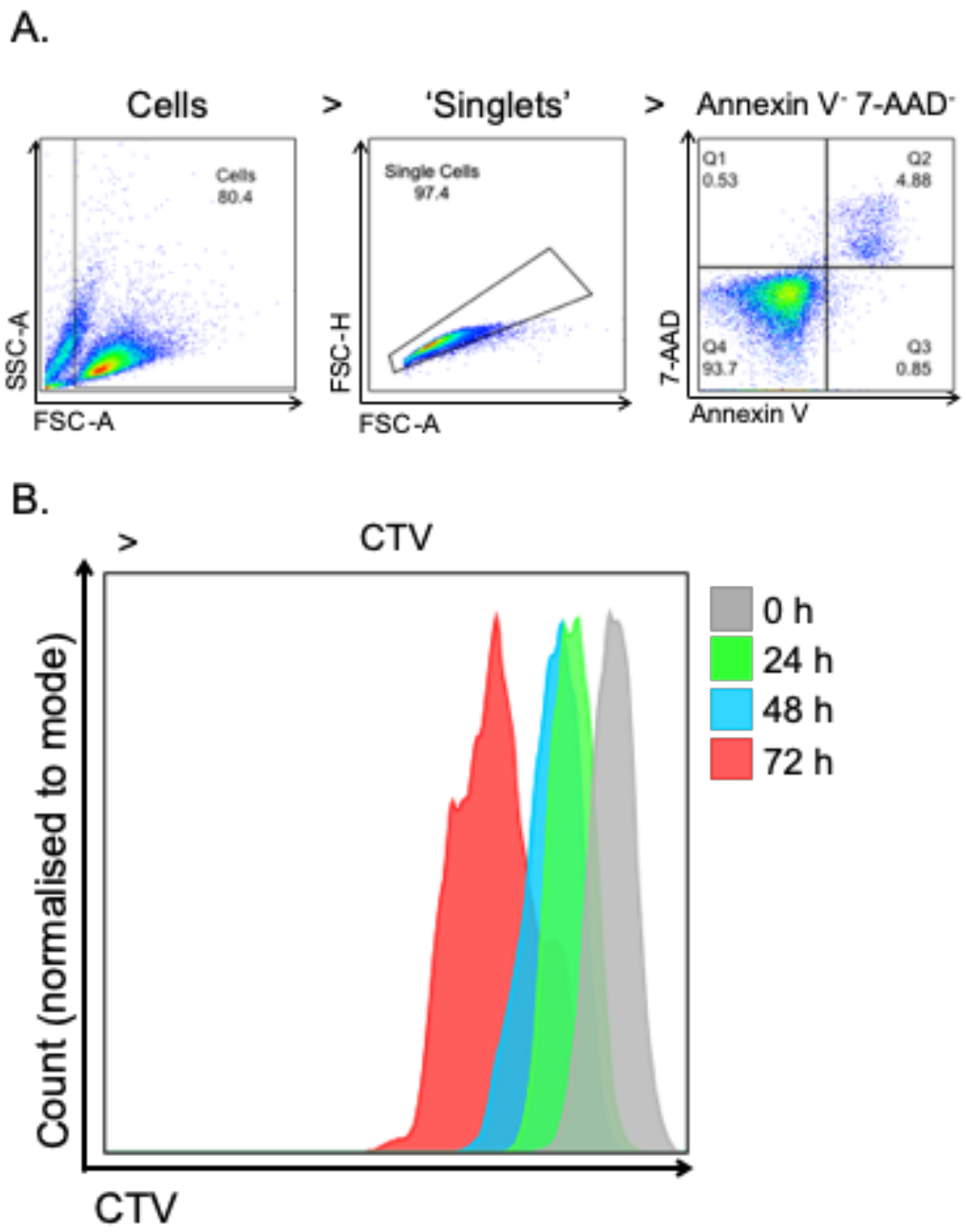

Figure 2.8 - Gating strategy for the CTV cell proliferation assay (HG-3 / MEC-1 cells) Proliferation of CTV-labelled HG-3 and MEC-1 cells was assessed following drug treatment. The following describes the gating strategy performed to assess proliferation of HG-3 and MEC-1 cell lines. **(A)** FSC and SSC were used to gate cells (left panel) and subsequently select for singlets (middle panel). Next, Annexin V 7-AAD staining was performed to select for viable cells (Annexin V^- 7-AAD^-) (right panel). **(B)** Of the viable cells gated, a univariate histogram was used to examine fluorescent intensity of CTV-labelled cells (bottom-right panel) across 4 timepoints: 0 h (grey), 24 h (green), 48 h (blue) and 72 h (red). 10,000 Q4 (Annexin V^- 7-AAD^-) events were recorded.

2.2.3 Immunofluorescence

The immunofluorescence (IF) procedure described here was adapted from the protocol published by Abcam entitled, 'Immunocytochemistry and immunofluorescence protocol' (415).

2.2.3.1 Tissue preparation

IF was performed on PB-derived primary CLL cells, HG-3 and MEC-1 cell lines to assess localisation and intensity of FOXO1 staining following drug treatment and/or $F(ab')_2$ stimulations. To determine the spatial distribution and localisation of FOXO1 within the TME, frozen spleen sections from wild-type (WT) mice and our CLL-like PKCαKR mouse model were used.

Primary CLL cells, HG-3 and MEC-1 cells were treated with drug or vehicle control in the presence or absence of $F(ab')_2$ stimulation (sections 2.2.1.8-2.2.1.9). Following the stimulation period, the cells were harvested and transferred into 15 mL reaction tubes. The cells were centrifuged at 300*g* for 5 min and resuspended in 10 mL PBS. Following another centrifugation step, the cells were fixed at a concentration of 5 $x10^6$ cells/mL in 4 % paraformaldehyde (PFA) (Santa Cruz Biotech) for 15 min at RT. After fixation, the cells were washed 3 times with ice-cold PBS. Cells were stored at 4 °C and used within 3 days.

Following the end of experimentation, spleens were harvested from WT mice and the CLL-like PKCαKR mouse model. Spleens carrying CLL-like disease were acquired from experiments carried out by Dr. Jodie Hay as left-over spleen tissue from *in vivo* experiments. The tissue was submerged in OCT freezing medium (Sakura), manipulated to achieve the correct orientation and carefully 'snap' frozen using liquid nitrogen, ensuring the OCT medium did not 'crack'. OCT-frozen spleens were stored at -80 °C until required.

2.2.3.2 Slide preparation

For primary CLL cells and cell lines, 10-spot multispot microscope slides (Henley-Essex) were prepared by coating each spot with 20 μL poly-L-lysine solution (Sigma) for 1 h at RT. The spots were rinsed 3 times with sterile dH_2O and

allowed to dry at RT. Afterwards, 20 μL fixed cells (1 x10^5 cells/20 μL) was pipetted onto each 'spot' and left to adhere for 1–2 h.

Sectioning of OCT-frozen mouse spleens was performed by Mr. Colin Nixon of the Histology Service at the Cancer Research UK (CRUK) Beatson Institute, Glasgow, UK. Cryo-sections were cut at 7μm and mounted onto coated histological slides. The sections were air-dried for 30 min at RT to prevent sections from falling off the slides during antibody incubations. Following this, the spleen sections were stored at -80 °C until required. Of note, 'unstained' and 'secondary-only' controls were included.

2.2.3.3 Fixation and permeabilization

After adhering to the slide, the cells were rinsed 3 times with 20 μL PBS. At this point, the cells were observed under a light microscope to observe seeding density. The cells were then permeabilised with 'perm buffer' (PBS, 0.25% Triton X-100) for 15 min at RT. Following incubation, the cells were washed 3 times with 20 μL PBS, 5 min each.

Immediately upon removal of splenic sections from -80 °C, 100 μL ice-cold 4 % PFA was added to the sections for 15 min at RT. After fixation, the cells were washed 3 times with 100 μL ice-cold PBS. At this step, a hydrophobic barrier was drawn around the specimen. The sections were then permeabilised with 100 μL perm buffer for 15 min at RT. Following incubation, the cells were washed 3 times with 100 μL PBS, 5 min each.

2.2.3.4 Blocking and immunostaining

For blocking unspecific antibody binding, the cells and spleen sections were incubated with 20 μL or 100 μL blocking solution (PBS, 1 % BSA, 10 % Normal Goat Serum, 0.1 % Tween 20), respectively, for 1 h at RT.

Following the blocking step, primary CLL cells and cell lines were stained with 20 μL anti-FOXO1 antibody (1:100; diluted in blocking solution) (Cell Signalling Technology) O/N at 4 °C in a humidified staining chamber (Biolegend). Spleen sections were stained with 100 μL anti-FOXO1 antibody (1:100) and AlexFluor-

594 anti-CD45R/B220 antibody (1:200) (Biolegend) simultaneously O/N at 4 °C in a humidified staining chamber.

After O/N incubation, the cells and spleen sections were washed 3 times with 20 μL or 100 μL wash buffer (PBS, 0.1% Tween 20), respectively, 5 min each. Next, the cells and spleen sections were incubated with 20 μL or 100 μL secondary goat-anti rabbit IgG-AlexaFluor 488 (1:500; diluted in blocking solution) (ThermoFisher Scientific) for 1 hr at RT, protected from light. Following a final washing step with wash buffer, the specimens were mounted in ProLong™ Diamond antifade mountant with DAPI (one drop/slide) (ThermoFisher Scientific), which stained the cell nuclei. The slides were left to cure for 24 h at RT, protected from light. The slides were stored at 4 °C until required.

2.2.3.5 Image acquisition

The specimens were visualised using a Zeiss Axio Imager M1 fluorescence microscope (Zeiss) connected to AxioVision v4.8.1 software (Zeiss). A range of objectives were used to visualise the specimens including 10x, 20x, 40x and 100x (oil) in the red, green and blue fluorescence channels. Where possible, z-stacks were acquired. Z-stack images, typically >25 individual images per stack, were used for deconvolution. The resultant images would be exported for use in image analysis software.

2.2.3.6 Image analysis

CellProfiler v2.2.0 image analysis software (CellProfiler) was used to quantify co-localisation using object-based quantification of signal localisation for the FOXO1 (green) and DAPI (blue) fluorescent channels. CellProfiler is free open-source software that enables users to create customised pipelines containing image-processing modules. CellProfiler runs a customisable co-localisation pipeline, which provides various outputs for quantifying co-localisation including Pearson's correlation coefficient, Manders' overlap coefficient (MOC) and the Costes threshold method. Values for the Manders' coefficient range from 0 to 1. Values closer to 1 correspond to greater co-localisation (284, 416). Signal thresholds were calculated using the Costes Auto threshold method. >360 cells were quantified per condition from each sample (284).

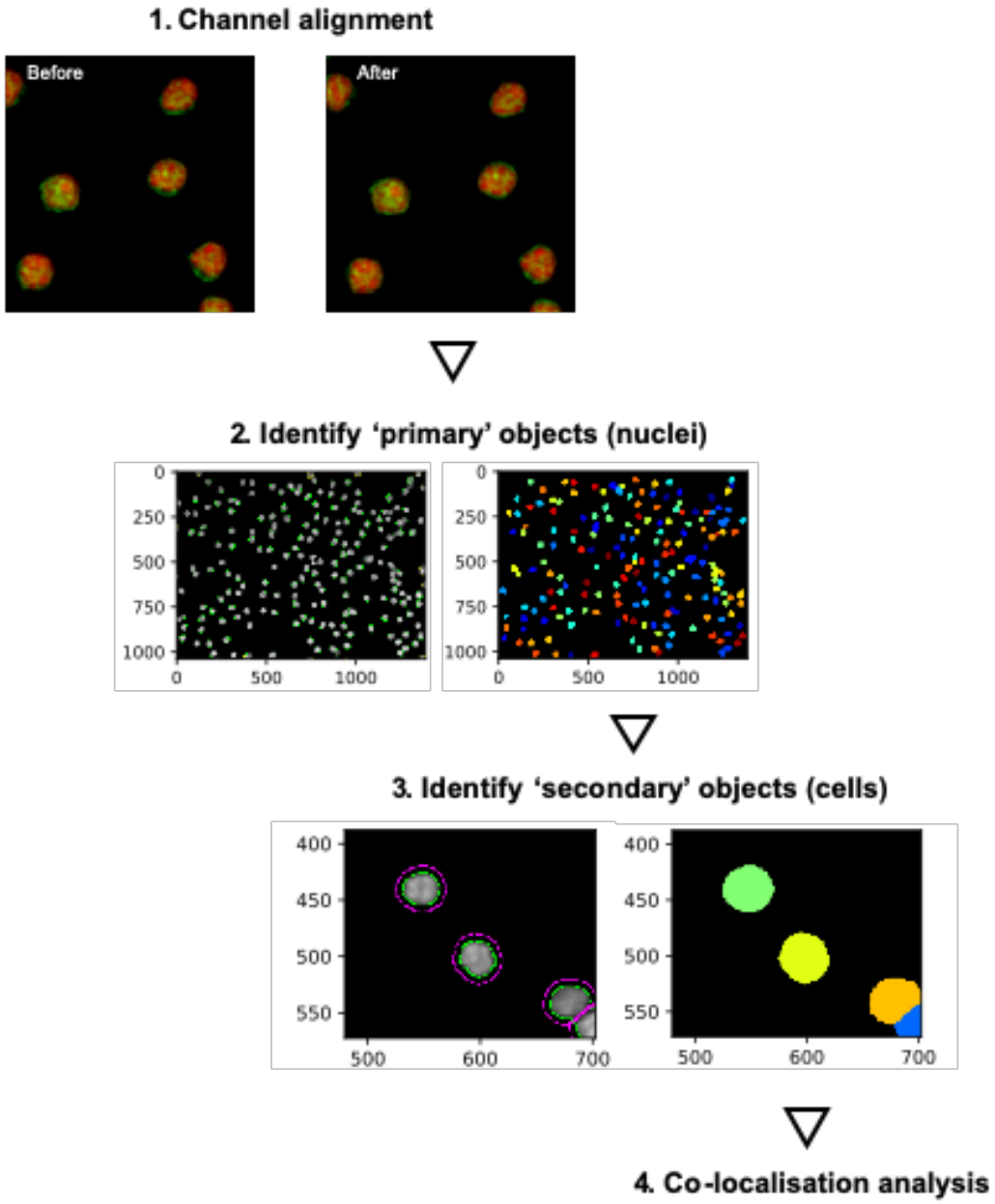

Figure 2.9 - Co-localisation pipeline (CellProfiler)
CellProfiler v2.2.0 image analysis software runs a customisable co-localisation pipeline, which provides various outputs for quantifying co-localisation. The software requires grey scale images (.PNG / .TIF / .JPG) from corresponding channels such as DAPI (blue) and FOXO1 (green) channels. Firstly, the software aligns the two images (same image, different channels) using normalised cross correlation to ensure correct co-localisation. Next, the software identifies 'primary' objects, which are represented by cell nuclei (DAPI). The software then calculates 'secondary' objects or 'cells' by expanding the 'primary' object field. Finally, co-localisation analysis provides various outputs for quantifying co-localisation including Pearson's correlation coefficient, Manders' overlap coefficient (MOC) and the Costes threshold method.

2.2.4 Immunohistochemistry

The immunohistochemistry (IHC) procedure described here was adapted from the protocol published by Abcam entitled, 'Immunohistochemistry (IHC): the complete guide' (417).

2.2.4.1 Sample preparation

Spleen tissue from WT mice were harvested at the end of experimentation. Spleens were acquired from Dr. Natasha Malik as left-over spleen tissue from *in vivo* experiments. Sample preparation, including formaldehyde fixation, paraffin-embedding and sectioning (microtome sections) were performed by the Histology Service at the CRUK Beatson Institute.

Sample preparation, staining and image acquisition of CLL patient LN biopsies was performed by Dr Mark Catherwood, Department of Histopathology, Belfast City Hospital, Belfast, UK.

2.2.4.2 Antigen retrieval

Heat-induced epitope retrieval was performed with specimens immersed in sodium citrate buffer (10 mM Tri-sodium citrate, 0.05 % Tween 20, pH 6.0). Sodium citrate buffer was stored at RT for <3 months. 1 L sodium citrate antigen retrieval buffer was added to a pressure cooker. The pressure cooker was positioned on a pre-heated hot plate on full power. Of note, the lid of the pressure cooker should not be secured. In the meantime, the sections were de-paraffinised and rehydrated by placing the slides into a rack and performing the subsequent washes sequentially in a Coplin jar (all volumes 50 mL): Xylene (3 min), Xylene (3 min), 1:1 Xylene:100 % ethanol (3 min), 100 % ethanol (3 min), 100 % ethanol (3 min), 95 % ethanol (3 min), 70 % ethanol (3 min), 50 % ethanol (3 min). Following the washes, the slides were placed in cold running tap water to rinse off the excess ethanol. As soon as the antigen retrieval buffer was boiling, the slides were placed into the pressure cooker and the lid was securely fixed. Once the pressure cooker had reached full pressure, the slides were left for 3 min. After the time had elapsed, the pressure cooker was transferred to a sink and de-pressurised. Afterwards, cold tap water was run into the pressure cooker (still containing the slides) for 10 min.

2.2.4.3 Staining procedure

Following antigen retrieval, the slides were washed 2 times in 50 mL ‘wash buffer’ (1X TBS, 0.025 % Triton X-100) with gentle agitation. At this step, a hydrophobic barrier was drawn around the specimen. The sections were blocked

in 100 μL blocking solution (1X TBS, 1 % BSA, 10 % Normal Goat Serum) for 2 h at RT. After the incubation period, the slides were drained and then stained with 100 μL anti-FOXO1 antibody (1:100) or anti-AKT^{S473} antibody (1:100) (Cell Signalling Technology) diluted in SignalStain antibody dilutent (Cell Signalling Technology). The sections were incubated in a humidified staining chamber O/N at 4 °C. The following morning, the slides were rinsed twice in wash buffer with gentle agitation. As the sections would be incubated with an HRP-conjugates secondary antibody, the specimens were immersed in 100 μL 0.3 % hydrogen peroxide (H_2O_2) (Sigma) in TBS for 15 min to suppress endogenous peroxide activity. After rinsing off the 0.3 % H_2O_2 with wash buffer, the sections were covered with 50 μL SignalStain Boost IHC Detection Reagent (HRP, Rabbit) (Cell Signalling Technology) and incubated in a humidified chamber for 30 min at RT. The sections were then rinsed 4 times in 100 μL TBS and incubated with 50 μL DAB Substrate Kit (Abcam) according to the manufacturer's instructions. The slides were developed for up to 10 min for the desired colour to emerge. Of note, a 'secondary only' control was used to determine the incubation period with chromogen substrate. The slides were placed in a sink and rinsed in running tap water for 5 min and subsequently counterstained with haemtoxylin (Sigma) for 1 min. Following counterstaining, the sections were dehydrated (washing step for rehydration in reverse e.g. starting with 50 % ethanol) and mounted using a drop of HistoLab mounting medium (Pertex). The slides were then cured for 24 hr at RT and stored at 4 °C until required.

2.2.4.4 Image acquisition

Sections were visualised using EVOS XL Core Cell Imaging System. 10x and 40x objectives were used to acquire images.

2.2.5 Western blotting

Western blotting was performed to examine the expression, phosphorylation status and subcellular localisation of proteins in response to cell stimulation and/or drug treatment. This technique, alongside the expression of a loading control, enables conclusions to be drawn about the effect of drug treatment and/or stimulation on protein expression and activity.

2.2.5.1 Preparation of protein lysates

Cells	Cell pellet	Volume of Protein Lysis Buffer (uL)
Primary CLL cells	~ 1 x10^7	35
MEC-1 / HG-3	~ 2 x10^6	55

Table 2.15 - Cell numbers for western blotting

Following cell stimulation and/or drug treatment, cells were harvested and transferred to pre-cooled 15 mL reaction tubes. Of note, all reagents required were placed on ice prior to harvesting the cells. The cells were washed with 1 mL ice-cold PBS and centrifuged at 300*g* for 5 min at 4 °C. Following another centrifugation and washing step, the cells were resuspended in 500 μL PBS and transferred to a 1.5 mL reaction tube. The cells underwent a final centrifugation step at 300*g* to pellet the cells. The cell pellet was then resuspended in 35 μL/50μL protein lysis buffer (1X Tris-EDTA pH 8.0, 1 % Triton X-100, 1 mM DTT) containing 1X c0mplete mini, EDTA-free protease inhibitor cocktail (Sigma) and 1X PhosSTOP phosphatase inhibitor cocktail (Sigma). The lysate was vortexed for 10 s at the highest setting and then placed on ice for 20 min. After the incubation period, the lysate was centrifuged at 15000*g* for 20 min at 4 °C to pellet the cellular debris. The supernatant (protein lysate) was transferred to a new pre-cooled 1.5 mL reaction tube and the cellular debris was discarded. For the purpose of protein quantitation, 5 μL protein lysate was transferred to a 0.5 mL reaction tube. The lysates were stored at -80 °C until required.

2.2.5.2 Cellular fractionation

Cellular fractionation was performed to assess translocation of proteins from nuclear to cytoplasmic compartments, or *vice versa*, in response to drug treatment and/or stimulation using the Nuclear Extract Kit (Active Motif). Of note, a whole-cell lysate was generated as a 'fractionation' control. Unless otherwise stated, cells were pre-treated with drug or DMSO vehicle control for 30 min followed by a 1 h $F(ab')_2$ stimulation.

The protocol for generating nuclear, cytoplasmic and whole-cell fractions was followed according to the manufacturer's instructions 'Protocol I: Adherent or Suspension Cells', with the following exceptions: 1 $x10^7$ primary CLL cells (per

condition) and 2 x10^6 HG-3 or MEC-1 cells (per condition) were used as starting material. At Step 2.1 and 2.2, both primary CLL cells and cell lines were resuspended in 50 μL Hypotonic Buffer and subsequently lysed with 1.67 μL detergent (418). For the purpose of protein quantitation, 5 μL of the nuclear, cytoplasmic and whole-cell lysates was transferred to a 0.5 mL reaction tube. The lysates were stored at -80 °C until required.

2.2.5.3 Protein quantitation

Protein concentration of cellular lysates or subcellular fractions was quantified using the Bicinchoninic acid (BCA) assay (Thermo Fisher Scientific) according to the manufacturer's instructions for the 'Microplate Procedure'. All reagents were pre-cooled on ice prior to commencing the assay.

To prepare the protein samples, 45 μL of ice-cold dH_2O was added to the 5 μL aliquots removed from the original protein lysates, creating a 1:10 dilution. Next, 20 μL of each standard and unknown sample was added to one well of a 96-well assay plate in duplicate. Following this, 200 μL of the working reagent, as determined by the number of samples to be analysed, was added to each well and mixed on a plate shaker for 30 s. The plate was covered and placed in a 37 °C incubator for 30 min. After incubation, the plate was cooled to RT and measured at 562 nm on a SpectraMax M5 microplate reader (Molecular Devices).

2.2.5.4 Gel electrophoresis and transfer

Gel electrophoresis and 'transfer' was performed using the XCell SureLock Mini-Cell electrophoresis system (Thermo Fisher Scientific) and XCell II Blot Module (Thermo Fisher Scientific), respectively, according to the manufacturer's instructions.

Following protein quantitation, 20-40 μg of protein was transferred to a 1.5 mL reaction tube. Of note, equal amounts of protein were added across each condition. If necessary, dH_2O was added to the reaction tubes to create an equal final volume. Next, appropriate volumes of 4X LDS Sample Buffer (Thermo Fisher Scientific) and 10X Sample Reducing Agent (Thermo Fisher Scientific) were added to the lysate and mixed thoroughly. The lysates were then 'boiled' at 70

°C for 10 min. After a quick vortex, the samples were loaded into either 10-, 12- or 15-well NuPAGE™ 4-12 % Bis-Tris Protein Gels (Thermo Fisher Scientific) immersed in 1X MES or MOPS Running Buffer (Thermo Fisher Scientific). Of note, the HyperPAGE Molecular Weight Marker (Bioline) was loaded next to the lysates to identify the approximate size of target proteins separated by gel electrophoresis. When necessary, two gels were run simultaneously containing equal amounts of protein lysate in duplicate, termed 'mirror' blots. Mirror blots were performed to interpret relative differences between the amount of phosphorylated and 'total' protein in response to drug treatment and/or stimulation.

For protein transfer, the gels and apparatus were assembled as per the manufacturer's instructions. The 1X Transfer Buffer (Thermo Fisher Scientific) contained either 10 % or 20 % methanol depending on whether one or two gels were being transferred, respectively. Separated proteins were transferred onto 0.45 μm Polyvinylidene Fluoride (PVDF) membranes (Thermo Fisher Scientific), which had been activated in methanol prior to protein transfer. In contrast to the manufacturer's protocol, protein transfer was run at 30V for 70 min.

2.2.5.5 Immunoblotting

At the end of transfer, the 'sandwich' was dissembled, and the membranes were rinsed in dH_2O to remove excess transfer buffer. To check for transfer efficiency, the proteins were visualised by staining the membranes with 5 mL Ponceau solution (Sigma). If necessary, the membranes were cut at this point to probe for different proteins simultaneously. The membranes were then washed 3 times with 10 mL TBST (1X TBS, 0.1 % Tween 20) to remove protein-bound Ponceau solution. Once all the Ponceau had been removed, the membranes were then blocked with 10 mL 5 % (w/v) Milk/TBST for 1 h at RT. After the blocking step, the membranes were transferred to 50 mL reaction tubes and washed 4 times in 5 mL TBST, 5 min each. The membranes were then incubated with 5 mL primary antibody diluted in 5 % (w/v) BSA/TBST or 5 % (w/v) Milk/TBST according to the antibody datasheet provided by the manufacturer. The membranes were incubated with primary antibody O/N at 4 °C.

The following morning, the primary antibody was decanted, and the membranes were washed 4 times in 5 mL TBST, 5 min each. Of note, primary antibodies were re-used up to 4 times or stored for <2 weeks at 4 °C. Furthermore, multiple primary antibodies were sometimes incubated together. After the washing step, 5 mL HRP-linked secondary anti-rabbit IgG (1:2000) or anti-mouse IgG (1:2000) (Cell Signalling Technology) diluted in 2 % (w/v) Milk/TBST was incubated with the membrane for 1 h at RT. On occasions, 5 mL fluorescently-linked IRDye 680RD goat anti-rabbit (1:15000) or IRDye 700CW goat anti-mouse (1:15000) secondary antibodies (LI-COR) diluted in TBST were used for near-infrared (NIR) detection. After a final washing step, proteins were visualised using the Odyssey Fc Imaging System (LI-COR) connected to ImageStudio v5.2.5 software (LI-COR). Membranes probed with HRP-linked secondary antibodies were immersed in Immobilon Forte Western HRP Substrate (Millipore) prior to chemiluminescent detection. Conversely, membranes probed with fluorescently-linked secondary antibodies were visualised directly in the imaging system using either 700 nm or 800 nm channels. Following acquisition, the membranes were rinsed in 10 mL dH_2O and stored at 4 °C, submerged in 50 mL dH_2O for re-probing. For long-term storage, membranes were dried O/N at RT and stored at – 20 °C.

2.2.5.6 Membrane re-probing

Membranes were re-probed without 'stripping', as long as subsequent antibodies did not target proteins of similar sizes or where non-specific background staining had occupied targeted regions of the membrane.

Following acquisition of Western blot images, membranes were rinsed in dH_2O to remove excess chemiluminescent ECL reagent, as necessary. The membranes were then washed 4 times in TBST for 5 min each and subsequently probed with the next primary antibody O/N at 4 °C. The protocol was followed therein in accordance with the standard immunoblotting procedure.

2.2.5.7 Densitometry

Densitometry (via quantitation of signal intensity) was performed using Image Studio™ Lite (version 5.2.5) software (LI-COR) with images acquired on the Odyssey Fc acquisition system. The procedure for densitometry was adapted

from the 'Image Studio™ Lite V5.x Quick Start Guide' and 'Image Studio™ Software Background Subtraction Guide' available on the manufacturer's website. For a detailed description of the methods used, please refer to our recently published methods paper (418).

2.2.6 RT-qPCR

In 'two-step' reverse transcription-quantitative PCR (RT-qPCR), RNA is reverse transcribed to complementary DNA (cDNA). The cDNA is then used as a template for the qPCR reaction in an entirely different reaction (419). TaqMan gene expression assays (ThermoFisher Scientific) were used to assess target gene expression in the qPCR reaction. The methods are outlined below.

2.2.6.1 RNA isolation

RNA was isolated using the RNeasy Mini Plus Kit (QIAGEN) according to the manufacturer's instructions.

After drug treatment and/or stimulation, cells were harvested as per the protocol described (section 2.2.5.1). Cell pellets were then resuspended and lysed in an appropriate volume of RLT Plus buffer (Table 2.16). The lysate was then homogenised by vortexing for 30 s. The lysate was stored at -80 °C until required. The protocol was then followed in accordance with the manufacturer's instructions.

Cells	Cell number	Volume of RLT Plus Buffer (uL)
Primary CLL cells	~5 x10^6	350
MEC-1/HG-3	~1 x10^6	350

Table 2.16 - Cell numbers for RT-qPCR

For pelleted *ex vivo* primary CLL cells, the pellet (~2 $x10^7$ cells) was thawed on ice and gently 'flicked' to dislodge the pellet. The cells were then lysed in an appropriate volume of RLT Plus buffer (Table 2.16) and homogenised by vortexing for 30 s. The protocol was then followed in accordance with the manufacturer's instructions.

The concentration and purity of RNA was determined using the NanoDrop spectrophotometer (ThermoFisher Scientific), according to the manufacturer's instructions. Of note, RNA concentration (ng/μL), 260/280 and 260/230 ratios were considered. RNA was stored at -80 °C until required.

2.2.6.2 First-strand cDNA synthesis

Total RNA was reverse-transcribed to cDNA with SuperScript III Reverse Transcriptase (ThermoFisher Scientific) according to the manufacturer's instructions. Of note, equal quantities of RNA (>150 ng) were used across each condition for first-strand cDNA synthesis. A maximum of 500 ng RNA from each condition/sample was used in the reaction. cDNA was generated using the ProFlex PCR system (ThermoFisher Scientific), following the thermal conditions described in the manufacturer's protocol. Of note, reverse transcriptase (RT) minus (RT-) controls were used, where possible. cDNA was diluted 1:5 with RT-PCR grade water (ThermoFisher Scientific) and stored at -20 °C until required.

First-Strand cDNA Synthesis	
Component	**Volume (uL)**
Oligo(dT) 12-18 Primer	1
dNTP Mix PCR Grade 10 mM	1
500 ng RNA	x
dH2O to a final volume of 13 uL **==> Heat mixture to 65 'C, 5 min. Incubate on ice for >1 min.**	
5X First-Strand Buffer	4
0.1 M DTT	1
RNaseOUT Recombinant RNase Inhibitor	1
SuperScript III RT	1
==> Heat mixture to 50 'C, 60 min. Inactivate reaction by heating to 70 'C, 15 min.	

Table 2.17 – First-strand cDNA synthesis

2.2.6.3 Polymerase Chain Reaction (PCR)

The TaqMan assays used in the qPCR reaction are listed in Table 2.6. The reaction was followed according to the manufacturer's instructions. Glucuronidase beta (*GUSB*) was used as a 'housekeeping' or internal reference gene in all reactions. The cDNA and qPCR reagents were loaded into MicroAmp Optical 384-Well Reaction Plates (ThermoFisher Scientific). The qPCR reaction was performed in a 7900HT Fast Real-Time PCR System (ThermoFisher Scientific) running SDS v2.4 software. The reaction underwent the following thermal cycling conditions: Stage 1: 50 °C (2 min); Stage 2: 95 °C (10 min); Stage 3: 95 °C (15 s) 60 °C (1 min). The reaction (stage 3) underwent 40 cycles. C_T values were generated with RQ Manager software.

	Volume for 10 uL	
PCR reaction components	**Single Reaction (uL)**	**3 replicates (uL)**
20X TaqMan Gene Expression Assay	0.5	1.5
2X TaqMan Universal PCR Master Mix	5	15
cDNA Template	2	6
RT-PCR grade H2O	2.5	7.5

Table 2.18 - RT-qPCR reaction

2.2.7 FOXO1 activity assay

The TransAM FKHR (FOXO1) Activity Kit (Active Motif) is a DNA-binding ELISA used to study FOXO1 transcription factor activation in cell (nuclear) extracts.

2.2.7.1 Preparation of nuclear lysates

The TransAM method requires the generation of highly enriched nuclear fractions from cellular lysates. For this purpose, we used the protocol described in section 2.2.5.2. Although the cytoplasmic fraction is not required in the assay, both the cytoplasmic and nuclear fractions can be used to assess FOXO1 translocation in response to drug treatment and/or stimulation by Western blotting. Nuclear lysates were stored at -80 °C until required.

2.2.7.2 TransAM™ FKHR (FOXO1) Activity Kit

The procedure for the TransAM FOXO1 Activity Kit was followed according to the manufacturer's instructions. Equal amounts of nuclear lysate (>4 μg) were used as starting material. Relevant controls, including Raji nuclear extract as a positive control and 'blank' negative control wells, were used. In addition, 'competitive binding' experiments were performed to monitor the specificity of the assay using WT and mutated consensus oligonucleotides to compete with activated FOXO1 in nuclear extracts.

Of note, for 'Step 4: Colorimetric Reaction', the developing solution was incubated for <10 min in all cases. Following incubation, absorbance was read at 450 nm (reference wavelength 655 nm) using a SpectraMax M5 microplate reader. Of note, absorbance must be read within 5 min.

2.2.8 shRNA-mediated knockdown of FOXO1

RNA interference (RNAi)-mediated knockdown of FOXO1 expression was achieved via lentiviral-delivery of short hairpin RNA (shRNA) molecules. The method below describes the procedures performed to deliver and expand shRNA constructs, generating stably-transduced MEC-1 cells to assess the impact of FOXO1 knockdown on cell survival and proliferation.

a

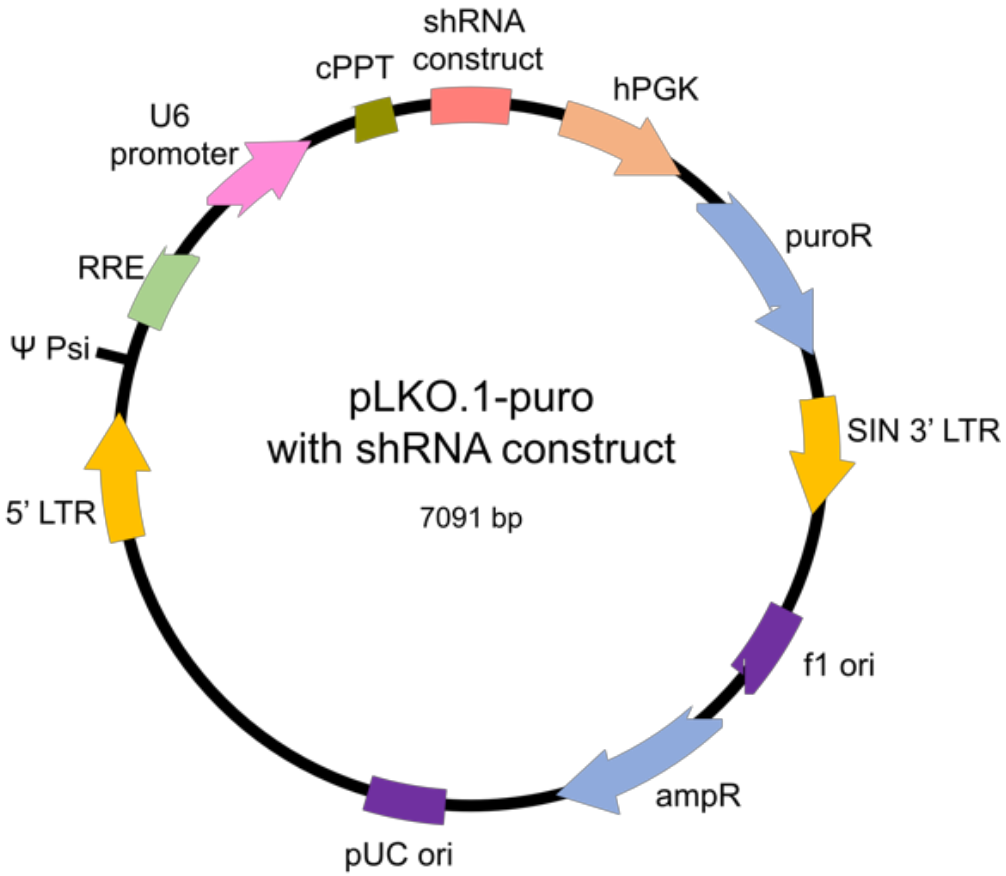

Figure 2.10 - pLKO.1-puro shRNA construct (420)
(A) Schematic of the pLKO.1-puro vector with shRNA insert. Image was modified from Addgene's 'Protocol – pLKO.1–TRC Cloning Vector', available at addgene.org.

2.2.8.1 Glycerol stocks of shRNA constructs

Multiple shRNA constructs (pLKO.1-puro TRC cloning vector containing shRNA target sequence) targeting FOXO1 were assessed (Table 2.19).

Symbol	Clone ID	Target sequence	Vector ID	Clone name	Region
FOXO1A	TRCN0000039582	GCCGGAGTTTAGCCAGTCCAA	pLKO.1	NM_002015.2-472s1c1	CDS
FOXO1A	TRCN0000039581	CAGGACAATAAGTCGAGTTAT	pLKO.1	NM_002015.2-1712s1c1	CDS
FOXO1A	TRCN0000039580	GCCACCAAACACCAGTTTGAA	pLKO.1	NM_002015.2-1609s1c1	CDS
FOXO1A	TRCN0000039579	GCTTAGACTGTGACATGGAAT	pLKO.1	NM_002015.2-2211s1c1	CDS
FOXO1A	TRCN0000039578	GCCTGTTATCAATCTGCTAAA	pLKO.1	NM_002015.2-2941s1c1	3' UTR

Table 2.19 - FOXO1 shRNA constructs (Sigma)

The aforementioned pre-cloned, sequence-verified shRNA constructs targeting FOXO1 were derived from a bacterial glycerol stock (Terrific Broth (TB), 100 μg/mL carbenicillin, 15 % glycerol) library (MISSION shRNA; Sigma) belonging to Dr. Xu Huang (University of Glasgow, Glasgow, UK). Of note, the pLKO.1-puro clones were transformed into *Escherichia coli* prior to the generation of a glycerol stock. pLKO.1-puro includes ampicillin and puromycin antibiotic resistance genes for selection in bacteria or mammalian cell lines, respectively (Figure 2.10).

2.2.8.2 Isolation of bacterial colonies and inoculation of liquid cultures

As glycerol stocks will be used isolate plasmid DNA, it was important to isolate individual bacterial clones (single colonies), which reduced the chance of obtaining an assortment of different plasmids in the purified DNA. Of note, the following protocol was performed using aseptic technique in a sterile environment.

Luria Broth (LB) agar (LB-amp) plates containing 100 μg/mL ampicillin were prepared (Table 2.20). Sterility was maintained by working near a flame. Using a sterile toothpick, a small amount of bacteria was scratched from the surface of a glycerol stock and gently spread over the surface of a LB-amp plate. A second sterile toothpick was used to drag through the previous streak into another section of the plate. A third sterile toothpick was used to drag the second streak of bacteria over the last section of the plate. The plate was incubated O/N at 37 °C. Of note, this was repeated for each construct (glycerol stock) in a fresh LB agar plate. In addition, a LB-amp plate without bacteria was used as a negative control for bacterial growth.

LB-Agar		
Component	**-**	**Final Concentration (ug/mL)**
InvivoGen Fast-Media LB Agar Base	1 pouch	-
dH20	200 mL	-
==> microwave in pulses. Allow to cool.		
Ampicillin 100 mg/mL	500 uL	100 ug/mL

Table 2.20 – LB-Agar preparation

Prior to picking individual colonies, TB containing 100 μg/mL ampicillin (TB-amp) was prepared (Table 2.21). The procedure has been adapted from the protocol 'Inoculating a Liquid Bacterial Culture' (421).

Teriffic Broth (TB)- ampicillin (TB-amp)		
Component	**-**	**Final Concentration (ug/mL)**
TB	23.5 g	-
dH2O	500 mL	-
==> Autoclave. Allow to cool.		
Ampicillin 100 mg/mL	500 uL	100

Table 2.21 - TB-amp preparation

Following O/N incubation, the plates were observed for individual bacterial colonies. If required, the plates were placed at 37 °C to allow for further growth. In the meantime, 5 mL TB-amp was transferred to a sterile 13 mL inoculation tube (Fisher Scientific). Once single colonies were observed, a single colony was selected from the LB agar plate using a pipette tip (without filter) and dropped directly into the liquid TB-amp. The liquid culture was swirled and then loosely covered with the lid of the inoculation tube. The bacterial culture was incubated O/N, shaking (200 rpm) at 37 °C. Thereafter, the liquid cultures were examined for bacterial growth. Of note, a TB-amp liquid culture without bacteria was used as a negative control for bacterial growth.

2.2.8.3 Miniprep

Minipreparation or ‘miniprep’ of plasmid DNA from bacteria was performed using the QIAprep Spin Miniprep Kit (QIAGEN) according to the manufacturer’s instructions. The plasmid DNA isolated from the miniprep procedure is used to visualise the presence of a shRNA sequence (target sequence) within the PLKO.1-TRC cloning vector by diagnostic digests.

From the original 5 mL TB-amp liquid bacterial culture, 4 mL was used for the miniprep procedure, whilst the remaining 1 mL was used in subsequent large-scale liquid bacterial cultures for ‘maxiprep’ procedures or to generate glycerol stocks. Of note, large-scale liquid bacterial cultures were only performed once the presence of a shRNA sequence insert was confirmed, as determined by a diagnostic digest.

The concentration and purity of the plasmid DNA was determined using the NanoDrop spectrophotometer, according to the manufacturer’s instructions. The plasmid DNA was then used for diagnostic digests or stored at -20 °C until required.

2.2.8.4 Maxiprep

Following the presence of shRNA sequence inserts in plasmid DNA generated by the miniprep procedure, the remaining 1 mL bacterial liquid culture from each construct was transferred to separate sterile conical flasks containing 100 mL TB-amp. The liquid culture was swirled and then loosely covered with aluminium foil. The bacterial culture was incubated O/N, shaking at 37 °C. Liquid cultures were examined for bacterial growth. Of note, a TB-amp liquid culture without bacteria was used as a negative control for bacterial growth.

Following incubation, a maxipreparation or ‘maxiprep’ was performed using the EndoFree Plasmid Maxi Kit (QIAGEN) according to the manufacturer’s instructions. The concentration and purity of plasmid DNA was determined using the NanoDrop spectrophotometer, according to the manufacturer’s instructions. The plasmid DNA was then used for diagnostic digests or stored at -20 °C until required.

2.2.8.5 Diagnostic digests

Diagnostic digests were performed to confirm the presence of an shRNA sequence insert before commencing subsequent steps. The protocol for diagnostic digests were generated using NEBcloner v1.3.14 software (New England Biolabs) and followed according to the manufacturer's protocol. Protocols generated by NEBcloner software differed depending on the specific restriction enzymes used. In brief, 500 ng plasmid DNA, isolated using either the miniprep or maxiprep protocol, was digested with Nde1 (New England Biolabs) and Spe1_HF (New England Biolabs) or Nde1 and BamH1_HF (New England Biolabs) restriction enzymes, theoretically generating ~555 base pairs (bp) or ~812 bp insert and ~6495 bp or ~6238 bp backbone fragments, respectively. The reaction was performed in the presence of 1X CutSmart Buffer (New England Biolabs) for 1 h at 37 °C. Of note, uncut, 'single' cut and non-template (dH_2O) controls were run alongside test samples. The fragments generated from the diagnostic digest were assessed by gel electrophoresis (Figure 2.11).

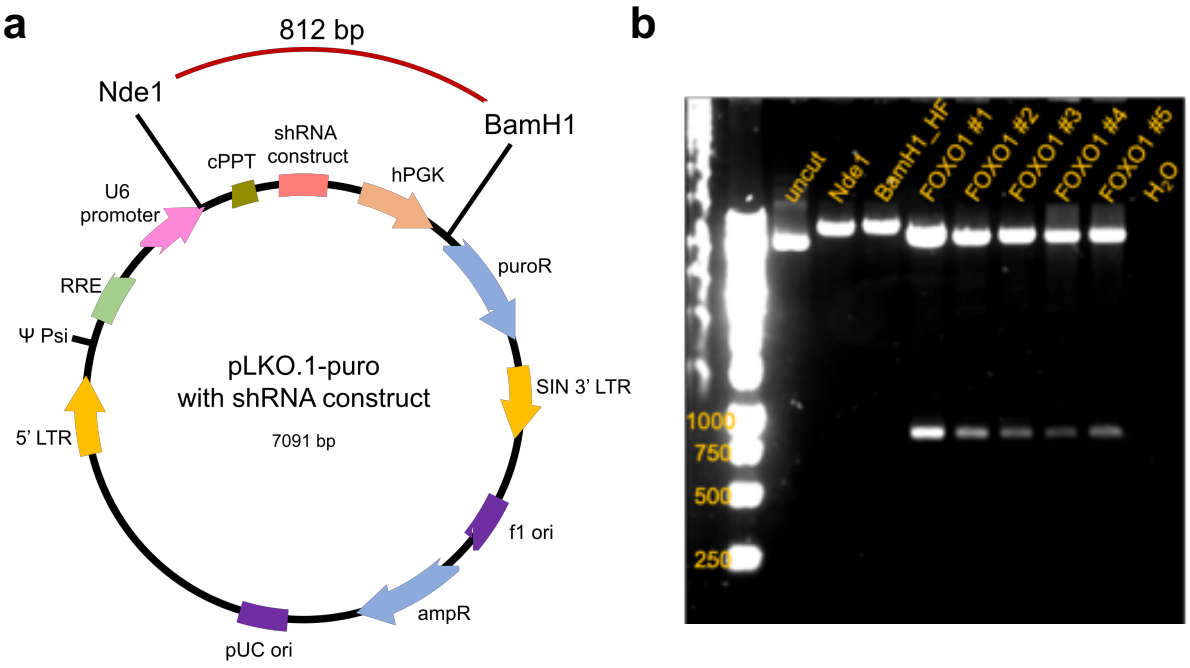

Figure 2.11 - Diagnostic digest and gel electrophoresis (including pLKO.1-puro construct) **(a)** Schematic of the pLKO.1-puro plasmid indicating restriction sites Nde1 and BamH1, creating a 812 bp fragment. **(b)** Gel electrophoresis of diagnostic digest (FOXO1 shRNA constructs).

2.2.8.6 DNA gel electrophoresis

Gel electrophoresis was performed to visualise the resulting DNA fragments generated by the diagnostic digests. The pattern of fragments on the gel determined the presence (or absence) of shRNA sequence inserts within the pLKO.1-puro plasmids.

To make a 1 % agarose gel, 1 g agarose (Sigma) was added to 100 mL 1X TAE buffer (diluted from a 50X TAE buffer stock solution (40 mM Tris, 20 mM acetate, 1 mM EDTA, pH 8.2) in a microwaveable flask. The agarose was dissolved in the microwave in 'pulses', ensuring the mixture did not over boil. Once the agarose solution had cooled, 10 μL 10000X SYBR Safe DNA gel Stain concentrate (Thermo Fisher Scientific) was added to the solution and gently swirled to prevent bubble formation. The agarose was subsequently poured into a gel tray with an appropriate well comb in place and allowed to solidify for ~1 h.

To prepare the samples, 1-part 6X TriTrack DNA Loading Dye (ThermoFisher Scientific) was added to 5-parts DNA digest. Once the agarose gel had set, it was placed in a suitable gel box, which was subsequently filled with 1X TAE buffer. First, the GeneRuler 1 kb DNA ladder (Thermo Fisher Scientific) was loaded into the first well, followed by the uncut, single-cut and digested DNA samples. A non-template (dH_2O) control was loaded in the final well.

The gel was run as 5 V/cm until the 'dye line' had reached ~70 % of the way down the gel. The DNA fragments were visualised using the Odyssey Fc Imaging System connected to ImageStudio v5.2.5 software. Of note, the 600 nm channel was used for visualising DNA gels (Figure 2.11).

2.2.8.7 Transfection / 2nd Generation Lentiviral Plasmids

The following procedure was adapted from the protocol 'pLKO.1–TRC Cloning Vector' (420). Transfection of HEK293T cells was performed adopting the calcium phosphate method to produce lentiviral particles (containing shRNA constructs) used to infect target cells.

For each shRNA construct to be transfected, including 'scrambled' and GFP control constructs, 5 $x10^5$ HEK293T cells were seeded in 5 mL serum/antibiotic-

free DMEM media in 6 cm tissue culture plates (Greiner Bio-One). The cells were incubated O/N at 37 °C, 5 % CO_2. 3 h prior to transfection, the HEK293T cells were monitored under a microscope to determine cell density. The cells should be between 70-80 % confluent. The cells were then replenished with fresh serum/antibiotic-free DMEM. For each transfection, Solution A (1.25 μg shRNA construct, 0.75 μg VSV.G envelope vector, 0.5 μg HIV-1 packaging vector, 50 μL 2.5 M $CaCl_2$, made up to 150 μL with sterile dH_2O) and Solution B (150 μL 2X HEPES buffer saline (Sigma)) was prepared in two separate polypropylene tubes (Greiner Bio-One). Solution A was slowly added to Solution B, whilst vigorously bubbling air through Solution B. The mixture was briefly vortexed and incubated at RT for 20 min (enabling a precipitate to form). Following incubation, the mixture was added dropwise to the culture medium containing the HEK293T cells. The plate was gently agitated back and forth to ensure the precipitate was evenly distributed and incubated O/N at 37 °C, 5 % CO_2. The following morning (<15 h), the transfection solution was removed and replaced with fresh complete DMEM. The cells were then incubated for 24 h at 37 °C, 5 % CO_2.

After the incubation period, the media was harvested from the cells using a sterile 10 mL syringe and filtered directly into a 15 mL reaction tube using a 0.45 μm filter (Sartorius) to remove the cells. This media contains lentiviral particles (viral supernatant). The viral supernatant was then stored at 4 °C. Another 5 mL fresh complete DMEM was added to the cells and incubated for a further 24 h at 37 °C, 5 % CO_2. After incubation, the media was harvested, filtered and pooled with the media from the previous day. If the viral supernatant was not required immediately, it was aliquoted and stored at -80 °C.

2.2.8.8 Lentiviral infection / transduction

1 x10^6 target cells/mL were seeded in 6-well culture plates the evening before transduction and incubated O/N at 37 °C, 5 % CO_2. The following day, the cells (MEC-1 and HG-3) were harvested, centrifuged at 300*g* for 5 min and resuspended in 1 mL fresh complete DMEM containing 10 μg/mL polybrene (Sigma). The cell suspension was then transferred to a new 6-well culture plate.

To begin lentiviral infection/transduction, 1 mL fresh or thawed viral supernatant (section 2.2.8.7) was added to the corresponding cell suspension. Importantly, the addition of the viral supernatant dilutes the concentration of polybrene in the cell suspension 2-fold, creating a culture with a desired concentration of 5 μg/mL polybrene. Of note, aliquots of frozen viral supernatant were thawed slowly on ice for around 2-3 h prior to transduction.

The cells were incubated for 24 h at 37 °C, 5 % CO_2 before puromycin selection and the generation of stable cell lines.

2.2.8.9 Generation of stable FOXO1-knockdown MEC-1 cell lines

Following 24 h of lentiviral infection, cells were given fresh complete DMEM supplemented with 2 μg/mL puromycin to select for transduced cells. Puromycin was only added to the culture 24 h after infection to enable expression of puromycin resistance gene. Non-transduced cells were cultured in parallel as a positive control for puromycin selection. The efficiency of transduction was monitored by examining the cells transduced with the GFP-expressing construct either qualitatively under a fluorescence microscope or quantitatively by flow cytometry.

Fresh puromycin-containing complete DMEM was given to cells every 3 days. Cell density of puromycin-selected cells was monitored to optimise cell growth and increase cell number by transferring cells to appropriately sized culture plates/flasks. Cell viability of non-transduced/uninfected cells was examined 72 h after the introduction of puromycin by Annexin V/7-AAD staining (section 2.2.2.3). Once all the non-transduced cells were Annexin V^+ 7-AAD^+, the infected cells were monitored for growth.

At 7- and 13-days post-infection, viable transduced cells were counted and approximately 1 $x10^6$ cells were removed from culture for RNA isolation and protein lysate preparation (sections 2.2.6.1 and 2.2.5.1, respectively). The expression levels of FOXO1 for each construct, including scrambled control, were subsequently determined by RT-qPCR and Western blotting. The two constructs that resulted in the most sufficient knockdown of FOXO1 in MEC-1 cells were

expanded in the presence of 1 μg/mL puromycin to maintain a selection pressure for transduced cells.

2.2.9 Resazurin assay

Resazurin (Sigma) is a non-toxic, non-fluorescent and cell-permeable compound. Upon exposure to viable cells, resazurin is reduced to resorufin, a highly fluorescent red-coloured compound (422). As such, changes in cell viability in response to drug treatment can be assessed using a fluorescence-based plate reader.

Resazurin solution (25 mM)		
Components	**-**	**Final Concentration (M)**
Resazurin Sodium Salt (MW = 251.17)	313 mg	0.025
dH_2O	50 mL	
Of note, Resazurin solution was filter-sterilised prior to use.		

Table 2.22 - Resazurin solution (25 mM)

Before each timepoint, 500 μM resazurin was prepared by diluting 25 mM Resazurin stock solution (1:50) with pre-warmed complete growth media (Table 2.22). Of note, suitable controls including cell-free wells with and without Resazurin was used to blank the experiment.

2.2.9.1 Dose-response curves

Dose-response curves were generated to determine the half maximal effective concentration (EC_{50}), defined as the concentration of drug that gives half-maximal response (423).

Freshly isolated or thawed primary CLL cells were seeded into each well of a 96-well culture plate in triplicate (3 x 10^5 cells/200 μL growth medium). The cells were then treated with increasing concentrations of drug (typically log or half-log concentrations) for 44 h at 37 °C, 5 % CO_2. Following incubation, 20 μL 500 μM resazurin (1:10) was added to the cells and incubated for 4 h at 37°C, 5 %

CO_2. Fluorescence was read on a SpectraMax M5 microplate reader using a fluorescence excitation wavelength at 570 nm and emission wavelength at 585 nm. Dose-response curves and resultant EC_{50} values were generated using Prism 6 software (GraphPad).

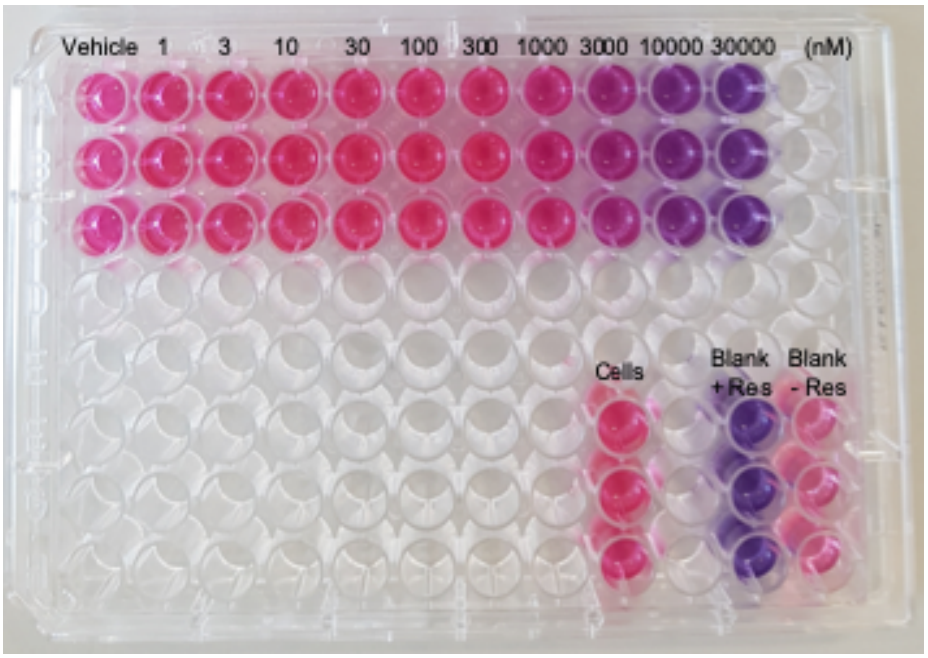

Figure 2.12 – Resazurin assay (dose-response curves)
Dose-response curves can be generated using the Resazurin assay. Cells are seeded into each well of a 96-well plate in triplicate. Of note, complete media (without cells) is used to 'blank' the reaction. Next, the cells are treated with increasing concentration of drug. After 44 h incubation, resazurin was added to the wells and incubated for a further 4 h at 37'C. Fluorescence was read on a microplate reader using a fluorescence excitation wavelength at 570 nm and emission wavelength at 585 nm. Dose-response curves and resultant EC_{50} values were generated using Prism 6 software (GraphPad).

2.2.9.2 Analysis of drug synergy

Combination therapy represents a highly effective treatment modality for cancer patients (424). Drug synergism is defined as the interaction between two or more drugs that evokes an effect greater than the sum of their individual parts (425).

Drug synergy between AZD8055/AZD2014 and ibrutinib was determined *in vitro* using primary CLL samples via the resazurin cell viability assay. Following O/N recovery, thawed CLL cells (1 x 10^7 cells/mL) were resuspended in RPMI complete medium. 3 x 10^5 cells/200 µL were seeded per well of a 96-well plate and treated with increasing concentrations of drug at a non-constant ratio. The following concentrations were used in the combination experiment: AZD8055

(6.25, 12.5, 25, 50, 100, 200 nM); AZD2014 (0.125, 0.25, 0.5, 1, 2, 4 µM); and ibrutinib (0.0625, 0.125, 0.25, 0.5, 1, 2 µM). Cells were incubated for 44 h at 37°C, 5% CO_2. Thereafter, 20 µL 500 µM resazurin (1:10) was added to the cells and incubated for 4 h at 37°C, 5 % CO_2. Following incubation, fluorescence was read on a SpectraMax M5 microplate reader using a fluorescence excitation wavelength at 570 nm and emission wavelength at 585 nm. Combination index (CI) values were calculated using the median-drug effect analysis method (425) with the CompuSyn software package (Biosoft), where a CI < 1 indicates synergy and CI > 1 indicates an antagonistic effect. Of note, drug concentrations were chosen based on clinically achievable doses calculated from dose escalation studies (439-441). With reference to the Chou and Talalay method (425), it is often necessary to calculate IC_{50} values for each drug to ascertain accurate CI values. However, IC_{50} values generated *in vitro* are not always applicable *in vivo*. Fortunately, IC_{50} values can be extrapolated using this method. Thus, the Chou and Talalay method can accommodate data points entirely above or below the IC_{50} of a given drug (425). Experimentally, this simplifies the use of heterogenous primary samples with variable IC_{50} values.

2.2.10 Statistics

Data were analysed using Prism 6 software (GraphPad) and are presented as mean values ± standard error of the mean (SEM), unless otherwise stated. All *n* values refer to the number of biological replicates. *P* values were determined by paired and unpaired, two-tailed Student's *t* test for analysis of two groups. One-way ANOVA with Tukey's multiple comparisons test was used for ≥ 3 groups. *P* values ≤0.05 were considered statistically significant. Unless otherwise stated, significant results are indicated by asterisks: $P \leq 0.05$ *, $P \leq 0.01$ **, $P \leq 0.001$ ***, $P \leq 0.0001$ ****, n.s. not significant.

3 Results I

3.1 Introduction

The advent of small-molecule inhibitors targeting BCR signalling components have revolutionized management strategies for CLL patients (45). Indeed, the BTK inhibitor ibrutinib (72, 131, 426) has proven tremendously effective among previously-treated, R/R and/or patients harbouring poor prognostic features (45). However, the emergence of drug resistance, treatment relapse and therapy discontinuation (87-89, 148) highlights the need to develop novel therapeutic strategies for CLL patients.

The clinical activity of BCR kinase inhibitors emphasises the significance of BCR signalling in CLL pathogenesis (9), most notably within the LN microenvironment (45, 207). mTOR kinase, through the coordinated activities of protein complexes mTORC1 and mTORC2, orchestrates PI3K-mediated growth and survival signals emanating from BCR engagement in normal B cells (266, 269). In fact, mTOR is prominently placed to integrate PI3K- and MAPK/ERK-mediated signals from a multitude of microenvironment stimuli (270). However, little is known about the role of mTOR signalling in CLL pathogenesis.

Despite encouraging preclinical data with the mTORC1-selective inhibitor rapamycin (313, 336, 337, 428), the rapalogue everolimus only had modest anti-tumour activity in a CLL clinical trial (339). Clinical activity of mTORC1-selective inhibitors are limited due to incomplete blockade of mTORC1-induced 4E-BP1 phosphorylation (312) and abrogation of negative feedback loops (mediated via S6K1) that enhance pro-survival signalling via increased mTORC2-AKT activity (314-317). The development of ‘second generation’ ATP-competitive mTOR inhibitors avoid these issues by inhibiting both mTORC1 and mTORC2 (293). As such, we sought to address whether inhibition of mTORC1 and mTORC2 with the dual mTOR kinase inhibitor AZD8055 would represent an effective therapeutic approach for CLL.

3.1.1 Aims

I. Explore mTOR activity in PB-derived CLL cells and patient LN biopsies.

II. Investigate *in vitro* modulation of mTOR activity downstream of TME stimuli.

III. Examine the ability of AZD8055, rapamycin and ibrutinib to inhibit mTOR activity in CLL cells.

IV. Determine and compare the functional impact of inhibiting mTOR with AZD8055 and rapamycin on CLL cell survival, growth and proliferation.

3.2 Results

3.2.1 mTOR is active in *ex vivo* primary CLL cells

Mindful that studies have previously demonstrated constitutively active PI3K (252) and AKT (285) in freshly isolated CLL cells, it was of interest to discover the activation status of mTOR complexes mTORC1 and mTORC2 in *ex vivo* primary CLL cells. To determine the basal level of mTOR activity in different prognostic subgroups of CLL patients, the phosphorylation status of mTORC1 (4E-BP1$^{T37/46}$ and S6$^{S235/236}$) and mTORC2 (AKT^{S473}) downstream targets was assessed in *ex vivo* primary CLL cells (derived from PB) compared with B cells from healthy donors (Figure 3.1). These data revealed that phosphorylation of AKT^{S473}, 4E-BP1$^{T37/46}$ and S6$^{S235/236}$ was present among CLL patient samples, but at varying levels (Figure 3.1a). In comparison to healthy donor B cells, phosphorylation levels of AKT^{S473}, 4E-BP1$^{T37/46}$ and S6$^{S235/236}$ were significantly lower in CLL cells (Figure 3b-d). Interestingly, while there was no difference in AKT expression (Figure 3.1f), a trend towards increased 4E-BP1 (p = 0.12; Figure 3.1g) and decreased S6 (p = 0.07; Figure 3.1h) expression was observed in CLL patient samples compared to B cells from healthy donors. Within this CLL patient cohort, stratification of AKT^{S473}, 4E-BP1$^{T37/46}$ and S6$^{S235/236}$ phosphorylation levels based upon distinct cytogenetic alternations showed no significant difference (Figure 3.1i-k). However, a modest trend towards decreased levels of AKT^{S473} and 4E-BP1$^{T37/46}$ phosphorylation was observed in poor-prognostic CLL patients with del(17p), compared to patients with undetected abnormalities in del(11q) or del(17p) (no del(11q)/del(17p)) (Figure 3.1i-k).

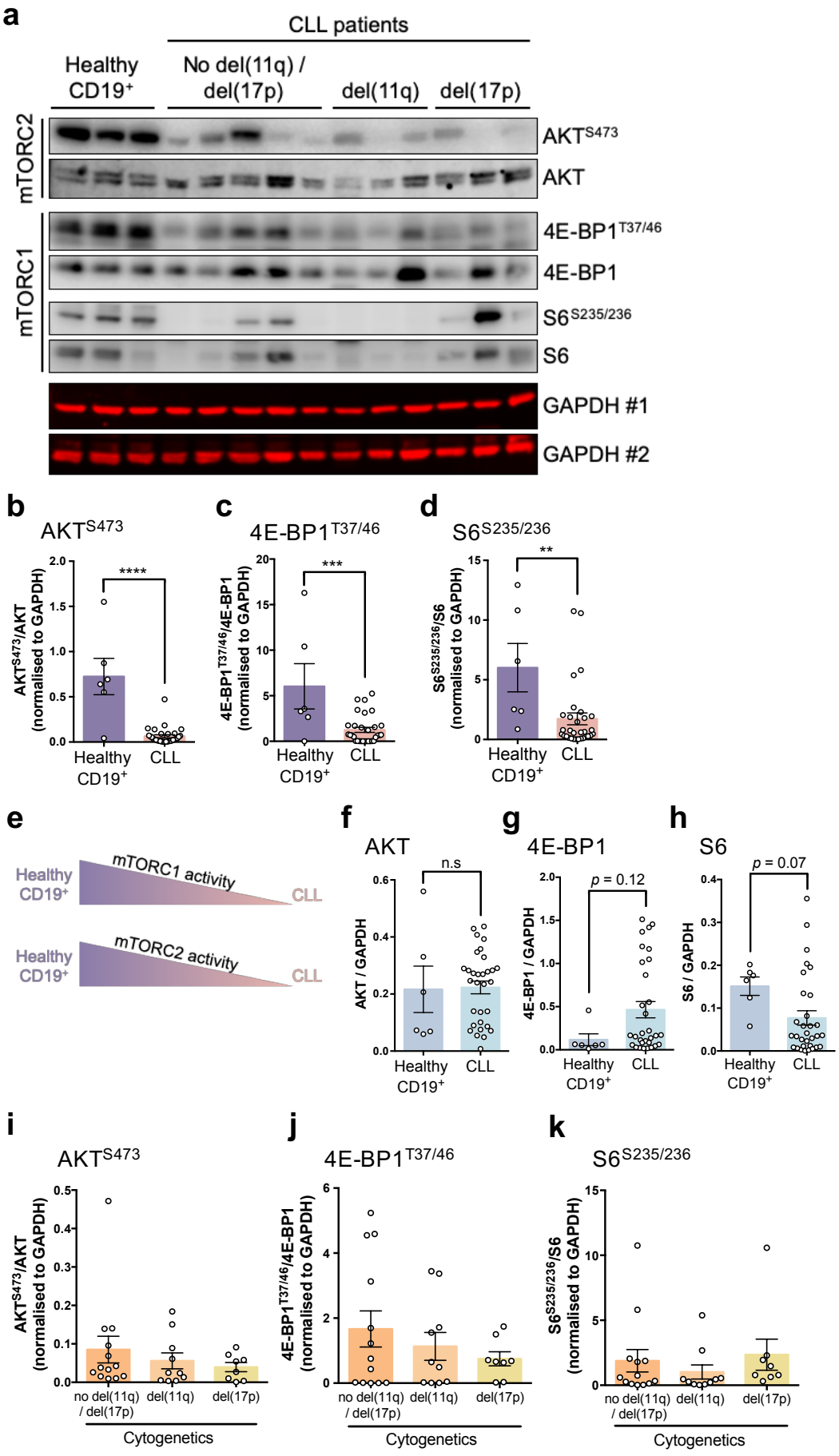

Figure 3.1 - mTOR is active in ex vivo primary CLL cells
(a) Western blot of healthy donor B cells (Healthy CD19$^+$; n=3) and CLL patients (n=11), subdivided into cytogenetic alterations 'No del(11q) / del(17p)' (n=5), del(11q) (n=3) and del(17p)

(n=3). 'No del(11q) / del(17p)' refers to an absence of detected del(11q) or del(17p) alterations. Blots were probed for AKT^{S473}, AKT, 4E-$BP1^{T37/46}$, 4E-BP1, $S6^{S235/236}$, S6 and GAPDH (loading control; #1 and #2 referring to mirror blots). (b, c, d) Relative phosphorylation levels of (b) AKT^{S473}, (c) 4E-$BP1^{T37/46}$ and (d) $S6^{S235/236}$ in Healthy $CD19^+$ (n=6; purple bars) and CLL samples (CLL; n = 31; peach bars) calculated by first normalising phosphorylation and expression levels by GAPDH, followed by normalised phosphorylation divided by normalised expression levels. (e) Schematic demonstrating mTORC1/2 activity between Healthy $CD19^+$ and CLL, showing increased mTORC1/2 activity in healthy donor B cells. (f,g,h) Normalised expression levels of (f) AKT, (g) 4E-BP1 and (h) S6 in Healthy $CD19^+$ (n=6; dark blue bars) and CLL samples (CLL; n = 31; light blue bars) calculated by normalising expression levels by GAPDH. (i, j, k) Relative phosphorylation levels of (i) AKT^{S473}, (j) 4E-$BP1^{T37/46}$ and (k) $S6^{S235/236}$ in CLL patients stratified according to cytogenetics 'No del(11q) / del(17p)' (n=13), del(11q) (n=10) and del(17p) (n=8). Individual patient datapoints are represented by white circles. Data expressed as the mean ± SEM. Statistics calculated by unpaired Student's t-test for two groups and one-way ANOVA for three groups, where * $p \leq 0.05$, ** $p \leq 0.01$, *** $p \leq 0.001$, **** $p \leq 0.0001$.

3.2.2 Regulation of mTORC1 activity in CLL patient LN biopsies

Following the assessment of basal mTOR activity in freshly isolated CLL cells, it was of interest to investigate mTOR activity within the CLL lymphoid compartment (Figure 3.2). The CLL-TME promotes BCR, CD40 and chemokine receptor engagement, which transmits signals through the PI3K-AKT-mTOR axis to promote cell survival, growth and proliferation (9, 207). To examine mTOR activity within the CLL-TME, the phosphorylation status of mTORC1 (4E-$BP1^{T37/46}$ and $S6^{S235/236}$) downstream targets was assessed by IHC of LN biopsies derived from distinct prognostic subgroups of CLL patients (Figure 3.2). The patients had previously been categorised into 'indolent' or 'progressive' disease, based upon cytogenetics, *IGVH* gene mutational status and CD38 expression. These experiments showed that 4E-$BP1^{T37/46}$ phosphorylation was observed at varying levels in CLL patient LN biopsies (Figure 3.2a). Of the 20 CLL patients examined, 5 (25 %) had undetected 4E-$BP1^{T37/46}$ phosphorylation. Moreover, no significant difference was observed in 4E-$BP1^{T37/46}$ phosphorylation levels between indolent or progressive CLL patients (Figure 3.2b). Interestingly, despite the presence of 4E-$BP1^{T37/46}$ phosphorylation, little or no $S6^{S235/236}$ phosphorylation was detected (Figure 3.2c). Only 3 (15 %) of the 20 CLL patients assessed exhibited $S6^{S235/236}$ phosphorylation (Figure 3.2d). Phosphorylation levels were scored as an intensity score (IS) by an experienced histopathologist.

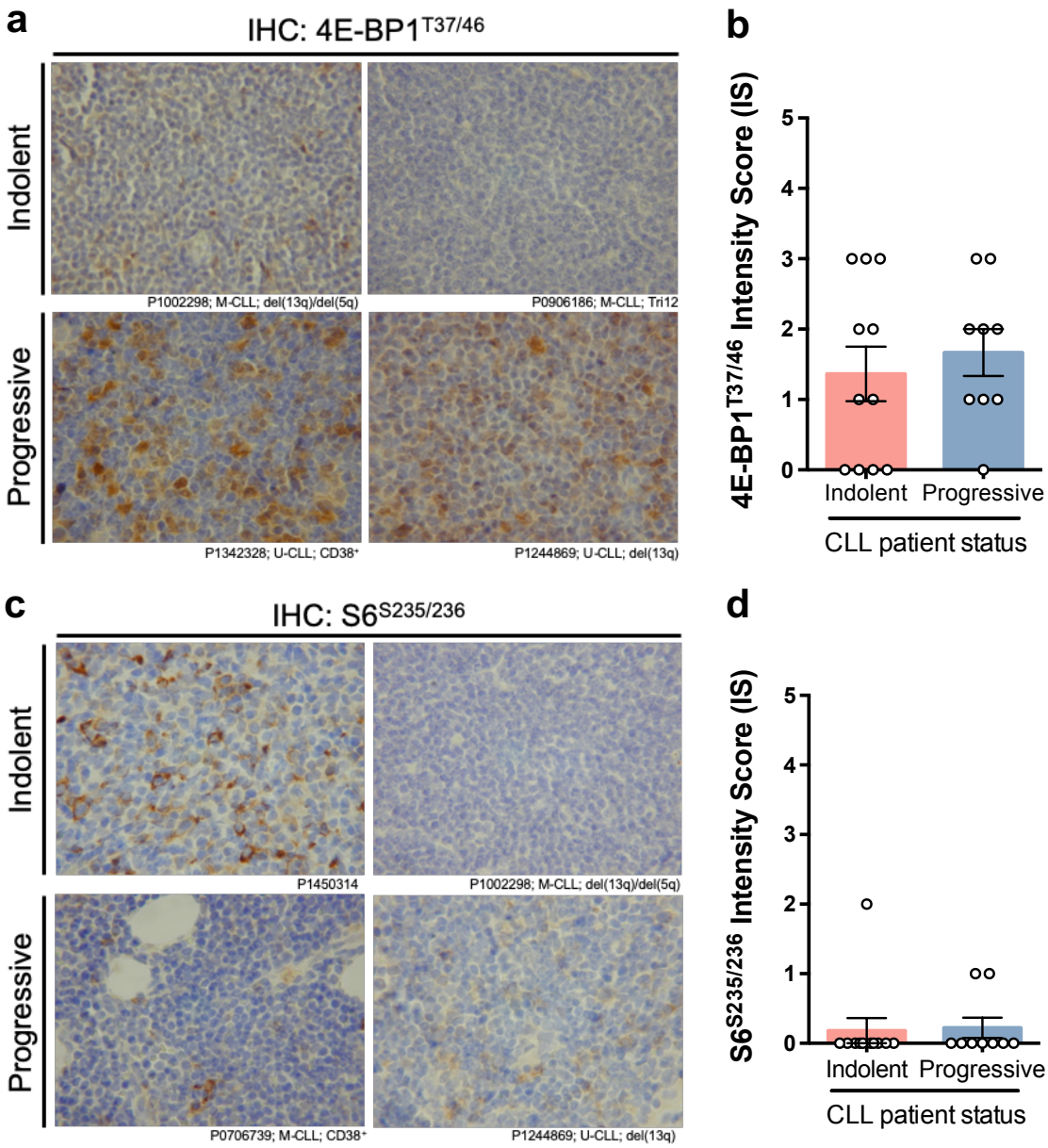

Figure 3.2 – Regulation of mTORC1 activity in CLL patient LN biopsies
(a, c) IHC of CLL patient LN biopsies stratified into 'indolent' and 'progressive' disease based on cytogenetics and *IGVH* gene mutational status. LN sections were stained for (a) 4E-BP1$^{T37/46}$ and (c) S6$^{S235/236}$. Prognostic information is found below each micrograph. Staining was performed by Dr. Mark Catherwood (Belfast City Hospital, Belfast). (b) 4E-BP1$^{T37/46}$ and (d) S6$^{S235/236}$ intensity score (IS) for CLL patient LN biopsies subdivided into indolent (n=11; salmon bars) and progressive (n=9; blue bars) disease. IS is scored from 0 to 5; 0 indicating undetected signal and 5 corresponding to highest signal. All slides were scored by an experienced histopathologist. Individual patient datapoints are represented by white circles. Data expressed as the mean ± SEM.

3.2.3 BCR stimulation enhances mTOR activity *in vitro*

To explore mTOR activation downstream of BCR ligation *in vitro*, primary CLL cells derived from PB were stimulated with soluble F(ab')$_2$ fragments (213). Following short-term F(ab')$_2$ stimulation, the phosphorylation status of mTORC1 (4E-BP1$^{T37/46}$ and S6$^{S235/236}$) and mTORC2 (AKT^{S473}) downstream targets was assessed (Figure 3.3). As BCR engagement elicits activation of MAPK/ERK

signalling in CLL cells (234) and mTORC1 is a downstream effector of the MAPK/ERK pathway (429, 430), ERK1/2$^{T202/Y204}$ phosphorylation was assessed. Western blotting of F(ab')$_2$-stimulated primary CLL samples revealed an increase in phosphorylation of the aforementioned mTORC1/2 targets and ERK1/2$^{T202/Y204}$ (Figure 3.3a). Importantly, these data demonstrated the heterogeneity of BCR signalling responses among CLL patients, where a subset of CLL samples are virtually unaffected by F(ab')$_2$ engagement (Figure 3.3a). Nevertheless, F(ab')$_2$ stimulation of primary CLL samples resulted in a significant increase in relative phosphorylation levels of ERK1/2$^{T202/Y204}$ (Figure 3.3e) and mTORC1 downstream target S6$^{S235/236}$ (Figure 3.3d). Additionally, near-significant increases in relative phosphorylation of mTORC2 substrate AKT^{S473} (p = 0.068; Figure 3.3b) and mTORC1 substrate 4E-BP1$^{T37/46}$ (p = 0.07; Figure 3.3c) were observed.

mTOR activity was further characterised in CLL cell lines HG-3 and MEC-1, which have cytogenetic alterations associated with favourable and poor prognosis, respectively (431, 432). Of note, HG-3 and MEC-1 cells are immortalised, Epstein-Barr virus (EBV)-transformed cell lines with unlimited proliferative capacity (431, 432). It must be stressed that while HG-3 and MEC-1 cells are reflective of certain aspects of CLL disease biology (i.e. cytogenetic alterations), one cannot make direct comparisons between these cell lines and primary CLL cells. Indeed, HG-3 and MEC-1 cells are characterised by hyperactive oncogenic signalling (distinct from CLL cells that require external stimulation), which will likely influence drug sensitivity/activity. This being said, MEC-1 cells display constitutive BTK activation (501) and express unmutated *IGHV* genes (409, 410), highlighting possible BCR signalling involvement. Thus, it was of interest to address mTOR activity in these cell lines. Additionally, unrestricted proliferation of HG-3 and MEC-1 cells will offer insights into the cytostatic ability of mTOR kinase inhibitors. To determine the activity of mTOR in HG-3 and MEC-1 cells, the phosphorylation status of mTORC1 (4E-BP1$^{T37/46}$ and S6$^{S235/236}$) and mTORC2 (AKT^{S473}) downstream targets was examined (Figure 3.3f-i). ERK1/2$^{T202/Y204}$ phosphorylation was also assessed (Figure 3.3f,j). These data revealed that phosphorylation of AKT^{S473}, 4E-BP1$^{T37/46}$ and S6$^{S235/236}$ was present in HG-3 and MEC-1 cells (Figure 3.3f). In comparison to HG-3 cells, relative phosphorylation levels of mTORC2 substrate AKT^{S473} was significantly decreased in MEC-1 cells (Figure 3.3g). In contrast, MEC-1 cells possessed significantly higher levels of

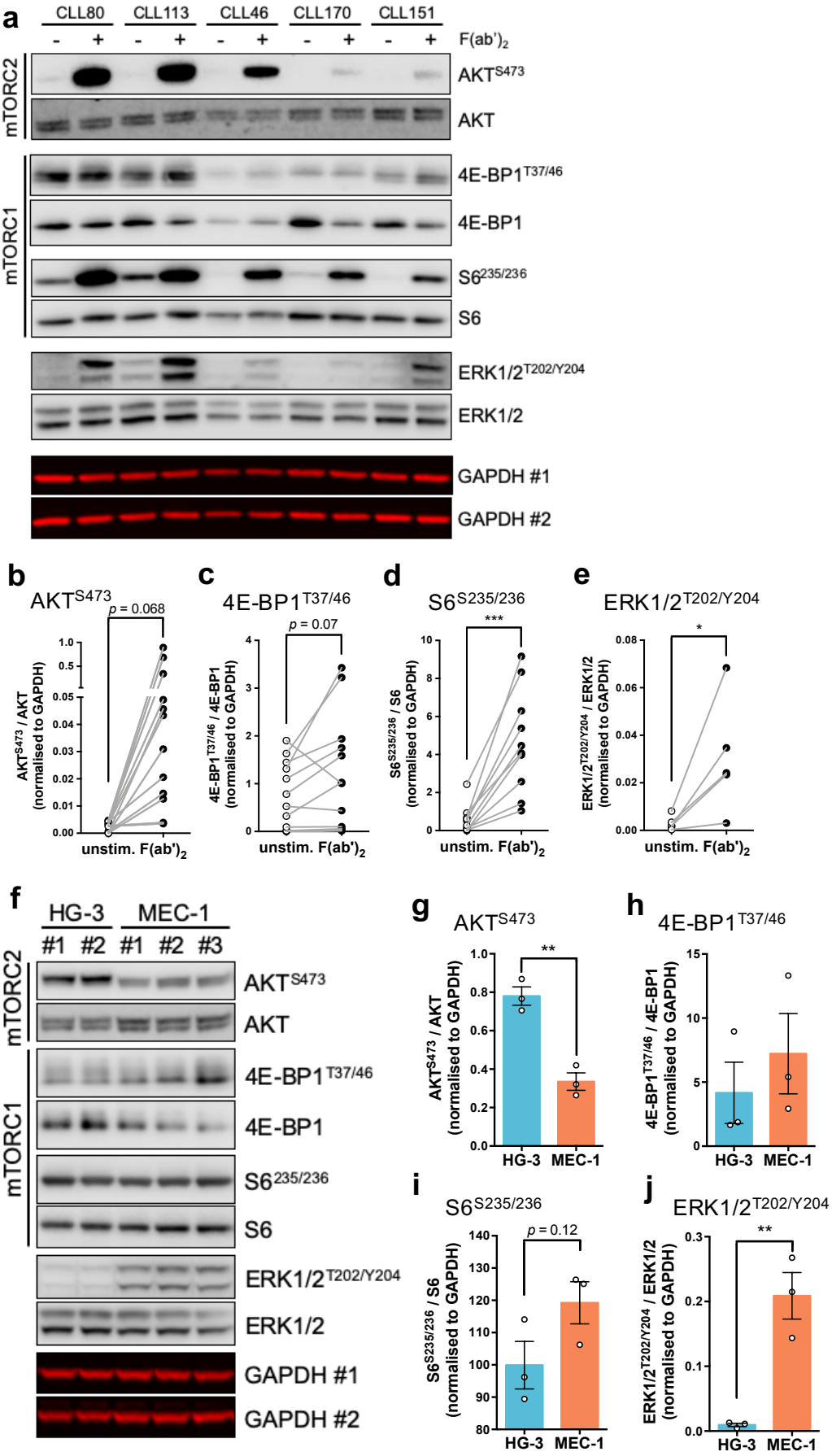

Figure 3.3 - BCR stimulation enhances mTOR activity *in vitro*

(a) Western blot of individual primary CLL samples (n=5) unstimulated (-) or stimulated (+) with F(ab')$_2$ fragments (10 ng/mL) for 1 h. Blots were probed for AKT^{S473}, AKT, 4E-BP1$^{T37/46}$, 4E-BP1, S6$^{S235/236}$, S6, ERK1/2$^{T202/Y204}$, ERK1/2 and GAPDH (loading control; #1 and #2 referring to mirror blots). (b, c, d, e) Relative phosphorylation levels of (b) AKT^{S473}, (c) 4E-BP1$^{T37/46}$, (d) S6$^{S235/236}$ and (e) ERK1/2^{T202Y204} between unstimulated (unstim.; white circles) and F(ab')$_2$-stimulated (black circles) CLL samples (AKT^{S473}, 4E-BP1$^{T37/46}$ n=12; S6$^{S235/236}$ n=10; ERK1/2^{T202Y204} n=5). For each CLL patient sample, relative phosphorylation levels for unstim. and F(ab')$_2$ are connected by a grey line. Relative phosphorylation is calculated by first normalising phosphorylation and expression levels by GAPDH, followed by normalised phosphorylation divided by normalised expression levels. (f) Representative western blot of HG-3 (n=2) and MEC-1 (n=3) protein lysates probed for AKT^{S473}, AKT, 4E-BP1$^{T37/46}$, 4E-BP1, S6$^{S235/236}$, S6, ERK1/2$^{T202/Y204}$, ERK1/2 and GAPDH. (g, h, i, j) Relative phosphorylation levels of (g) AKT^{S473}, (h) 4E-BP1$^{T37/46}$, (i) S6$^{S235/236}$ and (j) ERK1/2^{T202Y204} in HG-3 (n=3; blue bars) and MEC-1 (n=3; orange bars) cells. Individual datapoints are represented by white circles. Data expressed as the mean ± SEM. Statistics calculated by paired and unpaired Student's t-test, where * $p \leq 0.05$, ** $p \leq 0.01$, *** $p \leq 0.001$, **** $p \leq 0.0001$.

ERK1/2$^{T202/Y204}$ phosphorylation (Figure 3.3j). Despite no significant difference between the relative phosphorylation levels of 4E-BP1$^{T37/46}$ in HG-3 and MEC-1 cells (Figure 3.3 h), a trend towards increased levels of S6$^{S235/236}$ phosphorylation was observed in MEC-1 cells (p =0.12; Figure 3.3i). Importantly, while there was no difference in AKT, S6 or ERK1/2 expression (Figure 3.3f; data not shown), a trend towards increased 4E-BP1 (p = 0.12; Figure 3.3f; data not shown) expression was observed in HG-3 cells compared to MEC-1 cells.

3.2.4 AZD8055 inhibits phosphorylation of mTORC1/2 downstream targets in F(ab')$_2$-stimulated CLL cells

After demonstrating that mTOR is a downstream effector of BCR stimulation in CLL cells (Figure 3.4b), it was important to address whether pharmacological inhibition of mTOR using the dual mTOR kinase inhibitor AZD8055 possessed anti-tumour activity. To examine AZD8055 selectivity for mTORC1 and mTORC2 in unstimulated and F(ab')$_2$-stimulated CLL cells, the phosphorylation status of mTORC1 (4E-BP1$^{T37/46}$ and S6$^{S235/236}$) and mTORC2 (AKT^{S473}) downstream targets was assessed following short-term treatment with increasing doses of AZD8055 (Figure 3.4). After 30 min pre-treatment with the indicated doses of AZD8055, CLL cells remained unstimulated or were F(ab')$_2$-stimulated for 1 h. This experiment showed that AZD8055 treatment resulted in a dose-dependent inhibition of F(ab')$_2$-dependent 4E-BP1$^{T37/46}$, S6$^{S235/236}$ and AKT^{S473} phosphorylation (Figure 3.4a). With the exception of 4E-BP1$^{T37/46}$, phosphorylation levels of S6$^{S235/236}$ and AKT^{S473} were undetectable or noticeably reduced in unstimulated CLL cells (Figure 3.4a). In F(ab')$_2$-stimulated CLL cells, phosphorylation of AKT^{S473} and 4E-BP1$^{T37/46}$ was eliminated at a clinically

achievable dose of AZD8055, while $S6^{S235/236}$ phosphorylation was reduced (Figure 3.4a). Importantly, AZD8055 was effective in blocking a $F(ab')_2$-dependent increase in mTOR activity (Figure 3.4a,c). Unexpectedly, treatment with AZD8055 also resulted in a dose-dependent inhibition of $F(ab')_2$-induced AKT^{T308} phosphorylation (Figure 3.4a).

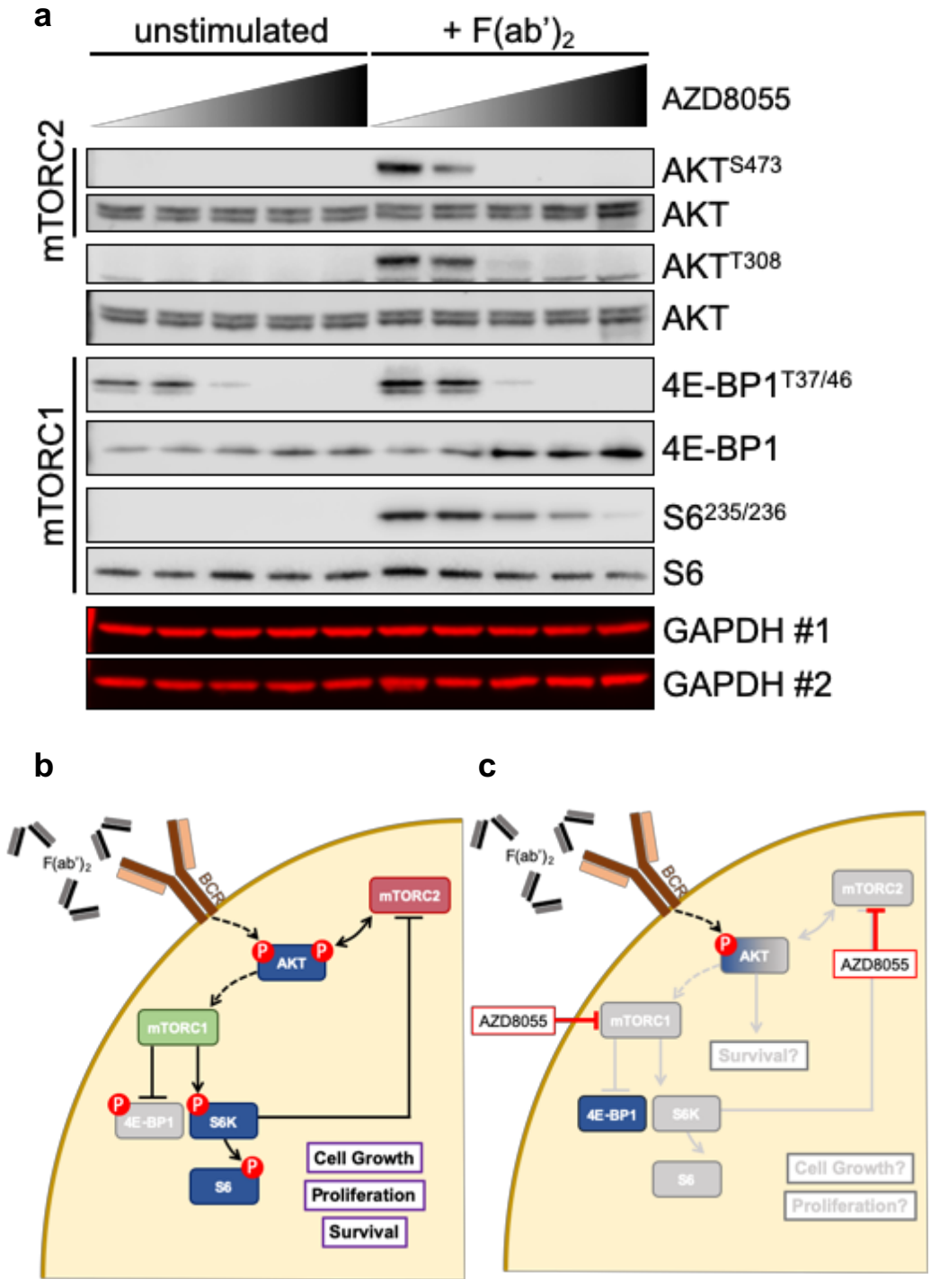

Figure 3.4 - Treatment of primary CLL cells with the dual mTOR inhibitor AZD8055 reveals a dose-dependent inhibition of mTORC1/2 activity
(a) Representative western blot of a primary CLL sample (CLL80; n=3 CLL samples) unstimulated or $F(ab')_2$-stimulated for 1 h following 30 min pre-treatment with increasing concentrations of AZD8055 (Vehicle, 10, 100, 1000, 10000 nM). Blots were probed for AKT^{S473}, AKT^{T308}, AKT, 4E-

BP1$^{T37/46}$, 4E-BP1, S6$^{S235/236}$, S6 and GAPDH (loading control; #1 and #2 referring to mirror blots). (b, c) Schematic of (b) mTOR pathway activation following F(ab')$_2$ stimulation and (c) AZD8055 drug selectivity for mTORC1/2, inhibiting phosphorylation of downstream targets AKT^{S473}, 4E-BP1$^{T37/46}$ and S6$^{S235/236}$.

To further explore drug selectivity for mTORC1 and mTORC2, AZD8055 was compared with the mTORC1-selective inhibitor rapamycin and BTK inhibitor ibrutinib (Figure 3.5). As treatment of BCR-stimulated CLL cells with ibrutinib has been shown to abrogate MAPK/ERK signalling (126), ERK1/2$^{T202/Y204}$ phosphorylation was also assessed. Following pre-treatment with AZD8055 (100 nM), rapamycin (10 nM) or ibrutinib (1 μM) for 30 min, CLL cells remained unstimulated or were F(ab')$_2$-stimulated for 1 h (Figure 3.5a). Consistent with Figure 3.4, these data showed that F(ab')$_2$-dependent phosphorylation of mTORC1 (4E-BP1$^{T37/46}$ and S6$^{S235/236}$) and mTORC2 (AKT^{S473}) downstream targets were inhibited following short-term AZD8055 treatment, resulting in a near-significant trend towards reduced AKT^{S473} phosphorylation (p = 0.09; Figure 3.5b). In contrast, AZD8055 treatment did not reduce ERK1/2$^{T202/Y204}$ phosphorylation levels (Figure 3.5a). Consistent with observation that rapamycin differentially affects 4E-BP1 and S6K activity (312), these data showed that 4E-BP1$^{T37/46}$ phosphorylation remained largely unaffected by rapamycin (Figure 3.5a,c), whereas S6$^{S235/236}$ phosphorylation was significantly inhibited in unstimulated CLL cells (Figure 3.5d). Moreover, increased F(ab')$_2$-dependent S6$^{S235/236}$ phosphorylation was also blocked with rapamycin to a similar extent as AZD8055 (Figure 3.5d). Conversely, rapamycin did not significantly affect AKT^{S473} (Figure 3.5b) and ERK1/2$^{T202/Y204}$ phosphorylation levels (Figure 3.5a). Short term treatment of F(ab')$_2$-stimulated CLL cells with ibrutinib resulted in a near-significant reduction in AKT^{S473} phosphorylation compared to F(ab')$_2$-stimulated vehicle control (p = 0.08; Figure 3.5b). While ibrutinib treatment did not significantly impact phosphorylation levels of mTORC1 downstream targets 4E-BP1$^{T37/46}$ (Figure 3.5c) and S6$^{S235/236}$ (Figure 3.5d) in unstimulated CLL cells, phosphorylation of 4E-BP1$^{T37/46}$ and S6$^{S235/236}$ was reduced in F(ab')$_2$-stimulated CLL cells (Figure 3.5a,c,d). However, whereas inhibition of F(ab')$_2$-dependent S6$^{S235/236}$ phosphorylation was readily observable, 4E-BP1$^{T37/46}$ inhibition was much more variable. Consistent with previous studies (126), ibrutinib treatment of F(ab')$_2$-stimulated CLL cells effectively inhibited ERK1/2$^{T202/Y204}$ phosphorylation (Figure 3.5a).

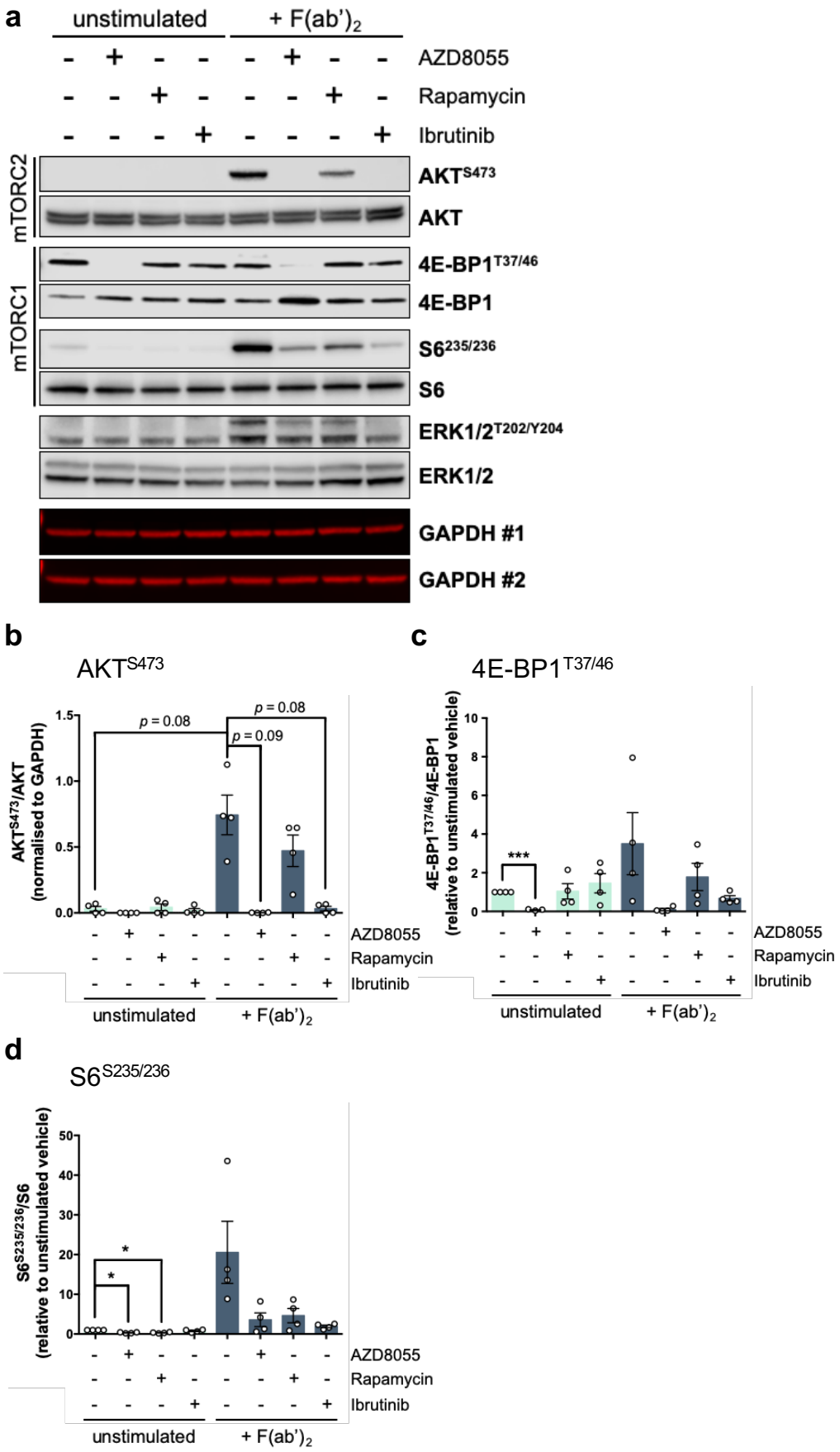

Figure 3.5 - A clinically-achievable dose of AZD8055 effectively inhibits phosphorylation of mTORC1/2 targets following F(ab')$_2$ stimulation, superior to the mTORC1-selective inhibitor rapamycin

(a) Representative western blot of a primary CLL sample (CLL57) unstimulated or F(ab')$_2$-stimulated for 1 h following 30 min pre-treatment with AZD8055 (100 nM), Rapamycin (10 nM),

Ibrutinib (1 μM) or DMSO vehicle control. Blots were probed for AKT^{S473}, AKT, 4E-$BP1^{T37/46}$, 4E-BP1, $S6^{S235/236}$, S6, $ERK1/2^{T202/Y204}$, ERK1/2 and GAPDH (loading control; #1 and #2 referring to mirror blots). (b, c, d) Relative phosphorylation levels of (b) AKT^{S473}, (c) 4E-$BP1^{T37/46}$ and (d) $S6^{S235/236}$ in primary CLL samples (n=4) treated as described in (a). Relative phosphorylation is calculated by first normalising phosphorylation and expression levels by GAPDH, followed by normalised phosphorylation divided by normalised expression levels. Relative phosphorylation levels are relative to unstimulated vehicle control. Unstimulated (teal bars) and $F(ab')_2$-stimulated (dark blue bars). Individual patient datapoints are represented by white circles. Data expressed as the mean ± SEM. Statistics calculated by one-way ANOVA, where * $p \leq 0.05$, ** $p \leq 0.01$, *** $p \leq 0.001$, **** $p \leq 0.0001$.

3.2.5 AZD8055 treatment does not affect HG-3 and MEC-1 cell viability

To examine the impact of dual mTOR inhibition upon CLL cell survival, HG-3 and MEC-1 cells were treated with AZD8055 (100 nM), rapamycin (10 nM) or ibrutinib (1 μM) for 48 h. Of note, ibrutinib treatment was included in recognition of the inhibitory effect upon $F(ab')_2$-dependent mTORC1 ($S6^{S235/236}$) and mTORC2 (AKT^{S473}) activity (Figure 3.5). Following treatment, the cells were stained with Annexin V/7-AAD and analysed by flow cytometry (Figure 3.6a). These data showed that treatment with AZD8055, rapamycin or ibrutinib did not significantly affect the viability of HG-3 or MEC-1 cells (Figure 3.6a-e). Notably, AZD8055 treatment modestly increased the percentage of viable (Annexin V^{neg} 7-AAD^{neg}) HG-3 cells (p = 0.056; Figure 3.6b). Consistent with this result, AZD8055 treatment corresponded to a visible decrease in the percentage of apoptotic (Annexin V^{pos} 7-AAD^{pos}) HG-3 cells (p = 0.08; Figure 3.6c). However, these data are likely explained by biological variability and do not represent biological significance. With hindsight, it would have been appropriate to treat the cells with a known apoptosis-inducing agent (as a positive control) to consider the scale of the effect of each treatment and enable comparisons to be drawn.

mTOR signalling plays a role in the regulation (activity and expression levels) of pro- and anti-apoptotic BCL2 family proteins, which shift the balance between cellular life and death (433, 434). Intrigued by the perceived lack of sensitivity of HG-3 and MEC-1 cells to mTOR inhibition, it was of interest to explore the regulation of anti-apoptotic (MCL-1, BCL-xL, BCL2 and Survivin) and pro-apoptotic (BIM) proteins in response to AZD8055, rapamycin or ibrutinib treatment (Figure 3.6f). The presence of PARP fragments or 'cleaved' PARP was also assessed as a marker for caspase-dependent apoptosis (435). These data revealed that although the presence of cleaved PARP was observable in HG-3

and MEC-1 cells, the levels were too low to resolve (Figure 3.6f). Interestingly, differential regulation of anti- and pro-apoptotic proteins was observed HG-3 and MEC-1 cells following treatment. For example, while the expression of anti-apoptotic MCL-1 was downregulated in HG-3 cells following treatment, MCL-1 expression was increased in MEC-1 cells. AZD8055 treatment downregulated MCL-1 expression to a greater extent than rapamycin or ibrutinib in HG-3 cells. Conversely, AZD8055 treatment upregulated MCL-1 expression to a larger extent than rapamycin or ibrutinib in MEC-1 cells (Figure 3.6f). Basal expression of the anti-apoptotic protein BCL-xL was higher in MEC-1 cells compared to HG-3 cells. Nevertheless, BCL-xL expression was elevated in HG-3 cells after rapamycin or ibrutinib treatment. AZD8055 treatment only caused a modest upregulation in BCL-xL expression in HG-3 cells. As for MEC-1 cells, treatment with AZD8055, rapamycin and ibrutinib resulted in an upregulation in BCL-xL expression (Figure 3.6f). Overexpression of the anti-apoptotic protein BCL2 is a central characteristic of CLL pathology (436). As such, high levels of BCL2 expression were observed in HG-3 and MEC-1 cells, which was maintained despite treatment with AZD8055, rapamycin or ibrutinib (Figure 3.6b). Basal expression of anti-apoptotic protein Survivin was higher in MEC-1 cells compared to HG-3 cells. Although the expression of Survivin was downregulated in HG-3 cells following treatment, Survivin expression was upregulated in MEC-1 cells with AZD8055 and rapamycin treatment. Interestingly, treatment with ibrutinib resulted in an upregulation of Survivin in HG-3 cells, while the same treatment caused a downregulation of Survivin in MEC-1 cells (Figure 3.6f). The expression of pro-apoptotic protein BIM (BIM_{EL}, BIM_L and BIM_S) was upregulated in HG-3 and MEC-1 cells following AZD8055, rapamycin and ibrutinib treatment. AZD8055 caused a modest increase in BIM expression in HG-3 cells, which was comparative to rapamycin. Similarly, AZD8055 treatment caused a larger increase in BIM expression (compared with rapamycin) in MEC-1 cells. Of note, AZD8055 upregulated the expression of BIM_S in MEC-1 cells, widely considered the most cytotoxic BIM isoform (437) (Figure 3.6f).

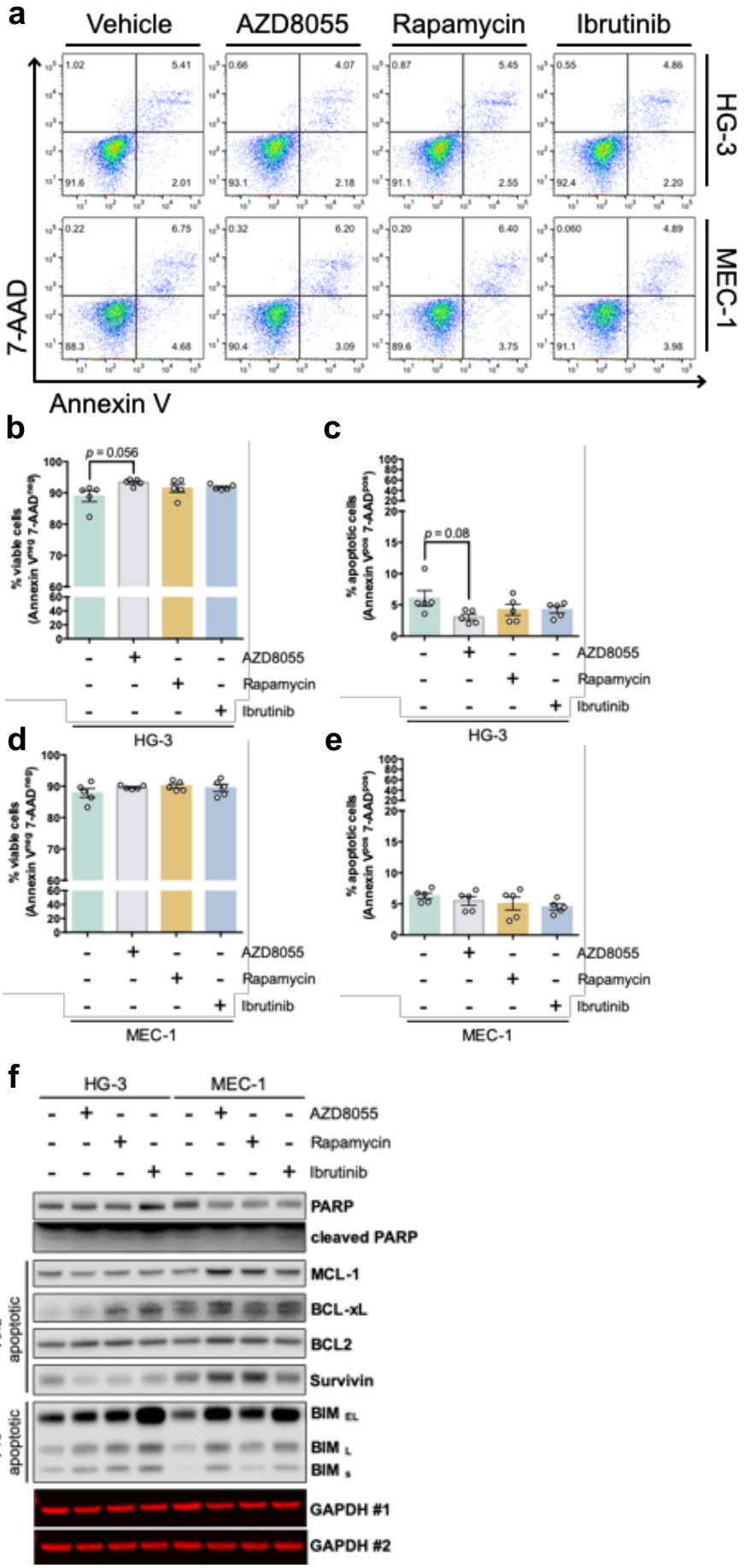

Figure 3.6 - AZD8055 promotes a modest increase in HG-3 cell viability
(a) Representative FACS plot of HG-3 (top panel) and MEC-1 (bottom panel) cells stained with Annexin V and 7-AAD to assess cell viability following treatment with AZD8055 (100 nM),

Rapamycin (10 nM), Ibrutinib (1 μM) or DMSO vehicle control (Vehicle) for 48 h. Please refer to section 2.2.2.3 for gating strategy. (b, d) Percentage viable (b) HG-3 (n=5) and (d) MEC-1 (n=5) cells treated with AZD8055 (grey bar), Rapamycin (gold bar), Ibrutinib (blue bar) or DMSO vehicle control (green bar) for 48 h, as described in (a). Viability is defined as Annexin V^{neg} and 7-AAD^{neg}. (c, e) Percentage apoptotic (c) HG-3 (n=5) and (e) MEC-1 (n=5) cells treated as described in (a). Apoptotic cells are defined as Annexin V^{pos} and 7-AAD^{pos}. (f) Representative western blot of HG-3 (n=3) and MEC-1 (n=3) cells treated with AZD8055, Rapamycin, Ibrutinib or DMSO vehicle control for 48 h. Blots were probed for PARP, MCL-1, BCL-xL, BCL2, Survivin, BIM (BIM_{EL}, BIM_L, and BIM_S) and GAPDH (loading control; #1 and #2 referring to mirror blots). Individual patient datapoints are represented by white circles. Data expressed as the mean ± SEM. Statistics calculated by one-way ANOVA, where * $p \leq 0.05$, ** $p \leq 0.01$, *** $p \leq 0.001$, **** $p \leq 0.0001$.

3.2.6 mTOR inhibition is sustained in F(ab')$_2$-stimulated CLL cells

Studies have previously highlighted the dynamic adaptability of various cancers in response to mTOR inhibition (293, 314, 324). To address whether mTOR inhibition is short-lived, primary CLL cells (Figure 3.7a) and MEC-1 cells (Figure 3.7b) were F(ab')$_2$-stimulated for the indicated time points in the presence of AZD8055. Thereafter, the phosphorylation status of mTORC1 (4E-$BP1^{T37/46}$ and $S6^{S235/236}$) and mTORC2 (AKT^{S473}) downstream targets was examined (Figure 3.7). Since AZD8055 has been shown to suppress feedback inhibition of RTKs, which ultimately results in PI3K-induced AKT^{T308} rephosphorylation (324), the phosphorylation status of AKT^{T308} was also assessed. F(ab')$_2$ stimulation of CLL cells conferred a transient increase in AKT^{T308}, AKT^{S473} and $S6^{S235/236}$ phosphorylation, while 4E-$BP1^{T37/46}$ phosphorylation was largely unaffected (Figure 3.7a). As demonstrated in Figure 3.4a, AZD8055 inhibited phosphorylation of mTORC1 (4E-$BP1^{T37/46}$ and $S6^{S235/236}$) and mTORC2 (AKT^{S473}) downstream targets in F(ab')$_2$-stimulated CLL cells (Figure 3.7a). Moreover, inhibition of mTORC1 (4E-$BP1^{T37/46}$ and $S6^{S235/236}$) and mTORC2 (AKT^{S473}) activity was sustained for up to 24 h. Interestingly, AZD8055 treatment also inhibited AKT^{T308} phosphorylation, which was maintained throughout the duration of the timecourse (Figure 3.7a).

As demonstrated in Figure 3.3f, mTORC1 (4E-$BP1^{T37/46}$ and $S6^{S235/236}$) and mTORC2 (AKT^{S473}) downstream targets were phosphorylated in MEC-1 cells. F(ab')$_2$ stimulation of MEC-1 cells did not confer an increase in AKT^{S473}, 4E-$BP1^{T37/46}$ and $S6^{S235/236}$ phosphorylation, while a modest increase in AKT^{T308} phosphorylation was observed (Figure 3.7b). Of note, relative phosphorylation levels of AKT^{T308}, AKT^{S473}, 4E-$BP1^{T37/46}$ and $S6^{S235/236}$ reduced towards the end of the timecourse (Figure 3.7b). Consistent with Figure 3.7a, AZD8055 inhibited phosphorylation of mTORC1 (4E-$BP1^{T37/46}$ and $S6^{S235/236}$) and mTORC2 (AKT^{S473}) downstream targets in

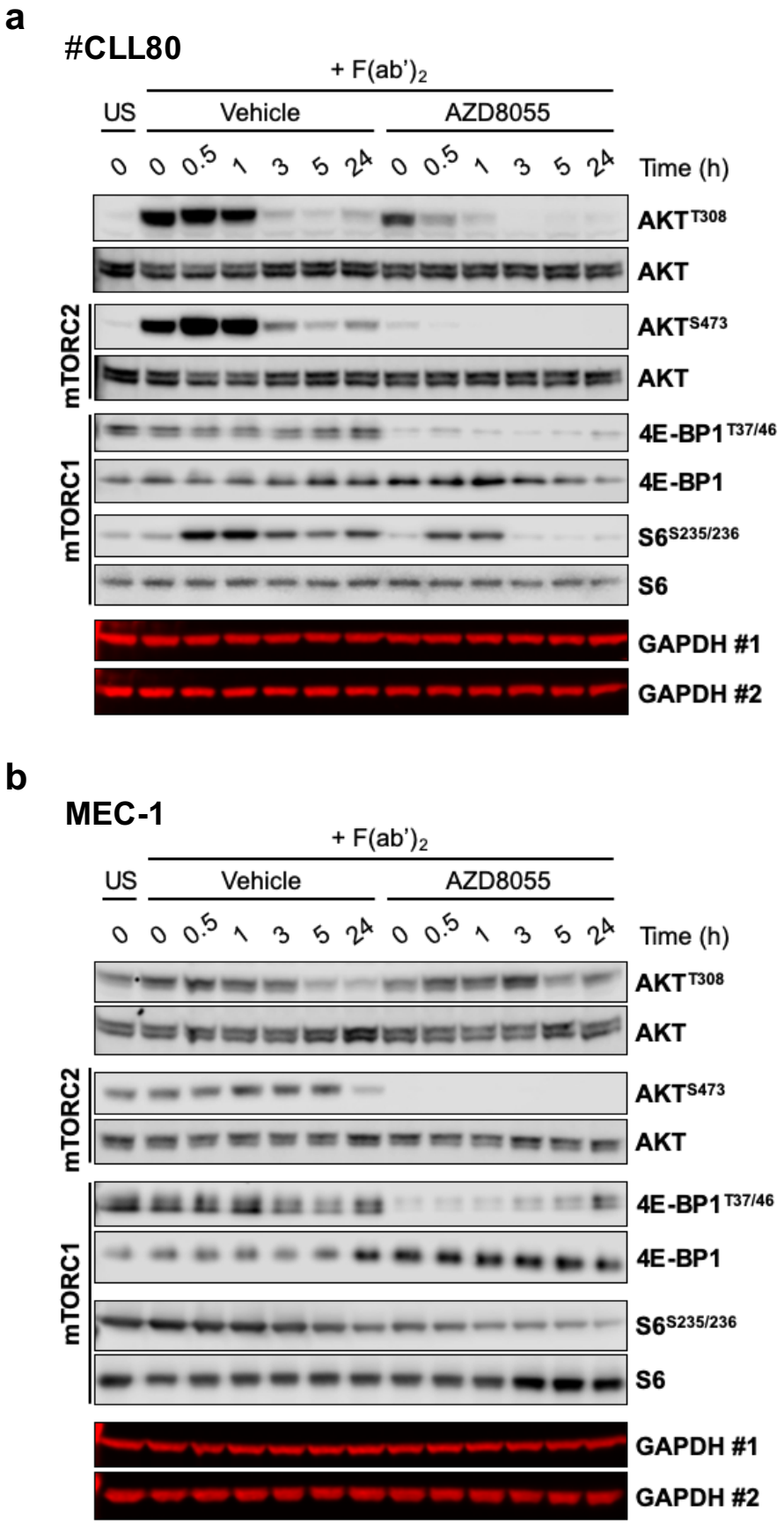

Figure 3.7 - mTOR inhibition is sustained in F(ab')$_2$-stimulated CLL cells
(a, b) Representative western blots of a (a) primary CLL sample (CLL80; n=3 primary CLL samples) and (b) MEC-1 cells (n=3) stimulated with F(ab')$_2$ for the indicated timepoints (0, 0.5, 1, 3, 5 and 24 h) following 30 min pre-treatment with AZD8055 (100 nM) or vehicle control. Blots were probed for AKT^{T308}, AKT^{S473}, AKT, 4E-BP1$^{T37/46}$, 4E-BP1, S6$^{S235/236}$, S6 and GAPDH (loading control; #1 and #2 referring to mirror blots).

F(ab')$_2$-stimulated MEC-1 cells (Figure 3.7b). However, unlike F(ab')$_2$-stimulated CLL cells, AZD8055 treatment did not inhibit AKT^{T308} phosphorylation in F(ab')$_2$-stimulated MEC-1 cells (Figure 3.7b). Importantly, inhibition of mTORC1 (S6$^{S235/236}$) and mTORC2 (AKT^{S473}) activity was sustained for the duration of the timecourse. However, an increase in 4E-BP1$^{T37/46}$ phosphorylation was observed at 24 h (Figure 3.7b). It is important to consider that MEC-1 cells are not 'wired' to be stimulated in the same way as primary CLL cells, owing to the fact that this cell line is EBV-transformed. Figure 3.7 highlights that MEC-1 cells are hyperactivated without external stimulation, whereas primary CLL cells require external stimulation (e.g. F(ab')$_2$ stimulation) to activate mTOR signalling. Thus, these factors demonstrably influence drug sensitivity/activity, inasmuch as AZD8055 cannot inhibit something that is almost unstimulated.

3.2.7 Dual mTOR inhibitors synergise with ibrutinib to enhance CLL cell death *in vitro*

To investigate the sensitivity of CLL cells to AZD8055, AZD2014 (AZD8055 clinical analogue) and ibrutinib, CLL cells were treated with increasing concentrations of drug for 48 h. The resazurin cell viability assay was subsequently used to quantify cell viability, from which the half-maximal effective concentration (EC_{50}) was calculated. As reported by Pike *et al.*, AZD8055 was shown to be a potent inhibitor of mTOR kinase (IC_{50}=0.00013) and inhibited mTORC1/2 downstream targets (S6$^{S235/236}$ IC_{50}=0.027 μM; AKT^{S472} IC_{50}=0.024 μM). Despite encouraging preclinical evaluation *in vitro*, AZD8055 exhibited unfavourable bioavailability (pharmacokinetics) among murine species (mouse=81 %; rat=12 %). Furthermore, AZD8055 was quickly metabolised in human hepatocytes (36.4μL/min/10^6). Given the potential risks associated with these factors, AZD8055 was further optimised to improve bioavailability, aqueous solubility and reduce turnover (318). A detailed explanation of the chemical modifications generated to synthesise AZD2014 was reviewed (318). In brief, AZD2014 was synthesised from AZD8055 in a stepwise process via modification of amide and methoxy groups to reduce turnover in human hepatocytes. AZD2014 demonstrated reduced metabolism (<4.2 μL/min/10^6), improved bioavailability in rodents (mouse=>100 %; rat=40 %), enhanced solubility (>600 μM) maintained good potency against mTOR kinase (IC_{50}=0.0028) and inhibited downstream targets (S6$^{S235/236}$ IC_{50}=0.2 μM; AKT^{S472} IC_{50}=0.08 μM). Like AZD8055, AZD2014 is

highly selective against other PIKK family members (IC_{50} >3 μM). However, chemical modifications rendered AZD2014 less potent than AZD8055 (318). Treatment of CLL cells with increasing concentrations of AZD8055 (Figure 3.8a), AZD2014 (Figure 3.8b) or ibrutinib (Figure 3.8c) resulted in a dose-dependent reduction in cell viability. However, CLL cells were largely insensitive to AZD8055 (EC_{50} = 12.415 μM) and AZD2014 (EC_{50} = 10.229 μM) at clinically achievable doses (Figure 3.8a,b). Conflicting with earlier reports (318), AZD2014 was slightly more potent than AZD8055 in primary CLL cells. Although CLL cells were more sensitive to ibrutinib (EC_{50} = 5.446 μM), only modest reductions in cell viability were observed at clinically achievable doses (Figure 3.8c).

As demonstrated in Figure 3.5a, AZD8055 or ibrutinib treatment as single agents targeted distinct components of pro-survival signalling pathways in $F(ab')_2$-stimulated CLL cells. For example, while ibrutinib failed to inhibit 4E-$BP1^{T37/46}$ phosphorylation, it diminished phosphorylation of $ERK1/2^{T202/Y204}$. Conversely, while AZD8055 was unable inhibit $ERK1/2^{T202/Y204}$ phosphorylation, it reduced phosphorylation of 4E-$BP1^{T37/46}$ (Figure 3.5a). Furthermore, although AZD8055 inhibited AKT^{S473} phosphorylation, AKT is unlikely to be completely inactivated due to the presence of PI3K-mediated AKT^{T308} phosphorylation (Figure 3.7b). Suppression of multiple oncogenic axes represents a rationale for drug combination studies (424). Given the inhibitory effect of ibrutinib on PI3K and MAPK/ERK pro-survival pathways (438), it was of interest to assess the impact of AZD8055 and ibrutinib combination therapy on cell viability *in vitro* (Figure 3.8d-f). To determine whether dual mTOR kinase inhibitors (AZD8055 and AZD2014) synergise with ibrutinib to enhance CLL cell apoptosis, a median-drug effect analysis was performed to calculate combination index (CI) values according to the Chou and Talalay method (425), where a CI<1 indicates synergism and CI>1 indicates antagonism (Figure 3.8d). Freshly isolated CLL cells were treated with various concentrations of AZD8055 (Figure 3.8d; left panel) or AZD2014 (Figure 3.8d; right panel) in combination with ibrutinib at a non-constant ratio for 48 h. Subsequently, the resazurin cell viability assay was performed to quantify cell viability, from which the CI values were calculated by CompuSyn software. The representative heat map depicts CI values (0 – 2) for each individual drug combination, where the yellow colouring indicates greater synergism (Figure 3.8d). These data revealed that while demonstrable antagonism existed, as

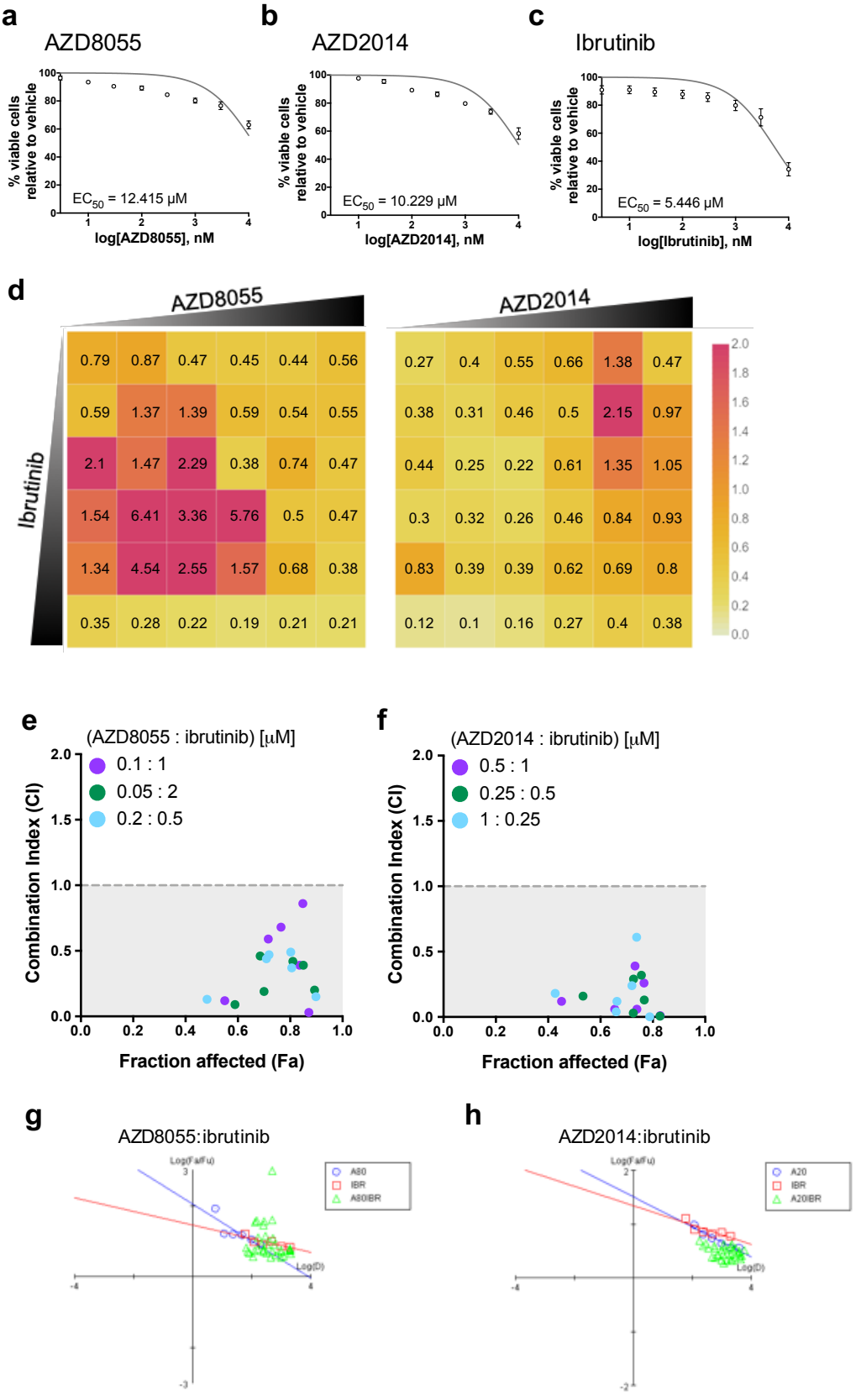

Figure 3.8 - Dual mTOR inhibitors synergise with ibrutinib to enhance CLL cell death in vitro
(a, b, c) Dose-response/dose-effect curve of primary CLL samples (n=5) treated with increasing concentrations of (a) AZD8055 (3, 10, 30, 100, 300, 1000, 3000, 10000 nM), (b) AZD2014 (3, 10, 30, 100, 300, 1000, 3000, 10000 nM), and (c) Ibrutinib (3, 10, 30, 100, 300, 1000, 3000, 10000 nM) as determined by the resazurin cell viability assay. EC_{50} values generated by nonlinear regression (curve fit) as an average of each primary CLL sample. (d) Representative median-effect analysis of a primary CLL sample (CLL158) examining drug synergy between combinations of AZD8055 and Ibrutinib (left panel) and AZD2014 and Ibrutinib (right panel). The following concentrations were

used at a non-constant ratio: AZD8055 (6.25, 12.5, 25, 50, 100, 200 nM), AZD2014 (0.0625, 0.125, 0.25, 0.5, 1, 2 μM) and Ibrutinib (0.0625, 0.125, 0.25, 0.5, 1, 2 μM). Indicated CI values were calculated using the median-drug effect analysis method with the CompuSyn software package, where CI < 1 indicates synergy and CI > 1 indicates an antagonistic effect. (e, f) Graphs depicting CI values plotted against fraction affected (Fa) for select combinations of (e) AZD8055:Ibrutinib (0.1:1 (purple circles); 0.05:2 (green circles); 0.2:0.5 (blue circles) μM) and (f) AZD2014:Ibrutinib (0.5:1 (purple circles); 0.25:0.5 (green circles); 1:0.25 (blue circles) μM). Individual datapoints within each combination represent different CLL patient samples (n=6). (g, h) Representative (CLL158) median-effect plots (Chou plot) for (g) AZD8055 and ibrutinib combination and (h) AZD2014 and ibrutinib combination where the x-intercept (log Dm) signifies drug potency. AZD8055 (blue circles), ibrutinib (red squares) and COMBO (green triangles).

represented by red datapoints, both AZD8055 and AZD2014 synergised with ibrutinib at multiple concentrations to enhance CLL cell death (Figure 3.8d and Table 3.1). For the combinations of AZD8055 and ibrutinib indicated (Figure 3.8e), the obtained CI values were 0.45±0.13, 0.15±0.06 and 0.34±0.06, respectively. Similarly, for the combinations of AZD2014 and ibrutinib presented (Figure 3.8f), the CI values were 0.15±0.05, 0.15±0.05 and 0.19±0.08, respectively. Importantly, AZD8055 and AZD2014 synergised with ibrutinib to enhance CLL cell death at clinically achievable doses (439-441) (Figure 3.8e,f). Furthermore, median-effect plots (Chou plots) indicated drug synergy at multiple concentrations for AZD8055 or AZD2014 in combination with ibrutinib (Figure 3.8g,h). CI values for AZD2014 and ibrutinib were generally lower than those calculated for AZD8055 and ibrutinib, which might be explained by the increased potency of AZD2014 (contrary to previous reports (318)) in CLL cells. Nevertheless, a conclusive explanation remains elusive.

3.2.8 AZD8055 and ibrutinib combination inhibits mTOR- and MAPK activity in HG-3 and MEC-1 cells

Encouraged by the enhanced, synergistic effect of AZD8055 and ibrutinib combination treatment (herein referred to as ‘COMBO’) on CLL cell viability (via the resazurin assay), it was of interest to explore the impact of the treatment on mTOR activity in HG-3 and MEC-1 cells. The phosphorylation status of mTORC1 (4E-BP1$^{T37/46}$ and S6$^{S235/236}$) and mTORC2 (AKT^{S473}) downstream targets was assessed following short-term AZD8055 (100 nM), ibrutinib (1 μM) or COMBO treatment. For the reasons stated previously, AKT^{T308} and ERK1/2$^{T202/Y204}$ phosphorylation was also examined (Figure 3.9). Consistent with Figure 3.7b, AZD8055 treatment inhibited phosphorylation of mTORC1 (4E-BP1$^{T37/46}$ and S6$^{S235/236}$) and mTORC2 (AKT^{S473}) downstream targets in MEC-1 cells, while

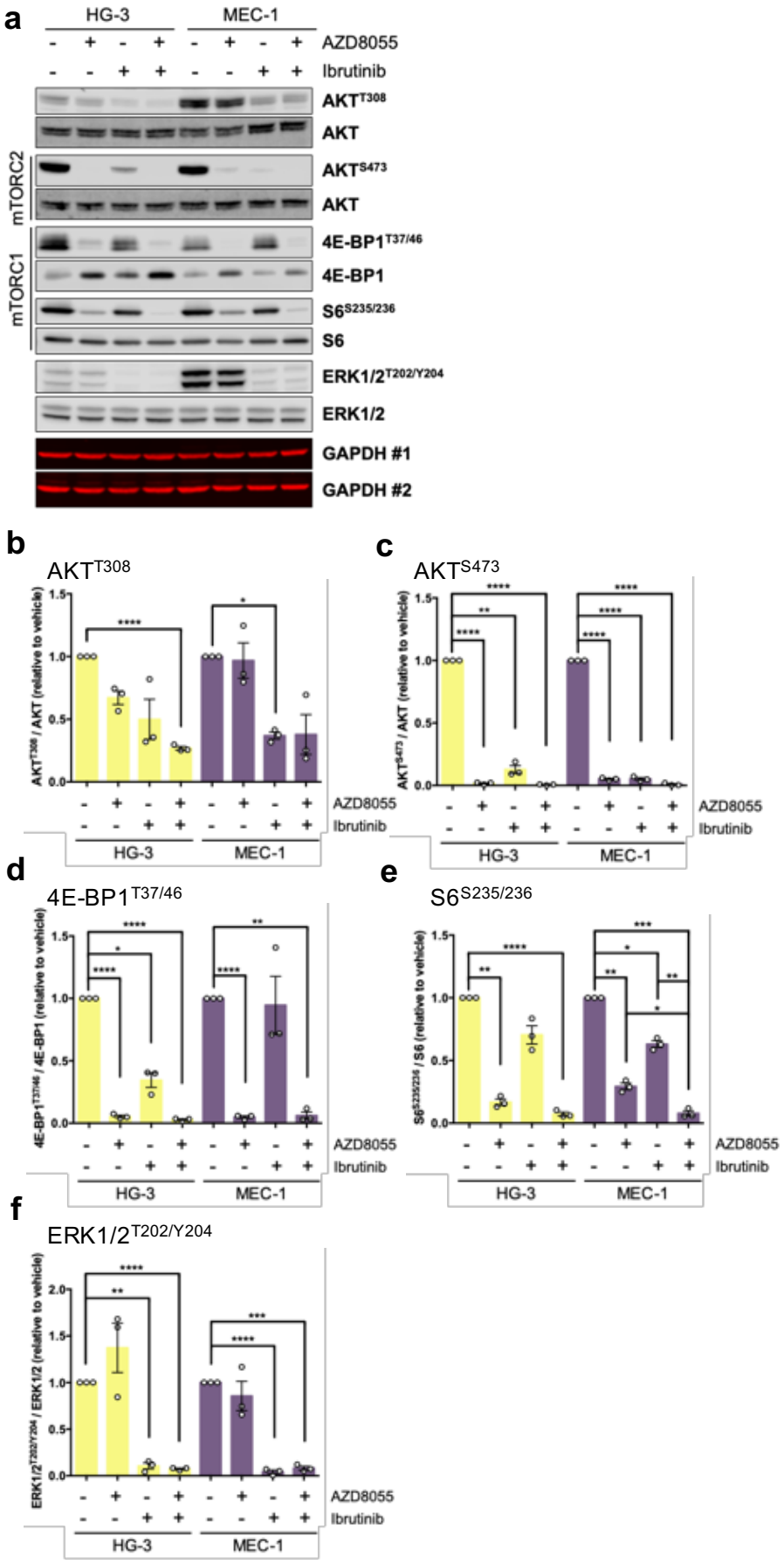

Figure 3.9 - AZD8055 and ibrutinib combination inhibits mTOR- and MAPK activity in HG-3 and MEC-1 cells

(a) Representative western blot of HG-3 (n=3) and MEC-1 (n=3) cells treated with AZD8055 (100 nM), Ibrutinib (1 μM), AZD8055 and Ibrutinib combination (COMBO) or DMSO vehicle control for 1

h. Blots were probed for AKT^{T308}, AKT^{S473}, AKT, 4E-BP1$^{T37/46}$, 4E-BP1, S6$^{S235/236}$, S6, ERK1/2$^{T202/Y204}$, ERK1/2 and GAPDH (loading control; #1 and #2 referring to mirror blots). (b, c, d, e, f) Relative phosphorylation levels of (b) AKT^{T308}, (c) AKT^{S473}, (d) 4E-BP1$^{T37/46}$ (e) S6$^{S235/236}$ and (f) ERK1/2$^{T202/Y204}$ in HG-3 (n=3; yellow bars) and MEC-1 (n=3; purple bars). Relative phosphorylation is calculated by first normalising phosphorylation and expression levels by GAPDH, followed by normalised phosphorylation divided by normalised expression levels. Relative phosphorylation levels for each condition are relative to vehicle control for HG-3 or MEC-1 cells. Individual datapoints are represented by white circles. Data expressed as the mean ± SEM. Statistics calculated by one-way ANOVA, where * $p \leq 0.05$, ** $p \leq 0.01$, *** $p \leq 0.001$, **** $p \leq 0.0001$.

AKT^{T308} and ERK1/2$^{T202/Y204}$ phosphorylation was largely unaffected (Figure 3.9a-e). Similarly, AZD8055 treatment blocked phosphorylation of mTORC1 (4E-BP1$^{T37/46}$ and S6$^{S235/236}$) and mTORC2 (AKT^{S473}) downstream targets in HG-3 cells, while a visible trend was observed towards reduced AKT^{T308} and increased ERK1/2$^{T202/Y204}$ phosphorylation (Figure 3.9a-e). Ibrutinib significantly reduced AKT^{T308} (Figure 3.9a,b), AKT^{S473} (Figure 3.9a,c), S6$^{S235/236}$ (Figure 3.9a,e) and ERK1/2$^{T202/Y204}$ (Figure 3.9a,f) phosphorylation in MEC-1 cells, while 4E-BP1$^{T37/46}$ (Figure 3.9a,d) was unaffected. Equally, ibrutinib treatment blocked AKT^{S473} (Figure 3.9a,c) and ERK1/2$^{T202/Y204}$ (Figure 3.9a,f) phosphorylation in HG-3 cells, while a noticeable trend towards reduced S6$^{S235/236}$ (Figure 3.9a,e) and AKT^{T308} (Figure 3.9a,b) phosphorylation was observed. Unlike MEC-1 cells, 4E-BP1$^{T37/46}$ phosphorylation was significantly reduced in HG-3 cells (Figure 3.9a,d). Importantly, the COMBO treatment significantly inhibited mTORC1 (4E-BP1$^{T37/46}$ and S6$^{S235/236}$) and mTORC2 (AKT^{S473}) downstream targets in MEC-1 cells (Figure 3.9a,c-e). Interestingly, COMBO enhanced inhibition of S6$^{S235/236}$ phosphorylation in MEC-1 cells, greater than the inhibitory effect of AZD8055 or ibrutinib alone (Figure 3.9e). Perhaps most crucially, COMBO significantly inhibited ERK1/2$^{T202/Y204}$ (Figure 3.9a,f) phosphorylation in MEC-1 cells, while a discernible trend towards reduced AKT^{T308} (Figure 3.9a,b) phosphorylation was observed. In HG-3 cells, COMBO treatment also conferred a robust inhibition of AKT^{T308} (Figure 3.9a,b), AKT^{S473} (Figure 3.9a,c), 4E-BP1$^{T37/46}$ (Figure 3.9a,d), S6$^{S235/236}$ (Figure 3.9a,e) and ERK1/2$^{T202/Y204}$ (Figure 3.9a,f) phosphorylation.

3.2.9 HG-3 and MEC-1 cell viability is unaffected by COMBO treatment

Combining AZD8055 with ibrutinib broadly inhibited AKT-mTOR and MAPK/ERK pro-survival pathways in HG-3 and MEC-1 cells (Figure 3.9). Given the lack of sensitivity of HG-3 and MEC-1 cells to AZD8055 or ibrutinib as single agents

(Figure 3.6), it was of interest to establish whether the COMBO treatment could enhance cell death. HG-3 and MEC-1 cells were treated with AZD8055 (100 nM) or ibrutinib (1 μM) alone and in combination for 48 h. Following treatment, the cells were stained with Annexin V/7-AAD and analysed by flow cytometry (Figure 3.10a). These data showed that the COMBO treatment did not affect the viability (Annexin V^{neg} 7-AAD^{neg}) of HG-3 or MEC-1 cells (Figure 3.10a,b,d). Although AZD8055 significantly reduced the proportion of apoptotic (Annexin V^{pos} 7-AAD^{pos}) HG-3 cells, this unlikely represents biological significance given the small percentages involved (Figure 3.10c). Consistently, treatment of HG-3 or MEC-1 cells with COMBO did not impact upon the relative levels of apoptotic cells (Figure 3.10c,e).

Considering these data, it was decided to explore the regulation of anti-apoptotic (MCL-1, BCL-xL, BCL2 and Survivin) and pro-apoptotic (BIM) proteins in response to the COMBO treatment (Figure 3.10f). Consistent with Figure 3.6f, differential regulation of anti- and pro-apoptotic proteins was observed following AZD8055 or ibrutinib treatment in HG-3 and MEC-1 cells (Figure 3.10f). Interestingly, COMBO resulted in an upregulation of anti-apoptotic MCL-1 and BCL-xL expression in HG-3 and MEC-1 cells, while Survivin was downregulated compared to vehicle control (Figure 3.10f). Concurrently, the expression of pro-apoptotic BIM (BIM_{EL}, BIM_L and BIM_S) was upregulated in HG-3 and MEC-1 cells in response to COMBO compared to vehicle control (Figure 3.10f). BCL2 expression remained unaffected by treatment in HG-3 or MEC-1 cells (Figure 3.10f).

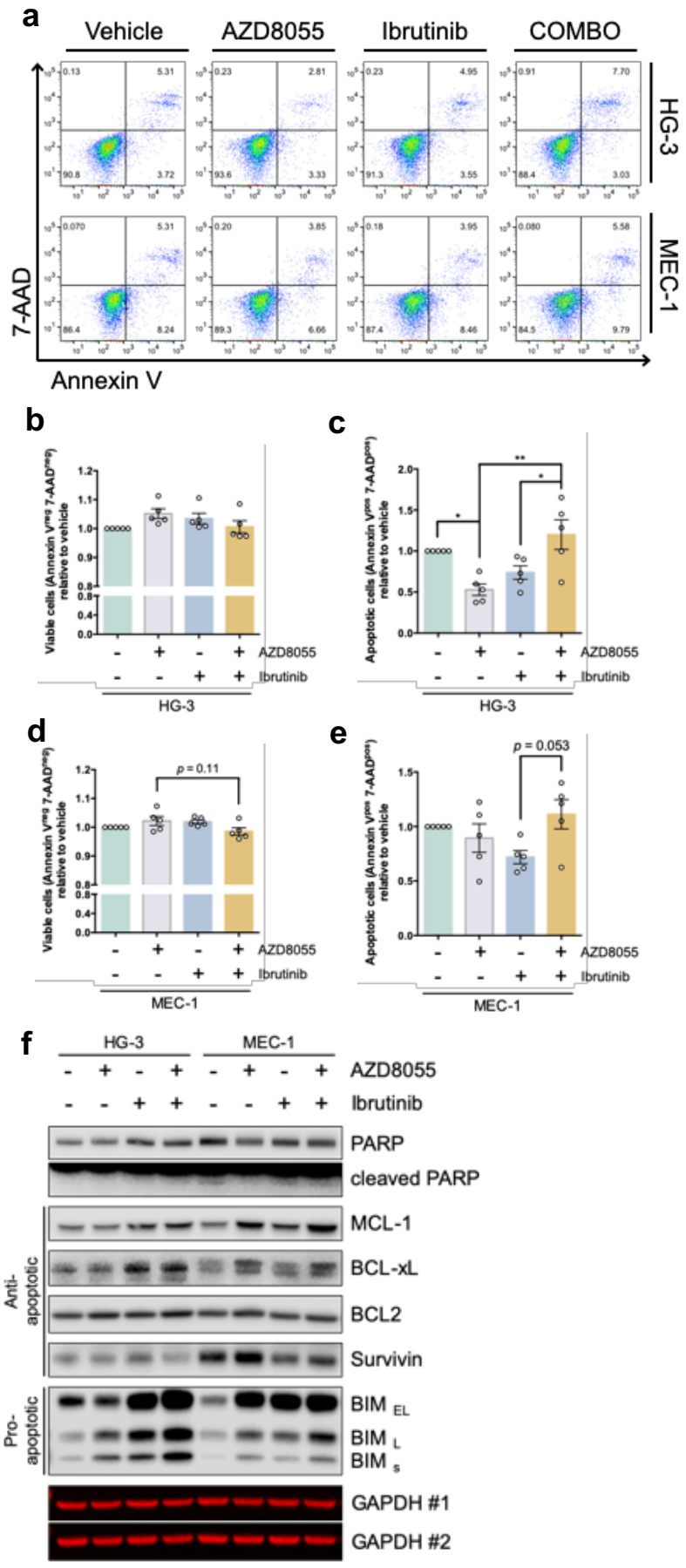

Figure 3.10 - HG-3 and MEC-1 cell viability is unaffected by AZD8055 and ibrutinib combination treatment

(a) Representative FACS plot of HG-3 (top panel) and MEC-1 (bottom panel) cells stained with Annexin V and 7-AAD to assess cell viability following treatment with AZD8055 (100 nM), Ibrutinib

(1 μM), AZD8055 and Ibrutinib combination (COMBO) or DMSO vehicle control (Vehicle) for 48 h. Please refer to section 2.2.2.3 for gating strategy. (b, d) Percentage viable (b) HG-3 (n=5) and (d) MEC-1 (n=5) cells treated with AZD8055 (grey bar), Ibrutinib (blue bar), COMBO (gold bar) or Vehicle (green bar) for 48 h, as described in (a). Viability is defined as Annexin V^{neg} and 7-AAD^{neg}. (c, e) Percentage apoptotic (c) HG-3 (n=5) and (e) MEC-1 (n=5) cells, treated as described in (a). Apoptotic cells are defined as Annexin V^{pos} and 7-AAD^{pos}. Percentage viable and apoptotic cells for each condition are relative to vehicle control for HG-3 or MEC-1 cells. (f) Representative western blot of HG-3 (n=3) and MEC-1 (n=3) cells treated with AZD8055, Ibrutinib, COMBO or Vehicle for 48 h. Blots were probed for PARP, MCL-1, BCL-xL, BCL2, Survivin, BIM (BIM_{EL}, BIM_L, and BIM_S) and GAPDH (loading control; #1 and #2 referring to mirror blots). Individual patient datapoints are represented by white circles. Data expressed as the mean ± SEM. Statistics calculated by one-way ANOVA, where * $p \leq 0.05$, ** $p \leq 0.01$, *** $p \leq 0.001$, **** $p \leq 0.0001$.

3.2.10 MEC-1 cell size is reduced by COMBO treatment

mTOR controls cell size, at least in part, through mTORC1-dependent phosphorylation of its downstream targets S6K1 and 4E-BP1 (270, 442). To examine the functional impact of mTOR inhibition on CLL cell size, HG-3 and MEC-1 cells were treated with AZD8055 (100 nM), ibrutinib (1 μM), COMBO or rapamycin (10 nM) for 48 h. Of note, rapamycin treatment was included to compare the effect of mTORC1-selective inhibition with dual mTOR inhibition. Following treatment, cell size was quantified as a measure of 'forward scatter-area (FSC-A)' by flow cytometry (Figure 3.11a). These data revealed an observable trend towards reduced cell size in HG-3 cells treated with AZD8055 or rapamycin (p = 0.12 and p = 0.11, respectively) compared to vehicle control (Figure 3.11b). However, there was neither a visible nor significant difference in HG-3 cell size between AZD8055 and rapamycin treatment (Figure 3.11b). Equally, ibrutinib or COMBO showed no significant difference in HG-3 cell size (Figure 3.11b). Conversely, treatment with AZD8055, ibrutinib, COMBO or rapamycin resulted in a significant reduction in MEC-1 cell size compared to vehicle control (Figure 3.11c). Furthermore, AZD8055 treatment caused a near-significant greater reduction in MEC-1 cell size compared to rapamycin (p = 0.11; Figure 3.11c). Importantly, the COMBO treatment resulted in a significant decrease in MEC-1 cell size, greater than each treatment alone (Figure 3.11c).

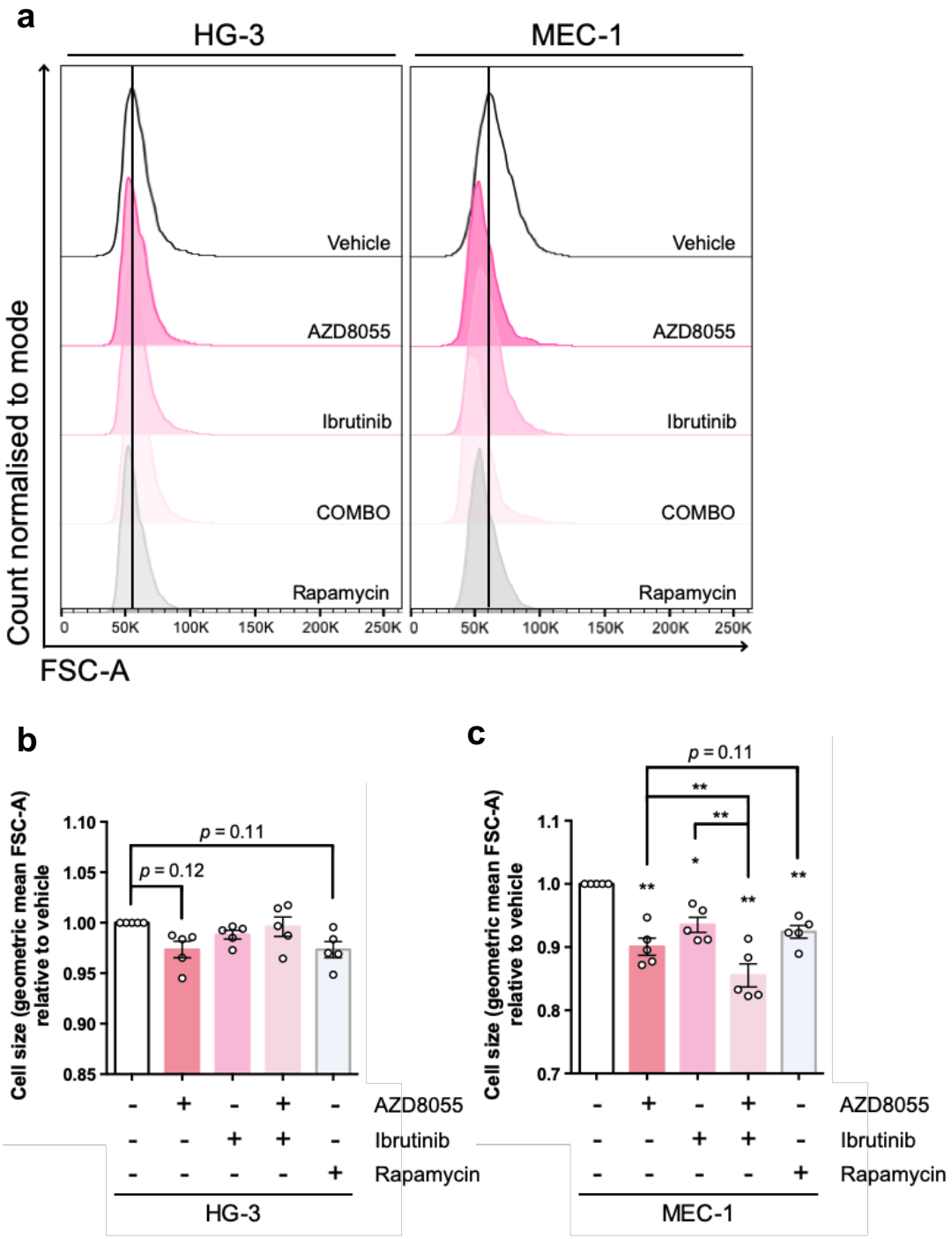

Figure 3.11 - MEC-1 cell size is reduced by AZD8055 and ibrutinib combination treatment
(a) Representative FACS histogram displaying geometric mean of forward scatter-area (FSC-A) of HG-3 (left panel) and MEC-1 (right panel) cells treated with AZD8055 (100 nM; dark pink histogram), Ibrutinib (1 μM; medium-pink histogram), AZD8055 and Ibrutinib combination (COMBO; light pink histogram), Rapamycin (10 nM; grey histogram) or DMSO vehicle control (Vehicle; white histogram) for 48 h. A black vertical line represents the peak of the Vehicle control histogram. (b, c) Relative cell size (geometric mean) of (b) HG-3 (n=5) and (c) MEC-1 (n=5) cells treated as described in (a). Geometric means for each condition are relative to vehicle control for HG-3 or MEC-1 cells. Individual datapoints are represented by white circles. Data expressed as the mean ± SEM. Statistics calculated by one-way ANOVA, where * p ≤ 0.05, ** p ≤ 0.01, *** p ≤ 0.001, **** p ≤ 0.0001.

3.2.11 COMBO treatment promotes G1 cell cycle arrest in HG-3 and MEC-1 cells

mTOR plays a crucial role in mediating cell cycle progression via the activity of S6K1 and 4E-BP1 (443). Rapamycin (444) and everolimus (445, 446) have been shown to inhibit the G1/S transition by prolonging the G1 phase of the cell cycle. Moreover, mTOR inhibitors have been shown to cause cell cycle arrest in CLL cells (313, 428). More recently, AZD8055 has been shown to inhibit proliferation by inducing G1 cell cycle arrest in adult T-cell leukaemia (ATL) (447). To assess the impact of dual mTOR kinase inhibition on cell cycle progression in CLL cells, HG-3 and MEC-1 cells were treated with AZD8055 (100 nM), ibrutinib (1 μM), COMBO or rapamycin (10 nM) for 48 h. Rapamycin treatment was included to compare the effect of mTORC1-selective inhibition with dual mTOR inhibition. Following treatment, HG-3 and MEC-1 cells were stained with PI to quantify DNA content by flow cytometry (Figure 3.12a). Interestingly, rapamycin, ibrutinib or COMBO caused a significant increase in the proportion of DNA in the G1/G0 phase of the cell cycle, while no significant difference was observed in AZD8055-treated HG-3 cells (Figure 3.12b). Furthermore, treatment of HG-3 cells with COMBO instigated a near-significant reduction in the proportion of DNA in S phase, compared to vehicle control (p = 0.06; Figure 3.12b). Conversely, AZD8055, ibrutinib, COMBO or rapamycin all conferred a significant elevation in the proportion of DNA in the G1/G0 phase of the cell cycle in MEC-1 cells compared to vehicle control (Figure 3.12c). While there was no significant difference between AZD8055 and rapamycin, a modest trend towards a higher proportion of DNA in the G1/G0 phase of the cell cycle was observed in AZD8055-treated MEC-1 cells compared to rapamycin (Figure 3.12c). Finally, treatment of MEC-1 cells with AZD8055, ibrutinib, COMBO or rapamycin corresponded to a significant reduction in the proportion of DNA in S phase compared to vehicle control (Figure 3.12c). The incubation time (48 h) was chosen to align with prior cell viability experiments. The doubling time for HG-3 (410) and MEC-1 cells (409) is approximately 40-50 hours. Upon reflection, the incubation time should have been extended to account for the intrinsic characteristics for each cell line. Moreover, cell synchronisation via ‘starvation’ may have enabled comparisons to be drawn between cell lines and quiescent CLL cells.

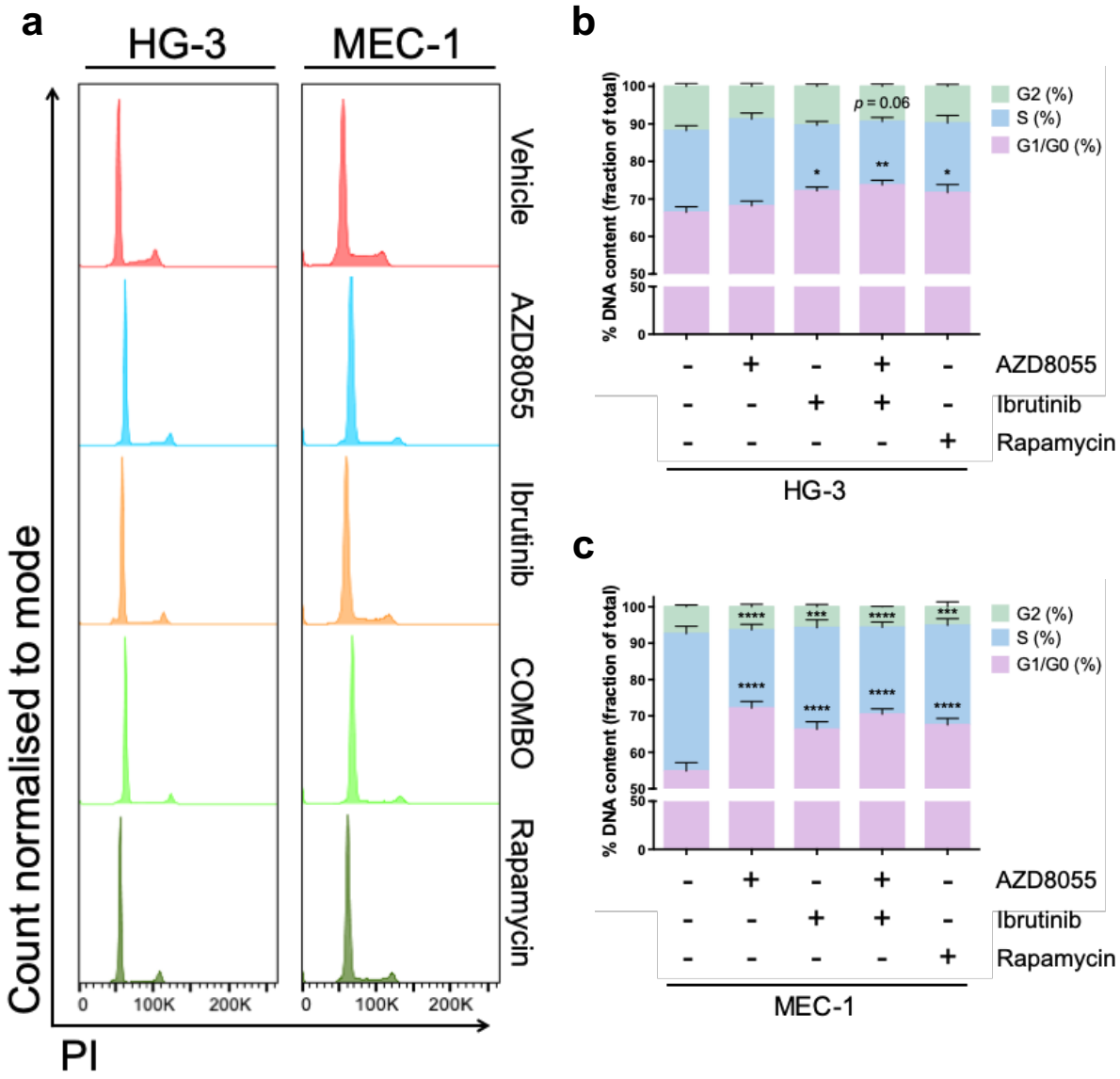

Figure 3.12 - AZD8055 and ibrutinib combination promotes G1 cell cycle arrest in HG-3 and MEC-1 cells
(a) Representative FACS histogram of HG-3 (left panel) and MEC-1 (right panel) cells stained with propidium iodide (PI) for cell cycle analysis by quantitation of DNA content following treatment with AZD8055 (100 nM; blue histogram), Ibrutinib (1 μM; orange histogram), AZD8055 and Ibrutinib combination (COMBO; light-green histogram), Rapamycin (10 nM; dark-green histogram) or DMSO vehicle control (Vehicle; red histogram) for 48 h. Please refer to section 2.2.2.4 for gating strategy. (b, c) Quantification of DNA content (%) for cycle cycle phase G1/G0 (purple bars), S (blue bars) and G2 (green bars) in (b) HG-3 (n=6) and (c) MEC-1 (n=5). Data from each replicate are depicted as 'fraction of total', where total values are equal to 100. Data expressed as the mean ± SEM. Statistics calculated by two-way ANOVA, where * $p \leq 0.05$, ** $p \leq 0.01$, *** $p \leq 0.001$, **** $p \leq 0.0001$.

3.2.12 COMBO treatment enhances inhibition of MEC-1 cell proliferation, corresponding to increased expression of $p27^{KIP1}$

CLL proliferation within 'proliferation centres' of SLOs is a key determinant for disease progression (9). Thus, treatments that block cell proliferation represent an attractive approach for CLL. Based on treatment-induced G1 cell cycle arrest

in MEC-1 cells (Figure 3.12), it was of interest to investigate the functional impact of mTOR inhibition on CLL cell proliferation. HG-3 and MEC-1 cells were treated with AZD8055 (100 nM), ibrutinib (1 μM), COMBO or rapamycin (10 nM) for 72 h. Prior to treatment, HG-3 and MEC-1 cells were stained with CTV to enable quantification of cell proliferation by flow cytometry (Figure 3.13a). These data revealed that AZD8055, COMBO and rapamycin resulted in a near-significant reduction in HG-3 cell proliferation (p = 0.08, p = 0.0503 and p = 0.13, respectively) compared to vehicle control (Figure 3.13b). Moreover, the COMBO treatment conferred a significant increase in CTV geometric mean, i.e. a greater inhibition of proliferation, compared to AZD8055 alone (Figure 3.13b). Interestingly, ibrutinib was unable to inhibit proliferation in HG-3 cells (Figure 3.13b), despite inducing G1 cell cycle arrest (Figure 3.12b). AZD8055 and COMBO treatment significantly inhibited MEC-1 cell proliferation compared to vehicle control (Figure 3.13c). Additionally, COMBO resulted in a near-significant greater inhibition of MEC-1 cell proliferation than AZD8055 alone (p = 0.07; Figure 3.13bc). Similarly, rapamycin conferred a near-significant inhibition of cell proliferation, though to a lesser extent than AZD8055 or COMBO (Figure 3.13c). As in Figure 3.13b, ibrutinib was unable to inhibit MEC-1 cell proliferation, however an observable trend towards increased inhibition was evident (Figure 3.13c).

Encouraged by the anti-proliferative effect of treatment on HG-3 and MEC-1 cells, the regulation of 'cell cycle proteins' was investigated, particularly those that govern the G1/S phase transition (Figure 3.13d,e,f). To explore treatment-induced cell cycle regulation at a molecular level, the expression of cell cycle proteins Cyclin E1, CDK2, Cyclin D2, CDK4, $p27^{KIP1}$ and $p21^{CIP1}$ were assessed by western blotting (Figure 3.13d). Basal expression levels of Cyclin E1, CDK4 and $p27^{KIP1}$ were visibly higher in MEC-1 cells compared to HG-3 cells (Figure 3.13d). AZD8055, ibrutinib, COMBO and rapamycin treatment upregulated the expression of Cyclin E1 in MEC-1 cells compared to vehicle control (Figure 3.13d). Moreover, the expression of CDK2 was largely unaffected by treatment in HG-3 and MEC-1 cells (Figure 3.13d). Interestingly, as demonstrated previously (Figures 3.6f and 3.10f), differential regulation was observed in HG-3 and MEC-1 cells in response to treatment. For example, while AZD8055 treatment increased the expression of Cyclin D2 in HG-3 cells, Cyclin D2 expression was downregulated in MEC-1

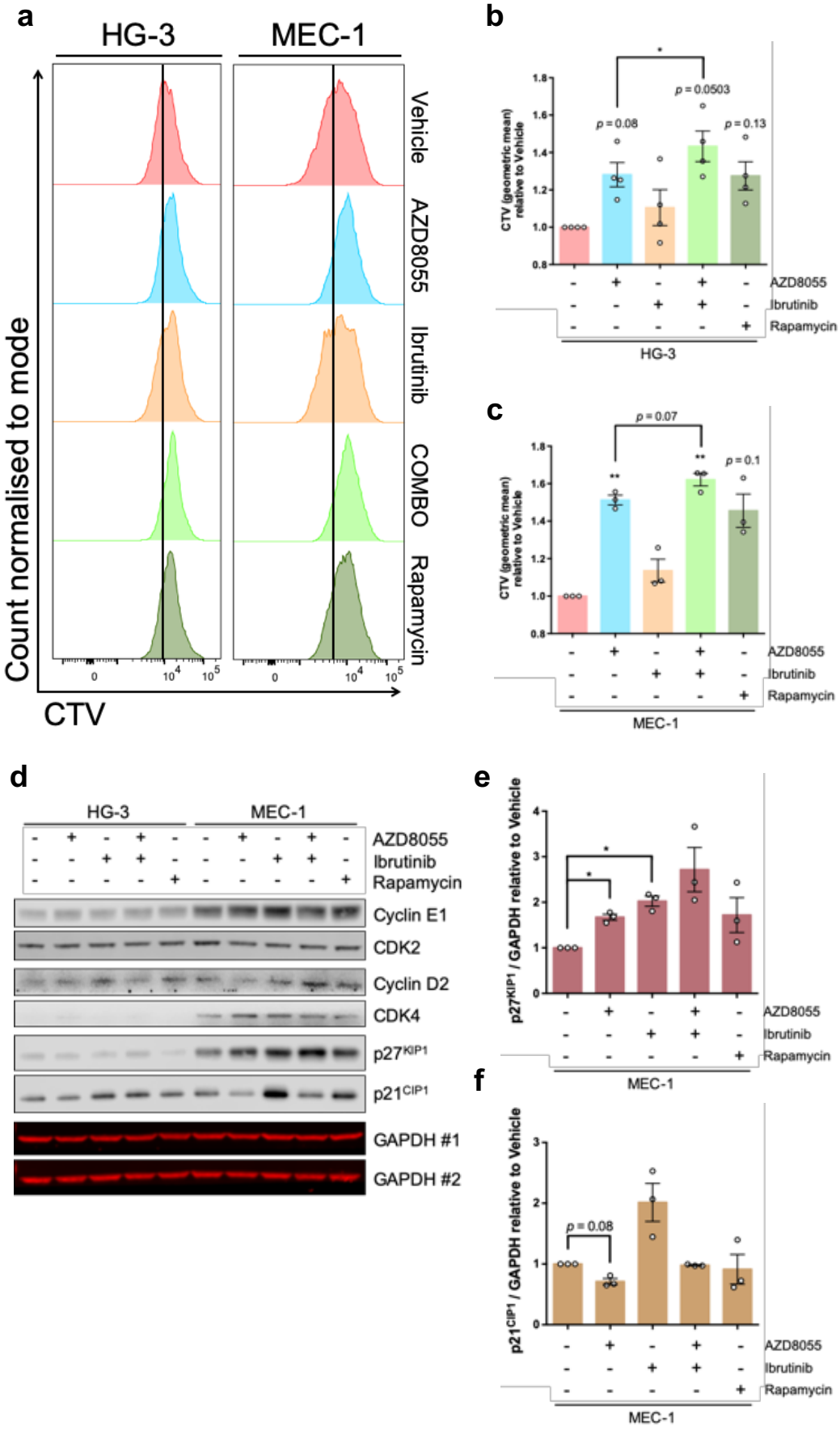

Figure 3.13 - AZD8055 and ibrutinib combination enhances inhibition of MEC-1 cell proliferation, corresponding to increased expression of p27^{KIP1}

(a) Representative FACS histogram of HG-3 (left panel) and MEC-1 (right panel) cells stained with CellTrace Violet (CTV) to assess cell proliferation following treatment with AZD8055 (100 nM; blue histogram), Ibrutinib (1 μM; orange histogram), AZD8055 and Ibrutinib combination (COMBO; light-

green histogram), Rapamycin (10 nM; dark-green histogram) and DMSO vehicle control (Vehicle; red histogram) for 72 h. A black vertical line represents the peak of the HG-3 and MEC-1 vehicle control histogram. Please refer to section 2.2.2.5 for gating strategy. (b, c) Assessment of CTV geometric mean for (b) HG-3 (n=4) and (c) MEC-1 (n=3) cells treated as described in (a). Geometric means for each condition are relative to vehicle control for HG-3 or MEC-1 cells. (d) Representative western blot of HG-3 (n=3) and MEC-1 (n=3) cells treated with AZD8055, Ibrutinib, COMBO, Rapamycin and Vehicle for 48 h. Blots were probed for Cyclin E1, CDK2, Cyclin D2, CDK4, $p27^{KIP1}$, $p21^{CIP1}$ and GAPDH (loading control; #1 and #2 referring to mirror blots). (e, f) Densitometry of (e) $p27^{KIP1}$ (dark brown bars) and (f) $p21^{CIP1}$ (light brown bars) expression in MEC-1 (n=3) cells following treatment as in (d). Normalised expression is relative to Vehicle for HG-3 or MEC-1 cells. Individual datapoints from each replicate are shown as white circles. Data expressed as the mean ± SEM. Statistics calculated by one-way ANOVA, where * $p \leq 0.05$, ** $p \leq 0.01$, *** $p \leq 0.001$, **** $p \leq 0.0001$.

cells. Furthermore, whereas COMBO did not visibly effect Cyclin D2 expression in HG-3 cells, Cyclin D2 was upregulated in MEC-1 cells (Figure 3.13d). Although AZD8055 or ibrutinib treatment alone resulted in an elevation of CDK4 expression in MEC-1 cells, COMBO did not noticeably effect CDK4 expression in MEC-1 cells (Figure 3.13d). Interestingly, CDK4 expression was not observed in HG-3 cells (Figure 3.13d). AZD8055 or ibrutinib treatment alone resulted in a significant upregulation of the cell cycle inhibitor $p27^{KIP1}$ in MEC-1 cells(Figure 3.13d,e). An observable trend towards enhanced $p27^{KIP1}$ expression was evident following the COMBO treatment, greater than each treatment alone (Figure 3.13d,e). Similarly, rapamycin treatment resulted in a trend towards increased $p27^{KIP1}$ expression in MEC-1 cells compared to vehicle control (Figure 3.13d,e). Interestingly, AZD8055 treatment caused a near-significant downregulation of $p21^{CIP1}$ expression in MEC-1 cells ($p = 0.08$), while ibrutinib conferred a demonstrable trend towards increased $p21^{CIP1}$ expression (Figure 3.13d,f). $p21^{CIP1}$ expression was largely unaffected by rapamycin or COMBO treatment in MEC-1 cells (Figure 3.13d,f).

3.2.13 mTOR and MAPK activity is inhibited by COMBO in F(ab')$_2$ stimulated CLL cells

To assess drug selectivity in F(ab')$_2$-stimulated primary CLL cells, the phosphorylation status of mTORC1 (4E-$BP1^{T37/46}$ and $S6^{S235/236}$) and mTORC2 (AKT^{S473}) downstream targets was assessed following short-term AZD8055 (100 nM), ibrutinib (1 μM) or COMBO treatment. After 30 min pre-treatment, CLL cells remained unstimulated or were F(ab')$_2$ stimulated for 1 h (Figure 3.14). As with Figure 3.3a-e, F(ab')$_2$ stimulation of primary CLL samples resulted in a near-significant increase in the relative phosphorylation levels of $ERK1/2^{T202/Y204}$ (p =

0.12; Figure 3.14e) and mTORC1 downstream target $S6^{S235/236}$ (p = 0.06; Figure 3.14d) relative to vehicle control. Additionally, phosphorylation of AKT^{S473} and AKT^{T308} was increased (Figure 3.14b), whereas 4E-$BP1^{T37/46}$ phosphorylation was largely unaffected (Figure 3.14c). Consistent with Figure 3.5, AZD8055 treatment inhibited phosphorylation of AKT^{S473} (Figure 3.14b) and 4E-$BP1^{T37/46}$ (Figure 3.14c) in unstimulated and F(ab')$_2$-stimulated CLL cells. Moreover, while AZD8055 treatment resulted in a near-significant decrease in $S6^{S235/236}$ phosphorylation (p = 0.08; Figure 3.14d), ERK1/$2^{T202/Y204}$ phosphorylation was only moderately reduced in the presence of BCR stimulation (p = 0.15; Figure 3.14e). As noted in Figure 3.7a, AZD8055 also eliminated AKT^{T308} phosphorylation in F(ab')$_2$ stimulated CLL cells (Figure 3.14a). Furthermore, short term treatment with ibrutinib resulted in decreased AKT^{S473} and AKT^{T308} phosphorylation (Figure 3.14a,b) in F(ab')$_2$ stimulated CLL cells (consistent with Figures 3.5a and 3.9a, respectively). Similarly, a near-significant decrease in $S6^{S235/236}$ (p = 0.07; Figure 3.14d) and ERK1/$2^{T202/Y204}$ (p = 0.13; Figure 3.14e) phosphorylation was observed. In contrast, 4E-$BP1^{T37/46}$ phosphorylation was largely unaffected by ibrutinib treatment in unstimulated and F(ab')$_2$ stimulated CLL cells (Figure 3.14c). Consistent with Figure 3.9, the COMBO treatment inhibited mTORC1 (4E-$BP1^{T37/46}$ (p = 0.09) and $S6^{S235/236}$) and mTORC2 (AKT^{S473}) downstream targets in unstimulated and F(ab')$_2$-stimulated CLL cells (Figure 3.14a-d). COMBO enhanced inhibition of $S6^{S235/236}$ phosphorylation compared to ibrutinib alone (p = 0.053; Figure 3.14d). Furthermore, COMBO elicited a near-significant inhibition of ERK1/$2^{T202/Y204}$ phosphorylation (p = 0.059; Figure 3.14e) and visibly reduced AKT^{T308} phosphorylation (Figure 3.14a) in the presence of BCR stimulation.

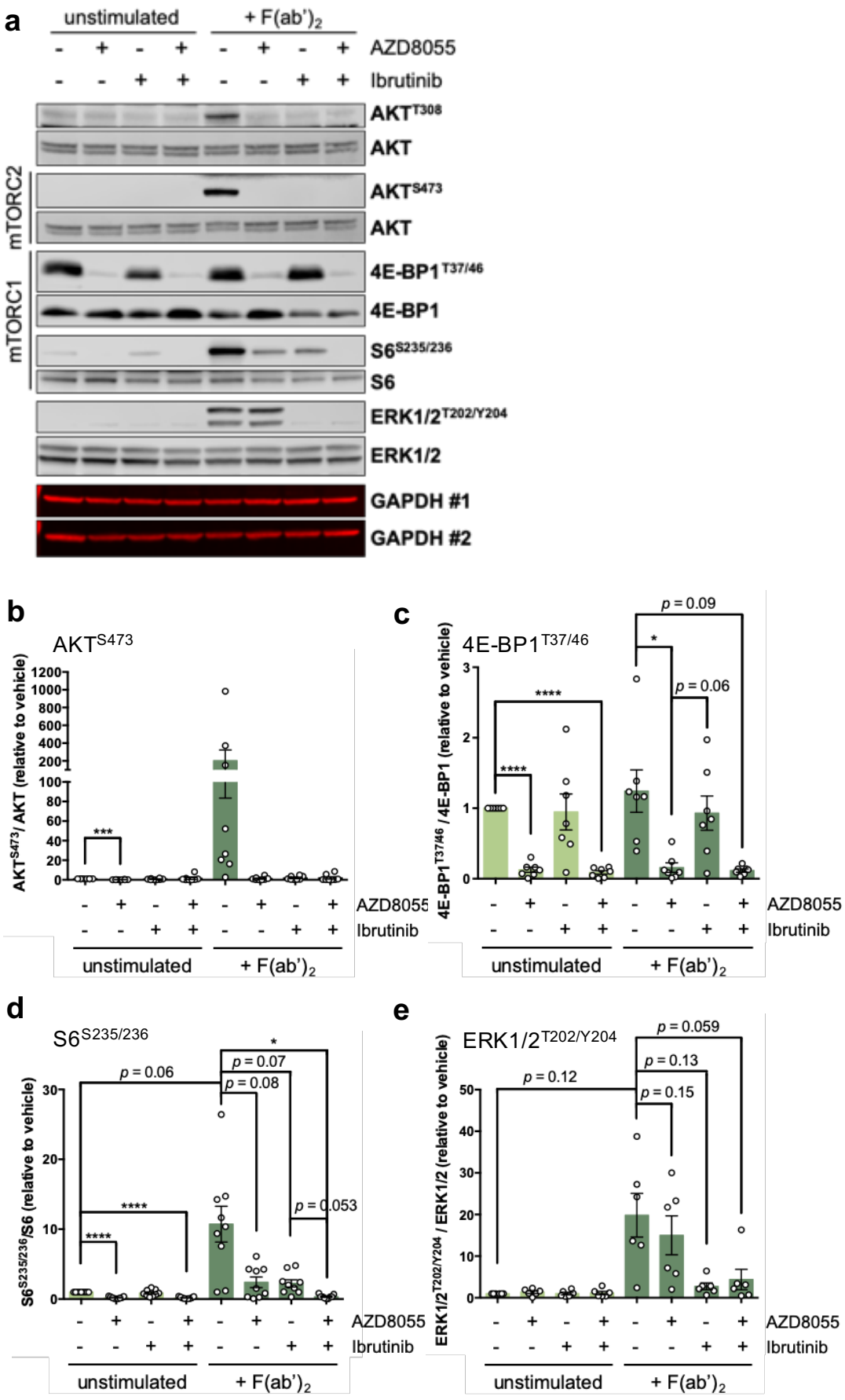

Figure 3.14 - mTOR and MAPK activity is inhibited by AZD8055 and ibrutinib combination in F(ab')$_2$-stimulated CLL cells

(a) Representative western blot of a primary CLL sample (CLL157) unstimulated or F(ab')$_2$ stimulated for 1 h following 30 min pre-treatment with AZD8055 (100 nM), Ibrutinib (1 μM),

AZD8055 and Ibrutinib combination (COMBO) or DMSO vehicle control (Vehicle). Blots were probed for AKT^{T308}, AKT^{S473}, AKT, 4E-$BP1^{T37/46}$, 4E-BP1, $S6^{S235/236}$, S6, $ERK1/2^{T202/Y204}$, ERK1/2 and GAPDH (loading control; #1 and #2 referring to mirror blots). (b, c, d, e) Relative phosphorylation levels of (b) AKT^{S473} (n=8), (c) 4E-$BP1^{T37/46}$ (n=7), (d) $S6^{S235/236}$ (n=9) and (e) $ERK1/2^{T202/Y204}$ (n=6) in primary CLL samples treated as described in (a). Unstimulated (light-green bars) and $F(ab')_2$ stimulated (dark-green bars). Relative phosphorylation is calculated by first normalising phosphorylation and expression levels by GAPDH, followed by normalised phosphorylation divided by normalised expression levels. Relative phosphorylation levels are relative to unstimulated vehicle control. Individual datapoints are represented by white circles. Data expressed as the mean ± SEM. Statistics calculated by one-way ANOVA, where * $p \leq 0.05$, ** $p \leq 0.01$, *** $p \leq 0.001$, **** $p \leq 0.0001$.

3.2.14 AZD8055 and ibrutinib combination overcomes BCR-mediated survival signals

Given the lack of sensitivity of HG-3 and MEC-1 cells to AZD8055, ibrutinib or COMBO treatment (Figure 3.10), it was of interest to establish whether COMBO could overcome BCR-mediated survival signals to enhance cell death (Figure 3.15). Primary CLL cells were pre-treated with AZD8055 (100 nM), ibrutinib (1 μM) or COMBO for 30 min. Thereafter, CLL cells remained unstimulated or $F(ab')_2$-stimulated for 48 h. Following treatment, the cells were stained with Annexin V/7-AAD and analysed by flow cytometry (Figure 3.15). These data showed a modest trend towards increased CLL cell viability as a consequence of $F(ab')_2$ stimulation (Figure 3.15a,b). Nevertheless, AZD8055 treatment resulted in a near-significant reduction in cell viability in unstimulated (p = 0.12) CLL cells, while a trend towards decreased viability was observed in $F(ab')_2$ stimulated CLL cells (Figure 3.15a,b). Furthermore, ibrutinib significantly reduced cell viability in unstimulated and, perhaps unsurprisingly, $F(ab')_2$ stimulated CLL cells (Figure 3.15a,b). Importantly, COMBO treatment caused a near-significant decrease in the viability of unstimulated (p = 0.054) and $F(ab')_2$-stimulated (p = 0.068) CLL cells (Figure 3.15a,b). A trend towards reduced cell viability existed between AZD8055 and COMBO in $F(ab')_2$ stimulated CLL cells (p = 0.11; Figure 3.15b).

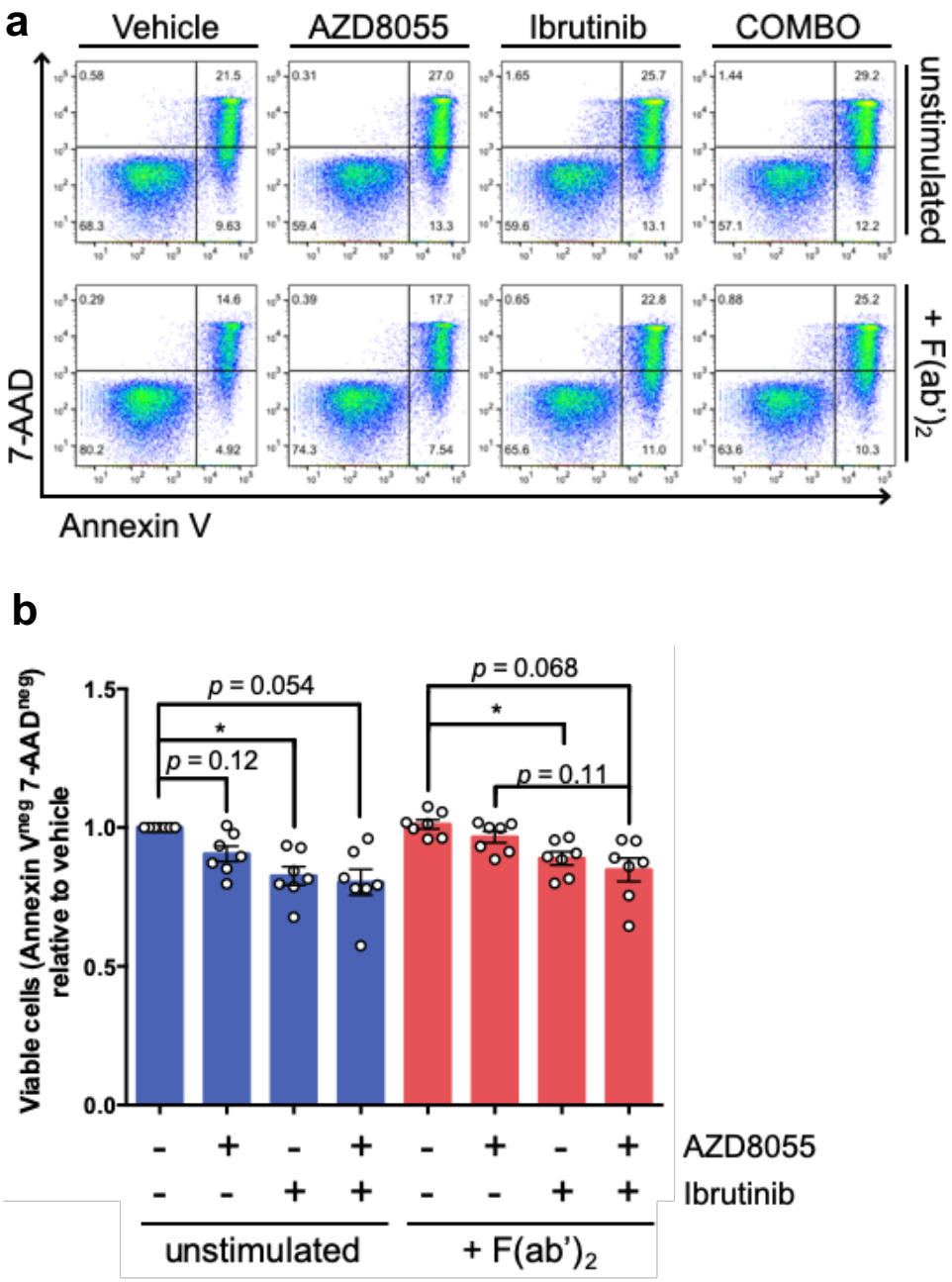

Figure 3.15 - Combination of AZD8055 and Ibrutinib reduces primary CLL cell survival and overcomes F(ab')$_2$-mediated survival signals
(a) Representative FACS plot of a primary CLL sample stained with Annexin V and 7-AAD following pre-treatment with AZD8055 (100 nM), Ibrutinib (1 μM), AZD8055 and Ibrutinib combination (COMBO) or DMSO vehicle control (Vehicle) and subsequent long-term F(ab')$_2$ stimulation for 48 h. (b) Relative viability (Annexin V^{neg} and 7-AAD^{neg} cells) of unstimulated (blue bars) or F(ab')$_2$ stimulated (red bars) primary CLL samples (n=7) treated as described in (a). Percentage viability for each condition is relative to unstimulated vehicle control. Individual datapoints are represented by white circles. Data expressed as the mean ± SEM. Statistics calculated by one-way ANOVA, where * p ≤ 0.05, ** p ≤ 0.01, *** p ≤ 0.001, **** p ≤ 0.0001.

Encouraged by these data, the regulation of anti- and pro-apoptotic proteins in response to treatment in unstimulated and F(ab')$_2$ stimulated CLL cells was explored (Figure 3.16). Initially the expression of anti-apoptotic *MCL-1* and *BCL2-L1* (BCL-xL) on a mRNA level was assessed (Figure 3.16a,b). Regulation of

MCL-1 expression varied in response to F(ab')$_2$ stimulation. Nevertheless, AZD8055 treatment resulted in a trend towards decreased *MCL-1* expression in unstimulated and F(ab')$_2$ stimulated CLL cells (Figure 3.16a). Ibrutinib treatment resulted in a significant downregulation of *MCL-1* in unstimulated CLL cells, while a near-significant downregulation of *MCL-1* was observed in F(ab')$_2$ stimulated CLL cells (p = 0.052) (Figure 3.16a). Interestingly, COMBO caused a significant reduction in *MCL-1* expression in unstimulated and F(ab')$_2$ stimulated CLL cells, significantly greater than AZD8055 treatment alone (Figure 3.16a). A trend towards increased *BCL2-L1* expression was evident as a consequence of F(ab')$_2$ stimulation (Figure 3.16b). Nevertheless, AZD8055 treatment resulted in a near-significant downregulation of *BCL2-L1* in unstimulated (p = 0.12) CLL cells, while a significant decrease in *BCL2-L1* expression was observed in F(ab')$_2$ stimulated CLL cells (Figure 3.16b). Moreover, ibrutinib treatment resulted in a significant downregulation of *BCL2-L1* in unstimulated and F(ab')$_2$-stimulated CLL cells (Figure 3.16b). Equally, while a visible trend towards decreased *BCL2-L1* expression was evident in unstimulated CLL cells, COMBO resulted in a significant downregulation of *BCL2-L1* in F(ab')$_2$-stimulated CLL cells (Figure 3.16b).

The regulation of anti-apoptotic (MCL-1 and BCL2) and pro-apoptotic (BIM) proteins were then assessed by western blotting (Figure 3.16c). These data showed a visible trend towards reduced levels of cleaved PARP in the presence of BCR stimulation (Figure 3.16c,d). Importantly, AZD8055, ibrutinib or COMBO treatment resulted in an increase in the presence of cleaved PARP in unstimulated and F(ab')$_2$ stimulated CLL cells (Figure 3.16c,d). COMBO conferred a trend towards elevated levels of cleaved PARP, greater than each single agent, in unstimulated and F(ab')$_2$ stimulated CLL cells (Figure 3.16c,d). Consistent with Figure 3.16a, regulation of anti-apoptotic MCL-1 protein expression varied in response to F(ab')$_2$ stimulation (Figure 3.16e). Nevertheless, AZD8055 treatment resulted in a significant downregulation of MCL-1 expression in unstimulated CLL cells, while a visible trend toward decreased MCL-1 was observed in F(ab')$_2$ stimulated CLL cells (Figure 3.16c,e). Ibrutinib treatment resulted in a trend towards decreased levels of MCL-1 in unstimulated and F(ab')$_2$ stimulated CLL cells (Figure 3.16c,e). Similarly, while COMBO caused a trend towards reduced MCL-1 in unstimulated CLL cells, a near-significant

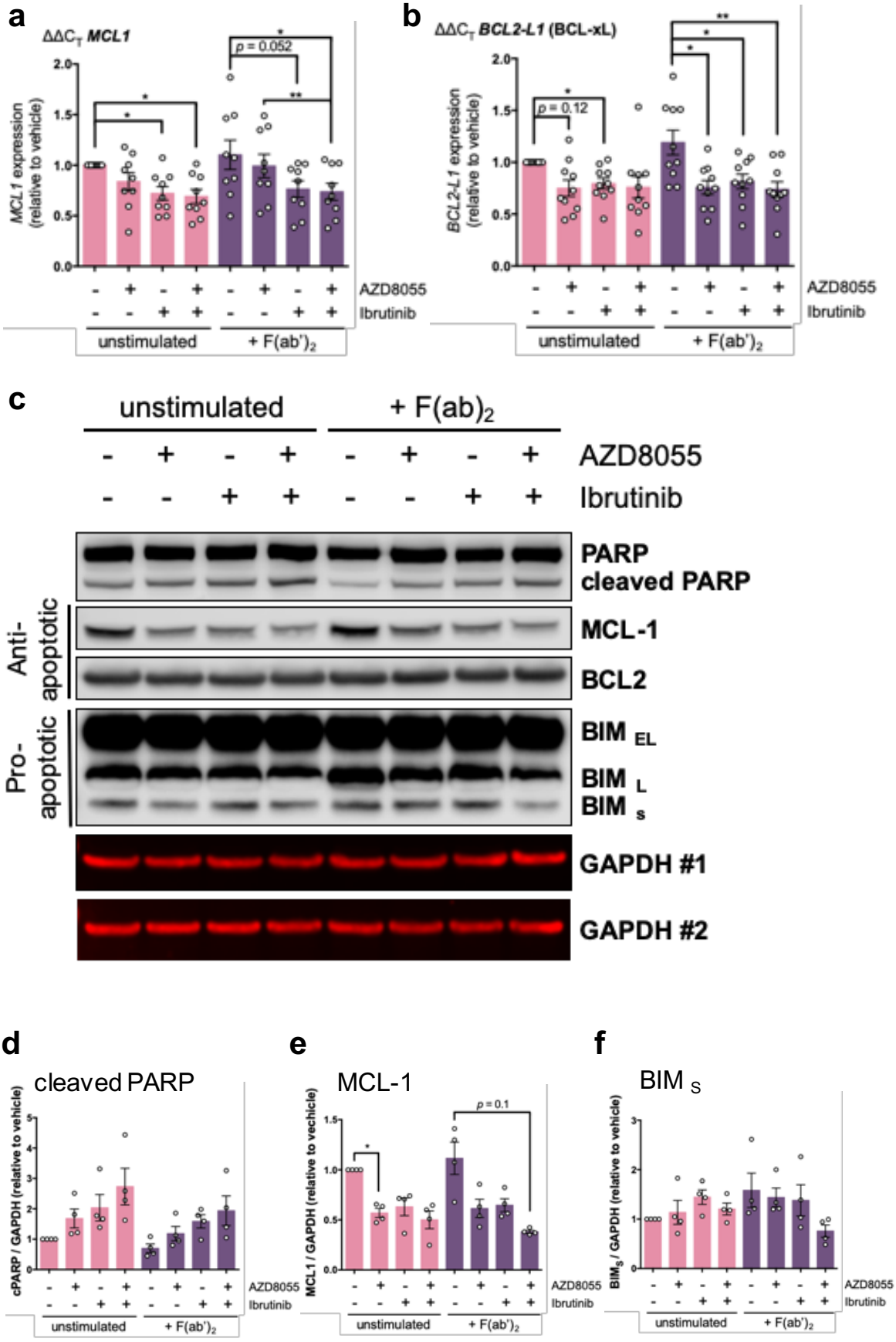

Figure 3.16 - Combination of AZD8055 and Ibrutinib reduces expression levels of anti-apoptotic *BCL2-L1* and *MCL1* in primary CLL cells

(a, b) RT-qPCR to assess expression of (a) *MCL-1* (n=9) and (b) *BCL2-L1* (n=10) in unstimulated (pink bars) or F(ab')$_2$ stimulated (purple bars) primary CLL samples (24 h stimulation) pre-treated with AZD8055 (100 nM), Ibrutinib (1 μM) and AZD8055 and Ibrutinib combination (COMBO). The ΔΔC$_T$ method was used to calculate expression levels, where samples were first normalised to the

internal reference gene *GUSB* and then made relative to unstimulated vehicle control. (c) Representative western blot of a primary CLL sample (CLL151; n=4 primary CLL samples) unstimulated or $F(ab')_2$ stimulated for 48 h following pre-treatment with AZD8055, Ibrutinib and COMBO. Blots were probed for PARP (cleaved PARP), MCL-1, BCL2, BIM (BIM_{EL}, BIM_L, and BIM_S) and GAPDH (loading control; #1 and #2 referring to mirror blots). (d, e, f) Densitometry of (d) cleaved PARP, (e) MCL-1 and (f) BIM_S in unstimulated (pink bars) or $F(ab')_2$ stimulated (purple bars) primary CLL samples (n=4) treated as described in (c). Normalised expression is relative to unstimulated vehicle control. Individual datapoints are represented by white circles. Data expressed as the mean ± SEM. Statistics calculated by one-way ANOVA, where * $p \leq 0.05$, ** $p \leq 0.01$, *** $p \leq 0.001$, **** $p \leq 0.0001$.

reduction in MCL-1 expression was observed in $F(ab')_2$ stimulated CLL cells (p = 0.1) (Figure 3.16c,e). Interestingly, a concurrent decrease in the expression of pro-apoptotic BIM isoform BIM_S was observed following treatment in $F(ab')_2$ stimulated CLL cells (Figure 3.16c, f). These data contrast with the observed results in HG-3 and MEC-1 cells (Figure 3.10f). Despite treatment, BCL2 expression remained constant (Figure 3.16c).

3.2.15 AZD8055 and COMBO inhibits mTOR activity in CLL cells co-cultured on NT-L and CD40L (+IL-4)

Within the CLL-TME, CLL cells co-localise with activated $CD4^+$ T cells expressing CD40L (via analysis of patient LN-biopsies) (182), which promotes proliferation and survival (183, 184). These findings, among others, facilitated the development of *in vitro* co-culture systems replicating the signals that promote CLL cell growth and survival in the CLL-TME (210). The established NT-L/CD40L (+IL-4) co-culture system is one such model mimicking T cell interactions in the CLL microenvironment (186, 217, 448). Given its inhibitory effect on mTOR activity downstream of BCR ligation, it was of interest to elucidate the impact of the COMBO treatment on mTOR activity downstream of CD40 engagement in CLL cells *in vitro*. Following overnight co-culture on NT-L and CD40L cells (+IL-4), CLL cells were treated with AZD8055 (100 nM), ibrutinib (1 µM) or COMBO for 1 h. Thereafter, the phosphorylation status of mTORC1 (4E-$BP1^{T37/46}$ and $S6^{S235/236}$) and mTORC2 (AKT^{S473}) downstream targets was assessed by western blotting (Figure 3.17). AZD8055 treatment resulted in a visible trend towards reduced AKT^{S473} phosphorylation in CLL cells co-cultured on NT-L and CD40L (Figure 3.17a,b). Moreover, ibrutinib caused a modest inhibition of AKT^{S473} phosphorylation in CLL cells co-cultured on NT-L and CD40L (+IL-4) (Figure 3.17a,b). Notably, COMBO mimicked the effect of AZD8055 treatment alone, conferring a more robust

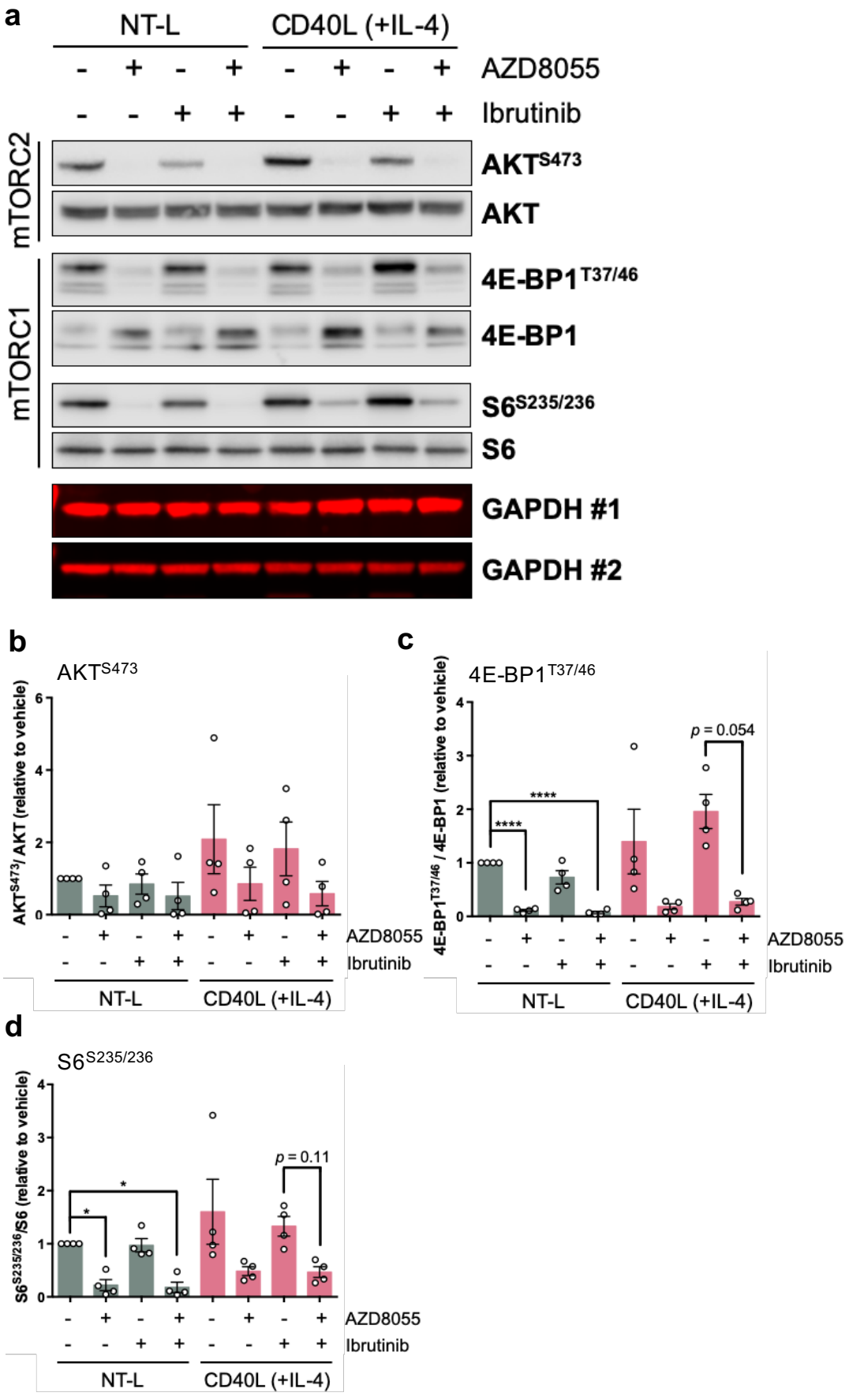

Figure 3.17 - AZD8055 treatment alone, and in combination with ibrutinib, inhibits mTOR activity in CLL cells co-cultured on NT-L and CD40L (+IL-4)
(a) Representative western blot of a primary CLL sample (CLL148; n=4 primary CLL samples) co-cultured on NT-L or CD40L (IL-4) overnight followed by treatment with AZD8055 (100 nM), Ibrutinib

(1 μM), AZD8055 and Ibrutinib combination (COMBO) and DMSO vehicle control (Vehicle) for 1 h. Blots were probed for AKT^{S473}, AKT, 4E-$BP1^{T37/46}$, 4E-BP1, $S6^{S235/236}$, S6 and GAPDH (loading control; #1 and #2 referring to mirror blots). (b, c, d) Relative phosphorylation levels of (b) AKT^{S473}, (c) 4E-$BP1^{T37/46}$ and (d) $S6^{S235/236}$ in primary CLL samples (n=4) co-cultured on NT-L (grey bars) and CD40L (+IL-4) (pink bars) treated as described in (a). Relative phosphorylation levels are relative to NT-L vehicle control. Individual datapoints are represented by white circles. Data expressed as the mean ± SEM. Statistics calculated by one-way ANOVA, where * $p \leq 0.05$, ** $p \leq 0.01$, *** $p \leq 0.001$, **** $p \leq 0.0001$.

inhibition of AKT^{S473} phosphorylation in CLL cells co-cultured on NT-L and CD40L (+IL-4) (Figure 3.17a,b). AZD8055 treatment resulted in a significant inhibition of mTORC1 downstream targets 4E-$BP1^{T37/46}$ (Figure 3.17a,c) and $S6^{S235/236}$ (Figure 3.17a,d) in CLL cells co-cultured on NT-L cells, while a observable trend towards reduced 4E-$BP1^{T37/46}$ (Figure 3.17a,c) and $S6^{S235/236}$ (Figure 3.17a,d) phosphorylation was present in CLL cells co-cultured on CD40L cells (+IL-4). Interestingly, ibrutinib was largely ineffective in reducing phosphorylation of 4E-$BP1^{T37/46}$ (Figure 3.17a,c) and $S6^{S235/236}$ (Figure 3.17a,d) in CLL cells co-cultured on NT-L or CD40L (+IL-4). Furthermore, COMBO treatment resulted in a significant inhibition of 4E-$BP1^{T37/46}$ (Figure 3.17a,c) and $S6^{S235/236}$ (Figure 3.17a,d) phosphorylation in CLL cells co-cultured on NT-L cells. Finally, the COMBO treatment visibly reduced phosphorylation of 4E-$BP1^{T37/46}$ (Figure 3.17a,c) and $S6^{S235/236}$ (Figure 3.17a,d) in CLL cells co-cultured on CD40L (+IL-4), resulting in a near-significant inhibition of 4E-$BP1^{T37/46}$ ($p = 0.054$) and $S6^{S235/236}$ ($p = 0.11$) compared to ibrutinib treatment alone (Figure 3.17a,c,d).

3.2.16 COMBO treatment overcomes stromal-mediated survival signals to enhance CLL cell death

Given the inhibitory effect of the COMBO treatment on mTOR activity downstream of stromal- and CD40L-mediated signals, it was of interest to establish whether the combination could overcome the enhanced survival advantages conferred by the NTL/CD40L (+IL-4) co-culture systems (Figure 3.18). Following overnight co-culture on NT-L and CD40L cells (+IL-4), CLL cells were treated with AZD8055 (100 nM), ibrutinib (1 μM) or COMBO for 48 h. Subsequently, the cells were stained with Annexin V/7-AAD and analysed by flow cytometry (Figure 3.18a-c). These data revealed that although CLL cells co-cultured on CD40L cells (+IL-4) were largely insensitive to AZD8055, ibrutinib or COMBO treatment, a small trend towards increased cell viability was seen with

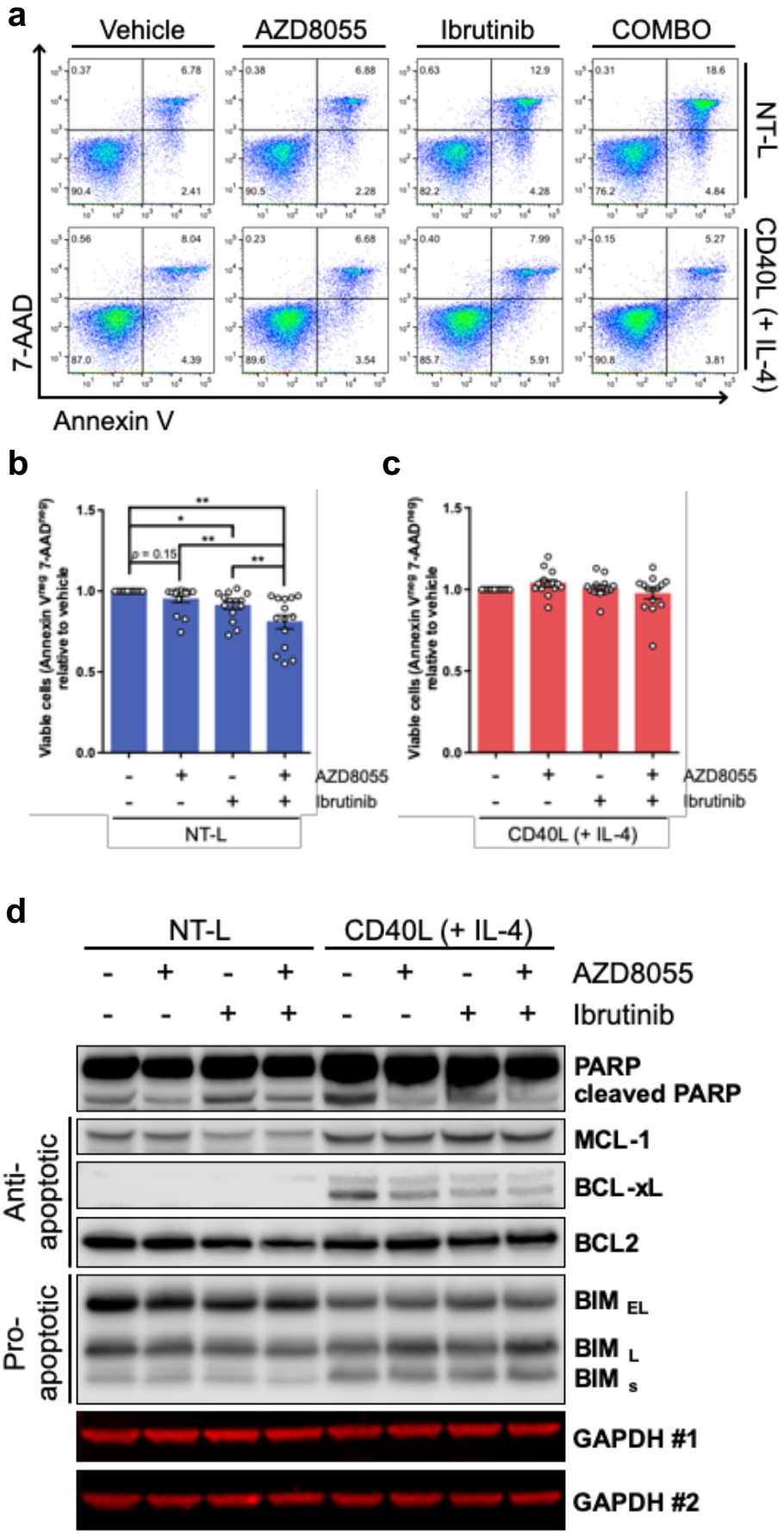

Figure 3.18 - AZD8055 and ibrutinib combination overcomes stromal-mediated survival signals to enhance CLL cell death

(a) Representative FACS plot of a primary CLL sample stained with Annexin V/7-AAD following overnight co-culture on NT-L (top panel) or CD40L (+IL-4) (bottom panel) and subsequent

treatment with AZD8055 (100 nM), Ibrutinib (1 μM), AZD8055 and Ibrutinib combination (COMBO) or DMSO vehicle control (Vehicle) for 48 h. (b, c) Relative viability (Annexin V^{neg} and 7-AAD^{neg} cells) of primary CLL samples (n=14) co-cultured on (b) NT-L (blue bars) or (c) CD40L (+IL-4) (red bars) treated as described in (a). Percentage viability for each condition is relative to vehicle control. Individual datapoints are represented by white circles. (d) Representative western blot of a primary CLL sample (CLL149; n=4 primary CLL samples) co-cultured on NT-L or CD40L (+IL-4) overnight and treated with AZD8055, Ibrutinib, COMBO or Vehicle for 48 h. Blots were probed for PARP (cleaved PARP), MCL-1, BCL-xL, BCL2, BIM (BIM_{EL}, BIM_L, and BIM_S) and GAPDH (loading control; #1 and #2 referring to mirror blots). Individual datapoints are represented by white circles. Data expressed as the mean ± SEM. Statistics calculated by one-way ANOVA, where * $p \leq 0.05$, ** $p \leq 0.01$, *** $p \leq 0.001$, **** $p \leq 0.0001$.

AZD8055 treatment (Figure 3.18a,c), akin to HG-3 and MEC-1 cells (Figure 3.10). Furthermore, a slight trend towards reduced cell viability was visible in response to the COMBO treatment (Figure 3.18a,c). Despite the lack of sensitivity in CLL cells co-cultured on CD40L cells (+IL-4), AZD8055 treatment resulted in a near-significant reduction in cell viability in CLL cells co-cultured on NT-L cells (p = 0.15; Figure 3.18a,b). Moreover, ibrutinib and COMBO treatment induced a significant decrease in cell viability (Figure 3.18a,b). Importantly, the COMBO treatment significantly enhanced cell death, greater than AZD8055 or ibrutinib treatment alone (Figure 3.18a,b).

The regulation of anti-apoptotic (MCL-1, BCL-xL and BCL2) and pro-apoptotic (BIM) proteins were assessed by western blotting (Figure 3.18d). AZD8055 and COMBO treatment resulted in a decrease in the presence of cleaved PARP in CLL cells co-cultured in NTL and CD40L (+IL-4) (Figure 3.18d), which conflicted with the viability data presented in Figure 3.18a-c. Nevertheless, anti-apoptotic MCL-1 was downregulated following COMBO treatment in CLL cells co-cultured on NT-L compared to vehicle control (Figure 3.18d). In contrast, MCL-1 expression was unaffected by COMBO treatment in CLL cells co-cultured on CD40L (+IL-4) (Figure 3.18d). As expected, the expression of anti-apoptotic BCL-xL was upregulated in CLL cells co-cultured on CD40L (+IL-4), which was downregulated following treatment with AZD8055, ibrutinib or COMBO (Figure 3.18d). A decrease in the expression of pro-apoptotic BIM isoform BIM_S was observed following COMBO treatment in CLL cells co-cultured on NT-L (Figure 3.18d), whereas BIM_S was unaffected by treatment in CLL cells co-cultured on CD40L (+IL-4) (Figure 3.18d). Despite treatment, BCL2 expression remained constant (Figure 3.16c).

3.2.17 AZD8055 and COMBO treatment inhibits CD40L (+IL-4)-induced increased CLL cell size

As demonstrated in Figure 3.11, AZD8055 and ibrutinib treatment alone significantly reduced MEC-1 cell size, which was further enhanced in combination. Co-culture on CD40L (+IL-4) activates mTORC1 signalling (Figure 3.17a), priming cellular growth and expansion (293). With this in mind, the functional impact of mTOR inhibition on CLL cell size downstream of CD40-ligation was explored (Figure 3.19). Following overnight co-culture on CD40L cells (+IL-4), CLL cells were treated with AZD8055 (100 nM), ibrutinib (1 μM) or COMBO treatment for 48 h. Thereafter, cell size was quantified as a measure of FSC-A by flow cytometry (Figure 3.19a,b). AZD8055 treatment resulted in a significant inhibition of CD40L (+IL-4)-induced CLL cell growth (Figure 3.19c). Moreover, a significant reduction was also observed in CLL cells treated with ibrutinib (Figure 3.19c). Despite this, the scale of inhibition was comparatively much larger in AZD8055-treated CLL cells (Figure 3.19c). Importantly, the COMBO treatment significantly blocked CLL cell growth facilitated by CD40L (+IL-4) co-culture (Figure 3.19c). Consistent with Figure 3.11, the COMBO treatment resulted in a significantly greater decrease in CLL cell size compared to ibrutinib treatment alone (Figure 3.19c), while a near-significant reduction was observed compared to AZD8055 treatment alone ($p = 0.13$; Figure 3.19c).

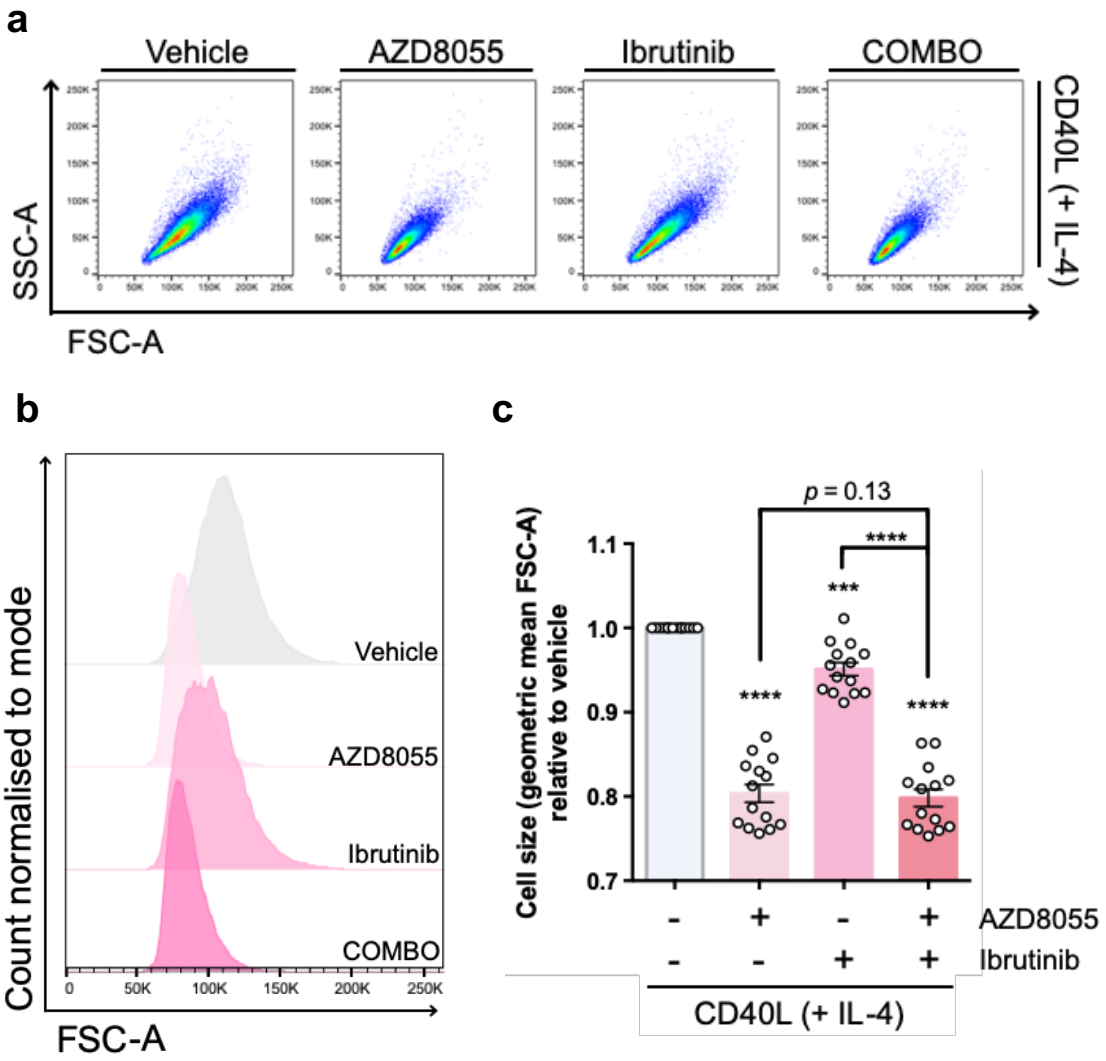

Figure 3.19 - AZD8055 treatment alone, and in combination with ibrutinib, inhibits CD40L (+IL-4)-mediated CLL cell growth
(a) Representative FACS plot (forward scatter-area (FSC-A) against sideward scatter-A (SSC-A)) assessing cell size of a primary CLL sample following overnight co-culture on CD40L (+IL-4) and subsequent treatment with AZD8055 (100 nM), Ibrutinb (1 μM), AZD8055 and Ibrutinib combination (COMBO) or DMSO vehicle control (Vehicle) for 48 h. (b) Representative FACS histogram displaying geometric mean of FSC-A of a primary CLL sample co-cultured on CD40L (+IL-4) and treated with AZD8055 (light-pink histogram), Ibrutinib (medium-pink histogram), COMBO (dark-pink histogram) or Vehicle (grey histogram) for 48 h. (c) (b, c) Relative cell size (geometric mean) of primary CLL samples (n=14) treated as described in (a). Geometric means for each condition are relative to Vehicle. Individual datapoints are represented by white circles. Data expressed as the mean ± SEM. Statistics calculated by one-way ANOVA, where * $p \leq 0.05$, ** $p \leq 0.01$, *** $p \leq 0.001$, **** $p \leq 0.0001$.

3.2.18 CD40-induced CLL cell proliferation is inhibited by AZD8055 and COMBO treatment

The CD40L co-culture system (supplemented with IL-4 or IL-21) has been implemented previously to induce proliferation of CLL cells *in vitro* (145, 180, 279). As demonstrated in Figure 3.17, mTOR signalling is active in CLL cells co-cultured on CD40L (+IL-4), which can be inhibited by AZD8055 or COMBO

treatment. Given the inhibitory effect of the COMBO treatment on cell proliferation in HG-3 and MEC-1 cells (Figure 3.13), the impact of treatment on CLL cell proliferation downstream of CD40-ligation was investigated (Figure 3.20). Following co-culture on NT-L (non-proliferative control) and CD40L (+IL-21) cells, CLL cells were treated with AZD8055 (100 nM), ibrutinib (1 μM), COMBO or rapamycin (10 nM) for 9 days. Prior to treatment, CLL cells were stained with CTV to qualitatively and quantitatively assess cell proliferation by flow cytometry (Figure 3.20a). Rapamycin treatment was included to compare the effect of mTORC1-selective inhibition with dual mTOR inhibition. These data revealed a significant increase in CD40L (+IL-21)-induced CLL cell proliferation compared to CLL cells co-cultured on NT-L, as represented by a smaller CTV geometric mean (Figure 3.20a,b). AZD8055 treatment resulted in a near-significant inhibition of cell proliferation compared to vehicle control (p = 0.11; Figure 3.20a,b). Moreover, the anti-proliferative effect of AZD8055 treatment was comparable with CLL cells co-cultured on NT-L (Figure 3.20b). Consistent with Figure 3.13, CLL cells co-cultured on CD40L (+IL-21) were largely unaffected by ibrutinib treatment, demonstrating enhanced cell proliferation akin to vehicle control (Figure 3.20b). Furthermore, this corresponded to a significant increase in cell proliferation compared to CLL cells co-cultured on NT-L (Figure 3.20b). COMBO treatment resulted in a trend towards reduced proliferation (Figure 3.20b). Equally, while rapamycin treatment showed a visible trend towards decreased proliferation, the inhibition conferred by AZD8055 was demonstrably greater than rapamycin (Figure 3.20b).

Subsequently, the regulation of ‘cell cycle proteins’ in response to treatment was assessed by western blotting (Figure 3.20c). Cyclin E1 expression was upregulated in CLL cells co-cultured on CD40L (+IL-21) compared to NT-L (Figure 3.20c,d). Consistent with Figure 3.13d, Cyclin E1 expression was upregulated following AZD8055 or ibrutinib treatment compared to vehicle treated cells, while the COMBO treatment downregulated Cyclin E1 (Figure 3.20c). Moreover, Cyclin E1 was upregulated by rapamycin treatment, noticeably greater than AZD8055 treatment alone (Figure 3.20c). CDK2 expression was marginally higher in CLL cells co-cultured on CD40L (+IL-21) compared to NT-L. Nevertheless, the expression of CDK2 in CD40L (+IL-21)-stimulated CLL cells was largely unaffected by treatment (Figure 3.20c). Cyclin D2 expression was downregulated in the

presence of AZD8055, while the COMBO treatment caused a modest upregulation in Cyclin D2 (Figure 3.20c). The expression of CDK4 was reduced in CLL cells

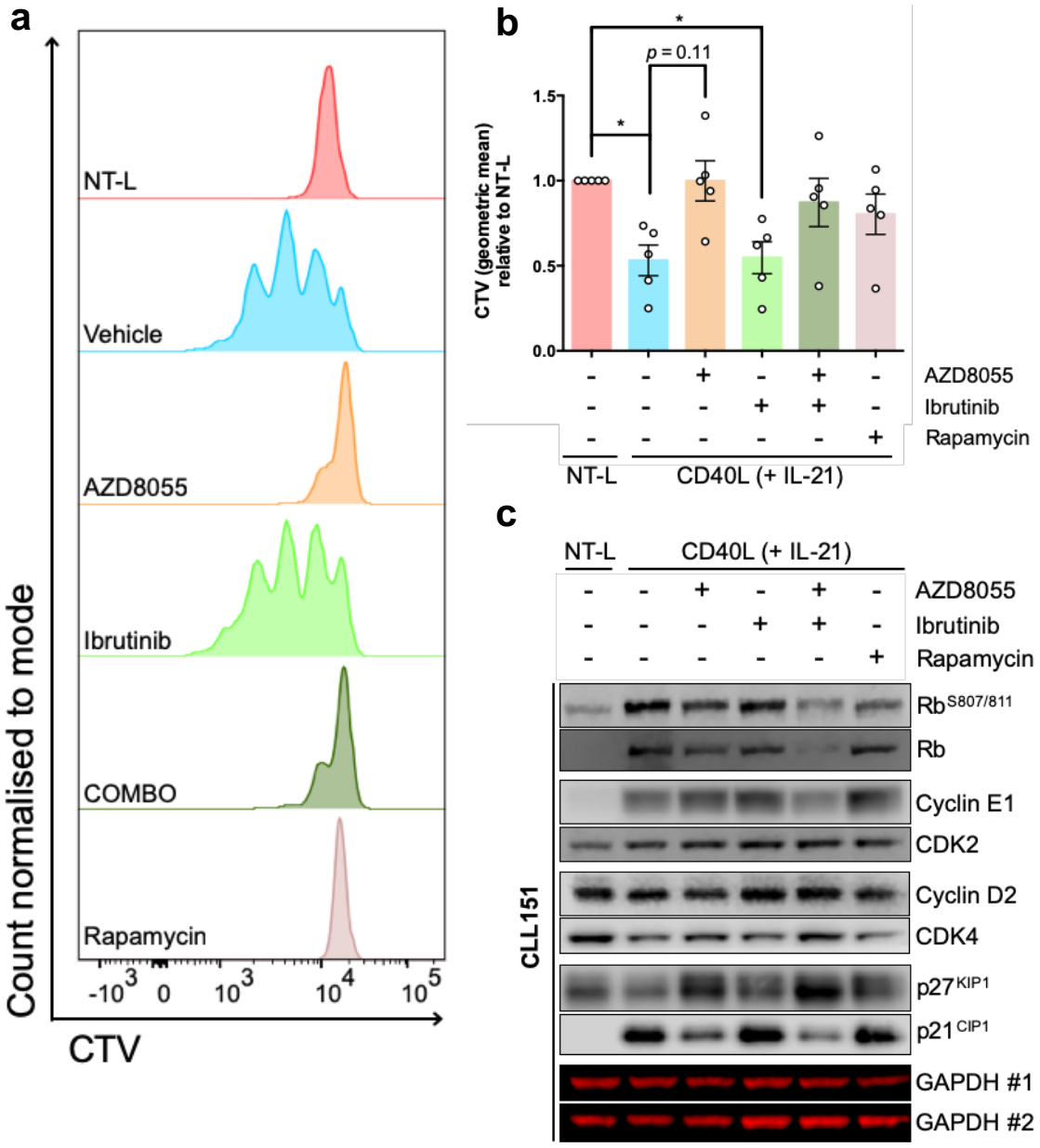

Figure 3.20 - CD40-induced CLL cell proliferation is inhibited by AZD8055 treatment alone and in combination with ibrutinib

(a) Representative FACS histogram of a primary CLL sample (CLL132) stained with CellTrace Violet (CTV) following long-term co-culture on CD40L (+IL-21) treated with AZD8055 (100 nM; orange histogram), Ibrutinib (1 μM; light-green histogram), AZD8055 and Ibrutinib combination (COMBO; dark-green histogram), Rapamycin (10 nM; pink histogram) or DMSO vehicle control (Vehicle; blue histogram) for 9 days. Primary CLL cells were co-cultured on NT-L as a non-proliferative control. Please refer to section 2.2.2.5 for gating strategy. (b) Assessment of CTV geometric mean for primary CLL samples (n=5) treated as described in (a). Geometric means for each condition are relative to NT-L non-proliferative control. Individual datapoints from each replicate are shown as white circles. (c) Representative western blot of primary CLL sample CLL151 (n=5 primary CLL samples) co-cultured on CD40L (+IL-21) and treated with AZD8055, Ibrutinib, COMBO, Rapamycin and Vehicle for 6 days. Primary CLL cells were co-cultured on NT-L as a non-proliferative control. Blots were probed for $Rb^{S807/811}$, Rb, Cyclin E1, CDK2, Cyclin D2, CDK4, $p27^{KIP1}$, $p21^{CIP1}$ and GAPDH (loading control; #1 and #2 referring to mirror blots). Data

expressed as the mean ± SEM. Statistics calculated by one-way ANOVA, where * $p \leq 0.05$, ** $p \leq 0.01$, *** $p \leq 0.001$, **** $p \leq 0.0001$.

co-cultured on CD40L (+IL-21) compared to NT-L. Notably, AZD8055 and the COMBO treatment upregulated CDK4 expression to levels similar to NT-L. In contrast, CDK4 expression was unaffected by ibrutinib or rapamycin treatment compared to vehicle control (Figure 3.20c). Interestingly, the expression of the CDKI $p27^{KIP1}$ was downregulated in CLL cells co-cultured on CD40L (+IL-21) compared to NT-L. Moreover, while each treatment caused an elevation in $p27^{KIP1}$ expression compared to vehicle control, the largest increase in $p27^{KIP1}$ expression occurred in the presence of AZD8055 and the COMBO treatment (Figure 3.20c). Perhaps most intriguingly, the expression of cell cycle inhibitor $p21^{CIP1}$ was upregulated in CLL cells co-cultured on CD40L (+IL-21) compared to NT-L. COMBO treatment downregulated $p21^{CIP1}$ expression, while ibrutinib and rapamycin elicited a noticeable upregulation in $p21^{CIP1}$ (Figure 3.20c). Of note, it would have been interesting to assess $p21^{CIP1}$ subcellular localisation following stimulation and/or treatment to ascertain $p21^{CIP1}$ activity in this context. Finally, these data revealed that phosphorylation of $Rb^{S807/811}$ increased in CLL cells co-cultured on CD40L (+IL-21) compared to NT-L, indicative of Rb inactivation and subsequent G1/S cell cycle progression (449) (Figure 3.20c).

3.2.19 AKT-dependent $FOXO1^{T24}$ phosphorylation is inhibited by COMBO treatment in $F(ab')_2$ stimulated CLL cells

BCR stimulation elevated phosphorylation levels of AKT^{T308} and AKT^{S473} in CLL cells, which were inhibited following pre-treatment with AZD8055, ibrutinib or COMBO (Figure 3.21a). As FOXO transcription factors are AKT substrates, which mediate cell cycle arrest and apoptosis (384), it was of interest to explore AKT-dependent regulation of FOXOs downstream of BCR ligation and mTOR inhibition (Figure 3.21). Previous studies have highlighted a prominent role for FOXO1 throughout B cell development (384, 387, 395). For these reasons, FOXO1 regulation was explored by assessing AKT-dependent $FOXO1^{T24}$ phosphorylation in unstimulated and $F(ab')_2$ stimulated CLL cells. As expected, $F(ab')_2$ stimulation of CLL cells elicited a significant increase in AKT-dependent $FOXO1^{T24}$ phosphorylation (Figure 3.21a,b). However, preincubation with AZD8055, ibrutinib or COMBO treatment resulted in a significant decrease in $FOXO1^{T24}$

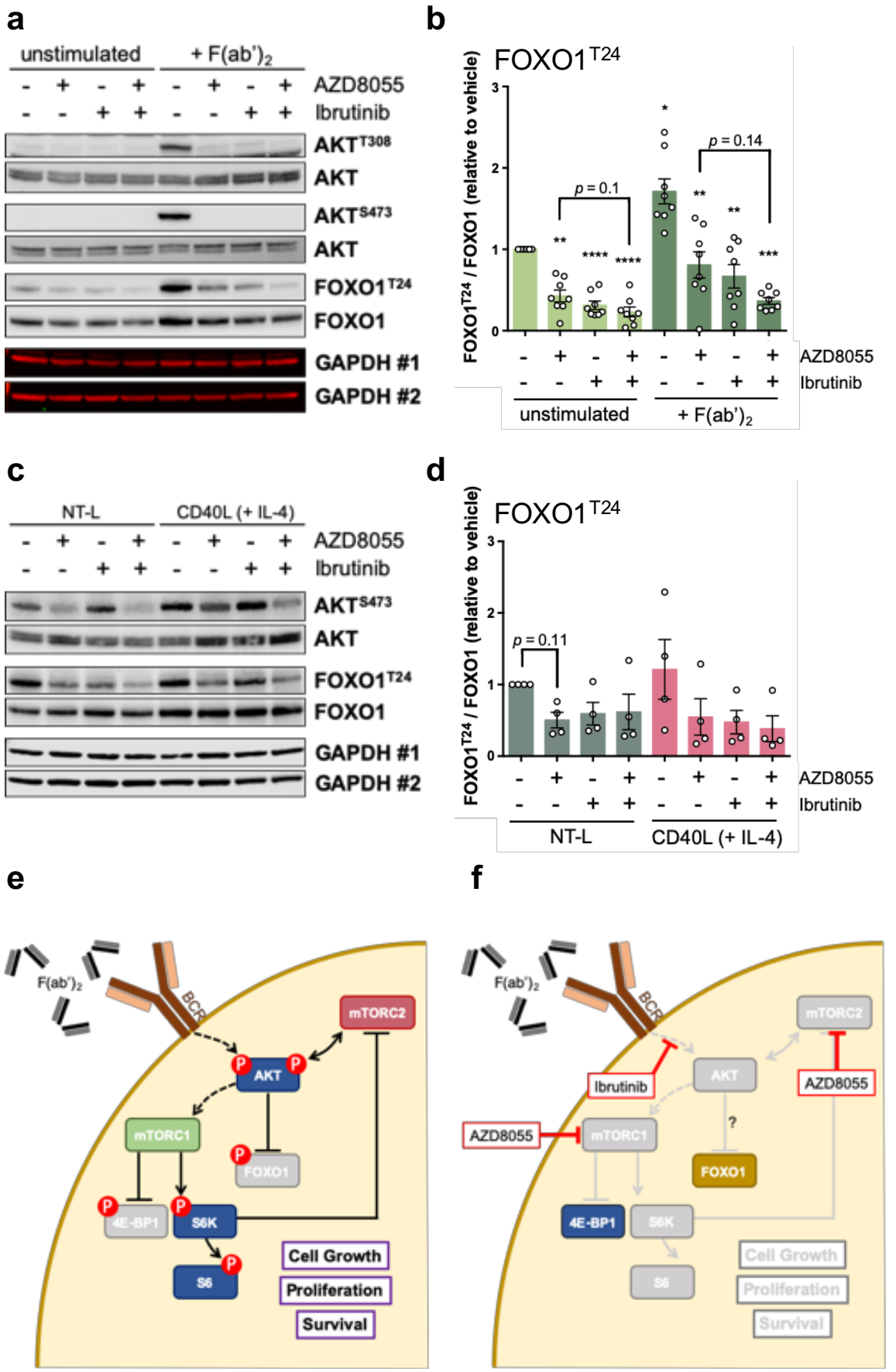

Figure 3.21 - AKT-dependent FOXO1^{T24} phosphorylation is inhibited by AZD8055 and ibrutinib combination in F(ab')$_2$ stimulated CLL cells

(a) Representative western blot of a primary CLL sample (#CLL151) unstimulated or F(ab')$_2$ stimulated for 1 h following 30 min pre-treatment with AZD8055 (100 nM), Ibrutinib (1 μM), AZD8055 and Ibrutinib combination (COMBO) or DMSO vehicle control (Vehicle). Blots were

probed for AKT^{T308}, AKT^{S473}, AKT, FOXO1^{T24}, FOXO1 and GAPDH (loading control; #1 and #2 referring to mirror blots). (b) Relative phosphorylation levels of FOXO1^{T24} in primary CLL samples (n=8) treated as described in (a). Unstimulated (light-green bars) or F(ab')$_2$ stimulated (dark-green bars). (c) Representative western blot of a primary CLL sample (#CLL143) co-cultured on NT-L or CD40L (+IL-4) overnight, followed by treatment with AZD8055 (100 nM), Ibrutinib (1 μM), AZD8055 and Ibrutinib combination (COMBO) or DMSO vehicle control (Vehicle). Blots were probed for AKT^{S473}, AKT, FOXO1^{T24}, FOXO1 and GAPDH. (d) Relative phosphorylation levels of FOXO1^{T24} in primary CLL samples (n=4) co-cultured on NT-L (grey bars) or CD40L (+IL-4) (pink bars) and treated as described in (c). Individual patient datapoints are shown as white circles. (e) Schematic depicting AKT-mediated FOXO1^{T24} phosphorylation as a consequence of F(ab')$_2$ stimulation. (f) Pre-treatment of primary CLL cells with AZD8055 and Ibrutinib combination inhibits F(ab')$_2$-dependent FOXO1^{T24} phosphorylation. Data expressed as the mean ± SEM. Statistics calculated by one-way ANOVA, where * $p \leq 0.05$, ** $p \leq 0.01$, *** $p \leq 0.001$, **** $p \leq 0.0001$.

phosphorylation (Figure 3.21a,b). In line with these findings, AZD8055, ibrutinib or COMBO treatment diminished basal levels of FOXO1^{T24} in unstimulated CLL cells (Figure 3.21a,b). Importantly, the COMBO treatment caused a near-significant reduction in FOXO1^{T24} phosphorylation in unstimulated (p = 0.1) and F(ab')$_2$ stimulated (p = 0.14) CLL cells, greater than AZD8055 treatment alone (Figure 3.21a,b). To address AKT-dependent regulation of FOXO1 downstream of CD40-ligation, phosphorylation levels of FOXO1^{T24} were assessed in CLL cells co-cultured on NT-L and CD40L (+IL-4) (Figure 3.21c,d). FOXO1^{T24} phosphorylation was observed in CLL cells co-cultured on NT-L and CD40L (+IL-4), corresponding to increased levels of AKT^{S473} (Figure 3.21c,d). AZD8055 and COMBO treatment reduced FOXO1^{T24} phosphorylation in CLL cells co-cultured on NT-L and CD40L (+IL-4), concordant with treatment-induced AKT^{S473} inhibition (Figure 3.21c,d). Consistent with Figure 3.17, ibrutinib treatment was unable to inhibit AKT^{S473} phosphorylation in CLL cells co-cultured on NT-L and CD40L (Figure 3.21c). Interestingly, however, a trend towards reduced FOXO1^{T24} phosphorylation was observed (Figure 3.21c,d). Therefore, BCR crosslinking induces FOXO1^{T24} phosphorylation (Figure 3.21e), which can be inhibited by AZD8055, ibrutinib or the COMBO treatment (Figure 3.21f).

3.3 Discussion

Here, we provide insights into mTOR activity in CLL cells derived from the periphery and in response to microenvironment stimuli *in vitro* and *ex vivo*. These findings have presented a rationale for targeted inhibition of mTOR kinase using AZD8055, which blocks the activity of both mTORC1 and mTORC2. However, AZD8055 anti-tumour activity appears to be limited as a monotherapy. We have shown that a synergistic combination of AZD8055 and the clinically approved BTK inhibitor ibrutinib has deleterious effects on CLL cell growth and survival - and the regulation of signalling pathways therein - which will be discussed in more detail here.

3.3.1 Basal mTOR activity in primary CLL cells is heterogeneous

The data presented here demonstrates the existence of basal mTOR activity, or heterogeneity thereof, among PB-derived CLL samples, as determined by phosphorylation of mTORC1 (4E-BP1$^{T37/46}$ and S6$^{S235/236}$) and mTORC2 (AKT^{S473}) downstream targets. These findings support previous studies reporting the presence of constitutively active PI3K (208, 252) and AKT (284-286) in primary CLL cells. These data suggest that PI3K-AKT-mTOR signalling might play an important role in CLL disease maintenance in the periphery.

Activation of the PI3K-AKT-mTOR axis in the PB compartment, constitutive or otherwise, might represent a 'functional snapshot' (247). Indeed, Packham *et al.* postulated that circulating CLL cells carry transient imprints of recent stimulation within lymphoid tissues, inasmuch as recent emigrants will possess an 'activated' phenotype that diminishes over time (256). For example, mTOR can be transiently activated in CLL cells through binding of chemokine receptors, such as CXCR4 and CXCR5, which regulate CLL cell migration from PB to the SLOs (333, 341, 450). These factors may explain a degree of heterogeneity in mTOR activity among peripheral CLL samples, distinct from constitutive activation. Nevertheless, one cannot assume that activation of signalling pathways is due to prior stimulation *in vivo* (256). In any case, there is evidence to suggest that PI3K-AKT-mTOR signalling is constitutively active in CLL cells. As mentioned previously, studies have demonstrated that PTEN is functionally comprised in CLL (288-290, 292), which describe a pathophysiological state

wherein aberrant PTEN function could potentially lead to constitutive activation of PI3K-AKT-mTOR signalling in CLL. Intriguingly, activation of the PI3K-AKT-mTOR axis in unstimulated CLL cells could also be indicative of antigen-independent autonomous or 'tonic' BCR signalling (247, 254, 255), supported by studies demonstrating constitutive activation of proximal BCR kinases LYN (250), SYK (251) and downstream component PI3K (252). Furthermore, one cannot exclude the influence of distinct pathways (e.g. MAPK/ERK) that converge upon mTOR (293). Finally, given the heterogeneity in responses to BCR stimulation among U-CLL and M-CLL patients (45), these data also raise an important point whether additional interpatient variability in disease biology impacts the regulation of mTOR. With hindsight, it would have been interesting to assess activation status of signalling components upstream of mTOR (proximal to the BCR), particularly in samples stratified according to *IGVH* mutational status.

Of note, despite reports on the contrary (284, 341, 343), mTOR activity was unexpectedly reduced in CLL cells compared with B cells from healthy donors. A likely explanation is the disparity between the methods of B cell isolation. While $CD19^{+}$ CLL cells were negatively selected, B cells derived from healthy donors were positively selected using anti-CD19 microbeads. Thus, without prior release of CD19 microbeads (252), CD19-mediated activation of PI3K signalling may have translated into increased mTOR activity.

3.3.2 Stratification of mTORC1/2 activity suggests dual mTOR inhibition might be efficacious across CLL prognostic subtypes

Stratification of mTOR activity among CLL samples revealed that phosphorylation of mTORC1 (4E-BP1$^{T37/46}$ and S6$^{S235/236}$) and mTORC2 (AKT^{S473}) downstream targets were irrespective of favourable- and poor-prognostic cytogenetic alterations. This suggests that pharmacological interventions targeting mTORC1 and mTORC2 might be efficacious across prognostic subtypes. However, these data contrast with a recent study that reported differential activation of mTOR substrates in CLL patient samples from different prognostic subsets. Here, Cosimo *et al*. found that stratification of basal phosphorylation levels of mTORC1 downstream targets in freshly isolated CLL samples were differentially regulated, with decreased S6$^{S235/236}$ phosphorylation and increased 4E-BP1$^{T37/46}$

phosphorylation in poorer prognostic del(17p) CLL samples (284). An explanation for the conflicting data could be due to the different approach taken to quantitatively assess relative phosphorylation levels of the aforementioned mTORC1 and mTORC2 downstream targets. For the data presented here, phosphorylation levels are relative to the expression of the 'total' protein, i.e. $S6^{S235/236}$ phosphorylation is relative to S6 expression. Cosimo *et al*. normalised the phosphorylation levels to the loading control, i.e. $S6^{S235/236}$ phosphorylation normalised to GAPDH expression (284). Despite being perfectly valid, the approach taken by the authors does not account for the differences in 'total' protein expression.

While it would have been interesting to stratify mTOR activity according to *IGVH* mutational status within our CLL cohort, the presence of favourable- or poor-prognostic cytogenetic alterations raises interesting questions regarding the regulation of mTOR activity. However, large patient cohorts are often required to tease out meaningful trends, owing to interpatient heterogeneity and the prevalence of certain cytogenetic abnormalities. This may explain, assuming there are differences, the absence of notable trends in mTOR activity among our stratified CLL cohort. To circumvent this experimental drawback, a crude method for distinguishing differences in mTOR activity according to cytogenetics is to use established cell lines with defined cytogenetic alterations. We used CLL cell lines HG-3 and MEC-1, which harbour cytogenetic abnormalities associated with favourable (del(13q)) and poor prognosis (del(17p)), respectively (431, 432). Interestingly, MEC-1 cells possessed elevated levels of 4E-$BP1^{T37/46}$, $S6^{S235/236}$ and $ERK1/2^{T202/Y204}$ phosphorylation, while HG-3 cells had increased levels of AKT^{S473} phosphorylation. Although mTOR is active in both cell lines, these data suggest that mTORC2 activity is greater in HG-3 cells, whereas mTORC1 activity is enhanced MEC-1 cells. Whether MEC-1 and HG-3 cells are more reliant on mTORC1 and mTORC2 activity, respectively, remains to be established. Clearly, the identification of cytogenetic abnormalities represents a powerful prognostic biomarker that ultimately governs treatment options for CLL patients (2). With reference to CLL patients harbouring del(17p) (loss of *TP53*) (451), studies have previously demonstrated communication between p53 and mTORC1 pathways to promote cell growth and proliferation (452). For example, p53 nullifies mTORC1 activity via activation and/or upregulation of mTORC1-

negative regulators (294, 453, 454). Additionally, p53 blocks mTORC1 activity through diminishing S6K activation or inhibiting eIF4E-mediated translation via 4E-BP1 dephosphorylation (294, 455). Considering the loss of *TP53* in MEC-1 cells, these findings may explain the increased levels of 4E-BP1$^{T37/46}$ and S6$^{S235/236}$ phosphorylation. Furthermore, MAPK/ERK activity positively regulates mTORC1 (293), providing another potential explanation for enhanced mTORC1 activity in MEC-1 cells. Equally, the deletion 13q14 (del(13q)) leads to overexpression of anti-apoptotic BCL2, owing to impairments of BCL2 negative regulators miR-15a and miR-16 (54). Interestingly, miR-16 has been shown to target *MTOR* and *RICTOR* mRNAs, albeit in CD4$^+$ T cells (456). Thus, loss of miR-16 in HG-3 cells may explain the enhanced levels of AKT^{S473} phosphorylation. Taken together, these findings indicate that CLL cytogenetic alterations may impact upon the activity of mTORC1 and mTORC2 in HG-3 and MEC-1 cells, which poses implications for treatment strategies targeting mTOR. In addition, this underscores the need for a sound understanding of the molecular networks affected by cytogenetic abnormalities to develop novel treatments for CLL. However, it is important to consider that a number of other alterations likely exist in HG-3 and MEC-1 cells, distinct from cytogenetics. Thus, comparisons drawn purely on the presence of different cytogenetic abnormalities are unlikely to yield meaningful conclusions. To assess the importance of cytogenetic alterations on mTOR activity, one might utilise isogenic mutants (e.g. *TP53* WT and null cell lines), which would lead to more accurate comparisons.

3.3.3 Differential regulation of mTORC1 downstream targets in patient LN biopsies suggests CLL growth and proliferation is driven, in part, by the activity of 4E-BP1

The ‘supportive’ LN microenvironment is a central compartment in CLL pathology (9), wherein BCR signalling and interactions with non-malignant accessory cells promote CLL cell survival, growth and proliferation (207, 457). Given its position downstream of many distinct signalling pathways, mTOR is prominently placed to integrate signals from a multitude of microenvironment stimuli (294). Interestingly, we observed differential regulation of mTORC1 downstream targets in CLL patient LN biopsies, which were independent of ‘indolent’ or ‘progressive’ clinical status. While 4E-BP1$^{T37/46}$ phosphorylation was readily detected in patient biopsies, little or no S6$^{S235/236}$ phosphorylation was

observed. This suggests the outcome of mTORC1 signalling in CLL cells is biased towards 4E-BP1 at the expense of S6K, albeit within the LN, which has implications for disease biology and treatment. Interestingly, studies have shown that the processes instigated by mTORC1-dependent 4E-BP1 phosphorylation are probably the most influential in terms of cancer initiation and progression (293, 315, 458-460). Indeed, Hsieh *et al.* demonstrated that mTORC1-dependent S6 phosphorylation was expendable for AKT-driven tumorigenesis, whereas activation of the 4E-BP1/eIF4E axis prompted translation (i.e. protein synthesis) of various transcripts (e.g. MCL-1) that promote lymphomagenesis in a mouse model of T cell lymphoma (458). Therefore, increased 4E-BP1$^{T37/46}$ phosphorylation in CLL patient LN biopsies may enhance eIF4E-mediated translation of proteins implicated in CLL pathogenesis (207, 284, 462). Decreased levels of S6$^{S235/236}$ phosphorylation in CLL patient LN biopsies suggests the activity of S6K1 is reduced. Alongside phosphorylation of S6$^{S235/236}$, S6K mediates a negative feedback loop between mTORC1 and mTORC2 (270, 284). Taken together, these findings indicate that the 4E-BP1/eIF4E axis may play a prominent role in CLL pathogenesis within the LN microenvironment. Equally, these data imply that AKT is active, owing to increased 4E-BP1$^{T37/46}$ phosphorylation and reduced S6K-dependent negative feedback on mTORC2/AKT signalling (299). However, in the absence of AKT^{S473} stained CLL patient LN sections, for example, these conclusions are difficult to convincingly resolve.

From a clinical standpoint, these results offer an alternative explanation as to why everolimus had only modest antitumor activity against CLL in clinical trial (339). Rapalogues (derivatives of rapamycin) do not entirely inhibit 4E-BP1 phosphorylation (312) and are unable to nullify negative feedback loops (mediated via S6K1) that enhance pro-survival signalling via increased mTORC2-AKT activity (270, 314, 315). Mindful of mTORC1 activity within the CLL LN, these findings point to a pathophysiological state whereby selective mTORC1 inhibitors have only limited efficacy in CLL. This suggests, therefore, that dual mTORC1/2 inhibition may elicit a more potent inhibitory response in CLL cells by blocking 4E-BP1 phosphorylation and mTORC2-AKT-mediated pro-survival signalling.

3.3.4 Increased mTORC1/2 activity in F(ab')$_2$ stimulated CLL cells suggests mTOR is a key effector downstream of BCR ligation

The CLL-TME appears to be the primary site of BCR activation for CLL cells (122, 207). As a key signalling node coordinating the activities of PI3K-AKT (269), mTOR integrates growth and survival signals emanating downstream of the BCR (266). Using anti-IgM F(ab')$_2$ fragments to ligate the BCR, we observed elevated phosphorylation levels of mTORC1 (4E-BP1$^{T37/46}$ and S6$^{S235/236}$) and mTORC2 (AKT^{S473}) downstream targets in CLL cells. These data indicate that mTOR is a downstream effector of BCR stimulation. Furthermore, this supports previous studies demonstrating the PI3K-AKT-mTOR axis is intact in BCR-stimulated CLL cells (284, 341, 343). Interestingly, mTOR activation was heterogenous among CLL samples, which is likely a reflection of the marked differences in responsiveness to BCR stimulation (45) pertaining to *IGVH* mutational status (4, 5) and ZAP-70 expression (258). However, without prior clinical assessment, i.e. classification of *IGVH* mutational status, the observed heterogeneity among CLL samples cannot be conclusively attributed to U-CLL or M-CLL. Nevertheless, these data indicate that dual mTOR inhibition may overcome PI3K-AKT-mediated survival signals downstream of the BCR. Therefore, among the current arsenal of BCR signalling inhibitors, targeted inhibition of mTORC1 and mTORC2 could represent a promising and innovative therapeutic approach for CLL.

3.3.5 AZD8055 targets both mTORC1 and mTORC2, which is necessary to inhibit subsequent rephosphorylation of AKT^{S473}

The rapalogue everolimus was less efficacious in CLL clinical trial than previously predicted from preclinical studies of rapamycin (270, 293, 313, 339, 463). With reference to the shortcomings associated with selective mTORC1 inhibitors (312, 314-317), 'second generation' ATP-competitive mTOR inhibitors, such as AZD8055 (318), were developed to avoid these issues by inhibiting the activity of mTORC1 *and* mTORC2 (293). Here, to initially assess AZD8055 specificity for mTORC1/2, unstimulated and F(ab')$_2$ stimulated CLL cells underwent short-term treatment with increasing concentrations of AZD8055. This revealed that AZD8055 overcame BCR stimulation to inhibit phosphorylation of mTORC1 (4E-BP1$^{T37/46}$ and S6$^{S235/236}$) and mTORC2 (AKT^{S473}) downstream targets in a dose

dependent manner, suggesting that AZD8055 is capable of inhibiting mTOR-coordinated growth and survival signals emanating from the BCR. Importantly, this was achieved at clinically achievable doses (441). These findings support previous studies that have demonstrated the selectivity and potency of AZD8055 for mTORC1 and mTORC2 *in vitro* (284, 319-322, 464). Interestingly, AZD8055 inhibited AKT^{T308} phosphorylation in a dose dependant manner, which has also been shown in earlier studies (319, 324). Interestingly, it has been proposed that AKT^{S473} stabilises AKT^{T308} phosphorylation (306, 465, 466), indicating that sustained inhibition of mTORC2 by AZD8055 destabilises AKT^{T308}. Furthermore, the mTOR kinase inhibitor PP242 also inhibited AKT^{T308} phosphorylation, indicating this is a not an AZD8055-specific 'off-target' effect but a typical feature of these inhibitors (324, 467). However, the rapid and transient nature of AZD8055-induced AKT^{T308} inhibition likely initiates PI3K-mediated feedback mechanisms, which may have implications for long-term AZD8055 treatment (324).

We next compared the ability of AZD8055, rapamycin and the BTK inhibitor ibrutinib to block mTOR substrate phosphorylation in unstimulated and $F(ab')_2$ stimulated CLL cells. A clinically achievable dose of AZD8055 inhibited phosphorylation of mTORC1 (4E-$BP1^{T37/46}$ and $S6^{S235/236}$) and mTORC2 (AKT^{S473}) downstream targets in the presence or absence of BCR stimulation. This suggested that mTORC2-AKT feedback activation was fully suppressed in AZD8055-treated CLL cells. Unsurprisingly, short-term rapamycin treatment was unable to fully inhibit phosphorylation of 4E-$BP1^{T37/46}$ and AKT^{S473}, while $S6^{S235/236}$ phosphorylation was reduced to levels comparable with AZD8055 in unstimulated and $F(ab')_2$ stimulated CLL cells. These findings further support studies demonstrating in the inability of rapamycin to completely inhibit 4E-BP1 phosphorylation (312, 468) and that ATP-competitive catalytic mTOR inhibitors can overcome the drawbacks associated with mTORC1 inhibitors (468). Furthermore, rapamycin was unable to inhibit the mTORC2 substrate AKT^{S473}. As explained earlier, inhibition of mTORC1 abolishes negative feedback loops mediated by S6K, resulting in enhanced mTORC2-dependent AKT^{S473} phosphorylation (and AKT reactivation) (316, 317, 341). Despite this, elevated AKT^{S473} phosphorylation was not observed in rapamycin-treated CLL cells following BCR ligation, possibly owing to the short treatment period or

transient effects of F(ab')$_2$ stimulation. Collectively, these data suggest that AZD8055 treatment may enhance CLL cell death by inhibiting pro-survival mTORC2/AKT signalling and enabling inhibitory 4E-BP1/eIF4E complex formation. Nevertheless, the functional response to long-term AZD8055 treatment remains to be elucidated. As BTK is required for BCR-mediated activation of AKT (469), we assessed the ability of ibrutinib to inhibit phosphorylation of mTORC1 (4E-BP1$^{T37/46}$ and S6$^{S235/236}$) and mTORC2 (AKT^{S473}) downstream targets in CLL. Equally, as ibrutinib has been shown to inhibit BCR-mediated MAPK/ERK signalling (126), ERK1/2$^{T202/Y204}$ phosphorylation was also evaluated. Ibrutinib treatment inhibited AKT^{S473} phosphorylation in F(ab')$_2$ stimulated CLL cells. This suggests PI3K-dependent phosphorylation of AKT^{T308} is inhibited, which is required for a SIN1-mediated positive feedback loop between mTORC2 and AKT (276). Moreover, ibrutinib reduced phosphorylation of S6$^{S235/236}$ in F(ab')$_2$ stimulated CLL cells. These findings correspond to recently published data showing the ability of ibrutinib to downregulate mTOR signalling in ABC-DLBCL (470). Interestingly, the impact of ibrutinib on S6$^{S235/236}$ phosphorylation was arguably greater than AZD8055 treatment alone. Mindful that short-term ibrutinib treatment inhibited BCR crosslinking-induced ERK1/2$^{T202/Y204}$ phosphorylation, this indicates that ibrutinib unleashes an additive effect via inhibition of distinct pathways, such as PI3K/AKT and MAPK/ERK signalling, that ultimately converge to regulate mTORC1 activity (293). However, this effect was not observed for 4E-BP1$^{T37/46}$, suggesting that ibrutinib may also perturb mTORC1-independent mechanisms regulating S6$^{S235/236}$ phosphorylation in CLL cells.

3.3.6 AZD8055 cytotoxicity is limited in HG-3 and MEC-1 cells, likely due to sustained AKT^{T308} phosphorylation

After assessing the ability of AZD8055, rapamycin and ibrutinib to block mTOR substrate phosphorylation in unstimulated and F(ab')$_2$ stimulated CLL cells, we next compared the impact of each drug on HG-3 and MEC-1 cell viability. As a monotherapy, rapamycin has limited toxicity, but elicits robust anti-proliferative effects in CLL cells (313, 428). Moreover, in early preclinical studies of ibrutinib, Herman *et al*. demonstrated only modest CLL cell apoptosis *in vitro* (126). Importantly, AZD8055 has been shown to induce caspase-dependent apoptosis, prevent eIF4E-dependent translation and eliminate reactivation of PI3K-AKT

signalling activation in primary AML cells (320). In contrast, HG-3 and MEC-1 cells were largely insensitive to AZD8055, rapamycin or ibrutinib treatment. These data highlight the immense adaptive capability of mTOR signalling (270), which poses implications for long term AZD8055 treatment. Indeed, Rodrik-Outmezguine *et al.* recently demonstrated that AZD8055 suppressed feedback inhibition of RTKs, which ultimately reactivated PI3K-AKT pro-survival signalling (324). Incidentally, AZD8055 has also been shown to induce autophagy (320), which can help maintain cancer cell survival (293). This being said, HG-3 and MEC-1 cells appear to be driven by overactive PI3K signalling, owing to the presence of constitutive AKT^{S473} phosphorylation, which may enhance or overwhelm the effect of AZD8055-induced PI3K activation. Indeed, Cosimo *et al.* recently compared the response of unstimulated CLL patient samples to AZD8055, rapamycin and ibrutinib treatment. Here, the authors reported a comparable, but modest, reduction in cell viability upon AZD8055 or ibrutinib treatment, whereas rapamycin did not affect CLL cell survival (284). This suggests, in the absence of sustained PI3K activation, AZD8055 is capable of inducing apoptosis in CLL cells, greater than the effect of rapamycin treatment.

While PI3K-mediated AKT^{T308} phosphorylation was not assessed alongside survival data, potential reactivation of AKT is an interesting and probable explanation for AZD8055 insensitivity in HG-3 and MEC-1 cells. There is growing evidence that AKT-mediated upregulation of the anti-apoptotic protein MCL-1 is crucial for CLL cell survival (278), particularly downstream of sustained BCR stimulation (471). Indeed, through its association with poor-prognostic markers, MCL-1 expression has clinical significance in CLL (462). As such, BCR signalling inhibitors have been shown to disrupt the delicate balance between pro- and anti-apoptotic proteins by decreasing MCL-1 expression (434, 472). Interestingly, AZD8055 has been shown to reduce MCL-1 expression in rhabdomyosarcoma (473), triple-negative breast cancer (474) and ovarian cancer (475). In contrast, we showed that AZD8055-treated MEC-1 cells upregulated MCL-1, BCL-xL and Survivin expression. This might be indicative of treatment-induced AKT reactivation (278). However, an exception to the rule was the upregulation of pro-apoptotic BIM isoforms (BIM_{EL}, BIM_L and BIM_S) in AZD8055-treated MEC-1 cells. Studies have shown that AKT-dependent BIM^{S87} phosphorylation induces its proteasomal degradation (434, 476). Nonetheless, the effect of AZD8055 treatment on the regulation of anti-

and pro-apoptotic proteins in HG-3 and MEC-1 cells might be specific to these cell lines, which is not replicated in primary CLL cells. Indeed, Cosimo *et al.* recently showed that treatment of F(ab')$_2$-stimulated CLL cells with AZD8055 and rapamycin inhibited BCR-mediated survival and reduced MCL-1 expression (284). This indicates that BCR-ligated CLL cells respond differently to dual mTOR inhibition than HG-3 and MEC-1 cells.

To assess whether extended AZD8055 treatment induced reactivation of AKT, we compared the response of F(ab')$_2$ stimulated CLL cells and MEC-1 cells to AZD8055 treatment at various timepoints up to 24 h. For primary CLL cells, the response to F(ab')$_2$ stimulation was transient (< 3h), as determined by phosphorylation of AKT^{T308} and AKT^{S473}. Importantly, the inhibition of mTORC1 (4E-BP1$^{T37/46}$ and S6$^{S235/236}$) and mTORC2 (AKT^{S473}) downstream targets was sustained for up to 24 h after AZD8055 treatment had commenced, corresponding to previous reports (324). Unlike AKT^{S473}, inhibition of AKT^{T308} phosphorylation was not immediate. This suggests elimination of AKT^{T308} phosphorylation is a secondary event to AKT^{S473} inhibition, supporting the notion that AKT^{S473} phosphorylation stabilises AKT^{T308} (306, 465, 466). This being said, rephosphorylation of AKT^{T308} was not observed in AZD8055-treated F(ab')$_2$ stimulated CLL cells up to 24 h. Although these findings conflict with the data posed by Rodrik-Outmezguine *et al.*, the authors based their findings on cell lines (324), which are unlikely to have the same response as primary cells. In some cases, however, AKT^{T308} rephosphorylation appeared 48 h after treatment (324), so it might be possible that reactivation of PI3K-AKT signalling occurs later, but this seems unlikely in primary CLL cells devoid of sustained stimulation. Nevertheless, prolonged inhibition of AKT^{T308} and AKT^{S473} phosphorylation in F(ab')$_2$ stimulated CLL cells suggests AKT kinase activity is eliminated, which may explain reduced MCL-1 expression in F(ab')$_2$ stimulated CLL cells following AZD8055 treatment (284). In the case of MEC-1 cells, the response to prolonged AZD8055 treatment was somewhat different. As with in F(ab')$_2$ stimulated CLL cells, inhibition of AKT^{S473} and S6$^{S235/236}$ phosphorylation was observed in MEC-1 cells throughout the treatment period. However, despite a gradual reduction in AKT^{T308} phosphorylation in vehicle control MEC-1 cells, AKT^{T308} phosphorylation was present for up to 24 h in AZD8055-treated MEC-1 cells. Since AZD8055 was unable to inhibit AKT^{T308} phosphorylation, this suggests

AKT is partially active and capable of eliciting kinase activity. Additionally, the presence of AKT^{T308} phosphorylation in AZD8055-treated MEC-1 cells at 24 h (compared to vehicle control) might indicate treatment-induced PI3K reactivation. Interestingly, despite initial suppression, 4E-BP1$^{T37/46}$ phosphorylation rebounded to near-basal levels between 5 and 24 h after incubation with AZD8055. This has also been observed previously (324), and was shown to be specific to AKT reactivation and not simply a drop in drug concentration (324). Therefore, rephosphorylation of 4E-BP1$^{T37/46}$ may promote eIF4E-dependent translation of mRNAs associated with CLL progression, establishing a new 'setpoint' that facilitates resistance to AZD8055 (324). Taken together, these findings may explain why MEC-1 cells were insensitive to long-term AZD8055 treatment, owing to enhanced MCL-1, BCL-xL and Survivin expression likely induced by partial reactivation of AKT-mTORC1-(4E-BP1) axis. This casts doubt over the efficacy of AZD8055 as a monotherapy, which subsequently invokes strategies for novel drug combinations that target both mTOR and PI3K/AKT signalling to confer a more robust inhibitory response in CLL.

3.3.7 Dual mTOR inhibitors synergise with ibrutinib to enhance CLL cell apoptosis, likely due to targeted inhibition of multiple survival pathways

The clinical effectiveness of combination therapies is underscored by the ability to perturb regulatory processes entwined within complex biological networks, which can often adapt to monotherapies via multiple feedback mechanisms to promote cellular resilience (477). Therefore, pharmacological inhibition of multiple oncogenes residing within distinct signalling pathways represents a rationale for drug combination studies (424). In MEC-1 cells, sustained AKT^{T308} phosphorylation amidst AZD8055 treatment likely induces downstream survival (and growth) processes sufficient to overcome monotherapy. Until now, we have assumed short-term ibrutinib treatment inhibits AKT^{T308} in MEC-1 cells, owing to the importance of BTK for AKT activation (469, 470) and the absence of AKT^{S473} in ibrutinib-treated MEC-1 cells, which implies the reciprocal feedback loop between mTORC2 and AKT is defunct (276). For these reasons, we hypothesised that combining AZD8055 with ibrutinib would block AKT-mediated survival signals, which would ultimately lead to enhanced CLL cell death. Additionally,

because ibrutinib also inhibits MAPK/ERK and NF-κB survival pathways (126), we envisage this might augment anti-cancer activity in CLL. Interestingly, a study performing a large-scale combinatorial screen to identify drugs that partner with ibrutinib to enhance apoptosis in ABC-DLBCL cells showed that inhibitors of PI3K-AKT-mTOR signalling were chief among the candidates that interacted favourably with ibrutinib to promote cell death (478). Following this, a study reported a synergistic interaction between ibrutinib and AZD2014 that potentiated apoptosis in ABC-DLBCL cells (470). As monotherapies, the ability of AZD8055, AZD2014 and ibrutinib to induce CLL cell apoptosis was negligible, especially at clinically achievable concentrations (439-441). To determine whether dual mTOR inhibitors, AZD8055 and AZD2014, synergise with ibrutinib to enhance CLL cell death, a median-drug effect analysis was performed to calculate CI values according to the Chou and Talalay method (425). This revealed that AZD8055 and AZD2014 synergised with ibrutinib at multiple clinically-achievable doses (439-441) to enhance apoptosis of primary CLL cells. These results were encouraging, not least because they supported the rationale that targeting multiple survival pathways would render CLL cells vulnerable to apoptosis. However, to confirm the ability of the combination to inhibit mTOR and MAPK/ERK activity, we needed to assess the phosphorylation status of mTORC1/2 downstream targets and ERK1/2$^{T202/Y204}$.

Initially, we determined the selectivity of the combination for mTOR and MAPK/ERK activity in HG-3 and MEC-1 cells. Along with the data presented in Figure 3.3f-j, this further suggested that MEC-1 cells might be more reliant on AKT/mTORC1 signalling than HG-3 cells, which may impact upon mTORC1-driven responses. While AZD8055 was unable to inhibit AKT^{T308} and ERK1/2$^{T202/Y204}$ phosphorylation in HG-3 and MEC-1 cells, the addition of ibrutinib successfully blocked activation of these targets. Similarly, while ibrutinib was unable to inhibit 4E-BP1$^{T37/46}$ in MEC-1 cells, AZD8055 effectively abrogated 4E-BP1$^{T37/46}$ phosphorylation. This suggests that synergy between AZD8055 and ibrutinib is due to 1) targeted inhibition of distinct signalling pathways, and 2) a more complete blockade of the same pathway (284). Combining AZD8055 and ibrutinib caused a stronger inhibition of S6$^{S235/236}$ than each agent alone, particularly in MEC-1 cells, indicating that ibrutinib targets distinct pathways that regulate S6K activity or S6$^{S235/236}$ directly. Indeed, S6K1 activation can occur in the absence of

AKT stimulation in DLBCL cell lines insensitive to AKT inhibition via increased expression of PIM2 (479). Interestingly, other kinases have been shown to modulate $S6^{S235/236}$ phosphorylation including RSK1-4 (480), PKC (481) and Protein Kinase A (PKA) (482), suggesting that ibrutinib may influence S6K1-S6 activity independently of mTOR (470).

We next sought to confirm the ability of the combination to inhibit mTOR and MAPK/ERK survival pathways in unstimulated and $F(ab')_2$ stimulated CLL cells. Consistent with the response in HG-3 and MEC-1 cells, AZD8055 and ibrutinib combination acted cooperatively to inhibit the activity of AKT/mTOR and MAPK/ERK in unmanipulated and BCR-stimulated primary CLL cells. These data indicate that following short-term treatment, BCR-mediated CLL survival can be overcome by a favourable interaction between AZD8055 and ibrutinib. Interestingly, we again observed an additive inhibitory effect of the combination treatment on $S6^{S235/236}$ phosphorylation in $F(ab')_2$-stimulated CLL cells, which further highlights the potential impact of ibrutinib on $S6^{S235/236}$ phosphorylation via a mechanism unrelated to mTORC1 (470), perhaps through established off-target activity (125). How this is resolved in the context of the CLL TME, where patient LN biopsies have revealed minimal $S6^{S235/236}$ phosphorylation, remains to be elucidated.

To assess the inhibitory effect of the combination treatment downstream of CD40 ligation, we used the well-established CD40L/IL-4 system (186, 217, 448). mTORC1 (4E-$BP1^{T37/46}$ and $S6^{S235/236}$) and mTORC2 (AKT^{S473}) downstream targets were activated in CLL cells co-cultured on NT-L or CD40L (+IL-4), indicating that mTORC1 and mTORC2 regulate stromal- and CD40L-induced CLL survival, which can be targeted by combining AZD8055 with ibrutinib. AZD8055 treatment successfully inhibited mTORC1 and mTORC2 activity. However, unlike in $F(ab')_2$ stimulated CLL cells, ibrutinib monotherapy only marginally reduced AKT^{S473} phosphorylation, while mTORC1 (4E-$BP1^{T37/46}$ and $S6^{S235/236}$) downstream targets were largely unaffected in CLL cells co-cultured on NT-L or CD40L (+IL-4). Partial inhibition of CD40L-induced AKT^{S473} phosphorylation by ibrutinib has been shown previously with soluble CD40L (126). Nevertheless, combining AZD8055 and ibrutinib blocks phosphorylation of mTORC1 (4E-$BP1^{T37/46}$ and $S6^{S235/236}$) and mTORC2 (AKT^{S473}) downstream targets, which is likely dependent upon AZD8055

treatment. However, without assessment of AKT^{T308} and ERK1/2$^{T202/Y204}$ phosphorylation, it is difficult to conclude the relative contributions of AZD8055 and ibrutinib in this context. Therefore, it remains to be seen whether this combination could reduce AKT-mediated survival signals emanating from CD40/IL-4R ligation. Nevertheless, ibrutinib is known to block interactions between CLL cells with non-malignant accessory cells of the CLL-TME (126, 127). Furthermore, ibrutinib treatment causes a downregulation of chemokine receptor CXCR4, which subsequently leads to CLL cell redistribution (or 'dropping out') into the periphery (124, 129, 483). Interestingly, unpublished data has also revealed that ibrutinib causes impaired IL-4R-signalling and blocks IL-4R-mediated survival in CLL cells (484).

3.3.8 AZD8055 and ibrutinib combination overcomes BCR-mediated survival, likely caused by inhibition of AKT-mediated MCL-1 expression

Ezell *et al*. demonstrated that combining ibrutinib with AZD2014 strongly induced apoptosis in ABC-DLBCL cell lines and OCI-LY10-derived xenograft models. In their case, the combination's mechanism of action converged on the regulation of 4E-BP1 and JAK/STAT3 signalling (470). Here, we proposed that the combination of AZD8055 and ibrutinib would act through concerted inhibition of multiple survival pathways, with emphasis on 'full' AKT inactivation through abrogation of AKT^{T308} rephosphorylation, to promote CLL cell apoptosis. Encouragingly, Cosimo *et al*. recently showed that treating a CLL-like mouse model (485) with a combination of AZD2014 and ibrutinib reduced the percentage of CLL-like cells in PB and decreased tumour burden in the BM and spleen (284). However, the underlying inhibitory mechanisms *in vivo* were not determined.

The initial approach was to assess the impact of the combination on HG-3 and MEC-1 cell viability. We previously demonstrated the relative insensitivity of HG-3 and MEC-1 cells to AZD8055 treatment as a monotherapy, citing sustained phosphorylation of AKT^{T308} following long-term AZD8055 treatment in MEC-1 cells. We subsequently determined that combining AZD8055 with ibrutinib inhibited both AKT^{S473} and AKT^{T308} phosphorylation, suggesting AKT kinase activity and ensuing AKT-mediated survival signals were blocked. Here, however,

we demonstrated that the COMBO treatment had minimal impact on cell viability or apoptosis compared to the single agents. While visible trends towards reduced cell viability and enhanced apoptosis were observed, these effects are unlikely to have biological significance. Therefore, this may suggest that AKT inactivation is transient and/or HG-3 and MEC-1 cells are capable of overcoming AKT, MAPK and NF-κB inhibition by distinct mechanisms. AZD8055 or ibrutinib monotherapy increased MCL-1 expression, which was surprisingly augmented when the drugs were combined. As such, considering the assumption that AKT is fully inactivated by COMBO treatment, these findings conflict with the notion that AKT mediates MCL-1 upregulation (278). AKT controls the expression of BCL2 family proteins through regulation of transcription factors (434). Indeed, AKT regulates NF-κB activation, which promotes anti-apoptotic BCL-xL upregulation (434, 486, 487). Conversely, AKT negatively regulates FOXO transcription factors, which supress expression of pro-apoptotic proteins (e.g. BIM) (375, 434). Confoundingly, we observed enhanced expression of both BCL-xL and BIM following COMBO treatment. Therefore, how these findings reconcile with the observation that AKT is fully inactivated after short-term treatment, remains to be elucidated. Nevertheless, concurrent upregulation of pro- (BIM) and anti-apoptotic (MCL-1 and BCL-xL) proteins perhaps suggests HG-3 cells and MEC-1 cells are capable of readdressing the balance of pro- and anti-apoptotic factors in response to treatment (434). Equally, constitutive expression of BCL2 could offer resistance to HG-3 and MEC-1 cells by sequestering BIM, which has been shown previously in CLL cells (488). Nevertheless, the response of HG-3 and MEC-1 cells in the face of agents altering this delicate balance warrants further investigation.

The impact of COMBO treatment on HG-3 and MEC-1 cell viability may be skewed due to their overactivated (PI3K-driven) phenotype, which is unlikely to mimic the effects of treatment in primary CLL cells. Indeed, Cosimo *et al.* already demonstrated that AZD8055 and ibrutinib as monotherapies are capable of inducing cell death in PB-derived CLL cells (284). Therefore, we next assessed the ability of AZD8055 and ibrutinib combination treatment to reduce cell viability in unstimulated and F(ab')$_2$-stimulated CLL cells. Stimulation of primary CLL cells with F(ab')$_2$ fragments modestly enhanced CLL survival and concurrently increased *MCL1* and *BCL2-L1* (BCL-xL) transcript expression, as

demonstrated previously (278). Encouragingly, the COMBO treatment reduced cell viability in unstimulated and F(ab')$_2$ stimulated CLL cells, which also corresponded to decreased *MCL1* and *BCL2-L1* transcript abundance and enhanced PARP cleavage. Moreover, while BCL2 levels remained consistent, MCL-1 protein expression was reduced following combination treatment in unstimulated and F(ab')$_2$ stimulated CLL cells. These data suggest that AZD8055 and ibrutinib act concertedly to inhibit multiple BCR-induced survival pathways to induce CLL cell apoptosis. Indeed, decreased MCL-1 expression is likely indicative of reduced AKT activation (278), while reduced *BCL2-L1* expression suggests abrogation of NF-κB transcriptional activity (486, 487).

Evaluating the ability of the COMBO treatment to overcome stromal- and CD40L/IL-4-mediated survival signals, we found that combining AZD8055 with ibrutinib reduced cell viability of CLL cells co-cultured on NT-L stromal cells to a greater extent than each drug alone. This corresponded to a decrease in MCL-1 expression, which implies a reduction in AKT activity (278) and perhaps highlights the importance of MCL-1 in CLL survival (462). Moreover, these findings aligned with an early preclinical study of ibrutinib that demonstrated enhanced cell death in ibrutinib-treated CLL cells co-cultured on Hs5 stromal cells (126). Thus, it was reassuring to observe an improved response through positive cooperation between AZD8055 and ibrutinib. However, AZD8055 and ibrutinib as monotherapies or in combination had minimal impact on the viability of CLL cells co-cultured on CD40L (+IL-4), despite overcoming CD40L/IL-4-induced upregulation of BCL-xL. Nevertheless, MCL-1 expression remained constant in CLL cells co-cultured on CD40L, which supports the notion that MCL-1 possesses a greater influence on CLL survival than BCL-xL (278, 462). This result was somewhat surprising, especially considering that studies have demonstrated the ability of ibrutinib to block survival signals emanating from CD40L-engagement (126) and IL-4R-ligation (484). This being said, it is possible that prolonged CD40-engagement in our co-culture system, as opposed to soluble factors (126), overwhelms the potential effect of the treatment. Indeed, sustained signalling downstream of CD40-ligation likely upregulates additional BCL2 family members (perhaps akin to overactivation of HG-3 and MEC-1 cells), which offers a degree of protection to CLL cells and confers resistance to the COMBO treatment (216). While this co-culture system focuses on the effects of

CD40L (+IL-4) stimulation, it cannot fully recapitulate the complex modes of stimulation (i.e. crosstalk) likely occurring within the CLL-TME *in vivo*. Nonetheless, given the profound effects of ibrutinib *in vivo*, including inhibition of cell proliferation, downregulation of chemokine receptors and subsequent redistribution into the periphery (124, 129, 483), this raises the possibility that the strengths of the COMBO treatment may lie elsewhere.

3.3.9 Combining AZD8055 with ibrutinib enhances inhibition of CLL cell proliferation, suggesting COMBO treatment could suppress clonal expansion in the LN microenvironment

The proliferative pool of CLL cells within 'proliferation centres' of the CLL-TME promotes rapid expansion of the malignant clone, facilitates clonal evolution and drives cancer progression (74, 76, 88, 489). Therefore, inhibiting the signals that orchestrate cell growth/proliferation are key to disrupting disease progression. Decker *et al*. demonstrated the ability of rapamycin to inhibit proliferation (i.e. cell cycle arrest) of CpG stimulated-CLL cells (313, 428). Although this underscores the importance of mTORC1 signalling for regulating cell growth, we were interested to assess whether dual mTOR kinase inhibition would augment cell growth arrest via abrogation of mTORC2-AKT signalling. AZD8055 has been shown to block proliferation of AML (320) and renal cell carcinoma (321) cell lines, with the latter demonstrating that AZD8055 conferred a greater inhibitory effect than rapamycin. Given the inhibitory effect of ibrutinib on CLL proliferation *in vivo* (127), we sought to explore whether combining AZD8055 with ibrutinib would augment cell growth arrest.

A prerequisite that permits cellular proliferative expansion is the accumulation of biomass (i.e. cells need to increase in size) (293). Fingar *et al*. showed that the reduction in cell size caused by rapamycin could be rescued by expression of a rapamycin-resistant mutants (mTOR or S6K1) or overexpression of eIF4E, demonstrating the importance of mTORC1 for this process (442). Interestingly, however, PI3K/mTOR-mediated coordination of cell growth and cell cycle progression also impinges upon mTORC2 (270). Therefore, we compared the ability of rapamycin and AZD8055 to regulate HG-3 and MEC-1 cell size. These data showed that AZD8055 and rapamycin significantly reduced MEC-1 cell size. Interestingly, the reduction in MEC-1 cell size caused by AZD8055 was arguably

greater than rapamycin, suggesting the involvement of mTORC2-mediated signalling. Indeed, a recent study demonstrated that genetic depletion of the mTORC2 component SIN1 decreased cell size and diminished proliferation in normal B cells. Interestingly, Li *et al*. showed that SIN1 controlled mTORC1 activity, in part, through AKT-dependent inactivation of TSC1/2 (490). This indicates that mTORC2/AKT activity augments mTORC1-mediated cell growth expansion to prime cells for proliferation, which may explain the enhanced inhibitory effect of AZD8055 over rapamycin. Mindful of the impact of the COMBO treatment on AKT/mTOR activity, the effects of COMBO treatment on cell growth were assessed. Ibrutinib treatment reduced MEC-1 cell size, possibly due to collective inhibition of ERK1/2$^{T202/Y204}$, mTORC1 (S6$^{S235/236}$) and mTORC2 (AKT^{S473}) activity. Interestingly, the COMBO treatment further decreased MEC-1 cell size to an extent greater than each single agent. This additive effect is likely explained by a more complete inhibition of AKT^{T308}, MAPK (ERK1/2$^{T202/Y204}$), mTORC1 (4E-BP1$^{T37/46}$ and S6$^{S235/236}$) and mTORC2 (AKT^{S473}). These findings suggest that AZD8055 and ibrutinib work cooperatively to enhance cell growth arrest, which might have implications for CLL cell cycle progression and proliferation. HG-3 cells were largely insensitive to treatment, despite near-significant reductions in cell size with AZD8055 and rapamycin. Although this requires further experimentation, these observations could be due to reduced basal mTORC1 activity in HG-3 cells compared to MEC-1 cells.

Rapamycin-induced G1 cell cycle arrest in CLL cells was shown to be a manifestation of reduced translation of mRNAs encoding proteins essential for G1 cell cycle progression (313, 428). Although mTORC1 substrates 4E-BP1 and S6K are key players in cell cycle progression (443), mTORC2 controls proliferation via ‘full’ activation of AKT (293, 465). Indeed, the decrease in cell size caused by rapamycin is seldom associated with an outright suppression of proliferation (491). Therefore, we initially sought to compare the effect of AZD8055 and rapamycin on cell cycle progression and proliferation in unsynchronised HG-3 and MEC-1 cells. We demonstrated that AZD8055 and rapamycin induced G1 cell cycle arrest in MEC-1 cells. Although marginal, a larger proportion of AZD8055-treated MEC-1 cells were arrested in G1, which aligns with previous studies demonstrating enhanced inhibitory effect of dual mTOR inhibitors on G1 cell cycle progression compared to rapamycin (and

rapalogues) (320, 321, 447, 492). As before, this suggests the involvement of mTORC2/AKT-mediated signals in cell cycle progression (490). Encouragingly, these findings translated into reduced proliferation following AZD8055 or rapamycin treatment in MEC-1 cells, with AZD8055 arguably conferring a larger inhibitory effect, albeit modest, compared to rapamycin. This indicates that dual mTOR inhibition is better placed to inhibit proliferative signals that are coordinated by both mTOR complexes. AZD8055 and rapamycin induced upregulation of the cell cycle inhibitor $p27^{KIP1}$, contrasting with a previous study (313). Whereas PB-derived CLL cells express high levels of $p27^{KIP1}$ (493), low expression levels of $p27^{KIP1}$ have been observed within 'proliferation centres' of the CLL LN microenvironment (494). This suggests that $p27^{KIP1}$ is an active participant in cell cycle regulation that is modulated in cycling CLL cells (463). The ability of AZD8055 to upregulate $p27^{KIP1}$ has been shown previously (495) and likely explains the inhibitory effect on G1 cell cycle progression in MEC-1 cells.

Subsequently, the effects of the COMBO treatment on cell cycle progression and proliferation were assessed. Ibrutinib treatment induced G1 cell cycle arrest in HG-3 and MEC-1 cells, which was likely a result of concurrent upregulation of cell cycle inhibitors $p21^{CIP1}$ and $p27^{KIP1}$. However, ibrutinib was unable to block HG-3 and MEC-1 cell proliferation to the same extent as AZD8055 or rapamycin. This contrasts with the prevailing view that ibrutinib is a potent inhibitor of CLL proliferation *in vivo* (127). However, ibrutinib likely affects CLL cell proliferation, in part, by promoting redistribution of CLL cells out of the 'proliferative niche' (124, 129, 483). Although the COMBO treatment induced G1 cell cycle arrest in MEC-1 cells, COMBO did not confer an additive effect upon cell cycle progression compared to each agent alone. Despite this, COMBO treatment surprisingly enhanced inhibition of HG-3 and MEC-1 proliferation. This suggests that COMBO treatment-induced AKT inactivation blocks proliferative signals downstream of PI3K/AKT. Indeed, enhanced upregulation of $p27^{KIP1}$ is indicative of relieved AKT-mediated negative regulation of FOXO transcription factors, which contribute towards cell cycle control (382). These findings suggest that COMBO treatment elicits its anti-proliferative effects, in part, through 'full' inhibition of AKT kinase activity and suppression of mTORC1-mediated processes.

To confirm these results, we tested the ability of the COMBO treatment to inhibit cell growth and proliferation in primary CLL cells. However, despite the importance of BCR signalling within the proliferative LN microenvironment *in vivo* (207), current *ex vivo* BCR stimulation protocols are unable to promote proliferation of CLL cells (496). Thus, we used the established CD40L/IL-4 (144) and CD40L/IL-21 co-culture systems (180). Consistent with MEC-1 cells, AZD8055 and ibrutinib as monotherapies blocked increased cell size induced by co-culture on CD40L (+IL-4), with AZD8055 conferring a greater inhibitory effect. This is likely due to complete inhibition of mTORC1/2 activity, whereas ibrutinib only poorly inhibits 4E-BP1$^{T37/46}$ phosphorylation. The inhibitory effect of COMBO on cell growth was larger than each agent alone, likely due to 'full' inhibition of AKT kinase activity alongside inhibition of signalling pathways and/or adaptive mechanisms that converge on mTORC1. Ibrutinib was unable to confer an anti-proliferative effect in CLL cells co-cultured on CD40L (+IL-21), which conflicted with reports on the contrary (127). Interestingly, however, studies have shown that CD40L (+IL-4)-stimulated 'normal' B cells retain the ability to proliferate following treatment with PI3K inhibitors (266, 497). Nevertheless, AZD8055 alone and COMBO inhibited CD40L (+IL-21)-induced CLL proliferation, highlighting the importance of mTOR signalling in coordinating proliferative signals downstream of CD40/IL-21R ligation. These data indicate that the COMBO treatment could represent an effective strategy to prevent clonal expansion within the CLL-TME.

3.3.10 Inactivation of AKT by COMBO treatment may reactivate FOXO1 activity to promote apoptosis and cell cycle arrest

A consequence of combining AZD8055 with ibrutinib involves the reduction of AKT kinase activity, through inhibition of AKT^{T308} and AKT^{S473} phosphorylation. This coincided with elevated p27^{KIP1} expression levels, which may contribute to the observed inhibition of cell cycle progression in MEC-1 cells. Interestingly, p27^{KIP1} is a target gene of FOXO transcription factors (382), which control diverse cellular processes such as survival and cell cycle progression (384). Since FOXOs are AKT substrates (246), we hypothesised that the combination's mechanism of action involved relieving AKT-mediated negative regulation of FOXOs to promote transactivation of FOXO target genes (348). To answer this question, we assessed the phosphorylation status of FOXO1^{T24}, an AKT-dependent FOXO1

phosphorylation site (345), downstream of BCR-ligation and NT-L/CD40L (+IL-4) co-cultures. Here, we found that BCR stimulation increased AKT^{T308}, AKT^{S473} and $FOXO1^{T24}$ phosphorylation in $F(ab')_2$ stimulated CLL cells, indicating that FOXO1 is a target of BCR crosslinking-induced AKT kinase activity. Because AKT negatively regulates FOXO1, this demonstrates that BCR simulation (albeit short-term) inhibits FOXO1 activity in CLL cells. Indeed, studies have shown that BCR crosslinking-induced activation of PI3K-AKT signalling inactivates FOXO1 in mature B cells, which decreases expression of FOXO1 target genes BIM and $p27^{KIP1}$ (275). Encouragingly, treatment with AZD8055, ibrutinib or COMBO inhibited BCR ligation-induced $FOXO1^{T24}$ phosphorylation. Interestingly, COMBO-induced AKT inactivation corresponded to a visibly enhanced inhibition of $FOXO1^{T24}$ phosphorylation. This suggests that COMBO treatment-induced inhibition of AKT kinase activity enables reactivation of FOXO1. This being said, residual $FOXO1^{T24}$ implies that AKT is active to an extent, which might be enough to promote CLL cell survival and proliferation. Interestingly, treatment reduced basal $FOXO1^{T24}$ phosphorylation in unstimulated CLL cells, indicating that AKT is also active in circulating CLL cells. In the absence of external stimulation, this may support the observation that PI3K (252) and AKT (285) are constitutively active in unmanipulated CLL cells, and may highlight the involvement of 'tonic' BCR signalling (247, 254, 255). Importantly, similar effects on $FOXO1^{T24}$ phosphorylation were observed in CLL cells co-cultured on NT-L and CD40L (+IL-4), indicating that AKT inactivation by the COMBO treatment is capable of reactivating FOXO1 activity to promote apoptosis and cell cycle arrest. However, whether FOXO1 is responsible for the observed inhibition in cell cycle progression remains to be elucidated.

3.3.11 Summary and future directions

Taken together, these findings demonstrate that mTOR is a key effector downstream of BCR stimulation in CLL cells. Enhanced mTORC1 and mTORC2 activity can be targeted by the dual mTOR kinase inhibitor AZD8055, which overcomes BCR-mediated cell survival. Importantly, AZD8055 does not induce enhanced mTORC2/AKT pro-survival signalling associated with selective-mTORC1 inhibitors. Nevertheless, AZD8055 anti-tumour activity is limited as a monotherapy. Interestingly, AZD8055 synergises with ibrutinib to enhance CLL cell apoptosis, and disables pro-survival signalling downstream of BCR ligation.

Furthermore, combining AZD8055 with ibrutinib blocks CD40L/IL-4-induced cell growth and CD40L/IL-21-induced proliferation. Collectively, this indicates that concurrent targeting of mTOR and BTK may promote anti-tumour activity in CLL. We propose that the combination treatment confers a ‘complete’ inhibition of AKT kinase activity, which relieves negative regulation of the FOXO1 transcription factor. Because active FOXO1 can promote cell death and cell cycle control, treatment-induced reactivation of FOXO1 may promote anti-cancer activity. In the following chapters, we will explore the regulation and function of FOXOs in CLL cells.

CLL158

	0	6.25	12.5	25	50	100	200	AZD8055 (nM)
0	1.000	0.980	0.981	0.951	0.930	0.901	0.807	
62.5	0.841	0.848	0.849	0.831	0.821	0.793	0.752	
125	0.832	0.827	0.845	0.844	0.817	0.797	0.748	
250	0.839	0.840	0.832	0.841	0.786	0.799	0.724	
500	0.821	0.818	0.849	0.835	0.846	0.766	0.719	
1000	0.826	0.798	0.827	0.813	0.799	0.765	0.687	
2000	0.723	0.741	0.732	0.720	0.700	0.679	0.597	

Ibrutinib (nM)

	0	125	250	500	1000	2000	4000	AZD2014 (nM)
0	1.000	0.867	0.884	0.861	0.798	0.765	0.583	
62.5	0.859	0.804	0.800	0.784	0.749	0.753	0.666	
125	0.855	0.804	0.778	0.767	0.725	0.785	0.659	
250	0.855	0.795	0.756	0.708	0.738	0.749	0.666	
500	0.832	0.766	0.756	0.715	0.712	0.708	0.654	
1000	0.814	0.782	0.750	0.732	0.728	0.689	0.639	
2000	0.717	0.696	0.667	0.666	0.660	0.635	0.560	

Ibrutinib (nM)

Table 3.1 – Drug combination studies: CLL158 cell viability
Cell viability of a representative CLL patient sample (CLL158) treated with AZD8055 and ibrutinib (top) or AZD2014 and ibrutinib (bottom) at non-constant ratios for 48 h (as indicated in Figure 3.8). Concentrations of each drug are indicated. Cell viability was assessed using the resazurin assay. The values depicted represent the 'fraction affected' (Fa) following treatment (relative to vehicle control). Fa values were used to generate CI values (depicted in Figure 3.8) according to the Chou and Talalay method (via Compusyn software).

AKT (T308)

HG-3					Statisitic (one-way ANOVA; Tukey's multiple comparisons test)				
Sample	Vehicle	AZD8055	Ibrutinib	COMBO	Vehicle/ AZD8055	Vehicle/ Ibrutinib	Vehicle/ COMBO	AZD8055/COMBO	Ibrutinib/ COMBO
1	1	0.704	0.820	0.297	ns	ns	****	ns	ns
2	1	0.745	0.320	0.252					
3	1	0.565	0.356	0.256					

MEC-1					Statisitic (one-way ANOVA; Tukey's multiple comparisons test)				
Sample	Vehicle	AZD8055	Ibrutinib	COMBO	Vehicle/ AZD8055	Vehicle/ Ibrutinib	Vehicle/ COMBO	AZD8055/COMBO	Ibrutinib/ COMBO
1	1	0.796	0.375	0.187	ns	*	ns	ns	ns
2	1	1.247	0.414	0.695					
3	1	0.861	0.316	0.252					

AKT (S473)

HG-3					Statisitic (one-way ANOVA; Tukey's multiple comparisons test)				
Sample	Vehicle	AZD8055	Ibrutinib	COMBO	Vehicle/ AZD8055	Vehicle/ Ibrutinib	Vehicle/ COMBO	AZD8055/COMBO	Ibrutinib/ COMBO
1	1	0.023	0.190	0.009	****	**	****	ns	ns

2	1	0.007	0.102	0.002					
3	1	0.020	0.092	0.007					
MEC-1					**Statisitic (one-way ANOVA; Tukey's multiple comparisons test)**				
Sample	Vehicle	AZD8055	Ibrutinib	COMBO	Vehicle/ AZD8055	Vehicle/ Ibrutinib	Vehicle/ COMBO	AZD8055/COMBO	Ibrutinib/ COMBO
1	1	0.060	0.071	0.003	****	****	****	ns	ns
2	1	0.052	0.048	0.003					
3	1	0.041	0.036	0.020					

4E-BP1 (T37/46)

HG-3					**Statisitic (one-way ANOVA; Tukey's multiple comparisons test)**				
Sample	Vehicle	AZD8055	Ibrutinib	COMBO	Vehicle/ AZD8055	Vehicle/ Ibrutinib	Vehicle/ COMBO	AZD8055/COMBO	Ibrutinib/ COMBO
1	1	0.075	0.400	0.036	****	*	****	ns	ns
2	1	0.049	0.406	0.033					
3	1	0.039	0.229	0.017					
MEC-1					**Statisitic (one-way ANOVA; Tukey's multiple comparisons test)**				
Sample	Vehicle	AZD8055	Ibrutinib	COMBO	Vehicle/ AZD8055	Vehicle/ Ibrutinib	Vehicle/ COMBO	AZD8055/COMBO	Ibrutinib/ COMBO
1	1	0.059	1.408	0.118	****	ns	**	ns	ns
2	1	0.030	0.718	0.031					
3	1	0.058	0.712	0.035					

S6 (S235/236)

HG-3					**Statisitic (one-way ANOVA; Tukey's multiple comparisons test)**				
Sample	Vehicle	AZD8055	Ibrutinib	COMBO	Vehicle/ AZD8055	Vehicle/ Ibrutinib	Vehicle/ COMBO	AZD8055/COMBO	Ibrutinib/ COMBO
1	1	0.217	0.695	0.060	**	ns	****	ns	ns
2	1	0.155	0.835	0.056					
3	1	0.131	0.584	0.104					
MEC-1					**Statisitic (one-way ANOVA; Tukey's multiple comparisons test)**				
Sample	Vehicle	AZD8055	Ibrutinib	COMBO	Vehicle/ AZD8055	Vehicle/ Ibrutinib	Vehicle/ COMBO	AZD8055/COMBO	Ibrutinib/ COMBO
1	1	0.288	0.585	0.061	**	*	***	*	**
2	1	0.249	0.627	0.057					
3	1	0.341	0.680	0.118					

ERK1/2 (T202/Y204)

HG-3					**Statisitic (one-way ANOVA; Tukey's multiple comparisons test)**				
Sample	Vehicle	AZD8055	Ibrutinib	COMBO	Vehicle/ AZD8055	Vehicle/ Ibrutinib	Vehicle/ COMBO	AZD8055/COMBO	Ibrutinib/ COMBO
1	1	0.844	0.118	0.082	ns	**	****	ns	ns
2	1	1.592	0.043	0.057					
3	1	1.681	0.154	0.082					
MEC-1					**Statisitic (one-way ANOVA; Tukey's multiple comparisons test)**				
Sample	Vehicle	AZD8055	Ibrutinib	COMBO	Vehicle/ AZD8055	Vehicle/ Ibrutinib	Vehicle/ COMBO	AZD8055/COMBO	Ibrutinib/ COMBO
1	1	0.656	0.052	0.074	ns	****	***	ns	ns

2	1	1.167	0.071	0.121
3	1	0.745	0.006	0.052

FOXO1 (T24)

HG-3				
Sample	Vehicle	AZD8055	Ibrutinib	COMBO
1	1	0.335	0.168	0.127
2	1	0.361	0.388	0.187
3	1	0.581	0.302	0.415

Statisitic (one-way ANOVA; Tukey's multiple comparisons test)				
Vehicle/ AZD8055	Vehicle/ Ibrutinib	Vehicle/ COMBO	AZD8055/COMBO	Ibrutinib/ COMBO
ns	*	ns	ns	ns

MEC-1				
Sample	Vehicle	AZD8055	Ibrutinib	COMBO
1	1	0.713	0.293	0.224
2	1	0.333	0.250	0.095
3	1	0.652	0.286	0.130

Statisitic (one-way ANOVA; Tukey's multiple comparisons test)				
Vehicle/ AZD8055	Vehicle/ Ibrutinib	Vehicle/ COMBO	AZD8055/COMBO	Ibrutinib/ COMBO
ns	****	*	ns	ns

Table 3.2 – Western blot densitometry: 1 h treatment (HG-3 and MEC-1 cells)
AKT^{T308}, AKT^{S473}, 4E-BP1$^{T37/46}$, S6$^{S235/236}$, ERK1/2$^{T202/Y204}$ and FOXO1^{T24} phosphorylation levels in HG-3 (n=3) and MEC-1 (n=3) cells following short-term (1 h) treatment with AZD8055, ibrutinib or COMBO (as described in Figure 3.9). Densitometry was calculated using Image Studio Lite software (relative to vehicle control). Statistical analysis was performed using a one-way ANOVA with Tukey's multiple comparisons test. $p > 0.05$ 'ns' = not significant; $p \leq 0.05$ *; $p \leq 0.01$ **; $p \leq 0.001$ ***; $p \leq 0.0001$ ****.

Viability (Annexin V negative / 7-AAD negative)

HG-3				
Sample	Vehicle	AZD8055	Ibrutinib	COMBO
1	1	1.016	0.974	1.009
2	1	1.113	1.085	1.106
3	1	1.031	0.974	1.006
4	1	1.062	1.016	1.029
5	1	1.035	0.981	1.022

Statisitic (one-way ANOVA; Tukey's multiple comparisons test)				
Vehicle/AZD8055	Vehicle/Ibrutinib	Vehicle/COMBO	AZD8055/COMBO	Ibrutinib/COMBO
ns	ns	ns	ns	ns

MEC-1				
Sample	Vehicle	AZD8055	Ibrutinib	COMBO
1	1	0.993	0.960	1.003
2	1	1.024	0.989	1.032
3	1	0.985	0.969	1.011
4	1	1.034	0.978	1.012
5	1	1.073	1.031	1.037

Statisitic (one-way ANOVA; Tukey's multiple comparisons test)				
Vehicle/AZD8055	Vehicle/Ibrutinib	Vehicle/COMBO	AZD8055/COMBO	Ibrutinib/COMBO
ns	ns	ns	ns	ns

Apoptosis (Annexin V positive / 7-AAD positive)

HG-3				
Sample	Vehicle	AZD8055	Ibrutinib	COMBO
1	1	0.752	1.283	0.898
2	1	0.389	0.619	0.491
3	1	0.529	1.450	0.932

Statisitic (one-way ANOVA; Tukey's multiple comparisons test)				
Vehicle/AZD8055	Vehicle/Ibrutinib	Vehicle/COMBO	AZD8055/COMBO	Ibrutinib/COMBO
*	ns	ns	**	*

4	1	0.374	0.996	0.635
5	1	0.598	1.652	0.730

MEC-1

Sample	Vehicle	AZD8055	Ibrutinib	COMBO
1	1	1.105	1.400	0.927
2	1	0.919	1.210	0.724
3	1	1.224	1.274	0.620
4	1	0.725	1.051	0.744
5	1	0.495	0.625	0.581

Statisitic (one-way ANOVA; Tukey's multiple comparisons test)

Vehicle/AZD8055	Vehicle/Ibrutinib	Vehicle/COMBO	AZD8055/COMBO	Ibrutinib/COMBO
ns	ns	ns	ns	ns

Table 3.3 - Cell viability analysis: 48 h treatment (HG-3 and MEC-1 cells)
HG-3 (n=5) and MEC-1 (n=5) cell viability (Annexin V/7-AAD staining) following long-term (48 h) treatment with AZD8055, ibrutinib or COMBO (as described in Figure 3.10). Values indicate the proportion of viable (top) and apoptotic (bottom) cells (relative to vehicle control). Statistical analysis was performed using a one-way ANOVA with Tukey's multiple comparisons test. $p > 0.05$ 'ns' = not significant; $p \leq 0.05$ *; $p \leq 0.01$ **; $p \leq 0.001$ ***; $p \leq 0.0001$ ****.

AKT (S473)

	unstimulated				F(ab')2			
Sample	Vehicle	AZD8055	Ibrutinib	COMBO	Vehicle	AZD8055	Ibrutinib	COMBO
CLL151	1	0.065	0.762	0.867	372.267	0.951	0.998	0.329
CLL157	1	0.642	0.294	1.566	983.808	4.717	0.315	8.488
CLL80	1	0.003	0.003	0.064	52.177	0.228	3.496	0.130
CLL138	1	0.234	0.596	0.333	2.678	0.474	0.544	0.193
CLL113	1	0.015	0.051	0.005	16.199	0.003	0.471	0.009
CLL148	1	0.300	1.400	0.600	20.500	1.200	3.600	0.800
CLL90	1	0.045	1.792	8.194	152.349	2.102	4.951	5.658
CLL69	1	0.041	0.032	0.002	26.532	0.027	0.384	0.048

Statisitic (one-way ANOVA; Tukey's multiple comparisons test)

unstimulated					F(ab')2					
Vehicle/ AZD8055	Vehicle/ Ibrutinib	Vehicle/ COMBO	AZD8055/COMBO	Ibrutinib/ COMBO	Vehicle/ AZD8055	Vehicle/ Ibrutinib	Vehicle/ COMBO	AZD8055/COMBO	Ibrutinib/ COMBO	Vehicle/ Vehicle
***	ns	ns	ns	ns	ns	ns	ns	ns	ns	ns

4E-BP1 (T37/46)

	unstimulated				F(ab')2			
Sample	Vehicle	AZD8055	Ibrutinib	COMBO	Vehicle	AZD8055	Ibrutinib	COMBO
CLL151	1	0.162	1.379	0.165	1.166	0.244	0.962	0.139
CLL157	1	0.060	0.582	0.048	1.160	0.092	1.509	0.216
CLL119	1	0.122	1.182	0.156	1.385	0.087	0.761	0.066
CLL80	1	0.073	0.492	0.016	0.530	0.027	0.393	0.137
CLL113	1	0.164	0.783	0.104	1.233	0.122	0.845	0.127
CLL90	1	0.007	0.089	0.005	0.394	0.010	0.075	0.030
CLL69	1	0.305	2.121	0.131	2.834	0.526	1.971	0.095

Statisitic (one-way ANOVA; Tukey's multiple comparisons test)

unstimulated					F(ab')2					
Vehicle/ AZD8055	Vehicle/ Ibrutinib	Vehicle/ COMBO	AZD8055/COMBO	Ibrutinib/ COMBO	Vehicle/ AZD8055	Vehicle/ Ibrutinib	Vehicle/ COMBO	AZD8055/COMBO	Ibrutinib/ COMBO	Vehicle/ Vehicle
****	ns	****	ns	ns	*	ns	ns	ns	ns	ns

S6 (S235/236)

	unstimulated				F(ab')2			
Sample	Vehicle	AZD8055	Ibrutinib	COMBO	Vehicle	AZD8055	Ibrutinib	COMBO
CLL151	1	0.455	1.377	0.410	10.371	4.260	2.012	0.831
CLL157	1	0.218	1.650	0.199	14.252	4.014	4.799	0.302
CLL119	1	0.039	0.838	0.040	1.192	0.072	1.000	0.042
CLL80	1	0.085	0.650	0.076	11.661	6.110	4.518	0.699
CLL138	1	0.385	0.769	0.137	1.005	0.258	0.313	0.324
CLL113	1	0.067	0.570	0.066	7.577	0.307	1.601	0.035
CLL148	1	0.167	0.417	0.357	14.732	4.274	2.536	0.333
CLL90	1	0.343	1.268	0.273	9.393	0.819	1.035	0.331
CLL69	1	0.195	0.277	0.083	26.424	1.534	2.418	0.152

Statisitic (one-way ANOVA; Tukey's multiple comparisons test)

unstimulated					F(ab')2					
Vehicle/ AZD8055	Vehicle/ Ibrutinib	Vehicle/ COMBO	AZD8055/COMBO	Ibrutinib/ COMBO	Vehicle/ AZD8055	Vehicle/ Ibrutinib	Vehicle/ COMBO	AZD8055/COMBO	Ibrutinib/ COMBO	Vehicle/ Vehicle
****	ns	****	ns	ns	ns	ns	*	ns	ns	ns

ERK1/2 (T202/Y204)

	unstimulated				F(ab')2			
Sample	Vehicle	AZD8055	Ibrutinib	COMBO	Vehicle	AZD8055	Ibrutinib	COMBO
CLL151	1	0.079	1.507	1.222	38.752	30.020	2.823	16.313
CLL157	1	2.311	2.195	2.868	24.225	23.283	2.823	3.132
CLL80	1	1.915	1.084	1.519	27.248	21.756	6.435	3.443
CLL113	1	1.055	0.330	0.396	2.413	2.015	0.644	0.479
CLL90	1	1.074	0.434	0.388	12.629	7.151	1.675	0.700
CLL69	1	1.632	0.529	0.448	13.650	5.821	2.116	2.195

Statisitic (one-way ANOVA; Tukey's multiple comparisons test)

unstimulated					F(ab')2					
Vehicle/ AZD8055	Vehicle/ Ibrutinib	Vehicle/ COMBO	AZD8055/COMBO	Ibrutinib/ COMBO	Vehicle/ AZD8055	Vehicle/ Ibrutinib	Vehicle/ COMBO	AZD8055/COMBO	Ibrutinib/ COMBO	Vehicle/ Vehicle
ns	ns	ns	ns	ns	ns	ns	ns	ns	ns	ns

FOXO1 (T24)

	unstimulated	F(ab')2

Sample	Vehicle	AZD8055	Ibrutinib	COMBO	Vehicle	AZD8055	Ibrutinib	COMBO
CLL151	1	0.668	0.567	0.363	2.436	1.311	1.101	0.464
CLL119	1	0.705	0.506	0.563	1.416	0.662	0.456	0.251
CLL80	1	0.399	0.195	0.067	1.429	0.572	1.146	0.297
CLL138	1	0.303	0.273	0.212	1.515	0.515	0.424	0.242
CLL113	1	0.389	0.207	0.037	1.199	0.938	0.295	0.545
CLL148	1	0.308	0.231	0.154	1.769	1.385	1.000	0.385
CLL90	1	0.089	0.198	0.205	1.654	0.018	0.075	0.282
CLL69	1	0.558	0.322	0.250	2.276	1.068	0.850	0.461

Statisitic (one-way ANOVA; Tukey's multiple comparisons test)

unstimulated					F(ab')2					
Vehicle/ AZD8055	Vehicle/ Ibrutinib	Vehicle/ COMBO	AZD8055/COMBO	Ibrutinib/ COMBO	Vehicle/ AZD8055	Vehicle/ Ibrutinib	Vehicle/ COMBO	AZD8055/COMBO	Ibrutinib/ COMBO	Vehicle/ Vehicle
**	****	****	ns	ns	**	**	***	ns	ns	*

Table 3.4 – Western blot densitometry: 1 h treatment (primary CLL cells)
AKT^{S473}, 4E-BP1$^{T37/46}$, S6$^{S235/236}$, ERK1/2$^{T202/Y204}$ and FOXO1^{T24} phosphorylation levels in primary CLL samples (pseudonym indicated) following short-term (1 h) treatment with AZD8055, ibrutinib or COMBO with or without F(ab')$_2$ stimulation (as described in Figure 3.14). Densitometry was calculated using Image Studio Lite software (relative to vehicle control). Statistical analysis was performed using a one-way ANOVA with Tukey's multiple comparisons test. $p > 0.05$ 'ns' = not significant; $p \leq 0.05$ *; $p \leq 0.01$ **; $p \leq 0.001$ ***; $p \leq 0.0001$ ****.

Viability (Annexin V negative / 7-AAD negative)

	unstimulated				F(ab')2			
Sample	Vehicle	AZD8055	Ibrutinib	COMBO	Vehicle	AZD8055	Ibrutinib	COMBO
CLL151	1	0.797	0.815	0.781	1.075	1	0.885	0.86
CLL69	1	1.007	0.935	0.96	0.996	1.018	0.965	0.956
CLL157	1	0.896	0.787	0.793	1.056	1.013	0.907	0.875
CLL90	1	0.852	0.677	0.574	0.959	0.932	0.816	0.645
CLL80	1	0.9354	0.8436	0.8188	0.962	0.913	0.895	0.8908
CLL113	1	0.9782	0.9269	0.9128	1.014	0.998	0.955	0.952
CLL119	1	0.8719	0.7964	0.7799	1.018	0.885	0.799	0.755

Statisitic (one-way ANOVA; Tukey's multiple comparisons test)

unstimulated					F(ab')2					
Vehicle/ AZD8055	Vehicle /Ibrutinib	Vehicle/ COMBO	AZD8055/COMBO	Ibrutinib/ COMBO	Vehicle/ AZD8055	Vehicle /Ibrutinib	Vehicle/ COMBO	AZD8055/COMBO	Ibrutinib/ COMBO	Vehicle/ Vehicle
ns	*	ns	ns	ns	ns	*	ns	ns	ns	ns

Apoptosis (Annexin V apoptosis positive / 7-AAD positive)

	unstimulated				F(ab')2			
Sample	Vehicle	AZD8055	Ibrutinib	COMBO	Vehicle	AZD8055	Ibrutinib	COMBO
CLL151	1	1.604	1.483	1.599	0.744	1	1.353	1.429
CLL69	1	0.96	1.256	1.176	1.045	1.023	1.147	1.1875

CLL157	1	1.889	2.83	2.83	0.521	0.961	1.769	1.979
CLL90	1	1.14	1.27	1.282	0.988	1.091	1.221	1.303
CLL80	1	1.078	1.026	1.184	0.936	1.047	1.034	1.005
CLL113	1	1.168	1.415	1.415	0.99	1.118	1.257	1.247
CLL119	1	1.258	1.4	1.445	1.008	1.275	1.42	1.45

Statisitic (one-way ANOVA; Tukey's multiple comparisons test)

unstimulated					F(ab')2					
Vehicle/ AZD8055	Vehicle/ Ibrutinib	Vehicle/ COMBO	AZD8055/COMBO	Ibrutinib/ COMBO	Vehicle/ AZD8055	Vehicle/ Ibrutinib	Vehicle/ COMBO	AZD8055/COMBO	Ibrutinib/ COMBO	Vehicle/ Vehicle
ns	ns	ns	ns	ns	ns	ns	ns	ns	ns	ns

Table 3.5 - Cell viability analysis: 48 h treatment (primary CLL cells)
Cell viability (Annexin V/7-AAD staining) of primary CLL samples (n=7) following long-term (48 h) treatment with AZD8055, ibrutinib or COMBO with or without F(ab')$_2$ stimulation (as described in Figure 3.15). Values indicate the proportion/percentage of viable (top) and apoptotic (bottom) CLL cells (relative to vehicle control). Statistical analysis was performed using a one-way ANOVA with Tukey's multiple comparisons test. $p > 0.05$ 'ns' = not significant; $p \leq 0.05$ *; $p \leq 0.01$ **; $p \leq 0.001$ ***; $p \leq 0.0001$ ****.

4 Results II

4.1 Introduction

Widely considered '*bona fide*' tumour suppressors, FOXO transcription factors regulate transcription of an array of genes involved in cell cycle arrest, apoptosis, metabolism and stress resistance (348). Subcellular localisation largely dictates FOXO transcriptional activity, which is influenced by multiple posttranslational modifications (345). Perhaps most prominently, AKT-dependent phosphorylation (T24, S256 and S319 in FOXO1) (344) promotes sequestration of FOXOs in the cytoplasm (277), which ultimately prevents transcription of FOXO target genes (365).

Although FOXOs has been extensively studied in normal and malignant B cells (384), little is known about the regulation of FOXO activity and subcellular localisation in CLL. Earlier, we demonstrated that BCR crosslinking elicited AKT-dependent FOXO1^{T24} phosphorylation in CLL cells, suggesting that FOXO1 inactivation is a functionally relevant consequence of CLL-BCR signalling. In 'activated' mature B cells, AKT-dependent FOXO1 nuclear export was essential for cell cycle progression and survival (390). Assuming CLL cells conform to the paradigm observed in normal B cells, re-activation of FOXOs might represent a promising anti-proliferative and apoptotic treatment strategy, as demonstrated *in vitro* in DLBCL (397) and classical Hodgkin lymphoma (cHL) (396). Encouragingly, we previously demonstrated that BCR crosslinking-induced FOXO1^{T24} phosphorylation was largely inhibited by AZD8055 and ibrutinib treatment as monotherapies or in combination, suggesting that FOXO1 might be an effector of BCR signalling inhibition.

In this chapter, we address FOXO1 subcellular localisation and DNA-binding activity following *in vitro* BCR ligation in CLL cells. We further explore whether AKT (AZD5363), mTOR kinase (AZD8055) and BTK (ibrutinib) inhibition has the ability to re-engage FOXO1 activity, potentially mediating the functional response to treatment.

4.1.1 Aims

I. Determine the expression and activity of FOXO family members in *ex vivo* primary CLL samples and healthy donor B cells.

II. Address the effect of BCR ligation on FOXO1 activity and subcellular localisation in CLL cells.

III. Investigate whether AKT, mTOR kinase and BTK inhibition impacts BCR crosslinking-induced FOXO1 activity and subcellular localisation.

IV. Visualise FOXO1 expression and distribution in CLL patient LN biopsies and spleen sections from a CLL-like mouse model.

4.2 Results

4.2.1 FOXO1 is the most highly expressed FOXO family member in *ex vivo* CLL cells

We first addressed the expression levels of each FOXO family member in PB-derived CLL cells (CLL) and B cells from healthy donors (Healthy $CD19^+$). The transcript abundance of *FOXO1*, *FOXO3* and *FOXO4* was measured by RT-qPCR, from which relative expression levels were calculated using the ΔC_T method (Figure 4.1a). These data showed that FOXO1 was the most highly expressed

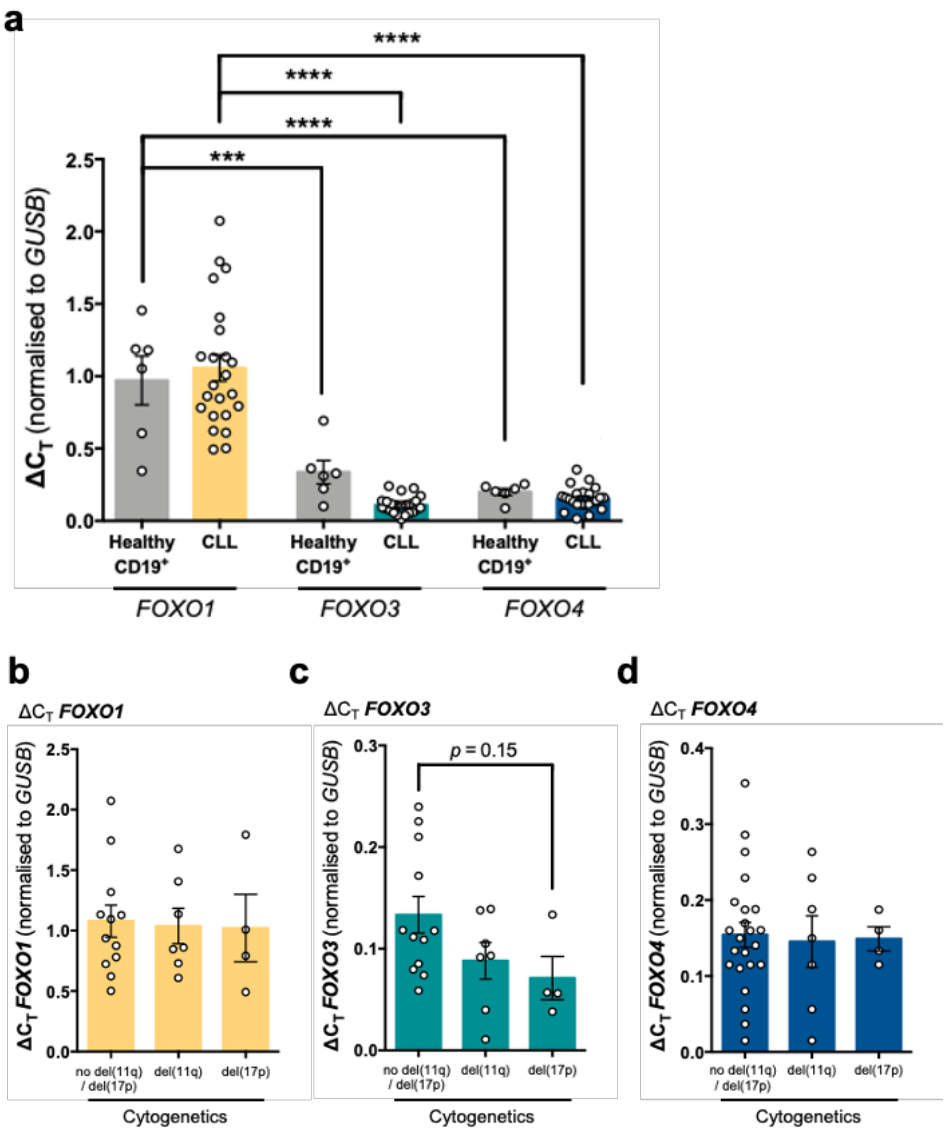

Figure 4.1 - FOXO1 is the most highly expressed FOXO family member in CLL cells.
(a) RT-qPCR to assess expression of *FOXO1*, *FOXO3* and *FOXO4* in healthy donor B cells (Healthy $CD19^+$; grey bars; n = 6) and CLL patient samples (CLL; *FOXO1* = yellow bars; *FOXO3* = turquoise bars; *FOXO4* = blue bars; n = 23). The ΔC_T method was used to calculate expression levels, where samples were normalised to the internal reference gene *GUSB*. (b, c, d) RT-qPCR to assess expression of (b) *FOXO1* (yellow bars), (c) *FOXO3* (turquoise bars) and (d) *FOXO4* (blue bars) in CLL patients stratified according to cytogenetic factors 'no del(11q) / del(17p)' (n = 12),

del(11q) (n = 7) or del(17p) (n = 4). The ΔC_T method was used to calculate expression levels, where samples were normalised to the internal reference gene *GUSB*. Individual datapoints are represented by white circles. Data expressed as the mean ± SEM. Statistics calculated by one-way ANOVA, where *** $p \leq 0.001$, **** $p \leq 0.0001$.

FOXO family member among CLL patient samples and, perhaps expectedly, B cells from healthy donors (Figure 4.1a). Although mRNA expression levels of *FOXO1*, *FOXO3* and *FOXO4* did not significantly differ between CLL cells and healthy donor B cells, *FOXO3* expression was visibly reduced in CLL cells (Figure 4.1a). Within this CLL patient cohort, stratification of *FOXO1* (Figure 4.1b), *FOXO3* (Figure 4.1c) and *FOXO4* (Figure 4.1d) expression based upon distinct cytogenetic alternations showed no significant difference. However, a modest but demonstrable trend towards decreased levels of *FOXO3* was observed in poor prognostic CLL patients with del(17p), compared to patients with undetected abnormalities in del(11q) or del(17p) ('no del(11q)/del(17p)) ($p = 0.15$; Figure 4.1c).

Through the assessment of basal mTOR activity, we observed varying levels of AKT^{S473} phosphorylation among CLL patient samples (Figure 3.1). Since AKT negatively regulates FOXO1 transcriptional activity via phosphorylation at conserved RxRxxS/T residues ($FOXO1^{T24}$, $FOXO1^{S256}$ and $FOXO1^{S319}$) (384), we assessed FOXO1 activity in *ex vivo* primary CLL cells compared with B cells from healthy donors (Figure 4.2). These data revealed that basal $FOXO1^{T24}$ phosphorylation levels were heterogenous among CLL patient samples; some patients exhibited high levels of $FOXO1^{T24}$ phosphorylation, while others demonstrated virtually undetectable levels (Figure 4.2a,b). Analysis of FOXO1 expression levels in CLL patient samples mirrored these findings; FOXO1 was elevated in some patients, while largely absent in others (Figure 4.2a,c). Subsequent stratification of $FOXO1^{T24}$ phosphorylation (Figure 4.2d) and FOXO1 expression levels (Figure 4.2e) according to cytogenetic factors showed no significant difference between favourable (no del(11q)/del(17p)) or poor prognostic (del(11q) or del(17p)) CLL patients. Nevertheless, relative $FOXO1^{T24}$ phosphorylation levels were noticeably higher in CLL patient samples compared to healthy donor B cells, albeit not significantly (Figure 4.2b). Conversely, FOXO1 expression was significantly reduced in CLL patient samples compared to normal B cells (Figure 4.2c).

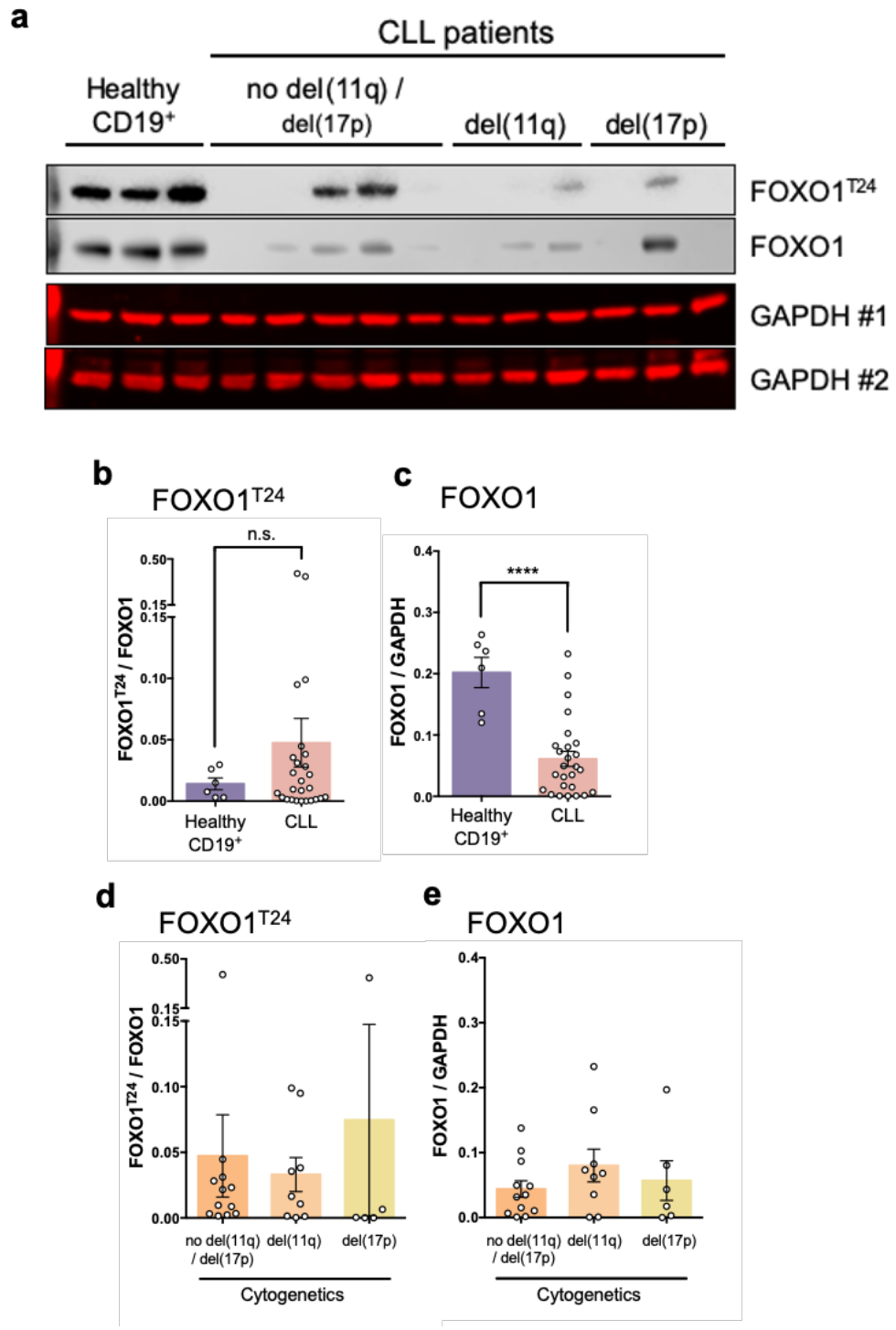

Figure 4.2 - FOXO1 expression is reduced in PB-derived primary CLL cells compared to healthy donor B cells.
(a) Western blot of healthy donor B cells (Healthy CD19$^+$; n=3) and CLL patients (n=11), subdivided into cytogenetic alterations 'No del(11q) / del(17p)' (n=5), del(11q) (n=3) and del(17p) (n=3). Blots were probed for FOXO1^{T24}, FOXO1 and GAPDH (loading control; #1 and #2 referring to mirror blots). (b) Relative phosphorylation levels FOXO1^{T24} and (c) relative expression levels of FOXO1 in Healthy CD19$^+$ (n=6; purple bar) and CLL samples (CLL; n = 31; peach bar). (d) Relative FOXO1^{T24} phosphorylation and (c) FOXO1 expression levels in CLL patients stratified according to cytogenetics 'No del(11q) / del(17p)' (dark orange bars; n=12), del(11q) (light orange bar; n=9) and del(17p) (yellow bar; n=6). Individual patient datapoints are represented by white circles. Data expressed as the mean ± SEM. Statistics calculated by unpaired Student's t-test for two groups and one-way ANOVA for three groups, where **** $p \leq 0.0001$.

4.2.2 F(ab')$_2$ stimulation transiently enhances AKT-dependent FOXO1^{T24} phosphorylation in CLL cells

We earlier demonstrated that BCR crosslinking transduced signals to FOXO1 via activation of AKT in CLL cells (Figure 3.21). However, F(ab')$_2$-induced AKT^{T308} and AKT^{S473} phosphorylation was only transient (Figure 3.7). We therefore asked whether AKT-dependent FOXO1^{T24} phosphorylation (and subsequent inactivation) is only short-lived following F(ab')$_2$ stimulation. To answer this question, CLL cells (Figure 4.3a) and MEC-1 cells (Figure 4.3b) underwent F(ab')$_2$ stimulation for the indicated time points. Thereafter, FOXO1^{T24} phosphorylation status and FOXO1 expression levels were examined (Figure 4.3a,b). Consistent with Figure 3.7, F(ab')$_2$ stimulation conferred a transient increase in AKT-dependent FOXO1^{T24} phosphorylation in CLL cells, whereas MEC-1 cells were unaffected (Figure 4.3a,b). Interestingly, F(ab')$_2$ stimulation also resulted in a transient increase in FOXO1 expression in CLL cells, followed by a brief downregulation before returning to basal levels within 24 h (Figure 4.3a). Notably, modulation of FOXO1 expression levels following F(ab')$_2$ stimulation appeared to be restricted to primary cells (Figure 4.3a,b). To build upon the observations in Figure 3.21, we analysed AKT-dependent FOXO1^{T24} phosphorylation following BCR crosslinking in CLL cells (Figure 4.3c). As expected, short-term F(ab')$_2$ stimulation elevated FOXO1^{T24} phosphorylation in CLL cells, which corresponded to increased AKT^{T308} and AKT^{S473} phosphorylation levels (Figure 4.3c,d). Consistent with earlier observations (Figure 4.3a), FOXO1 expression was significantly enhanced in CLL cells following short-term F(ab')$_2$ stimulation (Figure 4.3c,e). Because the intensity of FOXO1 expression varied among F(ab')$_2$-stimulated CLL patient samples, we wondered whether this heterogeneity corresponded to CLL patient prognosis (Figure 4.3f). Stratification of FOXO1 expression levels in F(ab')$_2$ stimulated CLL samples (relative to unstimulated) according to favourable (no del(11q)/del(17p)) or poor ((del(11q) or del(17p)) prognostic factors revealed no significant difference (Figure 4.3f).

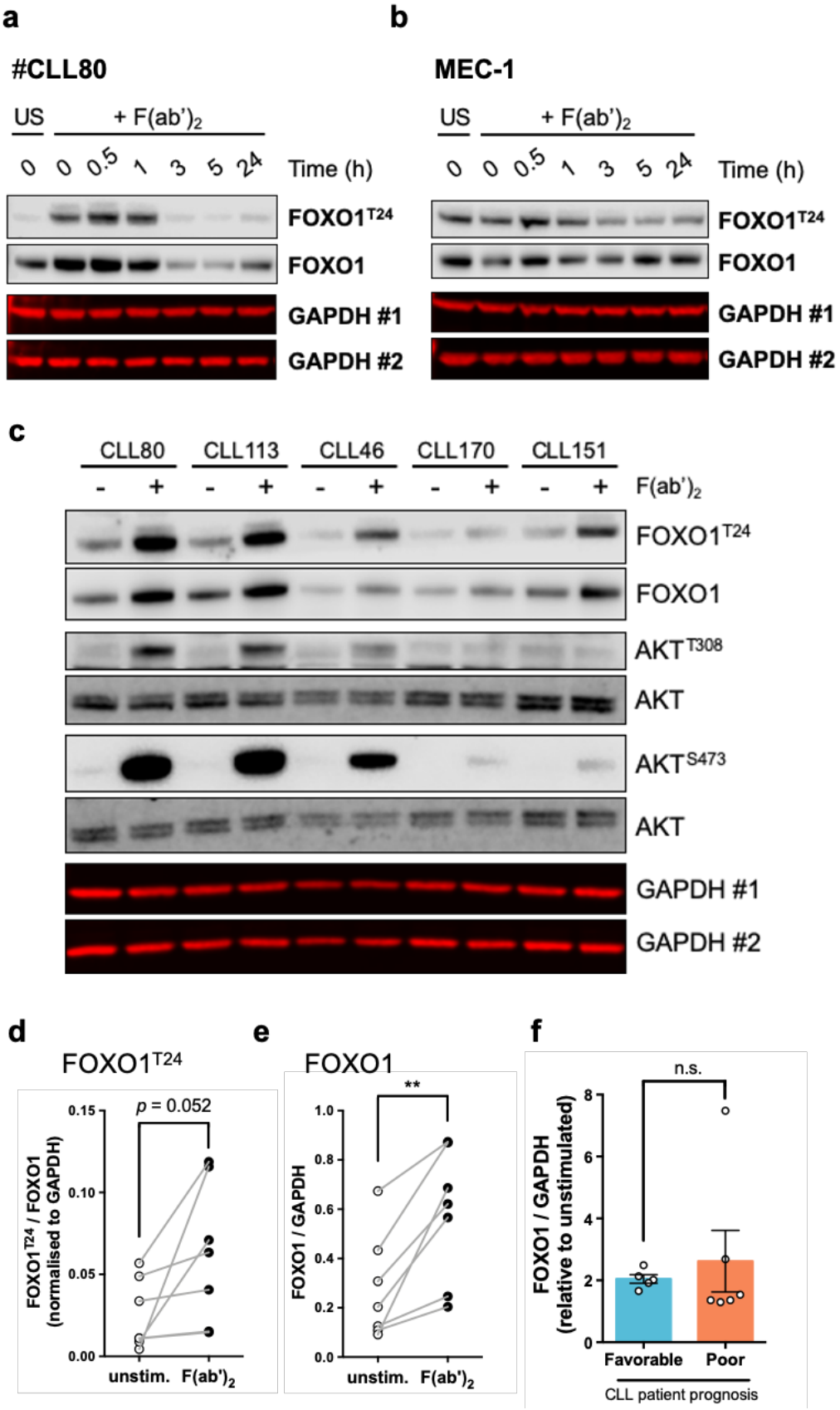

Figure 4.3 - Short-term F(ab')$_2$ stimulation increases FOXO1 expression and relative phosphorylation levels in primary CLL cells.
(a, b) Representative western blots of (a) primary CLL cells (#CLL80; n=3 primary CLL samples) and (b) MEC-1 cells (n=3) unstimulated (US) or F(ab')$_2$ stimulated for the indicated timepoints (0, 0.5, 1, 3, 5 and 24 h). Blots were probed for FOXO1^{T24}, FOXO1 and GAPDH (loading control; #1 and #2 referring to mirror blots). (c) Western blot of primary CLL samples (n=5; CLL# patient pseudonym) unstimulated (-) or F(ab')$_2$ stimulated (+) (10 ng/mL) for 1 h. Blots were probed for

FOXO1^{T24}, FOXO1, AKT^{T308}, AKT^{S473}, AKT and GAPDH (loading control; #1 and #2 referring to mirror blots). (d) Relative FOXO1^{T24} phosphorylation and (e) FOXO1 expression levels in unstimulated (unstim.; white circles) and F(ab')$_2$ stimulated (F(ab')$_2$; black circles) CLL samples (n=7). For each CLL sample, relative phosphorylation/expression levels for unstim. and F(ab')$_2$ are connected by a grey line. (f) Relative FOXO1 expression levels in 'favourable-' (n=5; blue bars) and 'poor-prognostic' (n=6; orange bars) CLL patient samples following F(ab')$_2$ stimulation for 1 h. FOXO1 expression is normalised to GAPDH and relative to unstimulated. Individual datapoints are represented by white circles. Data expressed as the mean ± SEM. Statistics calculated by paired and unpaired Student's t-test, where ** $p \leq 0.01$.

4.2.3 Short-term F(ab')$_2$ stimulation promotes FOXO1 nuclear export and subsequent decrease in FOXO1 activity

AKT phosphorylates nuclear FOXO1 to induce its association with 14-3-3 proteins, which ultimately shuttles FOXO1 out of the nucleus (350, 352, 361). Because short-term F(ab')$_2$ stimulation promotes AKT-dependent FOXO1^{T24} phosphorylation in CLL cells, we assessed localisation of FOXO1 following BCR crosslinking by IF (Figure 4.4a,b) and subcellular fractionation (Figure 4.4d-f). Both methods showed that FOXO1 was localised within the nucleus and cytoplasm of unstimulated CLL cells (Figure 4.4a,d). As expected, a greater proportion of FOXO1 was localised in the nuclear fraction compared to the cytoplasmic fraction in unstimulated CLL cells (Figure 4.4d). F(ab')$_2$ stimulation resulted in a large proportion of FOXO1 shuttling from the nucleus to the cytoplasm (Figure 4.4a), which was quantified by assessing the degree of co-localisation between FOXO1 and the nucleus (DAPI channel) using the Manders' colocalisation coefficient (Figure 4.4b). This was confirmed by subcellular fractionation (Figure 4.4d), which showed that FOXO1 expression significantly increased in the cytoplasmic fraction (Figure 4.4e) and concurrently decreased in the nuclear fraction (Figure 4.4f) following F(ab')$_2$ stimulation. These data demonstrated that short-term BCR crosslinking favoured cytoplasmic accumulation of FOXO1 in CLL cells (Figure 4.4c). Finally, we asked whether F(ab')$_2$-dependent FOXO1 nuclear export resulted in decreased FOXO1 transcriptional activity. Using the TransAM transcription factor activation assay we showed that FOXO1 DNA binding activity was significantly reduced in F(ab')$_2$ stimulated CLL cells (Figure 4.4g).

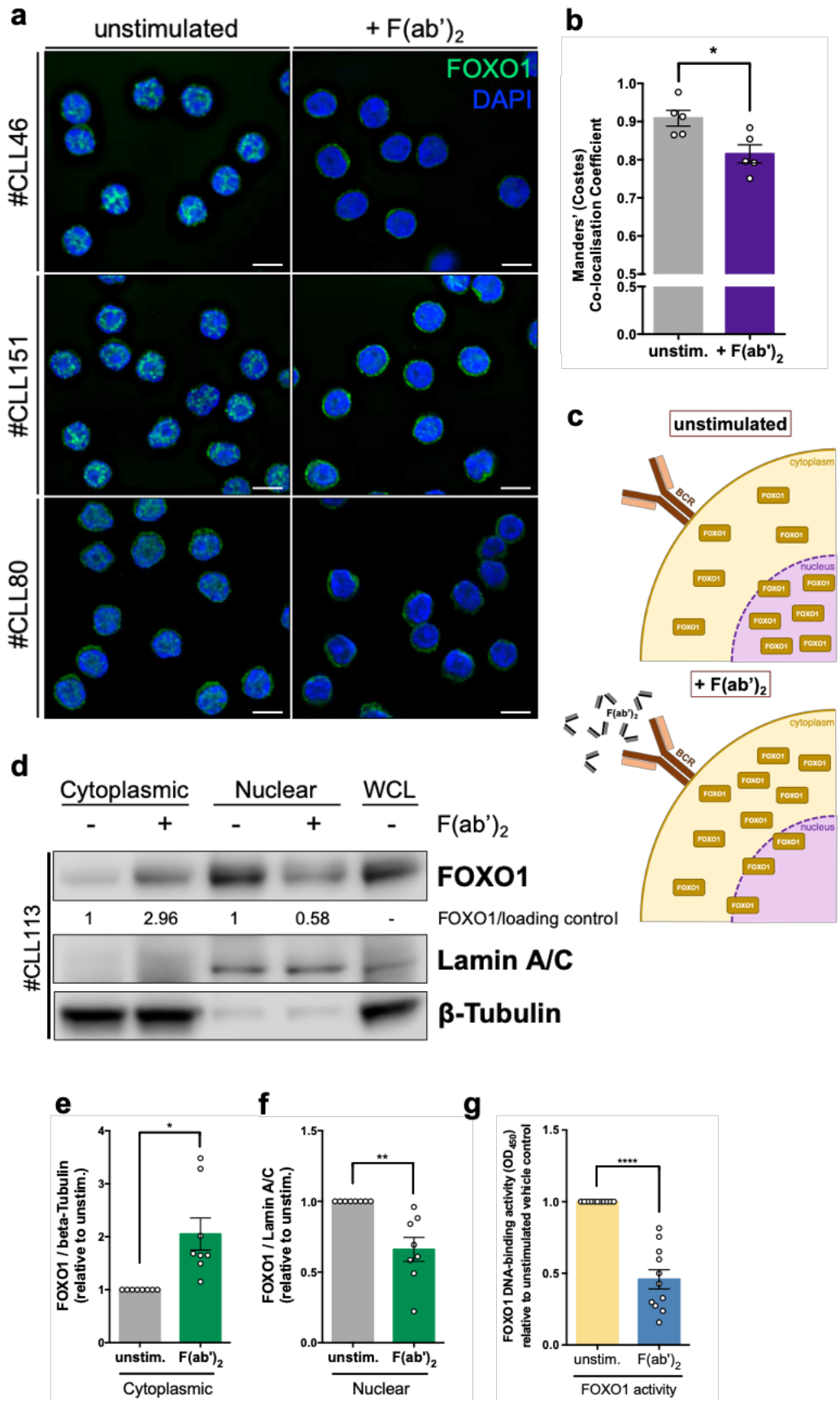

Figure 4.4 - Short-term F(ab')$_2$ stimulation promotes FOXO1 cytoplasmic translocation and reduces DNA-binding activity in primary CLL cells.
(a) IF micrographs (100x) of unstimulated (left panel) and F(ab')$_2$ stimulated (+ F(ab')$_2$; right panel) CLL patient samples (n=3; CLL# patient pseudonym) probed for FOXO1 (green) and counter stained with DAPI (DNA; blue). Scale bar = 5 μm. (b) Analyses of FOXO1 and DAPI co-localisation in unstimulated (unstim.; grey bar) and F(ab')$_2$ stimulated (+ F(ab')$_2$; purple bar) CLL patient

samples (n=5) using the Manders' (Costes) Co-localisation Coefficient (CellProfiler). >360 cells were quantified/condition from each sample. (c) Schematic depicting FOXO1 cytoplasmic translocation following F(ab')$_2$-mediated BCR ligation. (d) Subcellular fractionation of an unstimulated (-) and F(ab')$_2$ stimulated (+) CLL sample (#CLL113). Cytoplasmic, nuclear and whole cell lysate (WCL) fractions were generated. Blots were probed for FOXO1, Lamin A/C and β-Tubulin. β-Tubulin and Lamin A/C represent markers for cytoplasmic and nuclear fractions, respectively. Densitometry for cytoplasmic (FOXO1/β-Tubulin) and nuclear (FOXO1/Lamin A/C) FOXO1 expression are shown (relative to unstimulated). (e, f) Densitometry of FOXO1 expression in (e) cytoplasmic and (f) nuclear fractions from unstimulated (unstim.; grey bar) and F(ab')$_2$ stimulated (F(ab')$_2$; green bar) CLL samples (n=8), as calculated in (d). (g) FOXO1 DNA-binding activity (OD_{450}) of unstimulated (unstim.; yellow bar) and F(ab')$_2$ stimulated (F(ab')$_2$; blue bar) CLL patient samples (n=11), as determined by the TransAM FOXO1 activity assay (ActiveMotif). Individual datapoints are represented by white circles. Data expressed as the mean ± SEM. Statistics calculated by paired Student's t-test, where * $p \leq 0.05$, ** $p \leq 0.01$, **** $p \leq 0.0001$.

4.2.4 AKT inhibition blocks F(ab')$_2$-induced FOXO1 cytoplasmic translocation

After demonstrating that FOXO1 activity was diminished via BCR-induced FOXO1 nuclear export (Figure 4.4), we argued that FOXO1 may have a tumour suppressor role in the context of BCR activation in CLL cells. Therefore, pharmacological inhibition of BCR ligation-induced FOXO1 inactivation may favour nuclear retention and/or re-engage FOXO1 activity, as shown previously (277, 376, 377, 498). Because AKT plays a prominent role in the regulation of FOXO1 activity (277, 387) (Figure 4.5a), we examined FOXO1 phosphorylation (Figure 4.5b), localisation (Figure 4.5c-g) and DNA binding activity (Figure 4.5h) in unstimulated and F(ab')$_2$ stimulated CLL cells following short-term treatment with the AKT inhibitor AZD5363 (499). The ability of AZD5363 to inhibit AKT-dependent FOXO1 phosphorylation was assessed in CLL cells with or without BCR crosslinking by Western blotting (Figure 4.5b). AZD5363 treatment effectively inhibited F(ab')$_2$-induced FOXO1^{T24} and FOXO1^{S256} phosphorylation in a dose-dependent manner, whereas AKT^{T308} and AKT^{S473} phosphorylation was progressively enhanced in unstimulated and F(ab')$_2$ stimulated CLL cells (Figure 4.5b). Because AZD5363 inhibited BCR ligation-induced FOXO1 phosphorylation, we next addressed the ability of AZD5363 to block F(ab')$_2$-induced FOXO1 cytoplasmic translocation by IF and subcellular fractionation (Figure 4.5c-g). Although F(ab')$_2$ stimulation visibly promoted FOXO1 nuclear exclusion by IF (Figure 4.5c), subsequent analysis via the Manders' colocalisation coefficient did not support this observation (Figure 4.5d). Nevertheless, subcellular fractionation confirmed that short-term F(ab')$_2$ stimulation facilitated FOXO1 cytoplasmic translocation (Figure 4.6b). Consistent with Figure 4.4d-f, cytoplasmic FOXO1 expression was significantly enhanced following BCR ligation

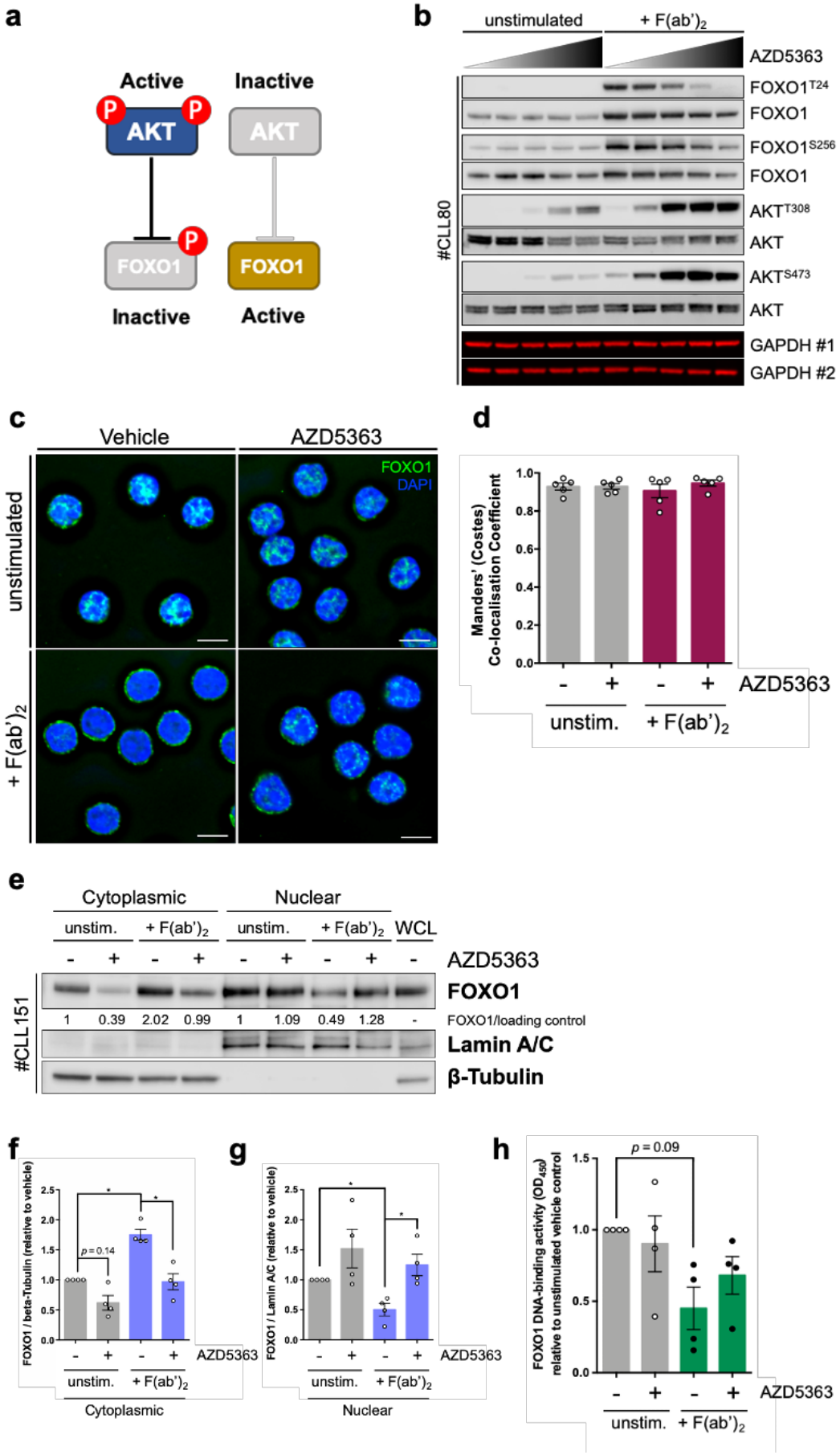

Figure 4.5 - The AKT inhibitor AZD5363 inhibits BCR ligation-induced FOXO1^{T24}/ FOXO1^{S256} phosphorylation and prevents F(ab')$_2$-mediated FOXO1 nuclear export.
(a) Schematic depicting AKT-dependent regulation of FOXO1 activity. Active AKT (blue) inactivates FOXO1 (grey), whereas inactive AKT (grey) enables FOXO1 activation (yellow). (b) Representative

western blot a primary CLL sample (#CLL80; n=3 CLL samples) unstimulated or F(ab')$_2$ stimulated (+F(ab')$_2$) for 1 h following 30 min pre-treatment with increasing concentrations of AZD5363 (Vehicle, 10, 100, 1000, 10000 nM). Blots were probed for FOXO1^{T24}, FOXO1^{S256}, FOXO1, AKT^{S473}, AKT^{T308}, AKT and GAPDH (loading control; #1 and #2 referring to mirror blots). (c) Representative IF micrographs (100x) of a CLL patient sample (#CLL80; n=5 CLL samples) unstimulated (top panel) or F(ab')$_2$ stimulated (+ F(ab')$_2$; bottom panel) for 1 h following 30 min pre-treatment with AZD5363 (1 μM). Cells were probed for FOXO1 (green) and counter stained with DAPI (DNA; blue). Scale bar = 5 μm. (d) Analyses of FOXO1 and DAPI co-localisation (Manders' (Costes) Co-localisation Coefficient) in unstimulated (unstim.; grey bars) and F(ab')$_2$ stimulated (+ F(ab')$_2$; red bars) CLL patient samples (n=5) treated with AZD5363 (+) or vehicle control (-). >360 cells were quantified/condition from each sample. (e) Subcellular fractionation of a CLL patient sample (#CLL151; n=4 CLL samples) unstimulated (unstim.) or F(ab')$_2$ stimulated (+ F(ab')$_2$) for 1 h following 30 min pre-treatment with 1 μM AZD5363 (+) or vehicle control (-). Cytoplasmic, nuclear and whole cell lysate (WCL) fractions were generated. Blots were probed for FOXO1, Lamin A/C and β-Tubulin. Densitometry for cytoplasmic (FOXO1/β-Tubulin) and nuclear (FOXO1/Lamin A/C) FOXO1 expression are shown (relative to unstimulated vehicle control). (f, g) Densitometry of FOXO1 expression in (f) cytoplasmic and (g) nuclear fractions from unstimulated (unstim.; grey bar) and F(ab')$_2$ stimulated (F(ab')$_2$; purple bar) CLL samples (n=4) treated with AZD5363 (+) or vehicle control (-), as calculated in (e). (h) FOXO1 DNA-binding activity (OD_{450}) of CLL patient samples (n=4) unstimulated (unstim.; grey bar) and F(ab')$_2$ stimulated (+ F(ab')$_2$; green bar) with (+) or without (-) AZD5363 treatment. Individual datapoints are represented by white or black circles. Data expressed as the mean ± SEM. Statistics calculated by one-way ANOVA, where * $p \leq 0.05$.

(Figure 4.5e,f), while nuclear FOXO1 expression was concomitantly decreased in F(ab')$_2$ stimulated CLL cells (Figure 4.5e,g). AZD5363 treatment enhanced retention of nuclear FOXO1 in F(ab')$_2$ stimulated CLL cells (Figure 4.5c), which was supported by the Manders' colocalisation coefficient (Figure 4.5d). In line with these findings, subcellular fractionation demonstrated that F(ab')$_2$-induced FOXO1 cytoplasmic translocation was inhibited by AZD5363 treatment (Figure 4.5e-g). AZD5363 treatment significantly reduced cytoplasmic FOXO1 expression in F(ab')$_2$ stimulated CLL cells (Figure 4.5a,b), which corresponded to a significant increase in nuclear FOXO1 expression compared to F(ab')$_2$ stimulated vehicle control (Figure 4.5a,c). Since AZD5363 inhibited F(ab')$_2$-induced FOXO1 cytoplasmic translocation, it was of interest to determine whether FOXO1 nuclear retention conferred an increase in FOXO1 DNA binding activity (Figure 4.5h). Consistent with Figure 4.4g, FOXO1 DNA-binding activity was reduced in response to F(ab')$_2$ stimulation (p = 0.09; Figure 4.5h). Furthermore, AZD5363 preincubation produced a notable trend, albeit modest, towards enhanced FOXO1 transcriptional activity in F(ab')$_2$ stimulated CLL cells (Figure 4.5h).

4.2.5 AZD8055 inhibits BCR crosslinking-induced FOXO1 nuclear export

Earlier experiments demonstrated that BCR-induced AKT^{S473} and FOXO1^{T24} phosphorylation was inhibited following treatment with AZD8055 (Figure 3.21),

demonstrating that mTOR kinase activity regulates AKT-dependent FOXO1^{T24} phosphorylation (Figure 3.21). To further examine the ability of AZD8055 to prevent AKT-mediated FOXO1 inactivation, the phosphorylation status of FOXO1^{T24}, AKT^{T308} and AKT^{S473} was assessed following treatment with increasing concentrations of AZD8055 with or without BCR crosslinking (Figure 4.6a). AZD8055 treatment resulted in a dose-dependent inhibition of AKT kinase activity (AKT^{T308} and AKT^{S473} phosphorylation) and AKT-dependent FOXO1^{T24} phosphorylation in F(ab')$_2$ stimulated CLL cells (Figure 4.6a). Importantly, inhibition of FOXO1^{T24} phosphorylation was achieved at clinically achievable concentrations (Figure 4.6a). Interestingly, while AKT expression levels were largely unaffected by AZD8055, FOXO1 expression was progressively reduced in response to increasing concentrations of AZD8055 (Figure 4.6a). Because AZD8055 inhibited AKT-dependent FOXO1^{T24} phosphorylation, we next assessed FOXO1 localisation in unstimulated and F(ab')$_2$ stimulated CLL cells with or without AZD8055 by IF (Figure 4.6b,c) and subcellular fractionation (4.7a-c). Consistent with Figure 4.4, IF analysis demonstrated that short-term F(ab')$_2$ stimulation promoted FOXO1 cytoplasmic translocation (Figure 4.6b), represented by a near-significant decrease in Manders' co-localisation coefficient compared to unstimulated vehicle control (p = 0.056; Figure 4.6c). Encouragingly, AZD8055 treatment inhibited BCR crosslinking-induced FOXO1 nuclear export in F(ab')$_2$ stimulated CLL cells (Figure 4.6b,c), resulting in a significant increase in Manders' co-localisation coefficient compared to F(ab')$_2$ stimulated vehicle control (Figure 4.6c). Finally, AZD8055 treatment visibly enhanced FOXO1 nuclear localisation in unstimulated CLL cells (Figure 4.6c).

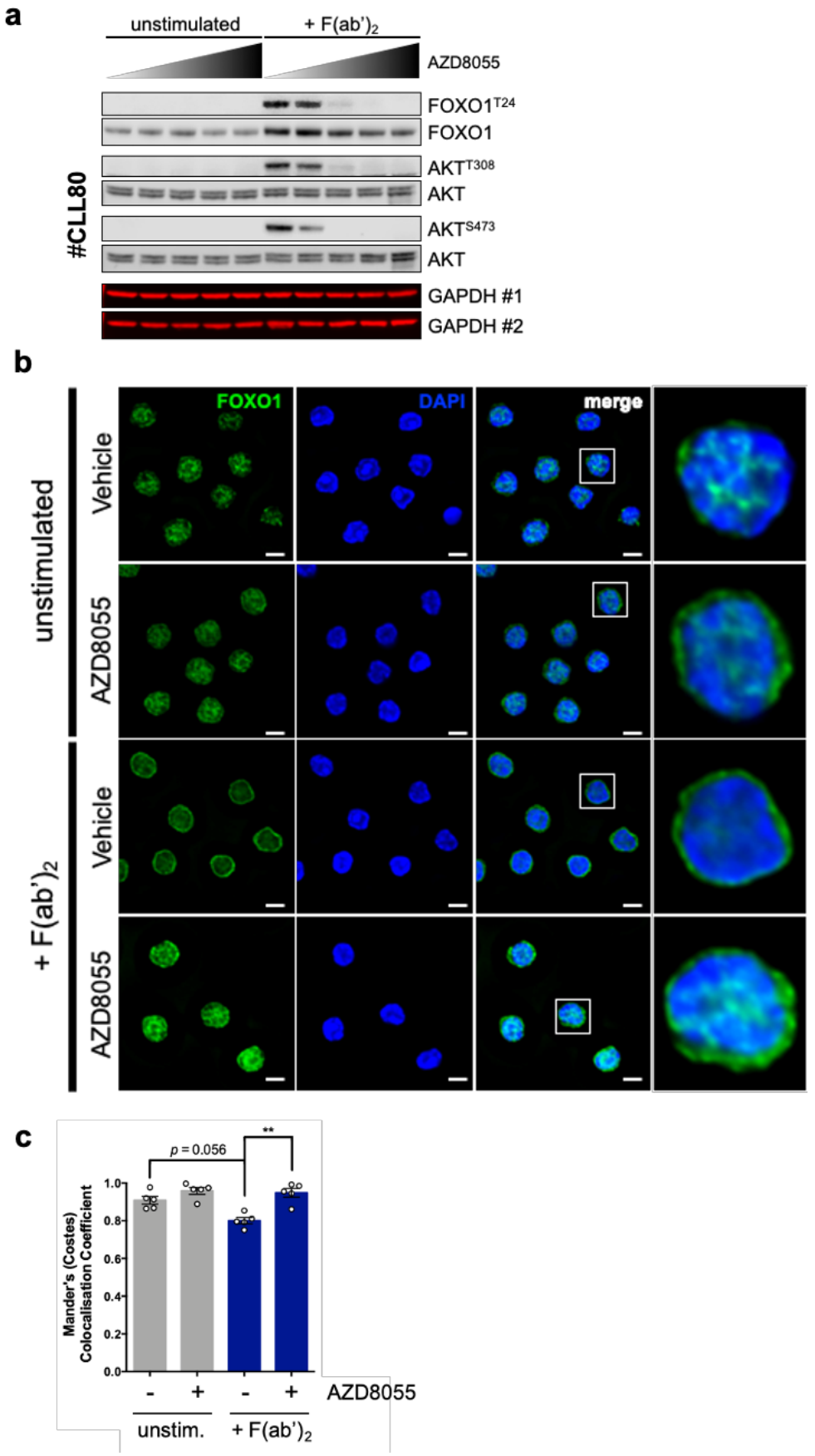

Figure 4.6 - AZD8055 inhibits BCR crosslinking-induced FOXO1 cytoplasmic translocation in primary CLL cells (1/2).
(a) Representative western blot a primary CLL sample (#CLL80; n=3 CLL samples) unstimulated or F(ab')$_2$ stimulated (+F(ab')$_2$) for 1 h following 30 min pre-treatment with increasing concentrations of AZD8055 (Vehicle, 10, 100, 1000, 10000 nM). Blots were probed for FOXO1^{T24}, FOXO1,

AKT^{S473}, AKT^{T308}, AKT and GAPDH (loading control; #1 and #2 referring to mirror blots). (b) Representative IF micrographs (100x) of a CLL patient sample (#CLL80; n=5 CLL samples) unstimulated or $F(ab')_2$ stimulated (+ $F(ab')_2$) for 1 h following 30 min pre-treatment with AZD8055 (100 nM) or vehicle control. Cells were probed for FOXO1 (green) and counter stained with DAPI (DNA; blue). Individual channel and merged images shown. Scaled image (far-right panel) of representative cell (white border; merged channel). Scale bar = 5 μm. (c) Analyses of FOXO1 and DAPI co-localisation (Manders' (Costes) Co-localisation Coefficient) in CLL patient samples (n=5) unstimulated (unstim.; grey bars) and $F(ab')_2$ stimulated (+ $F(ab')_2$; blue bars) for 1 h following 30 min pre-treatment with AZD8055 (+) or vehicle control (-). >360 cells were quantified/condition from each sample. Individual datapoints are represented by white or black circles. Data expressed as the mean ± SEM. Statistics calculated by one-way ANOVA, where ** $p \leq 0.01$.

Subcellular fractionation confirmed that $F(ab')_2$-induced FOXO1 cytoplasmic translocation was blocked by AZD8055 treatment (Figure 4.7a-c). Consistent with Figure 4.4d, cytoplasmic FOXO1 expression was enhanced following BCR crosslinking (Figure 4.7a,b), while nuclear FOXO1 expression was concurrently decreased in $F(ab')_2$ stimulated CLL cells (Figure 4.7a). AZD8055 treatment reduced cytoplasmic FOXO1 expression in unstimulated CLL cells ($p = 0.07$; Figure 4.7a,b), which corresponded to a concomitant increase in nuclear FOXO1 expression (Figure 4.7a,c). Moreover, $F(ab')_2$-induced cytoplasmic FOXO1 expression was reduced by AZD8055 (Figure 4.7a,b), which was paralleled by a concurrent increase in nuclear FOXO1 expression ($p = 0.08$; Figure 4.7a,c). As mentioned earlier, AKT-dependent $FOXO1^{T24}$ phosphorylation induces its nuclear export via association with 14-3-3 proteins (398). We therefore examined the localisation of AKT and 14-3-3 following BCR crosslinking with or without AZD8055 treatment by subcellular fractionation (Figure 4.7a). These data showed that AKT and 14-3-3 remained largely cytoplasmic irrespective of $F(ab')_2$ stimulation and/or treatment (Figure 4.7a). Previous experiments detected AKT kinase activity (Figure 3.3f,g and 3.7b) and AKT-dependent $FOXO1^{T24}$ (Figure 4.3b) phosphorylation in MEC-1 cells. We were therefore curious to assess FOXO1 localisation in MEC-1 cells following BCR crosslinking with or without AZD8055 treatment (Figure 4.7d,e). Interestingly, abundant nuclear and cytoplasmic FOXO1 expression was observed in unstimulated MEC-1 cells (Figure 4.7d). Furthermore, short-term $F(ab')_2$ stimulation induced FOXO1 cytoplasmic translocation, demonstrated by a visible reduction in Manders' co-localisation coefficient (Figure 4.7e). Consistent with earlier findings (Figure 4.6b,c), AZD8055 treatment enhanced FOXO1 nuclear accumulation in unstimulated and $F(ab')_2$ stimulated MEC-1 cells, as shown by a significant increase in Manders' co-localisation coefficient (Figure 4.7e).

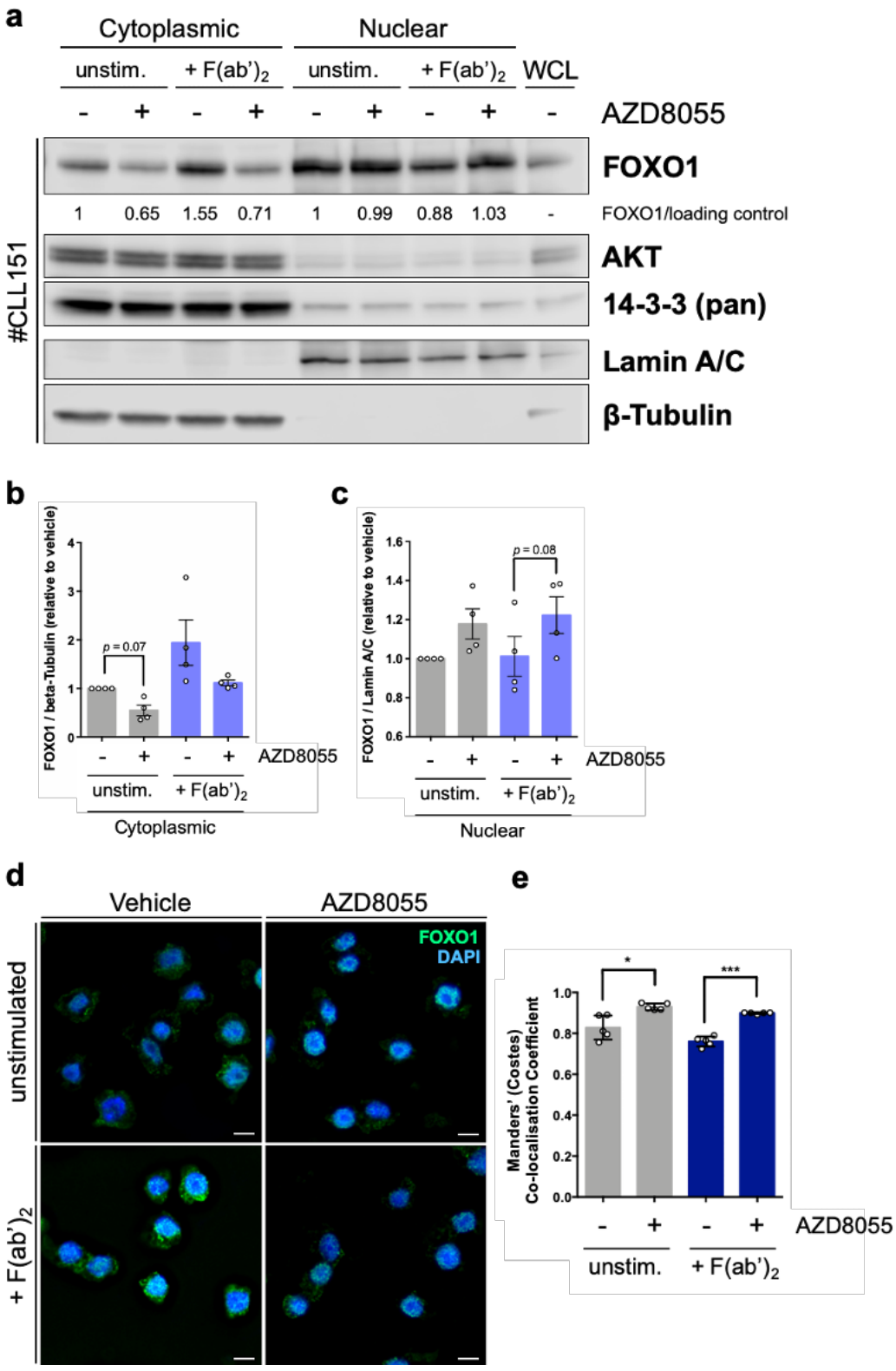

Figure 4.7 - AZD8055 inhibits BCR crosslinking-induced FOXO1 cytoplasmic translocation in primary CLL cells and MEC-1 cells (2/2).
(a) Subcellular fractionation of a CLL patient sample (#CLL151; n=4 CLL samples) unstimulated (unstim.) or F(ab')$_2$ stimulated (+ F(ab')$_2$) for 1 h following 30 min pre-treatment with 100 nM AZD8055 (+) or vehicle control (-). Cytoplasmic, nuclear and whole cell lysate (WCL) fractions were generated. Blots were probed for FOXO1, AKT, 14-3-3 (pan), Lamin A/C and β-Tubulin. Densitometry for cytoplasmic (FOXO1/β-Tubulin) and nuclear (FOXO1/Lamin A/C) FOXO1 expression are shown (relative to unstimulated vehicle control). (b, c) Densitometry of FOXO1 expression in (b) cytoplasmic and (c) nuclear fractions from unstimulated (unstim.; grey bar) and F(ab')$_2$ stimulated (F(ab')$_2$; purple bar) CLL samples (n=4) treated with AZD8055 (+) or vehicle control (-), as calculated in (a). (d) Representative IF micrographs (40x) of MEC-1 cells (n=5)

unstimulated (top panel) or F(ab')$_2$ stimulated (+ F(ab')$_2$; bottom panel) for 1 h following 30 min pre-treatment with AZD8055 (100 nM). Cells were probed for FOXO1 (green) and counter stained with DAPI (DNA; blue). Scale bar = 5 μm. (e) Analyses of FOXO1 and DAPI co-localisation (Manders' (Costes) Co-localisation Coefficient) in unstimulated (unstim.; grey bars) and F(ab')$_2$ stimulated (+ F(ab')$_2$; blue bars) MEC-1 cells (n=5 IF images/condition) treated with AZD8055 (+) or vehicle control (-). Individual datapoints are represented by white circles. Data expressed as the mean ± SEM. Statistics calculated by one-way ANOVA, where * $p \leq 0.05$, *** $p \leq 0.001$.

4.2.6 Rapamycin is unable to inhibit AKT-mediated FOXO1^{T24} phosphorylation and subsequent nuclear export

We earlier showed that AZD8055 (Figure 3.21 and 4.6a) or ibrutinib (Figure 3.21) treatment inhibited F(ab')$_2$ stimulation-induced AKT^{S473} and FOXO1^{T24} phosphorylation in CLL cells. These findings demonstrated the ability of these agents to inhibit 'full' mTORC2-dependent AKT activation, which is ordinarily required for FOXO inactivation (500). In contrast, mTORC1-selective rapamycin was unable to inhibit AKT^{S473} phosphorylation following BCR ligation (Figure 3.5). We therefore examined the effect of short-term rapamycin treatment on FOXO1^{T24} phosphorylation, alongside AZD8055 and ibrutinib, in unstimulated and F(ab')$_2$ stimulated CLL cells (Figure 4.8). Consistent with previous experiments, AZD8055 and ibrutinib successfully inhibited AKT^{S473} phosphorylation in F(ab')$_2$ stimulated CLL cells, whereas rapamycin was unable to block F(ab')$_2$-induced AKT^{S473} phosphorylation (Figure 4.8a). In support of Figure 3.21, AZD8055 treatment inhibited AKT-dependent FOXO1^{T24} phosphorylation in unstimulated CLL cells to a greater extent than rapamycin (p = 0.07; Figure 4.8a,b). Reproducibly, AZD8055 and ibrutinib (p = 0.09) treatment blocked BCR ligation-induced FOXO1^{T24} phosphorylation (Figure 4.8a,b). Perhaps expectedly, rapamycin was unable to inhibit AKT-dependent FOXO1^{T24} phosphorylation in F(ab')$_2$ stimulated CLL cells (Figure 4.8a,b). Consistent with Figure 4.3e, short-term BCR ligation resulted in a near-significant increase in FOXO1 expression (p = 0.059; Figure 4.8a,c). Interestingly, while AZD8055 and ibrutinib visibly reduced FOXO1 expression in unstimulated and F(ab')$_2$ stimulated CLL cells (Figure 4.8a,c), FOXO1 expression was largely unaffected by rapamycin treatment (Figure 4.8a,c).

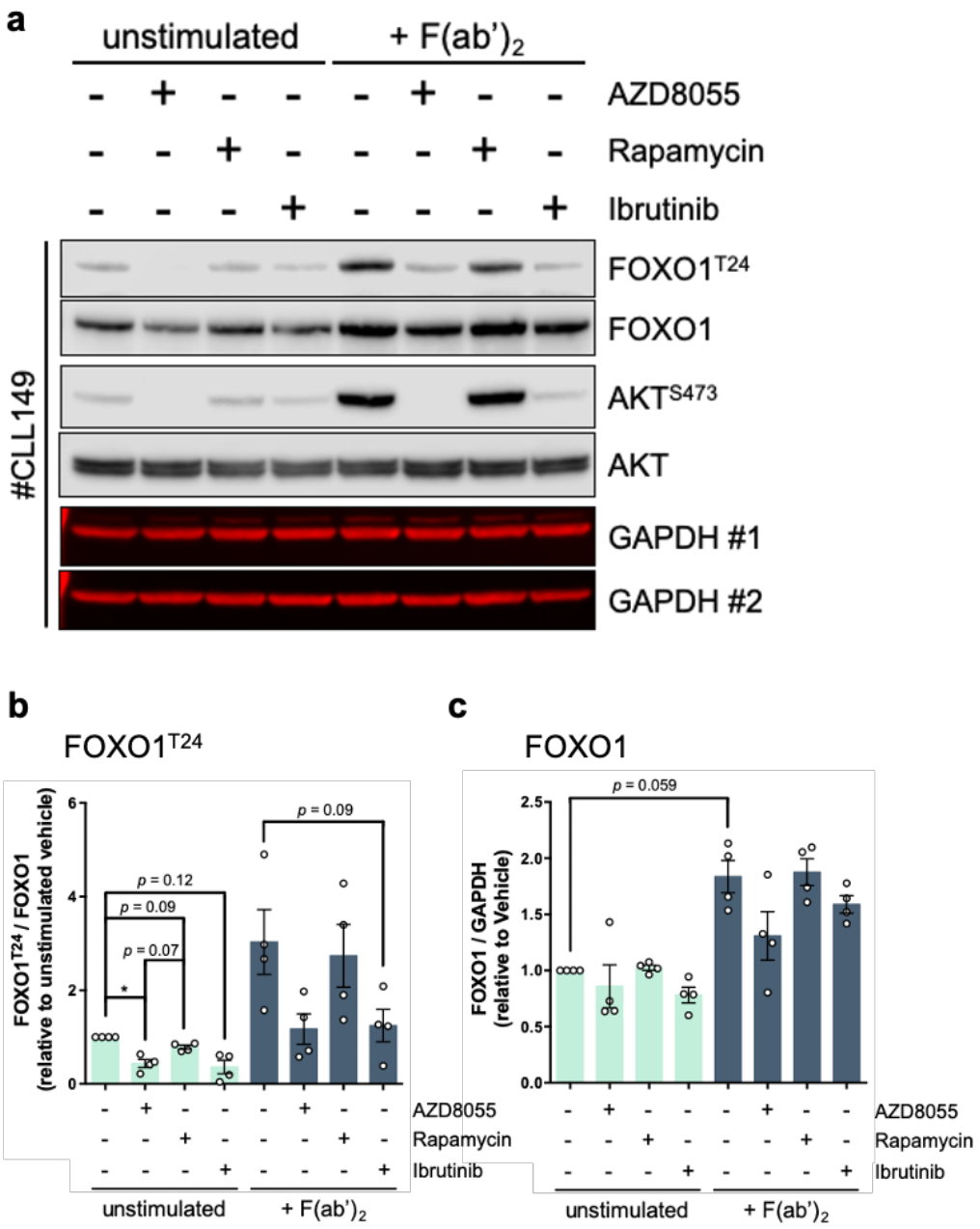

Figure 4.8 - Rapamycin does inhibit BCR ligation-induced AKT-mediated FOXO1^{T24} phosphorylation in primary CLL cells.
(a) Representative western blot of a primary CLL sample (#CLL149) unstimulated or F(ab')$_2$ stimulated for 1 h following 30 min pre-treatment with AZD8055 (100 nM), Rapamycin (10 nM), Ibrutinib (1 μM) or vehicle control. Blots were probed for FOXO1^{T24}, FOXO1, AKT^{S473}, AKT and GAPDH (loading control; #1 and #2 referring to mirror blots). (b) Relative FOXO1^{T24} phosphorylation and (c) FOXO1 expression levels in primary CLL samples (n=4), treated as described in (a). Unstimulated (teal bars) and F(ab')$_2$ stimulated (dark blue bars). Individual patient datapoints are represented by white circles. Data expressed as the mean ± SEM. Statistics calculated by one-way ANOVA, where * p ≤ 0.05.

We next assessed FOXO1 localisation in unstimulated and F(ab')$_2$ stimulated CLL cells following AZD8055 or rapamycin treatment by IF (Figure 4.9a) and subcellular fractionation (Figure 4.9b-d). IF showed that rapamycin was unable to inhibit FOXO1 cytoplasmic translocation in F(ab')$_2$ stimulated CLL cells (Figure 4.9a). However, as expected, AZD8055 treatment prevented F(ab')$_2$-induced

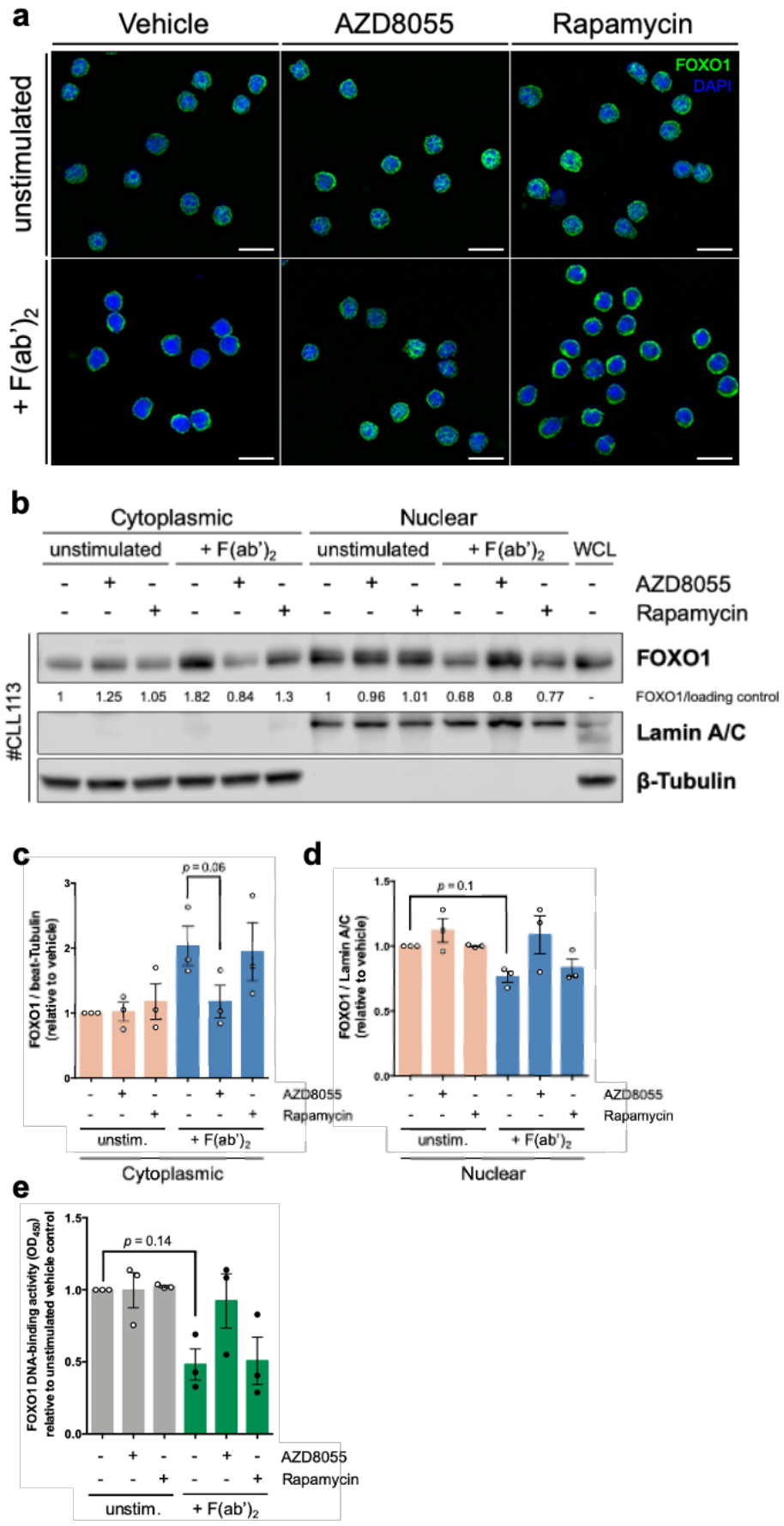

Figure 4.9 - Rapamycin does not prevent F(ab')$_2$-induced FOXO1 cytoplasmic translocation in primary CLL cells.
(a) Representative IF micrographs (40x) of a CLL patient sample (#CLL142; n=5 CLL samples) unstimulated (top panel) or F(ab')$_2$ stimulated (+ F(ab')$_2$; bottom panel) for 1 h following 30 min pre-

treatment with AZD8055 (100 nM) or rapamycin (10 nM). Cells were probed for FOXO1 (green) and counter stained with DAPI (DNA; blue). Scale bar = 5 μm. (b) Subcellular fractionation of a CLL patient sample (#CLL113; n=3 CLL samples) unstimulated (unstim.) or $F(ab')_2$ stimulated (+ $F(ab')_2$), treated as in (a). Cytoplasmic, nuclear and whole cell lysate (WCL) fractions were generated. Blots were probed for FOXO1, Lamin A/C and β-Tubulin. Densitometry for cytoplasmic (FOXO1/β-Tubulin) and nuclear (FOXO1/Lamin A/C) FOXO1 expression are shown (relative to unstimulated vehicle control). (c, d) Densitometry of FOXO1 expression in (c) cytoplasmic and (d) nuclear fractions from unstimulated (unstim.; peach bars) and $F(ab')_2$ stimulated ($F(ab')_2$; blue bars) CLL samples (n=3), treated as in (a). (e) FOXO1 DNA-binding activity (OD_{450}) of unstimulated (unstim.; grey bar) or $F(ab')_2$ stimulated (+ $F(ab')_2$; green bar) CLL patient samples (n=3), treated as in (a). Individual datapoints are represented by white or black circles. Data expressed as the mean ± SEM. Statistics calculated by one-way ANOVA.

FOXO1 nuclear exclusion (Figure 4.9a). In line with these findings, subcellular fractionation confirmed that $F(ab')_2$-induced FOXO1 nuclear-to-cytoplasmic translocation was unaffected by rapamycin treatment (Figure 4.9b-d). In contrast, $F(ab')_2$-induced cytoplasmic FOXO1 expression was reduced by AZD8055 treatment (p = 0.06; Figure 4.9b,c), which corresponded to a concomitant increase in nuclear FOXO1 expression (Figure 4.9b,d). To examine FOXO1 transcriptional activity in unstimulated and $F(ab')_2$ stimulated CLL cells following AZD8055 or rapamycin treatment, we determined the DNA binding activity of FOXO1. This experiment revealed that AZD8055 blocked $F(ab')_2$-induced FOXO1 inactivation to near-basal (unstimulated) levels (Figure 4.9d). Conversely, rapamycin was largely unable to prevent $F(ab')_2$-induced FOXO1 inactivation (Figure 4.9d). Of note, FOXO1 DNA-binding activity was unaffected by treatment in unstimulated CLL cells (Figure 4.9d).

4.2.7 AZD8055-induced inhibition of FOXO1^{T24} phosphorylation is sustained in CLL cells

We previously demonstrated that AZD8055 treatment sustained inhibition of AKT kinase activity in $F(ab')_2$ stimulated CLL cells for up to 24 hours (Figure 3.7a). We therefore asked whether inhibition of AKT-dependent FOXO1^{T24} phosphorylation was also endured. To answer this question, CLL cells underwent $F(ab')_2$ stimulation for the indicated time points in the presence of AZD8055. Thereafter, the phosphorylation status of FOXO1^{T24}, AKT^{T308} and AKT^{S473} was examined (Figure 4.10a,b). As expected, FOXO1^{T24} phosphorylation was influenced by the extent and duration of $F(ab')_2$-induced AKT^{S473} and AKT^{T308} phosphorylation (Figure 4.10a,b). Interestingly, $F(ab')_2$-induced modulation of FOXO1 expression appeared to correspond to the degree of AKT kinase activity (Figure 4.10a,b). Consistent with Figure 3.7a, AZD8055 treatment inhibited BCR

crosslinking-induced AKT^{S473} and AKT^{T308} phosphorylation for at least 24 h (Figure 4.10a,b). Encouragingly, AZD8055-induced inhibition of FOXO1^{T24} phosphorylation was also sustained for the duration of the timecourse compared to F(ab')$_2$-stimulated vehicle control (Figure 4.10a,b).

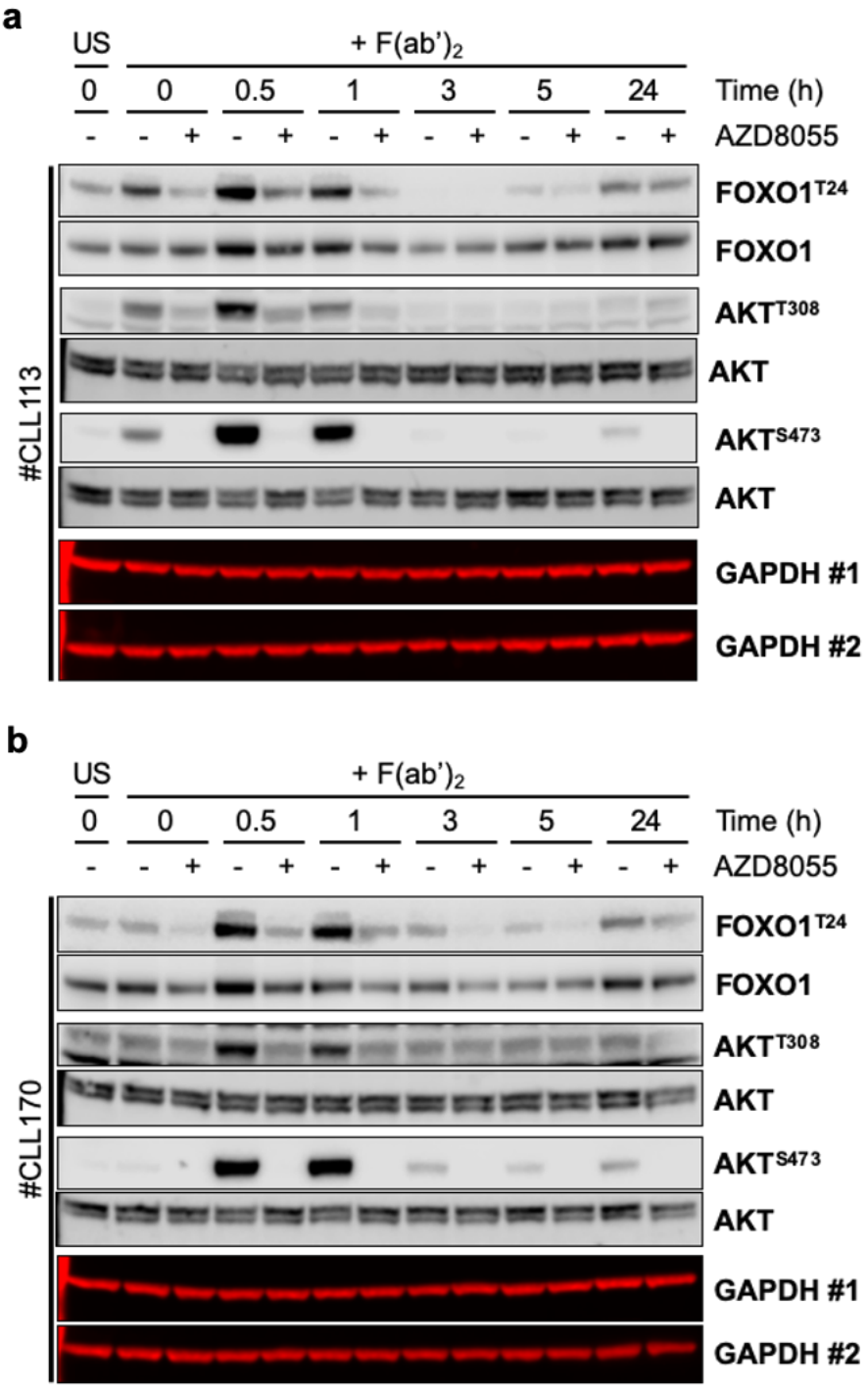

Figure 4.10 - AZD8055-induced inhibition of FOXO1^{T24} phosphorylation is sustained in CLL cells.
(a, b) Representative western blots of primary CLL samples (a) #CLL113 and (b) #CLL170 (n=3 primary CLL samples) stimulated with F(ab')$_2$ for the indicated timepoints (0, 0.5, 1, 3, 5 and 24 h) following 30 min pre-treatment with 100 nM AZD8055 (+) or vehicle control (-). Blots were probed for FOXO1^{T24}, FOXO1, AKT^{T308}, AKT^{S473}, AKT and GAPDH (loading control; #1 and #2 referring to mirror blots).

4.2.8 Ibrutinib inhibits F(ab')$_2$-induced FOXO1 nuclear exclusion

Earlier experiments showed that F(ab')$_2$-induced AKT^{S473} and FOXO1^{T24} phosphorylation was inhibited by treatment with ibrutinib (Figure 3.21). Furthermore, ibrutinib also reduced FOXO1^{T24} phosphorylation in unstimulated CLL cells (Figure 3.21), perhaps demonstrating that 'cell autonomous' (ligand-independent) BCR signalling induces AKT-dependent FOXO1 phosphorylation (397). To further examine the ability of ibrutinib to prevent AKT-mediated FOXO1 inactivation, the phosphorylation status of FOXO1^{T24}, AKT^{T308} and AKT^{S473} was assessed following treatment with increasing concentrations of ibrutinib with or without F(ab')$_2$ stimulation (Figure 4.11a). Ibrutinib treatment resulted in a dose-dependent inhibition of AKT kinase activity and AKT-dependent FOXO1^{T24} phosphorylation in F(ab')$_2$ stimulated CLL cells at clinically achievable levels (Figure 4.10a). Interestingly, as demonstrated with AZD8055 (Figure 4.6a), FOXO1 expression was progressively reduced in response to increasing concentrations of ibrutinib (Figure 4.11a). Because ibrutinib inhibited AKT-dependent FOXO1^{T24} phosphorylation, we next examined FOXO1 localisation in unstimulated and F(ab')$_2$ stimulated CLL cells with or without ibrutinib treatment by IF (Figure 4.11b,c) and subcellular fractionation (4.11d). Consistent with previous experiments (Figure 4.4a,b and 4.6b,c), short-term F(ab')$_2$ stimulation promoted FOXO1 nuclear exclusion (Figure 4.11b), resulting in a significant decrease in Manders' co-localisation coefficient compared to unstimulated vehicle control (Figure 4.11c). Ibrutinib inhibited F(ab')$_2$-induced FOXO1 cytoplasmic translocation (Figure 4.10b,c), represented by a significant increase in Manders' co-localisation coefficient compared to F(ab')$_2$ stimulated vehicle control (Figure 4.11b,c). Furthermore, ibrutinib treatment resulted in a notable trend towards enhanced FOXO1 nuclear localisation in unstimulated CLL cells (p = 0.12; Figure 4.11c). In support of these data, subcellular fractionation confirmed that F(ab')$_2$-induced FOXO1 nuclear-to-cytoplasmic translocation was blocked by ibrutinib treatment (Figure 4.11d). Cytoplasmic FOXO1 was enhanced following BCR ligation (Figure 4.11d), while nuclear FOXO1 was simultaneously decreased in F(ab')$_2$ stimulated CLL cells (Figure 4.11d). Furthermore, F(ab')$_2$-induced cytoplasmic FOXO1 expression was visibly reduced by ibrutinib treatment, which corresponded to a concurrent increase in nuclear FOXO1 expression (Figure 4.11d). Finally, in agreement with Figure 4.7a, AKT and 14-3-

3 localisation remained predominantly cytoplasmic irrespective of F(ab')$_2$ stimulation and/or treatment (Figure 4.11d).

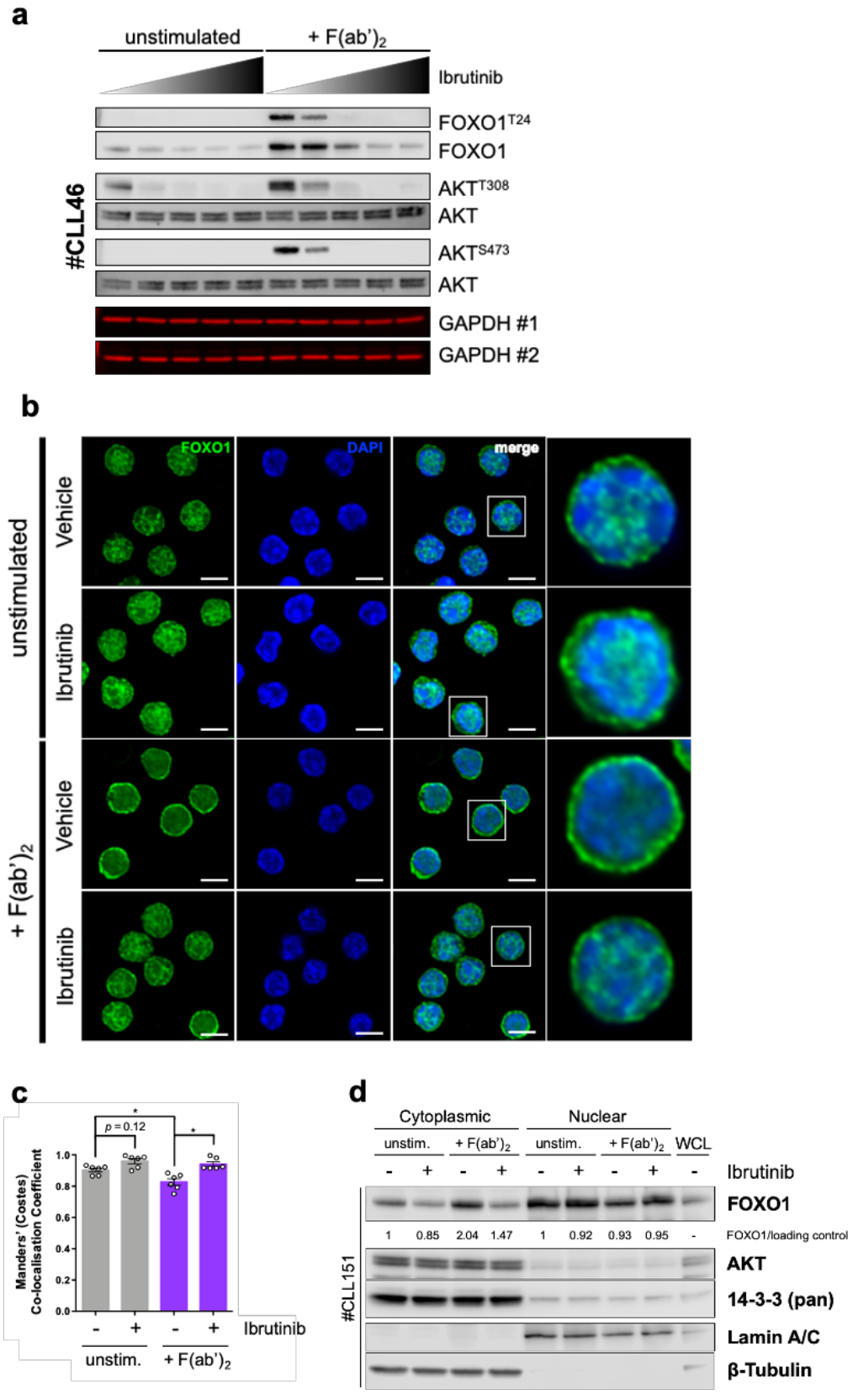

Figure 4.11 - Ibrutinib inhibits F(ab')$_2$-induced nuclear-to-cytoplasmic FOXO1 translocation in primary CLL cells.

(a) Representative western blot a primary CLL sample (#CLL46; n=3 CLL samples) unstimulated or F(ab')$_2$ stimulated (+F(ab')$_2$) for 1 h following 30 min pre-treatment with increasing concentrations of ibrutinib (Vehicle, 10, 100, 1000, 10000 nM). Blots were probed for FOXO1^{T24}, FOXO1, AKT^{S473}, AKT^{T308}, AKT and GAPDH (loading control; #1 and #2 referring to mirror blots). (b) Representative IF micrographs (100x) of a CLL patient sample (#CLL80; n=6 CLL samples) unstimulated or F(ab')$_2$ stimulated (+ F(ab')$_2$) for 1 h following 30 min pre-treatment with ibrutinib (1 μM) or vehicle control. Cells were probed for FOXO1 (green) and counter stained with DAPI (DNA; blue). Individual channel and merged images shown. Scaled image (far-right panel) of representative cell (white square; merged channel). Scale bar = 5 μm. (c) Analyses of FOXO1 and DAPI co-localisation (Manders' (Costes) Co-localisation Coefficient) in unstimulated (unstim.; grey bars) and F(ab')$_2$ stimulated (+ F(ab')$_2$; purple bars) CLL patient samples (n=5) treated with ibrutinib (+) or vehicle control (-). >360 cells were quantified/condition from each sample. (d) Subcellular fractionation of a CLL patient sample (#CLL151; n=4 CLL samples) unstimulated (unstim.) or F(ab')$_2$ stimulated (+ F(ab')$_2$) for 1 h following 30 min pre-treatment with 1 μM ibrutinib (+) or vehicle control (-). Cytoplasmic, nuclear and whole cell lysate (WCL) fractions were generated. Blots were probed for FOXO1, AKT, 14-3-3 (pan), Lamin A/C and β-Tubulin. Densitometry for cytoplasmic (FOXO1/β-Tubulin) and nuclear (FOXO1/Lamin A/C) FOXO1 expression are shown (relative to unstimulated vehicle control). Individual datapoints are represented by white circles. Data expressed as the mean ± SEM. Statistics calculated by one-way ANOVA, where * $p \leq 0.05$.

4.2.9 F(ab')$_2$ stimulation promotes FOXO1^{T24} phosphorylation in CLL patient samples with prior ibrutinib treatment

Studies have previously shown that FOXOs induce apoptosis in response to BTK (ibrutinib) (501) or PI3K/AKT (502) inhibitors in B cell malignancies and pancreatic cancer, respectively. On the other hand, FOXOs have been reported to mediate drug resistance in NHL (503), chronic myeloid leukaemia (CML) (K562) cells (504) and breast cancer (MCF-7/ADR) cells (505). Because ibrutinib treatment blocks short-term F(ab')$_2$-induced AKT kinase activity and AKT-dependent FOXO1^{T24} phosphorylation in CLL cells (Figure 3.21), thereby enabling FOXO1 nuclear exportation (Figure 4.11), we argued that FOXO1 behaves as a tumour suppressor in this context. To further examine the effect of ibrutinib on FOXO1 activity, we acquired serial samples from CLL patients before (pre) and after (post) ibrutinib treatment (Figure 4.12a). Pre- and post-ibrutinib treated CLL cells subsequently underwent short-term F(ab')$_2$ stimulation *ex vivo* to assess the phosphorylation status of FOXO1^{T24}, AKT^{T308}, AKT^{S473}, ERK1/2$^{T202/Y204}$ and BTK^{Y223} (an autophosphorylation site of activated BTK) (Figure 4.12b-d). As expected, *ex vivo* F(ab')$_2$ stimulation of CLL cells from patients before ibrutinib treatment enhanced FOXO1^{T24}, AKT^{T308}, AKT^{S473}, ERK1/2$^{T202/Y204}$ and BTK^{Y223} phosphorylation compared to unstimulated control (Figure 4.12b-d). Of note, basal activity of FOXO1^{T24} and BTK^{Y223} was observed in CLL patients CLL157 (Figure 4.12b) and CLL184 (Figure 4.12b) prior to ibrutinib treatment. Reassuringly, basal and F(ab')$_2$-induced BTK^{Y223} phosphorylation was inhibited in CLL cells from ibrutinib-treated patients (Figure 4.12b,d). Interestingly,

however, F(ab')$_2$ stimulation nevertheless elevated AKT^{T308}, AKT^{S473}, AKT-dependent FOXO1^{T24} and ERK1/2$^{T202/Y204}$ phosphorylation despite prior ibrutinib treatment (Figure 4.12b-d).

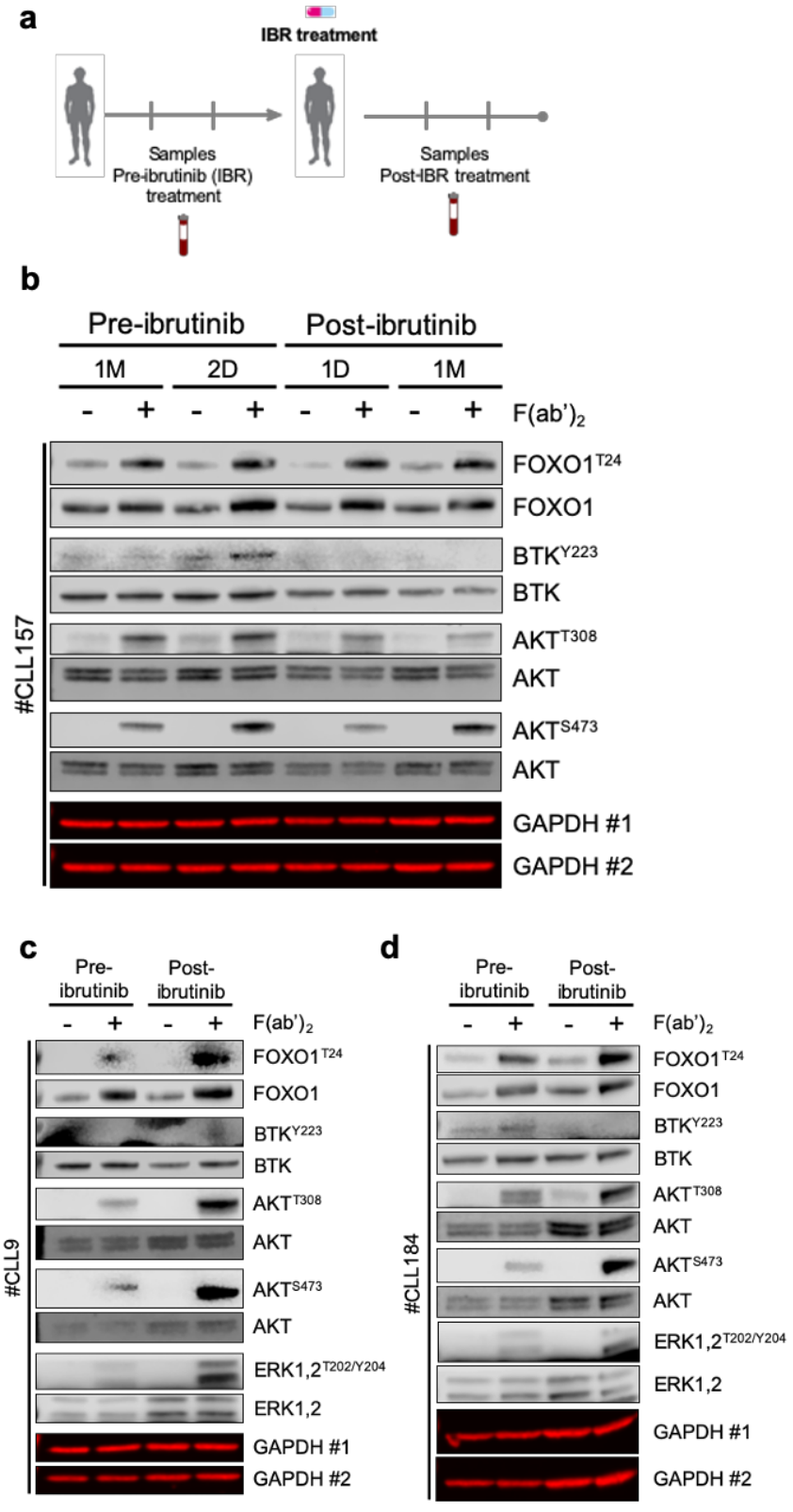

Figure 4.12 - F(ab')$_2$ stimulation promotes FOXO1^{T24} phosphorylation in CLL patient samples with prior ibrutinib treatment.
(a) Schematic depicting experimental design. Primary CLL cells were derived from CLL patients at defined timepoints before (pre-IBR) and after (post-IBR) ibrutinib treatment. (b - d) Western blots of

pre-IBR and post-IBR treated CLL patients (b) CLL157, (c) CLL9 and (d) CLL184 unstimulated (-) or F(ab')$_2$ stimulated (+) for 1 hour. Unless otherwise stated ('D' = days), pre-IBR represents 1 month (1M) prior to ibrutinib treatment and post-IBR signifies 1 month (1M) after ibrutinib treatment. Blots were probed for FOXO1^{T24}, FOXO1, BTK^{Y223}, BTK, AKT^{T308}, AKT^{S473}, AKT, ERK1,2$^{T202/Y204}$, ERK1,2 and GAPDH (loading control; #1 and #2 referring to mirror blots).

4.2.10 Combining AZD8055 with ibrutinib blocks F(ab')$_2$-dependent FOXO1 nuclear export in CLL cells

As shown previously, combining AZD8055 with ibrutinib visibly enhanced inhibition of AKT-dependent FOXO1^{T24} phosphorylation to a greater extent than AZD8055 alone in unstimulated and F(ab')$_2$ stimulated CLL cells (Figure 3.21). Building upon the experiments that demonstrated the ability of AZD8055 (Figure 4.6 and 4.7) or ibrutinib (Figure 4.11) to inhibit F(ab')$_2$-induced FOXO1 cytoplasmic translocation, we examined FOXO1 localisation following COMBO treatment in F(ab')$_2$-stimulated CLL cells by IF (Figure 4.13) and subcellular fractionation (Figure 4.14). Consistent with earlier experiments, F(ab')$_2$ stimulation promoted FOXO1 cytoplasmic translocation (Figure 4.13a), demonstrated by a significant reduction in Manders' co-localisation coefficient (Figure 4.13b). AZD8055 treatment resulted in a near-significant (p = 0.09) increase in Manders' co-localisation coefficient compared to F(ab')$_2$ stimulated CLL cells, while ibrutinib significantly blocked F(ab')$_2$-induced FOXO1 nuclear exclusion (Figure 4.13a,b). The COMBO treatment visibly enhanced FOXO1 nuclear retention (Figure 4.13a), resulting in a near-significant increase in Manders' co-localisation coefficient compared to F(ab')$_2$ stimulated CLL cells (p = 0.07; Figure 4.13b). Interestingly, the degree to which FOXO1 co-localised with the nucleus following the COMBO treatment was notably less than ibrutinib treatment alone (Figure 4.13b).

To further support these data, subcellular fractionation showed that F(ab')$_2$-induced FOXO1 cytoplasmic localisation was largely blocked by the COMBO treatment (Figure 4.14a-c). Cytoplasmic FOXO1 was visibly enhanced following BCR crosslinking (Figure 4.14a,b), while nuclear FOXO1 was concurrently decreased in F(ab')$_2$ stimulated CLL cells (Figure 4.14a,c). Treatment with AZD8055 or ibrutinib reduced cytoplasmic FOXO1 (Figure 4.13a,b), which corresponded to an increase in nuclear FOXO1 compared to F(ab')$_2$ stimulated vehicle control (Figure 4.14a,c). Finally, the COMBO treatment similarly reduced cytoplasmic FOXO1 (Figure 4.14a,b), which led to a simultaneous increase in

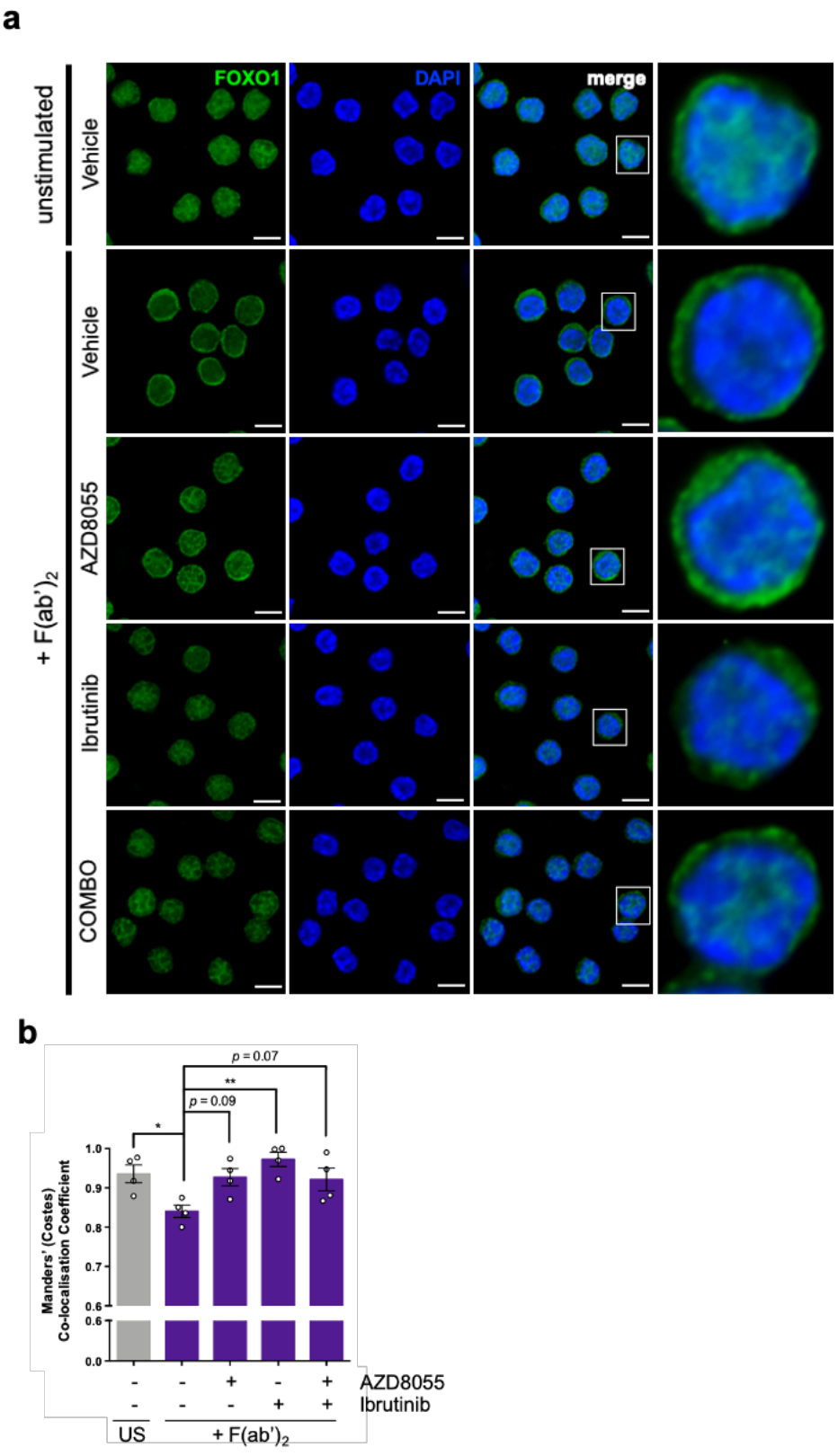

Figure 4.13 - AZD8055 and Ibrutinib combination inhibits BCR crosslinking-induced FOXO1 cytoplasmic sequestration in primary CLL cells (1).
(a) Representative IF micrographs (100x) of a CLL patient sample (#CLL80; n=4 CLL samples) unstimulated or F(ab')$_2$ stimulated (+ F(ab')$_2$) for 1 h following 30 min pre-treatment with AZD8055 (100 nM), ibrutinib (1 μM), AZD8055 and ibrutinib combination (COMBO) or vehicle control. Cells were probed for FOXO1 (green) and counter stained with DAPI (DNA; blue). Individual channel and merged images shown. Scaled image (far-right panel) of representative cell (region designated by white perimeter; merged channel). Scale bar = 5 μm. (b) Analyses of FOXO1 and DAPI co-

localisation (Manders' (Costes) Co-localisation Coefficient) in unstimulated (US; grey bar) and F(ab')$_2$ stimulated (+ F(ab')$_2$; purple bars) CLL patient samples (n=4), treated as described in (a). >360 cells were quantified/condition from each sample. Individual datapoints are represented by white circles. Data expressed as the mean ± SEM. Statistics calculated by one-way ANOVA, where * p ≤ 0.05, ** p ≤ 0.01.

nuclear FOXO1 expression (Figure 4.14a,c). These data demonstrate that BCR crosslinking-induced FOXO1^{T24} phosphorylation favours FOXO1 cytoplasmic translocation (Figure 4.14d), which can be inhibited by AZD8055 and ibrutinib as monotherapies or in combination via treatment-induced inhibition of AKT kinase activity (Figure 4.14e).

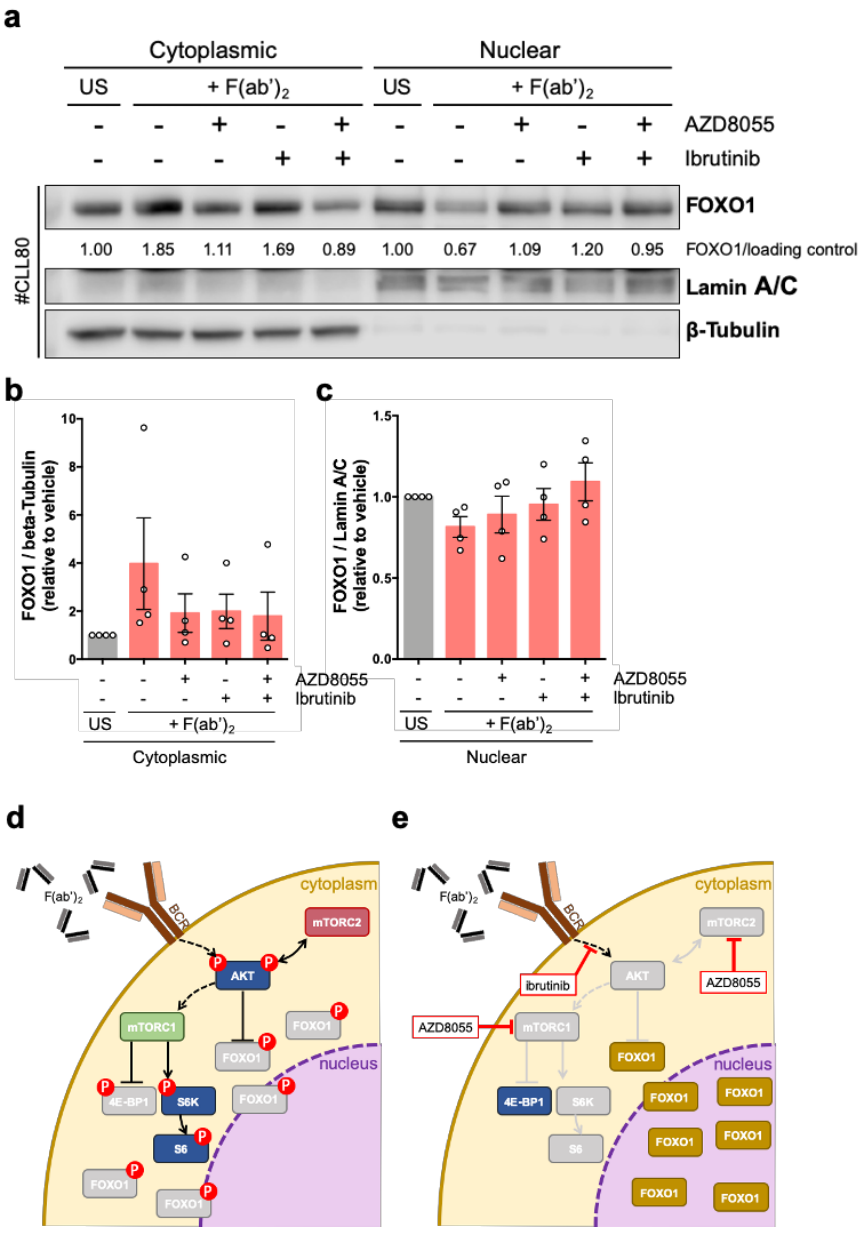

Figure 4.14 - AZD8055 and Ibrutinib combination inhibits BCR crosslinking-induced FOXO1 cytoplasmic sequestration in primary CLL cells (2).

(a) Subcellular fractionation of a CLL patient sample (#CLL80; n=4 CLL samples) unstimulated (US) or $F(ab')_2$ stimulated (+ $F(ab')_2$) for 1 h following 30 min pre-treatment with AZD8055 (100 nM), ibrutinib (1 μM), COMBO or vehicle control. Cytoplasmic, nuclear and whole cell lysate (WCL) fractions were generated. Blots were probed for FOXO1, Lamin A/C and β-Tubulin. Densitometry for cytoplasmic (FOXO1/β-Tubulin) and nuclear (FOXO1/Lamin A/C) FOXO1 expression are shown (relative to unstimulated vehicle control). (b, c) Densitometry of FOXO1 expression in (b) cytoplasmic and (c) nuclear fractions from unstimulated (US; grey bar) and $F(ab')_2$ stimulated (+ $F(ab')_2$; peach bars) CLL samples (n=4), treated as described in (a). Densitometry calculated as in (a). (d, e) Schematic of (d) $F(ab')_2$-induced AKT-dependent FOXO1 inactivation/cytoplasmic translocation and (e) COMBO-mediated inhibition of BCR crosslinking-induced FOXO1 nuclear export. Individual datapoints are represented by white circles. Data expressed as the mean ± SEM.

4.2.11 AZD8055 and ibrutinib combination enhances FOXO1 transcriptional activity in CLL cells

Since the COMBO treatment inhibited BCR crosslinking-induced FOXO1 nuclear export (Figure 4.13 and 4.14), it was of interest to determine whether treatment-induced FOXO1 nuclear localisation conferred an increase in FOXO1 transcriptional activity. Following treatment with AZD8055, ibrutinib or COMBO, CLL cells remained unstimulated or underwent short-term $F(ab')_2$ stimulation. Thereafter, FOXO1 DNA-binding activity was determined (Figure 4.15a). As expected, FOXO1 DNA-binding activity was reduced in response to short-term $F(ab')_2$ stimulation ($p = 0.053$; Figure 4.15a). AZD8055 or ibrutinib alone significantly enhanced FOXO1 transcriptional activity to near-basal levels in $F(ab')_2$ stimulated CLL cells (Figure 4.15a). The COMBO treatment evoked a near-significant increase in FOXO1 transcriptional activity in $F(ab')_2$ stimulated CLL cells ($p = 0.06$), which was notably greater than each monotherapy (Figure 4.15a). Statistically speaking, modulation of FOXO1 transcriptional activity in unstimulated CLL cells was largely unaffected by treatment (Figure 4.15a). However, the response was heterogenous; for example, some patient samples considerably enhanced FOXO1 activation in response to AZD8055 treatment, while others simultaneously downregulated FOXO1 DNA-binding activity (Figure 4.15a).

FOXOs regulate gene expression of targets involved in growth factor signalling, cell cycle arrest and apoptosis (344, 380, 506). We therefore measured the transcript abundance of a group of FOXO target genes, including *FOXO1*, *FOXO3*, *FOXO4*, *CCND1* (Cyclin D1), *CCND2* (Cyclin D2), *CDKN1A* ($p21^{CIP1}$), *CDKN1B* ($p27^{KIP1}$), *BCL2-L11* (BIM) and *GADD45A*, in unstimulated and $F(ab')_2$ stimulated CLL cells following treatment with AZD8055, ibrutinib or COMBO (Figure 4.15b-j). Despite notable trends towards enhanced *CCDN1*, *CCND2* and *CDKN1A*

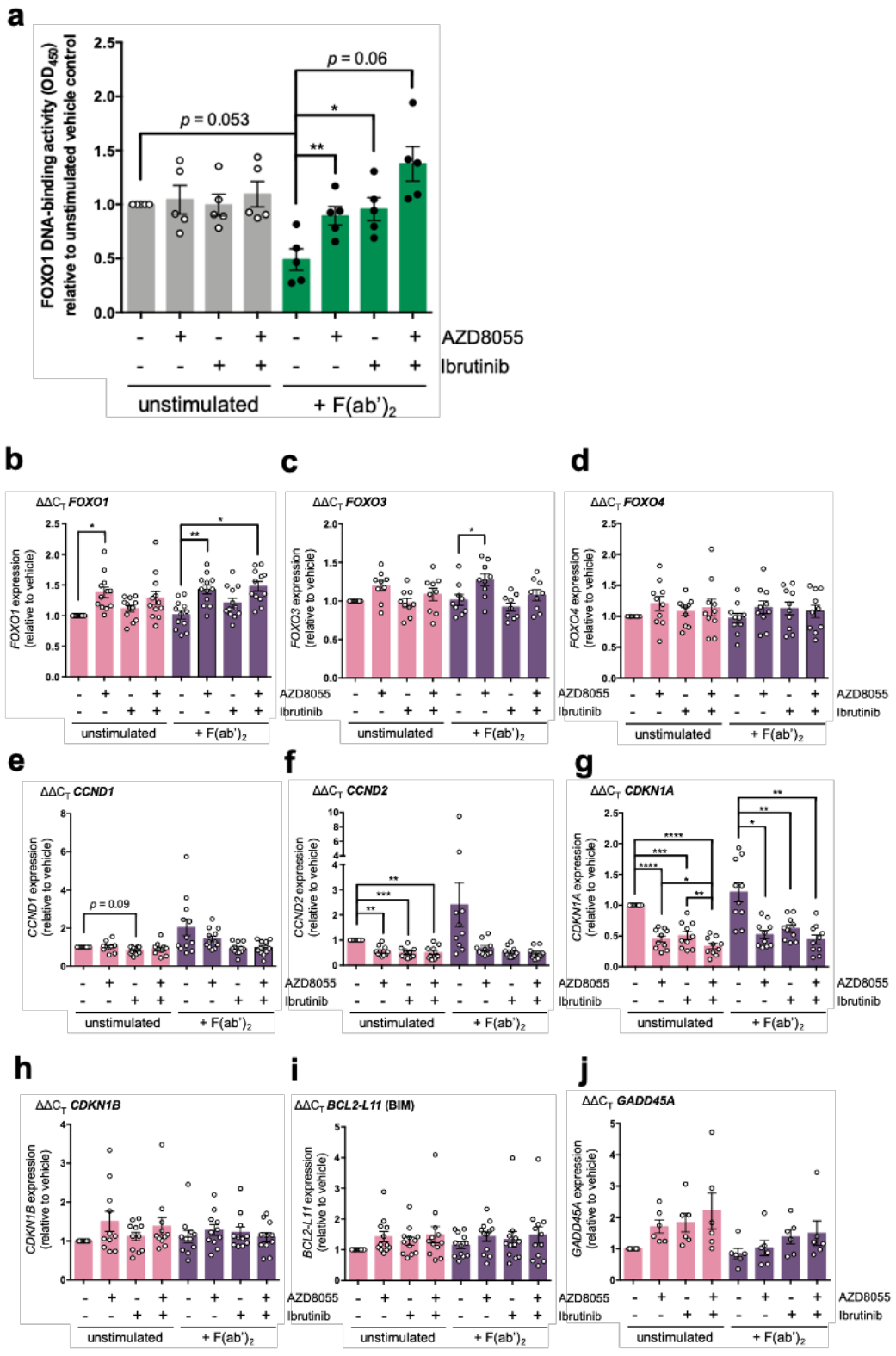

Figure 4.15 - COMBO treatment inhibits F(ab')$_2$-induced FOXO1 inactivation in primary CLL cells.

(a) FOXO1 DNA-binding activity (OD_{450}) of CLL patient samples (n=5) unstimulated (grey bars) or F(ab')$_2$ stimulated (+ F(ab')$_2$; green bars) for 1 h following 30 min pre-treatment with AZD8055 (100 nM), ibrutinib (1 μM), COMBO or vehicle control. (b – j) RT-qPCR to assess transcript abundance of (b) *FOXO1* (n=12), (c) *FOXO3* (n=9), (d) *FOXO4* (n=10), (e) *CCND1* (Cyclin D1) (n=12), (f) *CCND2* (Cyclin D2) (n=10), (g) *CDKN1A* ($p21^{CIP1}$) (n=10), (h) *CDKN1B* ($p27^{KIP1}$) (n=11), (i) *BCL2-L11* (BIM) (n=12) and (j) *GADD45A* (n=6) in unstimulated (pink bars) or F(ab')$_2$ stimulated (+ F(ab')$_2$; purple bars) primary CLL samples (24 h stimulation) pre-treated as described in (a). The $\Delta\Delta C_T$ method was used to calculate expression levels, where samples were first normalised to the internal reference gene *GUSB* and then made relative to unstimulated vehicle control. Individual

datapoints are represented by white or black circles. Data expressed as the mean ± SEM. Statistics calculated by one-way ANOVA, where * $p \leq 0.05$, ** $p \leq 0.01$, *** $p \leq 0.001$, **** $p \leq 0.0001$.

expression (Figure 4.15e,f,g), these data showed that transcript abundance of the selected FOXO target genes were largely unaffected by F(ab')$_2$-induced BCR crosslinking (Figure 4.15b-j). AZD8055 treatment significantly enhanced *FOXO1* expression in unstimulated CLL cells, while transcript levels of *CCND2* and *CDKN1A* were significantly decreased (Figure 4.15b,f,g). Moreover, AZD8055 treatment conferred visible trends towards increased *FOXO3*, *FOXO4*, *CDKN1B*, *BCL2-L11* and *GADD45A* expression in unstimulated CLL cells (Figure 4.15c,d,h,j). In F(ab')$_2$ stimulated CLL cells, *FOXO1* and *FOXO3* transcript levels were significantly enhanced following AZD8055 treatment, while *CDKN1A* was significantly reduced (Figure 4.15b,c,g). AZD8055 treatment also increased FOXO4 expression in F(ab')$_2$ stimulated CLL cells, whereas CCND1, CCND2, *CDKN1B*, *BCL2-L11* trended towards decreased expression (Figure 4.15d-f,h,i). Ibrutinib treatment significantly decreased *CCND2* and *CDKN1A* transcript abundance in unstimulated CLL cells, while trends towards enhanced *FOXO1* *CDKN1B*, *BCL2-L11* and *GADD45A* expression and decreased *CCND1* were observed (Figure 4.15b,e-j). In F(ab')$_2$ stimulated CLL cells, *CDKN1A* expression was significantly decreased following ibrutinib treatment, whereas notable trends towards increased transcript levels of *FOXO1*, *CDKN1B* and *GADD45A* and reduced *FOXO3*, *CCND1* and *CCND2* were detected (Figure 4.15b,c,e-h,j). The COMBO treatment significantly downregulated *CCDN2* and *CDKN1A* expression in unstimulated CLL cells, while trends towards increased *FOXO1*, *FOXO3*, *CDKN1B*, *BCL2-L11* and *GADD45A* were observed (Figure 4.15b,c,f-j). *FOXO1* transcript levels was significantly upregulated following COMBO treatment in F(ab')$_2$ stimulated CLL cells, whereas *CDKN1A* was significantly reduced (Figure 4.15b,g). Finally, the COMBO treatment increased transcript abundance of *FOXO3* and *GADD45A* in F(ab')$_2$ stimulated CLL cells, while trends towards reduced *CCND1* and *CCND2* were observed (Figure 4.15c,e,f,j). With the exception of *CDKN1A* expression in unstimulated CLL cells (Figure 4.15g), FOXO target transcript levels were not augmented by the COMBO treatment compared to AZD8055 or ibrutinib alone (Figure 4.15b-f,h-j).

4.2.12 FOXO1 is expressed in B220/CD45R$^+$ cells in *ex vivo* spleen sections derived from WT and PKCαKR CLL-like mice

In murine models, reports have established a key role for FOXO1 in the maintenance of the GC, where it regulates gene transcription favouring formation of the proliferative GC DZ (394, 395). In line with these findings, we sought to confirm the expression and localisation of FOXO1 in spleen sections from WT mice by IHC (Figure 4.16a,b) and IF (Figure 4.16a,c). As expected, FOXO1 expression was enhanced in structures resembling B cell follicles (Figure 4.16b). 'Dual' staining with the mouse B cell marker B220/CD45R revealed FOXO1 was almost exclusively expressed in B220/CD45R$^+$ cells (Figure 4.16c). Among B220/CD45R$^+$ cells, FOXO1 expression was elevated within a 'central core', surrounded by a band of B220/CD45R$^+$ cells with lower FOXO1 expression (Figure 4.16c). As observed previously (394, 395), B220/CD45R$^+$ cells showed almost exclusive nuclear expression of FOXO1 (Figure 4.16c). We subsequently examined AKT^{S473} phosphorylation (marker of PI3K-AKT activity (394, 395)) in WT spleen sections by IHC (Figure 4.16b). Interestingly, strong punctate AKT^{S473} staining was observed within an outer margin of B cell follicles, which was virtually absent towards the centre of the structure (Figure 4.16b). We next assessed FOXO1 expression and localisation in spleen sections from a poor prognostic CLL-like mouse model, generated as described in (485, 507) (Figure 4.17a). In brief, hematopoietic progenitor cells were retrovirally transduced with a dominant negative 'kinase-dead' PKCα (K368R) construct and adoptively transferred into RAG1$^{-/-}$ or, latterly, NSG mice. Splenocytes derived from these mice typically exhibit features of 'poor-prognostic' CLL patients including ZAP-70 expression, U-CLL and aberrant activation of signalling pathways (ERK and mTOR) (485, 507). Furthermore, these mice display upregulated BCR signalling (Michie 2020; personal communication). As such, it was of interest to assess FOXO1 expression and/or localisation within this model in the context of the TME. Spleens carrying CLL-like disease were acquired after completion of *in vivo* experiments as 'left-over' spleen tissue from vehicle control mice (Figure 4.17a). Dual staining with B220/CD45R revealed that FOXO1 was predominantly expressed in CLL-like B220/CD45R$^+$ cells (Figure 4.17b). Moreover, FOXO1 expression localised almost exclusively to the nucleus of B220/CD45R$^+$ cells

(Figure 4.17b). Interestingly, and somewhat confoundingly, AKT^{S473} was also largely detected in B220/CD45R^{+} cells (Figure 4.17c).

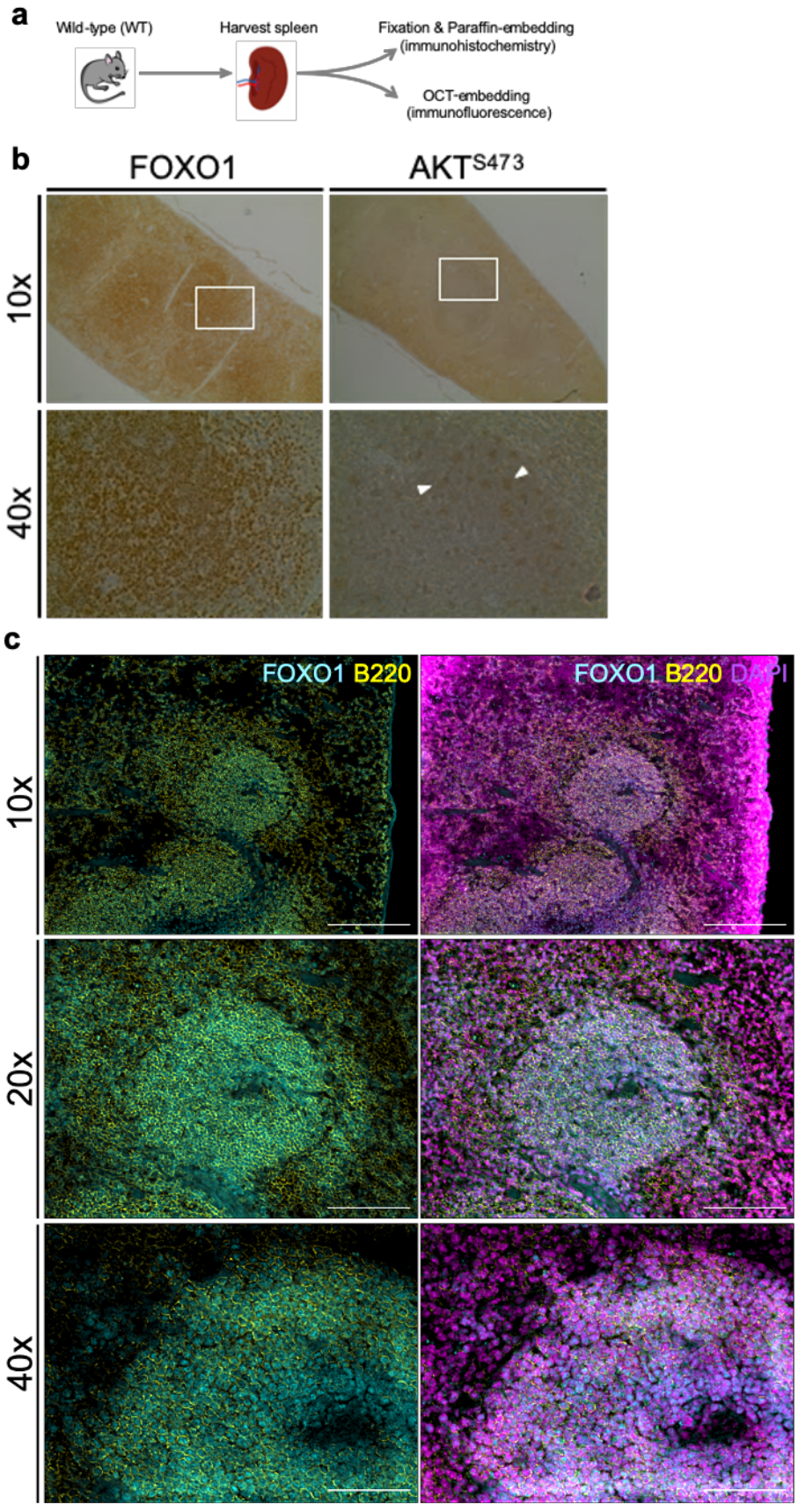

Figure 4.16 - FOXO1 expression in WT mouse spleen sections is upregulated in structures resembling B cell follicles.

(a) Schematic depicting experimental design. Spleens were harvested from WT mice and underwent either fixation/paraffin embedding (IHC) or OCT-embedding (IF). (b) IHC staining (10x and 40x) of a mouse WT spleen section (n=3) probed for FOXO1 and AKT^{S473}. White arrows indicate AKT^{S473} staining. Enlarged image (40x) representative of region designated within white rectangle (10x). (c) IF micrographs (10x, 20x and 40x) of a WT mouse spleen section. Sections were probed for FOXO1 (turquoise), B220 (yellow) and counter stained with DAPI (DNA; purple). FOXO1 and B220 staining (left panel) and merged image (right panel) are shown. Scale bar = 200 μm (10x), 100 μm (20x) and 50 μm (40x).

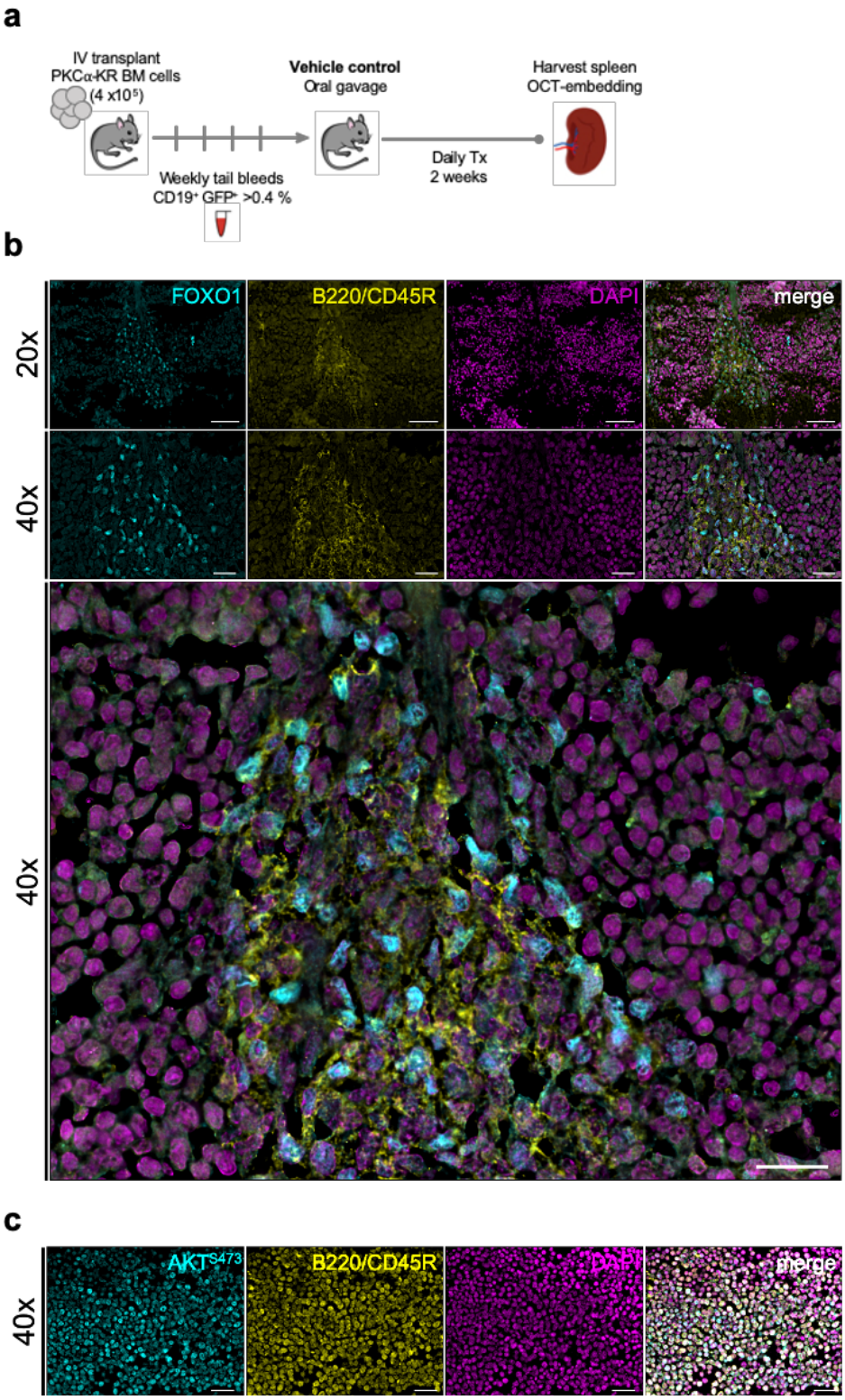

Figure 4.17 - FOXO1 is expressed in B220/CD45R^{+} cells in spleen sections derived from PKCαKR CLL-like mice.

(a) Schematic depicting experimental design. Spleens were harvested from PKCαKR CLL-like mice following 2 weeks of daily treatment with Kleptose (vehicle control). Spleen tissue underwent OCT-embedding (IF). (b) IF micrographs (20x and 40x) of a PKCαKR CLL-like mouse spleen section. Sections were probed for FOXO1 (turquoise), B220 (yellow) and counter stained with DAPI (DNA; purple). Individual channel and merged images are shown. Scale bar = 40 μm (20x) and 20 μm (40x). (c) IF micrographs (40x) of a PKCαKR CLL-like mouse spleen section probed for AKT^{S473} (turquoise), B220 (yellow) and counter stained with DAPI (DNA; purple). Individual channel and merged images are shown. Scale bar = 20 μm.

4.2.13 FOXO1 is upregulated in CLL patient LN biopsies of poor-prognostic patients, which correlates with increased Ki-67$^+$ staining

Nuclear FOXO1 expression has been observed in proliferating (Ki-67$^+$) GC B cells residing in the DZ (384, 394, 396). CLL cell proliferation within 'proliferation centres' of the LN microenvironment is inextricably linked to disease pathogenesis (9), therefore it was of interest to investigate FOXO1 expression within the CLL lymphoid compartment (Figure 4.18a-c). FOXO1 expression was assessed by IHC of LN biopsies derived from distinct prognostic subgroups of CLL patients (Figure 4.18a). As described in Figure 3.2, the patients had previously been categorised into 'indolent' or 'progressive' disease, based upon cytogenetics, *IGVH* gene mutational status and CD38 expression. Consistent with an earlier report (396), this experiment showed that FOXO1 expression was observed in CLL patient LN biopsies (Figure 4.18a,b). Of the 20 patients assessed, 19 (95%) possessed detectable levels of FOXO1 (Figure 4.18a,b). Interestingly, FOXO1 expression was significantly higher in patients harbouring poor-prognostic progressive disease markers compared to those with indolent disease (Figure 4.18a,b). Of the 9 progressive patients examined, 8 (89 %) demonstrated strong FOXO1 staining (intensity score ≥3) (Figure 4.18b). In contrast, only 3 (28%) of the 11 indolent patients exhibited strong FOXO1 staining (Figure 4.18b). Consistent with earlier findings (Figure 4.16 and 4.17), FOXO1 distribution appeared to be almost exclusively nuclear (Figure 4.18a). Ki-67 staining was subsequently aligned with FOXO1 in continuous sections among the CLL patient LN biopsies [data not shown]. Interestingly, the FOXO1 intensity score was positively correlated with % Ki-67 staining (R^2 = 0.49; p = 0.0006; n = 20) (Figure 4.18c).

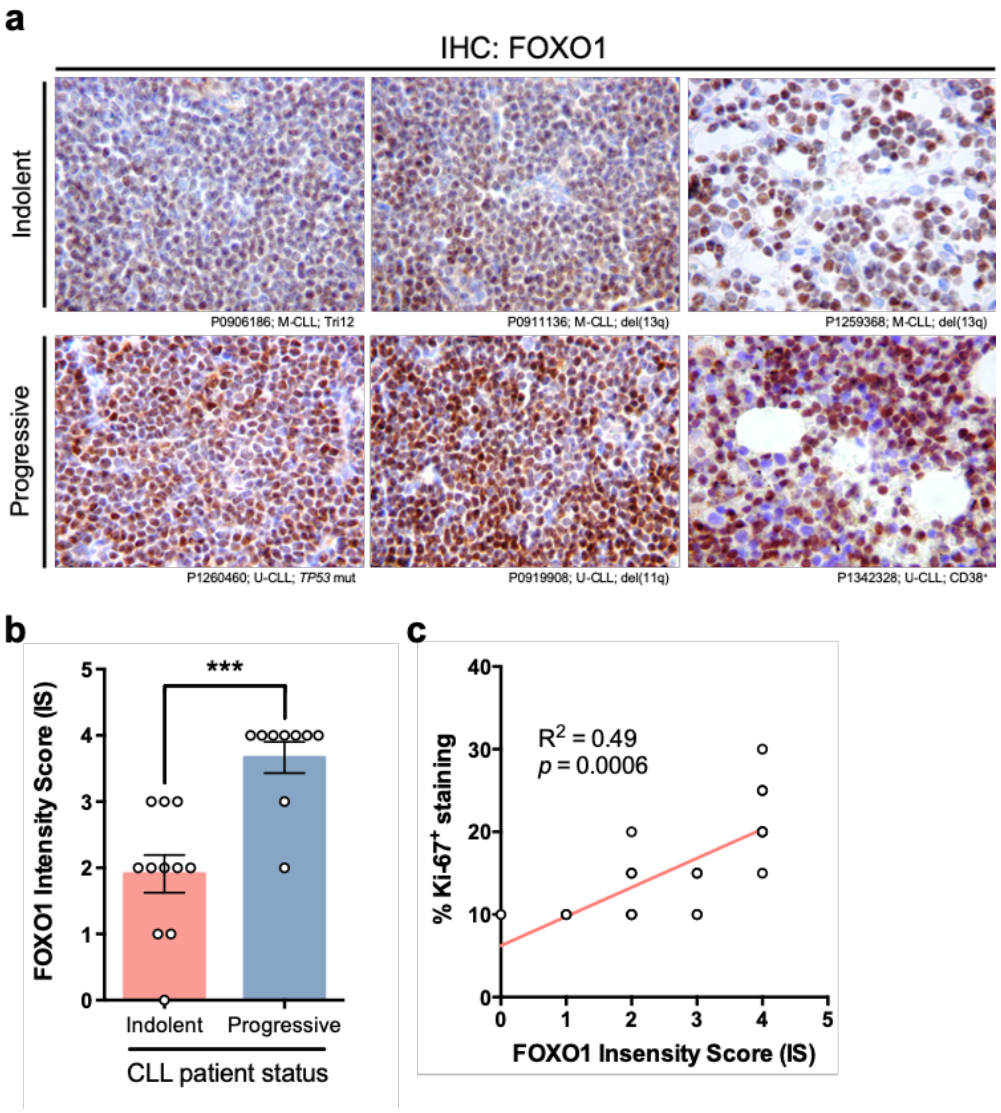

Figure 4.18 - FOXO1 is upregulated in CLL patient LN biopsies of poor-prognostic patients, which correlates with increased Ki-67⁺ staining.
(a) IHC of CLL patient LN biopsies stratified into 'indolent' and 'progressive' disease based on cytogenetics and IgVH gene mutational status. LN sections were stained for FOXO1. Prognostic information is found below each micrograph. (b) FOXO1 intensity score (IS) for CLL patient LN biopsies subdivided into indolent (n=11; salmon bars) and progressive (n=9; blue bars) disease. IS is scored from 0 to 5; 0 indicating undetected signal and 5 corresponding to highest signal. Staining performed by Dr. Mark Catherwood (Belfast City Hospital, Belfast). All slides were evaluated by a histopathologist. Individual patient datapoints are represented by white circles. Data expressed as the mean ± SEM. Statistics calculated by unpaired Student's t-test for two groups, where *** $p \leq 0.001$. (c) Correlation between FOXO1 intensity score (IS) and % Ki-67⁺ staining, as calculated by linear regression analysis (r^2).

4.2.14 'Proliferative' CLL cells possess diminished levels of FOXO1^{T24} phosphorylation and abundant nuclear FOXO1 expression

Previous reports have demonstrated that PI3K-induced inactivation of FOXO1 is required for B cell proliferation (275, 390). In contrast, a recent study demonstrated that T cell-induced proliferation of FOXO1-depleted GC B cells

was impaired (508). Because of these contradictory findings, it was of interest to explore FOXO1 phosphorylation and localisation in proliferating CLL cells *in vitro*

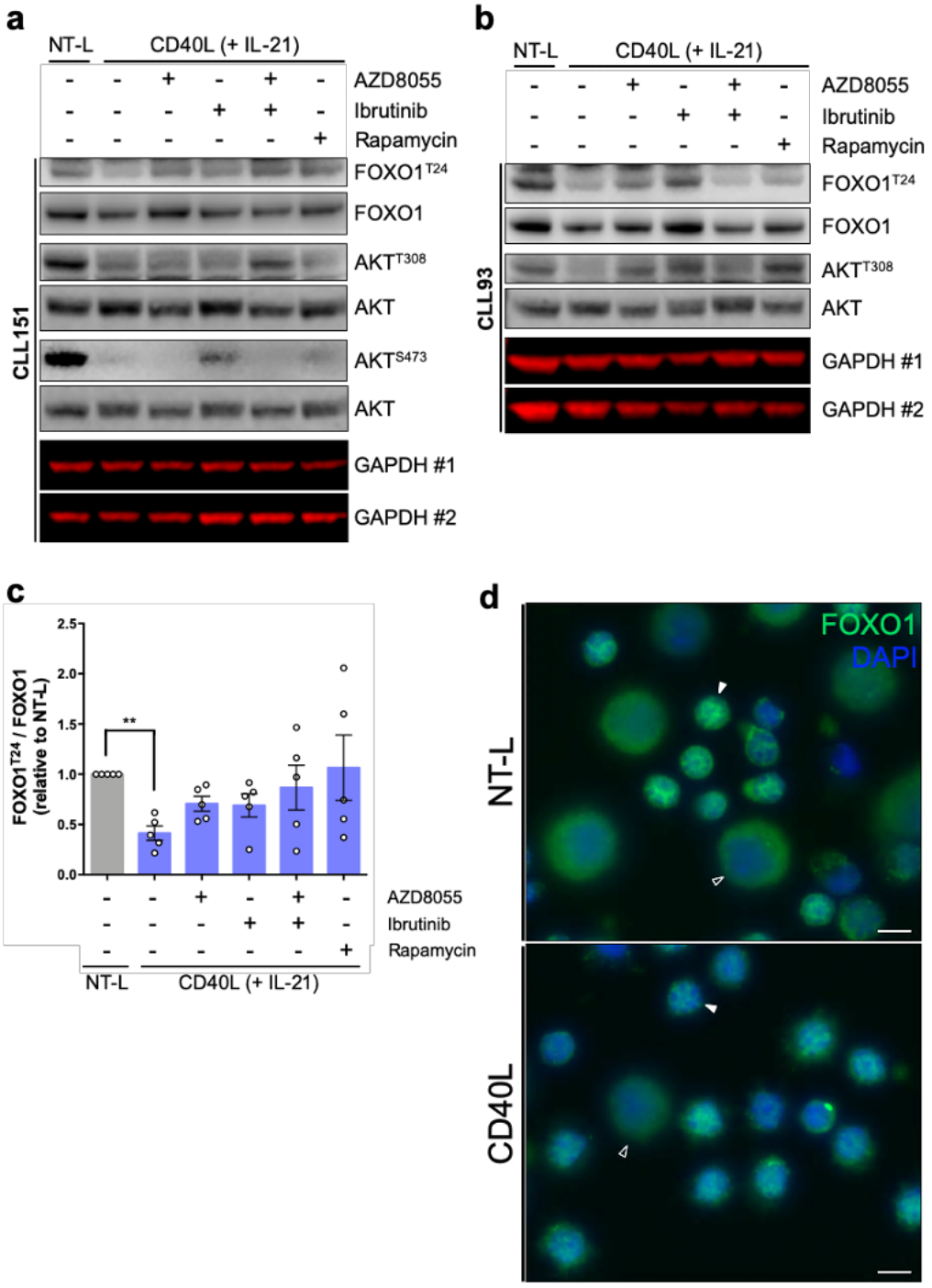

Figure 4.19 - 'Proliferative' CLL cells possess diminished levels of FOXO1^{T24} phosphorylation and abundant nuclear FOXO1 expression.
(a, b) Representative western blots of primary CLL samples (a) #CLL151 and (b) CLL93 (n=5 primary CLL samples) co-cultured on CD40L (+IL-21) and treated with AZD8055, Ibrutinib, COMBO, Rapamycin or vehicle control for 6 days. Primary CLL cells were co-cultured on NT-L as a non-proliferative control. Blots were probed for FOXO1^{T24}, FOXO1, AKT^{T308}, AKT^{S473}, AKT and GAPDH (loading control; #1 and #2 referring to mirror blots). (c) Relative FOXO1^{T24} phosphorylation levels (densitometry) in primary CLL samples (n=5) co-cultured on NT-L (grey bar) and CD40L (+IL-21) (purple bars), treated as described in (a). Relative phosphorylation levels are relative to NT-L vehicle control. Individual datapoints are represented by white circles. (d)

Representative IF micrographs (100x) of a CLL patient sample (#CLL157) co-cultured on NT-L (top image) or CD40L (+IL-21) (bottom image) for 72 h. Cells were probed for FOXO1 (green) and counter stained with DAPI (DNA; blue). Solid white arrows: CLL cells; empty arrows: stromal cells. Scale bar = 5 μm. Data expressed as the mean ± SEM. Statistics calculated by one-way ANOVA, where ** $p \leq 0.01$.

(Figure 4.19). As described earlier (Figure 3.20), *ex vivo* CLL cell proliferation was induced using the CD40L (+IL-21) co-culture system. Thereafter, the phosphorylation status of FOXO1^{T24}, AKT^{S473} and AKT^{T308} was assessed by Western blotting (Figure 4.19a-c), and the localisation of FOXO1 was examined by IF (Figure 4.19d). These data showed that the level of FOXO1^{T24} phosphorylation was significantly lower in proliferative CLL cells co-cultured on CD40L (+IL-21) compared to non-proliferative CLL cells co-cultured on NT-L cells (Figure 4.19a-c). Reduced FOXO1^{T24} phosphorylation coincided with decreased levels of AKT^{S473} and AKT^{T308} phosphorylation in CLL cells co-cultured on CD40L (+IL-21) compared to NT-L cells (Figure 4.19a,b). Furthermore, FOXO1^{T24} phosphorylation was visibly lower in proliferative vehicle control CLL cells compared to CLL cells treated with AZD8055, ibrutinib, COMBO or rapamycin (Figure 4.19a-c). IF showed that FOXO1 expression was mainly localised in the nucleus of CLL cells co-cultured on NT-L (Figure 4.19d). Interestingly, however, proliferative CLL cells co-cultured on CD40L (+IL-21) also possessed nuclear FOXO1 expression (Figure 4.19d), suggesting FOXO1 is active in proliferating CLL cells.

4.3 Discussion

Here, we provide insights into FOXO1 activity and subcellular localisation downstream of BCR crosslinking in CLL cells. BCR ligation-induced inactivation of FOXO1, the most abundantly expressed FOXO in CLL cells, demonstrates that the PI3K-AKT-FOXO1 axis likely plays an important role in CLL cell disease biology downstream of the BCR ligation. Additionally, re-engagement of FOXO1 DNA-binding activity by targeted elimination of BCR signalling, via AKT (AZD5363), mTOR kinase (AZD8055) or BTK (ibrutinib) inhibition, suggests that FOXO1 may mediate the functional response to treatment. However, given the expression of nuclear FOXO1 in poor prognostic CLL patient LN biopsies, it becomes tempting to speculate that FOXO1 might contribute towards CLL pathogenesis and progression in a context-specific manner.

4.3.1 BCR-dependent inactivation of FOXO1 suggests that the PI3K-AKT-FOXO1 axis contributes to CLL pathophysiology downstream of BCR ligation

The activity of FOXO transcription factors is primarily controlled by nucleo-cytoplasmic shuttling, governed largely by PI3K-AKT signalling (348). The results reported here demonstrate that BCR crosslinking enhances AKT-dependent FOXO1 phosphorylation, indicating that BCR signalling inactivates FOXO1 in CLL cells. In mature B cells, BCR ligation promotes PI3K-dependent phosphorylation and cytoplasmic translocation of FOXO1 (390). In line with these findings, we have shown that BCR ligation favours FOXO1 cytoplasmic accumulation and diminishes DNA-binding activity in CLL cells, suggesting that FOXO1 regulation in CLL cells observes the paradigm conveyed in normal B cells (390). Importantly, BCR crosslinking-induced FOXO1 phosphorylation was only temporary, potentially indicating that PI3K signalling must be diminished to enable FOXO1 re-activation (387). Consistent with its purported tumour suppressor role, Yusuf *et al*. further showed that expression of constitutively active FOXO1 (FOXO1-A3) induced apoptosis and cell cycle arrest in activated B cells (390). This demonstrated that inactivation of FOXO1 activity was an important functional outcome of BCR-mediated PI3K signalling in mature B cells (390). Given the significance of BCR signalling in driving CLL pathogenesis and progression (45), repression of pro-apoptotic (346, 365) and anti-proliferative (376, 377) pathways via PI3K-

dependent FOXO1 inactivation may fulfil an integral function in CLL pathophysiology. Indeed, our data demonstrates that mRNA expression of D-type cyclins *CCND1* and *CCND2* is elevated following BCR ligation, which are reportedly transcriptionally repressed by active FOXOs in mouse embryonic fibroblast cells (378). Therefore, these findings indicate that FOXO1 might be an effector of PI3K-AKT inhibition downstream of BCR ligation to promote cell cycle arrest and apoptosis in CLL cells, as demonstrated in pre-BCR^{+} BCP-ALL (402) and DLBCL (397).

Like mature B cells (222), studies have shown that CLL cell survival and expansion is dependent on both 'tonic' and antigen-triggered BCR signalling (122). As highlighted by Ushmorov *et al.,* the role of FOXO1 in the survival programme of B cells reliant on 'tonic' BCR signalling is somewhat contentious (384). For example, Dengler *et al*. showed that FOXO1 ablation using a conditional knockout (*Foxo1*$^{L/L}$*Cd21*^{Cre}) diminished survival (and proliferation) of mature B cells following F(ab')$_2$-induced BCR ligation, owing to reduced surface Ig expression and BCR signalling defects (384, 387). Accordingly, *SYK*, *BLNK* and *PI3KCA* were shown to be transcriptional targets of FOXOs, which are central components of BCR signalling, perhaps indicating that FOXO transcriptional activity is required to sustain 'tonic' signals (and survival, by extension) (384, 509, 510). On the other hand, Srinivasan *et al*. demonstrated that FOXO1 promoted apoptosis in BCR-negative (IgM^{neg}) B cells via upregulation of pro-apoptotic (*BCL2-L11*) and cytostatic (*CDKN1B*) transcripts, which was negated following *FOXO1* deletion, *PTEN*-knockout or expression of a constitutively active form of PI3K (P110α) (275, 384). As summarised by Ushmorov *et al.,* these findings likely indicate that FOXO1 activity (and the functional outcome) is finely balanced according to the strength and duration of BCR signalling, inasmuch as FOXO1 maintains B cell survival in response to optimal 'tonic' signalling, whereas FOXO1 mediates apoptosis in B cells with perturbed BCR signalling (384). Although Dengler *et al*. reported that FOXO1 was not necessary for B cell maintenance (387), others have shown that strict regulation of FOXO activity within an optimum contributes towards B cell homeostasis (403, 506, 511). Interestingly, Hornsveld *et al*. recently postulated that FOXOs are unlikely to distinguish between normal and malignant cells in accomplishing homeostatic activities (344). Indeed, FOXO1 was recently shown to produce 'bimodal'

responses in the maintenance of pre-BCR$^+$ BCP-ALL. For example, pharmacological inactivation of pre-BCR signalling or FOXO1-A3 overexpression resulted in FOXO1-induced cell death (402), whereas FOXO1 repression was shown to induce cell cycle arrest and apoptosis via CCND3 downregulation (403). How these findings are resolved in the context of CLL is yet to be determined. Still, it is intriguing to contemplate that FOXO1 may inadvertently promote CLL maintenance.

Similar to pre-BCR$^+$ BCP-ALL (512) and GCB-DLBCL (253), studies have demonstrated constitutive activation of PI3K (252) and AKT (284, 285) in circulating CLL cells, perhaps underscored by constitutive clustering of the BCR (247, 248), akin to normal B cells upon antigen stimulation (225, 513, 514). Despite AKT-dependent FOXO1^{T24} phosphorylation, we have shown that a proportion of FOXO1 is localised in nuclei of unstimulated CLL cells, similar to circulating B cells devoid of growth factor stimulation (390). In quiescent B cells, nuclear FOXO1 instructs transcription of genes favouring cell cycle arrest and redistribution between the blood and SLOs (266). In line with these findings, 'arrested' PB-derived CLL cells express elevated levels of cell cycle inhibitor p27^{KIP1} (493) and chemokine receptor CXCR4 (169), which are direct transcriptional targets of FOXO1 in B cells (275, 394). Importantly, BCR ablation enhances p27^{KIP1} expression in mature B cells (275), while IgM stimulation downregulates CXCR4 (515). Therefore, one might assume that optimal FOXO1 activity contributes to CLL cell homeostasis within the periphery, and that BCR ligation in the SLOs elicit commensurate changes in FOXO1 transcriptional activity to promote CLL cell expansion in a context-dependent manner. Although under the influence of PI3K-AKT signalling (401), it is likely that FOXO1 subcellular localisation exists in equilibrium (344), influenced largely by the extent of BCR signalling. Of note, we cannot exclude the effect BCR crosslinking on additional pathways, such as MAPK/ERK (366), NF-κB (516) or JNK (371), which also impact upon FOXO subcellular localisation (401, 517). Therefore, the influence of other posttranslational FOXO1 modifications (phosphorylation, acetylation, methylation and ubiquitination) downstream of BCR ligation warrants further investigation.

With reference to the outcome of BCR activation among CLL patients (i.e 'positive' signalling or anergy), this hypothesis could be tested by assessing FOXO1 localisation/expression in patient samples stratified according to IgM expression levels and/or *IGHV* mutational status.

4.3.2 Hindering F(ab')$_2$-mediated BCR signal transduction re-engages FOXO1 activity, suggesting FOXO1 is an effector of BCR signalling inhibition in CLL

Notwithstanding the potential homeostatic role of FOXO1 in CLL maintenance, the data presented here demonstrate that *in vitro* BCR ligation promotes FOXO1 inactivation in CLL cells, as evidenced by enhanced AKT-dependent FOXO1^{T24} phosphorylation, nuclear export and reduced DNA-binding activity. Because FOXOs are purported tumour suppressors (347), re-engagement of FOXO activity via PI3K-AKT inhibition has been mooted as an attractive therapeutic strategy (365). Indeed, the PI3K inhibitor LY294002 was shown to inhibit BCR crosslinking-induced FOXO1 cytoplasmic translocation in mature B cells, while ectopic expression of FOXO1-A3 resulted in cell cycle arrest and enhanced cell death (390). In GCB-DLBCL, a DLBCL subset characterised by increased activity of the PI3K-AKT pathway (253), elimination of BCR signalling via SYK inhibition increased FOXO1 activity and expression of direct FOXO targets including pro-apoptotic BCL2-L11 and the cell cycle inhibitor p27^{KIP1} (397). As such, we conjecture that FOXO1 operates as an effector of PI3K-AKT inhibition downstream of BCR engagement to promote cell cycle arrest and apoptosis in CLL cells.

Perhaps unsurprisingly (277, 350-353), the AKT inhibitor AZD5363 blocked AKT-dependent FOXO1^{T24} phosphorylation in F(ab')$_2$-stimulated CLL cells, which consequently diminished BCR crosslinking-induced FOXO1 nuclear export. Although the analysis of DNA-binding activity was inconclusive among the CLL samples tested, these data confirm that BCR engagement signals via AKT to promote cytoplasmic translocation (and inactivation) of FOXO1. Mechanistically, AKT-dependent FOXO1 phosphorylation (FOXO1^{T24} and FOXO1^{S256}) mediates interaction with 14-3-3 proteins (354, 355), which subsequently facilitate nuclear export via masking of the nuclear localisation sequence (277, 354) and disrupting DNA binding (359). Encouragingly, therefore, elimination of AKT

activity largely retains FOXO1 in the nucleus of CLL cells, which may instruct transcription of targets involved in cell cycle repression and apoptosis (365). Indeed, Szydlowski *et al*. showed that the AKT inhibitor MK2206 reduced proliferation of BCR-dependent DLBCL cell lines DHL4 and Ly7 in a FOXO1-dependent manner, inasmuch as FOXO1-depleted cells were resistant to the cytostatic effect of AKT inhibition (397). Furthermore, 'preprint' data has also revealed that FOXO is an effector of MK2206-induced cell cycle exit and cell death in multiple myeloma (MM) cells (518). Interestingly, Chapman *et al*. demonstrated that CD40L (+IL-4)-induced CLL cell proliferation was sensitive to AKT inhibition (AZD5363), which corresponded to enhanced $p27^{KIP1}$ levels (279). Although FOXOs were not assessed, it is interesting to speculate that FOXO1 might be an effector of AKT inhibition to suppress CLL cell proliferation. Notably, other AKT substrates, including GSK3α/β and TSC2 (246) are activated upon AKT inhibition in CLL cells (285, 519). Therefore, in the absence of a mechanistic approach targeting FOXO1, the influence of these substrates on cell growth, survival and proliferation must be considered.

Earlier, we demonstrated that inhibition of mTOR kinase inhibited BCR ligation-induced AKT (AKT^{S473} and AKT^{T308}) and $FOXO1^{T24}$ phosphorylation in CLL cells, indicating that AKT-dependent inactivation of FOXO1 is coordinated, in part, by mTOR signalling. In the present chapter, we show that AZD8055 treatment blocks BCR crosslinking-induced FOXO1 nuclear to cytoplasmic translocation, corresponding to enhanced DNA-binding activity and modulation of FOXO transcriptional targets *FOXO1*, *FOXO3*, *CCND2* and *CDKN1A* ($p21^{CIP1}$). Alongside our recent report (284), evidence supporting the role of mTOR kinase in the regulation of FOXO activity appears to be limited. However, the dual PI3K/mTOR inhibitors PI-103 and NVP-BEZ235 have been shown to enhance FOXO activity in neuroblastoma (520) and NHL (521), respectively. We further showed that the mTORC1-selective inhibitor rapamycin was unable to inhibit BCR crosslinking-induced AKT^{S473} and $FOXO1^{T24}$ phosphorylation in CLL cells, which resulted in FOXO1 cytoplasmic accumulation and diminished DNA-binding activity. Interestingly, a study showed that rapamycin treatment promoted FOXO1 inactivation via enhanced AKT^{S473} phosphorylation in colon cancer cell lines, limiting its anti-tumour efficacy (522). These data highlight the importance of mTORC2-dependent AKT^{S473} phosphorylation in regulating AKT kinase activity and

subsequent inactivation of FOXOs. Indeed, ablation of mTORC2 has been shown to compromise AKT-dependent FOXO3 phosphorylation in mice embryo fibroblasts (MEFs), whereas phosphorylation of AKT substrates GSK3β and TSC2 were unaffected (500). Interestingly, this finding indicates that PI3K-dependent AKT^{T308} phosphorylation is unable to 'fully' inactivate FOXOs (albeit FOXO3) without mTORC2-dependent AKT^{S473} phosphorylation (384). Nevertheless, our data demonstrates that AZD8055 inhibits AKT^{S473} and AKT^{T308} phosphorylation, indicating AZD8055 indirectly controls FOXO1 activity via 'full' AKT inactivation. Therefore, the relative importance of mTORC2-dependent AKT^{S473} phosphorylation over PI3K-dependent AKT^{T308} is difficult to decipher in this context.

Treatment with the BTK inhibitor ibrutinib blocked BCR ligation-induced AKT (AKT^{S473} and AKT^{T308}) and $FOXO1^{T24}$ phosphorylation, suggesting the BTK imbibition influences FOXO1 activity in CLL cells. In support of these data, Kapoor *et al*. recently demonstrated that ibrutinib (10 μM) inhibited $FOXO3a^{S253}$ phosphorylation in MEC-1 cells, leading to FOXO3a-dependent BIM expression (501). In pre-BCR^{+} BCP-ALL, ibrutinib was shown to inhibit baseline AKT-dependent $FOXO1^{T24}$, $FOXO3a^{T32}$ and $FOXO4^{T28}$ phosphorylation, which corresponded to a concomitant increase in $p27^{KIP1}$ (523). Here, we demonstrated that ibrutinib blocked BCR crosslinking-induced FOXO1 nuclear export in CLL cells, resulting in FOXO1 nuclear accumulation and enhanced DNA-binding activity. In line with these findings, ibrutinib treatment modulated transcript abundance of FOXO target genes *CCND2* and *CDKN1A* ($p21^{CIP1}$). Collectively, these data indicate that FOXO1 is an effector of BTK inhibition in CLL cells, which might contribute to the anti-proliferative and apoptotic properties of ibrutinib observed *in vitro* and *in vivo* (126, 127, 129). From a clinical point of view, FOXO1 might also represent a biomarker of clinical activity and/or resistance to BTK inhibitors. Indeed, Landau *et al*. recently generated an RNA sequencing (RNA-seq) dataset of serial CLL patient samples pre- and post-ibrutinib treatment (88). Using the gene expression profiling (GEP) data produced by the expression of FOXO1-A3 in Hodgkin lymphoma cell lines (524), it would be interesting to glean insights into FOXO1 transcriptional activity in CLL patient samples before and after ibrutinib treatment.

In a recent study, however, BCR ligation (via stimulation with anti-IgM) of CLL cells undergoing ibrutinib treatment was shown to induce signal transduction along the PI3K-AKT axis, despite inhibition of BTK and PLCγ2 activity (146). Consistent with these findings, we have shown that AKT (AKT^{S473} and AKT^{T308}), $FOXO1^{T24}$ and $ERK1/2^{T202/Y204}$ phosphorylation was still inducible upon $F(ab')_2$ stimulation of CLL samples undergoing ibrutinib treatment, despite inhibition of BTK^{Y223} phosphorylation. These data suggest that a proportion of CLL cells enduring long-term ibrutinib therapy adapt to treatment, in part, by preserving BCR signal transduction through PI3K-AKT-FOXO1 and MAPK/ERK (146), which may represent a precursor to treatment resistance (13). Indeed, Kapoor *et al*. recently showed that ibrutinib-resistant CLL (MEC-1) and ABC-DLBCL (RIVA) cell lines possess enhanced AKT^{S473} phosphorylation and aberrant cytoplasmic localisation of FOXO3a. Interestingly, inhibition of PI3Kδ (idelalisib) or AKT (MK2206) signalling, or restoration of nuclear FOXO3a, enhanced ibrutinib-induced apoptosis in ibrutinib-resistant cells, demonstrating that re-engagement of FOXO activity nullifies acquired ibrutinib resistance (501). Collectively, therefore, FOXO re-activation can be exploited by drug combinations targeting BCR-mediated PI3K-AKT signalling at multiple levels to promote apoptosis and inhibit compensatory pathways that promote therapy resistance (397, 501). Encouragingly, our findings demonstrate that combining AZD8055 with ibrutinib inhibits BCR crosslinking-induced AKT-dependent $FOXO1^{T24}$ phosphorylation, leading to FOXO1 nuclear retention and enhanced DNA-binding activity, as evidenced by modulation of FOXO targets *FOXO1*, *CCND2* and *CDKN1A* ($p21^{CIP1}$). These data suggest that FOXO1 may underscore the anti-proliferative and apoptotic response to mTOR kinase and BTK inhibition downstream of the BCR. Indeed, Szydlowski *et al*. showed that FOXO1-depleted BCR-dependent DLBCL cells were resistant to combined inhibition of SYK (R406) and AKT (MK2206), indicating that FOXO1 mediated the cytotoxic effect of this combination (397).

Considerable evidence demonstrates that FOXOs are heavily implicated in the cytostatic and apoptotic response to PI3K-AKT inhibitors (344). Importantly, however, FOXOs have also been shown to facilitate therapy resistance, as demonstrated in doxorubicin-resistant breast cancer (MCF-7) (505) and CML (K562) (504) cell lines (344). In CLL-like mouse models, resistance to the PI3Kδ inhibitor GS-649443 occurred via upregulation and activation of the insulin-like

growth factor 1 receptor (IGFR1), mediated by functional activation of FOXO1 (147). Furthermore, FOXO1 activating mutations in NHL have been implicated in the resistance to rituximab, cyclophosphamide, doxorubicin, vincristine and prednisone (R-CHOP). Here, Pyrzynska *et al.* showed that CD20 expression was negatively regulated by FOXO1 in NHL cell lines, which resulted in reduced efficacy of the clinically-approved CD20 monoclonal antibody rituximab (503). Intriguingly, a phase II clinical trial (#NCT02007044) comparing ibrutinib with or without rituximab in patients with R/R CLL or untreated del(17p) patients revealed no improvement in PFS or OS (median follow-up of 36 months) by combining the two agents (525). One might speculate, therefore, that ibrutinib-induced FOXO1 activation may repress CD20 expression, reducing the efficacy of rituximab in CLL. Taken together, treatments that re-activate FOXOs are potentially problematic, as FOXOs clearly partake in feedback mechanisms to support cellular resilience (344). Therefore, a detailed understanding of FOXO1 transcriptional output in a CLL- and context-specific manner is required.

4.3.3 BCR ligation transiently enhances FOXO1 expression in CLL cells, suggesting FOXO1 is protected from proteasomal degradation

In a study by Hinman *et al.*, BCR engagement downregulated *FOXO1* mRNA expression in normal B cells via a mechanism facilitated by PI3K and BTK signalling (391), which largely corresponds to the well-established paradigm of AKT-mediated FOXO1 nuclear export (348) and proteasomal degradation (362-364). Reproducibly, we have shown that FOXO1 expression was diminished within 3 h following BCR ligation in CLL cells, before returning to 'basal' expression levels within 24 h. Interestingly, however, FOXO1 expression was significantly upregulated in the initial stages of BCR stimulation in CLL cells, which was not reported in mature B cells (390). Importantly, inhibition of BTK (ibrutinib), AKT (AZD5363) or mTOR kinase (AZD8055) decreased BCR crosslinking-induced FOXO1 upregulation, suggesting that FOXO1 is transiently stabilised in the cytoplasm of CLL cells following BCR engagement (529). The E3 ubiquitin ligase SKP2 interacts with and polyubiquitinates AKT-phosphorylated FOXO1^{S256} for targeted degradation via the proteasome, inhibiting FOXO1's tumour suppressor function (364). Interestingly, a study showed that SKP2 expression was low in CLL cells (527), suggesting that SKP2-mediated FOXO1 degradation might be functionally

impaired. Furthermore, FOXO3 has been shown to repress *SKP2* transcription, representing a feedforward mechanism promoting stabilisation of FOXOs (528). Nevertheless, we have demonstrated the FOXO1 downregulation (and likely proteasomal degradation) eventually occurred following BCR engagement, akin to mature B cells (391), so it seems unlikely that ubiquitin-proteasome machinery is fundamentally compromised. In normal B cells, 14-3-3σ protein has been shown to stabilise FOXO1 at levels required for optimal BCR signalling (529). Here, we have shown that 14-3-3 (pan) expression was almost exclusively cytoplasmic in response to BCR ligation. Interestingly, Dobson *et al*. demonstrated that 14-3-3ζ binding increased steady-state FOXO3 levels and protected cytoplasmic FOXO3 from dephosphorylation (and ultimately degradation), suggesting that 14-3-3 abundance may control and/or stabilise FOXO protein levels (345, 530). Ordinarily the abundance of 14-3-3 proteins is tightly regulated in a context-dependent manner (345). Indeed, aberrant overexpression of 14-3-3 proteins have been linked to poor prognosis (531) in breast cancer (532), lung cancer (533), glioblastoma (534) and MM (535). Although expression levels of 14-3-3 proteins have not yet been established in CLL, a study has shown that 14-3-3ζ facilitated Wnt5a/ROR1 signalling-dependent CLL migration and proliferation (536). Taken together, enhanced BCR crosslinking-induced cytoplasmic FOXO1 expression might be linked to an aberrant abundance of 14-3-3 proteins in CLL cells, which directs FOXO1 activity in a context-dependent manner (345, 530). Therefore, an assessment of 'steady-state' 14-3-3 protein expression and modulation downstream of BCR ligation warrants further investigation.

4.3.4 Abundant nuclear FOXO1 expression in CLL patient LN biopsies is indicative of transcriptional activation, suggesting that FOXO1 may contribute to the oncogenic programme of CLL

The GC is a specialised (and transient) microanatomical structure within SLOs wherein activated B cells undergo rapid clonal expansion and Ig SHM to generate affinity-enhanced antibodies in support of the adaptive immune response (392-394). On a functional level, the GC is polarised into a highly proliferative DZ (where B cells undergo clonal expansion and SHM) and a LZ (where B cell 'mutants' are activated, selected and ultimately differentiate into memory B

cells) (392-394). FOXO1 is highly expressed in the nucleus of GC B cells within the proliferative DZ, where it directs a gene expression programme favouring DZ formation (394, 395). Although established markers delineating the DZ (AID), LZ (FDC-M2 or CD23) or follicular B cell compartment (IgD) were omitted (394, 395), our results confirmed that FOXO1 was mainly localised in the nucleus of B220/CD45R$^+$ cells within structures resembling B cell follicles in WT mice. Contradicting its well-established role as tumour suppressor (396, 397, 404, 537), Xie *et al.* showed that nuclear FOXO1 expression in the DZ co-localised with Ki-67$^+$ staining in human tonsillar tissue (396). Correspondingly, FOXO1 ablation towards a later stage of the GC reaction impaired GC B cell proliferation (508). Collectively, these findings demonstrate that FOXO1, perhaps in concert with other transcriptional regulators (394), mediates and/or promotes proliferation in the GC DZ (394, 395, 508). Relevantly, this highlights the ability of FOXOs to promote oncogenesis in a context-dependent manner, as demonstrated previously (401, 408, 538, 539).

Several B cell malignancies, such as Burkitt lymphoma (BL) and GCB-DLBCL, originate from GC B cells (393). In contrast, CLL subsets have distinct cellular origins, with U-CLL possessing features of mature pre-GC CD5$^+$ B cells and M-CLL deriving from a post-GC CD5$^+$CD27$^+$ subset (43). Unlike typical GCs, however, CLL cells form ‘proliferation centres’ or ‘pseudofollicles’ within SLOs (2). In an earlier report, CLL and BL patient lymphoid tissue biopsies demonstrated the highest levels of FOXO1 expression among B cell NHLs (396). Here, we demonstrated ubiquitous nuclear FOXO1 expression in CLL patient LN biopsies irrespective of prognosis, which positively correlated with Ki-67$^+$ staining. Along these lines, FOXO1 expression was localised in the nucleus of ‘proliferative’ CD40L (+IL-21)-stimulated CLL cells *in vitro*. In our PKCαKR CLL-like mouse model, which forms irregular splenic follicular structures (485), FOXO1 was similarly, albeit not exclusively, expressed in the nucleus of ‘expansive’ B220/CD45R$^+$ PKCαKR cells. Although the direct transcriptional targets are unknown, these findings suggest that ‘active’ nuclear FOXO1 may instruct a gene expression programme that facilitates CLL proliferation, akin to DZ GC B cells (394, 395).

Interestingly, AKT^{S473} phosphorylation was also detected in B220/CD45R^{+} PKCαKR cells. Consistent with the observations made by Kabrani *et al.*, these data indicate that nuclear FOXO1 expression paradoxically coincides with PI3K-AKT activity in CLL-like PKCαKR cells (401). In B cell malignancies, recurrent FOXO mutations frequently perturb AKT recognition motifs, leading to aberrant FOXO1 nuclear retention (384, 401). Although FOXO1 mutations are rare in CLL (Michie and Hay, personal communication), studies have shown that significant proportions of BL (541) and DLBCL (398) patients possess recurrent FOXO1 mutations, which render the transcription factor insensitive to AKT-dependent inactivation (394). From a clinical standpoint, these mutations are often associated with unfavourable response rates (398), demonstrating the pathogenic role of nuclear FOXO1 among B cell malignancies. Indeed, Kabrani *et al.* recently showed that aberrant FOXO1 nuclear localisation (via disruption of the FOXO1^{T24} phosphorylation site) enhanced survival and proliferation in BL cells (inducing a gene expression programme reminiscent of proliferative DZ GC B cells), demonstrating that FOXO1 nuclear localisation represents an initiating event in BL pathogenesis (401). Although the mechanisms that permit nuclear localisation of 'genetically intact' FOXO1 amidst active PI3K-AKT signalling remain unclear (401), it is intriguing to contemplate that nuclear FOXO1 may promote favourable conditions that facilitate CLL progression.

4.3.5 Summary and future directions

Taken together, these findings demonstrate that BCR crosslinking negatively regulates FOXO1 DNA-binding activity via AKT-dependent FOXO1 phosphorylation and nuclear export. Inactivation of FOXO1, the most abundantly expressed FOXO in CLL cells, likely represents a functionally important consequence of BCR engagement. Given its widely-considered role as a tumour suppressor, one might consider that FOXO1 inactivation might facilitate and/or enable favourable conditions for CLL cell survival and proliferation, akin to normal B cells (387, 390) and DLBCL (397). For this reason, subverting BCR signalling-induced FOXO1 inactivation might unleash its pro-apoptotic and anti-proliferative properties. Indeed, we have shown that elimination of BCR signal transduction, via AKT (AZD5363), mTOR kinase (AZD8055) or BTK (ibrutinib) inhibition, re-engaged FOXO1 DNA-binding activity by preventing FOXO1 nuclear export, suggesting that FOXO1 is an effector of BCR signalling inhibition and mediates treatment

response. This being said, nuclear FOXO1 expression in 'proliferative' CLL cells and CLL patient LN biopsies is at odds with its '*bona fide*' tumour suppressor role (347). Increasing evidence attests to the ability of FOXOs to elicit homeostatic functions that support cellular resilience (344, 506). Therefore, strict regulation of FOXO1 activity may facilitate CLL disease maintenance in a context-dependent manner. In the next chapter, we will investigate whether FOXO1 is an effector of treatment response using genetic (shRNA knockdown) and pharmacological inhibition. At the same time, these methods will enable us to assess the importance of FOXO1 in CLL disease maintenance.

5 Results III

5.1 Introduction

Alongside their well-established role as tumour suppressors (396, 404), considerable evidence supports the notion that FOXOs are mediators of cellular resilience (506). In the same vein, FOXOs have been shown to facilitate tumour development/progression in certain cellular contexts (344). Notwithstanding the context-dependent 'dual-faceted' properties of FOXO transcription factors in normal and malignant B cells (384), little is known about functionality of FOXOs in CLL disease biology.

Earlier, we demonstrated that elimination of BCR signal transduction inhibited AKT-dependent FOXO1^{T24} phosphorylation, upheld FOXO1 nuclear retention and enhanced FOXO1 DNA-binding activity in CLL cells. On a functional level, this corresponded to changes in FOXO target gene/protein expression, particularly those involved in signal transduction, cell cycle arrest and apoptosis. These findings suggest that FOXO1 operates as an effector of truncated BCR signalling. On the other hand, our data revealed that FOXO1 is localised in the nucleus of CLL patient LN biopsies and 'proliferative' CD40L (+IL-21)-stimulated CLL cells, indicating that FOXO1 might be implicated in CLL maintenance. One might speculate, therefore, that strict regulation of FOXO1 activity within an optimal range promotes CLL cell homeostasis, and drastic changes in FOXO1 activity away from this established 'setpoint' tilts the scales towards tumour suppression, as demonstrated in DLBCL (397) and pre-BCR^{+} BCP-ALL (402, 403). However, without assessing the importance of FOXO1 (either through genetic or pharmacological inhibition), these observations cannot be conclusively resolved.

In this chapter, we investigate the functional consequence of shRNA-mediated FOXO1 knockdown on both CLL maintenance and the response to COMBO treatment. Furthermore, we examine the sensitivity of CLL cells to the FOXO1 inhibitor AS1842856 and ask whether pharmacological FOXO1 inhibition protects CLL cells from the cytotoxic and cytostatic effect of the COMBO treatment.

5.1.1 Aims

I. Explore the expression, subcellular localisation and activity of FOXO1 in HG-3 and MEC-1 cells.

II. Generate FOXO1-targeting shRNA molecules to investigate the functional impact of FOXO1 knockdown on CLL maintenance and the response to the COMBO treatment.

III. Examine whether FOXO1 activity, via pharmacological FOXO1 inhibition (AS1842856), is required to elicit the functional response to the COMBO treatment.

IV. Analyse the transcriptional response (established FOXO target genes) to the COMBO treatment following FOXO1 inhibition.

5.2 Results

5.2.1 HG-3 and MEC-1 cells express nuclear FOXO1 amidst activated PI3K-AKT signalling

Previously, we demonstrated that FOXO1 expression was significantly higher in LN biopsies of patients harbouring poor-prognostic progressive disease markers compared to those with indolent disease (Figure 4.19a,b). We therefore

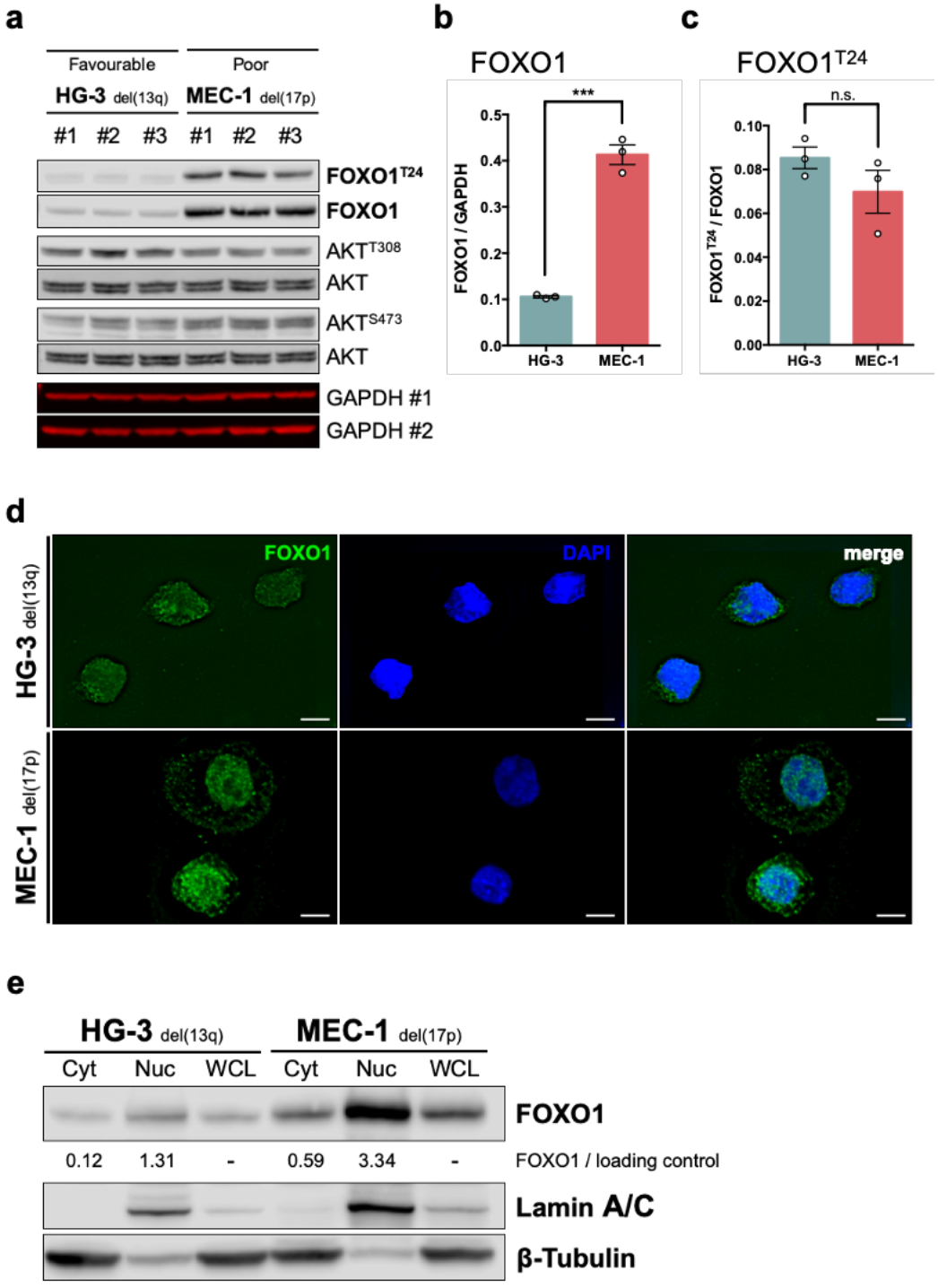

Figure 5.1 - CLL cell lines express nuclear FOXO1, despite AKT kinase activity.

(a) Western blot of FOXO1^{T24}, FOXO1, AKT^{T308}, AKT^{S473}, AKT and GAPDH (#1 and #2 representing mirror blots; loading control) expression in HG-3 (n=3) and MEC-1 (n=3) cells. (b) Relative FOXO1 expression and (c) FOXO1^{T24} phosphorylation levels in HG-3 (n=3; grey bars) and MEC-1 (n=3; red bars), as determined by densitometry. (d) Representative IF micrograph (100x) of HG-3 (n=2; top panel) and MEC-1 cells (n=2; bottom panel) stained with FOXO1 (green; left panel) and counter stained with DAPI (blue; middle panel). Individual channel and merged (merge; right panel) images are shown. Scale bar = 5 μm. (e) Representative western blot (n=2) depicting cellular fractionation of HG-3 and MEC-1 cells. Blots have been stained for FOXO1, Lamin A/C (nuclear marker; loading control) and β-Tubulin (cytoplasmic marker; loading control). Cyt = cytoplasmic fraction; Nuc = nuclear fraction; WCL = whole cell lysate. Relative FOXO1 expression within each compartment calculated by FOXO1 relative to β-Tubulin (cytoplasmic fraction) or Lamin A/C (nuclear fraction). Statistics calculated by unpaired Student's t-test, where *** $p \leq 0.001$.

assessed FOXO1 expression, activity and subcellular localisation in CLL cell lines HG-3 and MEC-1, which possess prognostic features associated with favourable and poor prognosis, respectively (Figure 5.1a,b). These data showed that FOXO1 expression was significantly higher in MEC-1 cells compared to HG-3 cells (Figure 5.1a,b). Despite marked differences in FOXO1 expression, relative AKT-dependent FOXO1^{T24} phosphorylation levels were comparable in HG-3 and MEC-1 cells, irrespective of prognostic factors (Figure 5.1a,c). We next assessed localisation of FOXO1 in HG-3 and MEC-1 cells by IF (Figure 5.1d) and subcellular fractionation (Figure 5.1e). Notably, despite AKT kinase activity (Figure 5.1a) and AKT-dependent FOXO1^{T24} phosphorylation (Figure 5.1a,c), both approaches confirmed that HG-3 and MEC-1 cells express nuclear FOXO1 (Figure 5.1d,e).

5.2.2 COMBO treatment promotes FOXO1 nuclear localisation and enhances activity in MEC-1 cells

Earlier experiments revealed that AZD8055 treatment inhibited AKT^{S473} phosphorylation in HG-3 and MEC-1 cells, whereas AKT^{T308} phosphorylation was largely unaffected (Figure 3.9). In contrast, single-agent ibrutinib or COMBO successfully diminished both AKT^{S473} and AKT^{T308} phosphorylation in HG-3 and MEC-1 cells (Figure 3.9). Because treatment reduced AKT kinase activity, it was of interest to discover whether this had a commensurate impact on AKT-dependent FOXO1^{T24} phosphorylation. HG-3 and MEC-1 cells were subjected to short-term treatment with AZD8055, ibrutinib or COMBO. Thereafter, the phosphorylation status of FOXO1^{T24} was assessed (Figure 5.2a,b). Ibrutinib significantly reduced AKT-dependent FOXO1^{T24} phosphorylation in HG-3 cells, while AZD8055 (p = 0.07) and the combination treatment (p = 0.056) resulted in a near-significant reduction in FOXO1^{T24} phosphorylation (Figure 5.2a,b). Furthermore, ibrutinib and the COMBO treatment significantly inhibited

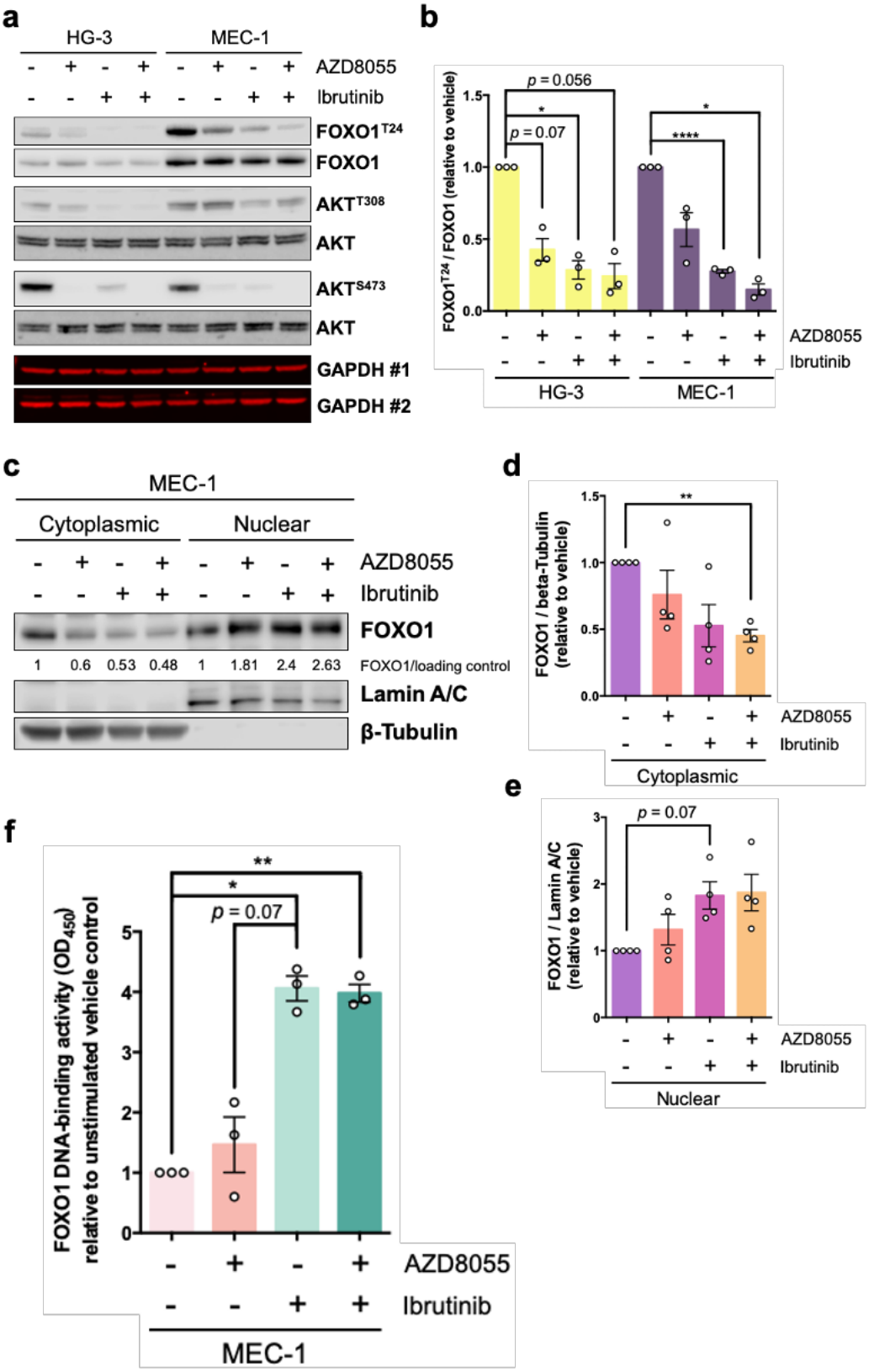

Figure 5.2 - COMBO treatment inhibits AKT-mediated FOXO1^{T24} phosphorylation, promotes FOXO1 cytoplasmic translocation and increases FOXO1 DNA-binding activity in MEC-1 cells.

(a) Representative western blot of HG-3 (n=3) and MEC-1 (n=3) cells treated with AZD8055 (100 nM), Ibrutinib (1 μM), COMBO or DMSO vehicle control for 1 h. Blots were probed for FOXO1^{T24}, FOXO1, AKT^{T308}, AKT^{S473}, AKT and GAPDH (loading control; #1 and #2 referring to mirror blots). (b) Relative FOXO1^{T24} phosphorylation levels in HG-3 (n=3; yellow bars) and MEC-1 cells (n=3; purple bars). (c) Subcellular fractionation of MEC-1 cells (n=3) treated with AZD8055 (100 nM), ibrutinib (1 μM), COMBO or vehicle control for 1 h. Cytoplasmic and nuclear fractions were

generated. Blots were probed for FOXO1, Lamin A/C and β-Tubulin. Densitometry for cytoplasmic (FOXO1/β-Tubulin) and nuclear (FOXO1/Lamin A/C) FOXO1 expression are shown (relative to unstimulated vehicle control). (d, e) Densitometry of FOXO1 expression in (d) cytoplasmic and (e) nuclear fractions from MEC-1 cells (n=4), treated as described in (a). Densitometry calculated as in (c). (f) FOXO1 DNA-binding activity (OD_{450}) of MEC-1 cells (n=3), treated as described in (a). Individual datapoints are represented by white circles. Data expressed as the mean ± SEM. Statistics calculated by one-way ANOVA, where * $p \leq 0.05$, ** $p \leq 0.01$, **** $p \leq 0.0001$.

$FOXO1^{T24}$ phosphorylation in MEC-1 cells, whereas AZD8055 visibly reduced $FOXO1^{T24}$ phosphorylation (Figure 5.2a,b). We next examined treatment-induced FOXO1 localisation in MEC-1 cells by subcellular fractionation (Figure 5.2c-e). These data showed that nuclear FOXO1 localisation was enhanced in response to AZD8055, ibrutinib and COMBO treatment (Figure 5.2c-e). AZD8055 and ibrutinib individually reduced cytoplasmic FOXO1 expression, which was concurrently elevated in the nuclear fraction (Figure 5.2c-e). Moreover, COMBO treatment significantly decreased FOXO1 expression in the cytoplasmic fraction, while nuclear FOXO1 was simultaneously enhanced (Figure 5.2c-e). Encouragingly, nuclear FOXO1 expression largely mirrored relative $FOXO1^{T24}$ phosphorylation levels (Figure 5.2a-e). Finally, we asked whether treatment-induced FOXO1 nuclear accumulation conferred an increase in FOXO1 activity in MEC-1 cells (Figure 5.2f). These data revealed that ibrutinib significantly elevated FOXO1 DNA-binding activity in MEC-1 cells, while AZD8055 treatment only modestly enhanced FOXO1 activity (Figure 5.2f). Interestingly, FOXO1 activity was near-significantly greater in ibrutinib-treated MEC-1 cells compared to AZD8055 treatment ($p = 0.07$; Figure 5.2f). The COMBO treatment significantly increased FOXO1 transcriptional activity comparable to ibrutinib-treated MEC-1 cells (Figure 5.2f).

5.2.3 Generation of *FOXO1* targeting shRNAs using the pLKO.1 lentiviral vector

Nuclear FOXO1 expression in HG-3 and MEC-1 cells indicates that FOXO1 is (to an extent) transcriptionally active (Figure 5.1). Therefore, one might speculate that FOXO1 facilitates CLL progression by maintaining cellular homeostasis. Equally, COMBO treatment-induced FOXO1 nuclear translocation (Figure 5.2c-e) and enhanced DNA-binding activity (Figure 5.2f) suggests FOXO1 may play a role in mediating the response to treatment. We therefore assessed the importance of FOXO1 by transducing MEC-1 cells with shRNA lentiviral vectors (Figure 5.3a). shRNA constructs targeting distinct regions of the *FOXO1* transcript were

evaluated (Table 2.19; referred to as #1, #2, #3, #4 and #5), alongside scrambled (Scr) shRNA control. FOXO1 depletion was verified by assessing transcript abundance and protein levels by RT-qPCR (Figure 5.3b) and Western blotting (Figure 5.3e), respectively, at 7- and 13-days post-transduction (relative to Scr control). *FOXO1* expression was repressed by constructs #2 (0.68), #4 (0.85) and #5 (0.41) at 13-days post-transduction, whereas constructs #1 (1.04) and #3 (1.23) enhanced *FOXO1* expression (Figure 5.3b). Of note, *FOXO1* transcript levels were efficiently depleted by construct #5 (0.5) at 7-days post-transduction, whereas constructs #2 (0.99) and #4 (0.92) were largely ineffective (Figure 5.3b). Western blotting revealed that constructs #4 (0.86) and #5 (0.34) repressed FOXO1 protein levels compared to Scr control 13-days post-transduction (Figure 5.3e). Although construct #2 reduced *FOXO1* transcript abundance (0.68), FOXO1 protein levels (1.01) were unaffected (Figure 5.3e). Interestingly, while construct #1 was ineffective at reducing *FOXO1* mRNA expression (1.04), FOXO1 protein levels (0.71) were repressed (Figure 5.3e). Notably, FOXO1 protein levels were also efficiently depleted by construct #1 (0.89), #4 (0.74) and #5 (0.4) at 7-days post-transduction (Figure 5.3e). As FOXOs exhibit functional redundancy in the context of tumour suppression (404), we assessed the transcript abundance of *FOXO3* (Figure 5.3c) and *FOXO4* (Figure 5.3d) in FOXO1-depleted MEC-1 cells. *FOXO3* transcript levels were enhanced in constructs #1 (1.22), #2 (1.29), #3 (1.33), #4 (1.35) and #5 (1.21) compared to Scr control 13-days post-transduction (Figure 5.3c). Conversely, *FOXO4* expression was decreased by constructs #1 (0.75), #2 (0.86), #4 (0.74) and #5 (0.88), whereas construct #3 (1.16) marginally elevated *FOXO4* expression (Figure 5.3d). Based on these data, we chose two shRNA constructs that reduced FOXO1 expression: #1 (Clone ID: TRCN0000039582) targeting the *FOXO1* coding region (CDS) and #5 (Clone ID TRCN0000039578) targeting the *FOXO1* 3' untranslated region (3' UTR). Repressing FOXO1 expression via shRNA-mediated knockdown reduces the proportion of transcriptionally active FOXO1 (Figure 5.3f). As such, this methodology will provide insights into the importance of FOXO1 in facilitating MEC-1 cellular homeostasis and mediating the response to treatment. Although FOXO1 knockdown by construct #1 was marginal, it was important to choose at least two constructs to validate the functional effect of FOXO1 knockdown. Equally, the data generated via construct #1 may provide interesting insights due to a 'graded' effect. Of note, because construct #1

appears to upregulate *FOXO1* mRNA expression, the construct may act post-translationally.

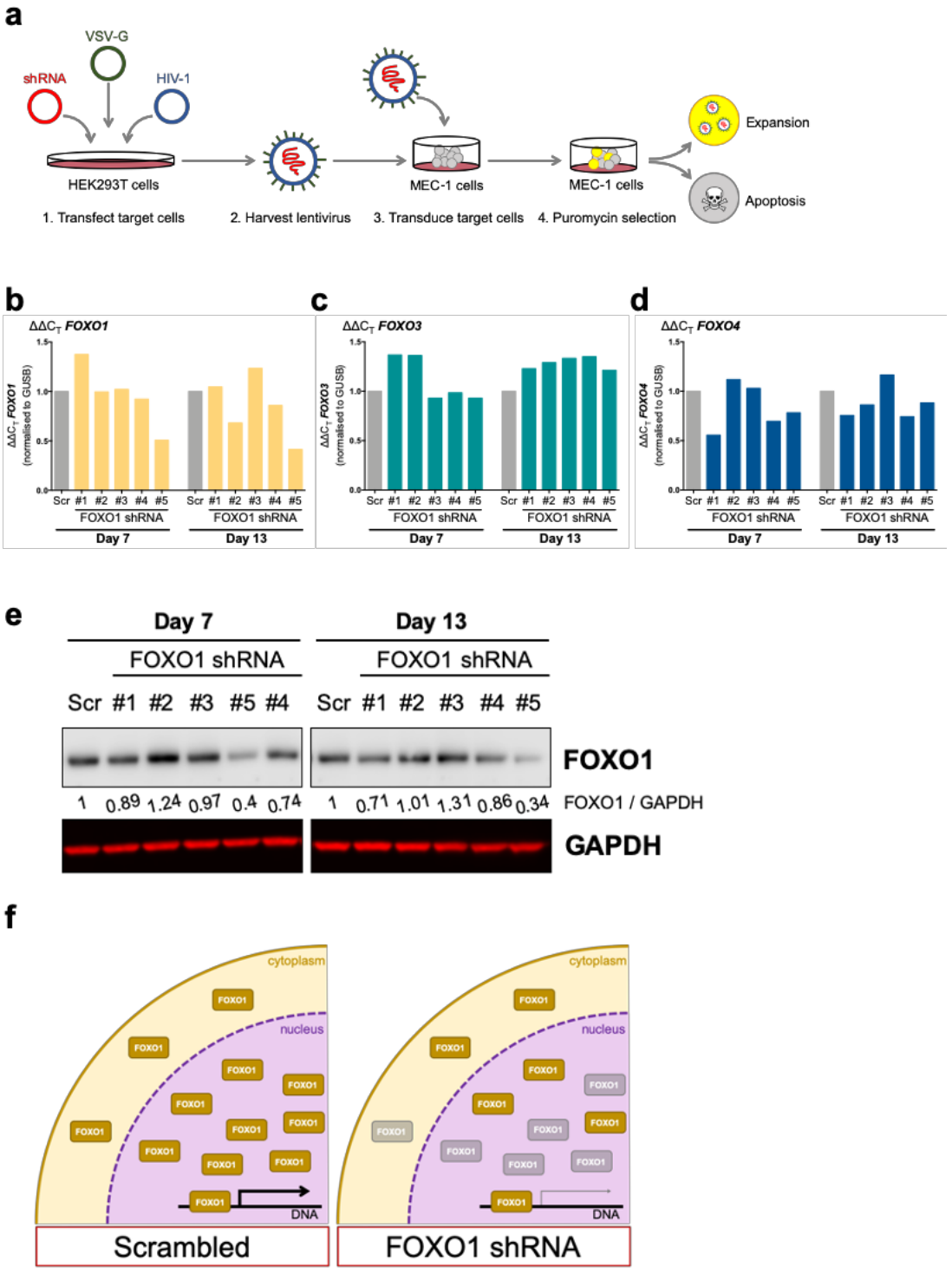

Figure 5.3 - Generation of FOXO1-targeting shRNA-expressing lentiviral constructs. (a) Schematic depicting experimental design (modified from (420)) . HEK293T cells were transfected and shRNA-containing lentiviral particles subsequently harvested. Lentiviral-transduced MEC-1 cells were puromycin selected and expanded. (b– d) RT-qPCR to assess expression of (b) *FOXO1* (yellow bars), (c) *FOXO3* (turquoise bars) and (d) *FOXO4* (dark blue bars) in puromycin-selected (7 and 13 days) MEC-1 cells transduced with FOXO1-targeting shRNA constructs #1, #2, #3, #4, #5 and Scr control. The $\Delta\Delta C_T$ method was used to calculate expression levels, where samples were first normalised to the internal reference gene *GUSB* and then made relative to Src control. (e) Representative western blot of puromycin-selected (7 and 13 days) MEC-1 cells

transduced with FOXO1-targeting shRNA constructs #1, #2, #3, #4, #5 Scr control. Blots were probed for FOXO1 and GAPDH (loading control). Densitometry (FOXO1/GAPDH) for each construct is shown. (f) Schematic depicting FOXO1 expression and activity in CLL cells transduced with Scr control (left panel) and *FOXO1*-targeting shRNA (right panel). Reduced FOXO1 expression via shRNA-mediated knockdown reduces the proportion of transcriptionally active FOXO1.

5.2.4 FOXO1 expression is enhanced in FOXO1-depleted MEC-1 cells treated with COMBO

We first assessed the effect of shRNA-mediated FOXO1 knockdown by interrogating the AKT-FOXO1 axis. Interestingly, studies have demonstrated that FOXO1 enhances mTORC2 activity and resultant AKT^{S473} phosphorylation via upregulation of the mTORC2 component RICTOR (542, 543). Therefore, we examined FOXO1 ($FOXO1^{T24}$) and AKT (AKT^{T308} and AKT^{S473}) activity in FOXO1-depleted MEC-1 cells with or without long-term (48 h) COMBO treatment. Western blotting showed that FOXO1 expression was diminished by constructs #1 and #5 compared to Scr control (Figure 5.4a). Notably, however, FOXO1 expression (relative to untreated) was elevated in COMBO-treated MEC-1 cells transduced with constructs #1 ($p = 0.13$) and #5, whereas FOXO1 levels were unaffected by COMBO treatment in Scr control cells (Figure 5.4a,b). Furthermore, FOXO1 expression appeared greater in COMBO-treated MEC-1 cells transduced with construct #5 compared to Scr control ($p = 0.07$; Figure 5.4a,b). $FOXO1^{T24}$ phosphorylation was moderately enhanced by construct #1 compared to Scr control, whereas $FOXO1^{T24}$ phosphorylation levels were near-significantly ($p = 0.051$) decreased by construct #5 (Figure 5.4a,c). Interestingly, $FOXO1^{T24}$ phosphorylation was largely unaffected by long-term COMBO treatment in MEC-1 cells transduced with constructs #1, #5 or Scr control (relative to untreated) (Figure 5.4c). However, relative $FOXO1^{T24}$ phosphorylation was significantly decreased in COMBO-treated MEC-1 cells transduced with construct #5 compared to construct #1 (Figure 5.4c). Additionally, a trend towards reduced $FOXO1^{T24}$ phosphorylation was observed in COMBO-treated MEC-1 cells transduced with construct #5 compared to Scr control cells ($p = 0.11$; Figure 5.4c). AKT^{T308} phosphorylation was largely unaffected by FOXO1 knockdown (constructs #1 and #5) compared to Scr control (Figure 5.4a,d). However, although long-term COMBO treatment had no effect on AKT^{T308} phosphorylation in Scr control cells, AKT^{T308} phosphorylation was significantly inhibited by COMBO treatment in FOXO1-depleted MEC-1 cells transduced with construct #1 and #5 (relative to

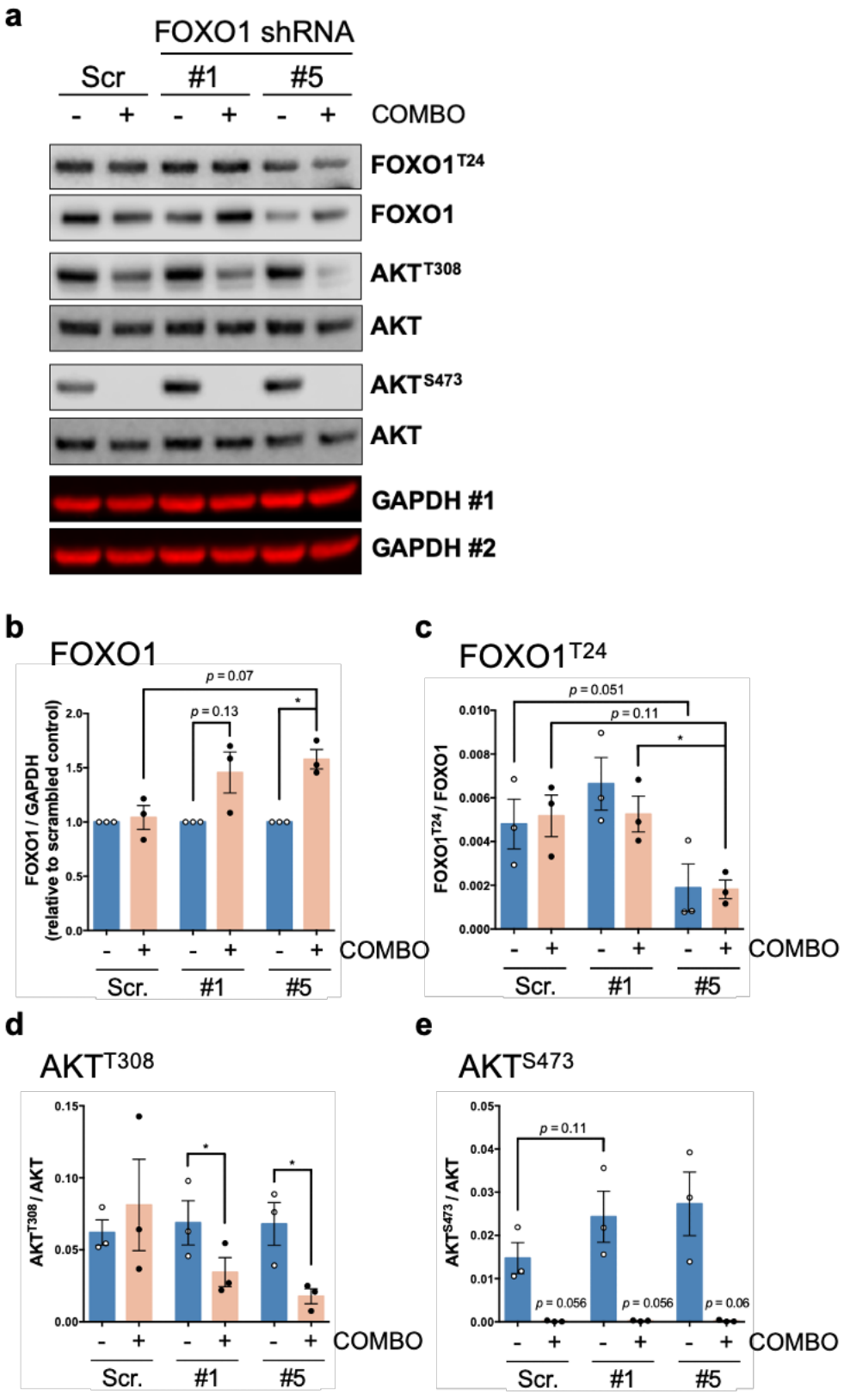

Figure 5.4 - FOXO1 knockdown reduces AKT-mediated FOXO1^{T24} phosphorylation and increases FOXO1 expression following COMBO treatment.
(a) Representative western blot of puromycin-selected MEC-1 cells (n=3) transduced with FOXO1-targeting shRNA constructs #1, #5 or Scr control and treated with COMBO or vehicle control for 48 h. Blots were probed for FOXO1, FOXO1^{T24}, AKT^{T308}, AKT^{S473}, AKT and GAPDH (loading control; #1 and #2 referring to mirror blots). (b) Relative FOXO1 expression and (c - e) phosphorylation levels of (c) FOXO1^{T24}, (d) AKT^{T308} and (e) AKT^{S473} in MEC-1 cells (n=3) transduced with FOXO1-targeting shRNA constructs #1, #5 or Scr control and treated with (+; peach bars) or without (-; blue bars) COMBO for 1 h. FOXO1 expression following COMBO treatment is relative to vehicle control

for each construct. Individual datapoints are represented by white or black circles. Data expressed as the mean ± SEM. Statistics calculated by one-way ANOVA, where * $p \leq 0.05$.

untreated) (Figure 5.4d). Furthermore, COMBO-induced AKT^{T308} phosphorylation levels were visibly less in FOXO1-depleted MEC-1 cells (constructs #1 and #5) compared with Scr control cells (Figure 5.4d). Interestingly, AKT^{S473} phosphorylation was modestly enhanced by FOXO1 repression via constructs #1 ($p = 0.11$) and #5 compared to Scr control (Figure 5.4e). In support of earlier findings (Figure 3.7b), COMBO treatment near-significantly inhibited AKT^{S473} phosphorylation in MEC-1 cells with all constructs (Figure 5.4a,e).

5.2.5 FOXO1 knockdown reduces COMBO-induced BIM upregulation in MEC-1 cells

Yusuf *et al*. showed that treatment of mature B cells with PI3K inhibitors or ectopic expression of FOXO1-A3 mediated cell death in a FOXO1-dependent manner (390). Although MEC-1 cell viability was largely insensitive to COMBO treatment (Figure 3.10a,d), previous experiments demonstrated that pro-apoptotic FOXO1-target BIM (387) was upregulated in response to COMBO treatment (Figure 3.10f). To determine the effect of FOXO1 depletion on cell viability, MEC-1 cells stably transduced with constructs #1, #5 or Scr control (Figure 5.5a) were incubated with or without COMBO for 48 h. Thereafter, the cells were stained with Annexin V/7-AAD and analysed by flow cytometry (Figure 5.5b-d). Although MEC-1 cell viability was largely unaffected by shRNA-mediated FOXO1 knockdown, a slight increase in cell viability was observed in MEC-1 cells transduced with construct #5 (Figure 5.5b,c). Consistent with these findings, apoptosis was modestly decreased in FOXO1-depleted MEC-1 cells (construct #5) compared to Scr control (Figure 5.5a,d). In contrast with earlier experiments (Figure 3.10a,d), COMBO treatment significantly reduced viability of Scr control cells (Figure 5.5b,c), corresponding to a significant increase in apoptosis (Figure 5.5b,d). Equally, however, cell viability of FOXO1-depleted MEC-1 cells was also significantly diminished by COMBO treatment (Figure 5.5b,c), reflected by a concomitant increase in apoptosis (Figure 5.5b,d). Thus, FOXO1 knockdown was unable to protect MEC-1 cells from COMBO-induced cell death (Figure 5.5b-d). Nevertheless, given that COMBO treatment upregulated BIM expression in MEC-1 cells (Figure 3.10f), it was of interest to determine whether COMBO-induced BIM modulation was dependent on FOXO1 expression. We therefore analysed BIM

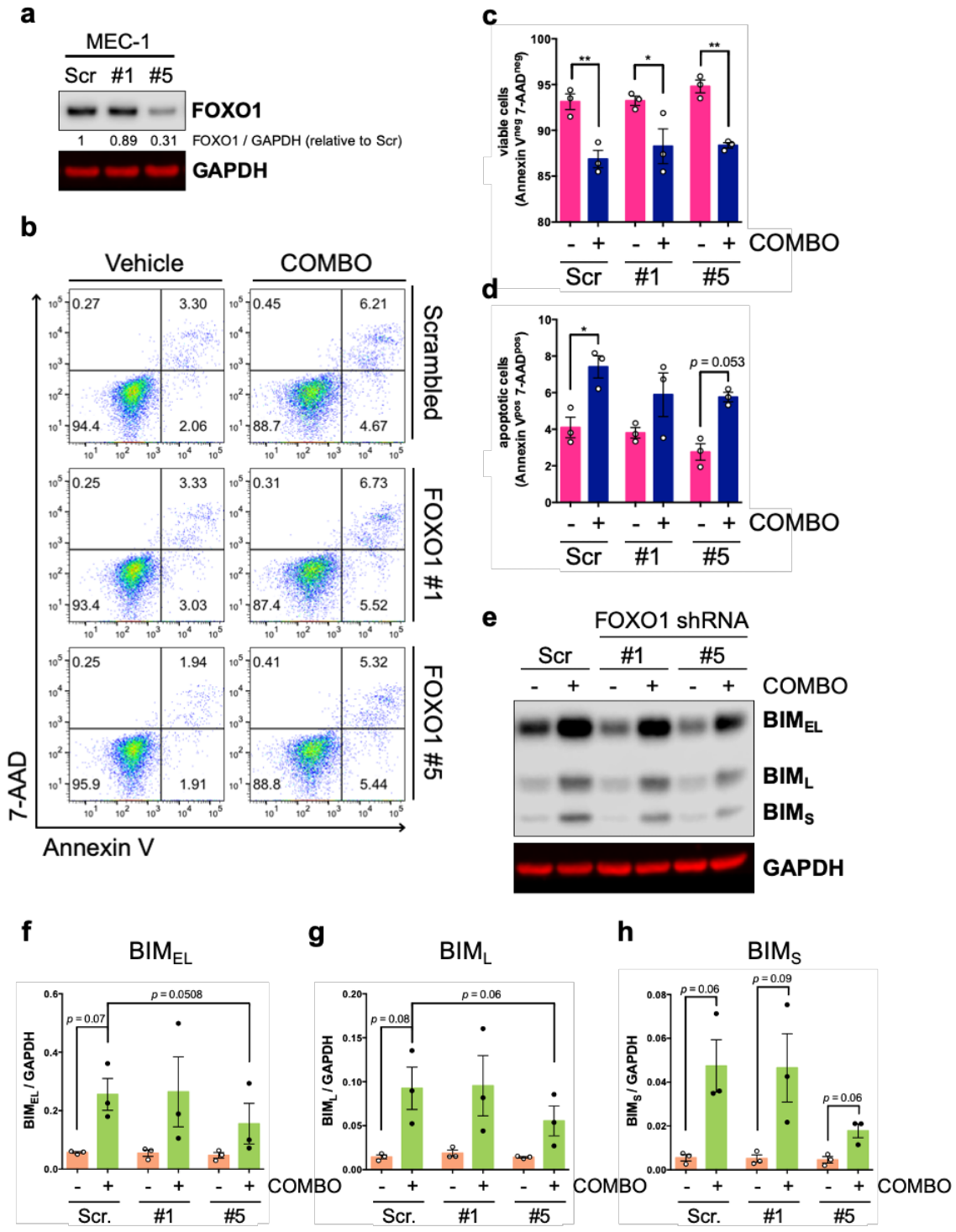

Figure 5.5 - shRNA-mediated knockdown of FOXO1 does not impact cell survival in MEC-1 cells.

(a) Representative western blot of FOXO1 expression in MEC-1 cells transduced with FOXO1-targeting shRNA constructs #1, #5 or Scr control. Blots were probed for FOXO1 and GAPDH (loading control). Densitometry (FOXO1/GAPDH) for each construct is shown. (b) Representative FACS plot of transduced (#1, #5 or Scr control) MEC-1 cells stained with Annexin V/7-AAD to assess cell viability following treatment with COMBO or vehicle control for 48 h. (c) Percentage viable and (d) apoptotic MEC-1 (n=3) cells transduced with FOXO1-targeting shRNA constructs #1, #5 or Scr control and treated with COMBO (pink bars) or vehicle control (blue bars) for 48 h, as described in (b). Viability is defined as Annexin V^{neg} and 7-AAD^{neg}; apoptotic cells are defined as Annexin V^{pos} and 7-AAD^{pos}. (e) Representative western blot of transduced (#1, #5 or Scr control) MEC-1 cells (n=3) treated with COMBO or vehicle control for 48 h. Blots were probed for BIM (BIM_{EL}, BIM_L, and BIM_S) and GAPDH (loading control). (f - h) Densitometry of (f) BIM_{EL}, (g) BIM_L and (h) BIM_S expression in transduced (#1, #5 or Scr control) MEC-1 cells (n=3) treated with COMBO (+; green bars) or vehicle control (-; orange bars) for 48 h, as described in (e). Expression

is relative to GAPDH. Individual datapoints are represented by white or black circles. Data expressed as the mean ± SEM. Statistics calculated by one-way ANOVA, where * p ≤ 0.05, ** p ≤ 0.01.

(BIM_{EL}, BIM_L, and BIM_S) protein expression in FOXO1-depleted MEC-1 cells following COMBO treatment (Figure 5.5e-h). Western blotting showed that BIM_{EL} (Figure 5.5e,f), BIM_L (Figure 5.5e,g), and BIM_S (Figure 5.5e,h) expression were largely unaffected by FOXO1 knockdown via constructs #1 or #5 (Figure 5.5e-h). As expected, COMBO treatment upregulated BIM_{EL} (p = 0.07; Figure 5.5e,f), BIM_L (p = 0.08; Figure 5.5e,g) and BIM_S (p = 0.06; Figure 5.5e,h) expression in Scr control cells. Although BIM_{EL}, BIM_L, and BIM_S expression was also notably elevated by COMBO treatment in FOXO1-depleted MEC-1 cells (Figure 5.5e-h), COMBO-induced upregulation of BIM_{EL} (p = 0.0508; Figure 5.5e,f), BIM_L (p = 0.06; Figure 5.5e,g), and BIM_S (Figure 5.5e,h) was visibly reduced in MEC-1 cells transduced with construct #5 compared with Scr control.

5.2.6 MEC-1 cell size is unaffected by shRNA-mediated FOXO1 repression

As explained earlier, mTORC1 regulates cell size via the coordinated activities of 4E-BP1 and S6K1 (442). FOXOs have been shown to downregulate mTORC1 activity through upregulation of sestrin 3 (SESN3), which activates mTORC1-negative regulators TSC1/2 (384, 542). Indeed, overexpression of FOXO1 has been reported to reduce cardiomyocyte cell size, which was blocked by expression of a dominant-negative FOXO1 construct (544). We therefore assessed the impact of FOXO1 knockdown on MEC-1 cell size by flow cytometry (Figure 5.6). These data showed that MEC-1 cell size was largely unaffected by shRNA-mediated FOXO1 knockdown (Figure 5.6a-c). However, we noted that cell size was modestly enhanced in FOXO1-depleted MEC-1 cells via construct #5 (Figure 5.6c). Because earlier experiments demonstrated that COMBO treatment reduced MEC-1 cell size (Figure 3.11), we determined whether FOXO1 knockdown could prevent MEC-1 cell size reduction upon COMBO treatment (Figure 5.6). As expected, COMBO treatment significantly decreased cell size in Scr control cells (Figure 5.6a-c). However, COMBO treatment also significantly decreased cell size in MEC-1 cells transduced with constructs #1 and #5 (Figure 5.6a-c). Thus, FOXO1 depletion had no effect on COMBO-induced MEC-1 cell size reduction (Figure 5.6a-c).

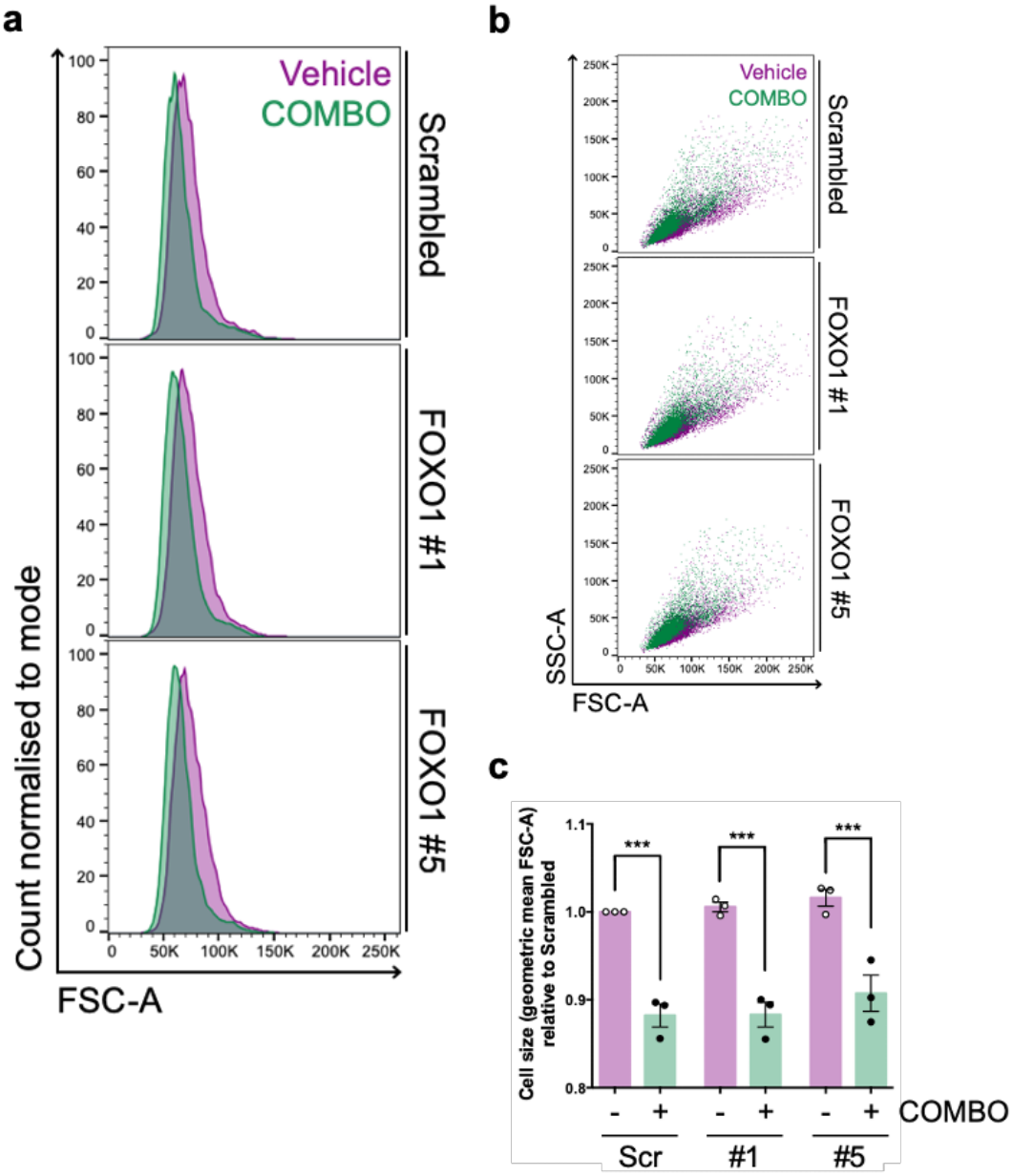

Figure 5.6 - FOXO1 knockdown does not affect MEC-1 cell size or COMBO-induced cell contraction.
(a) Representative FACS histogram displaying geometric mean of forward scatter-area (FSC-A) of transduced (FOXO1 #1, FOXO1 #5 or Scrambled control) MEC-1 cells treated with COMBO (green histograms) or DMSO vehicle control (Vehicle; purple histograms) for 48 h. (b) Representative FACS plot (forward scatter-area (FSC-A) against sideward scatter-A (SSC-A)) assessing cell size of transduced (FOXO1 #1, FOXO1 #5 or Scrambled control) MEC-1 cells, treated as described in (a). (c) Relative cell size (geometric mean) of transduced (#1, #5 or Scr control) MEC-1 (n=3) cells treated with (+; green bars) or without (-; purple bars), as described in (a). Geometric means for each condition are relative to Scrambled (Scr) vehicle control. Individual datapoints are represented by white or black circles. Data expressed as the mean ± SEM. Statistics calculated by one-way ANOVA, where *** $p \leq 0.001$.

5.2.7 Cytostatic impact of COMBO treatment is unaffected by FOXO1 depletion, despite reduced p27^{KIP1} expression

Overexpression of constitutively active FOXO1 (FOXO1-A3) in mature B cells (390), cHL cell lines (396) or DLBCL cell line DHL4 (397) has been shown to induce G1 cell cycle arrest. Equally, we earlier showed that COMBO treatment, which enhances FOXO1 activity (Figure 5.2f), inhibits G1/S cell cycle progression in MEC-1 cells (Figure 3.12). We therefore investigated the impact of FOXO1 depletion on cell cycle progression with and without COMBO treatment by flow cytometry (Figure 5.7). Analysis of DNA content revealed that FOXO1 knockdown had little effect on cell cycle progression in unsynchronized MEC-1 cells transduced with constructs #1 or #5 compared to Scr control (Figure 5.7a,b). As expected, COMBO treatment induced G1 cell cycle arrest in Scr control cells (Figure 5.7a,b). However, COMBO treatment also inhibited cell cycle progression in FOXO1-depleted MEC-1 cells (Figure 5.7a,b). As such, FOXO1 knockdown was unable to rescue MEC-1 cells from COMBO treatment-induced cell cycle arrest.

Earlier experiments demonstrated that MEC-1 cell proliferation was effectively inhibited by the COMBO treatment (Figure 3.13a-c), corresponding to an upregulation of the CDKI p27^{KIP1} (Figure 3.13d,e), a putative FOXO-target (377, 382). We therefore addressed whether the anti-proliferative effect of COMBO treatment depended on FOXO1 expression (Figure 5.8). Of note, a recent study showed that FOXO1-repressed DLBCL cell lines were effectively resistant to SYK or AKT inhibitor-induced cell growth inhibition (397). CTV-stained FOXO1-depleted MEC-1 cells were treated with or without COMBO for 72 h. Thereafter, cell proliferation was analysed by flow cytometry (Figure 5.8a,b). These data showed that FOXO1 knockdown via constructs #1 and #5 had no effect on cell proliferation (Figure 5.8a,b). Expectedly, COMBO treatment significantly inhibited cell proliferation in Scr control cells (Figure 5.8a,b). However, COMBO treatment also significantly inhibited cell proliferation in FOXO1-depleted MEC-1 cells (Figure 5.8a,b). Thus, FOXO1 knockdown was unable to protect MEC-1 cells from the cytostatic effect of the COMBO treatment. Nevertheless, studies have shown that FOXO1 knockdown reduces *CDKN1B* (p27^{KIP1}) expression in DLBCL cell lines DHL4 and Ly7 (397), while overexpression of FOXO1 elevates *CDKN1B* (p27^{KIP1}) expression in cHL cell lines (396). We therefore examined modulation of FOXO-targets p27^{KIP1} (Figure 5.8c,d) and p21^{CIP1} (Figure 5.8c,e) in FOXO1-

depleted MEC-1 cells with and without COMBO treatment by Western blotting. Compared to Scr control, these data showed that $p27^{KIP1}$ expression was largely unaffected by FOXO1 knockdown in MEC-1 cells (Figure 5.8c,d). However, we noted that FOXO1 depletion via construct #5 resulted in a modest

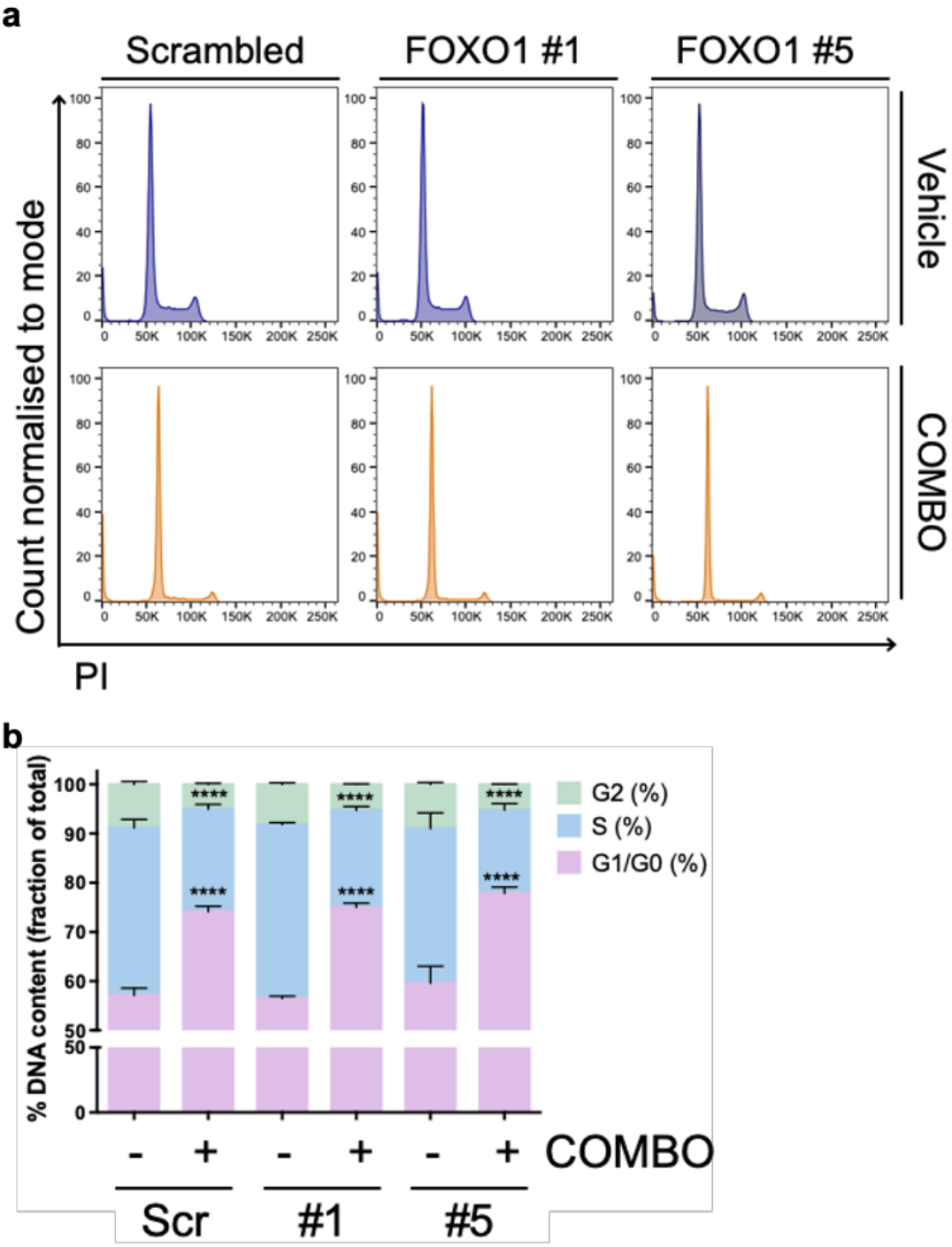

Figure 5.7 - shRNA-mediated FOXO1 knockdown does not influence cell cycle progression in MEC-1 cells.
(a) Representative FACS histograms of transduced (FOXO1 #1, FOXO1 #5 or Scrambled control) MEC-1 cells stained with PI for cell cycle analysis by quantitation of DNA content following treatment with COMBO (orange histograms; bottom panel) or DMSO vehicle control (Vehicle; purple histograms; top panel) for 48 h. (b) Quantification of DNA content (%) for cycle cycle phase G1/G0 (purple bars), S (blue bars) and G2 (green bars) in transduced (#1, #5 or Scr control) MEC-

1 cells (n=3) treated with (+) or without (-) COMBO. Data from each replicate are depicted as ‘fraction of total’, where total values are equal to 100. Data expressed as the mean ± SEM. Statistics calculated by two-way ANOVA, where **** p ≤ 0.0001.

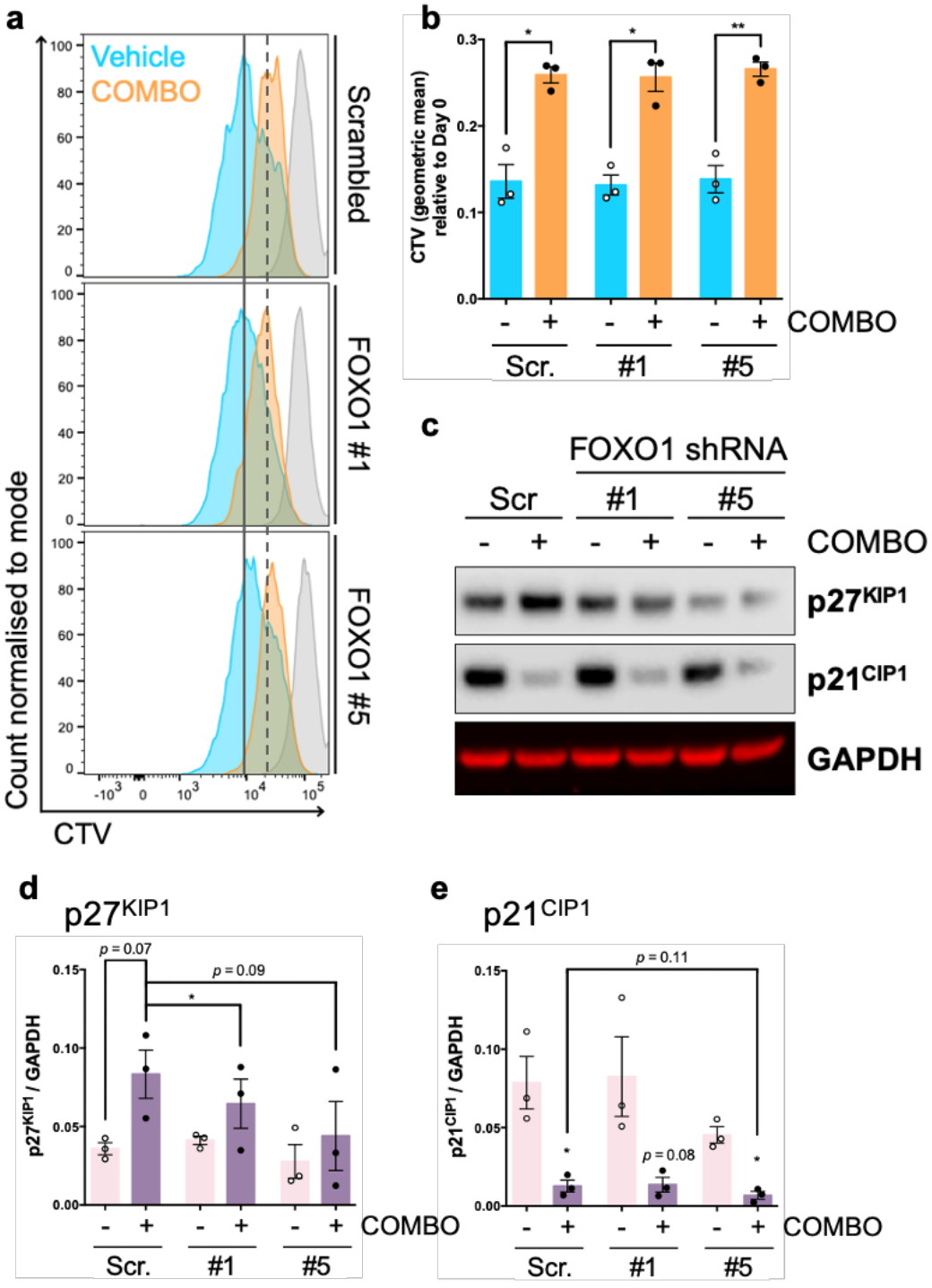

Figure 5.8 - FOXO1 knockdown does not affect cell proliferation, but p27^{KIP1} and p21^{CIP1} expression levels are modulated in FOXO1-depleted MEC-1 cells following COMBO treatment.
(a) Representative FACS histogram of transduced (FOXO1 #1, FOXO1 #5 or Scrambled control) MEC-1 cells stained with CTV to assess cell proliferation following treatment with COMBO (orange histograms) or DMSO vehicle control (Vehicle; blue histograms) for 72 h. A black vertical line represents the peak of the Scrambled vehicle control histogram. A black ‘dashed’ vertical line represents the peak of the Scrambled COMBO-treated histogram. Day 0 control (grey histograms)

are shown. (b) Assessment of CTV geometric mean for transduced (#1, #5 or Scr control) MEC-1 cells (n=3), treated as described in (a). (c) Representative western blot of transduced (#1, #5 or Scr control) MEC-1 cells (n=3) treated with (+) or without (-) COMBO for 48 h. Blots were probed for $p27^{KIP1}$, $p21^{CIP1}$ and GAPDH (loading control). (d, e) Densitometry of (d) $p27^{KIP1}$ and (e) $p21^{CIP1}$ expression in transduced (#1, #5 or Scr control) MEC-1 cells (n=3) following treatment with (+; purple bars) or without (-; pink bars) COMBO. Individual datapoints from each replicate are shown as white or black circles. Data expressed as the mean ± SEM. Statistics calculated by one-way ANOVA, where * $p \leq 0.05$, ** $p \leq 0.01$.

downregulation of $p27^{KIP1}$ expression (Figure 5.8c,d). Consistent with previous experiments (Figure 3.13d,e), COMBO treatment elicited a near-significant upregulation in $p27^{KIP1}$ expression in Scr control cells ($p = 0.07$; Figure 5.8c,d). Although COMBO treatment also visibly enhanced $p27^{KIP1}$ expression in FOXO1-depleted MEC-1 cells (compared to untreated), COMBO-induced upregulation of $p27^{KIP1}$ was significantly decreased in MEC-1 cells transduced with construct #1, and near-significantly reduced by construct #5 ($p = 0.09$) compared to COMBO-treated Scr control cells (Figure 5.8c,d). While $p21^{CIP1}$ expression was not affected by FOXO1 knockdown via construct #1, it was visibly reduced in MEC-1 cells transduced with construct #5 (Figure 5.8c,e). In contrast with Figure 3.13f, $p21^{CIP1}$ expression was significantly reduced by COMBO treatment in Scr control cells (Figure 5.8c,e). Interestingly, $p21^{CIP1}$ expression was also significantly reduced by COMBO treatment in FOXO1-depleted MEC-1 cells via construct #5 (compared to untreated), with a similar trend seen in COMBO treated MEC-1 cells transduced with construct #1 (Figure 5.8c,e).

5.2.8 Modulation of FOXO target transcript abundance demonstrates that FOXO1 regulates genes in a highly context-specific manner

Although FOXO1 knockdown had little effect on MEC-1 cell functionality or the physiological response to COMBO treatment, we were encouraged by the modulation of FOXO targets at the protein level (Figures 5.5e-h and 5.8c-e). We therefore assessed transcript abundance of known FOXO target genes: *FOXO1*, *IGF1R*, *SESN3*, *BCL2-L11* (BIM), *BBC3*, *GADD45A*, *CDKN1A*, *CDKN1B*, *CCNG2* and *CCND2* in FOXO1-depleted MEC-1 cells with or without COMBO treatment by RT-qPCR (Figure 5.9). As expected, *FOXO1* expression was significantly reduced in MEC-1 cells transduced with construct #5 (Figure 5.9a), corresponding to relative mRNA (Figure 5.3b) and protein (Figure 5.3e) levels demonstrated earlier. However, *FOXO1* expression was largely unaffected by construct #1 (Figure 5.9a). Nevertheless, *FOXO1* transcript abundance was visibly enhanced by

COMBO treatment in Scr control cells (p = 0.13; Figure 5.9a). Furthermore, *FOXO1* expression was similarly elevated in FOXO1-depleted MEC-1 cells (constructs #1 and #5) following COMBO treatment (Figure 5.9a). We also noted that COMBO-induced *FOXO1* upregulation in FOXO1-depleted or Scr control cells was discernibly proportionate to untreated *FOXO1* expression levels (Figure 5.9a). Irrespectively, COMBO-induced *FOXO1* upregulation was visibly less in MEC-1 cells transduced with construct #5 than in Scr control cells (p = 0.1; Figure 5.9a). 'Basal' *IGF1R* transcript levels were unaffected by FOXO1 knockdown (Figure 5.9b). However, *IGF1R* expression was notably enhanced following COMBO treatment in Scr control cells (Figure 5.9b). Interestingly, whereas COMBO treatment similarly induced *IGF1R* expression in MEC-1 cells transduced with construct #1 (p = 0.09; Figure 5.9b), COMBO treatment had no effect on *IGF1R* expression in FOXO1-depleted MEC-1 cells by construct #5 (Figure 5.9b). In support of this observation, *IGF1R* expression in COMBO-treated FOXO1-depleted MEC-1 cells (construct #5) was significantly less than COMBO-treated Scr control cells (Figure 5.9b). COMBO treatment visibly increased *SESN3* transcript abundance in Scr control cells, and to a lesser extent in MEC-1 cells transduced with construct #1 (Figure 5.9c). Interestingly, *SESN3* expression was significantly downregulated in FOXO1-depleted MEC-1 cells via construct #5 following COMBO treatment (Figure 5.9c). Unexpectedly, *BCL2-L11* expression was not affected by FOXO1 knockdown (Figure 5.9d). However, consistent with earlier observations (Figure 5.5e-h), COMBO treatment upregulated *BCL2-L11* expression in Scr control cells and those transduced with construct #1, while *BCL2-L11* expression was seemingly unaffected by COMBO treatment in FOXO1-depleted MEC-1 cells via construct #5 (Figure 5.9d). Furthermore, *BCL2-L11* transcript levels were significantly lower in COMBO-treated MEC-1 cells transduced with construct #5 compared to construct #1 (Figure 5.9d). Consistent with Figure 5.9d, expression of pro-apoptotic *BBC3* was largely unaffected by FOXO1 knockdown (Figure 5.9e). However, COMBO treatment produced a visible trend towards increased *BBC3* levels in Scr control cells and MEC-1 cells transduced with construct #1 (Figure 5.9e). Surprisingly, COMBO treatment further enhanced *BBC3* expression in FOXO1-depleted MEC-1 cells via construct #5, visibly greater than COMBO-induced *BBC3* expression in Scr control cells and MEC-1 cells transduced with construct #1 (Figure 5.9e). *GADD45A* expression decreased in FOXO1-depleted MEC-1 cells (constructs #1 and #5) compared

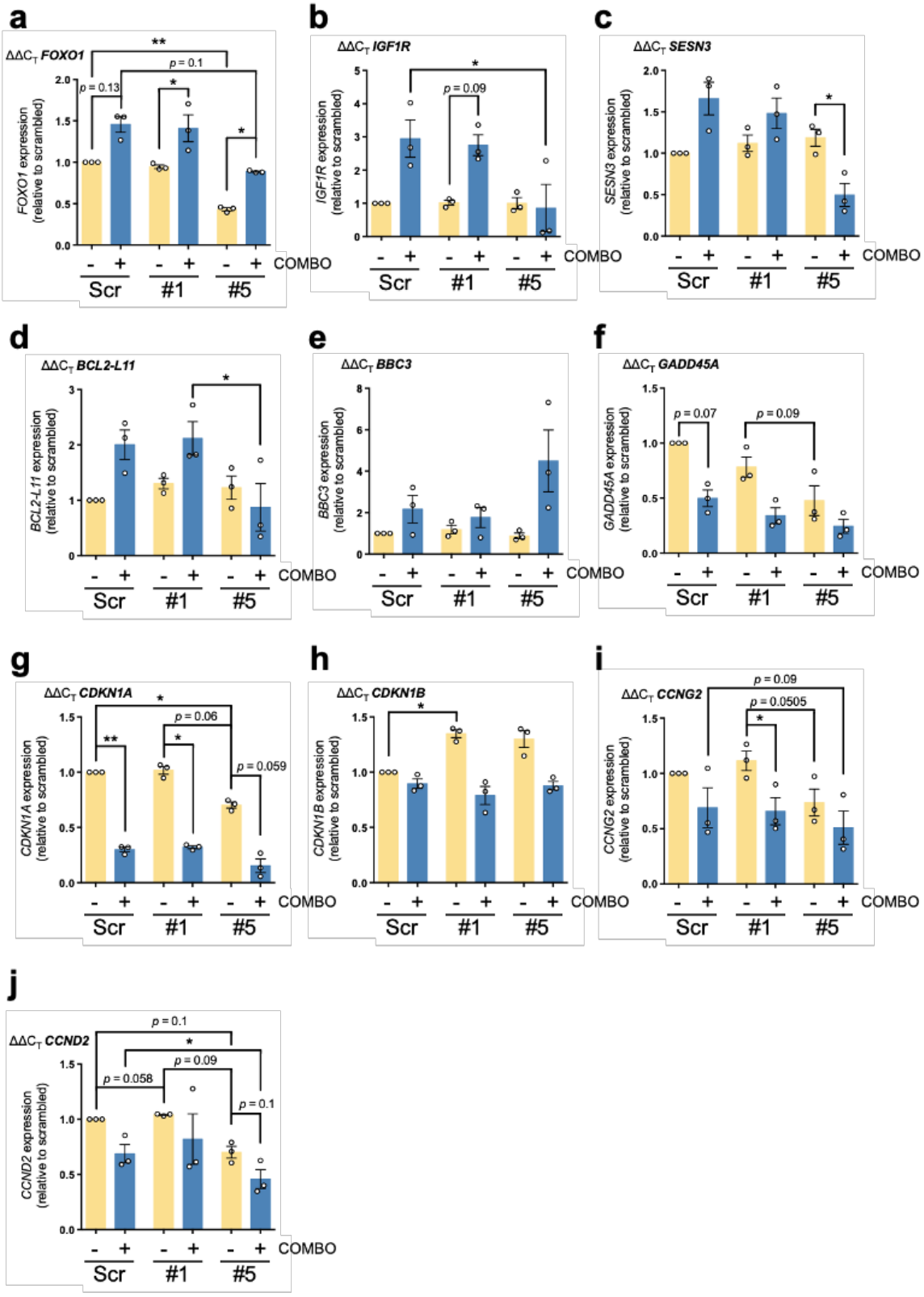

Figure 5.9 - shRNA-mediated knockdown of FOXO1 modulates expression (mRNA) levels of FOXO1 transcriptional targets.

(a - j) RT-qPCR to assess transcript abundance of (a) *FOXO1,* (b) *IGF1R*, (c) *SESN3*, (d) *BCL2-L11* (BIM), (e) *BBC3*, (f) *GADD45A*, (g) *CDKN1A* ($p21^{CIP1}$), (h) *CDKN1B* ($p27^{KIP1}$), (i) *CCNG2* and (j) *CCND2* in transduced (#1, #5 or Scr control) MEC-1 cells (n=3) treated with (+; blue bars) or without (-; yellow bars) COMBO for 48 h. The $\Delta\Delta C_T$ method was used to calculate expression levels, where samples were first normalised to the internal reference gene *GUSB* and then made relative to vehicle control. Individual datapoints are represented by white circles. Data expressed as the mean ± SEM. Statistics calculated by one-way ANOVA, where * $p \leq 0.05$, ** $p \leq 0.01$.

to Scr control, with the *GADD45A* transcript abundance being distinctly lower in MEC-1 cells transduced with construct #5 than construct #1 (p = 0.09; Figure 5.9f). COMBO treatment near-significantly downregulated *GADD45A* expression in Scr control cells (p = 0.07; Figure 5.9f). Similarly, *GADD45A* expression was also reduced in FOXO1-depleted MEC-1 cells (constructs #1 and #5) following COMBO treatment (Figure 5,9f). As before (Figure 5.9a), we noted that COMBO-induced *GADD45A* downregulation was largely proportionate to *GADD45A* expression levels in untreated cells (Figure 5.9f). Although *CDKN1A* transcript abundance was unaffected by FOXO1 knockdown via construct #1, *CDKN1A* expression was significantly, albeit counterintuitively, reduced in FOXO1-depleted MEC-1 cells transduced with construct #5 (Figure 5.9g). Moreover, *CDKN1A* expression was near-significantly decreased by construct #5 compared to construct #1 (p = 0.06; Figure 5.9g). Nevertheless, consistent with Figure 5.8e, COMBO treatment significantly downregulated *CDKN1A* expression in Scr control cells (Figure 5.9g). Equally, *CDKN1A* expression was also significantly reduced in COMBO-treated MEC-1 cells transduced with construct #1, and near-significantly reduced via construct #5 (p = 0.059; Figure 5.9g). Conflicting with Figure 5.8d, *CDKN1B* expression was significantly upregulated in FOXO1-depleted MEC-1 cells by construct #1, and comparably so by construct #5 (Figure 5.9h). Furthermore, COMBO treatment elicited a modest downregulation in *CDKN1B* expression in Scr control cells (Figure 5.9h). Intriguingly, however, *CDKN1B* transcript abundance was also observably reduced by COMBO treatment in FOXO1-depleted MEC-1 cells (construct #1 and #5) (Figure 5.9h). FOXO1 repression by construct #5 reduced *CCNG2* expression, compared with Scr and construct #1 cells (p = 0.0505; Figure 5.9i), while COMBO treatment visibly reduced *CCNG2* transcript abundance in Scr control cells (Figure 5.9i). Furthermore, *CCNG2* expression was significantly reduced by COMBO treatment in MEC-1 cells transduced with construct #1 (Figure 5.9i). While *CCNG2* expression was reduced in COMBO-treated MEC-1 cells transduced with construct #5, a notable trend towards reduced *CCNG2* expression existed between COMBO-treated Scr control cells and COMBO-treated FOXO1-depleted MEC-1 cells via construct #5 (p = 0.09; Figure 5.9i). FOXO1 knockdown- and COMBO treatment-induced *CCND2* modulation largely mirrored that of *CCNG2* (Figure 5.9j). *CCND2* expression was marginally, but near-significantly, enhanced in MEC-1 cells transduced with construct #1 compared to Scr control (p = 0.058; Figure 5.9j).

However, consistent with Figure 5.9i, *CCND2* expression was visibly downregulated in FOXO1-depleted MEC-1 cells via construct #5 (p = 0.1; Figure 5.9j), near-significantly less than construct #1 (p = 0.09; Figure 5.9j). COMBO treatment observably reduced *CCND2* transcript abundance in Scr control cells (Figure 5.9j). Equally, trends towards reduced *CCND2* expression were observed in MEC-1 cells transduced with construct #1 (Figure 5.9j) and construct #5 (p = 0.1; Figure 5.9j) following COMBO treatment. Of note, *CCND2* expression was significantly less in COMBO-treated MEC-1 cells transduced with construct #5 compared to COMBO-treated Scr control cells (Figure 5.9j).

5.2.9 HG-3 and MEC-1 cells are largely insensitive to FOXO1 inhibition with AS1842856

Since shRNA-mediated FOXO1 knockdown was only partial, we argued that residual FOXO1 was capable of eliciting a proportionate response to COMBO treatment via induction/repression of target gene transcription. We therefore adopted the FOXO1-specific inhibitor AS1842856, which inhibits FOXO1 DNA-binding activity (545). Nagashima *et al.* identified AS1842856 [5-amino-7-(cyclohexylamino)-1-ethyl-6-fluoro-4-oxo-1,4-dihydroquinoline-3-carboxylic acid] via high-throughput affinity selection-mass spectrometry screening of small-molecule compounds that bound to active (dephosphorylated) FOXO1. Using an insulin responsive element (IRE) promotor-driven reporter assay (luciferase), AS1842856 was shown to diminish FOXO1 DNA binding activity in HepG2 cells in a dose-dependent manner (IC_{50} = 0.033 μM). In contrast, FOXO3 and FOXO4 inhibition was considerably less potent (IC_{50} > 1 μM). The authors further showed that AS1842856 (100 nM) repressed FOXO1 DNA-binding activity by 70 %, while FOXO3 and FOXO4 DNA-binding activity was diminished by 3 % and 20 %, respectively. As such, AS1842856 is described as a 'selective' FOXO1 inhibitor. Furthermore, AS1842856 had no effect on FOXO1 phosphorylation status, insulin-induced $FOXO1^{S256}$ phosphorylation nor FOXO1 mRNA expression levels. Importantly, the authors confirmed that AS1842856 did not bind to inactive (phosphorylated) FOXO1 ($FOXO1^{S256}$), demonstrating that the compound specifically targets active (dephosphorylated) FOXO1. Although 'full' characterisation is lacking, Nagashima *et al.* proposed that AS1842856 interferes with FOXO1 binding to coactivators, such as cAMP-response-element-binding protein-binding protein (CBP), preventing FOXO1-DNA binding (545). In a later

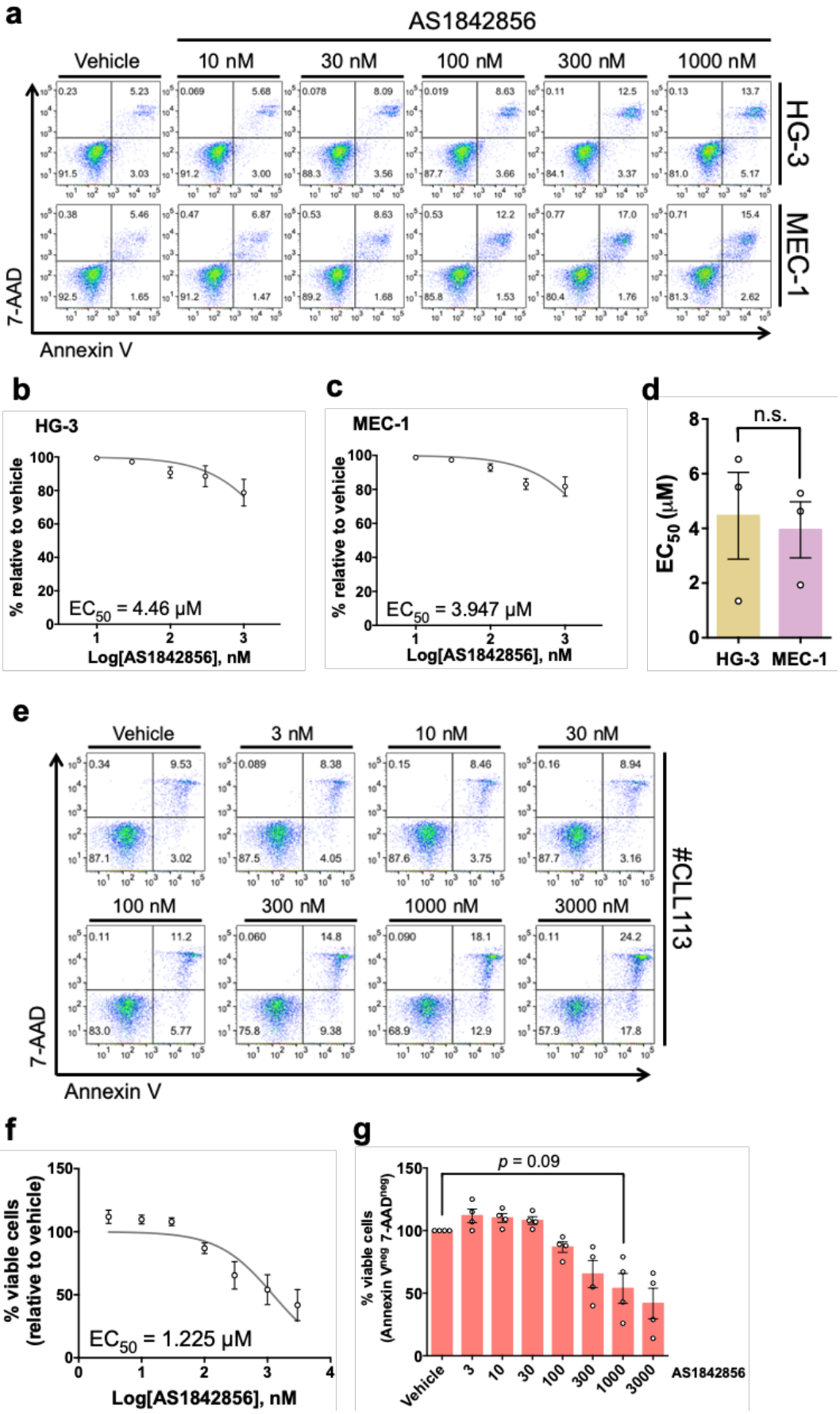

Figure 5.10 - The selective FOXO1 inhibitor AS1842856 confers a modest dose-dependent reduction in CLL cell survival.
(a) Representative FACS plot of HG-3 (top panel) and MEC-1 (bottom panel) cells stained with Annexin V/7-AAD to assess cell viability following treatment with increasing concentrations of

AS1842856 (vehicle, 10, 30, 100, 300, 1000 nM) for 48 h. (b, c) Dose-response / dose-effect curve of (b) HG-3 (n=3) and (c) MEC-1 cells (n=3) treated as described in (a). EC_{50} values generated by nonlinear regression (curve fit) as an average of each biological replicate. (d) Graphical comparison of EC_{50} values from (b, c) for HG-3 (yellow bar) and MEC-1 cells (pink bars) treated with AS1842856. (e) Representative FACS plot of a primary CLL sample (#CLL113) stained with Annexin V/7-AAD to assess cell viability following treatment with increasing concentrations of AS1842856 (vehicle, 3, 10, 30, 100, 300, 1000, 3000 nM) for 48 h. (f, g) Dose-response / dose-effect curve of primary CLL samples (n=4) treated as described in (e). (f) EC_{50} values generated by nonlinear regression (curve fit) as an average of each biological replicate. (g) Data represented as a bar chart. Individual datapoints (unless otherwise represented) are represented by white circles. Data expressed as the mean ± SEM. Statistics calculated by unpaired Student's t-test or one-way ANOVA. n.s. = not significant. EC_{50} values generated by extrapolation by GraphPad Prism.

study, Yu *et al*. demonstrated that AS1842856 promoted cytoplasmic sequestration of FOXO1 in human embryonic stem cells (hESCs) (547). In any case, AS1842856 inhibits FOXO1 DNA-binding activity, distinct from shRNA-mediated knockdown of FOXO1 expression. To assess the impact of AS1842856 treatment on cell viability, HG-3 and MEC-1 cells were incubated with increasing concentrations of drug for 48 h. Thereafter, cells were stained with Annexin V/7-AAD and analysed by flow cytometry (from which the EC_{50} was calculated) (Figure 5.10a-d). Treatment of HG-3 (Figure 5.10a,b) and MEC-1 cells (Figure 5.10a,c) with AS1842856 resulted in a dose-dependent reduction in cell viability. However, HG-3 (EC_{50} = 4.46 μM) and MEC-1 (EC_{50} = 3.94 μM) cells were largely insensitive to AS1842856 up to 1 μM (Figure 5.10d). In primary CLL cells treated with AS1842856, cell viability was maintained at concentrations up to 30 nM and then reduced in a dose-dependent manner (Figure 5.10e-g). Moreover, although primary CLL cells were more sensitive to AS1842856 (EC_{50} = 1.225 μM) than CLL cell lines, only modest reductions in cell viability were observed at doses achievable *in vivo* (403, 545) with minimal off-target effects (Figure 5.10e-g). Because AS1842856 selectively inhibited FOXO1 DNA-binding activity (IC_{50} = 33 nM) to a considerably larger extent than FOXO3 or FOXO4 (545), we proceeded with AS1842856 at 30 nM and 100 nM for *in vitro* experiments. Of note, EC_{50} values were generated by extrapolation using GraphPad Prism software.

5.2.10 AS1842856 does not prevent COMBO-induced FOXO1 nuclear translocation

AS1842856 has been shown to selectively inhibit 'active' FOXO1 (545, 546) and promote FOXO1 cytoplasmic retention in hESCs (547). To assess whether AS1842856 can block COMBO-induced FOXO1 nuclear translocation in MEC-1 cells, the localisation of FOXO1 was examined by subcellular fractionation

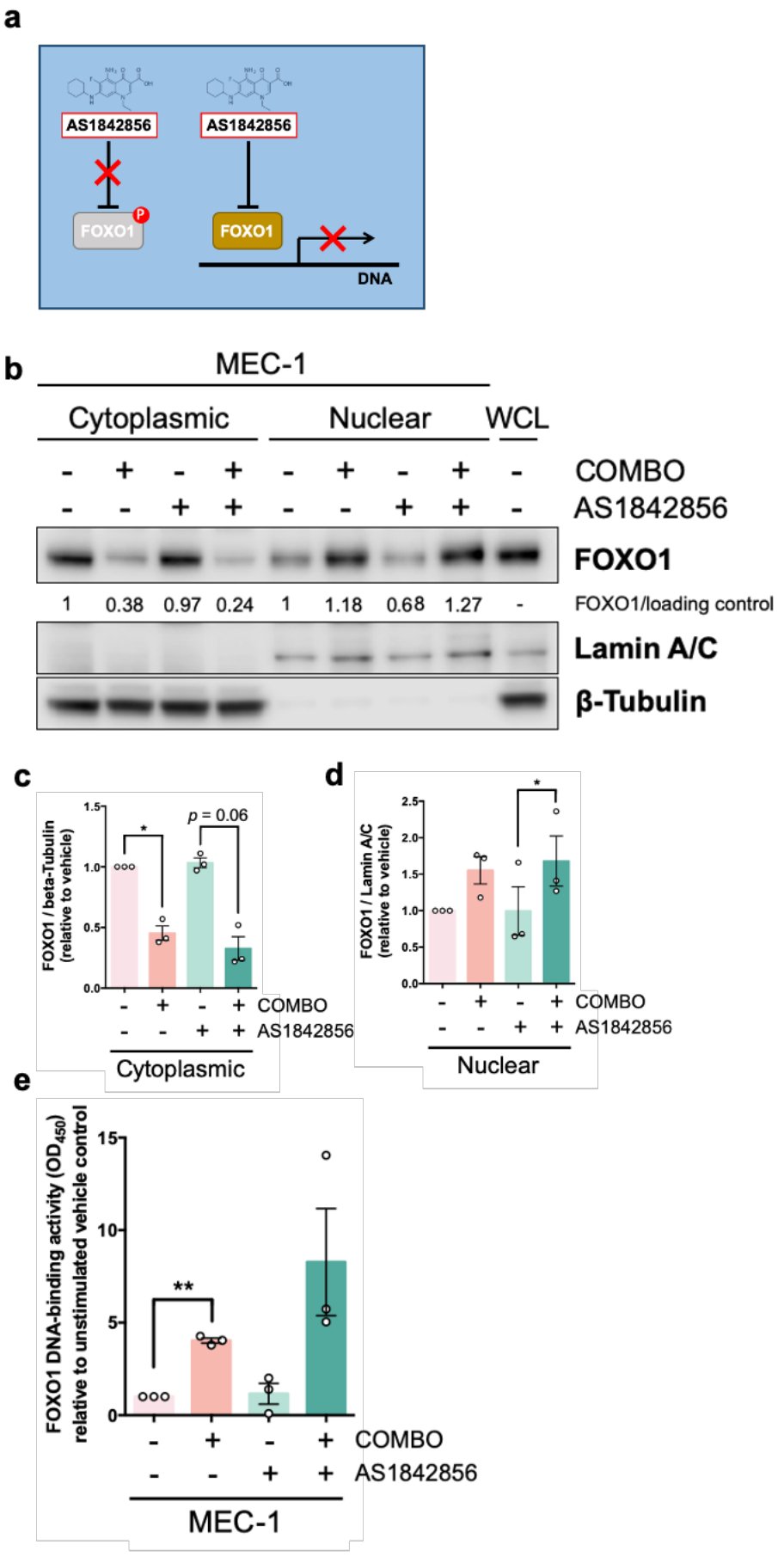

Figure 5.11 - Short-term AS1842856 treatment, simultaneously treated with or without COMBO, does not influence the FOXO1 localisation or transcriptional activity in MEC-1 cells.

(a) Schematic depicting AS1842856 mechanism of action. AS1842856 inhibits 'active' FOXO1, but not the 'inactive' phosphorylated form. (b) Subcellular fractionation of MEC-1 cells (n=3) treated with COMBO in the presence of absence of AS1842856 for 1 h. Cytoplasmic, nuclear and whole cell lysate (WCL) fractions were generated. Blots were probed for FOXO1, Lamin A/C and β-Tubulin. Densitometry for cytoplasmic (FOXO1/β-Tubulin) and nuclear (FOXO1/Lamin A/C) FOXO1 expression are shown (relative to unstimulated vehicle control). (c, d) Densitometry of FOXO1 expression in (c) cytoplasmic and (d) nuclear fractions from MEC-1 cells (n=4), treated as described in (b). Densitometry calculated as in (b). (e) FOXO1 DNA-binding activity (OD_{450}) of MEC-1 cells (n=3), treated as described in (b). Individual datapoints are represented by white circles. Data expressed as the mean ± SEM. Statistics calculated by one-way ANOVA, where * $p \leq 0.05$, ** $p \leq 0.01$.

following short-term COMBO treatment with or without AS1842856 (Figure 5.11b-d). Consistent with Figure 5.2c-e, COMBO treatment induced FOXO1 nuclear accumulation (Figure 5.11b-d), demonstrated by a significant reduction in cytoplasmic FOXO1 (Figure 5.11b,c) and concomitant increase in nuclear FOXO1 (Figure 5.11b,d). Interestingly, treatment with AS1842856 alone had no effect on FOXO1 cellular distribution (Figure 5.11b-d). Furthermore, COMBO-induced FOXO1 nuclear translocation was unaffected by simultaneous incubation with AS1842856 (Figure 5.11b-d). Cytoplasmic FOXO1 was reduced in COMBO-treated MEC-1 cells incubated with AS1842856 ($p = 0.06$; Figure 5.11b,c), which corresponded to a significant increase in nuclear FOXO1 to levels comparable with COMBO treatment alone (Figure 5.11b,d). As COMBO-induced FOXO1 nuclear accumulation was associated with enhanced DNA-binding activity (Figure 5.2f), we next addressed whether AS1842856 could block FOXO1 activity in COMBO-treated MEC-1 cells (Figure 5.11e). Consistent with earlier observations (Figure 5.2f), COMBO treatment significantly enhanced FOXO1 DNA-binding activity in MEC-1 cells. (Figure 5.11e). Unexpectedly, AS1842856 treatment alone had no effect on FOXO1 DNA-binding activity (Figure 5.11e). Surprisingly, simultaneously combining AS1842856 with the COMBO treatment visibly enhanced FOXO1 activity to levels greater than COMBO treatment alone (Figure 5.11e).

5.2.11 FOXO1 expression is unaffected by AS1842856 treatment in CLL cell lines, whereas AKT^{S473} phosphorylation is visibly reduced

Studies have shown that FOXO1 expression is unaffected by AS1842856 treatment in Fao cells (545), adipocytes (548) or hESCs (547). Furthermore, Nagashima *et al.* demonstrated that short-term AS1842856 treatment did not impact FOXO1^{S256}

or insulin-induced AKT^{S407} phosphorylation in Fao cells (545). In contrast, earlier experiments showed that FOXO1-depleted MEC-1 cells had reduced FOXO1^{T24} (Figure 5.4a,c) and increased AKT^{S473} phosphorylation levels (Figure 5.4a,e). In line with these findings, we addressed the long-term effect (48 h) of AS1842856 treatment on FOXO1/FOXO1^{T24} and AKT/AKT^{S473} expression/phosphorylation in CLL cell lines with or without COMBO (Figure 5.12). Consistent with the aforementioned studies, FOXO1 expression was largely unaffected by AS1842856 treatment in HG-3 and MEC-1 cells (Figure 5.12a,b). While FOXO1 expression was visibly enhanced by COMBO treatment in HG-3 cells, FOXO1 expression was not affected to the same extent in MEC-1 cells (Figure 5.12a,b). Furthermore, AS1842856 did not significantly impact FOXO1 expression levels in COMBO-treated HG-3 or MEC-1 cells (Figure 5.12a,b). Although the effect of AS1842856 treatment on FOXO1^{T24} phosphorylation varied markedly in HG-3 cells, FOXO1^{T24} phosphorylation was modestly reduced in MEC-1 cells (Figure 5.12a,c). Moreover, FOXO1^{T24} phosphorylation was unaffected by COMBO treatment in HG-3 cells, whereas FOXO1^{T24} phosphorylation was noticeably reduced in COMBO-treated MEC-1 cells (Figure 5.12a,c). Interestingly, simultaneous incubation with AS1842856 appeared to further diminish FOXO1^{T24} phosphorylation in COMBO-treated HG-3 and MEC-1 cells (Figure 5.12a,c). AS1842856 treatment discernibly reduced AKT expression in HG-3 cells (p = 0.1), while AKT expression in MEC-1 cells was largely unchanged (Figure 5.12a,d). Furthermore, AKT expression was visibly enhanced by COMBO treatment in HG-3 cells, whereas AKT expression in COMBO-treated MEC-1 cells was comparable with untreated control (Figure 5.12a,d). Interestingly, simultaneous incubation with AS1842856 further reduced AKT expression in COMBO-treated HG-3 (p = 0.1) and MEC-1 (p = 0.06) cells (Figure 5.12a,d). Furthermore, AKT^{S473} phosphorylation was significantly diminished by AS1842856 treatment in HG-3 cells (Figure 5.12a,e). Likewise, pharmacological inhibition of FOXO1 decreased AKT^{S473} phosphorylation in MEC-1 cells (Figure 5.12a,e). Encouragingly, COMBO treatment inhibited AKT^{S473} phosphorylation in HG-3 cells and MEC-1 cells (Figure 5.12a,e), while concurrently incubating COMBO-treated CLL cell lines with AS1842856 also diminished AKT^{S473} phosphorylation (Figure 5.12a,e).

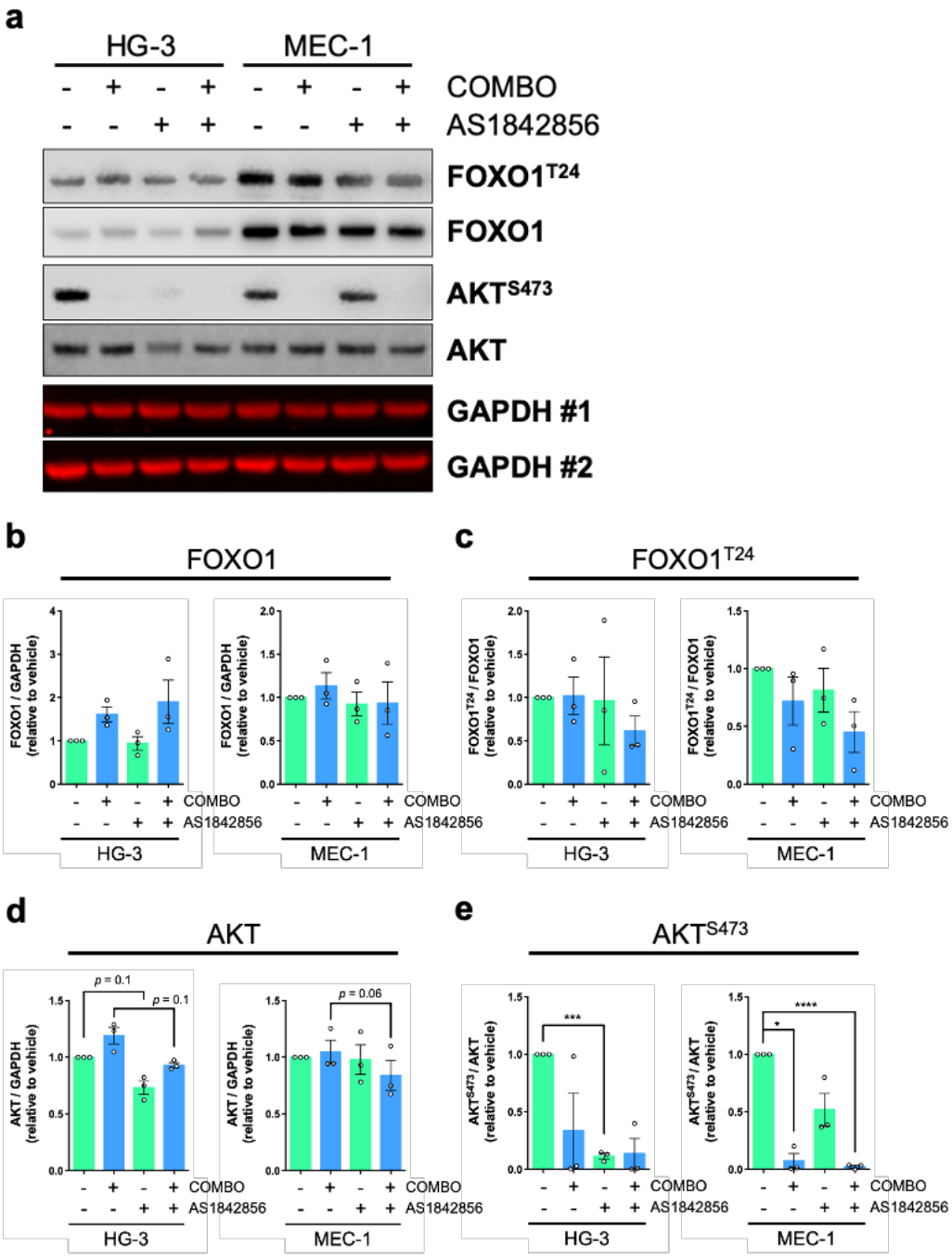

Figure 5.12 - Long-term AS1842856 treatment, in the presence or absence of COMBO, modulates FOXO1^{T24}/AKT^{S473} phosphorylation and FOXO1/AKT expression levels.
(a) Representative western blot of HG-3 (n=3) and MEC-1 cells (n=3) treated with COMBO in the presence of absence of AS1842856 (30 nM) for 48 h. Blots were probed for FOXO1^{T24}, FOXO1, AKT^{S473}, AKT and GAPDH (loading control; #1 and #2 referring to mirror blots). (b, d) Relative expression levels of (b) FOXO1 and (d) AKT in HG-3 (n=3) and MEC-1 cells (n=3), treated as described in (a). (c, e) Relative phosphorylation levels of (c) FOXO1^{T24} and (e) AKT^{S473} in HG-3 (n=3) and MEC-1 cells (n=3), treated as described in (a). Expression and phosphorylation levels are relative to vehicle control. Individual datapoints are represented by white circles. Data expressed as the mean ± SEM. Statistics calculated by one-way ANOVA, where * $p \leq 0.05$, *** $p \leq 0.001$, **** $p \leq 0.0001$.

5.2.12 FOXO1 activity mediates COMBO-induced cytotoxicity in MEC-1 cells

We earlier demonstrated that shRNA-mediated FOXO1 knockdown was unable to rescue MEC-1 cells from the cytotoxic effect of the COMBO treatment, yet COMBO-induced pro-apoptotic BIM upregulation was diminished in FOXO1-depleted MEC-1 cells (Figure 5.5). Therefore, we wondered whether inhibition of FOXO1 activity might render the COMBO treatment unable to induce cell death in CLL cell lines. To achieve this, we treated HG-3 and MEC-1 cells with AS1842856 and assessed the sensitivity of FOXO1-inhibited cells to the COMBO treatment by Annexin V/7-AAD staining (Figure 5.13a-c). These data revealed that COMBO treatment alone visibly decreased HG-3 and MEC-1 cell viability (Figure 5.13a-c), which corresponded to enhanced apoptosis (Figure 5.13a). AS1842856 treatment protected MEC-1 cells from COMBO-induced cytotoxicity (Figure 5.13a,c). As expected, treatment of HG-3 and MEC-1 cells with AS1842856 modestly reduced cell viability in a dose-dependent manner (Figure 5.13a-c). Although HG-3 cells appeared to be protected from COMBO-induced apoptosis by concomitant incubation with 30 nM AS1842856, cell viability rebounded to levels comparable with COMBO treatment alone when combined with 100 nM AS1842856 (Figure 5.13a,b). In MEC-1 cells, COMBO-induced cytotoxicity was discernibly reduced following simultaneous incubation with 30 nM (p = 0.13) or 100 nM AS1842856 (Figure 5.13a,c), which was associated with a concurrent decrease in apoptosis (Figure 5.13a). As explained earlier, BIM expression was reduced in FOXO1-depleted MEC-1 cells following COMBO treatment (Figure 5.5e-h). Because BIM is an important mediator of FOXO1-dependent cell death (384), we addressed the effect of AS1842856 treatment on COMBO-induced BIM (BIM_{EL}, BIM_L, and BIM_S) upregulation by Western blotting (Figure 5.13d-g). Consistent with Figure 5.5e-h, basal levels of BIM_{EL} (Figure 5.13d,e), BIM_L (Figure 5.13d,f) or BIM_S (Figure 5.13d,g) were unaffected by AS1842856 treatment in HG-3 and MEC-1 cells. As expected, COMBO treatment alone noticeably enhanced expression of BIM in HG-3 and MEC-1 cells (Figure 5.13d-g). Equally, BIM expression was visibly upregulated in COMBO-treated HG-3 and MEC-1 cells simultaneously treated with AS1842856 (Figure 5.13d-g). However, in support of earlier findings (Figure 5.5e-h), COMBO-induced BIM_{EL} (Figure 5.13d,e), BIM_L (p = 0.08; Figure 5.13d,f) and BIM_S (Figure 5.13d,g) upregulation was diminished in AS1842856-treated MEC-1 cells. Similarly,

upregulation of BIM_L (Figure 5.13d,f) and BIM_S (Figure 5.13d,g) in COMBO-treated HG-3 cells was moderately reduced in the presence of AS1842856.

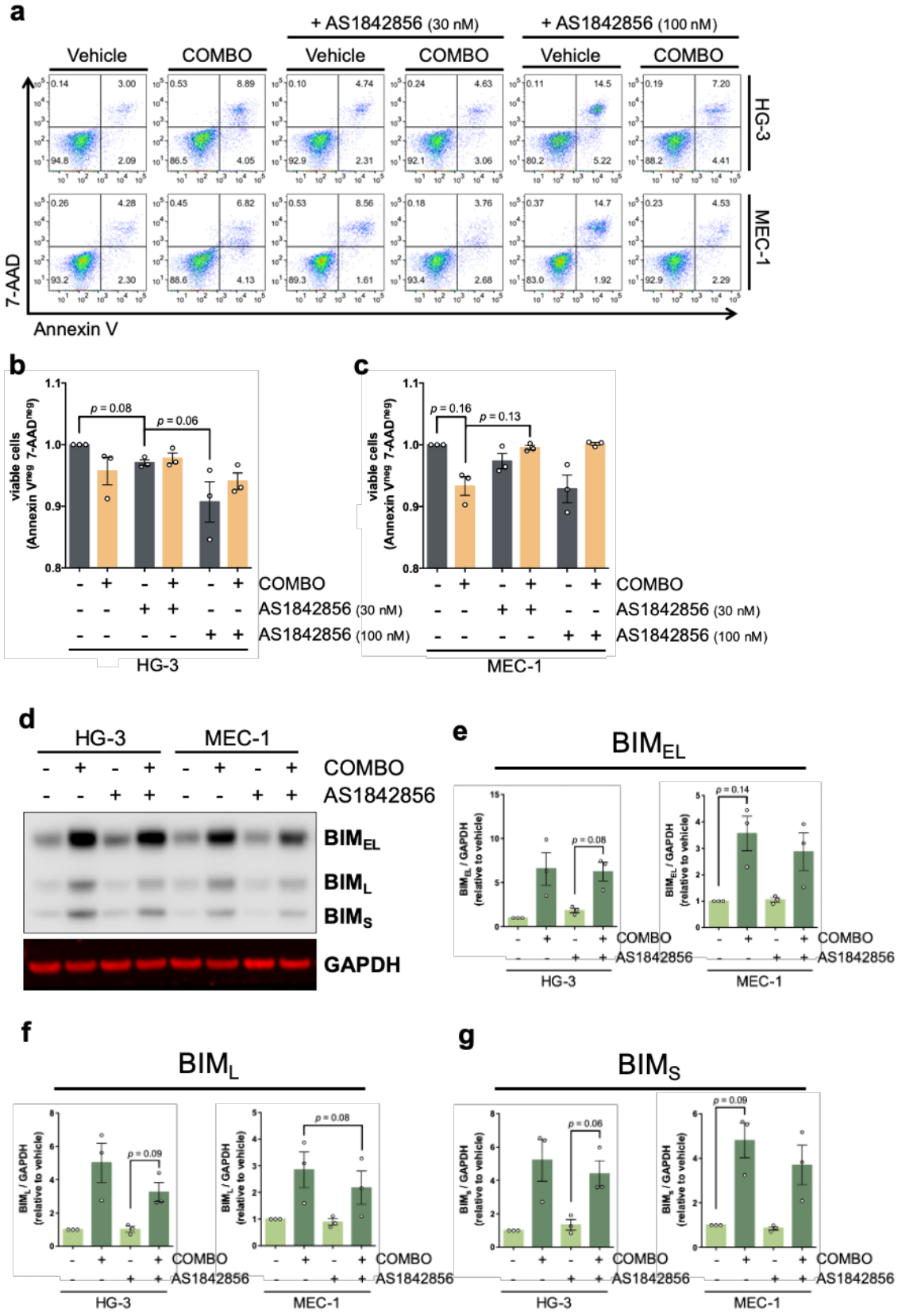

Figure 5.13 - AS1842856 treatment rescues the reduction in cell viability caused by COMBO treatment in MEC-1 cells.

(a) Representative FACS plot of HG-3 (top panel) and MEC-1 (bottom panel) cells stained with Annexin V/7-AAD to assess cell viability following treatment with COMBO in the presence or absence of AS1842856 (30 nM and 100 nM) for 48 h. (b, c) Relative viability (Annexin V^{neg} and 7-AAD^{neg} cells) of (b) HG-3 (n=3) and (c) MEC-1 cells (n=3) treated as described in (a). Percentage viability is relative to vehicle control. (d) Representative western blot of HG-3 (n=3) and MEC-1 cells (n=3) treated with COMBO in the presence or absence of AS1842856 (30 nM) for 48 h. Blots were probed for BIM (BIM_{EL}, BIM_L, and BIM_S) and GAPDH (loading control). (e - g) Densitometry of (e) BIM_{EL}, (f) BIM_L and (g) BIM_S expression in HG-3 (n=3) and MEC-1 cells (n=3) treated as described in (d). Expression is relative to GAPDH. Individual datapoints are represented by white circles. Data expressed as the mean ± SEM. Statistics calculated by one-way ANOVA.

5.2.13 FOXO1 activity is required to regulate MEC-1 cell size and plays an active role mediating the effects of the COMBO treatment

Although FOXO1 knockdown had minimal impact on MEC-1 cell size or the physiological response to COMBO treatment (Figure 5.6), we sought to determine whether a functional effect, if any, was dependent on transcriptional activity as opposed to relative expression levels. We therefore assessed the impact of FOXO1 inhibition via AS1842856 on HG-3 and MEC-1 cell size (Figure 5.14). AS1842856 (100 nM) treatment modestly enhanced HG-3 cell size (p = 0.059; Figure 5.14a,b). Equally, in contrast with earlier observations (Figure 5.6), MEC-1 cell size was significantly increased as a consequence of FOXO1 inhibition by AS1842856 (100 nM) (Figure 5.14a,c). We also noted moderate trends towards enlarged HG-3 (Figure 5.14a,b) and MEC-1 (Figure 5.14a,c) cell size in response to AS1842856 (30 nM) treatment. Unexpectedly, HG-3 cell size was minimally enhanced by the COMBO treatment alone (Figure 5.14b), which conflicted with previous experiments (Figure 3.11a,b). Additionally, HG-3 cell size was unaffected by COMBO treatment in the presence of AS1842856 (30 nM or 100 nM) (Figure 5.14a,b). Consistent with Figure 3.11c, COMBO treatment significantly reduced MEC-1 cell size (Figure 5.14a,c). Furthermore, MEC-1 cell size also significantly contracted following COMBO treatment in the presence of AS1842856 (30 nM or 100 nM) (Figure 5.14a,c). Interestingly, FOXO1 appeared to play an active role mediating the effects of the COMBO treatment on MEC-1 cell size (Figure 5.14d). The relative reduction in cell size was significantly greater in COMBO-treated MEC-1 cells than in COMBO-treated MEC-1 cells simultaneously incubated with AS1842856, indicating that inhibition of FOXO1 activity partially rescued the effect of COMBO treatment on MEC-1 cell size (Figure 5.14d).

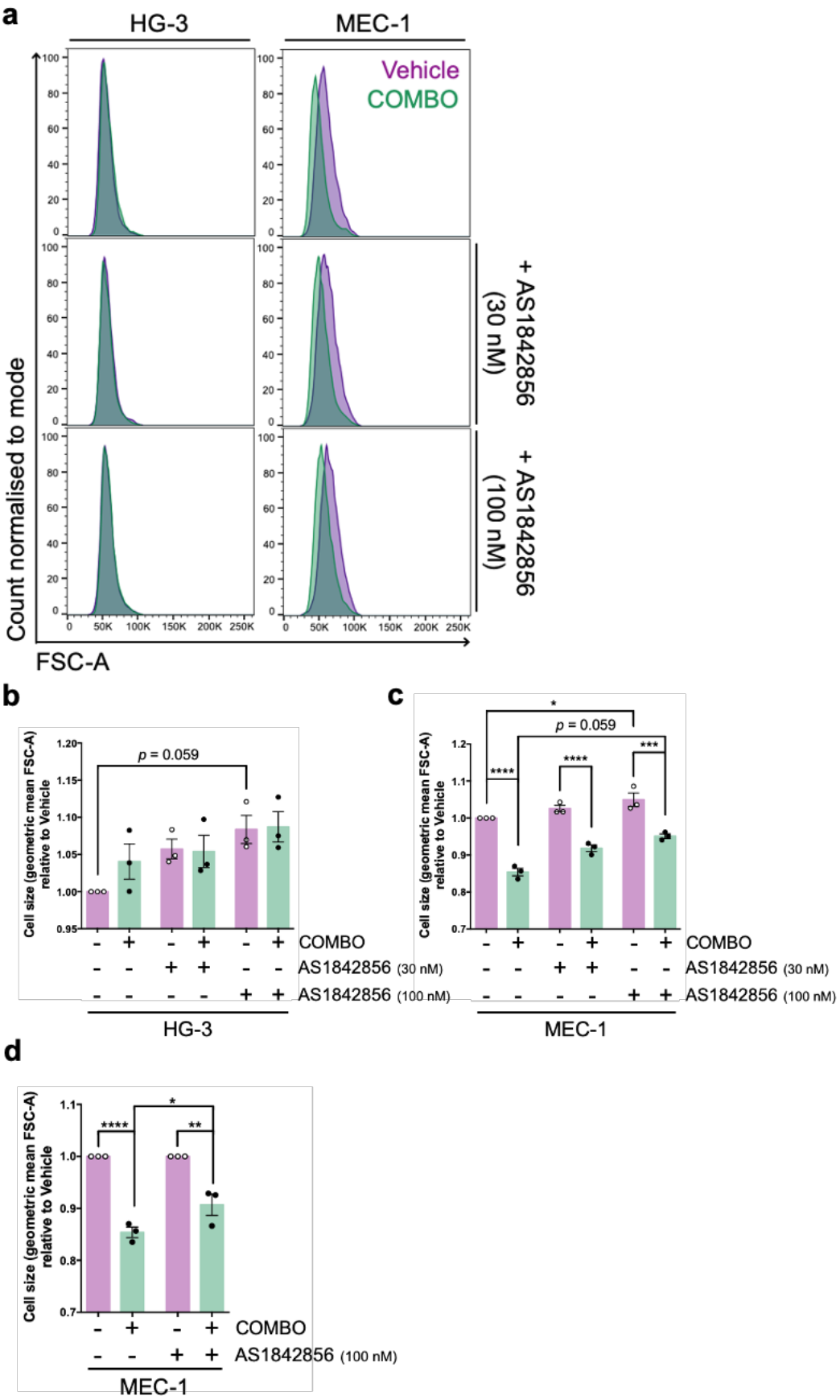

Figure 5.14 - AS1842856 treatment increases the size of MEC-1 cells, while rescuing the reduction in cell size associated with COMBO treatment.
(a) Representative FACS histogram displaying geometric mean of forward scatter-area (FSC-A) of HG-3 and MEC-1 cells treated with COMBO (green histograms) or DMSO vehicle control (Vehicle; purple histograms) in the presence or absence of AS1842856 (30 nM and 100 nM) for 48 h. (b, c)

Relative cell size (geometric mean) of HG-3 (n=3) and MEC-1 cells (n=3) treated as described in (a). Geometric means are relative to vehicle control. (d) Relative cell size (geometric mean) of MEC-1 cells (n=3) treated as described in (a). Data relative to vehicle control and AS1842856 (100 nM) alone. Individual datapoints are represented by white or black circles. Data expressed as the mean ± SEM. Statistics calculated by one-way ANOVA, where * $p \leq 0.05$, ** $p \leq 0.01$, *** $p \leq 0.001$, **** $p \leq 0.0001$.

5.2.14 Inhibition of FOXO1 activity rescues HG-3 and MEC-1 cells from COMBO-induced G1 cell cycle arrest, corresponding to reduced expression of $p27^{KIP1}$

Encouraged by the ability of AS1842856 to shield MEC-1 cells from COMBO-induced apoptosis (Figure 5.13) and cell size contraction (Figure 5.14), we next addressed the effect of FOXO1 inhibition on COMBO-induced cell cycle arrest (Figure 5.15). ShRNA-mediated FOXO1 knockdown did not influence the ability of the COMBO treatment to induce G1 cell cycle arrest in MEC-1 cells (Figure 5.7). Therefore, to assess whether FOXO1 activity is necessary to elicit the cytostatic effects of COMBO treatment, HG-3 and MEC-1 cells underwent long-term (48 h) COMBO treatment with or without AS1842856 (30 nM and 100 nM). Thereafter, cellular DNA content was analysed by flow cytometry via PI staining (Figure 5.15). These data showed that FOXO1 inhibition by AS1842856 alone did not affect cell cycle DNA content distribution in HG-3 or MEC-1 cells (Figure 5.15a-c). As expected, COMBO treatment inhibited cell cycle progression at G1 phase in HG-3 and MEC-1 cells, corresponding to a significant increase in G1/G0 and concomitant decrease in S phase DNA content (Figure 5.15a-c). In contrast to earlier observations (Figure 5.7), AS1842856 protected HG-3 and MEC-1 cells from COMBO-induced G1 cell cycle arrest (Figure 5.15a-c). In the presence of 30 nM or 100 nM AS1842856, G1/G0 DNA content was significantly lower in COMBO-treated HG-3 and MEC-1 cells compared to COMBO treatment alone, comparable to that of vehicle control (Figure 5.15a-c). Likewise, S phase DNA content was significantly greater in COMBO-treated HG-3 and MEC-1 cells simultaneously incubated with 30 nM or 100 nM AS1842856 (comparable to vehicle control) compared to COMBO treatment alone (Figure 5.15a-c).

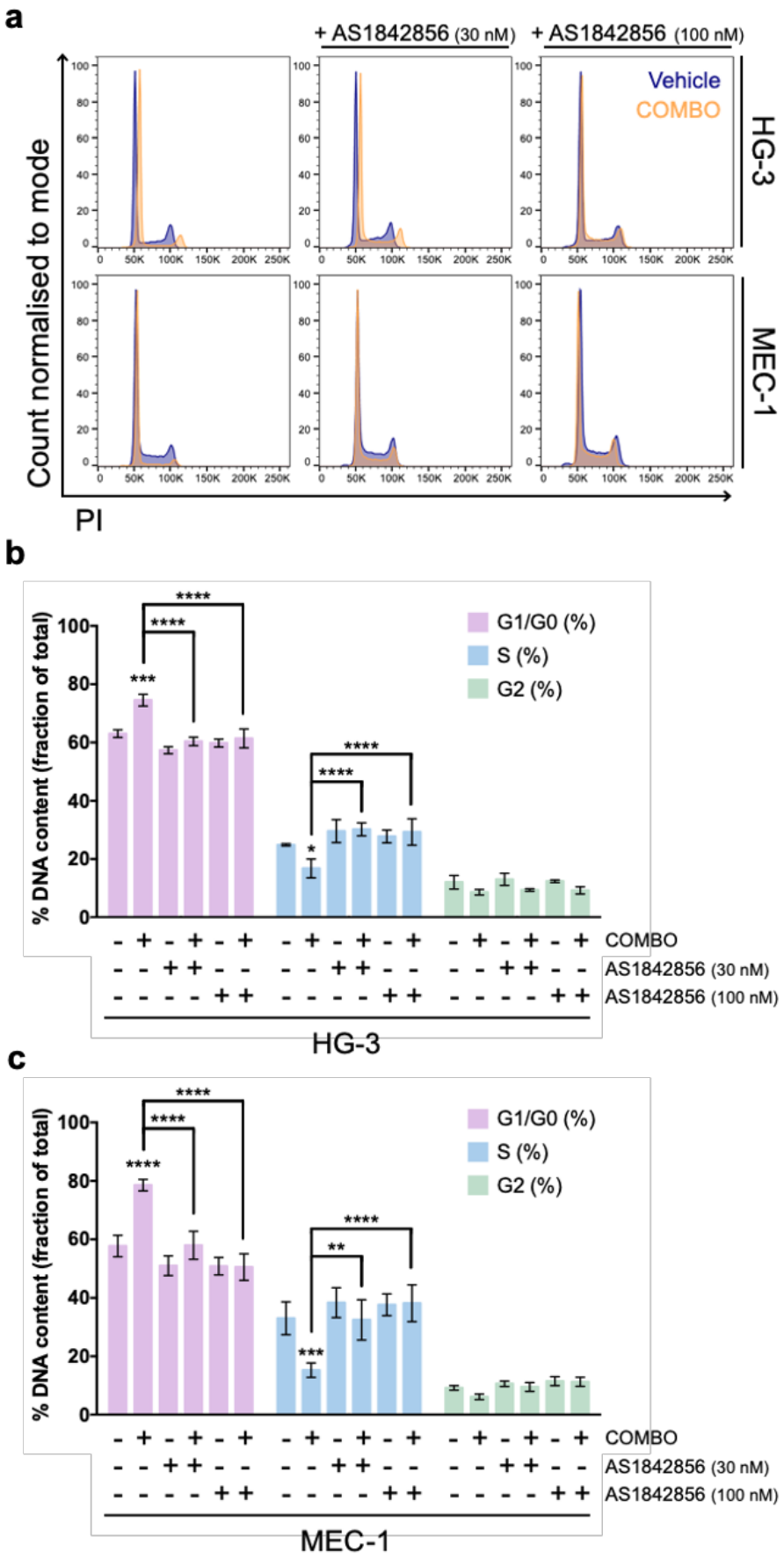

Figure 5.15 - AS1842856 treatment rescues the increased proportion of cells in G1 caused by COMBO treatment in HG-3 and MEC-1 cells.
(a) Representative FACS histograms of HG-3 (top panel) and MEC-1 cells (bottom panel) stained with PI for cell cycle analysis by quantitation of DNA content following treatment with COMBO

(orange histograms; bottom panel) or DMSO vehicle control (Vehicle; purple histograms; top panel) in the presence or absence of AS1842856 (30 nM and 100 nM) for 48 h. (b, c) Quantification of DNA content (%) for cycle phase G1/G0 (purple bars), S (blue bars) and G2 (green bars) in (b) HG-3 (n=3) and (c) MEC-1 cells (n=3) treated as described in (a). Data expressed as the mean ± SEM. Statistics calculated by two-way ANOVA, where ** $p \leq 0.01$, *** $p \leq 0.001$, **** $p \leq 0.0001$.

Our earlier observations concluded that FOXO1 knockdown visibly depleted COMBO-induced $p27^{KIP1}$ expression levels in MEC-1 cells (Figure 5.8d), whereas $p21^{CIP1}$ was largely unaffected (Figure 5.8e). As AS1842856 treatment shielded HG-3 and MEC-1 cells from COMBO-induced cell cycle arrest, we assessed whether inhibition of FOXO1 activity had a commensurate impact on COMBO-induced modulation of $p27^{KIP1}$ and $p21^{CIP1}$ expression levels (Figure 5.16). While FOXO1 inhibition by AS1842856 resulted in a trend towards reduced $p27^{KIP1}$ expression in HG-3 cells, $p27^{KIP1}$ expression was significantly depleted in MEC-1 cells (Figure 5.16a,b). Expectedly, COMBO treatment alone visibly enhanced $p27^{KIP1}$ in HG-3 cells, and significantly upregulated $p27^{KIP1}$ expression in MEC-1 cells (Figure 5.16a,b). Notably, induction of $p27^{KIP1}$ expression by COMBO treatment was visibly less in the presence of AS1842856 than COMBO treatment alone in HG-3 and MEC-1 cells (Figure 5.16a,b). AS1842856 treatment alone increased $p21^{CIP1}$ expression in HG-3 cells, whereas $p21^{CIP1}$ expression was largely unaffected by FOXO1 inhibition in MEC-1 cells (Figure 5.16a,c). Interestingly, COMBO-induced modulation of $p21^{CIP1}$ expression contrasted markedly between HG-3 and MEC-1 cells (Figure 5.16a,c). While COMBO treatment modestly enhanced $p21^{CIP1}$ expression in HG-3 cells, $p21^{CIP1}$ expression was reduced in COMBO-treated MEC-1 cells (Figure 5.16a,c). Nevertheless, $p21^{CIP1}$ expression was further enhanced in COMBO-treated HG-3 cells in the presence of AS1842856 (Figure 5.16a,c). Furthermore, unlike COMBO treatment alone, $p21^{CIP1}$ expression appeared unaffected in COMBO-treated MEC-1 cells simultaneously incubated with AS1842856 (Figure 5.16a,c).

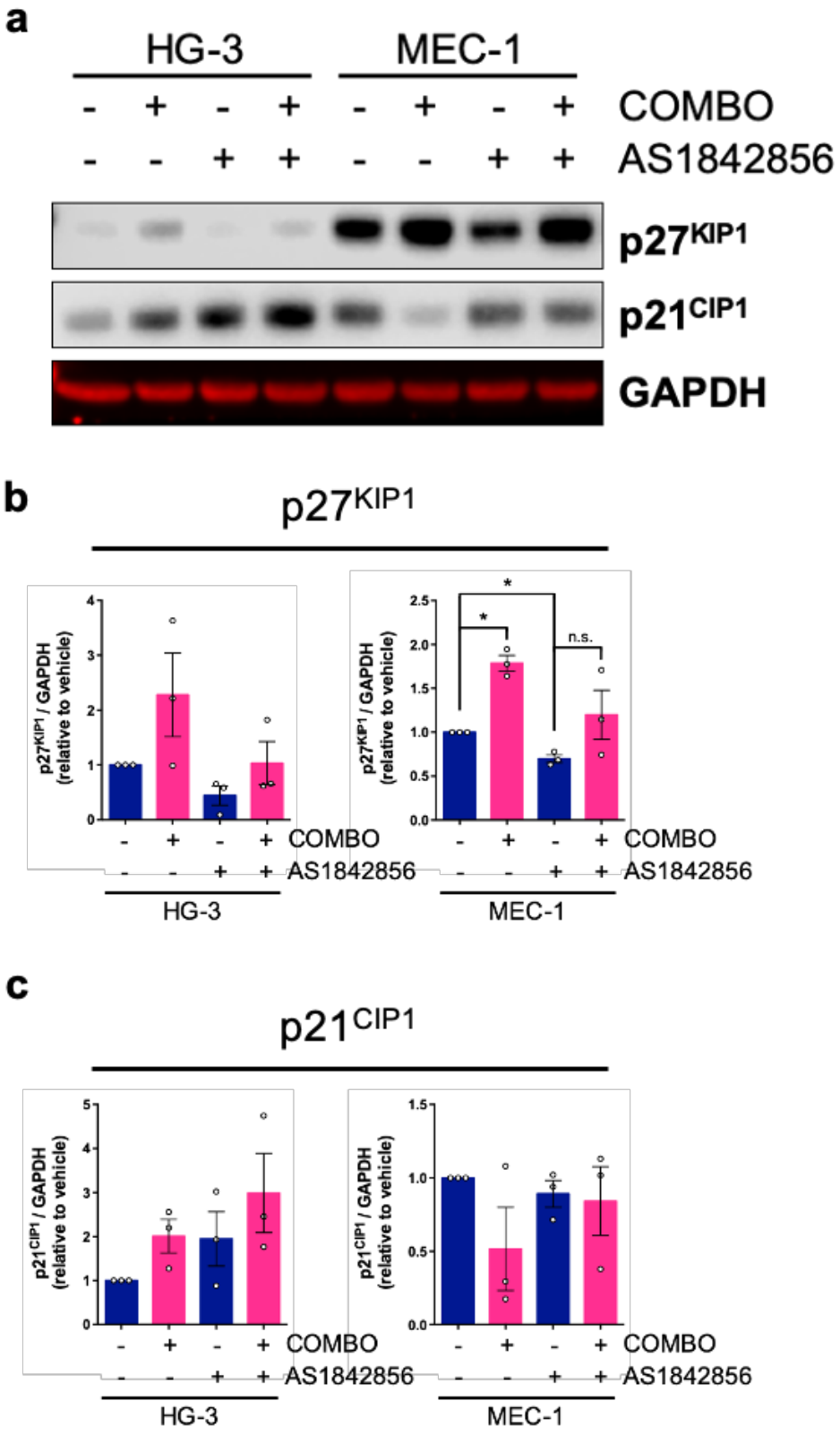

Figure 5.16 - AS1842856 decreases the expression of $p27^{KIP1}$ in MEC-1 cells.
(a) Representative western blot of HG-3 (n=3) and MEC-1 cells (n=3) treated with COMBO in the presence or absence of AS1842856 (30 nM) for 48 h. Blots were probed for $p27^{KIP1}$, $p21^{CIP1}$ and GAPDH (loading control). (b, c) Densitometry of (b) $p27^{KIP1}$ and (c) $p21^{CIP1}$ expression in HG-3 (n=3) and MEC-1 cells (n=3) treated as described in (a). Expression relative to vehicle control. Individual datapoints from each replicate are shown as white circles. Data expressed as the mean ± SEM. Statistics calculated by one-way ANOVA, where * $p \leq 0.05$.

5.2.15 FOXO1 mediates the cytostatic effect of the COMBO treatment in CLL cell lines and primary CLL cells co-cultured on CD40L (+IL-21)

FOXO1 activity plays a prominent role mediating COMBO-induced cell cycle arrest (Figure 5.15) and $p27^{KIP1}$ expression (Figure 5.16a,b) in CLL cell lines. We therefore focussed on the importance of FOXO1 activity for CLL cell proliferation (Figures 5.17 and 5.18). CTV-stained HG-3 and MEC-1 cells were treated with AZD8055, ibrutinib, COMBO or rapamycin for 72 h in the presence or absence of AS1842856. Thereafter, cell proliferation was analysed by flow cytometry (Figure 5.17). HG-3 and MEC-1 cell proliferation was unaffected by AS1842856 treatment alone (Figure 5.17a-c). Consistent with prior experiments (Figure 3.13a-c), AZD8055 and COMBO treatment inhibited HG-3 and MEC-1 cell proliferation, whereas ibrutinib was unable to confer a cytostatic effect (Figure 5.17a-c). Interestingly, simultaneous incubation with AS1842856 rescued AZD8055- (p = 0.08) and COMBO-induced (p = 0.08) inhibition of HG-3 cell proliferation (Figure 5.17a,b). Furthermore, the cytostatic effect of AZD8055 or COMBO treatment on MEC-1 cells was also significantly reduced by concurrent FOXO1 inhibition (Figure 5.17a,c). We also noted that rapamycin-induced inhibition of MEC-1 cell proliferation was also significantly alleviated in the presence of AS1842856 (Figure 5.17a,c).

Given that pharmacological FOXO1 inhibition rescued CLL cell lines from the anti-proliferative effect of the COMBO treatment (Figure 5.17), it was of interest to examine the impact of AS1842856 on the proliferative capacity of primary CLL cells. Following co-culture on NT-L (non-proliferative control) and CD40L (+IL-21) cells, CLL cells were treated with COMBO in the presence or absence of AS1842856 for 9 days. Prior to treatment, CLL cells were stained with CTV to qualitatively and quantitatively assess cell proliferation by flow cytometry (Figure 5.18a-c). Interestingly, FOXO1 inhibition resulted in a trend towards enhanced CLL cell proliferation compared to CD40L (+IL-21) vehicle control (relative to NT-L) (p = 0.13; Figure 5.18a,b). However, relative to CD40L (+IL-21) vehicle control, AS1842856 treatment alone significantly increased CLL cell proliferation (Figure 5.18a,c). Consistent with previous experiments (Figure 3.20a,b), COMBO treatment reduced CLL cell proliferation (Figure 5.18a-c). Of

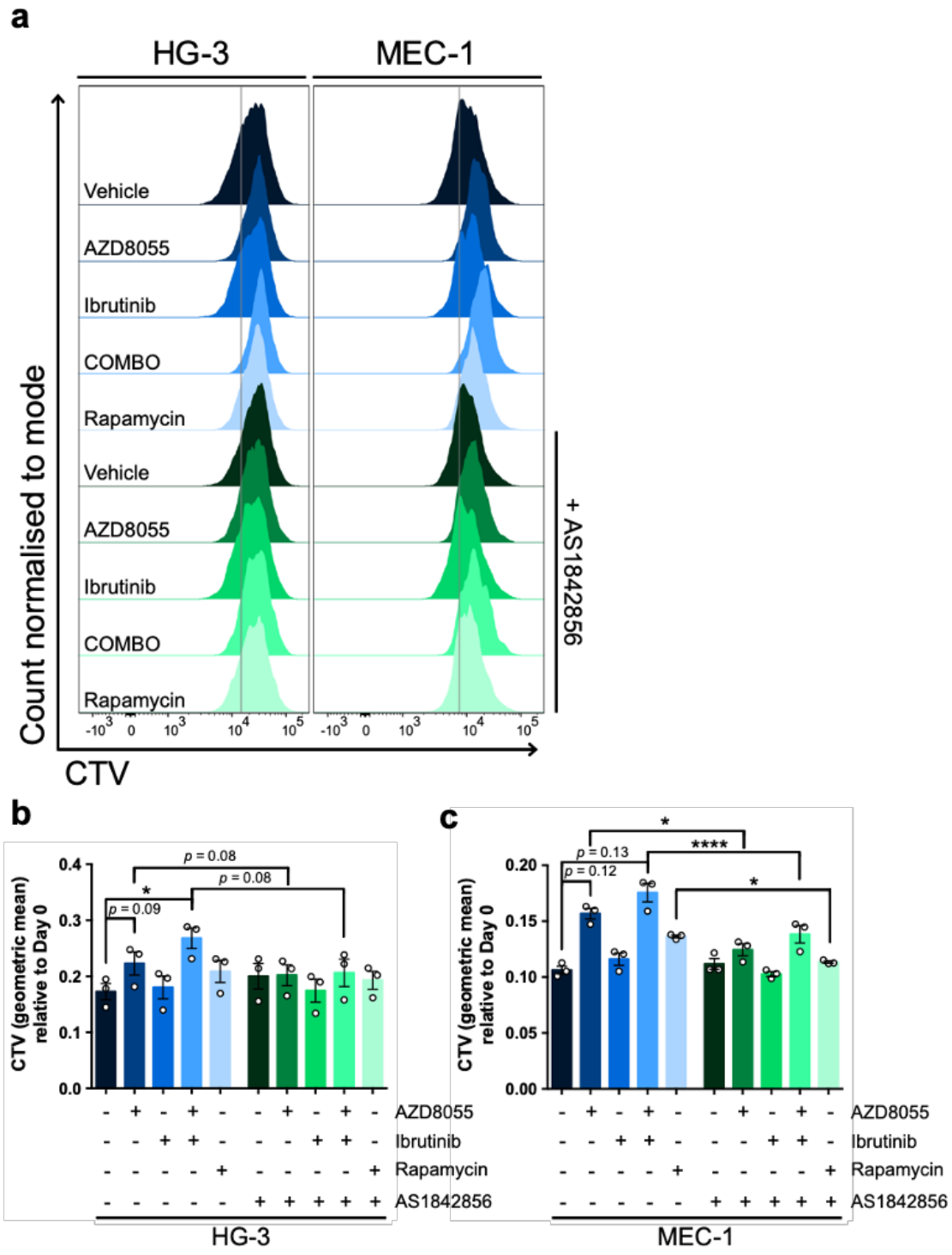

Figure 5.17 - AS1842856 treatment rescues the reduction in cell proliferation caused by COMBO treatment in HG-3 and MEC-1 cells.
(a) Representative FACS histogram of HG-3 and MEC-1 cells stained with CTV to assess cell proliferation following treatment with AZD8055 (100 nM), ibrutinib (1 μM), COMBO, rapamycin (10 nM) or DMSO vehicle control (Vehicle) in the presence (green histograms) or absence (blue histograms) of AS1842856 for 72 h. A grey vertical line represents the peak of the vehicle control histogram for HG-3 and MEC-1 cells. (b) Assessment of CTV geometric mean for HG-3(n=3) and MEC-1 cells (n=3), treated as described in (a). Individual datapoints from each replicate are shown as white circles. Data expressed as the mean ± SEM. Statistics calculated by one-way ANOVA, where * $p \leq 0.05$, **** $p \leq 0.0001$.

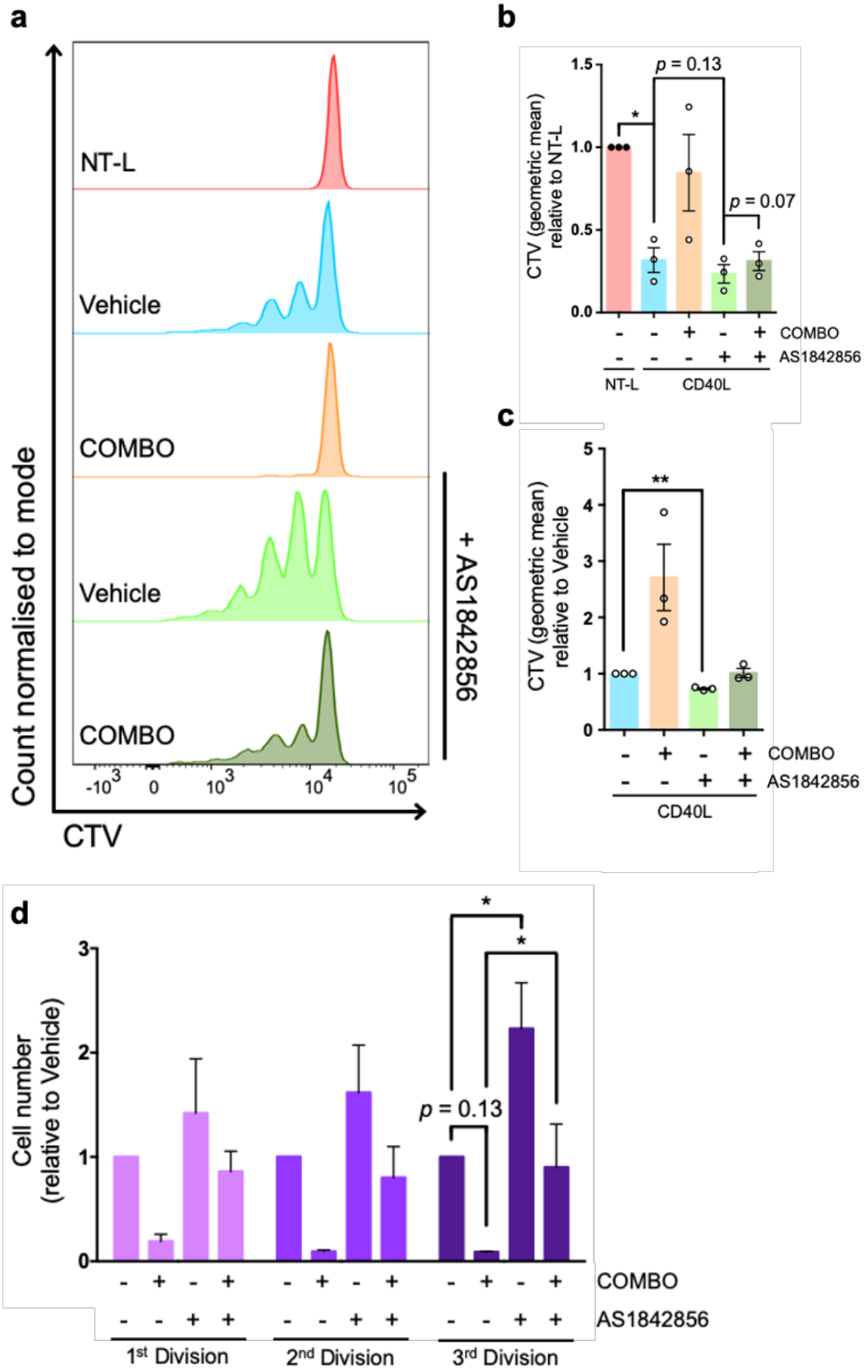

Figure 5.18 - AS1842856 enhances CD40L (+IL-21)-induced primary CLL cell proliferation and rescues CLL cells from the cytostatic effect of COMBO treatment.
(a) Representative FACS histogram of a primary CLL sample stained with CTV following long-term co-culture on CD40L (+IL-21) treated with COMBO or DMSO vehicle control (Vehicle) in the presence of absence of AS1842856 (30 nM) for 9 days. Primary CLL cells were co-cultured on NT-L as a non-proliferative control. (b) Assessment of CTV geometric mean for primary CLL samples

(n=3) treated as described in (a). Geometric means for each condition are relative to NT-L non-proliferative control. (c) Assessment of CTV geometric mean for primary CLL samples (n=3) treated as described in (a). Geometric means for each condition are relative to vehicle control. Individual datapoints from each replicate are shown as white circles. (d) Quantified cell counts of CLL cells co-cultured on CD40L (+IL-21) treated as described in (a). CLL cells were incubated with 'CountBright' counting beads prior to data acquisition. The 1st, 2nd and 3rd generations are shown. Data expressed as the mean ± SEM. Statistics calculated by one-way ANOVA, where * $p \leq 0.05$, ** $p \leq 0.01$.

note, simultaneous incubation with AS1842856 protected CLL cells from COMBO-induced proliferative arrest to levels comparable with CD40L (+IL-21) vehicle control (Figure 5.18a-c). Incubating CLL cells with 'CountBright Absolute Counting Beads' prior to analysis by flow cytometry enabled us to quantify cell numbers in discrete generations (divisions) by comparing the ratio of bead events to cell events (Figure 5.18d). For CLL cells that had undergone 3 divisions (3rd division), the number of AS1842856-treated CLL cells was significantly greater than vehicle control CLL cells (Figure 5.18d), corresponding to enhanced proliferative capacity (Figure 5.18a,c). Consistent with the cytostatic effect of COMBO treatment (Figure 5.18a-c), very few COMBO-treated CLL cells had undergone 3 divisions compared with vehicle control CLL cells ($p = 0.13$; Figure 5.18d). Interestingly, the number of COMBO-treated CLL cells simultaneously incubated with AS1842856 was significantly higher than the number of CLL cells treated with COMBO alone (Figure 5.18d).

5.2.16 COMBO-induced transcription of FOXO gene targets *IGFR1*, *SESN3*, *BCL2-L11* (BIM) and *CDKN1A* are repressed by AS1842856 in MEC-1 cells

Analysis of FOXO transcriptomic data (from various lineages) revealed that FOXO transcription factors regulate their targets in a highly context- and cell type-specific manner (344, 380, 387, 404, 549). We therefore compared basal transcript levels of FOXO target genes *FOXO1*, *IGF1R*, *SESN3*, *BCL2-L11* (BIM), *BBC3*, *GADD45A*, *CDKN1A*, *CDKN1B*, *CCNG2* and *CCND2* in HG-3 and MEC-1 cells (Figure 5.19). These data showed that transcript abundance of *SESN3* (Figure 5.19c), *GADD45A* (Figure 5.19f), *CDKN1A* (Figure 5.19g) and *CCND2* (Figure 5.19j) was significantly higher in HG-3 cells, whereas *FOXO1* (Figure 5.19a), *IGF1R* (Figure 5.19b) and *CCNG2* (Figure 5.19i) expression was significantly greater in MEC-1 cells. Expression levels of *BCL2-L11* (BIM) (Figure 5.19d), *BBC3* (Figure 5.19e) and *CDKN1B* (Figure 5.19h) were comparable between HG-3 and MEC-1 cells.

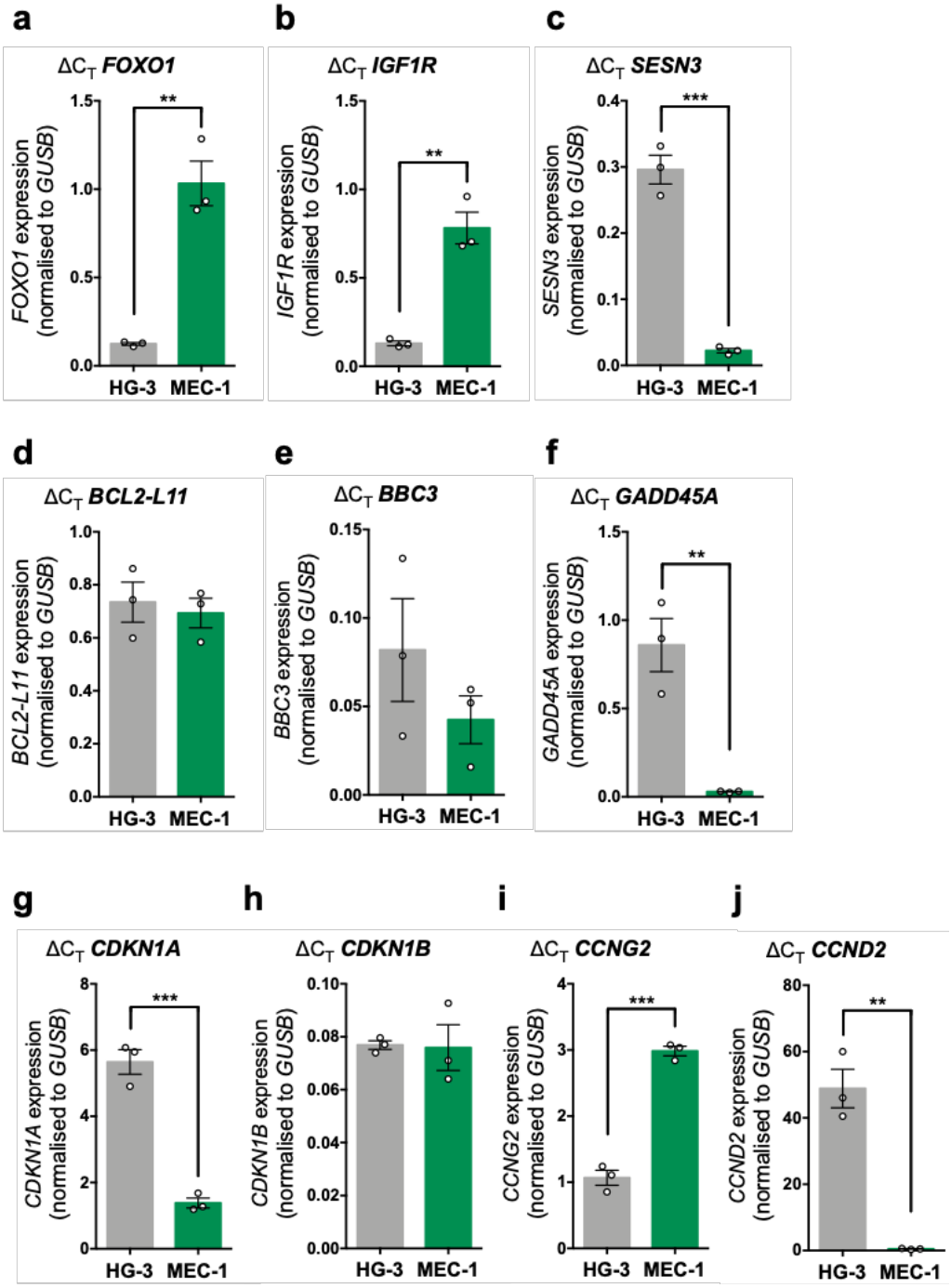

Figure 5.19 - RT-qPCR analysis reveals differential regulation of FOXO1 transcriptional targets between HG-3 and MEC-1 cells.
(a - j) RT-qPCR to assess transcript abundance of (a) *FOXO1,* (b) *IGF1R*, (c) *SESN3*, (d) *BCL2-L11* (BIM), (e) *BBC3*, (f) *GADD45A*, (g) *CDKN1A* ($p21^{CIP1}$), (h) *CDKN1B* ($p27^{KIP1}$), (i) *CCNG2* and (j) *CCND2* in HG-3 (grey bar; n=3) and MEC-1 cells (green bar; n=3). The ΔC_T method was used to calculate expression levels. Samples were normalised to the internal reference gene *GUSB*. Individual datapoints are represented by white circles. Data expressed as the mean ± SEM. Statistics calculated by one-way ANOVA, where ** $p \leq 0.01$, *** $p \leq 0.001$.

We next assessed expression of the aforementioned FOXO target genes in COMBO-treated HG-3 and MEC-1 cells with or without AS1842856 treatment by RT-qPCR (Figures 5.20). *FOXO1* expression was marginally enhanced by AS1842856 treatment alone in HG-3 cells, while transcript levels of *FOXO1* were

unaffected by FOXO1 inhibition in MEC-1 cells (Figure 5.20a). Expectedly, COMBO treatment alone elevated *FOXO1* expression in HG-3 and MEC-1 cells (Figure 5.20a). Notably, however, *FOXO1* transcript abundance was significantly augmented in COMBO-treated HG-3 cells simultaneously incubated with AS1842856, whereas inhibition of FOXO1 activity in MEC-1 cells appeared to block COMBO-induced *FOXO1* upregulation (Figure 5.20a). AS1842856 treatment resulted in a trend towards reduced *IGF1R* expression in HG-3 cells ($p = 0.11$), while FOXO1 inhibition significantly downregulated basal *IGF1R* transcript levels in MEC-1 cells (Figure 5.20b). Furthermore, *IGF1R* expression was upregulated by COMBO treatment alone in HG-3 ($p = 0.06$) and MEC-1 cells (Figure 5.20b). In support of these observations, COMBO-induced *IGF1R* upregulation was reduced by concurrent AS1842856 treatment in HG-3 ($p = 0.059$) and MEC-1 cells ($p = 0.1$; Figure 5.20b). Interestingly, while FOXO1 inhibition significantly enhanced *SESN3* expression in HG-3 cells, *SESN3* transcript abundance was significantly downregulated in MEC-1 cells (Figure 5.20c). Furthermore, COMBO treatment alone did not notably affect *SESN3* expression in HG-3 cells, whereas *SESN3* levels were visibly enhanced by COMBO treatment in MEC-1 cells (Figure 5.20c). Intriguingly, FOXO1 inhibition further enhanced *SESN3* expression in COMBO-treated HG-3 cells, near significantly than AS1842856 treatment alone ($p = 0.057$; Figure 5.20c). Conversely, AS1842856 treatment notably blocked COMBO-induced *SESN3* upregulation in MEC-1 cells (Figure 5.20c). A trend towards elevated levels of *BCL2-L11* was observed in HG-3 cells treated with AS1842856 alone ($p = 0.11$), whereas *BCL2-L11* expression was unaffected by FOXO1 inhibition in MEC-1 cells (Figure 5.20d). As expected, COMBO treatment modestly enhanced *BCL2-L11* transcript levels in HG-3 and MEC-1 cells (Figure 5.20d). Notably, while AS1842856 treatment significantly increased *BCL2-L11* expression in COMBO-treated HG-3 cells compared to COMBO treatment alone, *BCL2-L11* expression was visibly downregulated in COMBO-treated MEC-1 cells simultaneously incubated with AS1842856 (Figure 5.20d). Counterintuitively, expression of pro-apoptotic *BBC3* was significantly downregulated by FOXO1 inhibition in HG-3 cells, and observably reduced in MEC-1 cells (Figure 5.20e). Furthermore, COMBO treatment alone modestly downregulated *BBC3* expression in HG-3 and MEC-1 cells (Figure 5.20e). FOXO1 inhibition downregulated *BBC3* transcript abundance in COMBO-treated HG-3 cells to levels comparable with AS1842856 treatment alone (Figure 5.20e). Similarly, *BBC3* expression was

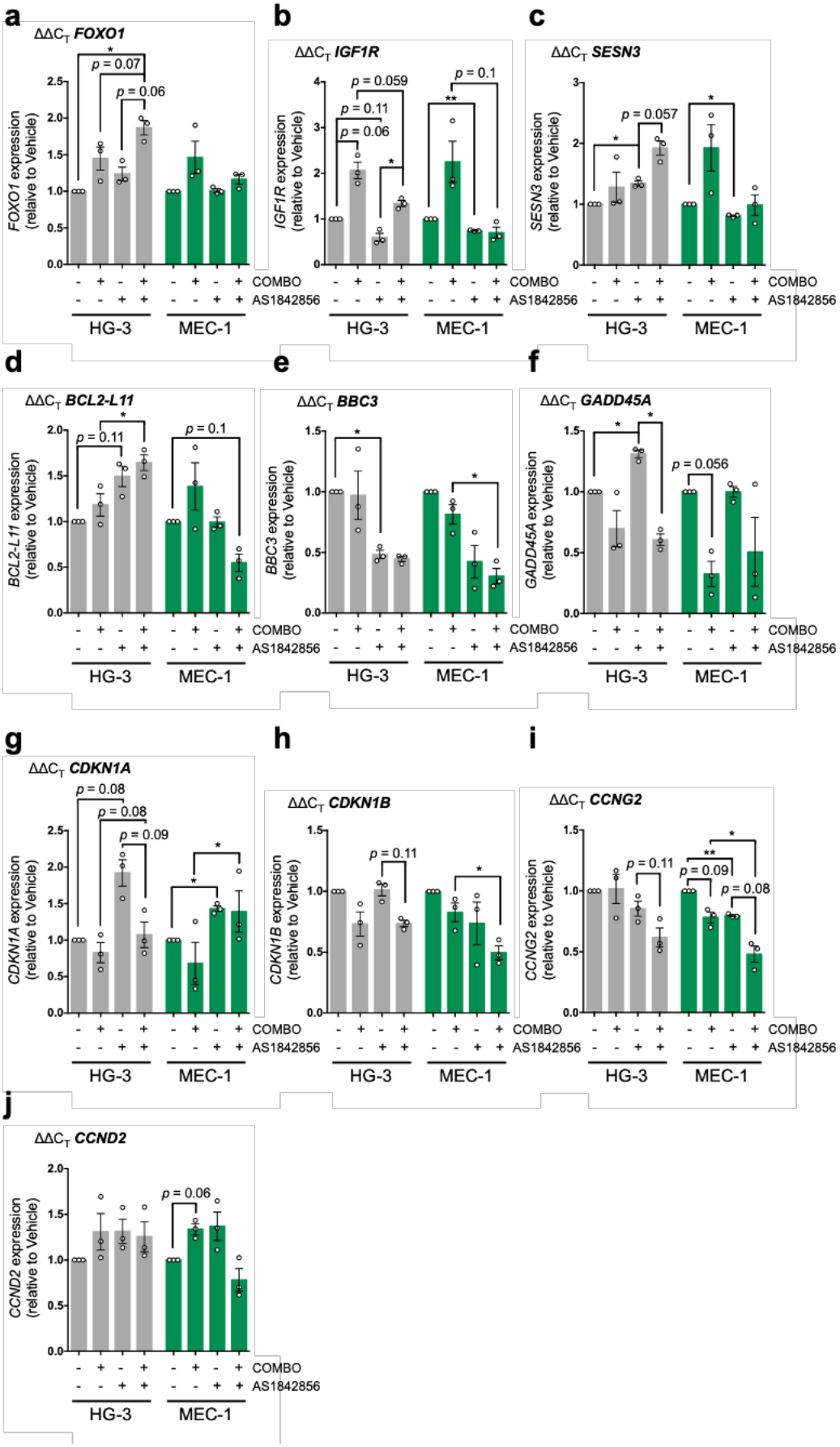

Figure 5.20 - Aberrant regulation of FOXO1 transcriptional targets following AS1842856 treatment in HG-3 and MEC-1 cells.

(a - j) RT-qPCR to assess transcript abundance of (a) *FOXO1,* (b) *IGF1R*, (c) *SESN3*, (d) *BCL2-L11* (BIM), (e) *BBC3*, (f) *GADD45A*, (g) *CDKN1A* (p21^{CIP1}), (h) *CDKN1B* (p27^{KIP1}), (i) *CCNG2* and

(j) *CCND2* in HG-3 (grey bars; n=3) and MEC-1 cells (green bars; n=3) treated with COMBO or vehicle control in the presence or absence of AS1842856 for 48 h. The $\Delta\Delta C_T$ method was used to calculate expression levels, where samples were first normalised to the internal reference gene *GUSB* and then made relative to vehicle control for each cell line. Individual datapoints are represented by white circles. Data expressed as the mean ± SEM. Statistics calculated by one-way ANOVA, where * $p \leq 0.05$, ** $p \leq 0.01$.

reduced in COMBO-treated MEC-1 cells concurrently treated with AS1842856, significantly downregulated compared to COMBO treatment alone (Figure 5.20e). *GADD45A* expression was significantly upregulated by AS1842856 treatment in HG-3 cells, whereas *GADD45A* transcript levels were unaffected by FOXO1 inhibition in MEC-1 cells (Figure 5.20f). Moreover, COMBO treatment visibly downregulated *GADD45A* expression in HG-3 and MEC-1 ($p = 0.056$) cells (Figure 5.20f). Concomitant incubation of COMBO-treated HG-3 cells with AS1842856 decreased *GADD45A* expression to levels comparable with COMBO treatment alone, and significantly less than AS1842856 treatment alone (Figure 5.20f). Similarly, *GADD45A* expression was downregulated in COMBO-treated MEC-1 cells in the presence of AS1842856 (Figure 5.20f). Inhibition of FOXO1 activity near-significantly enhanced *CDKN1A* expression in HG-3 cells ($p = 0.08$), while AS1842856 treatment significantly upregulated *CDKN1A* transcript abundance in MEC-1 cells (Figure 5.20g). Although inconclusive, *CDKN1A* expression appeared reduced by COMBO treatment in HG-3 and MEC-1 cells (Figure 5.20g). Nevertheless, FOXO1 inhibition in COMBO-treated HG-3 cells modestly increased *CDKN1A* transcript levels compared to COMBO treatment alone ($p = 0.08$; Figure 5.20g). Furthermore, AS1842856-induced *CDKN1A* upregulation was near-significantly reduced by concurrent incubation with the COMBO treatment in HG-3 cells ($p = 0.09$; Figure 5.20g). Compared to COMBO treatment alone, COMBO treatment in the presence of AS1842856 enhanced *CDKN1A* expression in MEC-1 cells to levels similar to AS1842856 treatment alone (Figure 5.20g). Although *CDKN1B* expression was unaffected by FOXO1 inhibition in HG-3 cells, *CDKN1B* was visibly downregulated by AS1842856 treatment in MEC-1 cells (Figure 5.20h). Expectedly, COMBO treatment resulted in a trend towards reduced *CDKN1B* transcript levels in HG-3 and MEC-1 cells (Figure 5.20h). Compared to AS1842856 treatment alone, *CDKN1B* expression was discernibly reduced in COMBO-treated HG-3 cells in the presence of AS1842856 ($p = 0.11$; Figure 5.20h). Intriguingly, inhibition of FOXO1 in COMBO-treated MEC-1 cells further decreased *CDKN1B* expression, significantly greater than COMBO treatment alone (Figure 5.20h). Whereas *CCNG2* transcript abundance was moderately downregulated by

AS1842856 treatment in HG-3 cells, *CCNG2* expression was significantly decreased in AS1842856-treated MEC-1 cells (Figure 5.20i). Furthermore, while *CCNG2* expression was unaffected by COMBO treatment in HG-3 cells, a near-significant reduction in *CCNG2* transcript levels was observed in MEC-1 cells ($p = 0.09$; Figure 5.20i). Inhibition of FOXO1 activity in COMBO-treated HG-3 cells further downregulated *CCNG2* expression, greater than each drug alone (Figure 5.20i). Equally, COMBO treatment in the presence of AS1842856 augmented *CCNG2* downregulation in MEC-1 cells, near-significantly greater than AS1842856 treatment alone ($p = 0.08$) and significantly less than COMBO treatment alone (Figure 5.20i). Inhibition of FOXO1 activity noticeably increased *CCND2* expression in HG-3 and MEC-1 cells (Figure 5,20j). Similarly, COMBO treatment modestly upregulated *CCND2* in HG-3 and MEC-1 ($p = 0.06$) cells to levels comparable with AS1842856 treatment alone (Figure 5.20j). While *CCND2* expression was unchanged in COMBO-treated HG-3 cells in the presence of AS1842856 (compared to each drug alone), *CCND2* was notably downregulated in COMBO-treated MEC-1 cells concomitantly incubated with AS1842856 (Figure 5.20j).

5.3 Discussion

Here, we provide insights into the functional consequence of genetic and pharmacological FOXO1 inhibition on CLL maintenance and the response to COMBO treatment. Despite modulation of direct FOXO targets, shRNA-mediated FOXO1 knockdown did not affect cellular pathophysiology, indicating that MEC-1 cells are largely resilient to changes in FOXO1 expression levels. Furthermore, FOXO1-depleted MEC-1 cells remained sensitive to the COMBO treatment, perhaps suggesting that residual FOXO1 is capable of mediating treatment response. In contrast, the FOXO1 inhibitor AS1842856 largely shielded CLL cells from the pro-apoptotic and anti-proliferative effects of the COMBO treatment. Indeed, pharmacological FOXO1 inhibition potentiated CD40L (+IL-21)-induced CLL proliferation, demonstrating that treatment-induced FOXO1 activity likely evokes a context-dependent gene expression programme favouring tumour suppression.

5.3.1 FOXO1 nuclear localisation in HG-3 and MEC-1 cells suggest PI3K-AKT signalling and 'active' FOXO1 paradoxically coincide in the same cells

In the preceding chapter, we demonstrated that FOXO1 expression was elevated among poor prognostic CLL patient LN biopsies compared to those with indolent disease. Notably, FOXO1 intensity score (i.e. FOXO1 expression) positively correlated with Ki-67^{+} staining. Here, largely mimicking the findings observed in lymphoid tissue, FOXO1 expression was significantly greater in MEC-1 cells (del(17p); poor prognostic) compared with HG-3 cells (del(13q); favourable prognostic). While it is intriguing to speculate about the biological importance of enhanced FOXO1 expression in poor-prognostic tissues, these data would need to be validated further to unearth a potential pathogenic role. Nevertheless, FOXO1 downregulation in patients with indolent disease might indicate an important (and perhaps perturbed) biological function for FOXOs in CLL progression. As summarised by Szydlowski *et al.*, evidence from other B cell malignancies highlight various mechanisms that modulate FOXO1 activity and/or expression levels (397), which could explain the differences observed between indolent and progressive disease. For instance, FOXO1 depletion is caused by 13q14 chromosomal deletions harbouring the *FOXO1* locus in cHL (396, 397).

Although FOXO1 loss has not been associated with 'indolent' 13q14 aberrations in CLL (and, by extension, HG-3 cells) (550, 551), analysis of primary Hodgkin and Reed/Sternberg (HRS) cells revealed only a fraction (~11 %) of cases with 13q14 deletions included FOXO1 involvement (396). Thus, it would be interesting to re-evaluate genomic (552, 553), transcriptomic (88) and copy-number (554) data for potential FOXO1 involvement in this CLL patient subset. Indeed, analysis of established FOXO gene targets via RNA-seq or ChIP-seq would further illuminate FOXO involvement. Additionally, aberrant expression of FOXO1-specific miRNAs, such as *miR-96*, *miR-182* and *miR-183* in cHL (396) and *miR-21* in DLBCL (555), have been shown to repress FOXO1 expression and activity (397). In CLL, *miR-29* is upregulated specifically in patients with indolent disease (556, 557). Interestingly, Guérit *et al.* demonstrated that FOXO3 was a direct target of *miR-29* in mesenchymal stem cells (MSCs) (558), suggesting that *miR-29* might downregulate FOXO expression in indolent CLL patients. Therefore, analysis of the FOXO-targeting miRNA landscape among CLL prognostic subtypes (559), particularly downstream of BCR ligation (560), warrants further assessment.

Earlier, our results demonstrated that FOXO1 was localised in the nucleus of 'proliferative' CD40L (+IL-21)-stimulated CLL cells, murine CLL-like PKCαKR cells and CLL patient LN biopsies (irrespective of prognosis). As discussed, these findings suggested that 'active' nuclear FOXO1 (particularly for LN-resident CLL cells) may instruct a gene expression programme promoting CLL maintenance. Notwithstanding the presence of AKT kinase activity (AKT^{S473} and AKT^{T308} phosphorylation), a sizeable fraction of FOXO1 was localised in the nuclei of HG-3 and MEC-1 cells, indicating that nuclear FOXO1 expression paradoxically coincides with PI3K-AKT activity. Consistently, a recent study similarly reported nuclear FOXO3a expression alongside phosphorylated AKT (AKT^{S473}) in MEC-1 cells (501). Although it is unlikely that FOXOs strictly exist as 'cytoplasmic' or 'nuclear' (344), these observations raised important points regarding the regulation and functional importance of FOXOs in HG-3 and MEC-1 cells. As mentioned previously, FOXO activity in the presence of constitutive PI3K-AKT signalling has also been reported in other B cell malignancies, such as BL (401) and pre-BCR^+ BCP-ALL (403), where FOXO activity supported an oncogenic phenotype. Nevertheless, without prior characterisation of 'activating' FOXO1 mutations in CLL, the presence of nuclear FOXO1 amidst AKT kinase activity

cannot be conclusively resolved (401). However, FOXOs are routinely under the influence of different posttranslational and/or posttranscriptional modifications, such as JNK-mediated phosphorylation (371) or miRNAs (561), which can promote FOXO nuclear localisation and transcriptional activity, respectively (347). Furthermore, as mentioned earlier, strict regulation of FOXO1 activity within the confines of an established setpoint (403, 506) might permit simultaneous PI3K- and FOXO1 activity.

FOXOs regulate their transcriptional targets in a highly context- and cell type-specific manner (344, 380, 387, 404, 549). Indeed, FOXO1 activity fulfils many distinct functions throughout B cell development (387) and among different B cell malignancies (384). Alongside established 'conserved' targets (380), one might conjecture that FOXOs regulate a unique array of context-dependent target genes in CLL. Interestingly, despite similar levels of FOXO1^{T24} phosphorylation, the data presented here revealed marked differences in FOXO target expression in HG-3 and MEC-1 cells. These findings suggest that HG-3 and MEC-1 prognostic might factors influence FOXO activity in a context-dependent manner, which may generate distinct FOXO-induced gene signatures on a prognostic-level. Other B cell malignancies have demonstrated differences in FOXO1 activity among disease- and subtype-specific cell lines, including cHL (524), DLBCL (397) and BCP-ALL (403), further indicating that FOXO1 activity is probably affected by intrinsic factors such as genomic mutations (562) and epigenetic regulation (563). However, since the FOXO transcriptional targets were arbitrarily chosen on the basis of prior functional data (344, 348), they were not necessarily exclusive to CLL cells. Therefore, it would be interesting to perform ChIP-seq binding analysis to uncover direct FOXO targets specifically in HG-3 and MEC-1 cells (or primary CLL cells, for that matter). Of note, HG-3 and MEC-1 cells are EBV-transformed (431, 432, 564), which has been shown to repress FOXO1 activity via Latent Membrane Protein (LMP)-1 and -2A-mediated PI3K-AKT activation (565). Unlike endemic BL (566) and EBV^{+} posttransplant lymphoproliferative disorder (PTLD) (567, 568), however, EBV infection is not involved in CLL pathogenesis (564). Therefore, while EBV-induced FOXO1 inactivation might contribute to HG-3 and MEC-1 oncogenesis, one must be cautious of drawing comparisons between cell lines and primary CLL cells.

5.3.2 MEC-1 cells were unaffected by shRNA-mediated FOXO1 knockdown, suggesting that these cells are largely resilient to changes in FOXO1 levels

In their study, Srinivasan *et al.* postulated that small changes in FOXO1 levels have major effects on mature B cell physiology (275). Largely supporting the notion that FOXOs maintain cellular homeostasis within a narrow range (506), this view indicated that deviations outside this optimum have deleterious consequences for normal (387) and malignant B cells (384). To investigate the importance of FOXO1 in CLL maintenance and the functional response to COMBO treatment, we adopted *FOXO1*-targetting shRNA lentiviral vectors to stably 'knockdown' FOXO1 expression in HG-3 and MEC-1 cells. Although MEC-1 cells were successfully transduced, several attempts to simultaneously expand infected HG-3 cells (including Scr control) were unsuccessful. Going forward, protocols for transducing HG-3 cells will need to be optimised to glean meaningful comparisons between HG-3 and MEC-1 cells. In pre-BCR$^-$ and pre-BCR$^+$ BCP-ALL cell lines, shRNA-mediated FOXO1 depletion induced G1 cell cycle arrest and enhanced caspase-dependent cell death, indicating that BCP-ALL cell maintenance is reliant on FOXO1 expression (403). In contrast, BCR-dependent DLBCL (DHL4, DHL6, Ly1 and Ly7) and cHL (U-HO1) cell lines were largely unaffected by FOXO1 repression (397, 403). In fact, FOXO1 knockdown actually enhanced proliferation in another cHL cell line (L428) (403), supporting FOXO1's reported tumour suppressor role in this malignancy (396). Although FOXO1 depletion modulated transcript abundance of certain FOXO targets (indicating perturbed FOXO target regulation), our results demonstrated that shRNA-mediated FOXO1 knockdown did not affect MEC-1 cell survival, size or proliferative capacity. Consistent with the findings observed in DLBCL and cHL (U-HO1) cell lines (397, 403), these data suggest that MEC-1 cells are largely resilient to changes in FOXO1 expression levels. As functional redundancy exists among FOXO transcription factors (404), FOXO1 expression might be superfluous in the context of MEC-1 cell maintenance. Here, we demonstrated that *FOXO3* mRNA expression was enhanced following FOXO1 knockdown in MEC-1 cells, perhaps indicating the existence of an adaptive mechanism. Whether this finding confers functional redundancy among FOXOs in MEC-1 cells remains to be elucidated. With experimental hindsight, incubation periods should have been extended from 2/3 days (48/72 h) up to a maximum of 9 days to properly

evaluate the functional impact of FOXO1 knockdown in MEC-1 cells. For example, the doubling time for MEC-1 cells is reportedly ~40 hours (409). In their study, Wang *et al*. assessed the proportion of FOXO1-depleted and scrambled control BCP-ALL cell lines on day 3, 6 and 9. Interestingly, the functional effect of FOXO1 repression was only apparent after 3 days (403). Taken together, although FOXO1 depletion in other B cell malignancies elicit 'positive' and 'negative' consequences for cellular function (403), this is not necessarily the case in MEC-1 cells. Notwithstanding potential experimental limitations, these findings suggest MEC-1 cells may adapt to perturbed FOXO1 levels.

5.3.3 FOXO1-depleted MEC-1 cells are sensitive to COMBO treatment, perhaps suggesting residual FOXO1 is capable of mediating treatment response

ShRNA-mediated FOXO1 repression protected BCR-dependent DLBCL cell lines from the cytotoxic and anti-proliferative effect of combined SYK (R406) and AKT (MK2206) inhibition (397), indicating that FOXO1 is an effector of truncated BCR signalling. Furthermore, pharmacological (PRT318 or LY294002) inactivation of pre-BCR signalling or FOXO1-A3 expression resulted in FOXO1-dependent pre-BCR^{+} BCP-ALL cell death and reduced proliferation, respectively (402). Collectively, these findings suggest that BCR signalling inhibitors unleash abnormal levels of FOXO1 activity (straying from the established setpoint) that promotes FOXO1-dependent tumour suppressor activity in B cell malignancies. Largely corresponding to earlier findings in primary CLL cells, our results demonstrated that COMBO treatment inhibited AKT-dependent FOXO1^{T24} phosphorylation (HG-3 and MEC-1 cells), augmented FOXO1 nuclear accumulation and enhanced FOXO1 DNA-binding activity in MEC-1 cells, suggesting that FOXO1 mediates the functional response to the COMBO treatment. Interestingly, increased FOXO1 activity appeared to be driven predominantly by ibrutinib treatment (over that of AZD8055) in MEC-1 cells, perhaps indicative of constitutive BTK activation (501) and enhanced BCR signalling capacity via the expression of unmutated (94% homology to germline) *IGVH* (*IGHV4-59*) genes (432, 564). However, shRNA-mediated FOXO1 depletion was unable to rescue MEC-1 cells from the pro-apoptotic, cell-contracting and anti-proliferative effects of the COMBO treatment. This result was unexpected, especially considering the impact of FOXO1 knockdown on the regulation of COMBO-

induced FOXO gene targets such as *IGFR1*, *SESN3* and *BCL2-L11*. Additionally, FOXO1 repression diminished COMBO-induced upregulation of BIM (BIM_{EL}, BIM_L and BIM_S) and $p27^{KIP1}$. Thus, FOXO1-depleted MEC-1 cells remained sensitive to COMBO treatment, despite aberrant modulation of FOXO targets on a mRNA and protein level. This implicated the 'incomplete' nature of FOXO1 knockdown as a possible explanation for the sensitivity of FOXO1-repressed MEC-1 cells, with residual FOXO1 activity being capable of conferring a commensurate response to treatment. This is reflected in the ability of FOXO1-depleted cells to enhance FOXO1 (mRNA and protein) expression upon COMBO treatment, a potential adaptive response that dampens the effect of FOXO1 knockdown. Nevertheless, how these findings are resolved amidst the narrative that FOXO elicits homeostatic functions within an optimal range remains to be elucidated. Going forward, the shRNA constructs and/or protocols for transduction must be optimised to improve the levels of FOXO1 knockdown; perhaps combining *FOXO1*-targeting constructs or choosing different constructs targeting multiple FOXOs, as described (403). Equally, it would be interesting to adopt CRISPR-Cas9 technology to achieve full inactivation of FOXO1 (or site-directed mutagenesis (401)). Furthermore, a future perspective would be to assess inducible FOXO1-A3 expression in CLL cells, alongside dominant-negative (DN) FOXO1 (FOXO1-DN) constructs, to complement our work on pharmacological-induced FOXO1 activation.

5.3.4 Inhibition of FOXO1 activity protects CLL cells from the effects of COMBO treatment, indicating FOXO1 mediates the functional response to treatment

Since shRNA-mediated FOXO1 knockdown was only partial, we argued that remnants of FOXO1 might have retained the ability to facilitate cellular maintenance and induce a proportional response to COMBO treatment. Thus, inhibition of FOXO1 transcriptional activity represents an attractive means to prevent induction or repression of FOXO target genes. The FOXO1 inhibitor AS1842856 has been reported to diminish FOXO1 DNA-binding activity by targeted inhibition of 'active' FOXO1 (545, 546). In BCP-ALL cells lines (RS4;11 and UoCB6), transcriptomic analysis uncovered >800 modulated probe sets following AS1842856 treatment, with 9 of the top 20 downregulated genes being established FOXO transcriptional targets (403). Here, AS1842856 treatment

modulated FOXO targets *IGFR1*, *SESN3*, *BBC3*, *GADD45A*, *CDKN1A* and *CCNG2* in CLL cell lines, indicating that FOXO1 activity is repressed. As a next step, it would be interesting to assess AS1842856-induced transcriptome changes to better understand the FOXO transcriptional landscape in CLL cells. Alongside its ability to prevent FOXO1 DNA-binding (545, 546), AS1842856 has been shown to sequester FOXO1 in the cytoplasm of hESCs (547). Interestingly, our results demonstrated that short-term AS1842856 treatment had no effect on FOXO1 localisation or COMBO-induced FOXO1 nuclear translocation. Moreover, FOXO1 DNA-binding activity was largely unaffected by AS1842856 in the presence or absence of the COMBO treatment. While these data were surprising, one possible explanation was the simultaneous incubation of AS1842856 and the COMBO treatment. With hindsight, pre-treating MEC-1 cells with AS1842856 prior to the introduction of COMBO might have yielded different results.

In B cell malignancies, studies adopting AS1842856 to address the functional importance of FOXO1 are limited. Interestingly, however, these findings appear to highlight FOXO1's oncogenic potential. Wang *et al*. showed that AS1842856 treatment reduced cell growth and survival in BCP-ALL cell lines. Furthermore, AS1842856 conferred anti-leukaemia activity in *ex vivo* patient-derived leukaemia cells and *in vivo* xenograft models (403). In another study, Pyrzynska *et al*. demonstrated that FOXO1 transcriptional activity was implicated in the resistance of NHLs to R-CHOP therapy via a mechanism that negatively regulated CD20 expression. AS1842856 treatment eliminated FOXO1-mediated CD20 repression in NHL cell lines (503). At odds with these findings, our results point towards a context-dependent tumour suppressor role for FOXO1. Here, we showed that AS1842856 treatment essentially rescued CLL cells from the pro-apoptotic, cell-contracting and anti-proliferative effects of the COMBO treatment, indicating that FOXO1 mediates the functional response to treatment. Moreover, pharmacological FOXO1 inhibition potentiated CD40L (+IL-21)-induced CLL cell proliferation, suggesting that FOXO1 operates as a 'molecular break' that regulates CLL proliferative capacity.

5.3.4.1 Apoptosis

Whilst largely insensitive to pharmacological FOXO1 inhibition, treatment of HG-3 and MEC-1 cells with AS1842856 resulted in a modest dose-dependent

reduction in cell viability. In primary CLL cells, cell viability was initially maintained at lower concentrations before decreasing in a dose-dependent manner. Notably, calculated EC_{50} values revealed that primary CLL cells were more sensitive to AS1842856 treatment compared to CLL cell lines. However, these values far exceeded the IC_{50} (33 nM) of AS1842856 established in HepG2 cells (545). Therefore, we cannot exclude potential off-target effects that may explain the elevated levels of apoptosis (at higher concentrations). Indeed, Nagashima *et al.* demonstrated that AS1842856 targets other FOXOs (FOXO3 and FOXO4) at concentrations exceeding 100 nM. Furthermore, pharmacokinetic analysis of AS1842856 revealed a maximum plasma concentration of 300 nM in mice (545), indicating that higher concentrations have deleterious off-target effects *in vivo*. Therefore, one should question the biological relevance of surpassing these concentrations. In their study, Wang *et al.* showed that AS1842856 induced apoptosis in BCP-ALL cell lines in a time- and dose-dependent manner (403). On reflection, the impact of AS1842856 on CLL cell viability should have been monitored daily for a period up to 96 h. At this point, we cannot conclude whether FOXO1 is implicated in the maintenance of CLL cells, but this warrants further investigation. On a molecular level, however, *BCL2-L11* (BIM) expression was unaffected by AS1842856 (30 nM) treatment, whereas pro-apoptotic *BBC3* (PUMA) transcript abundance was reduced in HG-3 and MEC-1 cells. These findings echo the modest effects of AS1842856 treatment on cell viability and points towards FOXO1 as a tumour suppressor in this context.

In normal and malignant cells, activated FOXOs drive the expression of pro-apoptotic genes that tip the scales towards cellular apoptosis (344, 346). As demonstrated earlier, COMBO treatment augmented FOXO1 DNA-binding activity, concomitantly upregulated pro-apoptotic *BCL2-L11* expression and reduced cell viability. Here, we showed that COMBO-induced cell death was seemingly negated in the presence of AS1842856 (30 nM and 100 nM) in MEC-1 cells, demonstrating that FOXO1 inhibition protected these cells from the pro-apoptotic effect of COMBO treatment. These findings suggest that FOXO1 mediates the apoptotic response of COMBO treatment in MEC-1 cells. In the case of HG-3 cells, the ability of AS1842856 to prevent COMBO-induced cell death remains unresolved. However, the low expression of FOXO1 in these cells might

be related to its limited efficacy. Nevertheless, enhanced COMBO-induced transcript abundance of *BCL2-L11* was diminished in the presence of AS1842856 in MEC-1 cells, indicating that FOXO1-mediated induction of pro-apoptotic *BCL2-L11* contributes to treatment-induced MEC-1 cell death. Importantly, Szydlowski *et al.* similarly showed, albeit by shRNA-mediated FOXO1 knockdown, that inhibiting BCR signalling in BCR-dependent DLBCL cell lines resulted in FOXO1-dependent cell death via a mechanism that involved FOXO1-mediated *BCL2-L11* upregulation (397).

5.3.4.2 Cell size

FOXOs have been implicated in the regulation of mTORC1 signalling via induction of *SESN3*, which activates mTORC1-negative regulators TSC1/2 (384, 542). As mTORC1 signalling plays a crucial role in the regulation of cell size (442), we assessed the impact of pharmacological FOXO1 inhibition on HG-3 and MEC-1 cell size. We demonstrated that AS1842856 treatment (100 nM) modestly enhanced MEC-1 cell size, which coincided with reduced levels of *SESN3* mRNA expression. These data indicate that FOXO1 regulates mTORC1 activity, in part, via induction of *SESN3* in MEC-1 cells. To confirm these findings, the impact of AS1842856 treatment on mTORC1 activity (4E-BP1$^{T37/46}$ and S6$^{S235/236}$) should be assessed. Although AS1842856 (100 nM) marginally enhanced HG-3 cell size, this paradoxically corresponded to enhanced levels of *SESN3* transcript levels. 'Basal' *SESN3* levels were shown to be higher in HG-3 cells than MEC-1 cells, perhaps reflecting reduced mTORC1 activity in HG-3 cells. A mechanism that permits SESN3 upregulation upon FOXO1 inhibition remains unknown. In any case, these results perhaps underscore a necessity of FOXO1 in mTORC1-dependent MEC-1 cell size regulation, which largely corresponds to a study demonstrating the association between FOXO1 overexpression and reduced cardiomyocyte cell size (544).

Along these lines, enhanced COMBO-induced FOXO1 activity coincided with reduced MEC-1 cell size. In search of a tangible link between elevated FOXO1 activity and MEC-1 cell contraction, we demonstrated that AS1842856 (100 nM) treatment marginally rescued the effect of COMBO treatment on MEC-1 cell size. Notably, COMBO treatment still significantly reduced cell size in the presence of AS1842856, which was likely a result of sustained mTORC1/2 inhibition.

Nevertheless, these findings potentially indicate that FOXO1 contributes to cell size regulation independent of mTORC1/2 signalling. Interestingly, Sengupta *et al.* demonstrated that FOXO1-mediated cell size reduction coincided with transactivation of autophagy-related genes *Gabarapl1* and *Atg12* in cardiomyocytes (544). Autophagy has been shown to inhibit cell growth (569). As FOXOs are known to promote autophagy (570), this ought to be considered as a potential response to COMBO treatment-induced FOXO activation in CLL cells. Thus, FOXO1 appears to be implicated in cell size regulation via mechanisms that involve mTORC1 inhibition and autophagy induction.

5.3.4.3 Cell cycle progression and proliferation

Supraphysiological FOXO activation (via PI3K-AKT inhibition or expression of constitutively active FOXO-AAA mutants) has been shown to induce cell cycle arrest (277, 344, 376, 377, 498). In BCR-dependent DLBCL cell lines DHL4 and Ly7, concurrent inhibition of SYK (R406) and AKT (MK2206) synergistically reduced proliferation in a FOXO1-dependent manner, inasmuch as FOXO1-depleted cells were resistant to the cytostatic effect of the combination treatment (397). Furthermore, ectopic FOXO1-A3 expression inhibited proliferation in cHL cell lines, which correlated with enhanced levels of the cell cycle kinase inhibitor *CDKN1B* ($p27^{KIP1}$) (396). Collectively, these studies suggest that abnormally high levels of FOXO1 activity elicit anti-proliferative tumour suppressive functions. Here, our results demonstrated that FOXO1 inhibition rescued HG-3 and MEC-1 cells from the anti-proliferative effect of COMBO treatment, indicating that enhanced FOXO1 activity mediates treatment response. Indeed, AS1842856 diminished COMBO-induced upregulation of FOXO target $p27^{KIP1}$, highlighting a potential FOXO-mediated mechanism for these observations. Thus, the anti-proliferative effects of FOXO1 in CLL cell lines correlate with the activation of its established tumour suppressor targets. Interestingly, FOXO1 inhibition similarly protected MEC-1 cells from the cytostatic effect of rapamycin, highlighting the involvement of FOXO1 in the functional response to mTORC1 inhibition. Of note, AS1842856 treatment alone had no effect on cell cycle regulation or proliferation in HG-3 or MEC-1 cells, despite downregulation of $p27^{KIP1}$.

In CD40L (+IL-21)-stimulated primary CLL cells, AS1842856 (30 nM) shielded 'proliferative' cells from the cytostatic effect of the COMBO treatment, further indicating that enhanced FOXO1 activity mediates treatment response. Although the regulation of FOXO1 targets was not assessed, earlier experiments revealed that COMBO-induced proliferation arrest coincided with $p27^{KIP1}$ upregulation. Therefore, it is interesting to speculate about the modulation of FOXO-induced cell cycle kinase inhibitors (e.g. $p27^{KIP1}$, $p21^{CIP1}$ and $p57^{KIP2}$) to delineate FOXO1's tumour suppressor function on a molecular level. Interestingly, pharmacological FOXO1 inhibition appeared to potentiate primary CLL cell proliferation, as demonstrated by CTV (geometric mean) and absolute cell counts. These findings suggest that FOXO1 operates as a 'molecular break' that tightly regulates the extent of CD40L (+IL-21)-induced CLL proliferation. Consistent with the pro-proliferative effect of FOXO1 depletion in cHL cell lines (L428) (403), these data imply that FOXO1 is a robust tumour suppressor in this context. Going forward, *FOXO1*-targeting shRNA constructs and protocols for transducing primary CLL cells must be optimised to complement these findings.

5.3.5 Summary

Taken together, these findings demonstrate that FOXO1 activity mediates the cytostatic and cytotoxic effects of the COMBO treatment, indicating that FOXO1 functions as a tumour suppressor in this context. Genetic or pharmacological FOXO1 inhibition did not impact HG-3 or MEC-1 cell maintenance, perhaps suggesting these cells can withstand reduced FOXO1 levels. However, a surplus of nuclear FOXO1 upon COMBO treatment overwhelms the cells and initiates cell cycle arrest and apoptosis in a FOXO1-dependent manner (397). These findings largely correlate to the notion of the 'Goldilocks principle' (403, 506), where only optimal ("just right") FOXO activity supports cellular maintenance (344, 403). As demonstrated in mature B cells (390), these data likely demonstrate that FOXO1 inactivation is an important outcome of CLL-BCR signal transduction (downstream of PI3K-AKT signalling) to prevent FOXO1-mediated cell cycle arrest and apoptosis. Thus, inhibition of FOXO negative regulators (such as PI3K-AKT) represent an interesting therapeutic strategy. However, one should be cautious of compensatory and/or resistance mechanisms induced by active FOXOs. Indeed, studies have shown that FOXOs induce transcription of growth factor receptors, such as IGF1R (147) and HER3 (324), which reactivate PI3K-AKT

signalling. Here, for example, we demonstrated that *IGF1R* is upregulated upon COMBO treatment in a FOXO1-depedent manner. Thus, while FOXO1 activation unleashes tumour suppressive functions, this should be complemented by an understanding of the transcriptome changes induced by aberrantly enhanced FOXO activity.

6 General Discussion

6.1 Summary of results

The data presented in this thesis demonstrates that mTOR is an effector of BCR crosslinking *in vitro*, playing a role in the coordination cellular behaviours emanating from BCR engagement (BCR-PI3K-AKT) in CLL cells. mTOR (mTORC1 and mTORC2) activity was effectively targeted by the 'second generation' mTOR kinase inhibitor AZD8055 (and its clinical analogue AZD2014), which disabled pro-survival feedback loops associated with the selective-mTORC1 inhibitor rapamycin. On a molecular level, AZD8055 inhibited mTOR signalling downstream of $F(ab')_2$-mediated BCR ligation and stromal cell (NT-L/CD40L) co-cultures, highlighting the ability of this compound to disrupt various microenvironmental stimuli. On a functional level, AZD8055 elicited potent inhibitory effects on CLL growth and proliferation, but only moderately affected cell viability *in vitro*. For these reasons, AZD8055 anti-tumour activity appeared to be limited as a monotherapy. A synergistic combination of AZD8055 and the BTK inhibitor ibrutinib promoted cell death, augmented cell size contraction and arrested proliferation, indicating that simultaneous inhibition of mTOR kinase and BTK in CLL cells evokes anti-tumour activity via targeted inhibition of multiple oncogenic pathways *and* at different levels within the same pathway.

In search of a mechanism of action, we proposed that the combination treatment conferred a more robust inhibition of AKT kinase activity, relieving negative regulation on tumour suppressive FOXO transcription factors. Our data demonstrated that BCR crosslinking negatively regulated FOXO1 (the most abundant FOXO in CLL cells) by AKT-dependent $FOXO1^{T24}$ phosphorylation, subsequent nuclear export and reduced DNA-binding activity. Like normal B cells, these data suggested that FOXO1 inactivation was an important consequence of BCR engagement in CLL cells. For this reason, we hypothesised that inhibiting BCR signalling would unleash FOXO1 tumour suppressor activity. We showed that elimination of BCR signal transduction, via AZD8055 or ibrutinib mono- and combination therapy, re-engaged FOXO1 DNA-binding activity by preventing FOXO1 nuclear export, which suggested that FOXO1 was an effector of BCR signalling inhibition that mediated treatment response. Through pharmacological FOXO1 inhibition, we demonstrated that FOXO1 activity

contributed to the cytotoxic, cell-contracting and cytostatic effects of the combination treatment, indicating that FOXO1 functions as a tumour suppressor in this context. Nevertheless, abundant nuclear FOXO1 expression in CLL patient LN biopsies points towards a context-dependent homeostatic role for FOXO1 in CLL maintenance, which requires further investigation though a comprehensive analysis of FOXO1 transcriptional targets in different compartments. In this concluding chapter, the implications of these results for prospective pre-clinical (translational) investigations and potential clinical studies are examined.

6.2 mTOR kinase (mTORC1/2) inhibition in CLL: a promising target for therapeutic intervention?

Despite promising results as a monotherapy (and in combination with other drugs) in clinical trials of 'solid' tumours and blood cancers, AstraZeneca discontinued AZD2014 (vistusertib) in November 2018 citing "re-prioritization [sic] of the R&D portfolio" (571). As a monotherapy, AZD2014 demonstrated anti-cancer effects in 'solid' tumours including breast (492) and small cell lung cancer (572), whereas a phase II clinical trial comparing AZD2014 and everolimus in renal cancer patients was terminated early due to lack of efficacy (573). Here, while the cytostatic effect of AZD8055/2014 likely represents a promising treatment modality to prevent proliferation-driven clonal evolution in CLL cells, the drugs are not particularly cytotoxic. As such, AZD8055/2014 is unlikely to eradicate the entirety of leukemic cells. Alongside the potential issues linked to the alleviation of adaptive feedback mechanisms, it is increasingly apparent that dual mTOR kinase inhibitors require partner drugs as novel combination strategies. In agreement with our results assessing the synergistic combination of AZD8055/2014 and ibrutinib in CLL cells, *in vitro* and *in vivo* pre-clinical studies of AZD2014 and acalabrutinib combination in DLBCL have demonstrated synergistic growth inhibition (574). As a result, the combination entered phase I/II trials in patients with R/R DLBCL (NCT03205046), which remained active until the discontinuation of AZD2014. In this section, recent pre-clinical data of novel mTOR inhibitors (dual PI3K/mTOR and mTOR/DNA-PK) will be discussed and an overview of intriguing treatment strategies combining mTOR inhibitors with BH3 mimetics will be provided.

6.2.1 Dual PI3K/mTOR inhibitors in CLL

The reported drawbacks associated with mTOR kinase inhibitors as monotherapies, i.e. diminished feedback inhibition of RTKs sufficient to reactivate AKT pro-survival signalling (324), have led to the development of novel targeted therapies designed to overcome subsequent activation of PI3K-AKT signalling (293). The dual PI3K/mTOR inhibitors PF-04691502 (341) and SAR245409 (342) have been adopted in CLL pre-clinical investigations. In their study, Blunt *et al*. demonstrated that PF-04691502 prevented AKT reactivation, induced caspase-dependent apoptosis irrespective of prognostic features, antagonised TME pro-survival signals and inhibited CXCL12-induced chemotaxis. Importantly, PF-04691502 was significantly more efficacious in reducing CLL cell viability than a synergistic combination of idelalisib and everolimus. In CLL-like Eμ-TCL1 mice, PF-04691502 reduced the number of $CD5^{+}B220^{+}$ leukemic cells in the blood, BM and SLOs (341). Along the same lines, Thijssen *et al*. showed that SAR245409 augmented CLL cell death compared to PI3Kδ/α selective inhibitors alone, abrogated proliferation and blocked cell adhesion *in vitro* (342). Phase 1b clinical data of SAR245409 (in combination with rituximab or rituximab+bendamustine) in R/R patients with B cell malignancies demonstrated encouraging clinical activity, with OR rates of 48.6 % (575). Alongside our data examining synergy between AZD8055 and ibrutinib (which equally inhibits PI3K-AKT signalling), these studies collectively indicate that targeted inhibition of PI3K and mTOR is a promising therapeutic strategy in CLL (particularly for high-risk patients) that negates elaborate resistance mechanisms, which ought to be investigated further. Therefore, one must speculate on the advantages of such a combination alongside the current arsenal of successful combination strategies (e.g. ibrutinib and venetoclax (165)). As ibrutinib treatment seemingly enhances PI3K-AKT-mTOR signalling (contributing to ibrutinib resistance) in CLL cells (146, 501), combining ibrutinib with mTOR inhibitors may restrict resistance mechanisms that might otherwise lead to disease progression and therapy discontinuation. Furthermore, enhanced AKT activity (due to ibrutinib treatment and/or resistance) may elevate BCL-xL or MCL-1 expression, limiting the effectiveness of venetoclax treatment (or other BH3 mimetics) (216, 278, 462). Given the effect of combining AZD8055 with ibrutinib on FOXO1 activity, it is tempting to conjecture that CLL patients could be selected the basis of FOXO1

expression. Although not conclusively resolved, patients with enhanced FOXO1 levels may benefit from COMBO-induced FOXO1 tumour suppressor activity.

Notably, the dual mTOR/DNA-PK inhibitor CC-115 has equally demonstrated pre-clinical and clinical potency in CLL. DNA-PK is a key regulator of the DNA damage repair pathway (343). CC-115 induced apoptosis independently of *TP53*, *ATM* or *NOTCH1* status, inhibited CD40L (+IL-21)-induced proliferation and blocked BCR signal transduction (also in idelalisib-resistant patient samples) *in vitro*. In a small cohort (8 patients) of R/R CLL patients, CC-115 similarly showed promising clinical efficacy (343).

6.2.2 mTOR and BCL2 inhibition: a promising combination strategy

In their recent review, Kater and Brown postulated the need to identify a partner drug for ibrutinib and discussed the rationale for combining ibrutinib with the BCL2 inhibitor venetoclax. The authors highlighted the ability of ibrutinib to antagonise chemotaxis towards the CLL-TME, but acknowledged its inability to induce robust apoptosis *in vitro* (576). In pre-clinical studies, *ex vivo* serial samples from ibrutinib-treated CLL patients demonstrated enhanced sensitivity to venetoclax treatment via ibrutinib-induced downregulation of MCL-1 and BCL-xL expression (577). In line with these data, Deng *et al.* showed that BTK inhibition (ibrutinib or acalabrutinib) augmented the cytotoxic effect of venetoclax *in vitro* and *ex vivo* via BTK inhibitor-induced enhanced mitochondrial BCL2 dependence (164). As such, clinical studies are now assessing venetoclax combined with ibrutinib in treatment naïve or R/R patients, which are ongoing and producing encouraging results (165, 166). Here, we showed that AZD8055 treatment inhibited $F(ab')_2$-induced MCL-1 and CD40L (+IL-4)-induced BCL-xL upregulation in primary CLL cells. Encouragingly, our preliminary data demonstrates that AZD8055 synergises with venetoclax to enhance apoptosis in MEC-1 cells (Smith, unpublished). Interestingly, recent evidence indicates that MCL-1- and BCL-xL-dependent resistance to venetoclax can be prevented by restricting PI3K-AKT-mTOR activation in DLBCL cell lines (578). The dual mTOR kinase inhibitor PQR620 has recently showed anti-tumour activity in a panel of 56 lymphoma cell lines, and synergised with venetoclax in GCB- and ABC-DLBCL cell lines (579). Dual PI3K/mTOR inhibitors have equally demonstrated synergism

with BH3 mimetics in DLBCL (580). Collectively, these data suggest that mTOR inhibitors (including dual PI3K/mTOR inhibitors) are promising partner drugs for venetoclax and represents a promising treatment modality for CLL patients. As such, our preliminary *in vitro* investigations should be expanded towards further *in vivo* studies.

6.3 mTOR kinase and CLL cell migration

A common thread that entwines BCR kinase inhibitors is the ability to antagonize CLL cell chemotaxis towards secreted chemokine gradients emanating from the CLL-TME (45). In a clinical setting, this manifests as a redistribution of CLL cells from the tissues to the PB compartment (124). Recently, Holroyd *et al*. expertly reviewed the role of mTOR signalling in the regulation of cellular motility, which emphasised CLL as an archetypal model for migration studies (333). Cell migration is orchestrated, in part, by the coordinated activities of mTORC1 and mTORC2, which regulate cellular adhesion (581) and actin cytoskeleton reorganisation via biosynthesis/activity of small Rho GTPases (305, 582-584). In clinical trial, the mTORC1-selective inhibitor everolimus promoted CLL cell redistribution from the lymphoid organs to the PB compartment (339), suggesting mTOR inhibition abrogates CLL cell infiltration into the tissues. Our group has generated interesting preliminary data that demonstrates the ability of AZD8055 to block CLL cell pseudoemperipolesis, reduce GTPase activity, overcome CXCL12-induced chemotaxis and diminish actin polymerisation (Holroyd, unpublished). In line with these data, AZD8055 reduced the migratory capacity of breast cancer cell lines (322). Furthermore, the PI3K/mTOR inhibitors PF-04691502 and SAR245409 inhibited CXCL12-induced CLL cell chemotaxis, which, in the case of SAR245409, had a greater anti-migratory effect than idelalisib alone (341, 342). Collectively, these studies demonstrate that mTOR plays a prominent role in the migratory potential of CLL cells, which can be targeted by mTOR inhibitors. Holroyd's data examining the effect of AZD8055 on CLL cell migration (233) is important as it aligns with the effect of everolimus (339) and other BCR-targeted therapies *in vivo* and *in vitro* (126-130, 139). This is a key point because CLL cell migration towards- and localisation within the CLL-TME precedes the ability of CLL cells to proliferate. Furthermore, treatment-induced redistribution of CLL cells from the tissues to the PB compartment relinquishes the ability of the CLL-TME to provide a protective

niche. As such, inhibitors that negate cell motility and homing represent an attractive therapeutic strategy, particularly in combination with cytotoxic agents such as venetoclax (164). Clearly, the data presented within this thesis only scratch the surface of mTOR's functional importance (and consequences of mTOR inhibition therein) for CLL pathogenesis. As mTOR signalling controls multiple functional behaviours, further pharmacological *in vitro* and *in vivo* studies are needed to elucidate mTOR's effects on CLL cells.

6.4 Reengaging tumour suppressor activity in CLL

In their study, Ventura *et al*. demonstrated that genetically restoring p53 function in lymphoma and sarcoma mouse models was capable of nullifying cancer cell growth (585), indicating that reactivation of tumour suppressors might represent a promising therapeutic strategy in human cancers (586). However, these treatments have not been forthcoming, owing primarily to the dearth of strategies to reengage tumour suppressors that have been genetically compromised (such as *TP53* and *ATM* in subsets of CLL patients) (586). This being said, tumour suppressors need not be genetically inactivated to contribute to tumorigenesis (587). As postulated by Berger *et al.*, functional inhibition of otherwise 'genetically intact' tumour suppressors via post-transcriptional and post-translational modifications similarly facilitate cancer progression in certain contexts (588). Indeed, FOXO transcription factors are seldom mutated in a way that impedes functionality (344), rather, they are deemed inoperable via negative regulation by overactive PI3K-AKT signalling (347). This has shifted the focus towards identifying and therapeutically targeting signalling networks and/or mechanisms that regulate tumour suppressor localisation, stability and activity (586). In this section, we summarise studies that aim to reactivate tumour suppressors in CLL and highlight potential druggable targets to unleash FOXO function. The roles of tumour suppressors in CLL was recently reviewed (586, 587).

6.4.1 Reactivating PTEN function: USP7 inhibition

As mentioned earlier, studies have demonstrated that the tumour suppressor PTEN, which negatively regulates PI3K-AKT signal transduction, is functionally compromised in CLL cells via posttranscriptional and posttranslational

modifications (288-290). More recently, Carra *et al*. demonstrated that PTEN tumour suppressor activity was negatively regulated by aberrant upregulation of the deubiquitinase USP7. Targeted inhibition of USP7 using the small-molecule inhibitor P5091 induced growth inhibition and apoptosis in MEC-1 cells (and apoptosis in primary CLL cells). Interestingly, PTEN was predominantly localised in the cytoplasm of CLL cells, whereas normal B cells displayed a 'diffuse pattern' throughout the cellular compartments. On a mechanistic level, P5091 disrupted the USP7-PTEN network, which promoted PTEN stabilisation and nuclear localisation in CLL cells, suggesting USP7 overexpression promoted aberrant PTEN localisation. To corroborate this, forced nuclear expression of PTEN induced apoptosis and cell cycle arrest in MEC-1 cells, akin to the effects of USP7 inhibition. This indicated that nuclear PTEN exerts tumour suppressive functions (292). Largely aligning with our data on FOXO1, reactivation of tumour suppressors (via pharmacological inhibition of negative regulators) exerts anti-cancer properties in CLL cells. Importantly, the functional consequences of USP7 inhibition were independent of *TP53* aberrations, suggesting reengagement of PTEN activity can fulfil tumour suppressive functions in patients with unmet clinical needs (288, 292). Although FOXO1 activity was not assessed on the basis of *TP53* status in primary CLL cells, our results demonstrated that COMBO-induced FOXO1 activity promoted growth arrest and apoptosis in *TP53*-deleted MEC-1 cells. Interestingly, USP7 has been shown to inactivate FOXOs via deubiquitination and subsequent nuclear export in response to oxidative stress (589), highlighting that P5091 may also promote FOXO nuclear localisation in CLL. These studies highlight the need for a more detailed analysis of posttranslational FOXO modifications (phosphorylation, acetylation, methylation and ubiquitination) in a context-dependent and temporal-specific manner, particularly downstream of microenvironmental stimuli. Nevertheless, these findings demonstrate that reactivation of tumour suppressors might represent a promising treatment strategy in CLL.

On a related note, studies have also investigated the tumour suppressive properties of the phosphatase SHIP1. SHIP1 dampens BCR ligation-induced PI3K-AKT signalling via dephosphorylation of PIP_3 (590). Recently, Lemm *et al*. showed that pharmacological activation of SHIP1 using AQX-435 induced apoptosis in CLL cells and overcame pro-survival signalling conferred by

microenvironment stimuli *in vitro*. Furthermore, combining AQX-435 with ibrutinib further downregulated PI3K-AKT signalling (591). Paradoxically, unpublished data has shown that pharmacological inhibition of SHIP1 using 3-a-Aminocholestane (3AC) induced CLL cell death via BCR overactivation (592). Collectively, these findings indicate that SHIP1 activity, akin to FOXO1 (408), is tightly regulated within a narrow range for optimal cellular maintenance. Therefore, a better understanding of tumour suppressor regulation and/or activity is necessary to harness tumour suppressors as mediators of novel targeted therapy in CLL.

6.4.2 Inhibition of FOXO negative regulators: ERK, CDK2 and CK1

Although AKT-dependent FOXO phosphorylation is perhaps the most prominent posttranslational modification affecting FOXO activity and subcellular localisation (345), FOXO transcription factors are also negatively regulated by MEK1/2-ERK (366, 367), CDK2 (368) and CK1 (369, 370) pathways. ERK-dependent inactivation of FOXO3a (via phosphorylation at Ser294, Ser344 and Ser425 residues) resulted in its nuclear exclusion and MDM2-mediated degradation, which enhanced proliferation and tumorigenesis in a mouse model of breast cancer (366). In CLL, inhibition of MEK1/2 using binimetinib diminished ERK1/2 activity and overcame *in vitro* TME stimuli (IgM, SDF-1α and CD40L co-cultures) to induce apoptosis (593, 594). Although the impact of binimetinib on FOXO activity was not assessed, subsequent investigations (including our group's ongoing study of the ERK1/2 inhibitor AZ6197 in CLL) should address the functional consequence of MEK1/2 and ERK1/2 inhibition on FOXO dynamics. In their study, Huang *et al*. demonstrated that CDK2 phosphorylated FOXO1 at Ser249 ($FOXO1^{S249}$), which promoted its cytoplasmic translocation and inactivation. Upon DNA damage, CDK2-dependent $FOXO1^{S249}$ phosphorylation is diminished. Importantly, FOXO1 knockdown interfered with DNA damage-induced apoptosis irrespective of cellular p53 status. Thus, CDK2 and FOXO1 regulated the apoptotic DNA damage response (368). The CDK2 inhibitor roscovitine induced caspase-dependent apoptosis in CLL cells (595), while our group demonstrated that CDK2/7/9 inhibitor CR8 overcame *in vitro* TME stimuli to promote apoptosis, prevent CLL cell proliferation and inhibit NF-κB signalling (596). The CDK2/9 inhibitor CYC065 has recently entered phase I clinical trials in combination with venetoclax for R/R CLL patients (597). Thus, an investigation

of FOXO1 activity in response to CDK2 inhibitors warrants further investigation. Finally, CK1-dependent phosphorylation of FOXO1 at Ser322 facilitated FOXO1 nuclear export (369, 370). CK1 has emerged as a novel therapeutic target in CLL. In preclinical studies, the CK1 inhibitor PF670462 inhibited TME interactions (CXCL12/CCL19-induced chemotaxis and stromal cell communication), delayed CLL-like Eμ-TCL1 leukaemia development and synergised with ibrutinib to augment inhibition of chemotaxis (598). Thus, it is interesting to speculate about the role of FOXO1 following CK1 inhibition, particularly in combination with ibrutinib.

6.4.3 SINE inhibitors: preventing FOXO nuclear export?

In 'normal' cells, the nuclear export protein exportin 1 (XPO1), otherwise known as chromosomal region maintenance 1 (CRM1), plays an important homeostatic role mediating nuclear-to-cytoplasmic shuttling (and inactivation) of tumour suppressors including p53 and FOXO (599). XPO1 overactivation is frequently observed in cancer, which contributes towards the aberrant cytoplasmic localisation of tumour suppressor molecules. Deregulation of XPO1 is typically associated with poor prognosis and treatment resistance (600-603). In CLL, XPO1 is overexpressed (604), recurrently mutated (605) and plays a key role in CLL drug resistance linked with 'gain of short arm chromosome 2' (2p+) cytogenetic aberrations (606). As such, XPO1 has emerged as a novel target for therapeutic exploitation using selective inhibitors of nuclear export (SINE) compounds (607). In their study, Lapalombella *et al.* demonstrated that the small-molecule SINE KPT-185 inhibited XPO1-cargo complexes, induced apoptosis and, importantly, prevented nuclear export of FOXO3a in CLL cells (604). Although the functional importance of treatment-induced nuclear FOXO3a was not assessed, one can speculate about the tumour suppressor activity of FOXOs in this scenario. Interestingly, Corno *et al.* showed that FOXO1 knockdown reduced the sensitivity of ovarian cancer cells to the XPO1 inhibitor selinexor (KTP-330) (608), demonstrating that SINEs promote cytotoxicity, in part, via retention of nuclear FOXO activity. Preclinical studies further demonstrated that combining selinexor with ibrutinib synergistically enhanced cytotoxicity in CLL cells (609). This combination subsequently entered in phase I clinical trials (NCT02303392) in R/R CLL patients, for which FOXO localisation was a study outcome (610). In 2017, the FDA suspended this study, citing 'incomplete information in the

investigator's brochure' (611). Nevertheless, the effect of selinexor on FOXO1 subcellular localisation and activity in CLL warrants further investigation.

6.5 FOXO1 as a prognostic/predictive biomarker in CLL

The advent of targeted therapy has accelerated the ever-growing need to investigate novel prognostic/predictive biomarkers to identify CLL patients in need of therapy (including the type of treatment) and/or at risk of disease progression (612). Stratification of CLL patient LN biopsies into 'indolent' or 'progressive' disease revealed that FOXO1 expression was significantly higher in 'progressive' CLL patients compared to 'indolent' patients. Although the functional and/or pathological relevance remains unknown, it is possible that FOXO1 expression levels may represent a novel prognostic and/or predictive biomarker in CLL. These observations appear to be specific for histological specimens derived from the LN, as stratification of PB-derived CLL cells revealed no significant difference between favourable (no del(11q)/del(17p)) and poor prognostic (del(11q)/del(17p)) patients. While these findings were promising, Hornsveld *et al*. proposed that one must be careful of interpreting results from histopathological studies (344). Indeed, studies assessing FOXO expression levels as a prognostic indicator have generated conflicting results (344). For example, previous reports have correlated high FOXO3 expression levels to poor prognosis in AML and glioblastoma (405, 406), whereas another study observed a link between low FOXO3 and poor prognosis in colorectal cancer (616). Although this may represent a context-specific effect, interpreting correlations between FOXO1 expression levels and CLL disease progression requires further attention to glean meaningful insights (344). Equally, as mentioned earlier, FOXO1 activity ($FOXO1^{T24}$), subcellular localisation and/or transcriptional output may also offer prognostic insights into treatment response/relapse (specifically BCR signalling inhibitors) (344, 407, 613, 617), which similarly requires further investigation.

6.6 Concluding remarks

To those navigating the PhD journey (or seasoned professionals alike), I offer you this thesis in the hope it provides inspiration and/or the catalyst for exciting new avenues of research. This thesis has raised a number of important unanswered questions pertaining to 1) the functional importance of mTOR

signalling in CLL pathogenesis, 2) the identification of rational AZD8055/2014 drug combinations and 3) the role of FOXOs in CLL disease maintenance, prognosis and therapy response, which I have attempted to highlight throughout this thesis. Further investigation into these unknowns may uncover exciting data with the potential to form the basis of future pre-clinical investigations and CLL clinical trials.

Bibliography

1. Chiorazzi N, Rai KR, Ferrarini M. Chronic lymphocytic leukemia. N Engl J Med. 2005;352(8):804-15.
2. Kipps TJ, Stevenson FK, Wu CJ, Croce CM, Packham G, Wierda WG, et al. Chronic lymphocytic leukaemia. Nature Reviews Disease Primers. 2017;3:16096.
3. Zhang S, Kipps TJ. The pathogenesis of chronic lymphocytic leukemia. Annual review of pathology. 2014;9:103-18.
4. Damle RN, Wasil T, Fais F, Ghiotto F, Valetto A, Allen SL, et al. Ig V gene mutation status and CD38 expression as novel prognostic indicators in chronic lymphocytic leukemia. Blood. 1999;94(6):1840-7.
5. Hamblin TJ, Davis Z, Gardiner A, Oscier DG, Stevenson FK. Unmutated Ig V(H) genes are associated with a more aggressive form of chronic lymphocytic leukemia. Blood. 1999;94(6):1848-54.
6. Döhner H, Stilgenbauer S, Benner A, Leupolt E, Kröber A, Bullinger L, et al. Genomic aberrations and survival in chronic lymphocytic leukemia. N Engl J Med. 2000;343(26):1910-6.
7. Crespo M, Bosch F, Villamor N, Bellosillo B, Colomer D, Rozman M, et al. ZAP-70 expression as a surrogate for immunoglobulin-variable-region mutations in chronic lymphocytic leukemia. N Engl J Med. 2003;348(18):1764-75.
8. Wiestner A, Rosenwald A, Barry TS, Wright G, Davis RE, Henrickson SE, et al. ZAP-70 expression identifies a chronic lymphocytic leukemia subtype with unmutated immunoglobulin genes, inferior clinical outcome, and distinct gene expression profile. Blood. 2003;101(12):4944-51.
9. Ten Hacken E, Burger JA. Microenvironment interactions and B-cell receptor signaling in Chronic Lymphocytic Leukemia: Implications for disease pathogenesis and treatment. Biochim Biophys Acta. 2016;1863(3):401-13.
10. Burger JA, Wiestner A. Targeting B cell receptor signalling in cancer: preclinical and clinical advances. Nat Rev Cancer. 2018;18(3):148-67.
11. Korycka-Wolowiec A, Wolowiec D, Kubiak-Mlonka A, Robak T. Venetoclax in the treatment of chronic lymphocytic leukemia. Expert Opin Drug Metab Toxicol. 2019;15(5):353-66.
12. Hallek M. Chronic lymphocytic leukemia: 2020 update on diagnosis, risk stratification and treatment. Am J Hematol. 2019;94(11):1266-87.
13. Puła B, Gołos A, Górniak P, Jamroziak K. Overcoming Ibrutinib Resistance in Chronic Lymphocytic Leukemia. Cancers (Basel). 2019;11(12).
14. Tausch E, Close W, Dolnik A, Bloehdorn J, Chyla B, Bullinger L, et al. Venetoclax resistance and acquired. Haematologica. 2019;104(9):e434-e7.
15. Cancer Research UK. Chronic lymphocytic leukaemia (CLL) statistics 2017 [Available from: https://www.cancerresearchuk.org/health-professional/cancer-statistics/statistics-by-cancer-type/leukaemia-cll#heading-Three.
16. Parikh SA, Rabe KG, Kay NE, Call TG, Ding W, Schwager SM, et al. Chronic lymphocytic leukemia in young (≤ 55 years) patients: a comprehensive analysis of prognostic factors and outcomes. Haematologica. 2014;99(1):140-7.
17. Catovsky D, Wade R, Else M. The clinical significance of patients' sex in chronic lymphocytic leukemia. Haematologica. 2014;99(6):1088-94.
18. Slager SL, Kay NE. Familial chronic lymphocytic leukemia: what does it mean to me? Clin Lymphoma Myeloma. 2009;9 Suppl 3:S194-7.
19. Cerhan JR, Slager SL. Familial predisposition and genetic risk factors for lymphoma. Blood. 2015;126(20):2265-73.

20. Yang SM, Li JY, Gale RP, Huang XJ. The mystery of chronic lymphocytic leukemia (CLL): Why is it absent in Asians and what does this tell us about etiology, pathogenesis and biology? Blood Rev. 2015;29(3):205-13.
21. Baumann Kreuziger LM, Tarchand G, Morrison VA. The impact of Agent Orange exposure on presentation and prognosis of patients with chronic lymphocytic leukemia. Leuk Lymphoma. 2014;55(1):63-6.
22. Schinasi LH, De Roos AJ, Ray RM, Edlefsen KL, Parks CG, Howard BV, et al. Insecticide exposure and farm history in relation to risk of lymphomas and leukemias in the Women's Health Initiative observational study cohort. Ann Epidemiol. 2015;25(11):803-10.
23. Towle KM, Grespin ME, Monnot AD. Personal use of hair dyes and risk of leukemia: a systematic literature review and meta-analysis. Cancer Med. 2017;6(10):2471-86.
24. Hallek M, Cheson BD, Catovsky D, Caligaris-Cappio F, Dighiero G, Dohner H, et al. iwCLL guidelines for diagnosis, indications for treatment, response assessment, and supportive management of CLL. Blood. 2018;131(25):2745-60.
25. Rawstron AC, Kreuzer KA, Soosapilla A, Spacek M, Stehlikova O, Gambell P, et al. Reproducible diagnosis of chronic lymphocytic leukemia by flow cytometry: An European Research Initiative on CLL (ERIC) & European Society for Clinical Cell Analysis (ESCCA) Harmonisation project. Cytometry B Clin Cytom. 2018;94(1):121-8.
26. Rai KR, Sawitsky A, Cronkite EP, Chanana AD, Levy RN, Pasternack BS. Clinical staging of chronic lymphocytic leukemia. Blood. 1975;46(2):219-34.
27. Binet JL, Auquier A, Dighiero G, Chastang C, Piguet H, Goasguen J, et al. A new prognostic classification of chronic lymphocytic leukemia derived from a multivariate survival analysis. Cancer. 1981;48(1):198-206.
28. Rai K. A critical analysis of staging in CLL. Chronic Lymphocytic Leukemia, Recent Progress and Future Directions. 1987:253-64.
29. American Cancer Society. How Is Chronic Lymphocytic Leukemia Staged? 2018 [Available from: https://www.cancer.org/cancer/chronic-lymphocytic-leukemia/detection-diagnosis-staging/staging.html#references.
30. Wierda WG, O'Brien S, Wang X, Faderl S, Ferrajoli A, Do KA, et al. Prognostic nomogram and index for overall survival in previously untreated patients with chronic lymphocytic leukemia. Blood. 2007;109(11):4679-85.
31. Shanafelt TD, Jenkins G, Call TG, Zent CS, Slager S, Bowen DA, et al. Validation of a new prognostic index for patients with chronic lymphocytic leukemia. Cancer. 2009;115(2):363-72.
32. Pflug N, Bahlo J, Shanafelt TD, Eichhorst BF, Bergmann MA, Elter T, et al. Development of a comprehensive prognostic index for patients with chronic lymphocytic leukemia. Blood. 2014;124(1):49-62.
33. group IC-lw. An international prognostic index for patients with chronic lymphocytic leukaemia (CLL-IPI): a meta-analysis of individual patient data. Lancet Oncol. 2016;17(6):779-90.
34. Molica S, Giannarelli D, Levato L, Mirabelli R, Gentile M, Morabito F. Assessing time to first treatment in early chronic lymphocytic leukemia (CLL): a comparative performance analysis of five prognostic models with inclusion of CLL-international prognostic index (CLL-IPI). Leuk Lymphoma. 2017;58(7):1736-9.
35. Gentile M, Shanafelt TD, Mauro FR, Laurenti L, Rossi D, Molica S, et al. Comparison between the CLL-IPI and the Barcelona-Brno prognostic model: Analysis of 1299 newly diagnosed cases. Am J Hematol. 2018;93(2):E35-E7.

36. Gentile M, Shanafelt TD, Rossi D, Laurenti L, Mauro FR, Molica S, et al. Validation of the CLL-IPI and comparison with the MDACC prognostic index in newly diagnosed patients. Blood. 2016;128(16):2093-5.
37. Delgado J, Doubek M, Baumann T, Kotaskova J, Molica S, Mozas P, et al. Chronic lymphocytic leukemia: A prognostic model comprising only two biomarkers (IGHV mutational status and FISH cytogenetics) separates patients with different outcome and simplifies the CLL-IPI. Am J Hematol. 2017;92(4):375-80.
38. Gaidano G, Rossi D. The mutational landscape of chronic lymphocytic leukemia and its impact on prognosis and treatment. Hematology Am Soc Hematol Educ Program. 2017;2017(1):329-37.
39. Papavasiliou FN, Schatz DG. Somatic hypermutation of immunoglobulin genes: merging mechanisms for genetic diversity. Cell. 2002;109 Suppl:S35-44.
40. Fais F, Ghiotto F, Hashimoto S, Sellars B, Valetto A, Allen SL, et al. Chronic lymphocytic leukemia B cells express restricted sets of mutated and unmutated antigen receptors. J Clin Invest. 1998;102(8):1515-25.
41. Maloum K, Davi F, Merle-Béral H, Pritsch O, Magnac C, Vuillier F, et al. Expression of unmutated VH genes is a detrimental prognostic factor in chronic lymphocytic leukemia. Blood. 2000;96(1):377-9.
42. Parikh SA, Strati P, Tsang M, West CP, Shanafelt TD. Should IGHV status and FISH testing be performed in all CLL patients at diagnosis? A systematic review and meta-analysis. Blood. 2016;127(14):1752-60.
43. Seifert M, Sellmann L, Bloehdorn J, Wein F, Stilgenbauer S, Dürig J, et al. Cellular origin and pathophysiology of chronic lymphocytic leukemia. J Exp Med. 2012;209(12):2183-98.
44. Agathangelidis A, Darzentas N, Hadzidimitriou A, Brochet X, Murray F, Yan XJ, et al. Stereotyped B-cell receptors in one-third of chronic lymphocytic leukemia: a molecular classification with implications for targeted therapies. Blood. 2012;119(19):4467-75.
45. Ten Hacken E, Gounari M, Ghia P, Burger JA. The importance of B cell receptor isotypes and stereotypes in chronic lymphocytic leukemia. Leukemia. 2019;33(2):287-98.
46. Ghiotto F, Fais F, Valetto A, Albesiano E, Hashimoto S, Dono M, et al. Remarkably similar antigen receptors among a subset of patients with chronic lymphocytic leukemia. J Clin Invest. 2004;113(7):1008-16.
47. Messmer BT, Albesiano E, Efremov DG, Ghiotto F, Allen SL, Kolitz J, et al. Multiple distinct sets of stereotyped antigen receptors indicate a role for antigen in promoting chronic lymphocytic leukemia. J Exp Med. 2004;200(4):519-25.
48. Widhopf GF, Rassenti LZ, Toy TL, Gribben JG, Wierda WG, Kipps TJ. Chronic lymphocytic leukemia B cells of more than 1% of patients express virtually identical immunoglobulins. Blood. 2004;104(8):2499-504.
49. Tobin G, Thunberg U, Karlsson K, Murray F, Laurell A, Willander K, et al. Subsets with restricted immunoglobulin gene rearrangement features indicate a role for antigen selection in the development of chronic lymphocytic leukemia. Blood. 2004;104(9):2879-85.
50. Stamatopoulos K, Belessi C, Moreno C, Boudjograh M, Guida G, Smilevska T, et al. Over 20% of patients with chronic lymphocytic leukemia carry stereotyped receptors: Pathogenetic implications and clinical correlations. Blood. 2007;109(1):259-70.
51. Agathangelidis A, Vardi A, Baliakas P, Stamatopoulos K. Stereotyped B-cell receptors in chronic lymphocytic leukemia. Leuk Lymphoma. 2014;55(10):2252-61.

52. Baliakas P, Hadzidimitriou A, Sutton LA, Minga E, Agathangelidis A, Nichelatti M, et al. Clinical effect of stereotyped B-cell receptor immunoglobulins in chronic lymphocytic leukaemia: a retrospective multicentre study. Lancet Haematol. 2014;1(2):e74-84.
53. Calin GA, Dumitru CD, Shimizu M, Bichi R, Zupo S, Noch E, et al. Frequent deletions and down-regulation of micro- RNA genes miR15 and miR16 at 13q14 in chronic lymphocytic leukemia. Proc Natl Acad Sci U S A. 2002;99(24):15524-9.
54. Cimmino A, Calin GA, Fabbri M, Iorio MV, Ferracin M, Shimizu M, et al. miR-15 and miR-16 induce apoptosis by targeting BCL2. Proc Natl Acad Sci U S A. 2005;102(39):13944-9.
55. Kitada S, Andersen J, Akar S, Zapata JM, Takayama S, Krajewski S, et al. Expression of apoptosis-regulating proteins in chronic lymphocytic leukemia: correlations with In vitro and In vivo chemoresponses. Blood. 1998;91(9):3379-89.
56. Klein U, Lia M, Crespo M, Siegel R, Shen Q, Mo T, et al. The DLEU2/miR-15a/16-1 cluster controls B cell proliferation and its deletion leads to chronic lymphocytic leukemia. Cancer Cell. 2010;17(1):28-40.
57. Roberts AW, Ma S, Kipps TJ, Coutre SE, Davids MS, Eichhorst B, et al. Efficacy of venetoclax in relapsed chronic lymphocytic leukemia is influenced by disease and response variables. Blood. 2019;134(2):111-22.
58. Roberts AW, Davids MS, Pagel JM, Kahl BS, Puvvada SD, Gerecitano JF, et al. Targeting BCL2 with Venetoclax in Relapsed Chronic Lymphocytic Leukemia. New England Journal of Medicine. 2016;374(4):311-22.
59. Döhner H, Stilgenbauer S, James MR, Benner A, Weilguni T, Bentz M, et al. 11q deletions identify a new subset of B-cell chronic lymphocytic leukemia characterized by extensive nodal involvement and inferior prognosis. Blood. 1997;89(7):2516-22.
60. Döhner H, Stilgenbauer S, Fischer K, Bentz M, Lichter P. Cytogenetic and molecular cytogenetic analysis of B cell chronic lymphocytic leukemia: specific chromosome aberrations identify prognostic subgroups of patients and point to loci of candidate genes. Leukemia. 1997;11 Suppl 2:S19-24.
61. Catovsky D, Richards S, Matutes E, Oscier D, Dyer M, Bezares RF, et al. Assessment of fludarabine plus cyclophosphamide for patients with chronic lymphocytic leukaemia (the LRF CLL4 Trial): a randomised controlled trial. Lancet. 2007;370(9583):230-9.
62. Hallek M, Fischer K, Fingerle-Rowson G, Fink AM, Busch R, Mayer J, et al. Addition of rituximab to fludarabine and cyclophosphamide in patients with chronic lymphocytic leukaemia: a randomised, open-label, phase 3 trial. Lancet. 2010;376(9747):1164-74.
63. Van Dyke DL, Werner L, Rassenti LZ, Neuberg D, Ghia E, Heerema NA, et al. The Dohner fluorescence in situ hybridization prognostic classification of chronic lymphocytic leukaemia (CLL): the CLL Research Consortium experience. Br J Haematol. 2016;173(1):105-13.
64. Rigolin GM, Cibien F, Martinelli S, Formigaro L, Rizzotto L, Tammiso E, et al. Chromosome aberrations detected by conventional karyotyping using novel mitogens in chronic lymphocytic leukemia with "normal" FISH: correlations with clinicobiologic parameters. Blood. 2012;119(10):2310-3.
65. Rigolin GM, Cavallari M, Quaglia FM, Formigaro L, Lista E, Urso A, et al. In CLL, comorbidities and the complex karyotype are associated with an inferior outcome independently of CLL-IPI. Blood. 2017;129(26):3495-8.
66. Baliakas P, Iskas M, Gardiner A, Davis Z, Plevova K, Nguyen-Khac F, et al. Chromosomal translocations and karyotype complexity in chronic lymphocytic

leukemia: a systematic reappraisal of classic cytogenetic data. Am J Hematol. 2014;89(3):249-55.
67. Rigolin GM, Saccenti E, Bassi C, Lupini L, Quaglia FM, Cavallari M, et al. Extensive next-generation sequencing analysis in chronic lymphocytic leukemia at diagnosis: clinical and biological correlations. J Hematol Oncol. 2016;9(1):88.
68. Herling CD, Klaumünzer M, Rocha CK, Altmüller J, Thiele H, Bahlo J, et al. Complex karyotypes and KRAS and POT1 mutations impact outcome in CLL after chlorambucil-based chemotherapy or chemoimmunotherapy. Blood. 2016;128(3):395-404.
69. Le Bris Y, Struski S, Guièze R, Rouvellat C, Prade N, Troussard X, et al. Major prognostic value of complex karyotype in addition to TP53 and IGHV mutational status in first-line chronic lymphocytic leukemia. Hematol Oncol. 2017;35(4):664-70.
70. Thompson PA, O'Brien SM, Wierda WG, Ferrajoli A, Stingo F, Smith SC, et al. Complex karyotype is a stronger predictor than del(17p) for an inferior outcome in relapsed or refractory chronic lymphocytic leukemia patients treated with ibrutinib-based regimens. Cancer. 2015;121(20):3612-21.
71. Anderson MA, Tam C, Lew TE, Juneja S, Juneja M, Westerman D, et al. Clinicopathological features and outcomes of progression of CLL on the BCL2 inhibitor venetoclax. Blood. 2017;129(25):3362-70.
72. O'Brien S, Furman RR, Coutre S, Flinn IW, Burger JA, Blum K, et al. Single-agent ibrutinib in treatment-naive and relapsed/refractory chronic lymphocytic leukemia: a 5-year experience. Blood. 2018;131(17):1910-9.
73. Baliakas P, Jeromin S, Iskas M, Puiggros A, Plevova K, Nguyen-Khac F, et al. Cytogenetic complexity in chronic lymphocytic leukemia: definitions, associations, and clinical impact. Blood. 2019;133(11):1205-16.
74. Landau DA, Tausch E, Taylor-Weiner AN, Stewart C, Reiter JG, Bahlo J, et al. Mutations driving CLL and their evolution in progression and relapse. Nature. 2015;526(7574):525-30.
75. Puente XS, Beà S, Valdés-Mas R, Villamor N, Gutiérrez-Abril J, Martín-Subero JI, et al. Non-coding recurrent mutations in chronic lymphocytic leukaemia. Nature. 2015;526(7574):519-24.
76. Landau DA, Carter SL, Stojanov P, McKenna A, Stevenson K, Lawrence MS, et al. Evolution and impact of subclonal mutations in chronic lymphocytic leukemia. Cell. 2013;152(4):714-26.
77. Wang L, Lawrence MS, Wan Y, Stojanov P, Sougnez C, Stevenson K, et al. SF3B1 and other novel cancer genes in chronic lymphocytic leukemia. N Engl J Med. 2011;365(26):2497-506.
78. Quesada V, Conde L, Villamor N, Ordóñez GR, Jares P, Bassaganyas L, et al. Exome sequencing identifies recurrent mutations of the splicing factor SF3B1 gene in chronic lymphocytic leukemia. Nat Genet. 2011;44(1):47-52.
79. Zenz T, Eichhorst B, Busch R, Denzel T, Häbe S, Winkler D, et al. TP53 mutation and survival in chronic lymphocytic leukemia. J Clin Oncol. 2010;28(29):4473-9.
80. Gonzalez D, Martinez P, Wade R, Hockley S, Oscier D, Matutes E, et al. Mutational status of the TP53 gene as a predictor of response and survival in patients with chronic lymphocytic leukemia: results from the LRF CLL4 trial. J Clin Oncol. 2011;29(16):2223-9.
81. Stilgenbauer S, Schnaiter A, Paschka P, Zenz T, Rossi M, Döhner K, et al. Gene mutations and treatment outcome in chronic lymphocytic leukemia: results from the CLL8 trial. Blood. 2014;123(21):3247-54.

82. O'Brien S, Jones JA, Coutre SE, Mato AR, Hillmen P, Tam C, et al. Ibrutinib for patients with relapsed or refractory chronic lymphocytic leukaemia with 17p deletion (RESONATE-17): a phase 2, open-label, multicentre study. Lancet Oncol. 2016;17(10):1409-18.
83. Brown JR, Byrd JC, Coutre SE, Benson DM, Flinn IW, Wagner-Johnston ND, et al. Idelalisib, an inhibitor of phosphatidylinositol 3-kinase p110δ, for relapsed/refractory chronic lymphocytic leukemia. Blood. 2014;123(22):3390-7.
84. Stilgenbauer S, Eichhorst B, Schetelig J, Coutre S, Seymour JF, Munir T, et al. Venetoclax in relapsed or refractory chronic lymphocytic leukaemia with 17p deletion: a multicentre, open-label, phase 2 study. Lancet Oncol. 2016;17(6):768-78.
85. Landau DA, Carter SL, Getz G, Wu CJ. Clonal evolution in hematological malignancies and therapeutic implications. Leukemia. 2014;28(1):34-43.
86. Wang J, Khiabanian H, Rossi D, Fabbri G, Gattei V, Forconi F, et al. Tumor evolutionary directed graphs and the history of chronic lymphocytic leukemia. Elife. 2014;3.
87. Burger JA, Landau DA, Taylor-Weiner A, Bozic I, Zhang H, Sarosiek K, et al. Clonal evolution in patients with chronic lymphocytic leukaemia developing resistance to BTK inhibition. Nat Commun. 2016;7:11589.
88. Landau DA, Sun C, Rosebrock D, Herman SEM, Fein J, Sivina M, et al. The evolutionary landscape of chronic lymphocytic leukemia treated with ibrutinib targeted therapy. Nat Commun. 2017;8(1):2185.
89. Ahn IE, Underbayev C, Albitar A, Herman SE, Tian X, Maric I, et al. Clonal evolution leading to ibrutinib resistance in chronic lymphocytic leukemia. Blood. 2017;129(11):1469-79.
90. Apollonio B, Ramsay AG. Subclonal heterogeneity in chronic lymphocytic leukaemia: revealing the importance of the lymphoid tumour microenvironment. Br J Haematol. 2016;172(1):7-8.
91. Ibrahim S, Keating M, Do KA, O'Brien S, Huh YO, Jilani I, et al. CD38 expression as an important prognostic factor in B-cell chronic lymphocytic leukemia. Blood. 2001;98(1):181-6.
92. Dürig J, Naschar M, Schmücker U, Renzing-Köhler K, Hölter T, Hüttmann A, et al. CD38 expression is an important prognostic marker in chronic lymphocytic leukaemia. Leukemia. 2002;16(1):30-5.
93. Del Poeta G, Maurillo L, Venditti A, Buccisano F, Epiceno AM, Capelli G, et al. Clinical significance of CD38 expression in chronic lymphocytic leukemia. Blood. 2001;98(9):2633-9.
94. D'Arena G, Musto P, Cascavilla N, Dell'Olio M, Di Renzo N, Perla G, et al. CD38 expression correlates with adverse biological features and predicts poor clinical outcome in B-cell chronic lymphocytic leukemia. Leuk Lymphoma. 2001;42(1-2):109-14.
95. Deaglio S, Vaisitti T, Aydin S, Bergui L, D'Arena G, Bonello L, et al. CD38 and ZAP-70 are functionally linked and mark CLL cells with high migratory potential. Blood. 2007;110(12):4012-21.
96. Chen L, Huynh L, Apgar J, Tang L, Rassenti L, Weiss A, et al. ZAP-70 enhances IgM signaling independent of its kinase activity in chronic lymphocytic leukemia. Blood. 2008;111(5):2685-92.
97. Wang H, Kadlecek TA, Au-Yeung BB, Goodfellow HE, Hsu LY, Freedman TS, et al. ZAP-70: an essential kinase in T-cell signaling. Cold Spring Harb Perspect Biol. 2010;2(5):a002279.
98. Burger JA. Treatment of Chronic Lymphocytic Leukemia. N Engl J Med. 2020;383(5):460-73.

99. CTCG. Chemotherapeutic options in chronic lymphocytic leukemia: a meta-analysis of the randomized trials. CLL Trialists' Collaborative Group. J Natl Cancer Inst. 1999;91(10):861-8.
100. Keating MJ, O'Brien S, Lerner S, Koller C, Beran M, Robertson LE, et al. Long-term follow-up of patients with chronic lymphocytic leukemia (CLL) receiving fludarabine regimens as initial therapy. Blood. 1998;92(4):1165-71.
101. Rai KR, Peterson BL, Appelbaum FR, Kolitz J, Elias L, Shepherd L, et al. Fludarabine compared with chlorambucil as primary therapy for chronic lymphocytic leukemia. N Engl J Med. 2000;343(24):1750-7.
102. Bellosillo B, Villamor N, Colomer D, Pons G, Montserrat E, Gil J. In vitro evaluation of fludarabine in combination with cyclophosphamide and/or mitoxantrone in B-cell chronic lymphocytic leukemia. Blood. 1999;94(8):2836-43.
103. O'Brien SM, Kantarjian HM, Cortes J, Beran M, Koller CA, Giles FJ, et al. Results of the fludarabine and cyclophosphamide combination regimen in chronic lymphocytic leukemia. J Clin Oncol. 2001;19(5):1414-20.
104. Bosch F, Ferrer A, López-Guillermo A, Giné E, Bellosillo B, Villamor N, et al. Fludarabine, cyclophosphamide and mitoxantrone in the treatment of resistant or relapsed chronic lymphocytic leukaemia. Br J Haematol. 2002;119(4):976-84.
105. Eichhorst BF, Busch R, Hopfinger G, Pasold R, Hensel M, Steinbrecher C, et al. Fludarabine plus cyclophosphamide versus fludarabine alone in first-line therapy of younger patients with chronic lymphocytic leukemia. Blood. 2006;107(3):885-91.
106. Flinn IW, Neuberg DS, Grever MR, Dewald GW, Bennett JM, Paietta EM, et al. Phase III trial of fludarabine plus cyclophosphamide compared with fludarabine for patients with previously untreated chronic lymphocytic leukemia: US Intergroup Trial E2997. J Clin Oncol. 2007;25(7):793-8.
107. Goede V, Fischer K, Busch R, Engelke A, Eichhorst B, Wendtner CM, et al. Obinutuzumab plus chlorambucil in patients with CLL and coexisting conditions. N Engl J Med. 2014;370(12):1101-10.
108. Scheffold A, Stilgenbauer S. Revolution of Chronic Lymphocytic Leukemia Therapy: the Chemo-Free Treatment Paradigm. Curr Oncol Rep. 2020;22(2):16.
109. Huhn D, von Schilling C, Wilhelm M, Ho AD, Hallek M, Kuse R, et al. Rituximab therapy of patients with B-cell chronic lymphocytic leukemia. Blood. 2001;98(5):1326-31.
110. O'Brien SM, Kantarjian H, Thomas DA, Giles FJ, Freireich EJ, Cortes J, et al. Rituximab dose-escalation trial in chronic lymphocytic leukemia. J Clin Oncol. 2001;19(8):2165-70.
111. Di Gaetano N, Xiao Y, Erba E, Bassan R, Rambaldi A, Golay J, et al. Synergism between fludarabine and rituximab revealed in a follicular lymphoma cell line resistant to the cytotoxic activity of either drug alone. Br J Haematol. 2001;114(4):800-9.
112. Tam CS, O'Brien S, Wierda W, Kantarjian H, Wen S, Do KA, et al. Long-term results of the fludarabine, cyclophosphamide, and rituximab regimen as initial therapy of chronic lymphocytic leukemia. Blood. 2008;112(4):975-80.
113. Fischer K, Bahlo J, Fink AM, Goede V, Herling CD, Cramer P, et al. Long-term remissions after FCR chemoimmunotherapy in previously untreated patients with CLL: updated results of the CLL8 trial. Blood. 2016;127(2):208-15.
114. Thompson PA, Tam CS, O'Brien SM, Wierda WG, Stingo F, Plunkett W, et al. Fludarabine, cyclophosphamide, and rituximab treatment achieves long-term disease-free survival in IGHV-mutated chronic lymphocytic leukemia. Blood. 2016;127(3):303-9.

115. Fischer K, Cramer P, Busch R, Stilgenbauer S, Bahlo J, Schweighofer CD, et al. Bendamustine combined with rituximab in patients with relapsed and/or refractory chronic lymphocytic leukemia: a multicenter phase II trial of the German Chronic Lymphocytic Leukemia Study Group. J Clin Oncol. 2011;29(26):3559-66.
116. Fischer K, Cramer P, Busch R, Böttcher S, Bahlo J, Schubert J, et al. Bendamustine in combination with rituximab for previously untreated patients with chronic lymphocytic leukemia: a multicenter phase II trial of the German Chronic Lymphocytic Leukemia Study Group. J Clin Oncol. 2012;30(26):3209-16.
117. Eichhorst B, Fink AM, Bahlo J, Busch R, Kovacs G, Maurer C, et al. First-line chemoimmunotherapy with bendamustine and rituximab versus fludarabine, cyclophosphamide, and rituximab in patients with advanced chronic lymphocytic leukaemia (CLL10): an international, open-label, randomised, phase 3, non-inferiority trial. Lancet Oncol. 2016;17(7):928-42.
118. Patz M, Isaeva P, Forcob N, Müller B, Frenzel LP, Wendtner CM, et al. Comparison of the in vitro effects of the anti-CD20 antibodies rituximab and GA101 on chronic lymphocytic leukaemia cells. Br J Haematol. 2011;152(3):295-306.
119. Salles G, Morschhauser F, Lamy T, Milpied N, Thieblemont C, Tilly H, et al. Phase 1 study results of the type II glycoengineered humanized anti-CD20 monoclonal antibody obinutuzumab (GA101) in B-cell lymphoma patients. Blood. 2012;119(22):5126-32.
120. Hillmen P, Gribben JG, Follows GA, Milligan D, Sayala HA, Moreton P, et al. Rituximab Plus Chlorambucil In Patients with CD20-Positive B-Cell Chronic Lymphocytic Leukemia (CLL): Final Response Analysis of An Open-Label Phase II Study. Blood. 2010;116(21):697-.
121. Foa R, Ciolli S, Di Raimondo F, Poeta GD, Lauria F, Forconi F, et al. A Phase II Study of Chlorambucil Plus Rituximab Followed by Maintenance Versus Observation In Elderly Patients with Previously Untreated Chronic Lymphocytic Leukemia: Results of the First Interim Analysis. Blood. 2010;116(21):2462-.
122. Burger JA, Chiorazzi N. B cell receptor signaling in chronic lymphocytic leukemia. Trends Immunol. 2013;34(12):592-601.
123. Burger JA, Li KW, Keating MJ, Sivina M, Amer AM, Garg N, et al. Leukemia cell proliferation and death in chronic lymphocytic leukemia patients on therapy with the BTK inhibitor ibrutinib. JCI Insight. 2017;2(2):e89904.
124. Wodarz D, Garg N, Komarova NL, Benjamini O, Keating MJ, Wierda WG, et al. Kinetics of CLL cells in tissues and blood during therapy with the BTK inhibitor ibrutinib. Blood. 2014;123(26):4132-5.
125. Honigberg LA, Smith AM, Sirisawad M, Verner E, Loury D, Chang B, et al. The Bruton tyrosine kinase inhibitor PCI-32765 blocks B-cell activation and is efficacious in models of autoimmune disease and B-cell malignancy. Proc Natl Acad Sci U S A. 2010;107(29):13075-80.
126. Herman SE, Gordon AL, Hertlein E, Ramanunni A, Zhang X, Jaglowski S, et al. Bruton tyrosine kinase represents a promising therapeutic target for treatment of chronic lymphocytic leukemia and is effectively targeted by PCI-32765. Blood. 2011;117(23):6287-96.
127. Herman SE, Mustafa RZ, Gyamfi JA, Pittaluga S, Chang S, Chang B, et al. Ibrutinib inhibits BCR and NF-kappaB signaling and reduces tumor proliferation in tissue-resident cells of patients with CLL. Blood. 2014;123(21):3286-95.
128. Ponader S, Chen SS, Buggy JJ, Balakrishnan K, Gandhi V, Wierda WG, et al. The Bruton tyrosine kinase inhibitor PCI-32765 thwarts chronic lymphocytic

leukemia cell survival and tissue homing in vitro and in vivo. Blood. 2012;119(5):1182-9.
129. de Rooij MF, Kuil A, Geest CR, Eldering E, Chang BY, Buggy JJ, et al. The clinically active BTK inhibitor PCI-32765 targets B-cell receptor- and chemokine-controlled adhesion and migration in chronic lymphocytic leukemia. Blood. 2012;119(11):2590-4.
130. Burger JA, O'Brien S, Fowler N, Advani R, Sharman JP, Furman RR, et al. The Bruton's Tyrosine Kinase Inhibitor, PCI-32765, Is Well Tolerated and Demonstrates Promising Clinical Activity In Chronic Lymphocytic Leukemia (CLL) and Small Lymphocytic Lymphoma (SLL): An Update on Ongoing Phase 1 Studies. Blood. 2010;116(21):57-.
131. Byrd JC, Furman RR, Coutre SE, Flinn IW, Burger JA, Blum KA, et al. Targeting BTK with ibrutinib in relapsed chronic lymphocytic leukemia. N Engl J Med. 2013;369(1):32-42.
132. Byrd JC, Hillmen P, O'Brien S, Barrientos JC, Reddy NM, Coutre S, et al. Long-term follow-up of the RESONATE phase 3 trial of ibrutinib vs ofatumumab. Blood. 2019;133(19):2031-42.
133. Burger JA, Tedeschi A, Barr PM, Robak T, Owen C, Ghia P, et al. Ibrutinib as Initial Therapy for Patients with Chronic Lymphocytic Leukemia. N Engl J Med. 2015;373(25):2425-37.
134. Woyach JA, Ruppert AS, Heerema NA, Zhao W, Booth AM, Ding W, et al. Ibrutinib Regimens versus Chemoimmunotherapy in Older Patients with Untreated CLL. N Engl J Med. 2018;379(26):2517-28.
135. Fraser G, Cramer P, Demirkan F, Silva RS, Grosicki S, Pristupa A, et al. Updated results from the phase 3 HELIOS study of ibrutinib, bendamustine, and rituximab in relapsed chronic lymphocytic leukemia/small lymphocytic lymphoma. Leukemia. 2019;33(4):969-80.
136. Byrd JC, Harrington B, O'Brien S, Jones JA, Schuh A, Devereux S, et al. Acalabrutinib (ACP-196) in Relapsed Chronic Lymphocytic Leukemia. N Engl J Med. 2016;374(4):323-32.
137. Barf T, Covey T, Izumi R, van de Kar B, Gulrajani M, van Lith B, et al. Acalabrutinib (ACP-196): A Covalent Bruton Tyrosine Kinase Inhibitor with a Differentiated Selectivity and In Vivo Potency Profile. J Pharmacol Exp Ther. 2017;363(2):240-52.
138. Byrd JC, Wierda WG, Schuh A, Devereux S, Chaves JM, Brown JR, et al. Acalabrutinib monotherapy in patients with relapsed/refractory chronic lymphocytic leukemia: updated phase 2 results. Blood. 2020;135(15):1204-13.
139. Hoellenriegel J, Meadows SA, Sivina M, Wierda WG, Kantarjian H, Keating MJ, et al. The phosphoinositide 3'-kinase delta inhibitor, CAL-101, inhibits B-cell receptor signaling and chemokine networks in chronic lymphocytic leukemia. Blood. 2011;118(13):3603-12.
140. Furman RR, Sharman JP, Coutre SE, Cheson BD, Pagel JM, Hillmen P, et al. Idelalisib and rituximab in relapsed chronic lymphocytic leukemia. N Engl J Med. 2014;370(11):997-1007.
141. Sharman JP, Coutre SE, Furman RR, Cheson BD, Pagel JM, Hillmen P, et al. Final Results of a Randomized, Phase III Study of Rituximab With or Without Idelalisib Followed by Open-Label Idelalisib in Patients With Relapsed Chronic Lymphocytic Leukemia. J Clin Oncol. 2019;37(16):1391-402.
142. Quiroga MP, Balakrishnan K, Kurtova AV, Sivina M, Keating MJ, Wierda WG, et al. B-cell antigen receptor signaling enhances chronic lymphocytic leukemia cell migration and survival: specific targeting with a novel spleen tyrosine kinase inhibitor, R406. Blood. 2009;114(5):1029-37.

143. Hoellenriegel J, Coffey GP, Sinha U, Pandey A, Sivina M, Ferrajoli A, et al. Selective, novel spleen tyrosine kinase (Syk) inhibitors suppress chronic lymphocytic leukemia B-cell activation and migration. Leukemia. 2012;26(7):1576-83.
144. McCaig AM, Cosimo E, Leach MT, Michie AM. Dasatinib inhibits B cell receptor signalling in chronic lymphocytic leukaemia but novel combination approaches are required to overcome additional pro-survival microenvironmental signals. Br J Haematol. 2011;153(2):199-211.
145. McCaig AM, Cosimo E, Leach MT, Michie AM. Dasatinib inhibits CXCR4 signaling in chronic lymphocytic leukaemia cells and impairs migration towards CXCL12. PLoS One. 2012;7(11):e48929.
146. Spina V, Forestieri G, Zucchetto A, Bruscaggin A, Bittolo T, Terzi di Bergamo L, et al. Mechanisms of Adaptation to Ibrutinib in High Risk Chronic Lymphocytic Leukemia. Blood. 2018;132(Supplement 1):585-.
147. Scheffold A, Jebaraj BMC, Tausch E, Bloehdorn J, Ghia P, Yahiaoui A, et al. IGF1R as druggable target mediating PI3K-δ inhibitor resistance in a murine model of chronic lymphocytic leukemia. Blood. 2019;134(6):534-47.
148. Woyach JA, Furman RR, Liu TM, Ozer HG, Zapatka M, Ruppert AS, et al. Resistance mechanisms for the Bruton's tyrosine kinase inhibitor ibrutinib. N Engl J Med. 2014;370(24):2286-94.
149. Woyach JA, Ruppert AS, Guinn D, Lehman A, Blachly JS, Lozanski A, et al. BTK. J Clin Oncol. 2017;35(13):1437-43.
150. Walliser C, Hermkes E, Schade A, Wiese S, Deinzer J, Zapatka M, et al. The Phospholipase Cγ2 Mutants R665W and L845F Identified in Ibrutinib-resistant Chronic Lymphocytic Leukemia Patients Are Hypersensitive to the Rho GTPase Rac2 Protein. J Biol Chem. 2016;291(42):22136-48.
151. Reiff SD, Mantel R, Smith LL, Greene JT, Muhowski EM, Fabian CA, et al. The BTK Inhibitor ARQ 531 Targets Ibrutinib-Resistant CLL and Richter Transformation. Cancer Discov. 2018;8(10):1300-15.
152. Woyach J, Stephens DM, Flinn IW, Bhat SA, Savage RE, Chai F, et al. Final Results of Phase 1, Dose Escalation Study Evaluating ARQ 531 in Patients with Relapsed or Refractory B-Cell Lymphoid Malignancies. Blood. 2019;134(Supplement_1):4298-.
153. Allan JN, Patel K, Mato AR, Wierda WG, Pinilla Ibarz J, Choi MY, et al. Ongoing Results of a Phase 1B/2 Dose-Escalation and Cohort-Expansion Study of the Selective, Noncovalent, Reversible Bruton'S Tyrosine Kinase Inhibitor, Vecabrutinib, in B-Cell Malignancies. Blood. 2019;134(Supplement_1):3041-.
154. Vogler M, Walter HS, Dyer MJS. Targeting anti-apoptotic BCL2 family proteins in haematological malignancies – from pathogenesis to treatment. British Journal of Haematology. 2017;178(3):364-79.
155. Roberts AW, Huang DCS. Targeting BCL2 With BH3 Mimetics: Basic Science and Clinical Application of Venetoclax in Chronic Lymphocytic Leukemia and Related B Cell Malignancies. Clinical Pharmacology and Therapeutics. 2017;101(1):89-98.
156. Kipps TJ, Eradat H, Grosicki S, Catalano J, Cosolo W, Dyagil IS, et al. A phase 2 study of the BH3 mimetic BCL2 inhibitor navitoclax (ABT-263) with or without rituximab, in previously untreated B-cell chronic lymphocytic leukemia. Leuk Lymphoma. 2015;56(10):2826-33.
157. Stilgenbauer S, Eichhorst B, Schetelig J, Hillmen P, Seymour JF, Coutre S, et al. Venetoclax for Patients With Chronic Lymphocytic Leukemia With 17p Deletion: Results From the Full Population of a Phase II Pivotal Trial. J Clin Oncol. 2018;36(19):1973-80.

158. Coutre S, Choi M, Furman RR, Eradat H, Heffner L, Jones JA, et al. Venetoclax for patients with chronic lymphocytic leukemia who progressed during or after idelalisib therapy. Blood. 2018;131(15):1704-11.
159. Jones JA, Mato AR, Wierda WG, Davids MS, Choi M, Cheson BD, et al. Venetoclax for chronic lymphocytic leukaemia progressing after ibrutinib: an interim analysis of a multicentre, open-label, phase 2 trial. Lancet Oncol. 2018;19(1):65-75.
160. Guièze R, Liu VM, Rosebrock D, Jourdain AA, Hernández-Sánchez M, Martinez Zurita A, et al. Mitochondrial Reprogramming Underlies Resistance to BCL-2 Inhibition in Lymphoid Malignancies. Cancer Cell. 2019;36(4):369-84.e13.
161. Blombery P, Anderson MA, Gong JN, Thijssen R, Birkinshaw RW, Thompson ER, et al. Acquisition of the Recurrent Gly101Val Mutation in BCL2 Confers Resistance to Venetoclax in Patients with Progressive Chronic Lymphocytic Leukemia. Cancer Discov. 2019;9(3):342-53.
162. Kater AP, Seymour JF, Hillmen P, Eichhorst B, Langerak AW, Owen C, et al. Fixed Duration of Venetoclax-Rituximab in Relapsed/Refractory Chronic Lymphocytic Leukemia Eradicates Minimal Residual Disease and Prolongs Survival: Post-Treatment Follow-Up of the MURANO Phase III Study. J Clin Oncol. 2019;37(4):269-77.
163. Fischer K, Al-Sawaf O, Bahlo J, Fink AM, Tandon M, Dixon M, et al. Venetoclax and Obinutuzumab in Patients with CLL and Coexisting Conditions. N Engl J Med. 2019;380(23):2225-36.
164. Deng J, Isik E, Fernandes SM, Brown JR, Letai A, Davids MS. Bruton's tyrosine kinase inhibition increases BCL-2 dependence and enhances sensitivity to venetoclax in chronic lymphocytic leukemia. Leukemia. 2017;31(10):2075-84.
165. Hillmen P, Rawstron AC, Brock K, Muñoz-Vicente S, Yates FJ, Bishop R, et al. Ibrutinib Plus Venetoclax in Relapsed/Refractory Chronic Lymphocytic Leukemia: The CLARITY Study. J Clin Oncol. 2019;37(30):2722-9.
166. Wierda WG, Siddiqi T, Flinn I, Badoux XC, Kipps TJ, Allan JN, et al. Phase 2 CAPTIVATE results of ibrutinib (ibr) plus venetoclax (ven) in first-line chronic lymphocytic leukemia (CLL). Journal of Clinical Oncology. 2018;36(15_suppl):7502-.
167. Jain N, Keating M, Thompson P, Ferrajoli A, Burger J, Borthakur G, et al. Ibrutinib and Venetoclax for First-Line Treatment of CLL. N Engl J Med. 2019;380(22):2095-103.
168. Deaglio S, Malavasi F. Chronic lymphocytic leukemia microenvironment: Shifting the balance from apoptosis to proliferation. Haematologica. 2009;94(6):752-6.
169. Burger JA, Burger M, Kipps TJ. Chronic lymphocytic leukemia B cells express functional CXCR4 chemokine receptors that mediate spontaneous migration beneath bone marrow stromal cells. Blood. 1999;94(11):3658-67.
170. Burger JA, Tsukada N, Burger M, Zvaifler NJ, Dell'Aquila M, Kipps TJ. Blood-derived nurse-like cells protect chronic lymphocytic leukemia B cells from spontaneous apoptosis through stromal cell-derived factor-1. Blood. 2000;96(8):2655-63.
171. Burger JA, Zvaifler NJ, Tsukada N, Firestein GS, Kipps TJ. Fibroblast-like synoviocytes support B-cell pseudoemperipolesis via a stromal cell-derived factor-1- and CD106 (VCAM-1)-dependent mechanism. J Clin Invest. 2001;107(3):305-15.
172. Messmer BT, Messmer D, Allen SL, Kolitz JE, Kudalkar P, Cesar D, et al. In vivo measurements document the dynamic cellular kinetics of chronic lymphocytic leukemia B cells. J Clin Invest. 2005;115(3):755-64.

173. van Attekum MH, Eldering E, Kater AP. Chronic lymphocytic leukemia cells are active participants in microenvironmental cross-talk. Haematologica. 2017;102(9):1469-76.
174. Del Giudice I, Marinelli M, Wang J, Bonina S, Messina M, Chiaretti S, et al. Inter- and intra-patient clonal and subclonal heterogeneity of chronic lymphocytic leukaemia: evidences from circulating and lymph nodal compartments. Br J Haematol. 2016;172(3):371-83.
175. Arruga F, Gyau BB, Iannello A, Vitale N, Vaisitti T, Deaglio S. Immune Response Dysfunction in Chronic Lymphocytic Leukemia: Dissecting Molecular Mechanisms and Microenvironmental Conditions. Int J Mol Sci. 2020;21(5).
176. Serra S, Vaisitti T, Audrito V, Bologna C, Buonincontri R, Chen SS, et al. Adenosine signaling mediates hypoxic responses in the chronic lymphocytic leukemia microenvironment. Blood Adv. 2016;1(1):47-61.
177. Koczula KM, Ludwig C, Hayden R, Cronin L, Pratt G, Parry H, et al. Metabolic plasticity in CLL: adaptation to the hypoxic niche. Leukemia. 2016;30(1):65-73.
178. Smallwood DT, Apollonio B, Willimott S, Lezina L, Alharthi A, Ambrose AR, et al. Extracellular vesicles released by CD40/IL-4-stimulated CLL cells confer altered functional properties to CD4+ T cells. Blood. 2016;128(4):542-52.
179. Stache V, Verlaat L, Gätjen M, Heinig K, Westermann J, Rehm A, et al. The splenic marginal zone shapes the phenotype of leukemia B cells and facilitates their niche-specific retention and survival. Oncoimmunology. 2017;6(6):e1323155.
180. Pascutti MF, Jak M, Tromp JM, Derks IAM, Remmerswaal EBM, Thijssen R, et al. IL-21 and CD40L signals from autologous T cells can induce antigen-independent proliferation of CLL cells. Blood. 2013;122(17):3010-9.
181. Os A, Bürgler S, Ribes AP, Funderud A, Wang D, Thompson KM, et al. Chronic lymphocytic leukemia cells are activated and proliferate in response to specific T helper cells. Cell Reports. 2013;4(3):566-77.
182. Ghia P, Strola G, Granziero L, Geuna M, Guida G, Sallusto F, et al. Chronic lymphocytic leukemia B cells are endowed with the capacity to attract CD4+, CD40L+ T cells by producing CCL22. Eur J Immunol. 2002;32(5):1403-13.
183. Patten PE, Buggins AG, Richards J, Wotherspoon A, Salisbury J, Mufti GJ, et al. CD38 expression in chronic lymphocytic leukemia is regulated by the tumor microenvironment. Blood. 2008;111(10):5173-81.
184. Kitada S, Zapata JM, Andreeff M, Reed JC. Bryostatin and CD40-ligand enhance apoptosis resistance and induce expression of cell survival genes in B-cell chronic lymphocytic leukaemia. Br J Haematol. 1999;106(4):995-1004.
185. Granziero L, Ghia P, Circosta P, Gottardi D, Strola G, Geuna M, et al. Survivin is expressed on CD40 stimulation and interfaces proliferation and apoptosis in B-cell chronic lymphocytic leukemia. Blood. 2001;97(9):2777-83.
186. Willimott S, Baou M, Naresh K, Wagner SD. CD154 induces a switch in pro-survival Bcl-2 family members in chronic lymphocytic leukaemia. Br J Haematol. 2007;138(6):721-32.
187. Cuni S, Perez-Aciego P, Perez-Chacon G, Vargas JA, Sanchez A, Martin-Saavedra FM, et al. A sustained activation of PI3K/NF-kappaB pathway is critical for the survival of chronic lymphocytic leukemia B cells. Leukemia. 2004;18(8):1391-400.
188. Erik S, Kater AP, Thijssen R, Eldering E. Targeting BCR-Independent Proliferation of CLL Cells. Blood. 2015;126(23):2916-.

189. Cui B, Chen L, Zhang S, Mraz M, Fecteau JF, Yu J, et al. MicroRNA-155 influences B-cell receptor signaling and associates with aggressive disease in chronic lymphocytic leukemia. Blood. 2014;124(4):546-54.
190. Girbl T, Hinterseer E, Grössinger EM, Asslaber D, Oberascher K, Weiss L, et al. CD40-mediated activation of chronic lymphocytic leukemia cells promotes their CD44-dependent adhesion to hyaluronan and restricts CCL21-induced motility. Cancer Res. 2013;73(2):561-70.
191. Buschle M, Campana D, Carding SR, Richard C, Hoffbrand AV, Brenner MK. Interferon gamma inhibits apoptotic cell death in B cell chronic lymphocytic leukemia. J Exp Med. 1993;177(1):213-8.
192. Dancescu M, Rubio-Trujillo M, Biron G, Bron D, Delespesse G, Sarfati M. Interleukin 4 protects chronic lymphocytic leukemic B cells from death by apoptosis and upregulates Bcl-2 expression. J Exp Med. 1992;176(5):1319-26.
193. Mackus WJ, Frakking FN, Grummels A, Gamadia LE, De Bree GJ, Hamann D, et al. Expansion of CMV-specific CD8+CD45RA+CD27- T cells in B-cell chronic lymphocytic leukemia. Blood. 2003;102(3):1057-63.
194. Nunes C, Wong R, Mason M, Fegan C, Man S, Pepper C. Expansion of a CD8(+)PD-1(+) replicative senescence phenotype in early stage CLL patients is associated with inverted CD4:CD8 ratios and disease progression. Clin Cancer Res. 2012;18(3):678-87.
195. Brusa D, Serra S, Coscia M, Rossi D, D'Arena G, Laurenti L, et al. The PD-1/PD-L1 axis contributes to T-cell dysfunction in chronic lymphocytic leukemia. Haematologica. 2013;98(6):953-63.
196. Ramsay AG, Clear AJ, Fatah R, Gribben JG. Multiple inhibitory ligands induce impaired T-cell immunologic synapse function in chronic lymphocytic leukemia that can be blocked with lenalidomide: establishing a reversible immune evasion mechanism in human cancer. Blood. 2012;120(7):1412-21.
197. Ramsay AG, Evans R, Kiaii S, Svensson L, Hogg N, Gribben JG. Chronic lymphocytic leukemia cells induce defective LFA-1-directed T-cell motility by altering Rho GTPase signaling that is reversible with lenalidomide. Blood. 2013;121(14):2704-14.
198. Riches JC, Davies JK, McClanahan F, Fatah R, Iqbal S, Agrawal S, et al. T cells from CLLpatients exhibit features of T-cell exhaustion but retain capacity for cytokine production. Blood. 2013;121(9):1612-21.
199. Motta M, Rassenti L, Shelvin BJ, Lerner S, Kipps TJ, Keating MJ, et al. Increased expression of CD152 (CTLA-4) by normal T lymphocytes in untreated patients with B-cell chronic lymphocytic leukemia. Leukemia. 2005;19(10):1788-93.
200. Nishio M, Endo T, Tsukada N, Ohata J, Kitada S, Reed JC, et al. Nurselike cells express BAFF and APRIL, which can promote survival of chronic lymphocytic leukemia cells via a paracrine pathway distinct from that of SDF-1alpha. Blood. 2005;106(3):1012-20.
201. Bürkle A, Niedermeier M, Schmitt-Gräff A, Wierda WG, Keating MJ, Burger JA. Overexpression of the CXCR5 chemokine receptor, and its ligand, CXCL13 in B-cell chronic lymphocytic leukemia. Blood. 2007;110(9):3316-25.
202. Deaglio S, Vaisitti T, Bergui L, Bonello L, Horenstein AL, Tamagnone L, et al. CD38 and CD100 lead a network of surface receptors relaying positive signals for B-CLL growth and survival. Blood. 2005;105(8):3042-50.
203. Burger JA, Quiroga MP, Hartmann E, Bürkle A, Wierda WG, Keating MJ, et al. High-level expression of the T-cell chemokines CCL3 and CCL4 by chronic lymphocytic leukemia B cells in nurselike cell cocultures and after BCR stimulation. Blood. 2009;113(13):3050-8.

204. Binder M, Léchenne B, Ummanni R, Scharf C, Balabanov S, Trusch M, et al. Stereotypical chronic lymphocytic leukemia B-cell receptors recognize survival promoting antigens on stromal cells. PLoS One. 2010;5(12):e15992.
205. Bleul CC, Fuhlbrigge RC, Casasnovas JM, Aiuti A, Springer TA. A highly efficacious lymphocyte chemoattractant, stromal cell-derived factor 1 (SDF-1). J Exp Med. 1996;184(3):1101-9.
206. Jitschin R, Braun M, Qorraj M, Saul D, Le Blanc K, Zenz T, et al. Stromal cell-mediated glycolytic switch in CLL cells involves Notch-c-Myc signaling. Blood. 2015;125(22):3432-6.
207. Herishanu Y, Perez-Galan P, Liu D, Biancotto A, Pittaluga S, Vire B, et al. The lymph node microenvironment promotes B-cell receptor signaling, NF-kappaB activation, and tumor proliferation in chronic lymphocytic leukemia. Blood. 2011;117(2):563-74.
208. Herman SE, Gordon AL, Wagner AJ, Heerema NA, Zhao W, Flynn JM, et al. Phosphatidylinositol 3-kinase-δ inhibitor CAL-101 shows promising preclinical activity in chronic lymphocytic leukemia by antagonizing intrinsic and extrinsic cellular survival signals. Blood. 2010;116(12):2078-88.
209. de Gorter DJ, Beuling EA, Kersseboom R, Middendorp S, van Gils JM, Hendriks RW, et al. Bruton's tyrosine kinase and phospholipase Cgamma2 mediate chemokine-controlled B cell migration and homing. Immunity. 2007;26(1):93-104.
210. Crassini K, Shen Y, Mulligan S, Giles Best O. Modeling the chronic lymphocytic leukemia microenvironment in vitro. Leuk Lymphoma. 2017;58(2):266-79.
211. Bernal A, Pastore RD, Asgary Z, Keller SA, Cesarman E, Liou HC, et al. Survival of leukemic B cells promoted by engagement of the antigen receptor. Blood. 2001;98(10):3050-7.
212. Nédellec S, Renaudineau Y, Bordron A, Berthou C, Porakishvili N, Lydyard PM, et al. B cell response to surface IgM cross-linking identifies different prognostic groups of B-chronic lymphocytic leukemia patients. J Immunol. 2005;174(6):3749-56.
213. Rombout A, Lust S, Offner F, Naessens E, Verhasselt B, Philippé J. Mimicking the tumour microenvironment of chronic lymphocytic leukaemia in vitro critically depends on the type of B-cell receptor stimulation. British journal of cancer. 2016;114(6):704-12.
214. Panayiotidis P, Jones D, Ganeshaguru K, Foroni L, Hoffbrand AV. Human bone marrow stromal cells prevent apoptosis and support the survival of chronic lymphocytic leukaemia cells in vitro. Br J Haematol. 1996;92(1):97-103.
215. Willimott S, Baou M, Huf S, Wagner SD. Separate cell culture conditions to promote proliferation or quiescent cell survival in chronic lymphocytic leukemia. Leuk Lymphoma. 2007;48(8):1647-50.
216. Vogler M, Butterworth M, Majid A, Walewska RJ, Sun X-m, Martin JS, et al. Concurrent up-regulation of BCL-X L and BCL2A1 induces approximately 1000-fold resistance to ABT-737 in chronic lymphocytic leukemia Concurrent up-regulation of BCL-X L and BCL2A1 induces approximately 1000-fold resistance to ABT-737 in chronic lymphocyti. 2012;113(18):4403-13.
217. Hamilton E, Pearce L, Morgan L, Robinson S, Ware V, Brennan P, et al. Mimicking the tumour microenvironment: Three different co-culture systems induce a similar phenotype but distinct proliferative signals in primary chronic lymphocytic leukaemia cells. British Journal of Haematology. 2012;158(5):589-99.

218. Asslaber D, Grössinger EM, Girbl T, Hofbauer SW, Egle A, Weiss L, et al. Mimicking the microenvironment in chronic lymphocytic leukaemia - where does the journey go? Br J Haematol. 2013;160(5):711-4.
219. Barbaglio F, Belloni D, Scarfò L, Sbrana FV, Ponzoni M, Bongiovanni L, et al. 3D co-culture model of chronic lymphocytic leukemia bone marrow microenvironment predicts patient-specific response to mobilizing agents. Haematologica. 2020.
220. Decker T, Schneller F, Sparwasser T, Tretter T, Lipford GB, Wagner H, et al. Immunostimulatory CpG-oligonucleotides cause proliferation, cytokine production, and an immunogenic phenotype in chronic lymphocytic leukemia B cells. Blood. 2000;95(3):999-1006.
221. Liu W, Tolar P, Song W, Kim TJ. Editorial: BCR Signaling and B Cell Activation. Front Immunol. 2020;11:45.
222. Lam KP, Kühn R, Rajewsky K. In vivo ablation of surface immunoglobulin on mature B cells by inducible gene targeting results in rapid cell death. Cell. 1997;90(6):1073-83.
223. Kraus M, Alimzhanov MB, Rajewsky N, Rajewsky K. Survival of resting mature B lymphocytes depends on BCR signaling via the Igalpha/beta heterodimer. Cell. 2004;117(6):787-800.
224. Kurosaki T, Shinohara H, Baba Y. B cell signaling and fate decision. Annu Rev Immunol. 2010;28:21-55.
225. Harwood NE, Batista FD. Early events in B cell activation. Annu Rev Immunol. 2010;28:185-210.
226. Yasuda S, Zhou Y, Wang Y, Yamamura M, Wang JY. A model integrating tonic and antigen-triggered BCR signals to predict the survival of primary B cells. Sci Rep. 2017;7(1):14888.
227. Myers DR, Zikherman J, Roose JP. Tonic Signals: Why Do Lymphocytes Bother? Trends Immunol. 2017;38(11):844-57.
228. Pieper K, Grimbacher B, Eibel H. B-cell biology and development. J Allergy Clin Immunol. 2013;131(4):959-71.
229. Jung D, Alt FW. Unraveling V(D)J recombination; insights into gene regulation. Cell. 2004;116(2):299-311.
230. Mak TW, Saunders ME, Jett BD. Chapter 4 - The B Cell Receptor: Proteins and Genes. In: Mak TW, Saunders ME, Jett BD, editors. Primer to the Immune Response (Second Edition). Boston: Academic Cell; 2014. p. 85-110.
231. Treanor B. B-cell receptor: from resting state to activate. Immunology. 2012;136(1):21-7.
232. Decker DJ, Boyle NE, Koziol JA, Klinman NR. The expression of the Ig H chain repertoire in developing bone marrow B lineage cells. J Immunol. 1991;146(1):350-61.
233. Holroyd A. Elucidating the role of mTOR kinase in chronic lymphocytic leukaemia cell migration: University of Glasgow; 2019.
234. Stevenson FK, Krysov S, Davies AJ, Steele AJ, Packham G. B-cell receptor signaling in chronic lymphocytic leukemia. Blood. 2011;118(16):4313-20.
235. Dal Porto JM, Gauld SB, Merrell KT, Mills D, Pugh-Bernard AE, Cambier J. B cell antigen receptor signaling 101. Mol Immunol. 2004;41(6-7):599-613.
236. Fu C, Turck CW, Kurosaki T, Chan AC. BLNK: a central linker protein in B cell activation. Immunity. 1998;9(1):93-103.
237. Nishizumi H, Taniuchi I, Yamanashi Y, Kitamura D, Ilic D, Mori S, et al. Impaired proliferation of peripheral B cells and indication of autoimmune disease in lyn-deficient mice. Immunity. 1995;3(5):549-60.

238. Turner M, Mee PJ, Costello PS, Williams O, Price AA, Duddy LP, et al. Perinatal lethality and blocked B-cell development in mice lacking the tyrosine kinase Syk. Nature. 1995;378(6554):298-302.
239. Cheng AM, Rowley B, Pao W, Hayday A, Bolen JB, Pawson T. Syk tyrosine kinase required for mouse viability and B-cell development. Nature. 1995;378(6554):303-6.
240. Khan WN, Sideras P, Rosen FS, Alt FW. The role of Bruton's tyrosine kinase in B-cell development and function in mice and man. Ann N Y Acad Sci. 1995;764:27-38.
241. Vetrie D, Vorechovský I, Sideras P, Holland J, Davies A, Flinter F, et al. The gene involved in X-linked agammaglobulinaemia is a member of the src family of protein-tyrosine kinases. Nature. 1993;361(6409):226-33.
242. Tsukada S, Saffran DC, Rawlings DJ, Parolini O, Allen RC, Klisak I, et al. Deficient expression of a B cell cytoplasmic tyrosine kinase in human X-linked agammaglobulinemia. Cell. 1993;72(2):279-90.
243. Pal Singh S, Dammeijer F, Hendriks RW. Role of Bruton's tyrosine kinase in B cells and malignancies. Mol Cancer. 2018;17(1):57.
244. Li Z, Wahl MI, Eguinoa A, Stephens LR, Hawkins PT, Witte ON. Phosphatidylinositol 3-kinase-gamma activates Bruton's tyrosine kinase in concert with Src family kinases. Proc Natl Acad Sci U S A. 1997;94(25):13820-5.
245. Saito K, Scharenberg AM, Kinet JP. Interaction between the Btk PH domain and phosphatidylinositol-3,4,5-trisphosphate directly regulates Btk. J Biol Chem. 2001;276(19):16201-6.
246. Manning BD, Toker A. AKT/PKB Signaling: Navigating the Network. Cell. 2017;169(3):381-405.
247. Ziegler CGK, Kim J, Piersanti K, Oyler-Yaniv A, Argyropoulos KV, van den Brink MRM, et al. Constitutive Activation of the B Cell Receptor Underlies Dysfunctional Signaling in Chronic Lymphocytic Leukemia. Cell Rep. 2019;28(4):923-37 e3.
248. Gomes de Castro MA, Wildhagen H, Sograte-Idrissi S, Hitzing C, Binder M, Trepel M, et al. Differential organization of tonic and chronic B cell antigen receptors in the plasma membrane. Nat Commun. 2019;10(1):820.
249. Damle RN, Ghiotto F, Valetto A, Albesiano E, Fais F, Yan XJ, et al. B-cell chronic lymphocytic leukemia cells express a surface membrane phenotype of activated, antigen-experienced B lymphocytes. Blood. 2002;99(11):4087-93.
250. Contri A, Brunati AM, Trentin L, Cabrelle A, Miorin M, Cesaro L, et al. Chronic lymphocytic leukemia B cells contain anomalous Lyn tyrosine kinase, a putative contribution to defective apoptosis. J Clin Invest. 2005;115(2):369-78.
251. Gobessi S, Laurenti L, Longo PG, Carsetti L, Berno V, Sica S, et al. Inhibition of constitutive and BCR-induced Syk activation downregulates Mcl-1 and induces apoptosis in chronic lymphocytic leukemia B cells. Leukemia. 2009;23(4):686-97.
252. Ringshausen I, Schneller F, Bogner C, Hipp S, Duyster J, Peschel C, et al. Constitutively activated phosphatidylinositol-3 kinase (PI-3K) is involved in the defect of apoptosis in B-CLL: association with protein kinase Cdelta. Blood. 2002;100(10):3741-8.
253. Davis RE, Ngo VN, Lenz G, Tolar P, Young RM, Romesser PB, et al. Chronic active B-cell-receptor signalling in diffuse large B-cell lymphoma. Nature. 2010;463(7277):88-92.
254. Duhren-von Minden M, Ubelhart R, Schneider D, Wossning T, Bach MP, Buchner M, et al. Chronic lymphocytic leukaemia is driven by antigen-independent cell-autonomous signalling. Nature. 2012;489(7415):309-12.

255. Binder M, Müller F, Frick M, Wehr C, Simon F, Leistler B, et al. CLL B-cell receptors can recognize themselves: alternative epitopes and structural clues for autostimulatory mechanisms in CLL. Blood. 2013;121(1):239-41.
256. Packham G, Krysov S, Allen A, Savelyeva N, Steele AJ, Forconi F, et al. The outcome of B-cell receptor signaling in chronic lymphocytic leukemia: proliferation or anergy. Haematologica. 2014;99(7):1138-48.
257. D'Avola A, Drennan S, Tracy I, Henderson I, Chiecchio L, Larrayoz M, et al. Surface IgM expression and function are associated with clinical behavior, genetic abnormalities, and DNA methylation in CLL. Blood. 2016;128(6):816-26.
258. Chen L, Widhopf G, Huynh L, Rassenti L, Rai KR, Weiss A, et al. Expression of ZAP-70 is associated with increased B-cell receptor signaling in chronic lymphocytic leukemia. Blood. 2002;100(13):4609-14.
259. Muzio M, Apollonio B, Scielzo C, Frenquelli M, Vandoni I, Boussiotis V, et al. Constitutive activation of distinct BCR-signaling pathways in a subset of CLL patients: a molecular signature of anergy. Blood. 2008;112(1):188-95.
260. Lanemo Myhrinder A, Hellqvist E, Sidorova E, Söderberg A, Baxendale H, Dahle C, et al. A new perspective: molecular motifs on oxidized LDL, apoptotic cells, and bacteria are targets for chronic lymphocytic leukemia antibodies. Blood. 2008;111(7):3838-48.
261. Krysov S, Potter KN, Mockridge CI, Coelho V, Wheatley I, Packham G, et al. Surface IgM of CLL cells displays unusual glycans indicative of engagement of antigen in vivo. Blood. 2010;115(21):4198-205.
262. Chu CC, Catera R, Zhang L, Didier S, Agagnina BM, Damle RN, et al. Many chronic lymphocytic leukemia antibodies recognize apoptotic cells with exposed nonmuscle myosin heavy chain IIA: implications for patient outcome and cell of origin. Blood. 2010;115(19):3907-15.
263. Hoogeboom R, van Kessel KP, Hochstenbach F, Wormhoudt TA, Reinten RJ, Wagner K, et al. A mutated B cell chronic lymphocytic leukemia subset that recognizes and responds to fungi. J Exp Med. 2013;210(1):59-70.
264. Ortiz-Maldonado V, Garcia-Morillo M, Delgado J. The biology behind PI3K inhibition in chronic lymphocytic leukaemia. Ther Adv Hematol. 2015;6(1):25-36.
265. Hanahan D, Weinberg RA. Hallmarks of cancer: The next generation. Cell. 2011;144(5):646-74.
266. Limon JJ, Fruman DA. Akt and mTOR in B Cell Activation and Differentiation. Front Immunol. 2012;3:228.
267. Pongas G, Cheson BD. PI3K signaling pathway in normal B cells and indolent B-cell malignancies. Semin Oncol. 2016;43(6):647-54.
268. Yang J, Nie J, Ma X, Wei Y, Peng Y, Wei X. Targeting PI3K in cancer: mechanisms and advances in clinical trials. Mol Cancer. 2019;18(1):26.
269. Fruman DA, Chiu H, Hopkins BD, Bagrodia S, Cantley LC, Abraham RT. The PI3K Pathway in Human Disease. Cell. 2017;170(4):605-35.
270. Liu GY, Sabatini DM. mTOR at the nexus of nutrition, growth, ageing and disease. Nat Rev Mol Cell Biol. 2020.
271. Okkenhaug K, Burger JA. PI3K Signaling in Normal B Cells and Chronic Lymphocytic Leukemia (CLL). Curr Top Microbiol Immunol. 2016;393:123-42.
272. Ramadani F, Bolland DJ, Garcon F, Emery JL, Vanhaesebroeck B, Corcoran AE, et al. The PI3K isoforms p110alpha and p110delta are essential for pre-B cell receptor signaling and B cell development. Sci Signal. 2010;3(134):ra60.
273. Jou ST, Carpino N, Takahashi Y, Piekorz R, Chao JR, Wang D, et al. Essential, nonredundant role for the phosphoinositide 3-kinase p110delta in signaling by the B-cell receptor complex. Mol Cell Biol. 2002;22(24):8580-91.

274. Davids MS, Brown JR. Phosphoinositide 3'-kinase inhibition in chronic lymphocytic leukemia. Hematol Oncol Clin North Am. 2013;27(2):329-39.
275. Srinivasan L, Sasaki Y, Calado DP, Zhang B, Paik JH, DePinho RA, et al. PI3 kinase signals BCR-dependent mature B cell survival. Cell. 2009;139(3):573-86.
276. Yang G, Murashige DS, Humphrey SJ, James DE. A Positive Feedback Loop between Akt and mTORC2 via SIN1 Phosphorylation. Cell Rep. 2015;12(6):937-43.
277. Brunet A, Bonni A, Zigmond MJ, Lin MZ, Juo P, Hu LS, et al. Akt promotes cell survival by phosphorylating and inhibiting a forkhead transcription factor. Cell. 1999;96(6):857-68.
278. Longo PG, Laurenti L, Gobessi S, Sica S, Leone G, Efremov DG. The Akt/Mcl-1 pathway plays a prominent role in mediating antiapoptotic signals downstream of the B-cell receptor in chronic lymphocytic leukemia B cells. Blood. 2008;111(2):846-55.
279. Chapman EA, Oates M, Mohammad IS, Davies BR, Stockman PK, Zhuang J, et al. Delineating the distinct role of AKT in mediating cell survival and proliferation induced by CD154 and IL-4/IL-21 in chronic lymphocytic leukemia. Oncotarget. 2017;8(61):102948-64.
280. Edelmann J, Klein-Hitpass L, Carpinteiro A, Fuhrer A, Sellmann L, Stilgenbauer S, et al. Bone marrow fibroblasts induce expression of PI3K/NF-kappaB pathway genes and a pro-angiogenic phenotype in CLL cells. Leuk Res. 2008;32(10):1565-72.
281. Kienle D, Benner A, Kröber A, Winkler D, Mertens D, Bühler A, et al. Distinct gene expression patterns in chronic lymphocytic leukemia defined by usage of specific VH genes. Blood. 2006;107(5):2090-3.
282. Ali AY, Wu X, Eissa N, Hou S, Ghia JE, Murooka TT, et al. Distinct roles for phosphoinositide 3-kinases γ and δ in malignant B cell migration. Leukemia. 2018;32(9):1958-69.
283. Balakrishnan K, Peluso M, Fu M, Rosin NY, Burger JA, Wierda WG, et al. The phosphoinositide-3-kinase (PI3K)-delta and gamma inhibitor, IPI-145 (Duvelisib), overcomes signals from the PI3K/AKT/S6 pathway and promotes apoptosis in CLL. Leukemia. 2015;29(9):1811-22.
284. Cosimo E, Tarafdar A, Moles MW, Holroyd AK, Malik N, Catherwood MA, et al. AKT/mTORC2 Inhibition Activates FOXO1 Function in CLL Cells Reducing B-Cell Receptor-Mediated Survival. Clin Cancer Res. 2019;25(5):1574-87.
285. Zhuang J, Hawkins SF, Glenn MA, Lin K, Johnson GG, Carter A, et al. Akt is activated in chronic lymphocytic leukemia cells and delivers a pro-survival signal: the therapeutic potential of Akt inhibition. Haematologica. 2010;95(1):110-8.
286. Ticchioni M, Essafi M, Jeandel PY, Davi F, Cassuto JP, Deckert M, et al. Homeostatic chemokines increase survival of B-chronic lymphocytic leukemia cells through inactivation of transcription factor FOXO3a. Oncogene. 2007;26(50):7081-91.
287. Longo PG, Laurenti L, Gobessi S, Petlickovski A, Pelosi M, Chiusolo P, et al. The Akt signaling pathway determines the different proliferative capacity of chronic lymphocytic leukemia B-cells from patients with progressive and stable disease. Leukemia. 2007;21(1):110-20.
288. Bernardi R, Ghia P. Reactivating nuclear PTEN to treat CLL. Oncotarget. 2017;8(22):35486-7.
289. Zou ZJ, Fan L, Wang L, Xu J, Zhang R, Tian T, et al. miR-26a and miR-214 down-regulate expression of the PTEN gene in chronic lymphocytic leukemia, but not PTEN mutation or promoter methylation. Oncotarget. 2015;6(2):1276-85.

290. Shehata M, Schnabl S, Demirtas D, Hilgarth M, Hubmann R, Ponath E, et al. Reconstitution of PTEN activity by CK2 inhibitors and interference with the PI3-K/Akt cascade counteract the antiapoptotic effect of human stromal cells in chronic lymphocytic leukemia. Blood. 2010;116(14):2513-21.
291. Palacios F, Abreu C, Prieto D, Morande P, Ruiz S, Fernández-Calero T, et al. Activation of the PI3K/AKT pathway by microRNA-22 results in CLL B-cell proliferation. Leukemia. 2015;29(1):115-25.
292. Carra G, Panuzzo C, Torti D, Parvis G, Crivellaro S, Familiari U, et al. Therapeutic inhibition of USP7-PTEN network in chronic lymphocytic leukemia: a strategy to overcome TP53 mutated/deleted clones. Oncotarget. 2017;8(22):35508-22.
293. Saxton RA, Sabatini DM. mTOR Signaling in Growth, Metabolism, and Disease. Cell. 2017;168(6):960-76.
294. Mirabilii S, Ricciardi MR, Piedimonte M, Gianfelici V, Bianchi MP, Tafuri A. Biological Aspects of mTOR in Leukemia. Int J Mol Sci. 2018;19(8).
295. Sancak Y, Thoreen CC, Peterson TR, Lindquist RA, Kang SA, Spooner E, et al. PRAS40 is an insulin-regulated inhibitor of the mTORC1 protein kinase. Mol Cell. 2007;25(6):903-15.
296. Nojima H, Tokunaga C, Eguchi S, Oshiro N, Hidayat S, Yoshino K, et al. The mammalian target of rapamycin (mTOR) partner, raptor, binds the mTOR substrates p70 S6 kinase and 4E-BP1 through their TOR signaling (TOS) motif. J Biol Chem. 2003;278(18):15461-4.
297. Dorrello NV, Peschiaroli A, Guardavaccaro D, Colburn NH, Sherman NE, Pagano M. S6K1- and betaTRCP-mediated degradation of PDCD4 promotes protein translation and cell growth. Science. 2006;314(5798):467-71.
298. Gingras AC, Gygi SP, Raught B, Polakiewicz RD, Abraham RT, Hoekstra MF, et al. Regulation of 4E-BP1 phosphorylation: a novel two-step mechanism. Genes Dev. 1999;13(11):1422-37.
299. Dibble CC, Asara JM, Manning BD. Characterization of Rictor phosphorylation sites reveals direct regulation of mTOR complex 2 by S6K1. Mol Cell Biol. 2009;29(21):5657-70.
300. Harrington LS, Findlay GM, Gray A, Tolkacheva T, Wigfield S, Rebholz H, et al. The TSC1-2 tumor suppressor controls insulin-PI3K signaling via regulation of IRS proteins. J Cell Biol. 2004;166(2):213-23.
301. Shah OJ, Wang Z, Hunter T. Inappropriate activation of the TSC/Rheb/mTOR/S6K cassette induces IRS1/2 depletion, insulin resistance, and cell survival deficiencies. Curr Biol. 2004;14(18):1650-6.
302. Hsu PP, Kang SA, Rameseder J, Zhang Y, Ottina KA, Lim D, et al. The mTOR-regulated phosphoproteome reveals a mechanism of mTORC1-mediated inhibition of growth factor signaling. Science. 2011;332(6035):1317-22.
303. Yu Y, Yoon SO, Poulogiannis G, Yang Q, Ma XM, Villén J, et al. Phosphoproteomic analysis identifies Grb10 as an mTORC1 substrate that negatively regulates insulin signaling. Science. 2011;332(6035):1322-6.
304. Liu P, Gan W, Chin YR, Ogura K, Guo J, Zhang J, et al. PtdIns(3,4,5)P3-Dependent Activation of the mTORC2 Kinase Complex. Cancer Discov. 2015;5(11):1194-209.
305. Sarbassov DD, Ali SM, Kim DH, Guertin DA, Latek RR, Erdjument-Bromage H, et al. Rictor, a novel binding partner of mTOR, defines a rapamycin-insensitive and raptor-independent pathway that regulates the cytoskeleton. Curr Biol. 2004;14(14):1296-302.

306. Alessi DR, Andjelkovic M, Caudwell B, Cron P, Morrice N, Cohen P, et al. Mechanism of activation of protein kinase B by insulin and IGF-1. EMBO J. 1996;15(23):6541-51.
307. Yang J, Cron P, Good VM, Thompson V, Hemmings BA, Barford D. Crystal structure of an activated Akt/protein kinase B ternary complex with GSK3-peptide and AMP-PNP. Nat Struct Biol. 2002;9(12):940-4.
308. Jacinto E, Facchinetti V, Liu D, Soto N, Wei S, Jung SY, et al. SIN1/MIP1 maintains rictor-mTOR complex integrity and regulates Akt phosphorylation and substrate specificity. Cell. 2006;127(1):125-37.
309. Cross DA, Alessi DR, Cohen P, Andjelkovich M, Hemmings BA. Inhibition of glycogen synthase kinase-3 by insulin mediated by protein kinase B. Nature. 1995;378(6559):785-9.
310. Potter CJ, Pedraza LG, Xu T. Akt regulates growth by directly phosphorylating Tsc2. Nat Cell Biol. 2002;4(9):658-65.
311. Sarbassov DD, Ali SM, Sengupta S, Sheen JH, Hsu PP, Bagley AF, et al. Prolonged rapamycin treatment inhibits mTORC2 assembly and Akt/PKB. Mol Cell. 2006;22(2):159-68.
312. Choo AY, Yoon SO, Kim SG, Roux PP, Blenis J. Rapamycin differentially inhibits S6Ks and 4E-BP1 to mediate cell-type-specific repression of mRNA translation. Proc Natl Acad Sci U S A. 2008;105(45):17414-9.
313. Decker T, Hipp S, Ringshausen I, Bogner C, Oelsner M, Schneller F, et al. Rapamycin-induced G1 arrest in cycling B-CLL cells is associated with reduced expression of cyclin D3, cyclin E, cyclin A, and survivin. Blood. 2003;101(1):278-85.
314. Tabernero J, Rojo F, Calvo E, Burris H, Judson I, Hazell K, et al. Dose- and schedule-dependent inhibition of the mammalian target of rapamycin pathway with everolimus: a phase I tumor pharmacodynamic study in patients with advanced solid tumors. J Clin Oncol. 2008;26(10):1603-10.
315. Hsieh AC, Liu Y, Edlind MP, Ingolia NT, Janes MR, Sher A, et al. The translational landscape of mTOR signalling steers cancer initiation and metastasis. Nature. 2012;485(7396):55-61.
316. O'Reilly KE, Rojo F, She QB, Solit D, Mills GB, Smith D, et al. mTOR inhibition induces upstream receptor tyrosine kinase signaling and activates Akt. Cancer Res. 2006;66(3):1500-8.
317. Tamburini J, Chapuis N, Bardet V, Park S, Sujobert P, Willems L, et al. Mammalian target of rapamycin (mTOR) inhibition activates phosphatidylinositol 3-kinase/Akt by up-regulating insulin-like growth factor-1 receptor signaling in acute myeloid leukemia: rationale for therapeutic inhibition of both pathways. Blood. 2008;111(1):379-82.
318. Pike KG, Malagu K, Hummersone MG, Menear KA, Duggan HM, Gomez S, et al. Optimization of potent and selective dual mTORC1 and mTORC2 inhibitors: the discovery of AZD8055 and AZD2014. Bioorg Med Chem Lett. 2013;23(5):1212-6.
319. Chresta CM, Davies BR, Hickson I, Harding T, Cosulich S, Critchlow SE, et al. AZD8055 is a potent, selective, and orally bioavailable ATP-competitive mammalian target of rapamycin kinase inhibitor with in vitro and in vivo antitumor activity. Cancer Res. 2010;70(1):288-98.
320. Willems L, Chapuis N, Puissant A, Maciel TT, Green AS, Jacque N, et al. The dual mTORC1 and mTORC2 inhibitor AZD8055 has anti-tumor activity in acute myeloid leukemia. Leukemia. 2012;26(6):1195-202.

321. Kauffman EC, Lang M, Rais-Bahrami S, Gupta GN, Wei D, Yang Y, et al. Preclinical efficacy of dual mTORC1/2 inhibitor AZD8055 in renal cell carcinoma harboring a TFE3 gene fusion. BMC Cancer. 2019;19(1):917.
322. Jordan NJ, Dutkowski CM, Barrow D, Mottram HJ, Hutcheson IR, Nicholson RI, et al. Impact of dual mTORC1/2 mTOR kinase inhibitor AZD8055 on acquired endocrine resistance in breast cancer in vitro. Breast Cancer Res. 2014;16(1):R12.
323. Gupta M, Hendrickson AE, Yun SS, Han JJ, Schneider PA, Koh BD, et al. Dual mTORC1/mTORC2 inhibition diminishes Akt activation and induces Puma-dependent apoptosis in lymphoid malignancies. Blood. 2012;119(2):476-87.
324. Rodrik-Outmezguine VS, Chandarlapaty S, Pagano NC, Poulikakos PI, Scaltriti M, Moskatel E, et al. mTOR kinase inhibition causes feedback-dependent biphasic regulation of AKT signaling. Cancer Discov. 2011;1(3):248-59.
325. clinicaltrials.gov. AZD2014 2020 [09/2020]. Available from: https://clinicaltrials.gov/ct2/results?cond=&term=AZD2014&cntry=&state=&city=&dist=.
326. clinicaltrials.gov. MLN0128 2020 [09/2020]. Available from: https://clinicaltrials.gov/ct2/results?cond=&term=MLN0128&cntry=&state=&city=&dist=.
327. clinicaltrials.gov. OSI-027 2020 [09/2020]. Available from: https://clinicaltrials.gov/ct2/results?cond=&term=OSI-027&cntry=&state=&city=&dist=.
328. clinicaltrials.gov. CC-223 2020 [Available from: https://clinicaltrials.gov/ct2/results?cond=&term=CC-223&cntry=&state=&city=&dist=.
329. clinicaltrials.gov. PF-04691502 2020 [Available from: https://clinicaltrials.gov/ct2/results?cond=&term=PF-04691502&cntry=&state=&city=&dist=.
330. clinicaltrials.gov. VS-5584 2020 [Available from: https://clinicaltrials.gov/ct2/results?cond=&term=VS-5584&cntry=&state=&city=&dist=.
331. clinicaltrials.gov. SAR245409 2020 [Available from: https://clinicaltrials.gov/ct2/results?cond=&term=SAR245409+&cntry=&state=&city=&dist=.
332. clinicaltrials.gov. CC-115 2020 [Available from: https://clinicaltrials.gov/ct2/results?cond=&term=CC-115&cntry=&state=&city=&dist=.
333. Holroyd AK, Michie AM. The role of mTOR-mediated signaling in the regulation of cellular migration. Immunology Letters. 2018;196(December 2017):74-9.
334. Menon S, Manning BD. Common corruption of the mTOR signaling network in human tumors. Oncogene. 2008;27 Suppl 2:S43-51.
335. Grabiner BC, Nardi V, Birsoy K, Possemato R, Shen K, Sinha S, et al. A diverse array of cancer-associated MTOR mutations are hyperactivating and can predict rapamycin sensitivity. Cancer Discov. 2014;4(5):554-63.
336. Hayun R, Okun E, Berrebi A, Shvidel L, Bassous L, Sredni B, et al. Rapamycin and curcumin induce apoptosis in primary resting B chronic lymphocytic leukemia cells. Leuk Lymphoma. 2009;50(4):625-32.
337. Aleskog A, Norberg M, Nygren P, Rickardson L, Kanduri M, Tobin G, et al. Rapamycin shows anticancer activity in primary chronic lymphocytic leukemia cells in vitro, as single agent and in drug combination. Leuk Lymphoma. 2008;49(12):2333-43.

338. Dietrich S, Oleś M, Lu J, Sellner L, Anders S, Velten B, et al. Drug-perturbation-based stratification of blood cancer. J Clin Invest. 2018;128(1):427-45.
339. Zent CS, LaPlant BR, Johnston PB, Call TG, Habermann TM, Micallef IN, et al. The treatment of recurrent/refractory chronic lymphocytic leukemia/small lymphocytic lymphoma (CLL) with everolimus results in clinical responses and mobilization of CLL cells into the circulation. Cancer. 2010;116(9):2201-7.
340. Jordaan G, Liao W, Gera J, Sharma S. Rictor Overexpression and mTORC2 Signaling in Chronic Lymphocytic Leukemia. Blood. 2012;120(21):3884-.
341. Blunt MD, Carter MJ, Larrayoz M, Smith LD, Aguilar-Hernandez M, Cox KL, et al. The PI3K/mTOR inhibitor PF-04691502 induces apoptosis and inhibits microenvironmental signaling in CLL and the Emicro-TCL1 mouse model. Blood. 2015;125(26):4032-41.
342. Thijssen R, Ter Burg J, van Bochove GG, de Rooij MF, Kuil A, Jansen MH, et al. The pan phosphoinositide 3-kinase/mammalian target of rapamycin inhibitor SAR245409 (voxtalisib/XL765) blocks survival, adhesion and proliferation of primary chronic lymphocytic leukemia cells. Leukemia. 2016;30(2):337-45.
343. Thijssen R, Ter Burg J, Garrick B, van Bochove GG, Brown JR, Fernandes SM, et al. Dual TORK/DNA-PK inhibition blocks critical signaling pathways in chronic lymphocytic leukemia. Blood. 2016;128(4):574-83.
344. Hornsveld M, Dansen TB, Derksen PW, Burgering BMT. Re-evaluating the role of FOXOs in cancer. Semin Cancer Biol. 2018;50:90-100.
345. Tzivion G, Dobson M, Ramakrishnan G. FoxO transcription factors; Regulation by AKT and 14-3-3 proteins. Biochimica et Biophysica Acta - Molecular Cell Research. 2011;1813(11):1938-45.
346. Fu Z, Tindall DJ. FOXOs, cancer and regulation of apoptosis. Oncogene. 2008;27(16):2312-9.
347. Jiramongkol Y, Lam EW. FOXO transcription factor family in cancer and metastasis. Cancer Metastasis Rev. 2020.
348. Calnan DR, Brunet A. The FoxO code. Oncogene. 2008;27(16):2276-88.
349. van der Heide LP, Jacobs FM, Burbach JP, Hoekman MF, Smidt MP. FoxO6 transcriptional activity is regulated by Thr26 and Ser184, independent of nucleo-cytoplasmic shuttling. Biochem J. 2005;391(Pt 3):623-9.
350. Biggs WH, Meisenhelder J, Hunter T, Cavenee WK, Arden KC. Protein kinase B/Akt-mediated phosphorylation promotes nuclear exclusion of the winged helix transcription factor FKHR1. Proc Natl Acad Sci U S A. 1999;96(13):7421-6.
351. Nakae J, Park BC, Accili D. Insulin stimulates phosphorylation of the forkhead transcription factor FKHR on serine 253 through a Wortmannin-sensitive pathway. J Biol Chem. 1999;274(23):15982-5.
352. Rena G, Guo S, Cichy SC, Unterman TG, Cohen P. Phosphorylation of the transcription factor forkhead family member FKHR by protein kinase B. J Biol Chem. 1999;274(24):17179-83.
353. Tang ED, Nuñez G, Barr FG, Guan KL. Negative regulation of the forkhead transcription factor FKHR by Akt. J Biol Chem. 1999;274(24):16741-6.
354. Rena G, Prescott AR, Guo S, Cohen P, Unterman TG. Roles of the forkhead in rhabdomyosarcoma (FKHR) phosphorylation sites in regulating 14-3-3 binding, transactivation and nuclear targetting. Biochem J. 2001;354(Pt 3):605-12.
355. Dansen TB, Burgering BM. Unravelling the tumor-suppressive functions of FOXO proteins. Trends Cell Biol. 2008;18(9):421-9.

356. Brunet A, Kanai F, Stehn J, Xu J, Sarbassova D, Frangioni JV, et al. 14-3-3 transits to the nucleus and participates in dynamic nucleocytoplasmic transport. J Cell Biol. 2002;156(5):817-28.
357. Obsilova V, Vecer J, Herman P, Pabianova A, Sulc M, Teisinger J, et al. 14-3-3 Protein interacts with nuclear localization sequence of forkhead transcription factor FoxO4. Biochemistry. 2005;44(34):11608-17.
358. Obsil T, Ghirlando R, Anderson DE, Hickman AB, Dyda F. Two 14-3-3 binding motifs are required for stable association of Forkhead transcription factor FOXO4 with 14-3-3 proteins and inhibition of DNA binding. Biochemistry. 2003;42(51):15264-72.
359. Silhan J, Vacha P, Strnadova P, Vecer J, Herman P, Sulc M, et al. 14-3-3 protein masks the DNA binding interface of forkhead transcription factor FOXO4. J Biol Chem. 2009;284(29):19349-60.
360. Boura E, Silhan J, Herman P, Vecer J, Sulc M, Teisinger J, et al. Both the N-terminal loop and wing W2 of the forkhead domain of transcription factor Foxo4 are important for DNA binding. J Biol Chem. 2007;282(11):8265-75.
361. Zhang X, Gan L, Pan H, Guo S, He X, Olson ST, et al. Phosphorylation of serine 256 suppresses transactivation by FKHR (FOXO1) by multiple mechanisms. Direct and indirect effects on nuclear/cytoplasmic shuttling and DNA binding. J Biol Chem. 2002;277(47):45276-84.
362. Matsuzaki H, Daitoku H, Hatta M, Tanaka K, Fukamizu A. Insulin-induced phosphorylation of FKHR (Foxo1) targets to proteasomal degradation. Proc Natl Acad Sci U S A. 2003;100(20):11285-90.
363. Aoki M, Jiang H, Vogt PK. Proteasomal degradation of the FoxO1 transcriptional regulator in cells transformed by the P3k and Akt oncoproteins. Proc Natl Acad Sci U S A. 2004;101(37):13613-7.
364. Huang H, Regan KM, Wang F, Wang D, Smith DI, van Deursen JM, et al. Skp2 inhibits FOXO1 in tumor suppression through ubiquitin-mediated degradation. Proc Natl Acad Sci U S A. 2005;102(5):1649-54.
365. Zhang X, Tang N, Hadden TJ, Rishi AK. Akt, FoxO and regulation of apoptosis. Biochimica et Biophysica Acta - Molecular Cell Research. 2011;1813(11):1978-86.
366. Yang JY, Zong CS, Xia W, Yamaguchi H, Ding Q, Xie X, et al. ERK promotes tumorigenesis by inhibiting FOXO3a via MDM2-mediated degradation. Nat Cell Biol. 2008;10(2):138-48.
367. Yang JY, Chang CJ, Xia W, Wang Y, Wong KK, Engelman JA, et al. Activation of FOXO3a is sufficient to reverse mitogen-activated protein/extracellular signal-regulated kinase kinase inhibitor chemoresistance in human cancer. Cancer Res. 2010;70(11):4709-18.
368. Huang H, Regan KM, Lou Z, Chen J, Tindall DJ. CDK2-dependent phosphorylation of FOXO1 as an apoptotic response to DNA damage. Science. 2006;314(5797):294-7.
369. Rena G, Woods YL, Prescott AR, Peggie M, Unterman TG, Williams MR, et al. Two novel phosphorylation sites on FKHR that are critical for its nuclear exclusion. EMBO J. 2002;21(9):2263-71.
370. Rena G, Bain J, Elliott M, Cohen P. D4476, a cell-permeant inhibitor of CK1, suppresses the site-specific phosphorylation and nuclear exclusion of FOXO1a. EMBO Rep. 2004;5(1):60-5.
371. Essers MA, Weijzen S, de Vries-Smits AM, Saarloos I, de Ruiter ND, Bos JL, et al. FOXO transcription factor activation by oxidative stress mediated by the small GTPase Ral and JNK. EMBO J. 2004;23(24):4802-12.

372. Yun H, Park S, Kim MJ, Yang WK, Im DU, Yang KR, et al. AMP-activated protein kinase mediates the antioxidant effects of resveratrol through regulation of the transcription factor FoxO1. FEBS J. 2014;281(19):4421-38.
373. Daitoku H, Sakamaki J, Fukamizu A. Regulation of FoxO transcription factors by acetylation and protein-protein interactions. Biochim Biophys Acta. 2011;1813(11):1954-60.
374. Boccitto M, Kalb RG. Regulation of Foxo-dependent transcription by post-translational modifications. Curr Drug Targets. 2011;12(9):1303-10.
375. Dijkers PF, Medema RH, Lammers JW, Koenderman L, Coffer PJ. Expression of the pro-apoptotic Bcl-2 family member Bim is regulated by the forkhead transcription factor FKHR-L1. Curr Biol. 2000;10(19):1201-4.
376. Kops GJ, Medema RH, Glassford J, Essers MA, Dijkers PF, Coffer PJ, et al. Control of cell cycle exit and entry by protein kinase B-regulated forkhead transcription factors. Mol Cell Biol. 2002;22(7):2025-36.
377. Medema RH, Kops GJ, Bos JL, Burgering BM. AFX-like Forkhead transcription factors mediate cell-cycle regulation by Ras and PKB through p27kip1. Nature. 2000;404(6779):782-7.
378. Schmidt M, Fernandez de Mattos S, van der Horst A, Klompmaker R, Kops GJ, Lam EW, et al. Cell cycle inhibition by FoxO forkhead transcription factors involves downregulation of cyclin D. Mol Cell Biol. 2002;22(22):7842-52.
379. Stahl M, Dijkers PF, Kops GJ, Lens SM, Coffer PJ, Burgering BM, et al. The forkhead transcription factor FoxO regulates transcription of p27Kip1 and Bim in response to IL-2. J Immunol. 2002;168(10):5024-31.
380. Webb AE, Kundaje A, Brunet A. Characterization of the direct targets of FOXO transcription factors throughout evolution. Aging Cell. 2016;15(4):673-85.
381. Seoane J, Le HV, Shen L, Anderson SA, Massagué J. Integration of Smad and forkhead pathways in the control of neuroepithelial and glioblastoma cell proliferation. Cell. 2004;117(2):211-23.
382. Dijkers PF, Medema RH, Pals C, Banerji L, Thomas NS, Lam EW, et al. Forkhead transcription factor FKHR-L1 modulates cytokine-dependent transcriptional regulation of p27(KIP1). Mol Cell Biol. 2000;20(24):9138-48.
383. Galluzzi L, Vitale I, Aaronson SA, Abrams JM, Adam D, Agostinis P, et al. Molecular mechanisms of cell death: recommendations of the Nomenclature Committee on Cell Death 2018. Cell Death Differ. 2018;25(3):486-541.
384. Ushmorov A, Wirth T. FOXO in B-cell lymphopoiesis and B cell neoplasia. Semin Cancer Biol. 2018;50:132-41.
385. Welinder E, Mansson R, Mercer EM, Bryder D, Sigvardsson M, Murre C. The transcription factors E2A and HEB act in concert to induce the expression of FOXO1 in the common lymphoid progenitor. Proc Natl Acad Sci U S A. 2011;108(42):17402-7.
386. Amin RH, Schlissel MS. Foxo1 directly regulates the transcription of recombination-activating genes during B cell development. Nat Immunol. 2008;9(6):613-22.
387. Dengler HS, Baracho GV, Omori SA, Bruckner S, Arden KC, Castrillon DH, et al. Distinct functions for the transcription factor Foxo1 at various stages of B cell differentiation. Nat Immunol. 2008;9(12):1388-98.
388. Venigalla RK, McGuire VA, Clarke R, Patterson-Kane JC, Najafov A, Toth R, et al. PDK1 regulates VDJ recombination, cell-cycle exit and survival during B-cell development. EMBO J. 2013;32(7):1008-22.
389. Nahar R, Ramezani-Rad P, Mossner M, Duy C, Cerchietti L, Geng H, et al. Pre-B cell receptor-mediated activation of BCL6 induces pre-B cell quiescence through transcriptional repression of MYC. Blood. 2011;118(15):4174-8.

390. Yusuf I, Zhu X, Kharas MG, Chen J, Fruman DA. Optimal B-cell proliferation requires phosphoinositide 3-kinase-dependent inactivation of FOXO transcription factors. Blood. 2004;104(3):784-7.
391. Hinman RM, Bushanam JN, Nichols WA, Satterthwaite AB. B cell receptor signaling down-regulates forkhead box transcription factor class O 1 mRNA expression via phosphatidylinositol 3-kinase and Bruton's tyrosine kinase. J Immunol. 2007;178(2):740-7.
392. De Silva NS, Klein U. Dynamics of B cells in germinal centres. Nat Rev Immunol. 2015;15(3):137-48.
393. Basso K, Dalla-Favera R. Germinal centres and B cell lymphomagenesis. Nat Rev Immunol. 2015;15(3):172-84.
394. Dominguez-Sola D, Kung J, Holmes AB, Wells VA, Mo T, Basso K, et al. The FOXO1 Transcription Factor Instructs the Germinal Center Dark Zone Program. Immunity. 2015;43(6):1064-74.
395. Sander S, Chu VT, Yasuda T, Franklin A, Graf R, Calado DP, et al. PI3 Kinase and FOXO1 Transcription Factor Activity Differentially Control B Cells in the Germinal Center Light and Dark Zones. Immunity. 2015;43(6):1075-86.
396. Xie L, Ushmorov A, Leithauser F, Guan H, Steidl C, Farbinger J, et al. FOXO1 is a tumor suppressor in classical Hodgkin lymphoma. Blood. 2012;119(15):3503-11.
397. Szydlowski M, Kiliszek P, Sewastianik T, Jablonska E, Bialopiotrowicz E, Gorniak P, et al. FOXO1 activation is an effector of SYK and AKT inhibition in tonic BCR signal-dependent diffuse large B-cell lymphomas. Blood. 2016;127(6):739-48.
398. Trinh DL, Scott DW, Morin RD, Mendez-Lago M, An J, Jones SJ, et al. Analysis of FOXO1 mutations in diffuse large B-cell lymphoma. Blood. 2013;121(18):3666-74.
399. Novak AJ, Asmann YW, Maurer MJ, Wang C, Slager SL, Hodge LS, et al. Whole-exome analysis reveals novel somatic genomic alterations associated with outcome in immunochemotherapy-treated diffuse large B-cell lymphoma. Blood Cancer J. 2015;5:e346.
400. Schmitz R, Young RM, Ceribelli M, Jhavar S, Xiao W, Zhang M, et al. Burkitt lymphoma pathogenesis and therapeutic targets from structural and functional genomics. Nature. 2012;490(7418):116-20.
401. Kabrani E, Chu VT, Tasouri E, Sommermann T, Bassler K, Ulas T, et al. Nuclear FOXO1 promotes lymphomagenesis in germinal center B cells. Blood. 2018;132(25):2670-83.
402. Köhrer S, Havranek O, Seyfried F, Hurtz C, Coffey GP, Kim E, et al. Pre-BCR signaling in precursor B-cell acute lymphoblastic leukemia regulates PI3K/AKT, FOXO1 and MYC, and can be targeted by SYK inhibition. Leukemia. 2016;30(6):1246-54.
403. Wang F, Demir S, Gehringer F, Osswald CD, Seyfried F, Enzenmuller S, et al. Tight regulation of FOXO1 is essential for maintenance of B-cell precursor acute lymphoblastic leukemia. Blood. 2018;131(26):2929-42.
404. Paik JH, Kollipara R, Chu G, Ji H, Xiao Y, Ding Z, et al. FoxOs are lineage-restricted redundant tumor suppressors and regulate endothelial cell homeostasis. Cell. 2007;128(2):309-23.
405. Santamaría CM, Chillón MC, García-Sanz R, Pérez C, Caballero MD, Ramos F, et al. High FOXO3a expression is associated with a poorer prognosis in AML with normal cytogenetics. Leuk Res. 2009;33(12):1706-9.

406. Qian Z, Ren L, Wu D, Yang X, Zhou Z, Nie Q, et al. Overexpression of FoxO3a is associated with glioblastoma progression and predicts poor patient prognosis. Int J Cancer. 2017;140(12):2792-804.
407. Chen J, Gomes AR, Monteiro LJ, Wong SY, Wu LH, Ng TT, et al. Constitutively nuclear FOXO3a localization predicts poor survival and promotes Akt phosphorylation in breast cancer. PLoS One. 2010;5(8):e12293.
408. Hornsveld M, Smits LMM, Meerlo M, van Amersfoort M, Groot Koerkamp MJA, van Leenen D, et al. FOXO Transcription Factors Both Suppress and Support Breast Cancer Progression. Cancer Res. 2018;78(9):2356-69.
409. DSMZ. MEC-1 (ACC 497) 2020 [Available from: https://www.dsmz.de/collection/catalogue/details/culture/ACC-497.
410. DSMZ. HG-3 (ACC 765) 2020 [Available from: https://www.dsmz.de/collection/catalogue/details/culture/ACC-765.
411. ATCC. L cells 2020 [Available from: https://www.lgcstandards-atcc.org/products/all/CRL-2648.aspx?geo_country=de.
412. ATCC. HEK293T cells 2020 [Available from: https://www.lgcstandards-atcc.org/products/all/crl-3216.aspx?geo_country=de#culturemethod.
413. Abcam. Advantages Of immunoglobulin F(ab) and F(ab')2 fragments 2020 [Available from: https://www.abcam.com/secondary-antibodies/advantages-of-immunoglobulin-fab-and-fab2-fragments.
414. Scientific T. CellTrace Violet Cell Proliferation Kit, for flow cytometry 2020 [Available from: https://www.thermofisher.com/order/catalog/product/C34557.
415. Abcam. Immunocytochemistry and immunofluorescence protocol 2020 [Available from: https://www.abcam.com/protocols/immunocytochemistry-immunofluorescence-protocol.
416. Dunn KW, Kamocka MM, McDonald JH. A practical guide to evaluating colocalization in biological microscopy. Am J Physiol Cell Physiol. 2011;300(4):C723-42.
417. Abcam. Immunohistochemistry (IHC): the complete guide 2020 [Available from: https://www.abcam.com/content/immunohistochemistry-the-complete-guide.
418. Hay J, Moles MW, Cassels J, Michie AM. Subcellular Fractionation of Primary Chronic Lymphocytic Leukemia Cells to Monitor Nuclear/Cytoplasmic Protein Trafficking. J Vis Exp. 2019(152).
419. Scientific T. Basic Principles of RT-qPCR 2020 [Available from: https://www.thermofisher.com/de/de/home/brands/thermo-scientific/molecular-biology/molecular-biology-learning-center/molecular-biology-resource-library/spotlight-articles/basic-principles-rt-qpcr.html.
420. Addgene. pLKO.1 - TRC Cloning Vector 2006 [Available from: https://www.addgene.org/protocols/plko/.
421. Addgene. Inoculating a Liquid Bacterial Culture 2020 [Available from: https://www.addgene.org/protocols/inoculate-bacterial-culture/.
422. Scientific T. AlamarBlue Cell Viability Reagent 2020 [Available from: https://www.thermofisher.com/order/catalog/product/DAL1025#/DAL1025.
423. GraphPad. 50% of what? How exactly are IC50 and EC50 defined? 2010 [Available from: https://www.graphpad.com/support/faq/50-of-what-how-exactly-are-ic50-and-ec50-defined/.
424. Bayat Mokhtari R, Homayouni TS, Baluch N, Morgatskaya E, Kumar S, Das B, et al. Combination therapy in combating cancer. Oncotarget. 2017;8(23):38022-43.

425. Chou TC. Drug combination studies and their synergy quantification using the Chou-Talalay method. Cancer Res. 2010;70(2):440-6.
426. Ahn IE, Farooqui MZH, Tian X, Valdez J, Sun C, Soto S, et al. Depth and durability of response to ibrutinib in CLL: 5-year follow-up of a phase 2 study. Blood. 2018;131(21):2357-66.
427. Burger JA, O'Brien S. Evolution of CLL treatment - from chemoimmunotherapy to targeted and individualized therapy. Nat Rev Clin Oncol. 2018;15(8):510-27.
428. Ringshausen I, Peschel C, Decker T. Mammalian target of rapamycin (mTOR) inhibition in chronic lymphocytic B-cell leukemia: a new therapeutic option. Leuk Lymphoma. 2005;46(1):11-9.
429. Ma L, Chen Z, Erdjument-Bromage H, Tempst P, Pandolfi PP. Phosphorylation and functional inactivation of TSC2 by Erk implications for tuberous sclerosis and cancer pathogenesis. Cell. 2005;121(2):179-93.
430. Roux PP, Ballif BA, Anjum R, Gygi SP, Blenis J. Tumor-promoting phorbol esters and activated Ras inactivate the tuberous sclerosis tumor suppressor complex via p90 ribosomal S6 kinase. Proc Natl Acad Sci U S A. 2004;101(37):13489-94.
431. Rosén A, Bergh AC, Gogok P, Evaldsson C, Myhrinder AL, Hellqvist E, et al. Lymphoblastoid cell line with B1 cell characteristics established from a chronic lymphocytic leukemia clone by in vitro EBV infection. Oncoimmunology. 2012;1(1):18-27.
432. Stacchini A, Aragno M, Vallario A, Alfarano A, Circosta P, Gottardi D, et al. MEC1 and MEC2: two new cell lines derived from B-chronic lymphocytic leukaemia in prolymphocytoid transformation. Leuk Res. 1999;23(2):127-36.
433. Singh R, Letai A, Sarosiek K. Regulation of apoptosis in health and disease: the balancing act of BCL-2 family proteins. Nat Rev Mol Cell Biol. 2019;20(3):175-93.
434. Fulda S. Shifting the balance of mitochondrial apoptosis: therapeutic perspectives. Front Oncol. 2012;2:121.
435. Chaitanya GV, Steven AJ, Babu PP. PARP-1 cleavage fragments: signatures of cell-death proteases in neurodegeneration. Cell Commun Signal. 2010;8:31.
436. Majid A, Tsoulakis O, Walewska R, Gesk S, Siebert R, Kennedy DB, et al. BCL2 expression in chronic lymphocytic leukemia: lack of association with the BCL2 938A>C promoter single nucleotide polymorphism. Blood. 2008;111(2):874-7.
437. O'Connor L, Strasser A, O'Reilly LA, Hausmann G, Adams JM, Cory S, et al. Bim: a novel member of the Bcl-2 family that promotes apoptosis. EMBO J. 1998;17(2):384-95.
438. Wiestner A. Targeting B-Cell receptor signaling for anticancer therapy: the Bruton's tyrosine kinase inhibitor ibrutinib induces impressive responses in B-cell malignancies. J Clin Oncol. 2013;31(1):128-30.
439. Advani RH, Buggy JJ, Sharman JP, Smith SM, Boyd TE, Grant B, et al. Bruton tyrosine kinase inhibitor ibrutinib (PCI-32765) has significant activity in patients with relapsed/refractory B-cell malignancies. J Clin Oncol. 2013;31(1):88-94.
440. Basu B, Dean E, Puglisi M, Greystoke A, Ong M, Burke W, et al. First-in-Human Pharmacokinetic and Pharmacodynamic Study of the Dual m-TORC 1/2 Inhibitor AZD2014. Clin Cancer Res. 2015;21(15):3412-9.
441. Naing A, Aghajanian C, Raymond E, Olmos D, Schwartz G, Oelmann E, et al. Safety, tolerability, pharmacokinetics and pharmacodynamics of AZD8055 in advanced solid tumours and lymphoma. Br J Cancer. 2012;107(7):1093-9.

442. Fingar DC, Salama S, Tsou C, Harlow E, Blenis J. Mammalian cell size is controlled by mTOR and its downstream targets S6K1 and 4EBP1 / eIF4E. Genes Dev. 2002;16:1472-87.
443. Fingar DC, Richardson CJ, Tee AR, Cheatham L, Tsou C, Blenis J. mTOR controls cell cycle progression through its cell growth effectors S6K1 and 4E-BP1/eukaryotic translation initiation factor 4E. Mol Cell Biol. 2004;24(1):200-16.
444. Hashemolhosseini S, Nagamine Y, Morley SJ, Desrivières S, Mercep L, Ferrari S. Rapamycin inhibition of the G1 to S transition is mediated by effects on cyclin D1 mRNA and protein stability. J Biol Chem. 1998;273(23):14424-9.
445. Wanner K, Hipp S, Oelsner M, Ringshausen I, Bogner C, Peschel C, et al. Mammalian target of rapamycin inhibition induces cell cycle arrest in diffuse large B cell lymphoma (DLBCL) cells and sensitises DLBCL cells to rituximab. Br J Haematol. 2006;134(5):475-84.
446. Mabuchi S, Altomare DA, Cheung M, Zhang L, Poulikakos PI, Hensley HH, et al. RAD001 inhibits human ovarian cancer cell proliferation, enhances cisplatin-induced apoptosis, and prolongs survival in an ovarian cancer model. Clin Cancer Res. 2007;13(14):4261-70.
447. Kawata T, Tada K, Kobayashi M, Sakamoto T, Takiuchi Y, Iwai F, et al. Dual inhibition of the mTORC1 and mTORC2 signaling pathways is a promising therapeutic target for adult T-cell leukemia. Cancer Science. 2018;109(1):103-11.
448. van Attekum MHA, Terpstra S, Slinger E, von Lindern M, Moerland PD, Jongejan A, et al. Macrophages confer survival signals via CCR1-dependent translational MCL-1 induction in chronic lymphocytic leukemia. Oncogene. 2017;36(26):3651-60.
449. Narasimha AM, Kaulich M, Shapiro GS, Choi YJ, Sicinski P, Dowdy SF. Cyclin D activates the Rb tumor suppressor by mono-phosphorylation. Elife. 2014;3.
450. Phillips RJ, Mestas J, Gharaee-Kermani M, Burdick MD, Sica A, Belperio JA, et al. Epidermal growth factor and hypoxia-induced expression of CXC chemokine receptor 4 on non-small cell lung cancer cells is regulated by the phosphatidylinositol 3-kinase/PTEN/AKT/mammalian target of rapamycin signaling pathway and activation of hypoxia inducible factor-1alpha. J Biol Chem. 2005;280(23):22473-81.
451. Grever MR, Lucas DM, Dewald GW, Neuberg DS, Reed JC, Kitada S, et al. Comprehensive assessment of genetic and molecular features predicting outcome in patients with chronic lymphocytic leukemia: results from the US Intergroup Phase III Trial E2997. J Clin Oncol. 2007;25(7):799-804.
452. Hasty P, Sharp ZD, Curiel TJ, Campisi J. mTORC1 and p53: clash of the gods? Cell Cycle. 2013;12(1):20-5.
453. Feng Z, Zhang H, Levine AJ, Jin S. The coordinate regulation of the p53 and mTOR pathways in cells. Proc Natl Acad Sci U S A. 2005;102(23):8204-9.
454. Stambolic V, MacPherson D, Sas D, Lin Y, Snow B, Jang Y, et al. Regulation of PTEN transcription by p53. Mol Cell. 2001;8(2):317-25.
455. Horton LE, Bushell M, Barth-Baus D, Tilleray VJ, Clemens MJ, Hensold JO. p53 activation results in rapid dephosphorylation of the eIF4E-binding protein 4E-BP1, inhibition of ribosomal protein S6 kinase and inhibition of translation initiation. Oncogene. 2002;21(34):5325-34.
456. Marcais A, Blevins R, Graumann J, Feytout A, Dharmalingam G, Carroll T, et al. microRNA-mediated regulation of mTOR complex components facilitates discrimination between activation and anergy in CD4 T cells. J Exp Med. 2014;211(11):2281-95.

457. Burger Ja, Gribben JG. The microenvironment in chronic lymphocytic leukemia (CLL) and other B cell malignancies: Insight into disease biology and new targeted therapies. Seminars in Cancer Biology. 2014;24:71-81.
458. Hsieh AC, Costa M, Zollo O, Davis C, Feldman ME, Testa JR, et al. Genetic dissection of the oncogenic mTOR pathway reveals druggable addiction to translational control via 4EBP-eIF4E. Cancer Cell. 2010;17(3):249-61.
459. She QB, Halilovic E, Ye Q, Zhen W, Shirasawa S, Sasazuki T, et al. 4E-BP1 is a key effector of the oncogenic activation of the AKT and ERK signaling pathways that integrates their function in tumors. Cancer Cell. 2010;18(1):39-51.
460. Dowling RJ, Topisirovic I, Alain T, Bidinosti M, Fonseca BD, Petroulakis E, et al. mTORC1-mediated cell proliferation, but not cell growth, controlled by the 4E-BPs. Science. 2010;328(5982):1172-6.
461. De Benedetti A, Graff JR. eIF-4E expression and its role in malignancies and metastases. Oncogene. 2004;23(18):3189-99.
462. Pepper C, Lin TT, Pratt G, Hewamana S, Brennan P, Hiller L, et al. Mcl-1 expression has in vitro and in vivo significance in chronic lymphocytic leukemia and is associated with other poor prognostic markers. Blood. 2008;112(9):3807-17.
463. Decker T, Schneller F, Hipp S, Miething C, Jahn T, Duyster J, et al. Cell cycle progression of chronic lymphocytic leukemia cells is controlled by cyclin D2, cyclin D3, cyclin-dependent kinase (cdk) 4 and the cdk inhibitor p27. Leukemia. 2002;16(3):327-34.
464. Cirstea D, Santo L, Hideshima T, Eda H, Mishima Y, Nemani N, et al. Delineating the mTOR kinase pathway using a dual TORC1/2 inhibitor, AZD8055, in multiple myeloma. Mol Cancer Ther. 2014;13(11):2489-500.
465. Sarbassov DD, Guertin DA, Ali SM, Sabatini DM. Phosphorylation and regulation of Akt/PKB by the rictor-mTOR complex. Science. 2005;307(5712):1098-101.
466. Hresko RC, Mueckler M. mTOR.RICTOR is the Ser473 kinase for Akt/protein kinase B in 3T3-L1 adipocytes. J Biol Chem. 2005;280(49):40406-16.
467. Feldman ME, Apsel B, Uotila A, Loewith R, Knight ZA, Ruggero D, et al. Active-site inhibitors of mTOR target rapamycin-resistant outputs of mTORC1 and mTORC2. PLoS Biol. 2009;7(2):e38.
468. Thoreen CC, Kang SA, Chang JW, Liu Q, Zhang J, Gao Y, et al. An ATP-competitive mammalian target of rapamycin inhibitor reveals rapamycin-resistant functions of mTORC1. J Biol Chem. 2009;284(12):8023-32.
469. Craxton A, Jiang A, Kurosaki T, Clark EA. Syk and Bruton's tyrosine kinase are required for B cell antigen receptor-mediated activation of the kinase Akt. J Biol Chem. 1999;274(43):30644-50.
470. Ezell SA, Mayo M, Bihani T, Tepsuporn S, Wang S, Passino M, et al. Synergistic induction of apoptosis by combination of BTK and dual mTORC1/2 inhibitors in diffuse large B cell lymphoma. Oncotarget. 2014;5(13):4990-5001.
471. Petlickovski A, Laurenti L, Li X, Marietti S, Chiusolo P, Sica S, et al. Sustained signaling through the B-cell receptor induces Mcl-1 and promotes survival of chronic lymphocytic leukemia B cells. Blood. 2005;105(12):4820-7.
472. Bojarczuk K, Sasi BK, Gobessi S, Innocenti I, Pozzato G, Laurenti L, et al. BCR signaling inhibitors differ in their ability to overcome Mcl-1-mediated resistance of CLL B cells to ABT-199. Blood. 2016;127(25):3192-201.
473. Preuss E, Hugle M, Reimann R, Schlecht M, Fulda S. Pan-mammalian target of rapamycin (mTOR) inhibitor AZD8055 primes rhabdomyosarcoma cells

for ABT-737-induced apoptosis by down-regulating Mcl-1 protein. J Biol Chem. 2013;288(49):35287-96.
474. Li H, Liu L, Chang H, Zou Z, Xing D. Downregulation of MCL-1 and upregulation of PUMA using mTOR inhibitors enhance antitumor efficacy of BH3 mimetics in triple-negative breast cancer. Cell Death Dis. 2018;9(2):137.
475. Pétigny-Lechartier C, Duboc C, Jebahi A, Louis MH, Abeilard E, Denoyelle C, et al. The mTORC1/2 Inhibitor AZD8055 Strengthens the Efficiency of the MEK Inhibitor Trametinib to Reduce the Mcl-1/[Bim and Puma] ratio and to Sensitize Ovarian Carcinoma Cells to ABT-737. Mol Cancer Ther. 2017;16(1):102-15.
476. Qi XJ, Wildey GM, Howe PH. Evidence that Ser87 of BimEL is phosphorylated by Akt and regulates BimEL apoptotic function. J Biol Chem. 2006;281(2):813-23.
477. Sidorov P, Naulaerts S, Ariey-Bonnet J, Pasquier E, Ballester PJ. Predicting Synergism of Cancer Drug Combinations Using NCI-ALMANAC Data. Front Chem. 2019;7:509.
478. Mathews Griner LA, Guha R, Shinn P, Young RM, Keller JM, Liu D, et al. High-throughput combinatorial screening identifies drugs that cooperate with ibrutinib to kill activated B-cell-like diffuse large B-cell lymphoma cells. Proc Natl Acad Sci U S A. 2014;111(6):2349-54.
479. Ezell SA, Wang S, Bihani T, Lai Z, Grosskurth SE, Tepsuporn S, et al. Differential regulation of mTOR signaling determines sensitivity to AKT inhibition in diffuse large B cell lymphoma. Oncotarget. 2016;5(8).
480. Roux PP, Shahbazian D, Vu H, Holz MK, Cohen MS, Taunton J, et al. RAS/ERK signaling promotes site-specific ribosomal protein S6 phosphorylation via RSK and stimulates cap-dependent translation. J Biol Chem. 2007;282(19):14056-64.
481. House C, Wettenhall RE, Kemp BE. The influence of basic residues on the substrate specificity of protein kinase C. J Biol Chem. 1987;262(2):772-7.
482. Moore CE, Xie J, Gomez E, Herbert TP. Identification of cAMP-dependent kinase as a third in vivo ribosomal protein S6 kinase in pancreatic beta-cells. J Mol Biol. 2009;389(3):480-94.
483. Herman SE, Niemann CU, Farooqui M, Jones J, Mustafa RZ, Lipsky A, et al. Ibrutinib-induced lymphocytosis in patients with chronic lymphocytic leukemia: correlative analyses from a phase II study. Leukemia. 2014;28(11):2188-96.
484. Chen S-S, Tam CS, Ramsay AG, Couto-Francisco NC, Ibrahim M, Ferrer G, et al. CLL B Cells Develop Resistance to Ibrutinib By Reinvigorating the IL-4R - IL-4 Axis Blocked By Bruton's Tyrosine Kinase Inhibitors Including Acalabrutinib and Zanubrutinib. Blood2019.
485. Nakagawa R, Vukovic M, Tarafdar A, Cosimo E, Dunn K, McCaig AM, et al. Generation of a poor prognostic chronic lymphocytic leukemia-like disease model: PKCalpha subversion induces up-regulation of PKCbetaII expression in B lymphocytes. Haematologica. 2015;100(4):499-510.
486. Ozes ON, Mayo LD, Gustin JA, Pfeffer SR, Pfeffer LM, Donner DB. NF-kappaB activation by tumour necrosis factor requires the Akt serine-threonine kinase. Nature. 1999;401(6748):82-5.
487. Romashkova JA, Makarov SS. NF-kappaB is a target of AKT in anti-apoptotic PDGF signalling. Nature. 1999;401(6748):86-90.
488. Del Gaizo Moore V, Brown JR, Certo M, Love TM, Novina CD, Letai A. Chronic lymphocytic leukemia requires BCL2 to sequester prodeath BIM, explaining sensitivity to BCL2 antagonist ABT-737. J Clin Invest. 2007;117(1):112-21.

489. Herndon TM, Chen SS, Saba NS, Valdez J, Emson C, Gatmaitan M, et al. Direct in vivo evidence for increased proliferation of CLL cells in lymph nodes compared to bone marrow and peripheral blood. Leukemia. 2017;31(6):1340-7.
490. Li M, Lazorchak AS, Ouyang X, Zhang H, Liu H, Arojo OA, et al. Sin1/mTORC2 regulate B cell growth and metabolism by activating mTORC1 and Myc. Cell Mol Immunol. 2019;16(9):757-69.
491. Fumarola C, La Monica S, Alfieri RR, Borra E, Guidotti GG. Cell size reduction induced by inhibition of the mTOR/S6K-signaling pathway protects Jurkat cells from apoptosis. Cell Death Differ. 2005;12(10):1344-57.
492. Guichard SM, Curwen J, Bihani T, D'Cruz CM, Yates JW, Grondine M, et al. AZD2014, an Inhibitor of mTORC1 and mTORC2, Is Highly Effective in ER+ Breast Cancer When Administered Using Intermittent or Continuous Schedules. Mol Cancer Ther. 2015;14(11):2508-18.
493. Vrhovac R, Delmer A, Tang R, Marie JP, Zittoun R, Ajchenbaum-Cymbalista F. Prognostic significance of the cell cycle inhibitor p27Kip1 in chronic B-cell lymphocytic leukemia. Blood. 1998;91(12):4694-700.
494. Quintanilla-Martinez L, Thieblemont C, Fend F, Kumar S, Pinyol M, Campo E, et al. Mantle cell lymphomas lack expression of p27Kip1, a cyclin-dependent kinase inhibitor. Am J Pathol. 1998;153(1):175-82.
495. Chen Y, Lee CH, Tseng BY, Tsai YH, Tsai HW, Yao CL, et al. AZD8055 Exerts Antitumor Effects on Colon Cancer Cells by Inhibiting mTOR and Cell-cycle Progression. Anticancer Res. 2018;38(3):1445-54.
496. Schleiss C, Ilias W, Tahar O, Guler Y, Miguet L, Mayeur-Rousse C, et al. BCR-associated factors driving chronic lymphocytic leukemia cells proliferation ex vivo. Sci Rep. 2019;9(1):701.
497. Fruman DA, Snapper SB, Yballe CM, Davidson L, Yu JY, Alt FW, et al. Impaired B cell development and proliferation in absence of phosphoinositide 3-kinase p85alpha. Science. 1999;283(5400):393-7.
498. Kops GJ, de Ruiter ND, De Vries-Smits AM, Powell DR, Bos JL, Burgering BM. Direct control of the Forkhead transcription factor AFX by protein kinase B. Nature. 1999;398(6728):630-4.
499. Davies BR, Greenwood H, Dudley P, Crafter C, Yu DH, Zhang J, et al. Preclinical pharmacology of AZD5363, an inhibitor of AKT: pharmacodynamics, antitumor activity, and correlation of monotherapy activity with genetic background. Mol Cancer Ther. 2012;11(4):873-87.
500. Guertin DA, Stevens DM, Thoreen CC, Burds AA, Kalaany NY, Moffat J, et al. Ablation in mice of the mTORC components raptor, rictor, or mLST8 reveals that mTORC2 is required for signaling to Akt-FOXO and PKCalpha, but not S6K1. Dev Cell. 2006;11(6):859-71.
501. Kapoor I, Li Y, Sharma A, Zhu H, Bodo J, Xu W, et al. Resistance to BTK inhibition by ibrutinib can be overcome by preventing FOXO3a nuclear export and PI3K/AKT activation in B-cell lymphoid malignancies. Cell Death Dis. 2019;10(12):924.
502. Roy SK, Srivastava RK, Shankar S. Inhibition of PI3K/AKT and MAPK/ERK pathways causes activation of FOXO transcription factor, leading to cell cycle arrest and apoptosis in pancreatic cancer. J Mol Signal. 2010;5:10.
503. Pyrzynska B, Dwojak M, Zerrouqi A, Morlino G, Zapala P, Miazek N, et al. FOXO1 promotes resistance of non-Hodgkin lymphomas to anti-CD20-based therapy. Oncoimmunology. 2018;7(5):e1423183.
504. Hui RC, Francis RE, Guest SK, Costa JR, Gomes AR, Myatt SS, et al. Doxorubicin activates FOXO3a to induce the expression of multidrug resistance gene ABCB1 (MDR1) in K562 leukemic cells. Mol Cancer Ther. 2008;7(3):670-8.

505. Han CY, Cho KB, Choi HS, Han HK, Kang KW. Role of FoxO1 activation in MDR1 expression in adriamycin-resistant breast cancer cells. Carcinogenesis. 2008;29(9):1837-44.
506. Eijkelenboom A, Burgering BM. FOXOs: signalling integrators for homeostasis maintenance. Nat Rev Mol Cell Biol. 2013;14(2):83-97.
507. Nakagawa R, Soh JW, Michie AM. Subversion of protein kinase C alpha signaling in hematopoietic progenitor cells results in the generation of a B-cell chronic lymphocytic leukemia-like population in vivo. Cancer Res. 2006;66(1):527-34.
508. Inoue T, Shinnakasu R, Ise W, Kawai C, Egawa T, Kurosaki T. The transcription factor Foxo1 controls germinal center B cell proliferation in response to T cell help. J Exp Med. 2017;214(4):1181-98.
509. Ochiai K, Maienschein-Cline M, Mandal M, Triggs JR, Bertolino E, Sciammas R, et al. A self-reinforcing regulatory network triggered by limiting IL-7 activates pre-BCR signaling and differentiation. Nat Immunol. 2012;13(3):300-7.
510. Hui RC, Gomes AR, Constantinidou D, Costa JR, Karadedou CT, Fernandez de Mattos S, et al. The forkhead transcription factor FOXO3a increases phosphoinositide-3 kinase/Akt activity in drug-resistant leukemic cells through induction of PIK3CA expression. Mol Cell Biol. 2008;28(19):5886-98.
511. Müschen M. Autoimmunity checkpoints as therapeutic targets in B cell malignancies. Nat Rev Cancer. 2018;18(2):103-16.
512. Geng H, Hurtz C, Lenz KB, Chen Z, Baumjohann D, Thompson S, et al. Self-enforcing feedback activation between BCL6 and pre-B cell receptor signaling defines a distinct subtype of acute lymphoblastic leukemia. Cancer Cell. 2015;27(3):409-25.
513. Ketchum C, Miller H, Song W, Upadhyaya A. Ligand mobility regulates B cell receptor clustering and signaling activation. Biophys J. 2014;106(1):26-36.
514. Lee J, Sengupta P, Brzostowski J, Lippincott-Schwartz J, Pierce SK. The nanoscale spatial organization of B-cell receptors on immunoglobulin M- and G-expressing human B-cells. Mol Biol Cell. 2017;28(4):511-23.
515. Vlad A, Deglesne PA, Letestu R, Saint-Georges S, Chevallier N, Baran-Marszak F, et al. Down-regulation of CXCR4 and CD62L in chronic lymphocytic leukemia cells is triggered by B-cell receptor ligation and associated with progressive disease. Cancer Res. 2009;69(16):6387-95.
516. Hu MC, Lee DF, Xia W, Golfman LS, Ou-Yang F, Yang JY, et al. IkappaB kinase promotes tumorigenesis through inhibition of forkhead FOXO3a. Cell. 2004;117(2):225-37.
517. Van Der Heide LP, Hoekman MF, Smidt MP. The ins and outs of FoxO shuttling: mechanisms of FoxO translocation and transcriptional regulation. Biochem J. 2004;380(Pt 2):297-309.
518. Bloedjes TA, de Wilde G, Maas C, Eldering EE, Bende RJ, van Noesel CJM, et al. Targeting AKT elicits tumor suppressive functions of FOXO transcription factors and GSK3 kinase in Multiple Myeloma. bioRxiv. 2019:816694.
519. Ding W, Shanafelt TD, Lesnick CE, Erlichman C, Leis JF, Secreto C, et al. Akt inhibitor MK2206 selectively targets CLL B-cell receptor induced cytokines, mobilizes lymphocytes and synergizes with bendamustine to induce CLL apoptosis. Br J Haematol. 2014;164(1):146-50.
520. Santo EE, Stroeken P, Sluis PV, Koster J, Versteeg R, Westerhout EM. FOXO3a is a major target of inactivation by PI3K/AKT signaling in aggressive neuroblastoma. Cancer Res. 2013;73(7):2189-98.

521. Bhatt AP, Bhende PM, Sin SH, Roy D, Dittmer DP, Damania B. Dual inhibition of PI3K and mTOR inhibits autocrine and paracrine proliferative loops in PI3K/Akt/mTOR-addicted lymphomas. Blood. 2010;115(22):4455-63.
522. Abdelnour-Berchtold E, Cerantola Y, Roulin D, Dormond-Meuwly A, Demartines N, Dormond O. Rapamycin-mediated FOXO1 inactivation reduces the anticancer efficacy of rapamycin. Anticancer Res. 2010;30(3):799-804.
523. Kim E, Hurtz C, Koehrer S, Wang Z, Balasubramanian S, Chang BY, et al. Ibrutinib inhibits pre-BCR. Blood. 2017;129(9):1155-65.
524. Vogel MJ, Xie L, Guan H, Tooze RM, Maier T, Kostezka U, et al. FOXO1 repression contributes to block of plasma cell differentiation in classical Hodgkin lymphoma. Blood. 2014;124(20):3118-29.
525. Burger JA, Sivina M, Jain N, Kim E, Kadia T, Estrov Z, et al. Randomized trial of ibrutinib vs ibrutinib plus rituximab in patients with chronic lymphocytic leukemia. Blood. 2019;133(10):1011-9.
526. Zhao Y, Yang J, Liao W, Liu X, Zhang H, Wang S, et al. Cytosolic FoxO1 is essential for the induction of autophagy and tumour suppressor activity. Nat Cell Biol. 2010;12(7):665-75.
527. Caraballo JM, Acosta JC, Cortés MA, Albajar M, Gómez-Casares MT, Batlle-López A, et al. High p27 protein levels in chronic lymphocytic leukemia are associated to low Myc and Skp2 expression, confer resistance to apoptosis and antagonize Myc effects on cell cycle. Oncotarget. 2014;5(13):4694-708.
528. Wu J, Lee SW, Zhang X, Han F, Kwan SY, Yuan X, et al. Foxo3a transcription factor is a negative regulator of Skp2 and Skp2 SCF complex. Oncogene. 2013;32(1):78-85.
529. Su YW, Hao Z, Hirao A, Yamamoto K, Lin WJ, Young A, et al. 14-3-3sigma regulates B-cell homeostasis through stabilization of FOXO1. Proc Natl Acad Sci U S A. 2011;108(4):1555-60.
530. Dobson M, Ramakrishnan G, Ma S, Kaplun L, Balan V, Fridman R, et al. Bimodal regulation of FoxO3 by AKT and 14-3-3. Biochim Biophys Acta. 2011;1813(8):1453-64.
531. Pennington KL, Chan TY, Torres MP, Andersen JL. The dynamic and stress-adaptive signaling hub of 14-3-3: emerging mechanisms of regulation and context-dependent protein-protein interactions. Oncogene. 2018;37(42):5587-604.
532. Neal CL, Yao J, Yang W, Zhou X, Nguyen NT, Lu J, et al. 14-3-3zeta overexpression defines high risk for breast cancer recurrence and promotes cancer cell survival. Cancer Res. 2009;69(8):3425-32.
533. Fan T, Li R, Todd NW, Qiu Q, Fang HB, Wang H, et al. Up-regulation of 14-3-3zeta in lung cancer and its implication as prognostic and therapeutic target. Cancer Res. 2007;67(16):7901-6.
534. Yang X, Cao W, Zhou J, Zhang W, Zhang X, Lin W, et al. 14-3-3ζ positive expression is associated with a poor prognosis in patients with glioblastoma. Neurosurgery. 2011;68(4):932-8; discussion 8.
535. Gu Y, Xu K, Torre C, Samur M, Barwick BG, Rupji M, et al. 14-3-3ζ binds the proteasome, limits proteolytic function and enhances sensitivity to proteasome inhibitors. Leukemia. 2018;32(3):744-51.
536. Yu J, Chen L, Chen Y, Hasan MK, Ghia EM, Zhang L, et al. Wnt5a induces ROR1 to associate with 14-3-3zeta for enhanced chemotaxis and proliferation of chronic lymphocytic leukemia cells. Leukemia. 2017;31(12):2608-14.
537. Obrador-Hevia A, Serra-Sitjar M, Rodríguez J, Villalonga P, Fernández de Mattos S. The tumour suppressor FOXO3 is a key regulator of mantle cell lymphoma proliferation and survival. Br J Haematol. 2012;156(3):334-45.

538. Sykes SM, Lane SW, Bullinger L, Kalaitzidis D, Yusuf R, Saez B, et al. AKT/FOXO signaling enforces reversible differentiation blockade in myeloid leukemias. Cell. 2011;146(5):697-708.
539. Naka K, Hoshii T, Muraguchi T, Tadokoro Y, Ooshio T, Kondo Y, et al. TGF-beta-FOXO signalling maintains leukaemia-initiating cells in chronic myeloid leukaemia. Nature. 2010;463(7281):676-80.
540. Mlynarczyk C, Fontán L, Melnick A. Germinal center-derived lymphomas: The darkest side of humoral immunity. Immunol Rev. 2019;288(1):214-39.
541. Zhou P, Blain AE, Newman AM, Zaka M, Chagaluka G, Adlar FR, et al. Sporadic and endemic Burkitt lymphoma have frequent. Blood Adv. 2019;3(14):2118-27.
542. Chen CC, Jeon SM, Bhaskar PT, Nogueira V, Sundararajan D, Tonic I, et al. FoxOs inhibit mTORC1 and activate Akt by inducing the expression of Sestrin3 and Rictor. Dev Cell. 2010;18(4):592-604.
543. Lin A, Piao HL, Zhuang L, Sarbassov dos D, Ma L, Gan B. FoxO transcription factors promote AKT Ser473 phosphorylation and renal tumor growth in response to pharmacologic inhibition of the PI3K-AKT pathway. Cancer Res. 2014;74(6):1682-93.
544. Sengupta A, Molkentin JD, Yutzey KE. FoxO transcription factors promote autophagy in cardiomyocytes. J Biol Chem. 2009;284(41):28319-31.
545. Nagashima T, Shigematsu N, Maruki R, Urano Y, Tanaka H, Shimaya A, et al. Discovery of novel forkhead box O1 inhibitors for treating type 2 diabetes: improvement of fasting glycemia in diabetic db/db mice. Mol Pharmacol. 2010;78(5):961-70.
546. Diep CH, Charles NJ, Gilks CB, Kalloger SE, Argenta PA, Lange CA. Progesterone receptors induce FOXO1-dependent senescence in ovarian cancer cells. Cell Cycle. 2013;12(9):1433-49.
547. Yu F, Wei R, Yang J, Liu J, Yang K, Wang H, et al. FoxO1 inhibition promotes differentiation of human embryonic stem cells into insulin producing cells. Exp Cell Res. 2018;362(1):227-34.
548. Zou P, Liu L, Zheng L, Liu L, Stoneman RE, Cho A, et al. Targeting FoxO1 with AS1842856 suppresses adipogenesis. Cell Cycle. 2014;13(23):3759-67.
549. Tothova Z, Kollipara R, Huntly BJ, Lee BH, Castrillon DH, Cullen DE, et al. FoxOs are critical mediators of hematopoietic stem cell resistance to physiologic oxidative stress. Cell. 2007;128(2):325-39.
550. Migliazza A, Bosch F, Komatsu H, Cayanis E, Martinotti S, Toniato E, et al. Nucleotide sequence, transcription map, and mutation analysis of the 13q14 chromosomal region deleted in B-cell chronic lymphocytic leukemia. Blood. 2001;97(7):2098-104.
551. Ouillette P, Erba H, Kujawski L, Kaminski M, Shedden K, Malek SN. Integrated genomic profiling of chronic lymphocytic leukemia identifies subtypes of deletion 13q14. Cancer Res. 2008;68(4):1012-21.
552. Parker H, Rose-Zerilli MJ, Parker A, Chaplin T, Wade R, Gardiner A, et al. 13q deletion anatomy and disease progression in patients with chronic lymphocytic leukemia. Leukemia. 2011;25(3):489-97.
553. Ouillette P, Collins R, Shakhan S, Li J, Li C, Shedden K, et al. The prognostic significance of various 13q14 deletions in chronic lymphocytic leukemia. Clin Cancer Res. 2011;17(21):6778-90.
554. Ouillette P, Collins R, Shakhan S, Li J, Peres E, Kujawski L, et al. Acquired genomic copy number aberrations and survival in chronic lymphocytic leukemia. Blood. 2011;118(11):3051-61.

555. Go H, Jang JY, Kim PJ, Kim YG, Nam SJ, Paik JH, et al. MicroRNA-21 plays an oncogenic role by targeting FOXO1 and activating the PI3K/AKT pathway in diffuse large B-cell lymphoma. Oncotarget. 2015;6(17):15035-49.
556. Calin GA, Ferracin M, Cimmino A, Di Leva G, Shimizu M, Wojcik SE, et al. A MicroRNA signature associated with prognosis and progression in chronic lymphocytic leukemia. N Engl J Med. 2005;353(17):1793-801.
557. Santanam U, Zanesi N, Efanov A, Costinean S, Palamarchuk A, Hagan JP, et al. Chronic lymphocytic leukemia modeled in mouse by targeted miR-29 expression. Proc Natl Acad Sci U S A. 2010;107(27):12210-5.
558. Guérit D, Brondello JM, Chuchana P, Philipot D, Toupet K, Bony C, et al. FOXO3A regulation by miRNA-29a Controls chondrogenic differentiation of mesenchymal stem cells and cartilage formation. Stem Cells Dev. 2014;23(11):1195-205.
559. Calin GA, Liu CG, Sevignani C, Ferracin M, Felli N, Dumitru CD, et al. MicroRNA profiling reveals distinct signatures in B cell chronic lymphocytic leukemias. Proc Natl Acad Sci U S A. 2004;101(32):11755-60.
560. Bomben R, Gobessi S, Dal Bo M, Volinia S, Marconi D, Tissino E, et al. The miR-17~92 family regulates the response to Toll-like receptor 9 triggering of CLL cells with unmutated IGHV genes. Leukemia. 2012;26(7):1584-93.
561. Wang Y, Hu C, Cheng J, Chen B, Ke Q, Lv Z, et al. MicroRNA-145 suppresses hepatocellular carcinoma by targeting IRS1 and its downstream Akt signaling. Biochem Biophys Res Commun. 2014;446(4):1255-60.
562. Guièze R, Wu CJ. Genomic and epigenomic heterogeneity in chronic lymphocytic leukemia. Blood. 2015;126(4):445-53.
563. Xanthopoulos C, Kostareli E. Advances in Epigenetics and Epigenomics in Chronic Lymphocytic Leukemia. Current Genetic Medicine Reports. 2019;7(4):214-26.
564. Rasul E, Salamon D, Nagy N, Leveau B, Banati F, Szenthe K, et al. The MEC1 and MEC2 lines represent two CLL subclones in different stages of progression towards prolymphocytic leukemia. PLoS One. 2014;9(8):e106008.
565. Shore AM, White PC, Hui RC, Essafi A, Lam EW, Rowe M, et al. Epstein-Barr virus represses the FoxO1 transcription factor through latent membrane protein 1 and latent membrane protein 2A. J Virol. 2006;80(22):11191-9.
566. Dave SS, Fu K, Wright GW, Lam LT, Kluin P, Boerma EJ, et al. Molecular diagnosis of Burkitt's lymphoma. N Engl J Med. 2006;354(23):2431-42.
567. Uchida J, Yasui T, Takaoka-Shichijo Y, Muraoka M, Kulwichit W, Raab-Traub N, et al. Mimicry of CD40 signals by Epstein-Barr virus LMP1 in B lymphocyte responses. Science. 1999;286(5438):300-3.
568. Zhao B, Zou J, Wang H, Johannsen E, Peng CW, Quackenbush J, et al. Epstein-Barr virus exploits intrinsic B-lymphocyte transcription programs to achieve immortal cell growth. Proc Natl Acad Sci U S A. 2011;108(36):14902-7.
569. Neufeld TP. Autophagy and cell growth--the yin and yang of nutrient responses. J Cell Sci. 2012;125(Pt 10):2359-68.
570. Cheng Z. The FoxO-Autophagy Axis in Health and Disease. Trends Endocrinol Metab. 2019;30(9):658-71.
571. Fierce Biotech. AZ drops midstage cancer drug vistusertib 2018 [Available from: https://www.fiercebiotech.com/biotech/az-drops-mid-stage-cancer-drug-vistusertib.
572. Sakre N, Wildey G, Behtaj M, Kresak A, Yang M, Fu P, et al. RICTOR amplification identifies a subgroup in small cell lung cancer and predicts response to drugs targeting mTOR. Oncotarget. 2017;8(4):5992-6002.

573. Powles T, Wheater M, Din O, Geldart T, Boleti E, Stockdale A, et al. A Randomised Phase 2 Study of AZD2014 Versus Everolimus in Patients with VEGF-Refractory Metastatic Clear Cell Renal Cancer. Eur Urol. 2016;69(3):450-6.
574. Brugger W, Hattersley M, Bussey A, Reimer C, Tron AE, Staniszewska A, et al. Combined Inhibition of mTOR and BTK Signaling Is Required for Optimal Long Term Growth Inhibition in DLBCL Models. Blood. 2017;130(Supplement 1):4113-.
575. Awan FT, Gore L, Gao L, Sharma J, Lager J, Costa LJ. Phase Ib trial of the PI3K/mTOR inhibitor voxtalisib (SAR245409) in combination with chemoimmunotherapy in patients with relapsed or refractory B-cell malignancies. Br J Haematol. 2016;175(1):55-65.
576. Kater AP, Brown JR. Ibrutinib: searching for a partner drug. Lancet Oncol. 2019;20(1):3-5.
577. Cervantes-Gomez F, Lamothe B, Woyach JA, Wierda WG, Keating MJ, Balakrishnan K, et al. Pharmacological and Protein Profiling Suggests Venetoclax (ABT-199) as Optimal Partner with Ibrutinib in Chronic Lymphocytic Leukemia. Clin Cancer Res. 2015;21(16):3705-15.
578. Choudhary GS, Al-harbi S, Mazumder S, Hill BT, Smith MR, Bodo J, et al. MCL-1 and BCL-xL-dependent resistance to the BCL-2 inhibitor ABT-199 can be overcome by preventing PI3K/AKT/mTOR activation in lymphoid malignancies. Cell Death and Disease. 2015;6(1):e1593-e.
579. Tarantelli C, Gaudio E, Hillmann P, Spriano F, Sartori G, Aresu L, et al. The Novel TORC1/2 Kinase Inhibitor PQR620 Has Anti-Tumor Activity in Lymphomas as a Single Agent and in Combination with Venetoclax. Cancers (Basel). 2019;11(6).
580. Lee JS, Tang SS, Ortiz V, Vo TT, Fruman DA. MCL-1-independent mechanisms of synergy between dual PI3K/mTOR and BCL-2 inhibition in diffuse large B cell lymphoma. Oncotarget. 2015;6(34):35202-17.
581. Chen L, Xu B, Liu L, Liu C, Luo Y, Chen X, et al. Both mTORC1 and mTORC2 are involved in the regulation of cell adhesion. Oncotarget. 2015;6(9):7136-50.
582. Jacinto E, Loewith R, Schmidt A, Lin S, Rüegg MA, Hall A, et al. Mammalian TOR complex 2 controls the actin cytoskeleton and is rapamycin insensitive. Nat Cell Biol. 2004;6(11):1122-8.
583. Liu L, Chen L, Chung J, Huang S. Rapamycin inhibits F-actin reorganization and phosphorylation of focal adhesion proteins. Oncogene. 2008;27(37):4998-5010.
584. Liu L, Luo Y, Chen L, Shen T, Xu B, Chen W, et al. Rapamycin inhibits cytoskeleton reorganization and cell motility by suppressing RhoA expression and activity. J Biol Chem. 2010;285(49):38362-73.
585. Ventura A, Kirsch DG, McLaughlin ME, Tuveson DA, Grimm J, Lintault L, et al. Restoration of p53 function leads to tumour regression in vivo. Nature. 2007;445(7128):661-5.
586. Carra G, Taulli R, Morotti A. Tumor suppressors revival in CLL. Aging (Albany NY). 2017;9(6):1473-4.
587. Andreani G, Carrà G, Lingua MF, Maffeo B, Brancaccio M, Taulli R, et al. Tumor Suppressors in Chronic Lymphocytic Leukemia: From Lost Partners to Active Targets. Cancers (Basel). 2020;12(3).
588. Berger AH, Knudson AG, Pandolfi PP. A continuum model for tumour suppression. Nature. 2011;476(7359):163-9.
589. van der Horst A, de Vries-Smits AM, Brenkman AB, van Triest MH, van den Broek N, Colland F, et al. FOXO4 transcriptional activity is regulated by monoubiquitination and USP7/HAUSP. Nat Cell Biol. 2006;8(10):1064-73.

590. Pauls SD, Marshall AJ. Regulation of immune cell signaling by SHIP1: A phosphatase, scaffold protein, and potential therapeutic target. Eur J Immunol. 2017;47(6):932-45.
591. Lemm EA, Valle-Argos B, Smith LD, Richter J, Gebreselassie Y, Carter MJ, et al. Preclinical Evaluation of a Novel SHIP1 Phosphatase Activator for Inhibition of PI3K Signaling in Malignant B Cells. Clin Cancer Res. 2020;26(7):1700-11.
592. Ecker V, Braun M, Neumayer T, Muschen M, Ruland J, Buchner M. SHIP1 Inhibition As Novel Therapeutic Approach in Chronic Lymphocytic Leukemia. Blood. 2018;132(Supplement 1):894-.
593. Crassini K, Stevenson WS, Mulligan SP, Best OG. The MEK1/2 inhibitor, MEKi-1, induces cell death in chronic lymphocytic leukemia cells under conditions that mimic the tumor microenvironment and is synergistic with fludarabine. Leuk Lymphoma. 2015;56(12):3407-17.
594. Crassini K, Shen Y, Stevenson WS, Christopherson R, Ward C, Mulligan SP, et al. MEK1/2 inhibition by binimetinib is effective as a single agent and potentiates the actions of Venetoclax and ABT-737 under conditions that mimic the chronic lymphocytic leukaemia (CLL) tumour microenvironment. Br J Haematol. 2018;182(3):360-72.
595. Hahntow IN, Schneller F, Oelsner M, Weick K, Ringshausen I, Fend F, et al. Cyclin-dependent kinase inhibitor Roscovitine induces apoptosis in chronic lymphocytic leukemia cells. Leukemia. 2004;18(4):747-55.
596. Cosimo E, McCaig AM, Carter-Brzezinski LJ, Wheadon H, Leach MT, Le Ster K, et al. Inhibition of NF-κB-mediated signaling by the cyclin-dependent kinase inhibitor CR8 overcomes prosurvival stimuli to induce apoptosis in chronic lymphocytic leukemia cells. Clin Cancer Res. 2013;19(9):2393-405.
597. Wierda WG, Lee ST, Chen R, Zheleva D, Blake D, Chiao JH, et al. A Phase I Study Combining CDK2/9 Inhibitor CYC065 with Venetoclax, a BCL2 Inhibitor, to Treat Relapsed or Refractory Chronic Lymphocytic Leukemia (CLL). Blood. 2019;134(Supplement_1):1761-.
598. Janovska P, Verner J, Kohoutek J, Bryjova L, Gregorova M, Dzimkova M, et al. Casein Kinase 1 is a Therapeutic Target in Chronic Lymphocytic Leukemia. Blood. 2018;131(11):blood-2017-05-786947.
599. Parikh K, Cang S, Sekhri A, Liu D. Selective inhibitors of nuclear export (SINE)--a novel class of anti-cancer agents. J Hematol Oncol. 2014;7:78.
600. Yao Y, Dong Y, Lin F, Zhao H, Shen Z, Chen P, et al. The expression of CRM1 is associated with prognosis in human osteosarcoma. Oncol Rep. 2009;21(1):229-35.
601. Turner JG, Dawson J, Sullivan DM. Nuclear export of proteins and drug resistance in cancer. Biochem Pharmacol. 2012;83(8):1021-32.
602. Shen A, Wang Y, Zhao Y, Zou L, Sun L, Cheng C. Expression of CRM1 in human gliomas and its significance in p27 expression and clinical prognosis. Neurosurgery. 2009;65(1):153-9; discussion 9-60.
603. Camus V, Miloudi H, Taly A, Sola B, Jardin F. XPO1 in B cell hematological malignancies: from recurrent somatic mutations to targeted therapy. Journal of Hematology & Oncology. 2017;10(1):47-.
604. Lapalombella R, Sun Q, Williams K, Tangeman L, Jha S, Zhong Y, et al. Selective inhibitors of nuclear export show that CRM1/XPO1 is a target in chronic lymphocytic leukemia. Blood. 2012;120(23):4621-34.
605. Puente XS, Pinyol M, Quesada V, Conde L, Ordóñez GR, Villamor N, et al. Whole-genome sequencing identifies recurrent mutations in chronic lymphocytic leukaemia. Nature. 2011;475(7354):101-5.

606. Cosson A, Chapiro E, Bougacha N, Lambert J, Herbi L, Cung HA, et al. Gain in the short arm of chromosome 2 (2p+) induces gene overexpression and drug resistance in chronic lymphocytic leukemia: analysis of the central role of XPO1. Leukemia. 2017;31(7):1625-9.
607. Wang AY, Liu H. The past, present, and future of CRM1/XPO1 inhibitors. Stem Cell Investig. 2019;6:6.
608. Corno C, Stucchi S, De Cesare M, Carenini N, Stamatakos S, Ciusani E, et al. FoxO-1 contributes to the efficacy of the combination of the XPO1 inhibitor selinexor and cisplatin in ovarian carcinoma preclinical models. Biochem Pharmacol. 2018;147:93-103.
609. Hing ZA, Mantel R, Beckwith KA, Guinn D, Williams E, Smith LL, et al. Selinexor is effective in acquired resistance to ibrutinib and synergizes with ibrutinib in chronic lymphocytic leukemia. Blood. 2015;125(20):3128-32.
610. clinicaltrials.gov. Selinexor and Ibrutinib in Treating Patients With Relapsed or Refractory Chronic Lymphocytic Leukemia or Aggressive Non-Hodgkin Lymphoma 2020 [Available from: https://clinicaltrials.gov/ct2/show/study/NCT02303392.
611. Lymphoma Hub. The FDA halts clinical trials of selinexor in CLL and DLBCL 2017 [Available from: https://lymphomahub.com/medical-information/the-fda-halts-clinical-trials-of-selinexor-in-cll-and-dlbcl.
612. Cohen JA, Bomben R, Pozzo F, Tissino E, Härzschel A, Hartmann TN, et al. An Updated Perspective on Current Prognostic and Predictive Biomarkers in Chronic Lymphocytic Leukemia in the Context of Chemoimmunotherapy and Novel Targeted Therapy. Cancers (Basel). 2020;12(4).
613. Hagenbuchner J, Rupp M, Salvador C, Meister B, Kiechl-Kohlendorfer U, Müller T, et al. Nuclear FOXO3 predicts adverse clinical outcome and promotes tumor angiogenesis in neuroblastoma. Oncotarget. 2016;7(47):77591-606.
614. Wu Y, Elshimali Y, Sarkissyan M, Mohamed H, Clayton S, Vadgama JV. Expression of FOXO1 is associated with GATA3 and Annexin-1 and predicts disease-free survival in breast cancer. Am J Cancer Res. 2012;2(1):104-15.
615. Zhang H, Pan Y, Zheng L, Choe C, Lindgren B, Jensen ED, et al. FOXO1 inhibits Runx2 transcriptional activity and prostate cancer cell migration and invasion. Cancer Res. 2011;71(9):3257-67.
616. Bullock MD, Bruce A, Sreekumar R, Curtis N, Cheung T, Reading I, et al. FOXO3 expression during colorectal cancer progression: biomarker potential reflects a tumour suppressor role. Br J Cancer. 2013;109(2):387-94.
617. Kim HJ, Lee SY, Kim CY, Kim YH, Ju W, Kim SC. Subcellular localization of FOXO3a as a potential biomarker of response to combined treatment with inhibitors of PI3K and autophagy in PIK3CA-mutant cancer cells. Oncotarget. 2017;8(4):6608-22.